Second Microgravity Fluid Physics Conference

Proceedings of a conference hosted
by NASA Lewis Research Center
Cleveland, Ohio
June 21–23, 1994

Second Microgravity Fluid Physics Conference

TABLE OF CONTENTS

Drops and Bubbles

Solidification

Phase Transitions

Multiphase Flow/Heat Transfer

Complex Fluids

Biological Colloids & Electrohydrodynamics

Physicochemical Systems

Microgravity Fluids Program Information

PREFACE AND ACKNOWLEDGEMENTS

The Second Microgravity Fluid Physics Conference was held in Cleveland, Ohio, on June 21 to 23, 1994. It was attended by 326 people from academia, industry, and government, representing nine countries. The conference's purpose was to inform the fluid physics community of research opportunities in reduced-gravity fluid physics, present the status of the existing and planned reduced gravity fluid physics research programs, and inform participants of the upcoming NASA Research Announcement in this area.

The plenary sessions provided an overview of the Microgravity Fluid Physics Program, present and future areas of emphasis, information on NASA's ground-based and space-based flight research facilities, and the process by which future investigators enter the program. An international forum offered participants an opportunity to hear from speakers about the microgravity research programs in their respective countries. Keynote speakers provided broad technical overviews on multiphase flow and complex fluids research. An interactive discussion session, with the Fluid Dynamics Discipline Working Group serving as the panel, answered questions from the audience. Selected plenary presentations of general interest are included in the proceedings.

Sixty-two technical papers were presented in 21 sessions. Presenters briefed their peers on the scientific results of their ground-based and flight research. Fifty-eight of the papers are included here. Titles and authors on four papers that were not available are listed for completeness. Papers are grouped by subdisciplines rather than sessions in which they were presented. However, the conference agenda and an author index are included to facilitate the reader in locating papers.

Sincere appreciation is offered to the authors for providing the papers in a timely manner and to the members of the Microgravity Fluids Physics Branch of NASA Lewis Research Center for their many contributions. Assistance from the Logistics and Technical Information Division personnel at NASA Lewis Research Center in publishing this proceedings volume is gratefully acknowledged.

Dr. Bhim S. Singh, Conference Organizer
Mail Stop 500-102
NASA Research Center
21000 Brookpark Road
Cleveland, OH 44135
Phone (216) 433-5396 or fax (216) 433-8660
E-mail: BSINGH@LIMS01,LERC.NASA.GOV

Keynote

Future Directions in Two-Phase Flow and Heat Transfer in Space

12p

S. George Bankoff
Chemical Engineering Department
Northwestern University
Evanston, IL 60208

ABSTRACT

Some areas of opportunity for future research in microgravity two-phase flow and heat transfer are pointed out. These satisfy the dual requirements of relevance to current and future needs, and scientific/engineering interest.

INTRODUCTION

Two-phase flow (or more broadly, multiphase flow) covers an extremely wide variety of fluid physics. To narrow the scope, only flows where one or more free interfaces exist, since these interfaces are generally sensitive to the presence or absence of gravity. These include liquid-gas, liquid-vacuum (or passive gas), and liquid-liquid combinations. Further, particular attention is paid to processes involved in space power systems, since power generation systems and chemical processing are the traditional preserves of two-phase flow and heat transfer. Also, studies of this nature focus on a particular need for space-based research. Finally, the underlying phenomena are poorly understood, even on the ground, and particularly so in space.

WHERE IS THE LIQUID?

A basic problem with partially-filled containers in space is the uncertainty as to just where the liquid is. As a result of the accelerations experienced during and after launch, globs of liquid may be floating about, coalescing with each other and with the wall layers. Furthermore, if g-jitter has significant energy in resonant, or subharmonic resonant, frequencies, large surface disturbances can be induced [1]. Finally, a well-wetting liquid (positive spreading coefficient), will simply creep out of an open container, or distribute itself over all exposed surfaces in a closed container. The reverse is true if wetting is very poor, as with mercury on stainless steel. This has serious implications for the reliability of thermocouples, conductivity probes and hot-film anemometers. It may be possible to control the motion of the contact line by heating or cooling the dry surface ahead of it [2,3], owing to thermocapillary (Marangoni) effects.

BOILING

Boiling is normally an efficient heat transfer process, but saturated pool boiling becomes unstable at moderate heat fluxes in space. Bubble departure from the heating

surface is no longer assisted by buoyancy. As an example, n-pentane subcooled by 7 K gives a nucleate boiling flux of only 0.4 w/cm^2, but extrapolated towards saturated conditions, gives almost immediate film boiling (Fig. 10 of [4]. Subcooled pool boiling is more efficient, since the bubbles grow into the subcooled region and partially condense. Hence a steady heat flux can be sustained, provided that the subcooling can be maintained by external means. On the other hand, forced-convection boiling has minimum reliance on gravity to remove bubbles from the walls. Highly-subcooled forced-convection nucleate boiling is one of the most effective heat transfer processes known [5]. The critical heat flux in nucleate boiling, which represents local transition to film boiling, and hence is a key thermal design parameter, is poorly understood, even on earth.

CONDENSATION

Condensation runs into similar difficulties, in that gravity is no longer available to drain the condensate away. Furthermore, surface shear exerted by flowing vapor in the absence of gravity is not as effective, since the vapor velocity decreases as condensation proceeds. The ratio of the tube lengths for complete condensation of ammonia vapor has been calculated to be 1.5 for an 8 mm diameter tube in space vs. earth, and 30 for a 25 mm diameter tube [6]. It is, of course, always possible to add a non-condensible gas, such as air, to prevent complete condensation. However, it is well-known that even small quantities of air reduce the condensation heat transfer coefficients markedly. Capillary action, such as exerted by wicks and grooves in heat pipes, is used in space, but is limited in capacity, and can lead to low power-weight ratios in space radiators. An alternative, which does not seem to have been explored, is the use of rotating condensers, particularly for large space power applications.

GAS-LIQUID FLOWS

Cocurrent and countercurrent gas-liquid flows appear in many contexts on earth. Many flow regimes have been identified, depending on the orientation of the pipe and the flow directions of the two phases. However, in space countercurrent flow does not exist, and pipe orientation is immaterial. The situation is therefore much simpler, resolving down to three principal flow regimes: bubbly, slug and annular. Since the principal mechanisms for transport of heat and momentum are quite different for each flow regime, much more needs to be learned about the stability requirements for each regime, as well as for other regimes not yet identified.

BUBBLY FLOW

In a vertical pipe on earth, large bubbles rise more rapidly than small bubbles. Hence a large bubble acts as a "vacuum cleaner", coalescing with smaller bubbles above it, and eventually growing to be of the same order in diameter as the pipe. This does not happen at 0 g. The key distinction is that at 0 g the local relative velocity of gas and liquid, averaged over a local cell, is nearly zero, while at 1 g it is of the order of the rise velocity of a typical bubble in stagnant liquid. Hence, coalescence of neighboring bubbles is much less frequent in space, whereas breakup due to strong shear (large Reynolds numbers, pumps, expansions, etc.) continues as the mixture circulates through a closed loop. Hence one expects a nearly-uniform dispersion of fine bubbles after some time, with mean density and velocity which vary radially owing to wall shear effects. This is a considerable simplification, which may allow a simple treatment for pressure drop and void fraction calculations [7]. This is

4

equivalent to the drift flux model [8], with the local relative velocity set equal to zero. For more detailed calculations, recourse must be had to the ensemble-averaged momentum and mass transport equations [9,10]. These have been quite successful, with suitable models for the drag, lift and turbulent Reynolds stresses, in fitting extensive experimental data taken on earth. These models, however, take as their velocity scale the local average relative velocity, which goes nearly to zero at 0 g. Furthermore, the wettability of the wall is a powerful influence in space, determining the nature of the wall layer. More work is therefore needed.

SLUG FLOW

As the gas content is increased, long gas slugs separated by liquid slugs appear. The liquid slugs are more stable in the absence of buoyancy effects, and hence of rise velocity of the gas into the liquid. In the central portion of the gas slugs there will be a nearly-stationary liquid wall film, again provided that the wall is well-wetted. If the wall is poorly wetted, as with mercury-nitrogen flow [11], asymmetric gas slugs hugging the wall appear. In microgravity these slugs may be stationary. Hence, with either good and poor wetting, boiling can result in burnout even before the annular flow regime is reached. The stability to rupture of the wall film and its wetting tendency are thus important in determining the critical heat flux (CHF).

ANNULAR FLOW

In isothermal laminar gas-liquid flow with well-wetted walls, the wall film is unstable by a linear analysis [12,13]. This is probably also true for turbulent-turbulent flow. Because the restoring force is weak, droplets detach from the free interface and redeposit on the wall film. If, in addition, the wall film is evaporating, it eventually becomes unstable and ruptures. It can break down into rivulets, which can still provide effective cooling [14,15]. Further theoretical and experimental study of the necessary conditions is needed. With turbulent shear, as with nitrogen-Freon cocurrent flow [16], a transient dryout-rewetting zone may be expected prior to the development of rivulets. Wall wettability is again important.

THIN LIQUID FILMS

As noted above, these appear naturally on well-wetted walls in slug and annular flow. These films give excellent heat and mass transfer, but their rupture and dryout can lead to equipment overheating. Very thin films separate bubbles formed in forced-convection subcooled nucleate boiling from the wall. This causes the bubbles, growing and collapsing while attached to the heated wall, to act as miniature heat pipes. This is responsible, at least in part, for the very high heat fluxes observed on earth, as in cooling the throat section of rocket motors [17]. These films also appear in many other contexts, such as in manufacturing processes and biological functions. Because of their thinness, they are amenable to detailed computation and experimental analysis, with minimum reliance on empirical modeling [18]. Fig. 1 shows the computed unsteady film profile, based on a nonlinear evolution equation, for a thin heated film on a horizontal surface, taking into account van der Waals, surface tension, vapor recoil and mass loss effects [14]. The initial sinusoidal perturbation slowly deforms, but downwards fingering becomes important when the vapor recoil and van der Waals effects become important. The calculation seems to indicate film rupture, but surface wetting has not been taken into account. The final stages of rupture, consisting of the formation and spreading of a dry spot, have not yet been analyzed.

Fig. 2 shows a three-dimensional calculation for a falling film, with initially a two-

dimensional surface wave in the direction of flow down a heated wall. Marangoni effects enhance the transfer of energy from the streamwise wave to a cross-stream wave. This eventually results in longitudinal rolls, which further deepen into pre-rivulets [19].

ELECTROSTATIC LIQUID FILM RADIATOR

Electrohydrodynamic forces, which are generally weak compared to gravity on earth, can be significant in space. In keeping with the general theme of basic studies related to space power systems, a novel lightweight space radiator concept is discussed here. This is based on the fact that an electric field, regardless of its sign, always pulls a conductive liquid into a non-conductive region. This effect can be used to stop a leak of a thin liquid-metal film through a puncture of the radiator wall caused by micrometeorite impact [20-23]. A very thin membrane is used for the body of a closed hollow radiator with internal localized electric fields, switched on as necessary when a leak is detected. Such leaks will be quite infrequent, since nearly all micrometeorites are smaller than a few microns in diameter. Punctures of this size will be sealed by capillary effects, since the internal pressure is the vapor pressure of the liquid metal film flowing along the wall of the radiator (0.3 dynes/cm^2 for lithium at 700 K). This is not possible with heat pipes, which have a substantial internal pressure. There is thus a potential weight advantage of about 2 or 3 to one for this type of radiator compared to heat-pipe radiators. The electrostatic radiator may consist of stationary cylinders or rotating disks, with view factors greater than 0.8. Fig. 3 shows a stability calculation for a lithium liquid film, immediately after switching on the electrostatic film after detection of a surface leak. It is seen that a surface wave is immediately induced, but this has a maximum amplitude of about 0.15 mm, and then gets washed downstream. Hence there is no danger of shorting out the electrode, which is situated 1-2 cm. away from the film. The pressure depression is sufficient to stop the leak with a safety factor of about two. However, the stability of the entrance walljet and collection of the exiting liquid film in space need further study.

COMPUTATION

Advanced codes for efficient representation of large surface deformations on short time scales with heat and mass transfer are needed. In view of the enormous costs of experimentation in space, computations on earth have the potential for considerable cost savings. Work along these lines have been progressing in a number of locations. The Los Alamos code, RIPPLE [24], as an example, models surface as a volume force derived from a continuum surface force model. Free surface elements are represented by volume-of-fluid data. Another promising code is a general multidimensional hyperbolic equation solver [25,26], which uses a cubic polynomial interpolation scheme, with the gradient of the quantity as a free parameter, in a stable explicit scheme. This has produced good resolution for shock wave interaction with a liquid drop, and for laser-induced evaporation dynamics.

THERMOCAPILLARY EFFECTS

A number of papers in this conference deal with thermocapillary effects. These can dominate in the absence of gravity. As the Marangoni number, as well as other parameters, is increased, thermocapillary flows can become 3-D, time-dependent and eventually chaotic. G-jitter effects can additionally be superimposed. An evaporating drop can build up a surface temperature gradient until a critical Marangoni number is reached, leading to internal mixing. On the other hand, thermocapillary convection in fluid layers may be stabilized by nonplanar

6

flow oscillations or possibly by laser pulsing. Similarly, removal of entrapped bubbles from melts can be induced by imposing a mean temperature gradient on the liquid. The bubbles tend to "swim" towards the higher temperature.

CONCLUSIONS

A number of areas of opportunity for research related to two-phase flow and heat transfer in the presence of free interfaces have been pointed out. Ground-based analysis, experimentation and computation should be emphasized, in view of the high cost of space experiments. New phenomena result in the absence of gravity, and old ones can become much less important. There is considerable room for imaginative work.

REFERENCES
[1]   J. Casademunt, W. Zhang, J. Vinals and R. F. Sekerka, Stability of a Fluid Surface in a Microgravity Environment, AIAA Journal, 31 (1993) 2027.
[2]   P. Ehrhard and S. H. Davis, Non-Isothermal Spreading of Liquid Drops on Horizontal Plates, J. Fluid Mech. 229 (1991) 365.
[3]   D. M. Anderson and S. H. Davis, The Spreading of Volatile Liquid Droplets on Heated Surfaces, Physics of Fluids, (1994), pending publication.
[4]   T. Oka, Y. Abe, K. Tanaka, Y. Mori and A. Nagashima, Observational Study of Pool Boiling Under Microgravity, JSME International J. 35 (1992).
[5]   G. Tsung-Chang and S. G. Bankoff, On the Mechanism of Forced-Convection Subcooled Nucleate Boiling, J. Heat Transfer, 112 (1990) 213.
[6]   A. Delil, Gravity Dependence of Pressure Drop and Heat Transfer in Straight Two-Phase Heat Transport System Condenser Ducts, NLR TP 92167 U, National Aerospace Laboratory NLR, Netherlands (1992).
[7]   S. G. Bankoff, A. Variable-Density Single-Fluid Model for Two-Phase Flow with Particular Reference to Two-Phase Flow, J. Heat Transfer, 82 C (1960) 265.
[8]   N. Zuber and J. A. Findlay, Average Volumetric Concentration in Two-Phase Flow, J. Heat Transfer, 87 (1965) 453.
[9]   R. T. Lahey, Jr. and D. A. Drew, On the Development of Multidimensional Two-Fluid Models for Vapor/Liquid Two-Phase Flows, Chem. Eng. Communications, 118 (1992) 125.
[10]   I. Kataoka, D. C. Besnard, and A. Serizawa, Basic Equation of Turbulence and Modeling of Interfacial Transfer Terms in Gas-Liquid Two-Phase Flow, Chem. Eng. Communications, 118 (1992) 221.
[11]   L. G. Neal and S. G. Bankoff, A. High-Resolution Resistivity Probe for Determination of Local Void Properties in Gas-Liquid Flow, AIChE J., 9 (1963) 490.
[12]   D. Joseph and Y. Renardy, *Fundamentals of Two-Fluid Dynamics*, Springer-Verlag, N.Y. (1993).
[13]   B. S. Tilley, S. Y. Davis and S. G. Bankoff, Linear Stability Theory of Two-Layer Fluid Flow in an Inclined Channel, Physics of Fluids (1994), pending publication.
[14]   W. W. Joo, S. H. Davis and S. G. Bankoff, Long-Wave Instabilities of Heated Falling Films: Two-Dimensional Theory of Uniform Layers, J. Fluid Mech., 230 (1991) 117.
[15]   S. W. Joo, S. H. Davis and S. G. Bankoff, Instabilities in Evaporating Liquid Films, *Instabilities in Multiphase Flows*, ed. by G. Gouesbet and A. Berlemont, Plenum Press, N.Y. (1993).

[16]   J. C. Chung and S. G. Bankoff, Initial Breakdown of a Heated Liquid Film in Cocurrent Annular Flow: II. Rivulet and Drypatch Models, Chem. Eng. Communications, 4 (1980) 455.

[17]   F. C. Gunther and F. Kreith, Progress Report No. 4-120, Jet Propulsion Laboratory, California Institute of Technology, Pasadena, CA (1950).

[18]   S. W. Joo and S. H. Davis, Instabilities of Three Dimensional Viscous Falling Films, J. Fluid Mechanics, 242 (1992) 529.

[19]   S. W. Joo and S. H. Davis, Irregular Waves on Viscous Falling Films, Chem. Eng. Communications, 118 (1992) 111.

[20]   H. Kim, S. G. Bankoff and M. J. Miksis, The Effect of an Electrostatic Field on Film Flow Down an Inclined Plane, Phys. Fluids A 4(1992) 2117.

[21]   H. Kim, S. G. Bankoff and M. J. Miksis, Electrostatic Field Effects on a Rotating Liquid Film Conical Radiator, AIAA J. Propulsion and Power, 9 (1992) 245.

[22]   S. G. Bankoff, M. J. Miksis, H. Kim and R. Gwinner, Design Considerations for the Rotating Electrostatic Liquid-Film Radiator, Nuclear Eng. and Design (1994), in press.

[23]   H. Kim, S. G. Bankoff and M. J. Miksis, The Cylindrical Electrostatic Liquid Film Radiator for Heat Rejection in Space, J. Heat Transfer (1994), pending publication.

[24]   D. B.Kothe and R. C. Mjolsness, RIPPLE: A New Model for Incompressible Flows with Free Surfaces, AIAA Journal 30 (1992) 2694.

[25]   T. Yabe and T. Aoki, A. Universal Solver for Hyperbolic Equations by Cubic-Polynomial Interpolation I. One-dimensional Solver, Computer Physics Communications 66 (1991) 219.

[26]   T. Yabe, T. Ishikawa, P. Y. Yang, T. Aoki, Y. Kadota and F. Ikeda, A Universal Solver for Hyperbolic Equations by Cubic-Polynomial Interpolation II. Two- and Three-Dimensional Solvers, Comp. Phys. Comm. 66 (1991) 233.
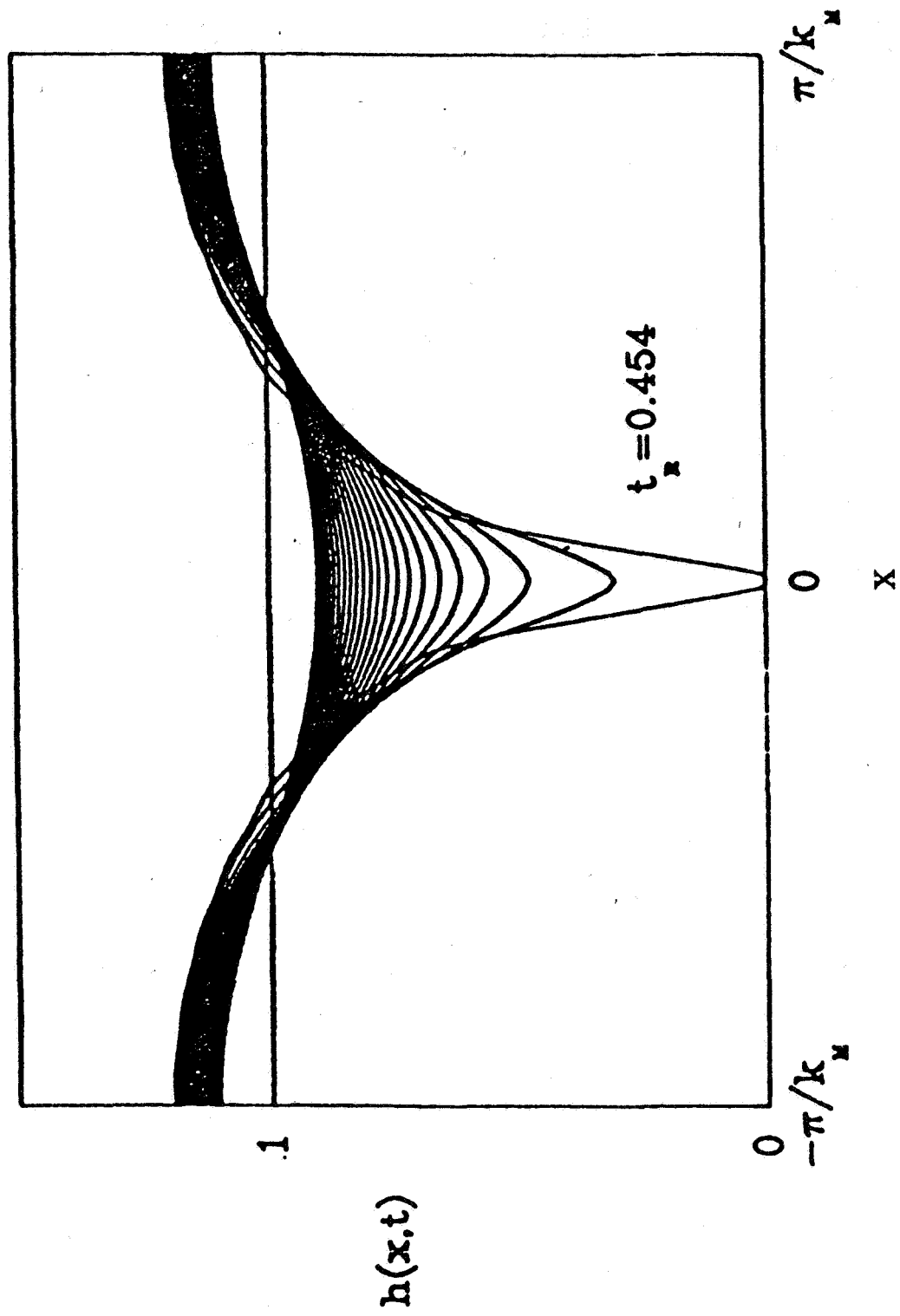
Fig. 1 Development of a Fingering-Type Instability in a Horizontal Evaporating Liquid Film with Surface Tension, Vapor Recoil, Mass Loss and van der Waals Effects
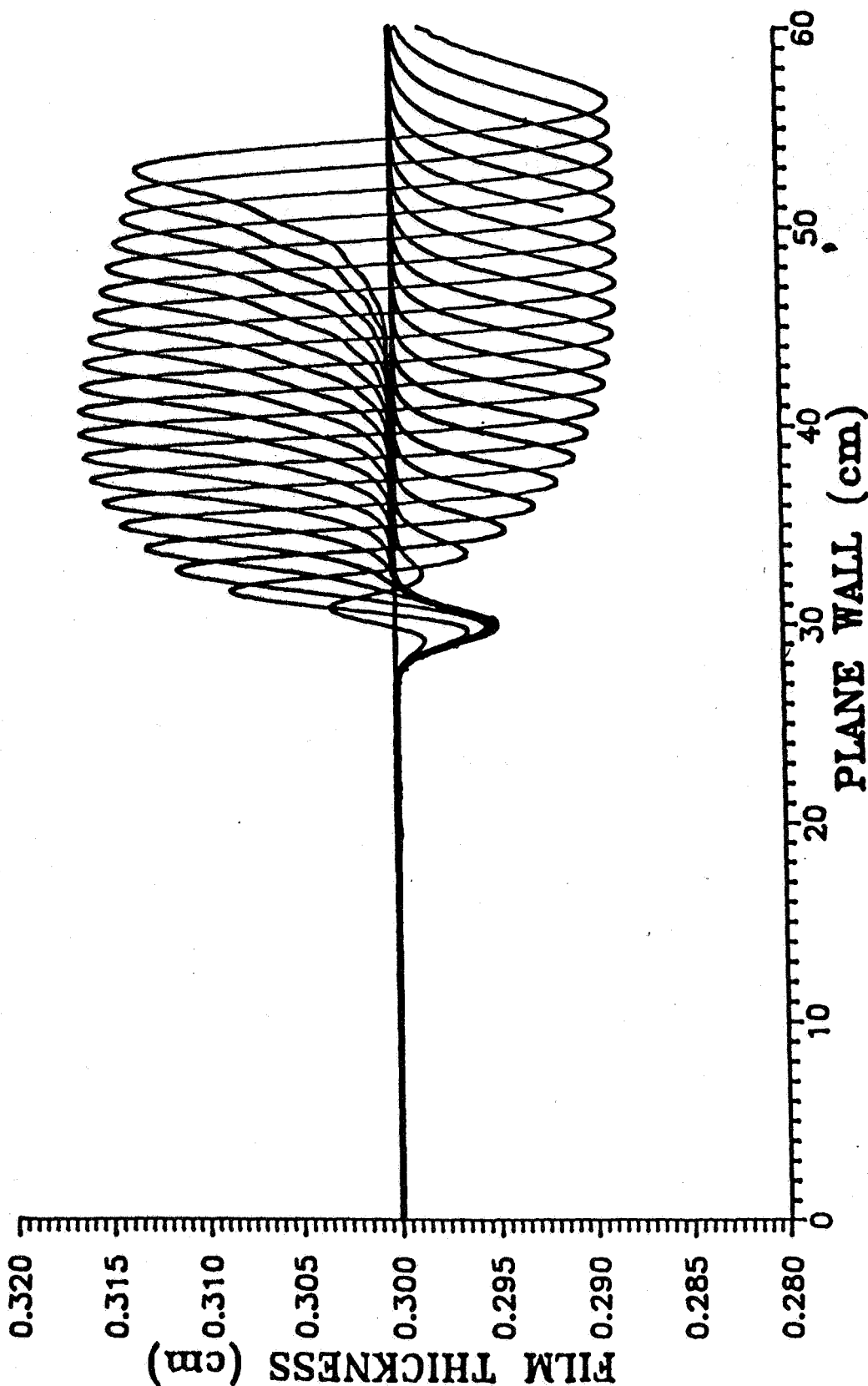
Fig. 2   Surface Wave in a Liquid Lithium Film Falling Down a Plane Wall after Switching on Electrostatic Field

(a)
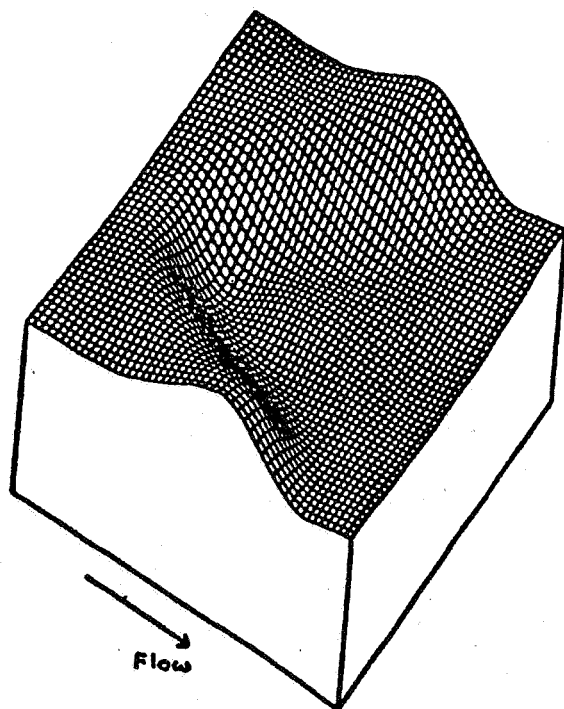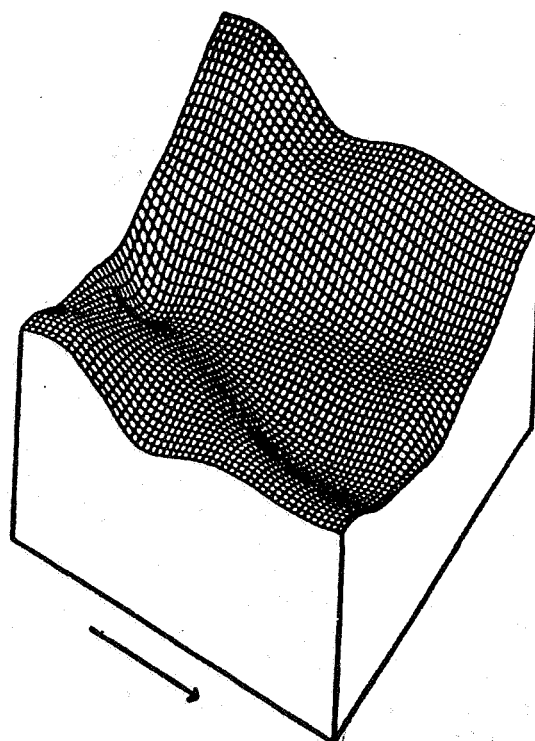
Flow

(b)

Fig. 3   Three-Dimensional Wave Growth into
Rivulet Precursors in a Heated Falling
Liquid Film, Owing to Marangoni Effect
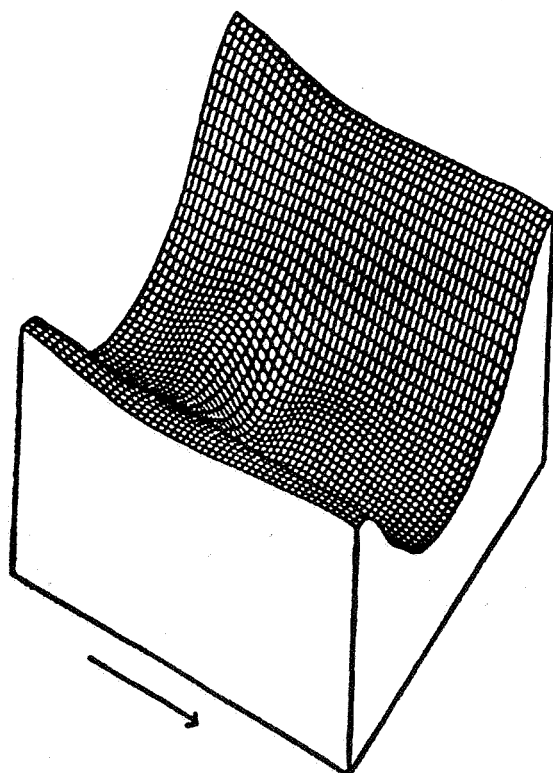
(c)
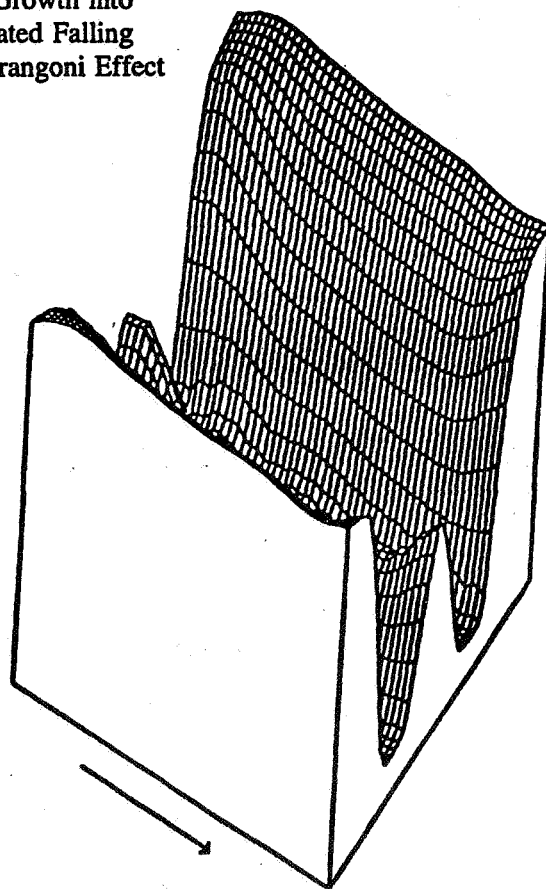
(d)

11

Thermocapillary Flows

13.

STABILIZATION OF THERMOCAPILLARY CONVECTION BY MEANS OF NONPLANAR FLOW OSCILLATIONS

R. E. Kelly
Arthur Or
Mechanical, Aerospace and Nuclear Engineering Department
University of California
Los Angeles, CA 90024-1597

ABSTRACT

Nonplanar flow oscillations have been shown to be effective in stabilizing buoyancy-induced Rayleigh-Benard convection. The present study was initiated to see if thermocapillary convection of the Marangoni type might also be stabilized by the same means. When surface deflection can be ignored, significant stabilization occurs. However, when the operating parameters are such that surface deflection is nonnegligible, destabilization can occur, in contrast to Rayleigh-Bénard convection. Mechanisms for both stabilization and destabilization are discussed.

INTRODUCTION

Thermal convection of the classical Rayleigh-Bénard type is predicted to begin in the form of convection rolls (or vortices) for the case of a Boussinesq fluid. Due to horizontal isotropy, no preferred direction occurs for the rolls and, unless a well-defined initial disturbance is imposed, the pattern of convection in a large aspect ratio container is somewhat jumbled. If a horizontal, unidirectional shear flow exists in the fluid layer that is heated, convection begins at the same value of critical Rayleigh number (Ra_c) as without shear but a well-defined pattern of rolls with axes in the flow direction (called "longitudinal rolls") is predicted to be the preferred pattern of convection and has been often observed in experiments (for a review, see ref. 1). This result means that the shear has a stabilizing effect upon all disturbances that have a nonzero wavenumber in the direction of the shear. For longitudinal rolls, the value of this wavenumber component is zero, and the stabilizing effect does not occur.

Now consider the situation when the shear flow has two horizontal components of velocity that vary in the vertical direction so that the direction of shear varies continuously with height. It is then impossible for a disturbance to orient itself so as to escape the effect of shear, and so we should expect disturbances associated with buoyancy to be stabilized, i. e. Ra_c will then increase with the Reynolds number, Re. This result should hold even when the shear is periodic in time, meaning that the effect can in principle be observed in a laboratory experiment by suitably oscillating one or both surfaces in their own planes, thereby eliminating the need for the kind of flow apparatus required for a steady flow with a net mass through-flow. Kelly and Hu (ref. 2) have made a detailed analysis of the case of oscillatory shear for small values of Re and concluded that stabilization does indeed occur, that the degree of stabilization increases with the Prandtl number (Pr), and that maximum stabilization occurs when the nondimensional forcing frequency is of order unity. They also predicted that the pattern of convection consists of rolls with axes in the direction of the dominant velocity component. In further work, Hu and Kelly (ref. 3) report results for finite values of Re which indicate that quite significant stabilization might occur, e. g. , Ra_c is increased by a factor of sixteen for $Pr = 10$ as Re increases up to a value of 100, which is probably small enough to avoid any hydrodynamic shear instability (although the critical value of Re for such an instability is difficult to predict).

It is felt that this result might be of value to certain applications in materials processing when it is desirable to avoid thermal convection in order to achieve a more uniform product. Whether or not it is of practical value depends on whether the effect can be realized in more practical configurations, such as an

oscillating disk.

Due to these encouraging results, we decided to see if similar stabilization is predicted for thermocapillary convection of the Marangoni type that occurs via an instability. Marangoni convection is generally regarded as being of importance in space applications when Rayleigh-Bénard convection is no longer dominant.

THE CASE OF MARANGONI CONVECTION

Marangoni convection (or thermocapillary convection of the Bénard type) occurs in a fluid layer with at least one free surface along which surface tension can act so as to drive convection if the surface tension varies in magnitude along the surface due to its dependence upon a spatially varying temperature associated with a thermal disturbance. The general problem of a deformable surface involves several nondimensional parameters, such as the Marangoni number (Ma), the Prandtl number (Pr), the Bond number (Bo), the Biot number (Bi), and the Crispation number (Cr) which tends to characterize the deformability of the surface. If gravity is nonnegligible, then the Rayleigh number must also be considered. Due to this complexity, a clear picture of the overall problem can be difficult to achieve, although understanding of the problem associated with a nondeformable surface has been available since the pioneering work of Pearson (ref. 4). Nonetheless, by considering various limits it is now understood that two distinct modes with different physical characteristics can participate in the instability, although each naturally involves the thermocapillary effect (e. g. , see ref. 5). For the Pearson mode, surface deformation is not essential, and the resulting convection is described by a wavelength of the same order as the layer depth. For the other mode which is associated with Scriven and Sternling (ref. 6) and Smith (ref. 7), surface deformation is essential, and the characteristic wavelength can be much greater than the layer depth. Hence, it will be referred to as the long wavelength mode in this paper, with the caveat that a clear distinction between the two modes is possible only under certain operating conditions.

We have considered the effects of a nonplanar flow oscillation upon the critical Marangoni number (Ma_c) by two approaches (ref. 8). In the first approach, the Reynolds number is assumed to be small, and an expansion is made in terms of Re, i. e.,

$$Ma_c = Ma_o + ReM_1 + Re^2 M_2 + \ldots$$

At each order of Re, the corresponding value of M_j is determined (e. g., $M_1 = 0, M_2 \neq 0$) by means of a solvability condition. For small Re, the change in Ma_c from the corresponding value without shear is small, but this approach helps us to obtain some feeling for how the result depends qualitatively on the various physical parameters. For finite values of Re, a numerical solution to the linear stability equations is obtained by means of a Fourier-Chebyshev expansion with time-dependent amplitudes. In this way, a set of coupled ordinary differential equations with time-periodic coefficients is obtained which can be analyzed by the use of Floquet theory (see ref. 8).

Some results for the case of a nondeformable surface as obtained from the small Re expansion are shown in Fig. 1. The factor M_2 is plotted versus the nondimensional frequency β. It is clear that stabilization occurs ($M_2 > 0$) with the degree of stabilization increasing with Pr. Furthermore, an optimal value of β exists that gives maximum stabilization. In Fig. 2, the effect of Biot number is shown, and it is clear that M_2 decreases as Bi increases. When the surface is allowed to be deformable, the same analysis indicates that long wavelength disturbances can be destabilized by the oscillation, as shown in Fig. 3. Stabilization occurs only for the highest wavenumber that is associated with the Pearson mode. Calculations are currently being done for the disturbance energy budget in order to gain insight into the destabilizing mechanism. It might be associated with the action of the perturbation shear stress at the deformed surface, which is the mechanism associated with the instability of steady film flow down an inclined plane (ref. 9). This conjecture is made on the basis of other results (not shown) that indicate that M_2 for this case is rather insensitive to changes in Bi and Pr. As a result, the effect of nonplanar oscillations upon the onset of Marangoni convection depends

upon which mode tends to be more unstable, which in turn depends upon the operating conditions (ref. 5). A more detailed presentation of the small Re results is forthcoming (ref. 10).

For cases when surface deformation can be ignored, Fig. 4 indicates that substantial stabilization is possible. Even for a relatively low value of $Re = 20$, an almost two-fold increase in Ma_c is possible for this high Pr case at $B_i = 0.5$. The same numerical code is currently being used to determine the maximum value of Re at which stabilization still occurs for the nondeformable case, as well as predicting the amount of destabilization possible at finite values of Re for the deformable case.

Some preliminary results for the deformable case when $Re=25$ are shown in Fig. 5, where Ma_c is shown as a function of wavenumber for two different values of β; the neutral curve for $Re = 0$ is also provided as a reference and indicates that long waves are most unstable for these operating conditions. The effect of the oscillations is shown to be strongly destabilizing, even causing instability in the normally stable regime $Ma < 0$. It should be noted that Yih (ref. 11) has shown already that instability can occur due to shear oscillations for the isothermal case ($Ma = 0$).

CONCLUSIONS

It is evident that nonplanar flow oscillations can have a significant effect upon the onset of Marangoni convection. In contrast to Rayleigh-Bénard convection, the effect can be stabilizing or destabilizing, depending upon the operating conditions. The present analysis has been done for a system that is infinite in both horizontal directions. Side boundaries must, of course, generally be considered for actual applications; these can affect the basic flow as well as stabilize the long wavelength disturbances. For the oscillating disk configuration, the effect of spatial inhomogeneity in the flow could also have a strong effect on the long wavelength disturbances.

Finally, it should be remarked that the oscillations should profoundly affect the subcritical instability characteristic of Marangoni convection, in a manner similar to that discussed in (ref. 12) for convection in a slightly non-Boussinesq fluid.

REFERENCES

1. Kelly, R. E., Adv. Appl. Mech. **30** (1994), 35-112.
2. Kelly, R. E. and Hu, H. -C., J. Fluid Mech. **249** (1993), 373-390.
3. Hu, H. C., and Kelly, R. E., Heat Transfer 1994 (Proc. 10th Int. Heat Transfer Conf.) to appear.
4. Pearson, J. R. A., J. Fluid Mech. **4** (1958), 489-500.
5. Goussis, D. A. and Kelly, R. E., Int. J. Heat Mass Transfer **33** (1990), 2237-2245.
6. Scriven, L. E. and Sternling, C. V., J. Fluid Mech. **19** (1964), 321-340.
7. Smith, K. A., J. Fluid Mech. **24** (1966), 401-414.
8. Or, A. C. and Kelly, R. E., AIAA Paper 94-0242 (1994).
9. Kelly, R. E., Goussis, D. A., Lin, S.P., and Hsu, F. K., Phys, Fluids A **1** (1989), 819-828.
10. Or, A.C. and Kelly, R.E., to be published in Int. J. Heat Mass Transfer (1994).
11. Yih, C. -S., J. Fluid Mech. **31** (1968), 737-751.
12. Hall, P. and Kelly, R.E., (1994), submitted for publication.
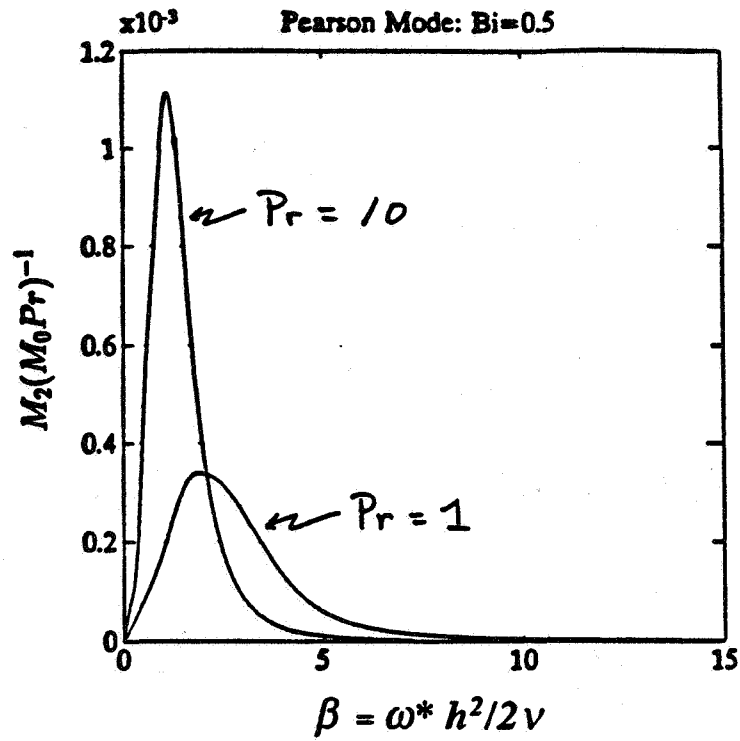
Fig. 1. The change (M_2) in the critical Marangoni number as a function of nondimensional frequency (β) at small values of Re. Nondeformable surface.
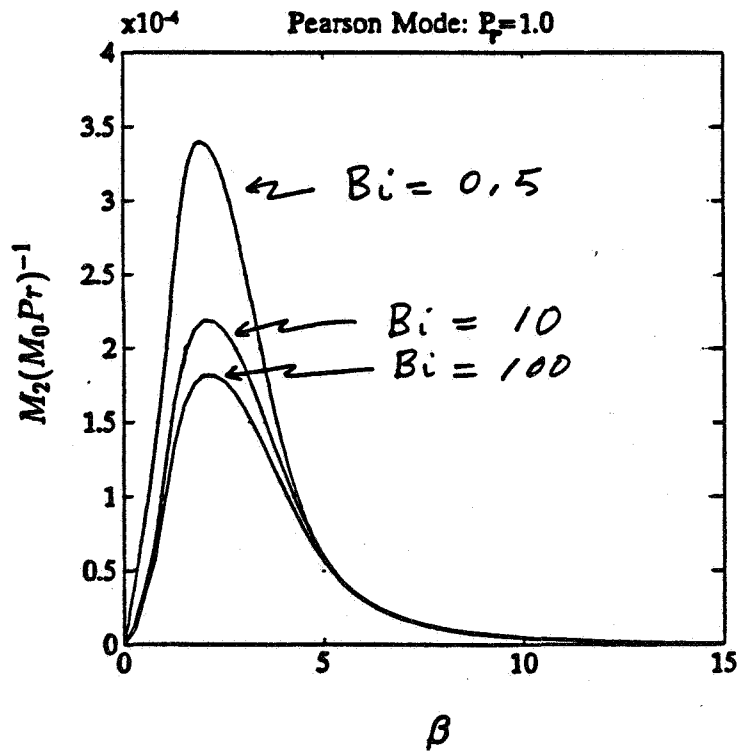
Fig. 2. The change (M_2) in the critical Marangoni number as a function of nondimensional frequency (β) at small values of Re for different values of Biot number. Nondeformable surface.
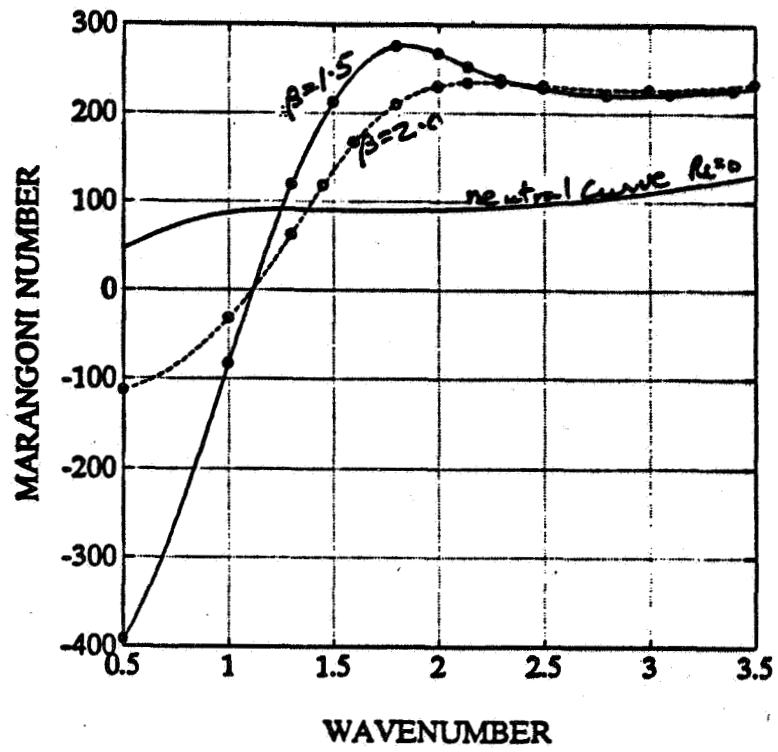
Fig. 5. The critical Marangoni number as a function of wavenumber for the case of a deformable surface with $Re = 25$, $Pr = 7$, $B_i = 0.5$, $Bo = 0.1$, and $\chi = 1.0$.
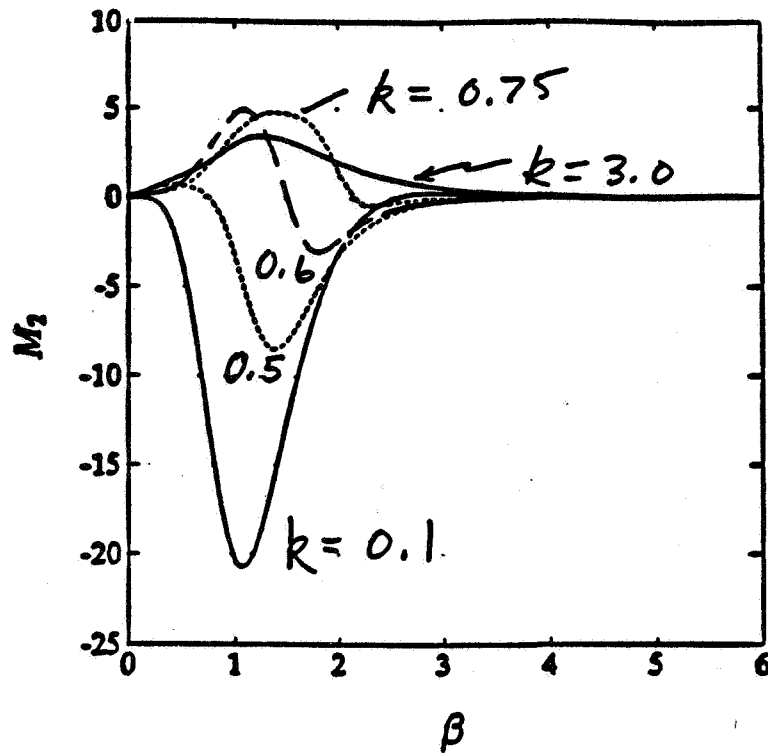
Fig. 3. The change (M_2) in the critical Marangoni number for a deformable surface as a function of frequency (β) for different wavenumbers at small Re. All other parameters are fixed.
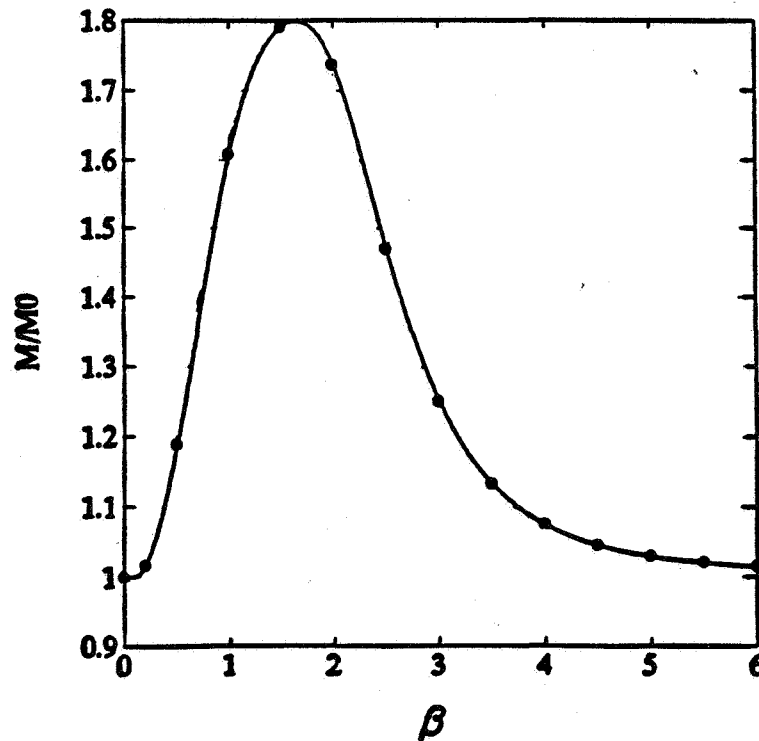
Fig. 4. The critical Marangoni number as a function of nondimensional frequency β for $Re = 20$, $Pr = 7$ and $B_i = 0.5$, with a nondeformable surface for the critical wavenumber at 2.14.

CONTROL OF OSCILLATORY THERMOCAPILLARY CONVECTION IN MICROGRAVITY

G. Paul Neitzel
The George W. Woodruff School of Mechanical Engineering
Georgia Institute of Technology
Atlanta, Georgia 30332-0405

ABSTRACT

Laboratory and numerical experiments are underway to generate, and subsequently suppress, oscillatory thermocapillary convection in a thin layer of silicone oil. The laboratory experiments have succeeded in characterizing the flow state in a limited range of Bond number—Marangoni number space of interest, identifying states of: *i*) steady, unicellular, thermocapillary convection; *i*) steady, multicellular, thermocapillary convection; and *iii*) oscillatory thermocapillary convection. Comparisons between experimental results and stability computations for a related basic state will be made.

INTRODUCTION

Thermocapillary convection is that motion induced in liquids with interfaces by a thermally induced interfacial-tension gradient. In the cases considered in this study, the interface will be a free surface between a liquid and gas and the surface tension will be a decreasing function of temperature, so that thermocapillary-induced surface motion will be from hot to cold regions. Thermocapillary convection occupies an important place in microgravity fluid dynamics because its existence is not swamped or masked, as in some terrestrial situations, by a stronger convection driven by buoyancy, which is significantly diminished in microgravity. In certain terrestrial applications such as the growth of semiconductor material using the float-zone process, the *instability* of thermocapillary convection is known to degrade crystal quality (1). In this case, the transition is to an *oscillatory* state which, when coupled with solidification, leads to the appearance of undesirable striations in the resulting material.

The transition to oscillatory thermocapillary convection in models of the float-zone process has lead to a great deal of research in identifying regions of stability and instability in so-called "half-zone" models of the process (2-5). The determination of such regions may make it possible, in some applications, to avoid the transition to oscillatory thermocapillary convection by operating a process in a region of guaranteed stability. This is not always practical, or even possible, however, and it is this fact which motivates the present research. In a situation for which oscillatory thermocapillary convection is both present and undesirable, we seek a method for detecting and suppressing this mode of convection through exploitation of the instability mechanism.

As a model for this approach, we use the problem studied extensively by Smith and Davis (6, 7), namely, thermocapillary convection in a layer driven by an imposed lateral temperature gradient. Among the basic states considered by Smith and Davis was one called a "return-flow," which would exist in a container of finite extent. This state, shown in Fig. 1, consists of a surface flow from the hot wall to the cold one and a flow along the bottom in the reverse direction driven by a pressure gradient established to conserve mass. For fluids of moderate Prandtl number $\mathrm{Pr} = v/\kappa$, where v is the kinematic viscosity and κ the thermal diffusivity, Smith and Davis found the preferred mode of instability to be in the form of a new instability they termed a "hydrothermal wave," which propagates obliquely with the dominant velocity component in the direction opposite to that of the basic-state free-surface motion. The mechanism behind the instability was described by Smith (7) and is driven by communication between the thermal disturbances on the free surface and those in the layer's interior. We shall attempt to suppress the oscillations by sensing and actively modifying the free-surface temperature distribution.

The project consists of both laboratory and numerical experiments. The laboratory experiments have succeeded in establishing a state of oscillatory thermocapillary convection; in addition, states of steady, multicellular convection are observed in certain regions of Marangoni number–Bond number space, where the dynamic Bond number $\mathrm{Bo_D}$ is defined to be $\mathrm{Bo_D} = \rho g \beta d^2 / \gamma$, where ρ is the density, g is the gravitational acceleration, β is the coefficient of volumetric expansion, σ is the mean surface tension and $\gamma = -d\sigma/dT$ is the rate of decrease of surface tension with temperature. Preliminary numerical work was utilized to assist in the design of the laboratory apparatus; more sophisticated numerical modeling of the flow is just commencing and will be reported on at a later date. A modification to the Smith and Davis (6) theory has been made to include the presence of buoyancy absent in the earlier work. Comparisons between these results and the laboratory observations will be made.

APPARATUS AND DIAGNOSTICS

The apparatus used for the laboratory experiments allows for a liquid layer of variable depth to be established between two aluminum walls located 30 mm apart. Temperature-controlled water is circulated through the endwalls to establish isothermal conditions of T_H and $T_C < T_H$; these are measured with the use of thermocouples embedded in these endwalls and are used in the computation of the Marangoni number $\mathrm{Ma} = \gamma \Delta T d^2 / \mu \kappa L$. In this expression, $\Delta T = T_H - T_C$ is the driving horizontal temperature difference, μ is the dynamic viscosity coefficient and d and L are the depth and length ($L = 30$ mm), respectively, defined in Fig. 1.

The layer is constrained laterally by two Plexiglas walls positioned 50 mm apart; the Plexiglas provides for a thermal condition approximating an adiabatic wall. The meniscus is pinned around its entire perimeter by having a sharp lip machined into the device. The horizontal surfaces of the lip are coated, prior to each set of experiments with a fluorinert compound which resists the wetting of these surfaces by the silicone oil ($\nu = 1$ cS, corresponding to $\mathrm{Pr} = 13.93$) used as the test liquid. Pinning the meniscus in this manner allows for a flat interface and well-defined layer depth. This is in contrast to earlier, related experiments by Villers and Platten (8) which appeared to make no apparent attempt to pin the meniscus. Schwabe *et al.* (9) conducted experiments in both rectangular and annular geometries; in the rectangular case, the meniscus appears to be pinned as in the present experiments. The depth is controlled by utilizing a false bottom of thick Plexiglas supported on three micrometers, allowing accurate positioning and depth control. Silicone oil also occupies a reservoir beneath the false bottom so that leakage through the bottom is not of concern in these experiments; this reservoir plays no role in the dynamics of the flow. A photograph of the apparatus is shown as Fig. 2; the view is similar to the sketch in Fig. 1, but from an angle above the horizontal.

Flow visualization experiments have been performed to characterize the various flow regimes in Ma–$\mathrm{Bo_D}$ space. Two types of flow visualization have been employed. In the first type of experiment, the layer is seeded with polystyrene spheres of sizes in the range 1.5 - 15 μm. A light sheet from an argon-ion laser is used to illuminate an x–y plane (See Fig. 1) of the flow and the particles are observed with either a digital camera and video recorder or with a still camera capable of taking time-exposure photographs. The second type of flow visualization employs a shadowgraphic technique. A collimated light source is used to illuminate the layer through one sidewall and the flow is observed through the other, i.e., in the z–direction of Fig. 1. The effect is therefore integrated across the layer and the images do not subject themselves to a simple interpretation (the patterns are representative of the second derivative of the density, or alternately, the second derivative of temperature). However, the technique appears to be very sensitive in detecting changes in flow structure and the onset of time dependence.

In addition to the flow-visualization work, various steady-flow states where characterized quantitatively using laser-Doppler velocimetry to map out the velocity fields for both steady, unicellular and steady, multicellular convection. These results are reported in the paper by Riley and Neitzel (10)

22

The primary interest in these experiments is in identifying the boundary associated with the onset of oscillatory thermocapillary convection, since this is the regime in which the control strategy will be implemented. Moreover, it is of interest to determine if there are regions in Ma–Bo_D space which exhibit a transition directly from steady, unicellular convection [the Smith and Davis (6) return-flow basic state] to oscillatory convection, in line with the Smith and Davis theory. It might be expected that the likelihood of this occurrence increases with decreasing Bo_D, since the calculations of Smith and Davis were performed assuming zero gravity. We shall see from the results that this is the case.

RESULTS

As just mentioned, the principal aim of these first experiments was to identify regions of Ma–Bo_D space which are likely to exhibit a transition directly from the steady basic state to oscillatory thermocapillary convection. The results of these experiments for a single silicone oil with Pr = 13.93 are shown in Fig. 3. It can be seen that such a transition occurs for Bond numbers in the range $0.075 < Bo_D < 0.2$. For Bond numbers above this range, the first transition from the steady basic state is to a state of steady, multicellular convection. Fig. 4 shows a comparison between a streak photograph and a shadowgraph for a case of this type, corresponding to (Ma, Bo_D) = (1350, 0.57). This value of Ma is significantly above the value (Ma = 680) at which the transition to steady, multicellular convection takes place for this Bond number. For a relatively deep layer such as seen in Fig. 4 ($d = 2.0$ mm), the multicellular structure nearly fills the entire layer; for smaller depths, the co-rotating cells shrink in size and are difficult to observe from the streak photographs, while the shadowgraphs still show a significantly distorted shape such as those seen here.

Fig. 5 is a photograph of the shadowgraphic image observed for a state which has undergone a transition directly to an oscillatory mode. This case corresponds to a layer depth of $d = 1.0$ mm with (Ma, Bo_D) = (460, 0.14), which is just slightly above the transition value of Ma = 455 for this Bo_D; in this regime, the transition to oscillatory convection is very sharp. The pattern seen here propagates to the left (toward the hot wall) in a very regular manner with a well-defined speed. It is the degree of this regularity, combined with the spatial nature of the instability, which makes it a candidate for active control and oscillation suppression.

Finally, it is worthwhile to examine the results of stability computations based on the Smith and Davis (6) theory with the inclusion of buoyancy. Fig. 6 shows the Marangoni number and wave speed as a function of wavenumber for the case of $Bo_D = 0.50$. The theoretical results reported here considered two-dimensional disturbances for simplicity. For Prandtl numbers in the range of the oil used in these experiments, the linear-theory Marangoni numbers are nearly indistinguishable for 2-D and oblique waves. The value of Ma_L corresponding to the minimum of the solid curve has an associated wave speed which yields waves propagating against the direction of the basic-state free surface. One observes from this graph that there does exist a wavenumber for which the wave speed is zero, possibly corresponding to a steady, multicellular mode. Fig. 7 shows the behavior of Ma_L and the Marangoni number corresponding to this zero-wave-speed value as a function of Bond number. At a value of $Bo_D = 0.75$, the critical state corresponds to one with zero phase speed, as compared to the occurrence of steady, multicellular states at $Bo_D \approx 0.2$ in the experiments.

One possible basis for differences in the magnitudes of the Marangoni numbers determined by experiment and theory is due to the fact that the theoretical calculations assume a basic state with a linear temperature gradient which is used to evaluate Ma. In the experiments, this gradient is approximated by $\Delta T/L$, which is much larger than the shallow gradient in the middle of the layer. Encouraging is the fact that the Smith and Davis, zero-gravity stability limit (indicated on Fig. 3 by an arrow) is in good agreement with the experimentally determined result for small Bond number, although the degree of this agreement is in need of further interpretation, given the statement in the previous sentence. Mid-layer surface-temperature gradients will be measured during the next phase of the research.

DISCUSSION AND FUTURE WORK

An apparatus has been constructed and used to demonstrate the existence of oscillatory thermocapillary convection. The apparatus is designed to pin the meniscus around the entire perimeter so that a flat interface and well-defined depth may be achieved. Three flow regimes have been identified and a stability map constructed for a limited range of Ma–Bo_D space. On a portion of this plane, the transition to oscillatory thermocapillary convection is a sharp one and occurs directly from the steady, return-flow basic state without passing through a steady, multicellular state.

Now that a range of Bo_D has been identified in which the transition occurs from steady, unicellular thermocapillary convection to oscillatory thermocapillary convection, we shall begin to implement the proposed control strategy. This involves detecting the surface-temperature variations with the use of an infrared camera and then actively supplying heat to regions of negative disturbance temperature to homogenize the free-surface temperature. The heat is to be supplied with a carbon-dioxide laser, making use of the properties of silicone oil determine by Pline (11) in support of the Surface-Tension-Driven Convection Experiment (STDCE).flown on the USML-1 Shuttle mission.

The control strategy to be employed is envisioned to utilize feed-forward control to detect the presence of waves at one spatial location and then suppress them at a distance downstream of this point, where by downstream, we refer to the direction of propagation.. If the instability mechanism postulated by Smith (7) is correct and if the flow being observed is indeed a hydrothermal-wave instability, then this strategy should result in the successful suppression of oscillatory convection downstream of the heating location.

ACKNOWLEDGMENT

REFERENCES

1. H.C. Gatos, in G.E. Rindone, (ed.) Materials Processing in the Reduced Gravity Environment of Space, Elsevier, 1982,

2. Y. Shen, *et al.*, J. Fluid Mech., 217 (1990), 639-660.

3. G.P. Neitzel, *et al.*, Phys. Fluids A, 3 (1991), 2841-2846.

4. G.P. Neitzel, *et al.*, Phys. Fluids A, 5 (1993), 108-114.

5. H. Kuhlmann and H. Rath, J. Fluid Mech., 247 (1993), 247-274.

6. M.K. Smith and S.H. Davis, J. Fluid Mech., 132 (1983), 119-144.

7. M.K. Smith, Phys. Fluids, 29 (1986), 3182-3186.

8. D. Villers and J.K. Platten, J. Fluid Mech., 224 (1992), 487-510.

9. D. Schwabe, *et al.*, Phys. Fluids A, 4 (1992), 2368-2381.

10. R.J. Riley and G.P. Neitzel, in G.P. Neitzel and M.K. Smith, (ed.) Surface-Tension-Driven Flows, ASME, 1993,

11. A.D. Pline, NASA-TM 101353 (1989), NASA Lewis Research Center.
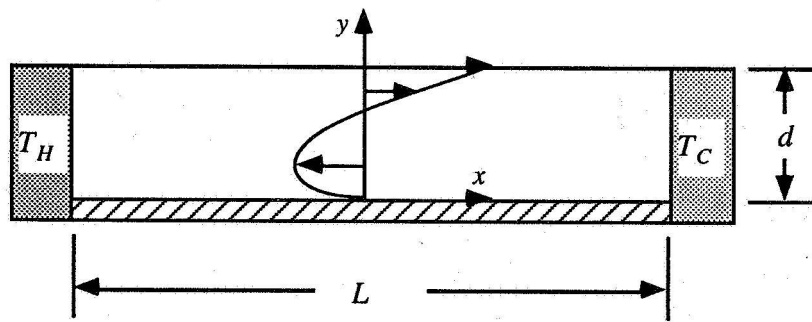
Thermocapillary convection return-flow basic state in a layer of finite length.
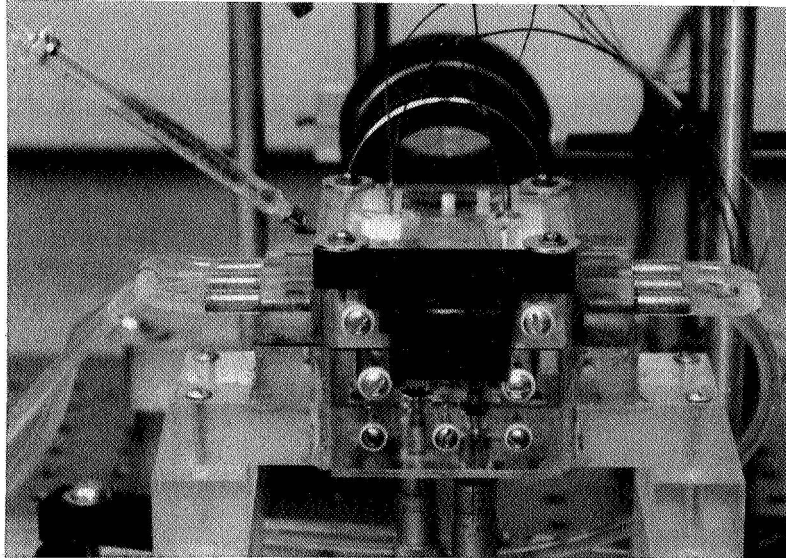
Fig. 2. Photograph of the experimental apparatus.
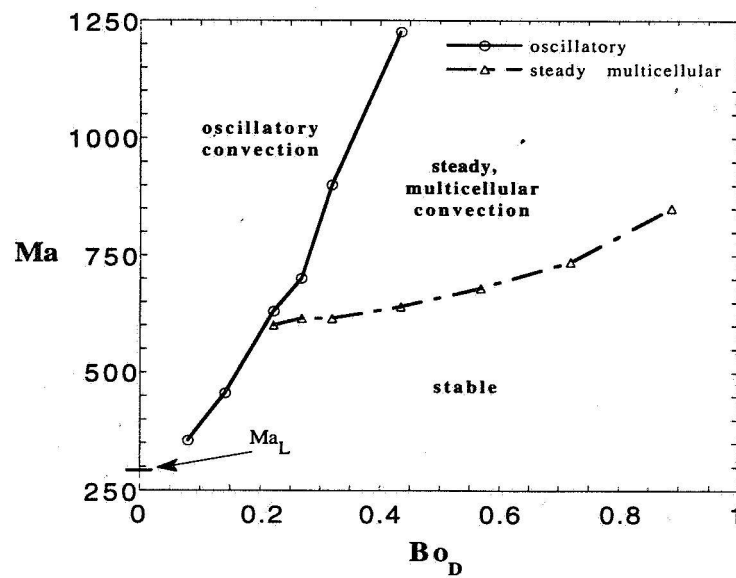
Fig. 3. Experimental results for 1 cS silicone oil with Pr = 13.93.
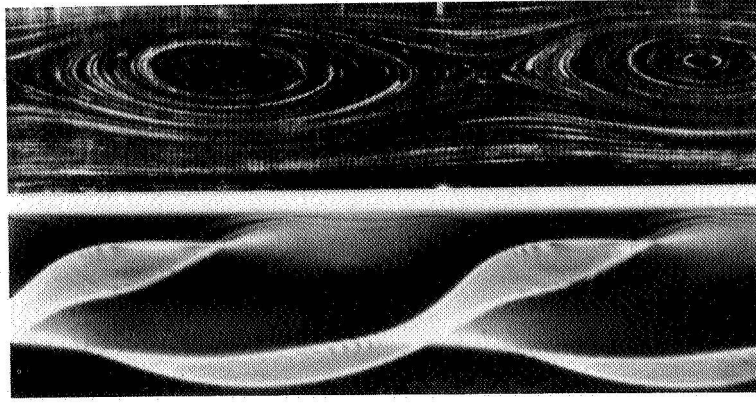
Fig. 4. Streak photograph and shadowgraph for a steady, multicellular case with $d = 2.0$ mm and $(Ma, Bo_D) = (1350, 0.57)$.

Fig. 5. Shadowgraph for an oscillatory case with $d = 1.0$ mm and $(Ma, Bo_D) = (460, 0.14)$.
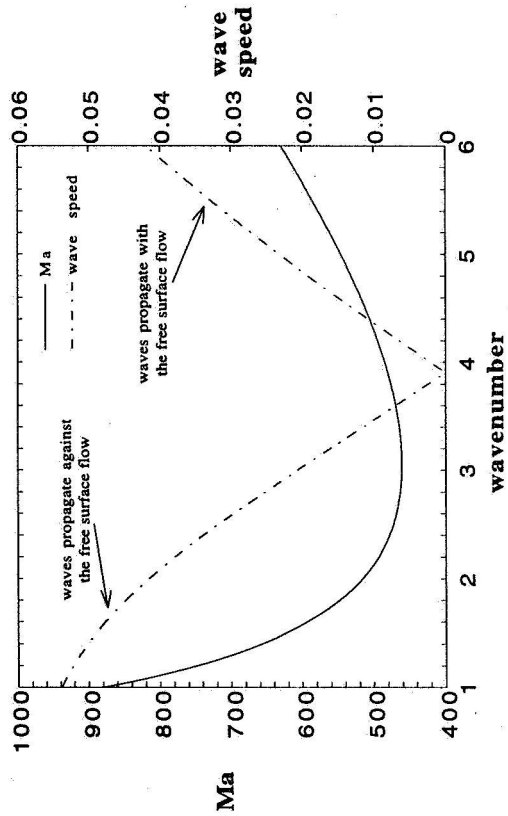
Fig. 6. Linear-stability calculations versus wavenumber.
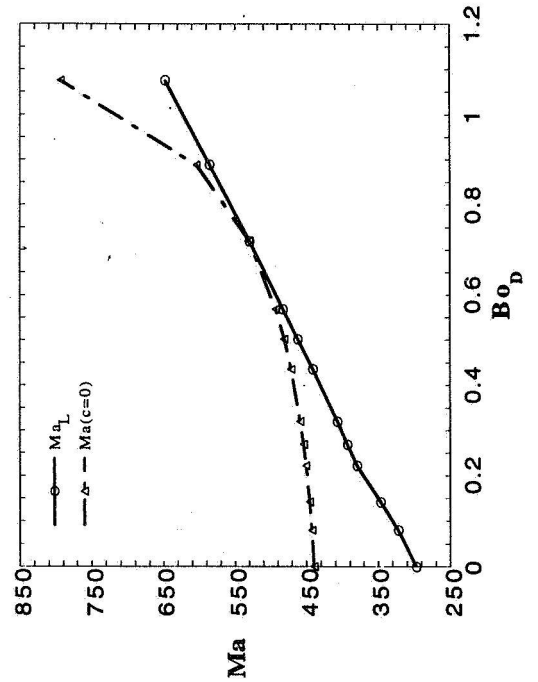
Fig. 7. Linear-stability results including buoyancy.

OSCILLATORY THERMOCAPILLARY CONVECTION

Michael R. Mundrane and Abdelfattah Zebib
Department of Mechanical and Aerospace Engineering
Rutgers University
Piscataway, NJ 08855-0909

ABSTRACT

We study thermocapillary and buoyant thermocapillary convection in rectangular cavities with aspect ratio $A = 4$ and $\mathbf{Pr} = 0.015$. Two separate problems are considered. The first is combined buoyant thermocapillary convection with a nondeforming interface. We establish neutral curves for transition to oscillatory convection in the $\mathbf{Re} - \mathbf{Gr}$ plane. It is shown that while pure buoyant convection exhibits oscillatory behavior for $\mathbf{Gr} > \mathbf{Gr}_{cr}$ (where $\mathbf{Gr}_{cr}$ is defined for the pure buoyant problem), pure thermocapillary convection is steady within the range of parameters tested. In the second problem, we consider the influence of surface deformation on the pure thermocapillary problem. For the range of parameters considered, thermocapillary convection remained steady.

INTRODUCTION

Understanding and controlling oscillatory thermocapillary convection is very important to material processing in microgravity. Thermocapillary flows, driven by tangential shear associated with temperature induced surface tension gradients at a free surface, are a primary mechanism for convection under reduced gravity. While steady convection reduces the diffusional boundary layer at the solidification interface during crystal growth, and thus is generally beneficial, unsteady convection has a negative impact on crystal morphology, rendering the resulting product unusable.

A number of recent numerical studies have predicted transitions in the pure thermocapillary problem for both small and large $\mathbf{Pr}$ [1, 2, 3] while others [4, 5, 6, 7] could only predict steady states. Calculations which included buoyant affects in addition to thermocapillary affects have also been performed and displayed both steady and unsteady behavior [8, 9].

Because the buoyant problem is well understood, an indirect approach is utilized in the present work to shed light on the behavior of the thermocapillary problem. We specifically consider the behavior of the Hopf bifurcation, which clearly exists in the pure buoyant case ($\mathbf{Re} = 0$) but subsequently disappears under pure thermocapillary conditions ($\mathbf{Gr} = 0$). Numerically estimated neutral stability curves are presented in a $\mathbf{Gr} - \mathbf{Re}$ parameter space and thereby the fate of the Hopf bifurcation under the influence of thermocapillary forces is displayed. We analize the transfer of energy between the steady and oscillatory components of the flow to identify the driving mechanism for time dependent flow.

We also consider pure thermocapillary convection in a cavity and incorporate a deforming interface using two different approaches. The first approach is an asymptotic expansion with respect to the small parameter $\mathbf{Ca}$. The $O(1)$ and $O(\mathbf{Ca})$ solutions are obtained. The second approach employs a linearized free surface condition.

MATHEMATICAL MODEL

The physical model consists of a rectangular calculation domain with aspect ratio $A = width/height$ (see Figure 1). There is a free surface ($y = H$) across which no mass transport takes place. A driving temperature difference ($T_h - T_c$) is imposed in the x direction by assuming differentially heated side walls and adiabatic conditions are assumed at the two remaining boundaries. The fluid is Boussinesq and the surface tension is assumed to be a monotonic, weak function of temperature $\sigma = \sigma_r - \gamma(T^* - T_r)$ where $\gamma = -d\sigma/dT^*$. The superscript on T indicates a dimensional quantity and T_r is a reference temperature. Other nondimensional parameters are the Prandtl ($\mathbf{Pr} = \nu/\alpha$), Reynolds ($\mathbf{Re} = \gamma T_r L/\mu\nu$), Grashof ($\mathbf{Gr} = g\beta T_r L^3/\nu^2$), Marangoni ($\mathbf{Ma} = \mathbf{RePr}$) numbers. The symbols ν and μ represent the kinematic and dynamic viscosities respectively. In addition, the Capillary number ($\mathbf{Ca} = \gamma T_r/\sigma_r$) provides some measure of the surface deflection in response to thermocapillary induced stresses. This parameter is small in value and in the limit $\mathbf{Ca} \to 0$, the free surface is flat.

For the combined problem, scales $L = H$, $T_r = (T_h - T_c)/A$, $\mathbf{Gr}\,\nu/L$, L^2/ν, and $\mathbf{Gr}\,\nu\mu/L^2$ are applied to length, temperature, velocity, time, and pressure respectively and permit the influence of both buoyant and thermocapillary effects [10, 11]. Scales $L = H$, $T_r = T_h - T_c$, $\gamma T_r/L$, L^2/ν, and $\gamma T_r/L$ are applied to length, temperature, velocity, time, and pressure respectively for the thermocapillary problem.

Free surface deformation is incorporated by performing an asymptotic expansion with respect to the small parameter $\mathbf{Ca}$. Grouping terms of $O(1)$ and terms of $O(\mathbf{Ca})$ yields a nonlinear and a linear system of equations and boundary conditions representing a leading order solution and a correction, respectively. A second approach is to linearize the free surface boundary conditions by performing an expansion with respect its equilibrium position [12].

RESULTS

Based on numerous computations at carefully selected parameter values, neutral stability curves (see Figure 2) have been generated in the $\mathbf{Re} - \mathbf{Gr}$ parameter space. The displayed curves represent both $\mathbf{Pr}$ and aspect ratio dependence for the Hopf bifurcation of the combined buoyant and thermocapillary problem. It can be seen that the generated curves do not intersect the $\mathbf{Gr} = 0$ line at any point. This has also been confirmed by calculations performed for $\mathbf{Pr} = 0$. The results are consistent with both steady and unsteady calculations performed by Hadid and Roux [9]. The neutral curve is shifted upwards (a stabilized flow) if either the aspect ratio is decreased or if the Prandtl number is increased.

Insight into the mechanism of instability can be obtained by computing the production and dissipation of energies for a given disturbance [13]. We assume that the flow field can be decoupled into a time averaged $\mathbf{U}$ calculated in a protracted fashion over many cycles and a perturbation $\mathbf{u}'$ extracted directly as the instantaneous difference between the actual and the "base" flow field given by $\mathbf{U}$. The analyses are performed for the limiting case of $\mathbf{Pr} = 0$ which prescribes a conduction profile and thereby eliminates the small contributions of the fluctuating temperature field present with small but nonzero $\mathbf{Pr}$. The vector dot product of the perturbation velocity and the momentum equation is integrated over the calculation domain to define the energy and thus obtain the Reynolds-Orr energy equation $\dot{\mathbf{K}}$ in terms of production P and dissipation D in the form

$$\int \dot{\mathbf{K}} d\mathbf{x} = \int \mathbf{Gr}\,\mathbf{P}\,dx - \int \mathbf{D}\,dx$$

This equation evaluates the net transfer of energy between the base flow and the perturbation. If the transfer is positive/negative, then the flow is unstable/stable to the perturbation.

Stream function contours for the averaged flow field and local rate of change of kinetic energy for reinforcing and opposing thermocapillarity, are indicated in Figures 3 and 4 respectively. They correspond to the same $\mathbf{Pr}$ and $\mathbf{Gr}$ with selected $\mathbf{Re}$ such that they are near the respective sides of the the neutral curve. For the reinforcing case (Figure 3) the flow consists of the buoyancy dominated clockwise corotation. Net

production which is positive, and thus representative of a transfer of energy between the underlying base flow and the unsteady perturbation flow, is present in the shear region between the two corotating cells and in the region where the cold wall cell interacts with the lower adiabatic boundary. In the opposing case (Figure 4) The base flow is seen to be separated into two distinct counter rotating cells. The lower one contains buoyancy driven clockwise corotating cells while the surface thermocapillary cells are counterclockwise and corotating. The regions of net energy transfer to the perturbation flow exist in the the shear region between the buoyancy driven corotating cells and also in the high shear region at the free surface where the buoyant cell interacts with the opposing thermocapillary surface near the hot corner. As the neutral stability curve is approached, the buoyant cell is pushed downwards into the cavity and this reduces its interaction with the free surface.

The indicated plots for energy production are not time invariant. The perturbation velocities u'_x and u'_y have the same period, but differ by some constant phase angle. However, the regions of intense shear for the opposing case remain the saddle point of the buoyant corotating cells and the interaction near the free surface between the thermocapillary and buoyant recirculations. For the reinforcing case, The relevant regions consist of the saddle point and the interaction between the buoyant recirculation and the lower surface. The contribution to the perturbation varies in importance through the limit cycle but remains associated with these respective regions. In both the opposing and the reinforcing case, energy transfer in the buoyant cells is reduced as the neutral stability curve is approached. Thus, the thermocapillary driven surface flow acts to diffuse energy transfer and ultimately net production is suppressed due to elimination of internal shear layers.

Thermocapillary convection with a deforming interface is shown in Figures 5 - 9, which corresponds to $Re = 1000, 5000$. These figures display both the $O(Ca)$ and combined flow fields. The combination is performed utilizing an assumed $Ca = 0.01$ which is consistent with the small parameter assumption in the original expansion $\phi \approx \phi_0 + \phi_1 Ca$. The combined and the $O(1)$ flow fields are indistinguishable for these parameter values. The flow is seen to be unicellular and attracted to the cold corner. This is consistent with other work [4]. The temperature field does not deviate substantially from a conduction profile for this Pr and Re. The calculated results were steady for the parameter values selected and the flow fields for the $O(1)$ and $O(Ca)$ calculations were of comparable orders of magnitude.

The surface deflection (see Figure 8) is nearly three times larger than that obtained for aspect ratio $A = 2$, $Pr = 0.01$ and $Re = 1000$ flows. However, this deflection is still $\approx 10^{-3}$ for the Ca utilized. Because h is very small, we also calculate the flow using linearized free surface boundary conditions. The results for the parameter values of Figure 5 are shown in Figure 6 where quantitative agreement of about 0.05% is indicated. The free surface velocities (see Figure 9) are qualitatively similar to profiles obtained using different aspect ratios. The peak surface velocity is near the cold wall for these calculations. This is consistent with the flow field profiles which indicate that the dominant circulation is attracted to the cold isothermal boundary for increasing Re.

CONCLUSIONS

We have investigated the combined buoyant thermocapillary convection oscillatory states and attempted to understand the origin of these transitions. When Gr is sufficiently large to admit periodic solutions in the pure buoyant problem and when thermocapillarity acts in support of buoyancy, the effect is stabilizing as a larger Gr is needed for transition. When it acts in opposition it is destabilizing for small $|Re|$ due to additional energy transfer to the fluctuating component at the free surface, but for larger $|Re|$ the flow eventually separates into two distinct recirculations. One is buoyancy driven and the other is thermocapillary driven with opposing circulation. Thermocapillarity is ultimately stabilizing as it smooths out the internal buoyant shear layers. Furthermore, surface deflection which is small for small Ca is found to have no significant effect on the transition process, ie. the flow remained steady for all parameters utilized.

Our computational techniques have been validated against numerous published works, however, our

results do not agree only with Chen and Hwu [2]. Further studies should be conducted to establish a complete picture of the technologically important case of low **Pr**, microgravity convection. In particular, there appears to be no experimental results in the literature for this case.

ACKNOWLEDGMENTS

REFERENCES

[1] M. Ohnishi and H. Azuma. Computer simulation of oscillatory Marangoni flow. *Acta. Astronautica*, 26(8-10):685–696, 1992.

[2] J. C. Chen and F. S. Hwu. Oscillatory thermocapillary flow in a rectangular cavity. *Int. J. Heat Mass Transfer*, 36(15):3743–3749, 1993.

[3] L. J. Peltier and S. Biringen. Time-dependent thermocapillary convection in a rectangular cavity: numerical results for a moderate Prandtl number fluid. *J. Fluid Mech.*, 257:339–357, 1993.

[4] A. Zebib, G. M. Homsy, and E. Meiburg. High Marangoni number convection in a square cavity. *Phys. Fluids*, 28(12):3467–3476, 1985.

[5] B. M. Carpenter and G. M. Homsy. High Marangoni number convection in a square cavity: Part 2. *Phys. Fluids A*, 2:137–148, 1990.

[6] U. Buckle and M. Peric. Numerical simulation of buoyant and thermocapillary convection in a square cavity. *Numerical Heat Transfer, Part A*, 21:121–141, 1992.

[7] A. Liakopoulos and G. W. Brown. Thermocapillary and natural convection in a square cavity. In G. P. Neitzel and M. K. Smith, editors, *Surface Tension Driven Flows*, volume AMD-170, pages 57–74, New York, NY, Dec 1993. Winter Annual Meeting, ASME.

[8] T. L. Bergman and J. R. Keller. Combined buoyancy, surface tension flow in liquid metals. *Numerical Heat Transfer*, 13:49–63, 1988.

[9] H. B. Hadid and B. Roux. Buoyancy- and thermocapillary-driven flows in differentially heated cavities for low-prandtl-number fluids. *J. Fluid Mech.*, 235:1–36, 1992.

[10] B. M. Carpenter. *Combined buoyant-thermocapillary flow in a cavity*. PhD thesis, Stanford University, Stanford, CA, 1989.

[11] M. Mundrane and A. Zebib. Oscillatory buoyant thermocapillary flow. *Phys. Fluids A.*, 1994. submitted.

[12] M. Mundrane and A. Zebib. Marangoni convection with a deforming interface. New York, NY, Jan 1994. IMECE, ASME. submitted.

[13] N. Ramanan and G. M. Homsy. Linear stability of lid-driven cavity flow, 1994. preprint.
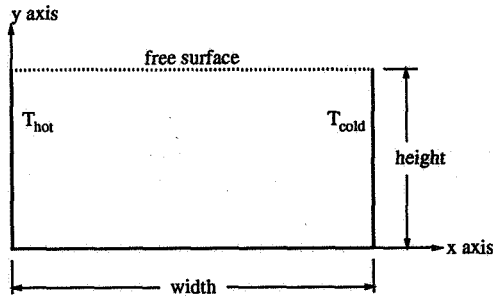
Figure 1: Physical diagram of calculation domain with solid walls as indicated. Hot and cold walls are located at $x = 0$ and $x = X_{max}$ respectively.
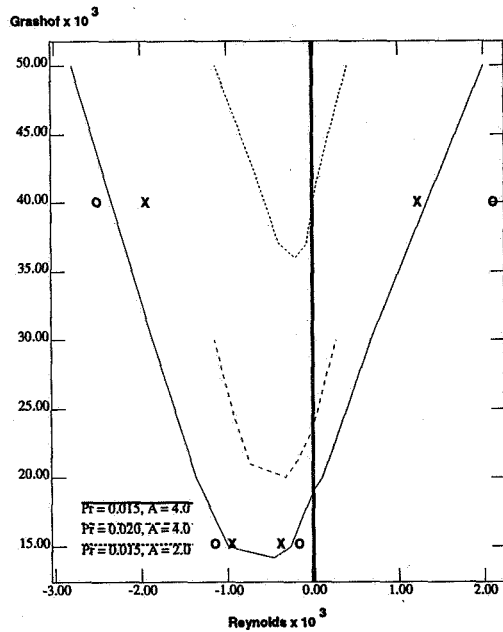
Figure 2: Neutral stability curves showing aspect ratio and **Pr** dependence. In all cases the flow is steady for **Gr** and **Re** combinations which are below the curve and unsteady for combinations which are above it. Points marked with an X (unsteady) or an O (steady) have been calculated by Hadid and Roux (1992) with aspect ratio $A = 4$ and **Pr** = 0.015.
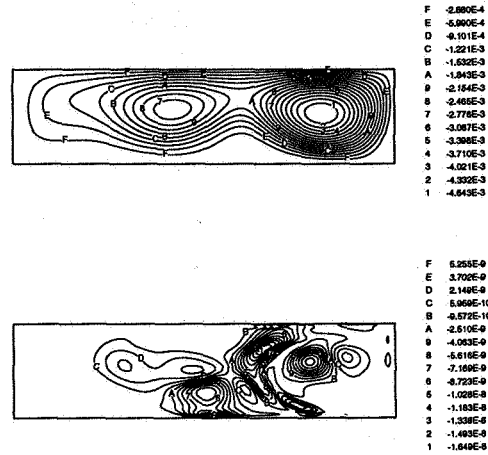
Figure 3: Averaged flow field, local production **P**, and local rate of change of kinetic energy $\dot{\mathbf{K}}$ corresponding to **Pr** = 0, **Gr** = 20000, and **Re** = 333.
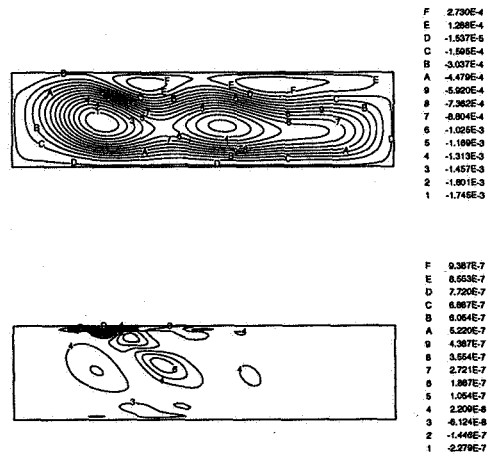
Figure 4: Averaged flow field, local production **P**, and local rate of change of kinetic energy $\dot{\mathbf{K}}$ corresponding to **Pr** = 0, **Gr** = 20000, and **Re** = −1550.

8	5.24558E-3
7	4.11746E-3
6	2.98933E-3
5	1.86121E-3
4	7.33089E-4
3	-3.95033E-4
2	-1.52316E-3
1	-2.65128E-3

F	8.82656E-3
E	8.33143E-3
D	7.73629E-3
C	7.14116E-3
B	6.54603E-3
A	5.95089E-3
9	5.35576E-3
8	4.76062E-3
7	4.16549E-3
6	3.57035E-3
5	2.97522E-3
4	2.38008E-3
3	1.78495E-3
2	1.18981E-3
1	5.94675E-4
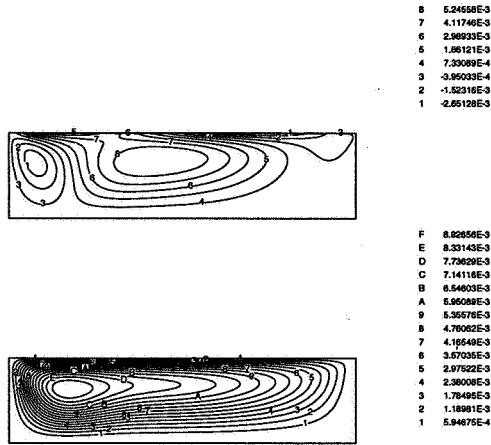
Figure 5: The upper/lower plots correspond to the $O(\mathbf{Ca})$ and combined flow fields respectively for parameter values $A = 4$, $\mathbf{Pr} = 0.015$, $\mathbf{Ca} = 0.01$, and $\mathbf{Re} = 1000$. The cold/hot isothermal boundaries are located at $x = 0, A$ respectively. The leading order flow field (not shown) is indistinguishable from the combined flow field for these parameter values.

F	8.93172E-3
E	8.33624E-3
D	7.74076E-3
C	7.14528E-3
B	6.54981E-3
A	5.95433E-3
9	5.35885E-3
8	4.76337E-3
7	4.16789E-3
6	3.57241E-3
5	2.97693E-3
4	2.38145E-3
3	1.78597E-3
2	1.19049E-3
1	5.95016E-4
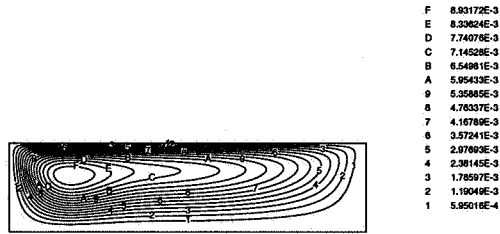
Figure 6: Complete flow field obtained utilizing the linearized approach with the same parameter values as in Figure 5. The flow fields calculated using the two different approaches differ by approximately 0.05%.

8	-3.53512E-4
7	-2.42762E-3
6	-4.50213E-3
5	-6.57644E-3
4	-8.65076E-3
3	-1.07251E-2
2	-1.27994E-2
1	-1.48737E-2

F	6.84968E-3
E	6.38265E-3
D	5.91543E-3
C	5.44820E-3
B	4.98098E-3
A	4.51375E-3
9	4.04653E-3
8	3.57931E-3
7	3.11208E-3
6	2.64486E-3
5	2.17763E-3
4	1.71041E-3
3	1.24318E-3
2	7.75959E-4
1	3.08734E-4
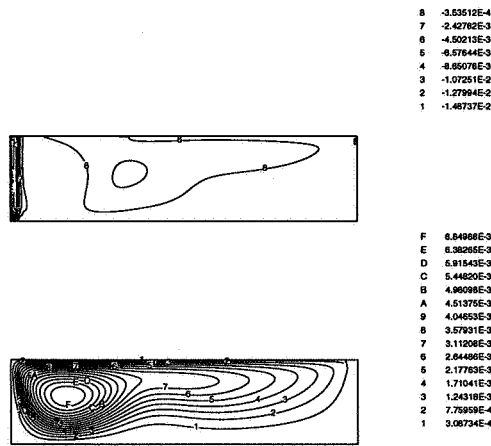
Figure 7: Similar to Figure 5, but with $\mathbf{Re} = 5000$.
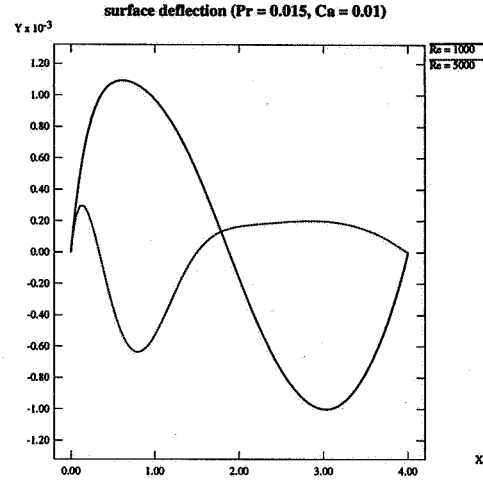
Figure 8: Free surface deflection for the same parameter values as in Figure 5 and $\mathbf{Re} = 1000, 5000$.
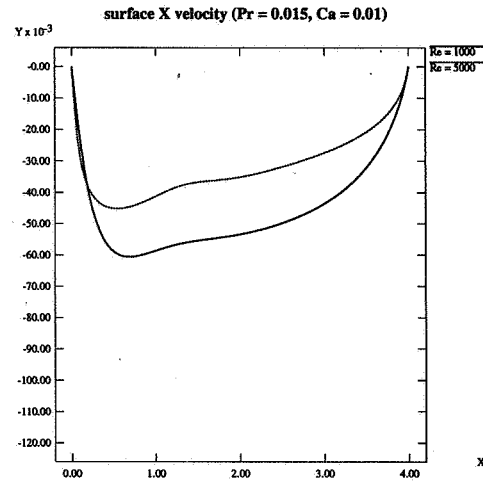
Figure 9: Free surface velocities associated with the flows of Figure 8.

32

/995-108//3
324 751

Lp

ONSET OF HEXAGONS IN SURFACE-TENSION-DRIVEN BENARD CONVECTION*

Michael F. Schatz**, Stephen J. VanHook, J. B. Swift,
W. D. McCormick, and Harry L. Swinney
Center for Nonlinear Dynamics and Department of Physics
The University of Texas at Austin
Austin, TX 78712

ABSTRACT

High resolution laboratory experiments with large aspect ratio are being conducted for thin fluid layers heated from below and bounded from above by a free surface. The fluid depths are chosen sufficiently small (< 0.06 cm) so that surface tension is the dominant driving mechanism; the Rayleigh number is less than 5 for the results reported here. Shadowgraph visualization reveals that the primary instability leading to hexagons is slightly hysteretic (-1%). Preliminary measurements of the convection amplitude using infrared imaging are also presented.

INTRODUCTION

Bénard's landmark experiment [1], which revealed striking hexagonal patterns that arise spontaneously in fluid heated from below, inspired the scientific study of convection and stimulated theoretical ideas ranging from classical hydrodynamic stability to modern notions of pattern formation and complexity in nature. More pertinently, surface-tension-driven Bénard convection (also referred to as Bénard-Marangoni convection) has been recognized as an important paradigm in low-gravity fluid dynamics since it represents a simple, clean example of capillarity-driven flows, which are dominant in the microgravity environment.

Despite its long-standing significance and current relevance, many fundamental questions about Bénard-Marangoni convection remain unanswered. Discrepancies between theory and experiment exist for the primary instability [2]. Secondary instabilities and the transition to turbulence have never been explored. The surface-tension-driven Bénard problem is poorly understood because in terrestrial experiments the effect of buoyancy is often comparable to that of surface tension. Only in space can instabilities and the transition to turbulence in Bénard-Marangoni convection be studied without influence from buoyancy effects. However, in terrestrial experiments on sufficiently thin layers, the effect of buoyancy is negligible at the onset of the primary instability. Such experiments can characterize the primary instability and serve as a basis for studies in space of higher instabilities. Finally, many of the experimental techniques developed and refined for Bénard-Marangoni convection will be directly applicable to other capillarity-driven flows.

In the following, we present results for the onset of convective motion in the Bénard-Marangoni problem. We compare our experimental observations qualitatively to a variational model. In addition, we present preliminary measurements of the temperature field at the fluid-air interface to illustrate the promise of infrared (IR) imaging as a means of obtaining quantitative flow amplitudes.

EXPERIMENTAL

Convection Cell. – The simplest geometry for Bénard-Marangoni convection is the system with a single liquid layer of thickness d_f and horizontal extent $2\Gamma d_f$ bounded at $z = 0$ by a solid surface of high thermal conductivity (1 cm thick aluminum mirror) and at $z = d_f$ by a gas layer of

negligible viscosity and density (Fig. 1). The thickness of the gas layer d_a in the experiments is fixed ($\approx d_f$) by bounding above with a solid surface of high thermal conductivity (1 mm thick sapphire window). A temperature gradient is imposed by heating the mirror to a temperature T_b and by cooling the sapphire window at a temperature T_t. Initially, the surface tension $\sigma(T)$ is uniform at the liquid-gas interface; however, if $T_b - T_t$ is sufficiently large, instability causes surface tension gradients that drive flow along the interface and in the bulk. The dimensionless number that characterizes the surface tension driving is the Marangoni number $M = \sigma_t d_f \Delta T_f / \rho \nu \kappa$, with the liquid density ρ, the liquid kinematic viscosity ν, the liquid thermal diffusivity κ, $\sigma_t = |d\sigma/dT|$, and $\Delta T_f = (T_b - T_t)(1 + k_f d_a/k_a d_f)^{-1}$ in terms of the thermal conductivities k_f and k_a. For any terrestrial experiment, the onset of convection will also depend on buoyancy, which is characterized by the Rayleigh number $R = g\alpha\Delta T_f d_f^3/\nu\kappa$ with the acceleration of gravity g and the temperature coefficient of volumetric expansion α. The importance of surface tension relative to buoyancy in Bénard-Marangoni convection is given by $\Psi \equiv M/R$; buoyancy effects are negligible when $\Psi \gg 1$.

The experiment is performed in a cylindrical cell of diameter $2\Gamma d_f = 3.81$ cm with $d_f = 0.045 \pm 0.0006$ cm and $d_a = 0.050 \pm 0.001$ cm. The thickness of both the fluid and the air layers varies by approximately ± 1 μm, as measured inteferometrically. Purified dimethylsiloxane silicone oil (96.7% --tetracosamethyldodecasiloxane) is used in the experiment to reduce the potential for subtle thermal cross-diffusive effects that can occur with polymer mixtures such as commercial silicone oils [3]. The heater power to the mirror is computer controlled; with constant heater power, the temperature of the bottom plate fluctuates by less than ± 0.0005 °C. The mean temperature of the sapphire window is held constant at 13.32 °C and regulated to ± 0.005 °C. The fundamental time scale in the experiment is set by the vertical diffusion time, $t_v = d_f^2/\kappa \approx 2.2$ s. For the present choice of geometry and working fluid, we have $\Psi = 33$; thus surface-tension effects clearly dominate buoyancy.

Imaging. – The behavior of patterns in Bénard-Marangoni convection is investigated by noninvasive optical methods. The shadowgraph technique is used to detect the onset of convection and to visualize pattern morphology. The shadowgraph images are digitized and enhanced to improve the signal-to-noise using standard image processing techniques. Additionally, infrared (IR) imaging techniques yield the temperature field at the fluid-air interface. The IR imager used in this study is the Amber Engineering Series 5256 ProView system, an LN2 cooled, indium antimonide staring array of size 256×256 pixels that operates in the MWIR band from 1.0 to 5.0 μm. To obtain maximum temperature sensitivity and accuracy, multiple data images (typically ~ 64) are acquired at 20 Hz and averaged; an equal number of images of a temperature controlled reference are subsequently averaged and subtracted. To insure that temperature measurements are not averaged over the bulk, a working fluid is used that is composed of methylhydropolysiloxane (30 cS viscosity) mixed with 10 cS Dow Corning 200 silicone oil in a 1:1 ratio by volume. As a result the extinction length for the detected infrared radiation (4.61 micron center wavelength with a bandpass width of 80 nm) is approximately 10 μm.

RESULTS

Hysteresis at Onset–The conduction state undergoes an abrupt transition to hexagons as ΔT_f is increased slowly (average rate $t_v dM/dt = 10^{-6}$). Just prior to onset, a weak circular conduction roll of diameter $\approx d_f$ arises near the boundary; this roll is believed to be driven by static forcing due to the slight mismatch of thermal conductivity between the sidewall and the fluid. Hexagons first appear in a localized section of this conduction roll (Fig. 2(a)). For a given experimental setup, this arc of cells always appears in the same section of the convection apparatus. With a single step increase of 0.15 in M, additional hexagons nucleate from the sidewall and propagate as a traveling front, invading the apparatus until the entire flow domain is filled with hexagons (Fig. 2(b)). The resulting hexagonal planform is free from defects since the lattice is grown from a single "seed crystal" of cells at the boundary. The front of hexagons

propagates across the apparatus in approximately 600 t_v, a time short compared to the *horizontal* diffusion time 4 $\Gamma^2 t_v \approx 7000\ t_v$. The critical Marangoni number is $M_c = 78 \pm 4$ with the uncertainty in the accuracy due to the uncertainty in d_f, d_a, and fluid properties. This compares well with $M_c = 80$ determined from linear stability calculations [4].

On decreasing ΔT_f quasistatically, hexagons continue to persist even as M is reduced to values below that for the first appearance of cells (Fig. 3 (a)-(d)). The hexagons begin to disappear first in regions of the apparatus where they appeared last at onset; thus, the front between convection and conduction propagates in a time-reversed way as compared to onset. However, several steps of size 0.15 in M are required before convection ceases. Moreover, if ΔT_f is held constant before the hexagons completely disappear from the apparatus, the remaining patch of cells persist; in Fig. 3 (c), for example, the patch of hexagons was observed to persist for more than 7000 t_v whereupon continued decrements in temperature caused a return to conduction (Fig. 3 (d)).

Theoretical Model–Near onset, the hexagonal planform arises from the interaction of three roll (plane wave) solutions, k_i, k_j, k_k, each of which has a magnitude equal to the critical wavenumber and makes an angle of $2\pi/3$ with the other roll solutions [5]. Under these conditions, the evolution of the planform is described the set of (real) amplitude equations of the form:

$$d_t A_i = \varepsilon A_i + \alpha A_j A_k - A_i(A_i^2 + \gamma(A_j^2 + A_k^2))$$
(1)

where the indices are cyclically permuted. Under certain assumptions, the coefficients can be computed from the full fluid equations [6, 7]. The existence of hexagons requires $\alpha \neq 0$; as a result, the bifurcation from the conduction state is *subcritical*, i.e., it occurs discontinuously like a first order phase transition. With $\varepsilon = (M/M_c - 1)$, the solutions for hexagons and for conduction are linearly stable over a range of parameter: $\varepsilon_\alpha < \varepsilon < 0$ with $\varepsilon_\alpha = -\alpha^2/(2+4\gamma)$ (the conduction state is linearly unstable for $M > M_c$).

The amplitude equations form a variational model; such a system is expected to exhibit relaxational time dependence governed by a potential function V [8]. Over the range of parameter where both conduction and hexagons exist, each solution corresponds to a minimum of V, where one solution represents the global minimum of V while the other solution, the metastable phase, represents a local minimum. However, there exists a parameter value ε_m (often called the Maxwell point) where both solutions have equal values of the potential; as the parameter value passes through ε_m, the solutions exchange the roles of global stability/metastability. For Eqs. (1), the conduction state is globally stable for $\varepsilon < \varepsilon_m = -8/9\ \varepsilon_\alpha$ and metastable for $\varepsilon_m < \varepsilon < 0$.

The experimental observations are consistent with this variational model. The conduction state enters a metastable regime $\varepsilon > \varepsilon_m$ as ΔT_f increases. The hexagons that first appear at the boundary provide a sufficient perturbation to push the system over the potential barrier and the front between the two states propagates in a way such that the globally stable state (hexagons) spreads. When ΔT_f is decreased, hexagons become metastable for $\varepsilon < \varepsilon_m$. Since the range of parameter values where hexagons are metastable is nearly an order of magnitude smaller than the region of metastability for conduction, the transition back to conduction will be more sensitive to small spatial variations in ε due to nonuniformities in the depths of both the fluid and air layers. As a result, the transition back to conduction occurs in stages, with the front halting as soon as the local value of ε is equal to ε_m.

Surface Temperature Measurements–Local amplitude measurements are necessary to provide direct, quantitative comparison to theoretical models (such as Eqs. (1)) and to numerical simulations. Toward this end, high-resolution infrared imaging is being investigated; Figure 4 illustrates a preliminary measurement of surface temperature near onset. A spatially varying ε is intentionally imposed by increasing the surface temperature (hence, decreasing ΔT_f) from left to

right in Fig. 4; the interface between conduction and convection is quite sharp, in qualitative agreement with the shadowgraph images in Fig. 3. This measurement demonstrates that the temperature resolution, which is better than 0.1 °C, is sufficient to examine quantitatively the behavior of Bénard-Marangoni convection near onset.

CONCLUSIONS

The experimental observations of an abrupt onset of convection and hysteretic return to the conduction state support the idea that the primary instability in Bénard-Marangoni convection is subcritical; further quantitative investigation is being conducted to characterize the degree of subcriticality. One outstanding question is the determination of the range in ε over which hysteresis occurs. Our initial measurements indicate that this range may depend on the size and rate at which the temperature (and, hence, ε) is stepped. Such behavior is not surprising since subcritical transitions may be triggered by finite amplitude perturbations (temperature fluctuations, nonuniformity at the boundary); it remains to be seen to what extent such perturbations may be reduced in our experiments. Additionally, we are developing more quantitative measures of experimental geometry and fluid properties to determine more accurately the critical Marangoni number M_c and are conducting extensive measurements of surface temperature near onset using infrared imaging.

**Author to whom correspondence should be directed--email: schatz@chaos.utexas.edu.

REFERENCES

1. Bénard, H., Rev. Gen. Sci. Pure Appl., 1 (1900), 1261.

2. Koschmieder, E. L. and Biggerstaff, M. I., J. Fluid Mech., 167 (1986), 49.

3. Moses, E. and Steinberg, V., Phys. Rev. Lett., 57 (1986), 2018.

4. Pearson, J. R. A., J. Fluid Mech., 4 (1958), 489.

5. Ciliberto, S., Coullet, P., Lega, J., Pampaloni, E. and Perez-Garcia, C., Phys. Rev. Lett., 65 (1990), 2370.

6. Davis, S. H., Annual Review of Fluid Mechanics, 19 (1987), 403.

7. Bestehorn, M., Phys. Rev. E, 48 (1993), 3622.

8. Malomed, B. A., Nepomnyashchy, A. A. and Tribelsky, M. I., Phys. Rev. A, 42 (1990), 7244.
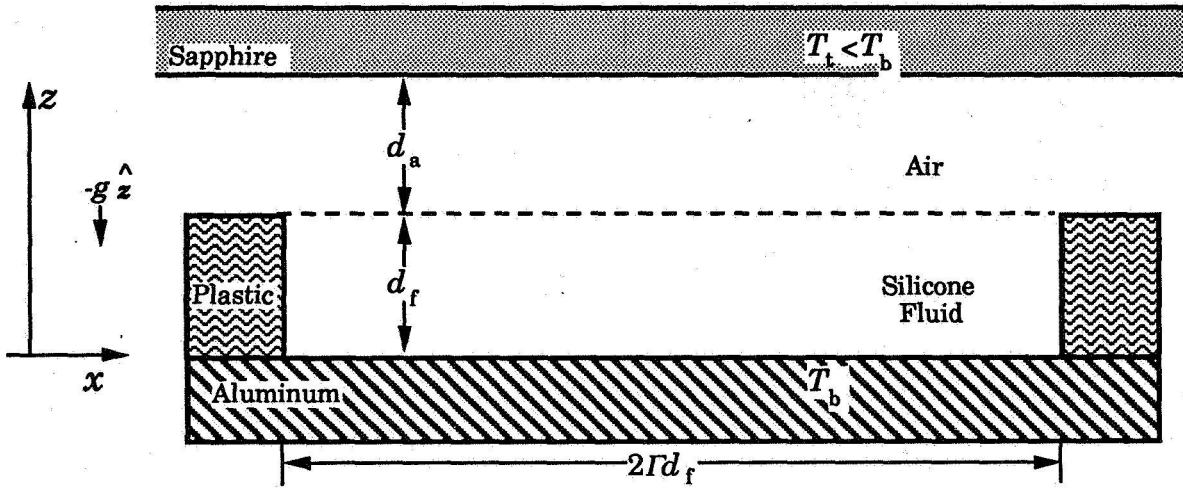
Figure 1: Geometry of Bénard-Marangoni convection

INCREASING M

(a) $M = 78.10$
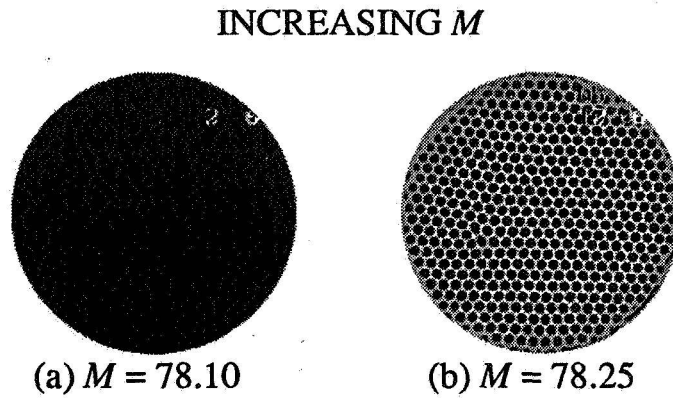
(b) $M = 78.25$

Figure 2: Shadowgraph images depict a sharp onset in surface-tension-driven Bénard convection.
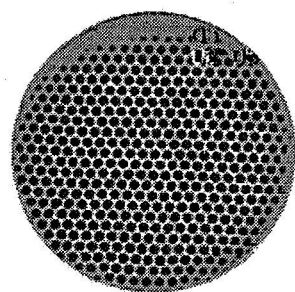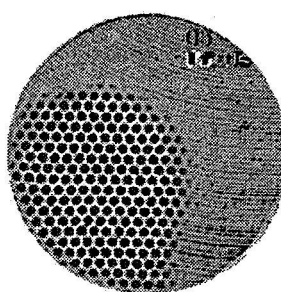
(a) $M = 78.25$ (b) $M = 77.75$
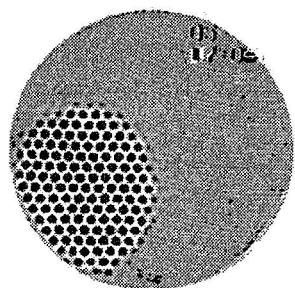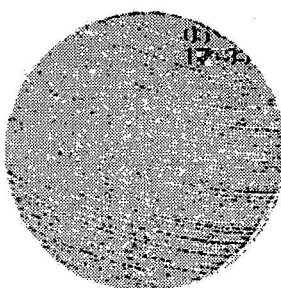
(c) $M = 77.50$ (d) $M = 77.30$

Figure 3: Hexagonal convection persists at values of M below onset, indicating a hysteretic transition (compare to Figure 2).
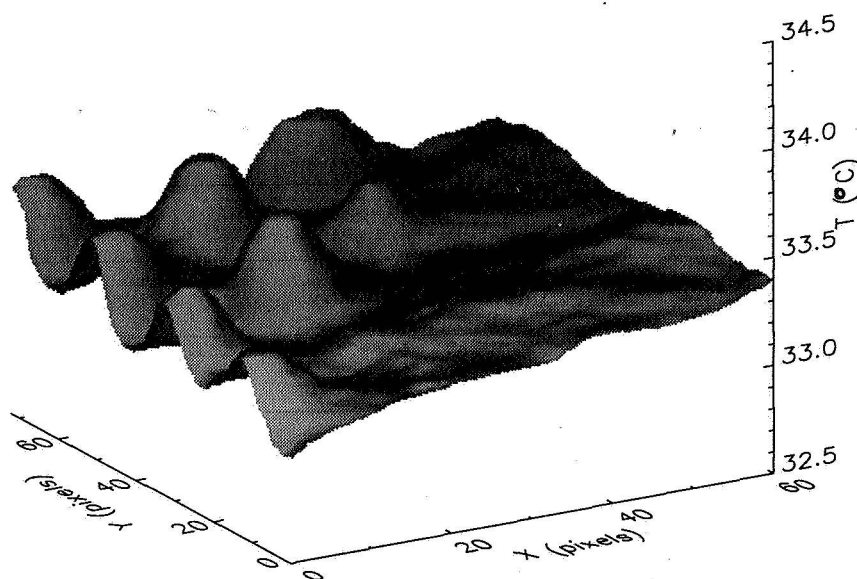
Figure 4: Fluid surface temperature measured near onset by infrared imaging.

EXPERIMENTAL INVESTIGATION OF THE MARANGONI EFFECT
ON THE STABILITY OF A DOUBLE-DIFFUSIVE LAYER

Josef Tanny and Chuan F. Chen
Department of Aerospace and Mechanical Engineering
The University of Arizona
Tucson, Arizona 85721

ABSTRACT

Stability experiments were carried out in a 4-cm-thick, salt-stratified fluid layer by heating from below and cooling from above. The bottom boundary was rigid while the top was either free or rigid. The initial solute Rayleigh number varied from 2.5×10^6 to 4.6×10^7. For the rigid-free case, at initial solute Rayleigh numbers $R_S > 5.4 \times 10^6$, thermal Marangoni instabilities were observed to onset along the free surface at a relatively low thermal Rayleigh number, R_T. The convection was very weak, and it had almost no effect on the concentration and temperature distributions. Double-diffusive instabilities along the top free surface were observed to onset at a higher R_T with much stronger convection causing changes in the concentration and temperature distributions near the top. At a yet higher R_T, double-diffusive convection was observed to onset along the bottom boundary. Fluid motion in the layer then evolved into fully developed thermal convection of a homogeneous fluid without any further increase in the imposed ΔT. For layers with $R_S < 5.4 \times 10^6$, Marangoni and double-diffusive instabilities onset simultaneously along the free surface first, while double-diffusive instabilities along the bottom wall onset at a higher R_T.

INTRODUCTION

The low-gravity environment in a space shuttle or a space station provides a unique opportunity to carry out experiments to study the interactions of surface tension and double-diffusive effects on the onset of instability and subsequent motion in a fluid layer. This problem not only has practical applications in materials processing in space, but also is of fundamental interest in understanding the behavior of fluids in response to the simultaneous inputs of stabilizing or destabilizing effects of surface and body forces.

When an alloy melt is solidified directionally by cooling from the bottom of the mold and the heavier element is preferentially crystallized out at the liquidus temperature, there is a region of vigorous finger convection above the mushy zone [see, for example, Chen and Chen (1991)]. Salt-finger convection is the result of a double-diffusive instability caused by the adverse density gradient generated by the slower diffusing component in the solution. It is easily demonstrated that using the property values of a lead-tin alloy as given by Coriell et al. (1980) and assuming a concentration difference of 0.5 wt% across a fluid layer depth of 1 cm, such convection will exist at 10^{-4} g_0, where g_0 is the gravitational acceleration at sea level. Such gravity levels were measured on board Skylab and shuttle missions at quiet times (Chassay and Schwaniger 1986). When a free surface is present, either due to shrinkage or an open mold, forces due to surface tension gradients become important and must be accounted for. The interactions between surface tension and double-diffusive effects may exacerbate or ameliorate the instability characteristics of the fluid layer. This will, in turn, affect the convection in the melt, which ultimately affects the quality of the casting.

The effect of surface tension on a fluid layer being heated from below was first studied by Nield (1964). Davis and Homsy (1980) generalized the problem to include the effect of a deformable free surface. McTaggart (1983) studied the stability of a layer with respect to surface tension effects when both temperature and concentration gradients are present in the layer. The layer is assumed to be in a zero-gravity environment. Recently, Chen and Su (1992) and Chen and Chen (1993) considered the combined Marangoni and double-diffusive instability problem including the effects of cross diffusion.

The effect of surface tension on the stability of a double-diffusive fluid was studied experimentally by Chen (1991). We have extended the investigation by conducting experiments over a range of initial solute Rayleigh numbers and by using an improved instrumentation and flow visualization technique. The results reported herein

not only provide a better understanding of the instability phenomenon but also will serve as a benchmark for the numerical simulation program based on the boundary element method currently under development.

EXPERIMENTAL APPARATUS AND PROCEDURES

The experiments were conducted in a rectangular test tank with inner dimensions of 24 × 12 × 5 cm high. The sidewalls of the tank were made of optical glass to facilitate Schlieren flow visualization. The top and bottom constant-temperature walls were made of stainless steel. In some of the experiments with the free surface, a brass top wall was used. In all cases, the removable top wall was provided with passages through which fluid from a constant-temperature bath could circulate. The tank was placed above an aluminum heat transfer plate, which was kept at a constant temperature by another constant-temperature bath. An RdF microfoil heat flux sensor with dimensions of 4 × 1.5 × 0.15 cm thick was placed between the stainless steel bottom and the plate. In order to minimize contact resistances, a thermal joint compound was applied to all contact surfaces. Thermocouples were embedded in the top and bottom walls near the inside surfaces. Their output was linearized and recorded using a data logger. The top and bottom walls were insulated with 5-cm-thick Styrofoam. The sidewalls were not insulated in order to allow for continuous flow visualization during the experiment. This did not seem to influence the results because the temperature differences attained were usually small (not more than 5°C above or below room temperature).

Vertical concentration and temperature profiles were measured by a dual probe consisting of a four-electrode micro-scale conductivity instrument (MSCI) and a thermocouple. The sensor of the MSCI and the thermocouple junction were located at the same vertical level, at a horizontal distance of 0.3 cm. The combined probe was traversed vertically through the stratified fluid at a constant speed of about 0.11 mm/sec, recording the conductivity and temperature each 10 seconds, which resulted in about 40 data points over the layer depth. Data were always recorded while the probe was traversed downward, with the two sensors ahead of the probe holder in order to minimize any disturbances at the measured region. The MSCI was calibrated before and after each experiment against six solutions of known concentration. For experiments with aqueous solutions of NaCl, the output voltage of the MSCI was translated into concentration using the local measured temperature and the relations given by Head (1983).

The convective motions were visualized using the Schlieren technique. The Schlieren system consisted of two spherical mirrors, 15.24 cm (6 inches) in diameter and 152.4 cm in focal length, a white light source, and a knife edge. The system was set up such that the circular parallel beam was passed horizontally through the mid-section of the tank, visualizing an approximately 16-cm section out of a total length of 24 cm. The output of the Schlieren system was imaged by a CCD camera and was displayed on a monitor and also recorded by time-lapse VCR for later reviewing.

In all experiments, the depth of the salt-stratified fluid layer was 4 cm. Stratification was obtained by filling the tank with eight layers of salt (NaCl) solution of equal thickness (0.5 cm) but with decreasing concentration. The filled tank was let stand for 2 hr. A one-dimensional time-dependent numerical calculation predicted that the eight-layer structure would become smooth by molecular diffusion within this time period; this was verified by the concentration profile measurement. During the 2-hr waiting period, the stratified fluid was brought to a uniform temperature by applying equal temperatures at the top and bottom walls.

The experiment was started by increasing the bottom wall temperature by 0.5°C and decreasing the top wall temperature by 0.5°C, thus imposing a temperature difference of 1°C across the layer. This temperature change was allowed to diffuse across the layer over a period of 50 min, the thermal diffusion time for a 2-cm-thick water layer. Then, an additional change of 1°C was imposed across the layer, and so on. In the experiments with a free surface, the top wall was placed 0.9 cm above the free surface and, because of the air gap, its temperature had to be reduced much more than 0.5°C for each adjustment. It was found by trial and error that a temperature reduction of 1.5°C was needed to reduce the free fluid surface temperature by 0.5°C. The vertical profiles of concentration and temperature were always measured before each temperature adjustment, when the system was in a quasi-steady state.

The temperature gradient was increased until double-diffusive instability plumes were observed at the bottom and top walls. In those experiments where instability started near one wall before the other, the temperature gradient was further increased until both the top and bottom regions became unstable. At this slightly supercritical condition, the system was allowed to stand for a few hours until a state of turbulent thermal convection across the layer was established.

RESULTS AND DISCUSSION

In this section, we first present the results of two experiments with the same initial stratification but with different boundary conditions in order to illustrate the effect of Marangoni instability on the stability characteristics of a double-diffusive layer. Experiment 18 was carried out with rigid-rigid (R-R) conditions, and experiment 30 was carried out with rigid-free (R-F) conditions. The initial salinity gradient was nominally the same, with the first 0.5 cm layer at 2.7 wt% and the top layer at 2.0 wt%. A series of six concentration profiles for both experiments are shown in Fig. 1 in order to illustrate the different phases of instability.

At t = 120 min after the filling of the test tank, the concentration profiles of isothermal fluid layers in the R-R (left) and R-F (right) cases are shown in Fig. 1a. The two profiles are essentially the same. The initial solute Rayleigh numbers, R_S, are 1.98×10^7 and 1.88×10^7, respectively. At t = 220 min, after two adjustments of ΔT, with the thermal Rayleigh number $R_T = 1.47 \times 10^6$ (Fig. 1b), Marangoni instability in the R-F case became observable in the Schlieren picture. We denote this critical thermal Rayleigh number by R_{T1}. The Marangoni convection cells appeared as short, vertical dark shadows, more or less equally spaced along the free surface. These are indicated in the sketch below the concentration profiles. The Marangoni convection was confined to the neighborhood of the free surface because of the stable density gradient in the fluid layer. The concentration of the fluid became uniform within a layer of 0.4 cm thickness below the free surface due to the convective mixing (Fig. 1b).

At t = 320 min and $R_T = 3.37 \times 10^6$, double-diffusive convection in the form of plumes (Shirtcliffe 1969) started near the free surface where the stabilizing salinity gradient was weakened by Marangoni convection. This critical Rayleigh number is denoted by R_{T2}. These plumes penetrated much deeper into the fluid, and the mixed layer extended down to approximately 0.8 cm (Fig. 1c). The upper mixed layer continued to deepen as ΔT was increased, and Marangoni convection cells disappeared as double-diffusive cells strengthened. At t = 370 min and $R_T = 4.03 \times 10^6$, it reached down to 1.3 cm (Fig. 1d). At t = 470, when R_T reached 4.97×10^6 (Fig. 1e), double-diffusive convection started at the bottom wall, which was clearly indicated by the concentration profile. This critical Rayleigh number is denoted by R_{T3}. At this time, the concentration profile in the R-R case was still evolving by diffusion. At t = 500-510 min (Fig. 1f), double-diffusive convection occurred both at the top and the bottom walls in the R-R case at $R_T = 6.96 \times 10^6$. In the terminology developed so far, for the R-R case, there is no R_{T1} and R_{T2} and R_{T3} approach each other. We denote this transition by $R_{T2,3} = 6.9 \times 10^6$. At that time, in the R-F case, the convection in both layers was well developed and the R_T actually decreased to 4.76×10^6 due to the slight drop in ΔT because of the four-fold increase in heat flux from the conductive state to the fully convective stage.

A total of thirteen experiments were conducted, seven of these were with rigid-free conditions and six with rigid-rigid conditions. Data from these experiments are shown in Fig. 2, in which the critical thermal Rayleigh number is shown as a function of the solute Rayleigh number. The initial solute Rayleigh number varied from 2.5×10^6 to 4.6×10^7. For the R-F cases, when $R_S > 5.4 \times 10^6$, the sequence of events is similar to what we described above: there are three distinct thermal Rayleigh numbers, R_{T1} (denoted by crosses), R_{T2} (denoted by filled squares), and R_{T3} (denoted by filled circles). But, for the two experiments with initial $R_S < 5.4 \times 10^6$, onset of Marangoni and double-diffusive instability at the top occurred simultaneously, thus $R_{T1} = R_{T2}$. For the R-R case, in general, double-diffusive instability at the bottom (denoted by open circles) and at the top (denoted by open squares) occurred at the same thermal Rayleigh number, $R_{T2} = R_{T3} = R_{T2,3}$. In this case, there is no R_{T1}. It is seen that due to the thermal Marangoni effect, the fluid layer with the R-F condition is less stable than that with the R-R condition.

, Straight lines were fitted through the data points by the least squares method. For the R-F cases with $R_S > 5.4 \times 10^6$, R_{T1} is nearly a horizontal line:

$$R_{T1} = 5.012 \times 10^5 \, R_s^{0.07} \qquad 5.4 \times 10^6 < R_s < 4.6 \times 10^7$$

while R_{T2} and $R_{T3} \propto R_s^{0.771}$ and $R_s^{0.7}$, respectively:

$$\left.\begin{array}{l} R_{T2} = 10.695 \times R_s^{0.771} \\[2mm] R_{T3} = 54.828 \times R_s^{0.7} \end{array}\right\} \qquad 2.5 \times 10^6 < R_s < 4.6 \times 10^7$$

For the R-R case, double-diffusive convection onsets simultaneously along the bottom and top walls, with one exception. A straight line correlation yields the following:

$$R_{T2,3} = 116.95 \, R_s^{0.664}$$

The full line denotes the theoretical onset condition for double-diffusive convection in a layer with linear gradients and stress-free boundaries, $R_{T2,3} \propto R_s$ (Turner 1973).

CONCLUSIONS

1. For a double-diffusive layer with a free surface, at high initial solute Rayleigh numbers ($R_s > 5.4 \times 10^6$), the first instability to occur is the Marangoni instability at the free surface. At successively higher thermal Rayleigh numbers, double-diffusive instability first appears at the free surface, then at the bottom rigid surface.

2. At lower initial solute Rayleigh numbers ($R_s < 5.4 \times 10^6$), Marangoni and double-diffusive instabilities occur simultaneously at the free surface. Double-diffusive instability appears at the bottom rigid boundary at a higher thermal Rayleigh number.

3. Although the Marangoni convection at the free surface is not strong enough to affect the concentration and temperature distributions, it contributes substantially to the reduction in the critical thermal Rayleigh number for the onset of double-diffusive convection, both at the top and the bottom of the layer.

ACKNOWLEDGEMENTS

REFERENCES

Chassay, R. P. and Schwaniger, A. J., 1986, NASA TM-86585.
Chen, C. F., 1991, Microgravity Sci. and Tech., 4, 108-109.
Chen, C. F. and Chen, C. C., 1993, Phys. Fluids, 6, 1482-1490.
Chen, C. F. and Chen, F., 1991, J. Fluid Mech., 227, 567-586.
Chen, C. F. and Su, T. F., 1992, Phys. Fluids A, 11, 2360-2367.
Coriell, S. R., Cordes, M. R., Boettinger, W. J., and Sekerka, R. F., 1980, J. Cryst. Growth, 49, 13-28.
Davis, S. H. and Homsy, G. M., 1980, J. Fluid Mech., 98, 527-553.
Head, M. J., 1983, Ph.D. Thesis, University of California, San Diego.
McTaggart, C. A., 1983, J. Fluid Mech., 134, 301-310.
Nield, D. A., 1964, J. Fluid Mech., 19, 341-352.
Shirtcliffe, T. G. L., 1969, J. Fluid Mech., 35, 677-688.
Turner, J. S., 1973, Buoyancy Effects in Fluids, Cambridge University Press, p. 255.
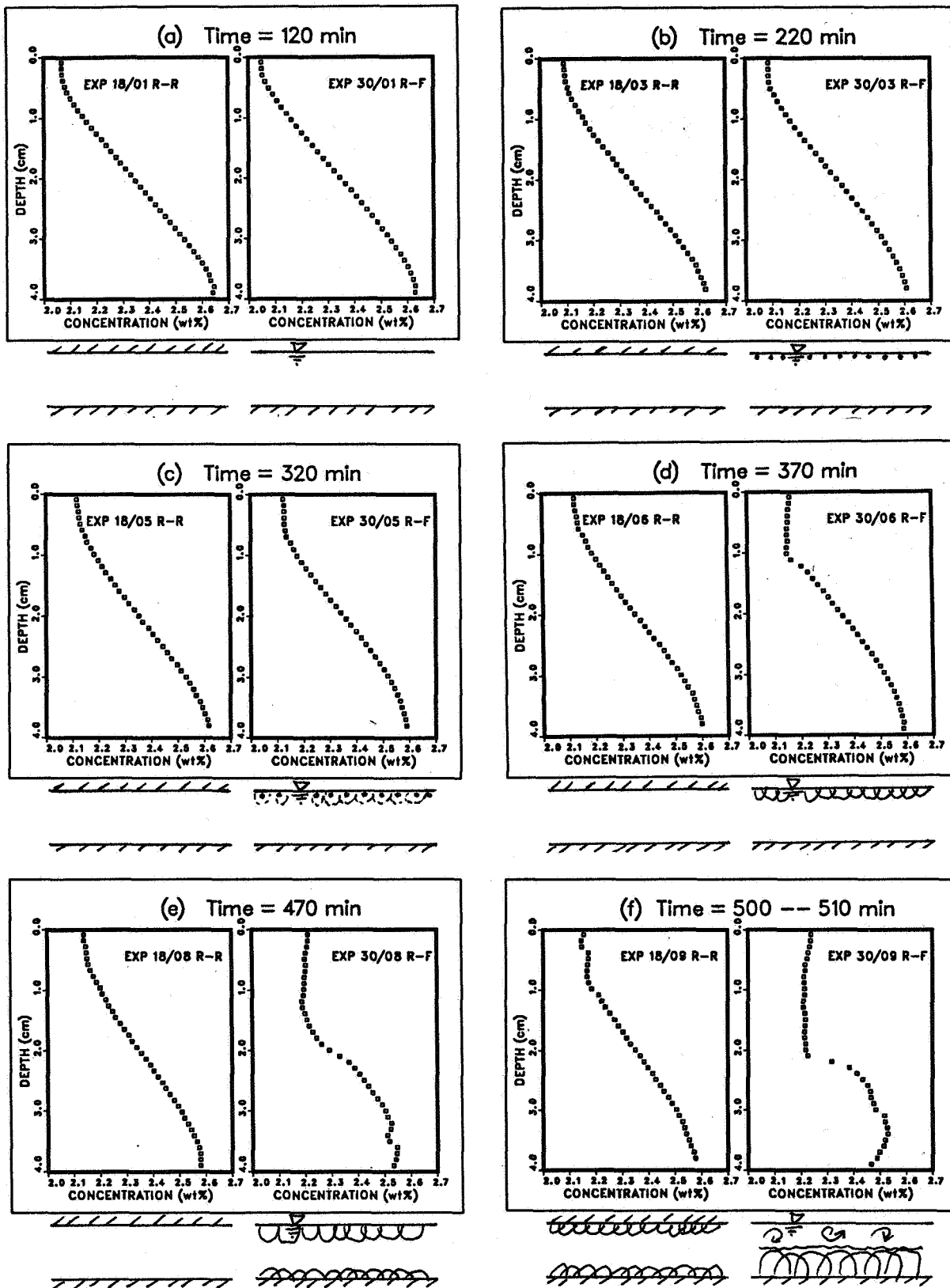
Fig. 1. Evolution of concentration profile for the R-R case (left) and the R-F case (right) as R_T is increased. Sketch below each graph illustrates the flow pattern observed.
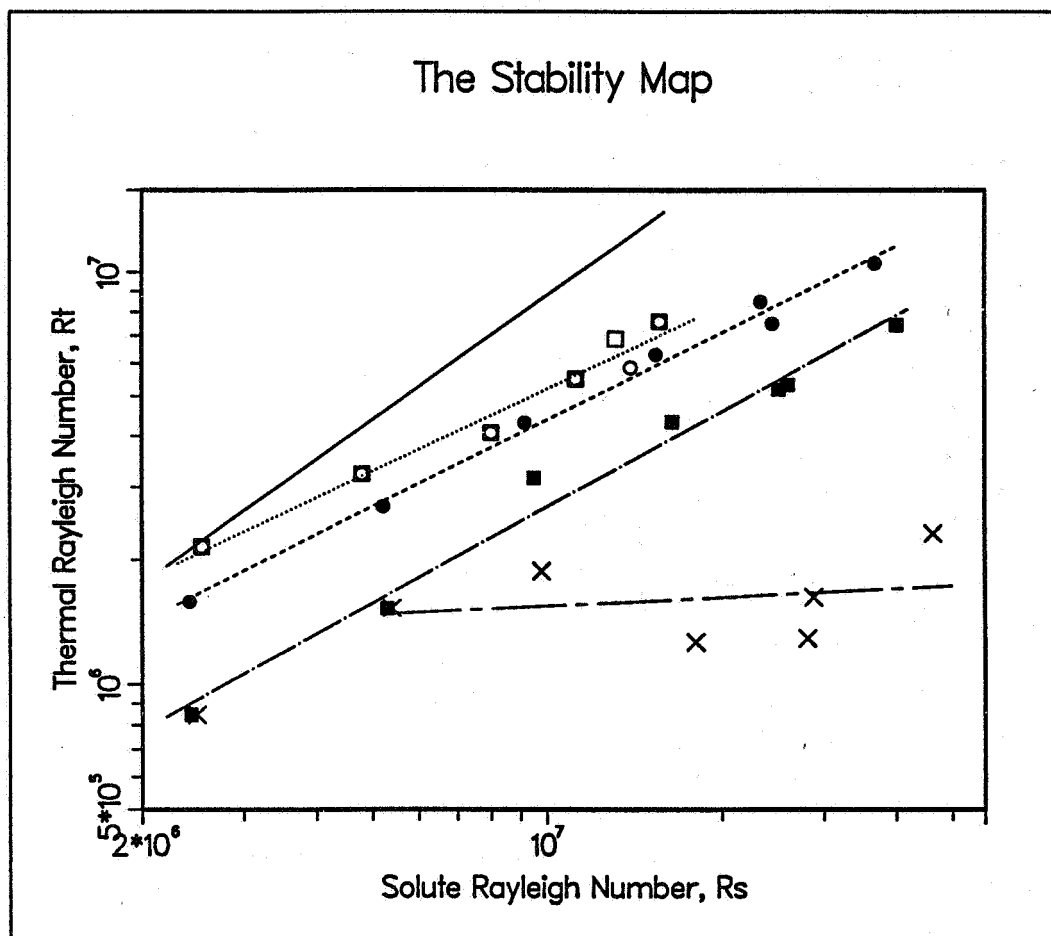
Fig. 2. The stability map. ✗ Marangoni instability; ■, ● double-diffusive instability at the top and the bottom, respectively, for the R-F case; □, O double-diffusive instability at the top and the bottom, respectively, for the R-R case; ——— theoretical result.

THERMOCAPILLARY CONVECTION IN FLOATING ZONES UNDER SIMULATED REDUCED-GRAVITY CONDITIONS

Y. Tao, B. Xiong and S. Kou
Department of Materials Science and Engineering
University of Wisconsin
Madison, WI 53706

ABSTRACT

The present study demonstrated that calculated thermocapillary convection in a non-cylindrical floating zone can now be compared with measured one, by considering the lens effect of the floating zone. Flow visualization and computer simulation of thermocapillary convection in a silicone oil zone and a molten zone in an $NaNO_3$ rod were conducted. The calculated results agree very well with the measured ones, including the free surface shapes, the solid/melt interface shapes and the velocity fields.

INTRODUCTION

Thermocapillary convection becomes significantly more important as gravity and hence gravity-induced natural convection are reduced. Flow visualization has been widely used to study thermocapillary convection in floating zones. In ground-based experiments simulating the reduced-gravity condition the floating zones, though dominated by thermocapillary convection, are often non-cylindrical in shape. In flight experiments the floating zones have to be non-cylindrical in shape, if the significant effect of the free-surface shape on thermocapillary convection is to be studied. The optical distortions due to the lens effect of these non-cylindrical floating zones prevent the visualized results from being used to verify the calculated ones or from being interpreted properly. Recently, equations have been derived to quantitatively describe such a lens effect [1]. The objective of the present study is to demonstrate that measured and calculated velocity fields can now be compared quantitatively by considering the lens effect.

In the present study flow visualization and computer simulation are conducted in a silicone oil zone and a molten zone of $NaNO_3$. The calculated and measured results are compared to each other.

FLOW VISUALIZATION

A 5-centistoke silicone oil zone about 0.3 cm long was established between two 0.4 cm diameter Cu rods, the upper and lower rods being held constant at 37.9 and 27.9°C, respectively. A small zone length and diameter help insure that thermocapillary convection dominates over natural convection in ground-based experiments as in flight experiments.

A laser light-cut technique and fine aluminum tracer particles were used to reveal the flow pattern. A beam chopper, a high contrast film and a macrophoto system were used for photographing. The developed negative film was projected onto a large graph paper screen of 1 mm grid spacing, the floating zone covering an area of about 20 cm by 30 cm. The locations of the particle images were used to construct the velocity fields.

A molten zone was produced in a 0.4 cm diameter NaNO$_3$ rod in a vacuum chamber with the help of a Pt ring heater. The same light-cut technique was used for flow visualization.

In both cases, thermocapillary convection was steady and axisymmetric. No flow oscillation was observed.

COMPUTER SIMULATION

Convection in the floating zone is assumed to be at the steady state, laminar and axisymmetric. The governing equations, boundary conditions and method of solution are similar to those described elsewhere [2,3]. In brief, a control-volume finite difference method was used, with body-fitted general (non-orthogonal) curvilinear coordinates having variable grid spacing. The free surface is calculated based on the normal stress balance. The physical properties have been given elsewhere [2,3].

RESULTS AND DISCUSSION

In order to show what the flow pattern looks like, results from a similar oil zone reported in the previous year [3] are shown in Fig. 1. This comparison between the calculated and converted flow pattern (LHS) and the observed one (RHS) is believed to be the first one for a non-cylindrical zone.

The measured velocity field in the present silicone oil zone is shown on the LHS of Fig. 2a. It is interpolated and shown on the RHS of the same figure, only on some (not all) grid points in order to be legible.

As shown in Fig. 3a, the calculated free surface shape agrees very well with the observed one. The grid mesh is shown on the LHS of Fig. 3b. The calculated velocity field is shown on the LHS of Fig. 2b on selected grid points. It is then converted, by considering the lens effect of the floating zone (refractive index n = 1.396), and shown on the RHS of the same figure. Due to the significant lens effect this conversion causes several layers of velocity vectors near the free surface to fuse together into a thin dark strip (deleted for clarity) along the free surface.

Figure 4 shows the calculated and measured velocity distributions along the grid lines shown on the RHS of Fig. 3b. As shown, the agreement is very good.

Similar results are shown in Figs. 5 and 6 for the NaNO3 molten zone. As shown, the agreement between the calculated and measured results is very good. Since the melt is about 10 pct lighter than the solid, the melt diameter is on the average larger than the solid diameter. Near the top of grid line (f), however, the calculated solid/melt interface appears somewhat higher than the observed one, thus causing the calculated local axial velocity to deviate significantly from the measured one. More detailed discussion will be given elsewhere [4].

FUTURE PLANS

An image analysis system, consisting of a PC, a frame grabber, a CCD camera and a particle tracking software, will be set up to automatically generate the measured velocity fields.

REFERENCES

1.   C. W. Lan and S. Kou, J. Crystal Growth 132 (1993) 471.
2.   C. W. Lan and S. Kou, J. Crystal Growth 108 (1991) 351.
3.   T. Tao, R. Sakidja and S. Kou, Int. J. Heat Mass Transfer, in press.
4.   T. Tao, B. Xiong and S. Kou, manuscripts in preparation.
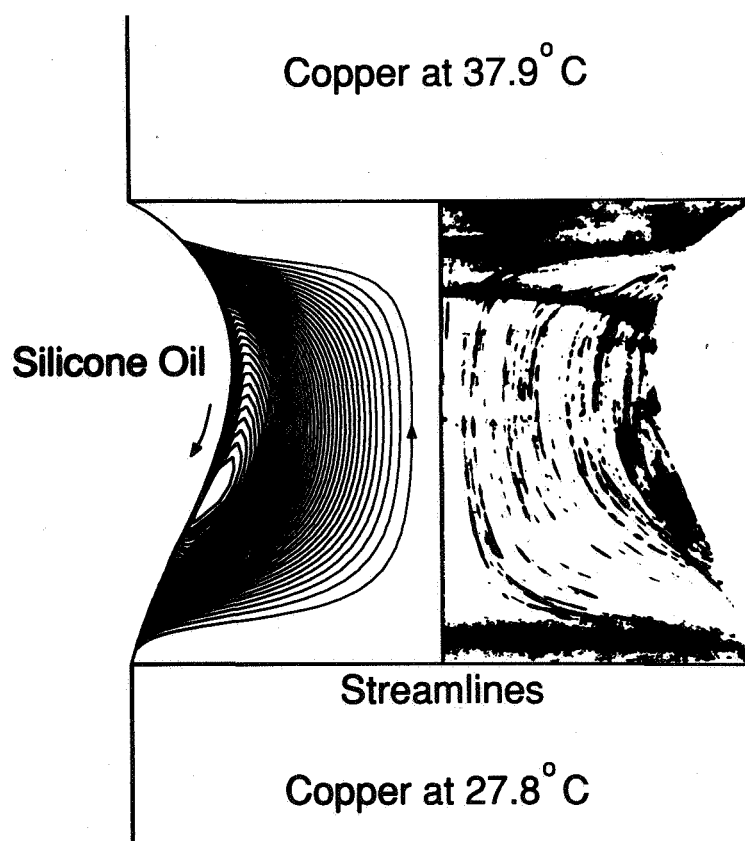
Fig. 1 Calculated and converted streamlines (LHS) and observed flow pattern (RHS) in a silicone oil zone[3].
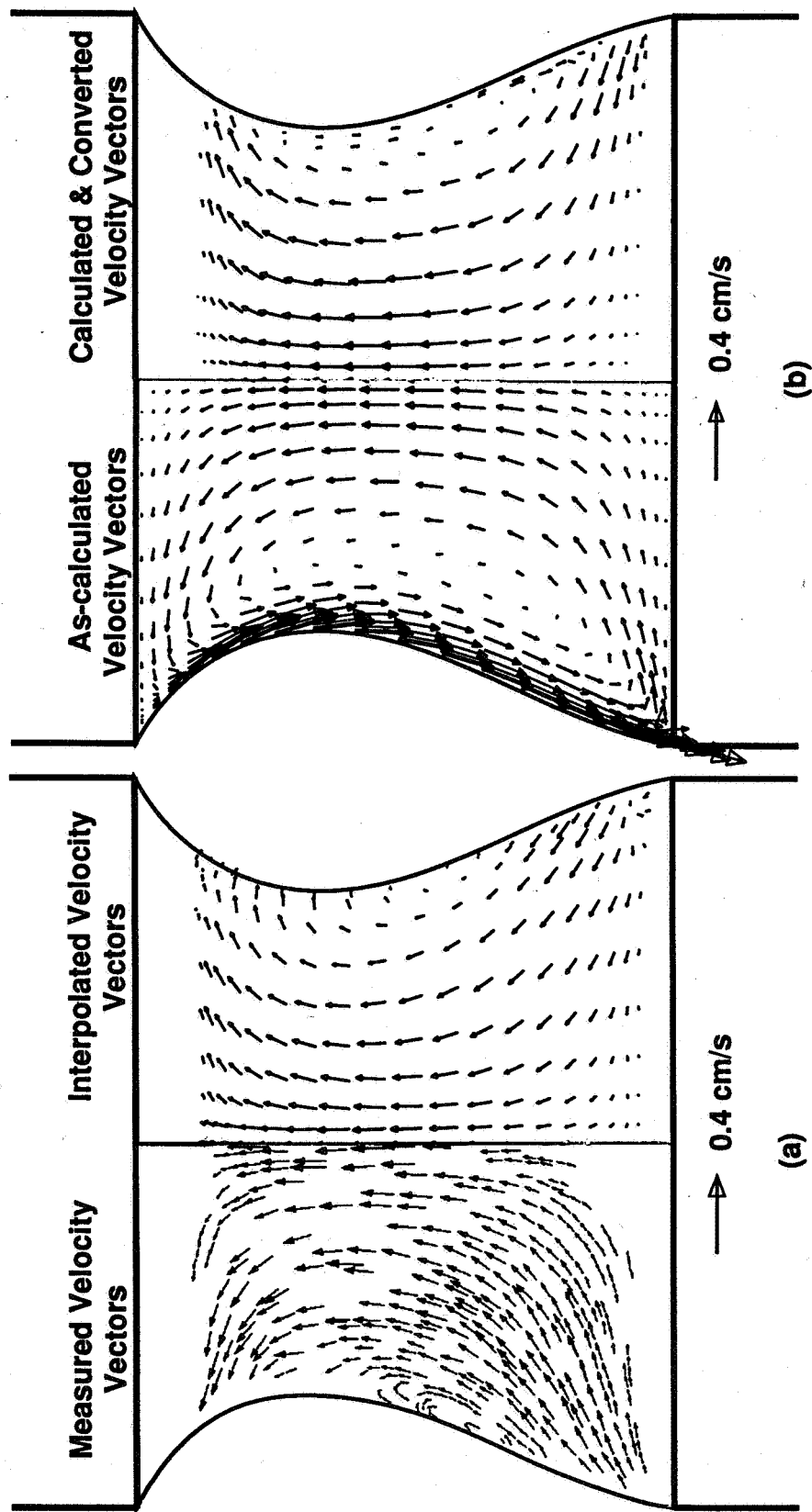
Fig. 2 Velocity vectors in silicone oil zone; (a) measured; (b) calculated
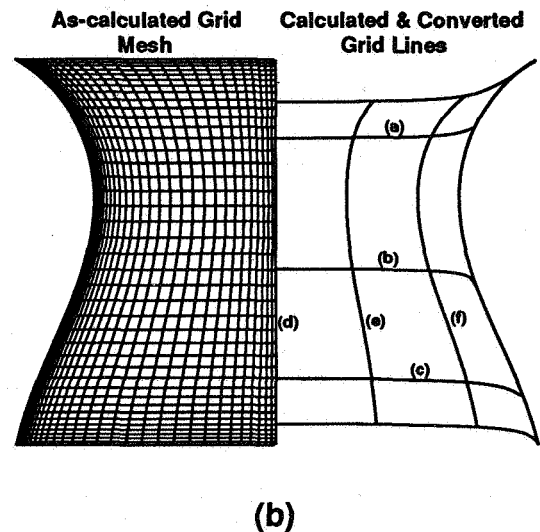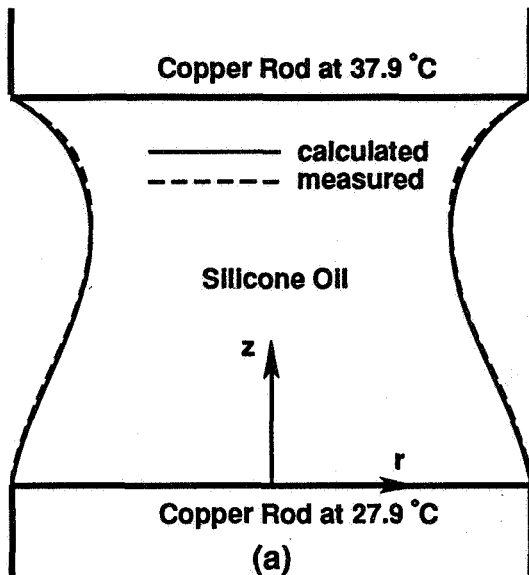
Fig. 3 Silicone oil zone: (a) calculated and measured free surfaces;
(b) grid mesh and lines.
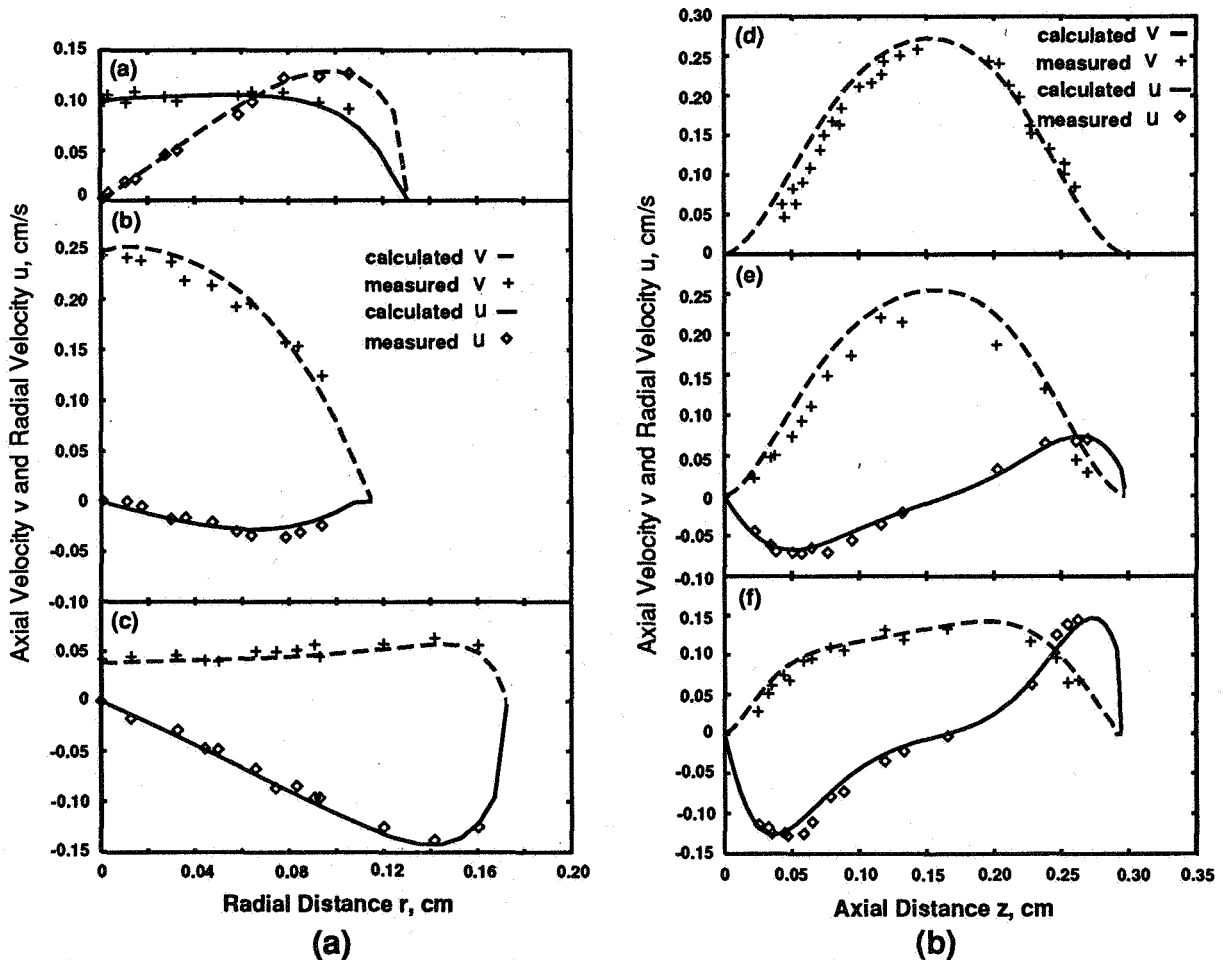
Fig. 4 Comparison between calculated and measured velocity vectors: (a) along lines
(a), (b) and (c) in Fig. 2; (b) along lines (d), (e) and(f).
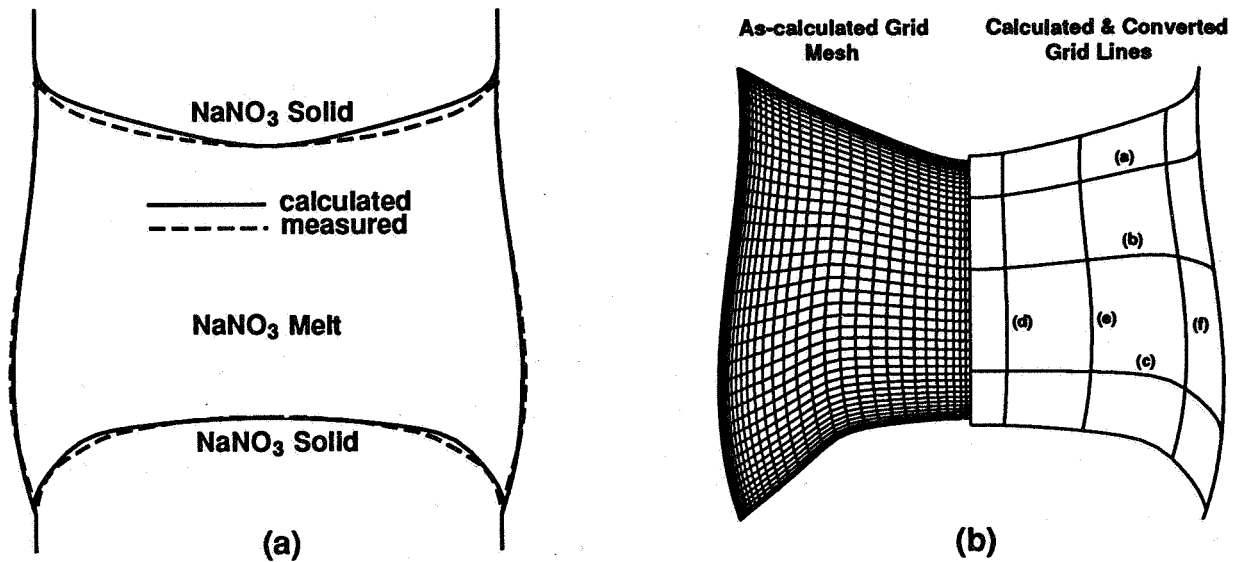
Fig. 5 NaNO$_3$ molten zone: (a) calculated and measured free surfaces; (b) grid mesh and lines.
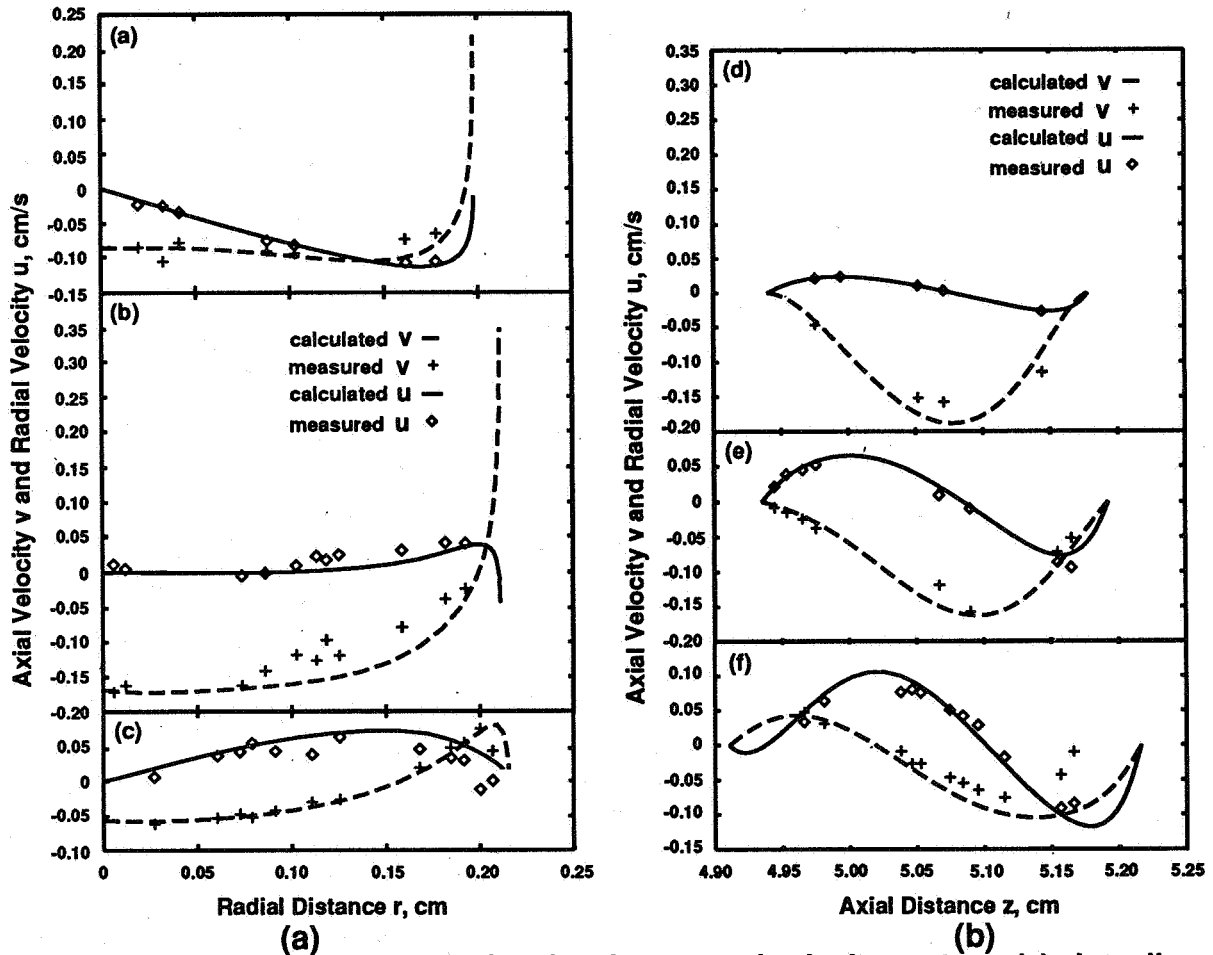
Fig. 6 Comparison between calculated and measured velocity vectors: (a) along lines (a), (b) and (c) in Fig. 4; (b) along lines (d), (e) and (f).

THE BEHAVIOR OF UNSTEADY THERMOCAPILLARY FLOWS

David R. Vrane and Marc K. Smith
The George W. Woodruff School of Mechanical Engineering
Georgia Institute of Technology
Atlanta, Georgia

ABSTRACT

The thermocapillary-driven flow of a liquid in a shallow slot provides a simple model to explore the effects of free-surface deflection and end walls on the stability of the flow. Such an investigation may be useful in understanding the complex flow seen in processes such as the float-zone refining of single crystals. A linear stability analysis of the viscously-dominated slot flow indicates stable basic states to both two- and three-dimensional infinitesimal disturbances for capillary numbers below 43.3. Above this capillary number steady solutions do not exist. We also discuss current work involving the development of an inertially-dominated slot-flow model using singular perturbation methods. If these flows are unstable, inertial effects would be the only possible cause of the instability.

INTRODUCTION

Thermocapillary flows are driven by temperature-induced surface tension gradients at the interface between two immiscible fluids. For most liquids, the surface tension decreases with increasing temperature. Thus, when the interface experiences a positive temperature gradient the bulk fluids on each side of the interface must balance an effective negative shear stress. Through this mechanism, the thermal fields in the fluids are coupled to the velocity fields.

One important process in which thermocapillary flows are seen is the float-zone processing of crystalline materials. Here, an amorphous rod of semiconducting material passes through a ring heater producing a local melt-zone along the rod. Ideally, as the material travels past the heater, the leading portion of the molten material solidifies and forms a single, uniform crystal. However, since the conditions at the freezing end of the zone dictate the uniformity of the material, the presence of unsteady thermocapillary flows in the melt-zone can compromise crystal quality.

The present work describes the first two of a series of analytical models designed to isolate the mechanisms that cause thermocapillary-driven flows in finite regimes, such as the float zone, to become time dependent. The basic model, originally investigated by Sen and Davis (1), is the flow in a single liquid layer bounded by two end walls. This geometry is also called the flow in a shallow slot. Sen and Davis (1) provided a steady, asymptotic solution (small depth to width ratios) for a viscously-dominated flow in the slot with first-order surface deflections. Sen (2) extended this analysis to leading-order surface deflections. In our current work, we find that steady solutions for the flow are only possible for capillary numbers below 43.3. A linear stability analysis shows that these steady solutions are stable to both two- and three-dimensional infinitesimal disturbances. In our second flow model, we consider an inertially-dominated flow in the slot in an effort to investigate the role of fluid inertia on the instability of the slot flow. Previous work by Smith and Davis (3) has shown that fluid inertia plays a significant role in the stability mechanism for long wavelength surface wave instabilities.

ANALYSIS

In the earlier work of Sen and Davis (1) and Sen (2), hereafter referred to as SD and Sen respectively, the authors analyzed thermocapillary flows in a rectangular slot of aspect ratio A, defined as the depth of the fluid layer over the width of the slot, in the limit $A \rightarrow 0$. Their analyses

were based on the assumption that the Reynolds and Marangoni numbers were both $O(A)$. However, SD considered capillary numbers of $O(A^4)$ while Sen looked at capillary numbers of $O(A^3)$. The former scaling resulted in nearly parallel flows in the core matched to return flows in the end layers with only small corrections to the flat interface. The latter scaling produced nonparallel core flows with $O(1)$ surface deflections. The present work focuses on the stability of the results found in Sen, but will make frequent references to the derivations originally developed in SD.

Written in stream function form, the dynamics of the fluid within the cavity are described by the following dimensionless equations (see SD for notation):

$$
RA\left[\left(\psi_{yyt} + \psi_y\psi_{xyy} - \psi_x\psi_{yyy}\right) + A^2\left(\psi_{xxt} + \psi_y\psi_{xxx} - \psi_x\psi_{xxy}\right)\right]
$$
$$
= \psi_{yyyy} + 2A^2\psi_{xxyy} + A^4\psi_{xxxx}
$$
(1a)

$$
MA\left[T_t + \psi_yT_x - \psi_xT_y\right] = T_{yy} + A^2T_{xx}.
$$
(1b)

The dimensionless boundary conditions are given by

$x = \pm\frac{1}{2}$: $\psi_x = \psi_y = 0$, $T = \mp\frac{1}{2}$ (2a)

$y = 0$: $\psi_x = \psi_y = 0$, $T_y = 0$ (2b)

$y = h(x,t)$: $h_t = -\psi_yh_x - \psi_x$ (2c)

$$
-p + 2A^2(1 + A^2h_x^2)^{-1}\left[\left(-\psi_{xy} - h_x\psi_{yy}\right) + A^2h_x\left(\psi_{yy} + h_x\psi_{xy}\right)\right]
$$
$$
= A^3C^{-1}h_{xx}(1 + A^2h_x^2)^{-3/2}(1 - A^{-1}CT)
$$
(2d)

$(1 - A^2h_x^2)(\psi_{yy} - A^2\psi_{xx}) - 4A^2h_x\psi_{xy} = -(1 + A^2h_x^2)^{1/2}(T_x + h_xT_y)$ (2e)

$(1 + A^2h_x^2)^{-1/2}(T_y - A^2h_xT_x) + L(T + x) = 0.$ (2f)

The constant-volume condition is given by

$$
\int_{-1/2}^{1/2} h(x,t)dx = 1,
$$
(3a)

and for steady flow, a zero mass-flux condition holds across the depth of the fluid

$$
\int_0^{h(x)} \psi_{oy}(x,y)dy = \psi_o(h(x)) - \psi_o(0) = 0.
$$
(3b)

Finally, for the case where the ends of the interface are of fixed height, we impose

$$
h\left(\pm\frac{1}{2}\right) = 1.
$$
(4)

For the viscously-dominated flow, Sen took $R = \overline{R}A$, $M = \overline{M}A$, and $C = \overline{C}A^3$, where the overbarred terms are all $O(1)$. In the limit $A \to 0$, the core flow was derived by expanding the dependent variables of the system in terms of an asymptotic series in A. Substituting these expansion into equations (1-4), and solving the leading-order system in terms of $h(x)$, Sen obtained the following approximations for the stream function and the interface position in the core

$$\psi_o(x,y) = \frac{1}{4}y^2\left[\frac{y}{h(x)} - 1\right] \tag{5}$$

$$h_o h_{oxxx} = -3\overline{C}/2. \tag{6}$$

At both end walls, the leading-order, inner systems required that the interface remain flat throughout the boundary-layers, making equation (6) valid across the entire slot and subject to the pinned-end conditions (4).

In the current work, equation (6) was solved using a Chebyshev pseudo-spectral method in conjunction with a Newton-Kantorovich iteration scheme. The results of these computations are shown in figure 1 for several values of the capillary number. Steady interface solutions were found in the range $0 \le \overline{C} \le 43.3$. For capillary numbers above this limit, the Newton-Kantorovich scheme failed to converge, perhaps indicating the existence of unsteady basic-states. Further investigation of this behavior near this limit and for even larger capillary numbers still remains to be done.

We determined the stability to three-dimensional small disturbances of this viscously-dominated system by perturbing the steady interface as follows

$$h(x,z,t) = H(x) + \hat{h}(x)e^{st+\alpha z}, \tag{7}$$

where $H(x)$ is the steady interface solution, $\hat{h}(x)$ is the disturbance mode shape, s is the disturbance growth rate, and α is the disturbance wave number transverse to the flow direction. Note that for two dimensional disturbances $\alpha = 0$. Substituting equation (7) into the stream function equation (5) and the three-dimensional form of the kinematic equation (2c), substituting equation (5), evaluated at the interface, into equation (2c), and then linearizing yields the general linearized disturbance interface equation

$$s\hat{h} = \frac{1}{2}\left(H_x + H\hat{h}_x\right) - \frac{H^2}{3\overline{C}}\left(3H_x(\hat{h}_{xxx} - \alpha^2\hat{h}_x) + H(\hat{h}_{xxxx} - 2\alpha^2\hat{h}_{xx} + \alpha^4\hat{h})\right), \tag{8}$$

subject to the conditions

$$x = \pm\tfrac{1}{2}: \quad \hat{h} = \hat{h}_{xxx} = 0 \tag{9a,b}$$

$$\int_{-1/2}^{1/2} \hat{h}(x,t)dx = 0. \tag{10}$$

Condition (9b) is the perturbation form of the zero volume flux condition (3b), which becomes restricted to the endwalls for unsteady flow.

The system of equations (8-10) presents an eigenvalue problem in s that was solved using a Chebyshev spectral method in combination with an IMSL eigenvalue routine. The results of these computations are shown in figure 2. Here, the most dangerous growth rate is plotted against its respective capillary number for various wave numbers. Note that all of the disturbance growth rates are negative for the viscously-dominated flow, signifying that the steady solutions of this flow model are always stable. In addition, for any capillary number, transverse disturbances have a stabilizing effect. Finally, it is interesting that for two-dimensional disturbances the growth rate approaches zero as the capillary number approaches the upper limit for the existence of steady-flow solutions.

Since the viscously-dominated slot is unconditionally stable to small disturbances, there will be no doubt as to the origin of resulting instabilities when new effects are added to the model. In our second model, we add the effect of fluid inertia. This addition is accomplished by changing the

Reynolds number scaling from $R = \overline{R}A$ to $R = \overline{R}A^{-1}$. Physically, this means that we have gone from considering an $O(1)$ Prandtl number fluid to an $O(A^2)$ Prandtl number fluid. Such a rescaling may provide a better approximation to the thermocapillary flows of low Prandtl number fluids such as liquid silicon. Substituting this scaling into equations (1) and (2) yields the following leading-order, core-flow system

$$R\left[\psi_{oyyt} + \psi_{oy}\psi_{oxyy} - \psi_{ox}\psi_{oyyy}\right] = \psi_{oyyyy} \tag{11a}$$

$$T_{oyy} = 0 \tag{11b}$$

$$y = 0: \quad \psi_{ox} = \psi_{oy} = 0, \; T_{oy} = 0 \tag{12a}$$

$$y = h_o(x,t): \quad h_{ot} = -\psi_{oy}h_{ox} - \psi_{ox} \tag{12b}$$

$$-p_o = \overline{C}^{-1}h_{oxx} \tag{12c}$$

$$\psi_{oyy} = -(T_{ox} + h_{ox}T_{oy}) \tag{12d}$$

$$T_{oy} + L(T_o + x) = 0. \tag{12e}$$

Clearly, the solution of this system will require a numerical approach, but it is still far simpler than the full Navier-Stokes equations. Fortunately, since the thermal field remains conduction-dominated to leading order, the inner conditions still require a flat interface in the end layers. Therefore, the leading-order outer solution may be obtained by solving for the interface position and stream function simultaneously subject to the additional conditions

$$\int_{-1/2}^{1/2} h_o(x,t)dx = 1 \tag{13a}$$

$$\int_0^{h(x)} \psi_{oy}(x,y)dy = \psi_o(h(x)) - \psi_o(0) = 0 \tag{13b}$$

$$h\left(\pm\tfrac{1}{2}\right) = 1. \tag{13c}$$

The numerical approach used to solve this system of equations will employ a double iteration scheme as follows. Using the leading-order solution provided by Sen as an initial guess, a spectral, Newton-Kantorovich scheme will be used to solve the nonlinear equation (11a) subject to conditions (12a, b, d) and (13b). This will provide an intermediate solution for the stream function. The intermediate solution will then be used to calculate the pressure field from the x-momentum equation. Once the pressure is known, condition (12c) may be integrated subject to conditions (13a, c) to give a corrected interface shape. This process is repeated until both the stream function and the interface shape converge to a solution.

FUTURE PLANS

Once the inertially-dominated flow has been computed and explored with regard to its stability, we wish to explore other effects that can be easily incorporated into this slot-flow model. These effects can be summarized with the following model problems.

(1) A flat, annular geometry in which the flow is in the radial direction and the transverse direction is periodic. In this model we shall explore the effect of the geometric deceleration of the flow as it moves radially outward from the center. The interface itself remains relatively flat for small capillary numbers. This geometry is also relevant to the space flight experiment of Ostrach (4).

(2) A vertical, annular geometry in which the flow is in the vertical direction and the transverse direction is periodic. With this model, we include the capillary pressure associated with the curvature of the interface in this cylindrical geometry. Such curvature has the potential to balance the stabilizing effect of surface tension seen in the original flat-slot model.

(3) A cylindrical geometry. Here, we let the inner wall of the annular geometry go to zero and obtain a long capillary bridge. This geometry is the most relevant to the float-zone geometry, but it still keeps the end effects as only a boundary condition on the flow in the core.

With these three model problems, we shall explore a variety of effects that can contribute to the instability of the thermocapillary flow. The advantage of using this succession of models is that the individual effects are included one at a time. This will allow an unambiguous study of their relative effect on the stability. Such a treatment may succeed in identifying the underlying mechanism of the thermocapillary instabilities seen in these systems.

In each model, we shall consider a viscously-dominated and an inertially-dominated flow field. Once the numerical codes are developed to handle the inertial problem in the original flat-slot geometry, the inclusion of the effects represented in the other models is relatively straightforward.

CONCLUSION

By constructing a series of models that successively includes more and more effects, this research will seek to clarify the roles of both fluid inertia and flow geometry in contributing to the nature of the instabilities seen in thermocapillary flows. The viscously- and inertially-dominated slot models addressed in this paper are just the first two models in this series.

We have found that the viscously-dominated flow in the flat-slot geometry has steady, two-dimensional solutions for capillary numbers less than 43.3, and that these solutions are stable to both two- and three-dimensional infinitesimal disturbances. The inertially-dominated flow problem has been posed and is now in the process of numerical code development.

ACKNOWLEDGMENTS

REFERENCES

1. Sen, A. K. and Davis, S. H., Steady thermocapillary flows in two-dimensional slots, J. Fluid Mech., 121, 1982, 163-186.

2. Sen, A. K., Thermocapillary convection in a rectangular cavity with a deformable interface, Phys. Fluids, 29, 1986, 3881-3883.

3. Smith, M. K. and Davis, S. H., Instabilities of dynamic thermocapillary liquid layers. Part 2. Surface-wave instabilities., J. Fluid Mech., 132, 1983, 145-162.

4. Ostrach, S., Surface Tension Driven Convection Experiment, NASA Tech. Mem. 4569, 1994, II-80-82.
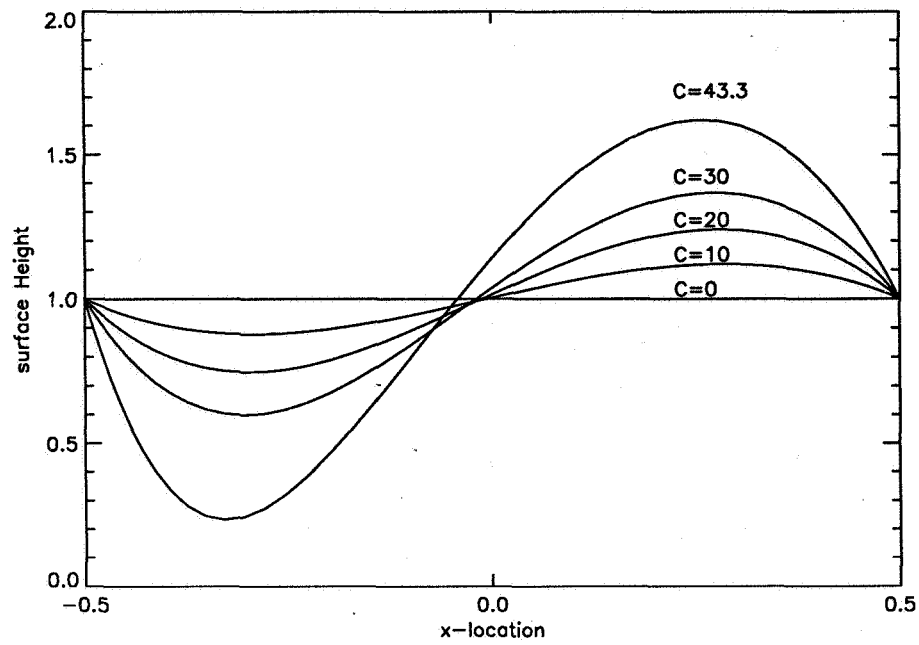
Figure 1 – The interface shape for various values of the scaled capillary number $\overline{C}$.
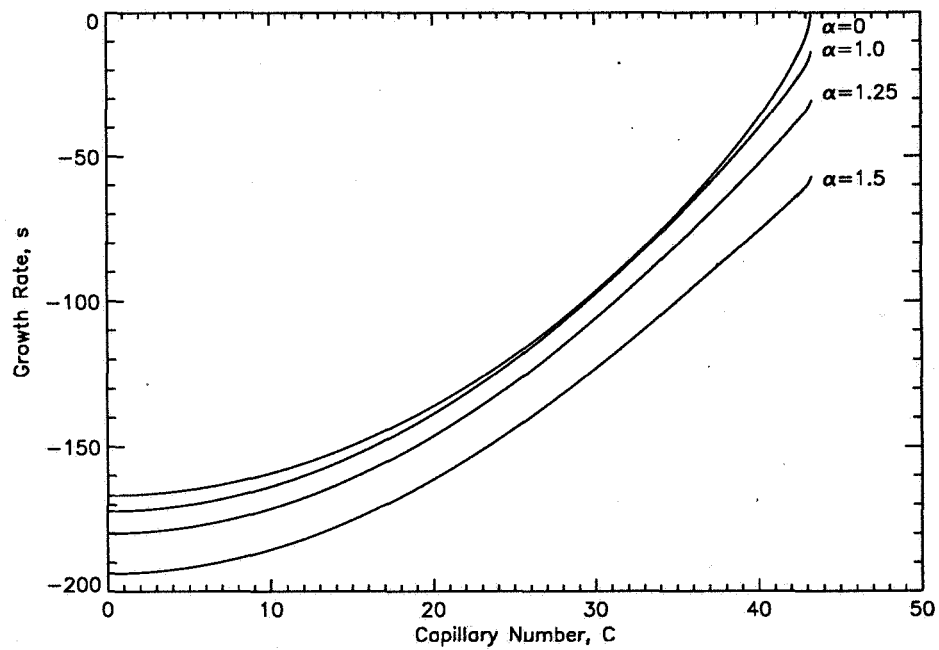
Figure 2 – The growth rate as a function of the scaled capillary number $\overline{C}$ for various values of the wave number α.

1995 117

324757

Oscillatory/Chaotic Thermocapillary Flow Induced by Radiant Heating

Kwang-Chung Hsieh, [†] Robert L. Thompson, and David Van Zandt [*]
NASA Lewis Research Center
Cleveland, OH 44135

Kenneth DeWitt, and Jon Nash
The University of Toledo
Toledo, OH 44606

Abstract

The objective of this paper is to conduct ground-based experiments to measure the onset conditions of oscillatory Marangoni flow in laser-heated silicone oil in a cylindrical container. For a single fluid, experimental data are presented using the aspect ratio and the dynamic Bond number. It is found that for a fixed aspect ratio, there seems to be an asymptotic limit of the dynamic Bond number beyond which no onset of flow oscillation could occur. Experimental results also suggested that there could be a lower limit of the aspect ratio below which there is no onset of oscillatory flow.

I. Introduction

Surface tension driven convection (STDC) and its instabilities have been a subject of great interest in recent years. The microgravity environment provided by the space shuttle allows detailed study of the flow phenomena without the interference of the effect of buoyancy forces. In terms of the relative direction between the temperature and the surface tension gradients, instability of STDC can be divided into two categories, namely the B'enard–Marangoni (BMI) and the Marangoni flow instabilities. The B'enard–Marangoni flow is established by a temperature gradient normal to a liquid-liquid or a liquid-gas interface (heated from the bottom of the container). Infinitesimally small disturbances grow and develop into a steady state flow pattern when the Marangoni number exceeds a critical value for the first transition. This is recognized as the famous B'enard cell[1] in a thin liquid layer. Higher transitions to oscillatory and chaotic flows are being studied but are still in the exploratory stage[2,3].

As opposed to the B'enard – Marangoni flow instability (BMI), Marangoni flow starts once there is a temperature gradient established along the free surface such that there is no first transition. For higher flow transition, a Hopf bifurcation similar to that in the BMI could exist in this configuration. Transition from steady state to oscillatory flow has been observed in experiments with various container geometries.[4,5,6] The possibility of further flow transition to the chaotic mode (second transition) at a higher Marangoni number (Ma) has not yet been well studied. Basically, two configurations have been adopted by various researchers to study the Marangoni flow instabilities. One is a floating zone and the other is an open-top container (square or cylindrical) filled with liquid. The floating zones are vertical liquid columns held between two cylindrical rods.

In the floating-zone configurations, Schwabe et al.[7] concluded that the oscillatory state of thermocapillary flow is a distortion of the laminar state in the form of a wave travelling in the azimuthal direction. Napolitano et al.[8] conducted float zone experiments on the Spacelab-D1 mission. This was the first microgravity experiment where large liquid bridges were produced, the largest being 6 cm in diameter and 8 cm in length. However, the oscillatory flow results were inconclusive. Vargas et al.[9] observed thermocapillary flow oscillations for hexadecone, Fluorinert, and methyl alcohol test fluids in a simulated float zone configuration. Critical temperature differences for the onset of oscillations and the resulting frequencies of oscillation were determined for several aspect ratios. It was found that the critical Marangoni number is not the proper dimensionless parameter to describe the onset of oscillation. It was also shown that the oscillation mechanism is not in the form of an azimuthal travelling wave. Instead, once the oscillation appeared, a pair of vortices grew and decayed alternately in a cross-sectional (vertical) plane. Based on the phase shifts of the thermocouples, Velten et al.[10,11] concluded that there are

---

three discernable spatiotemporal structures of oscillatory convection. These are azimuthal running waves, axial running waves with a symmetric wave front, and axial running waves with a deformed wave front. Chun[12] and Velten[10] both reported experimental results on time-dependent (oscillatory and turbulent) thermocapillary flow under microgravity and normal gravity conditions for simulated floating zone configurations. The latter stated that gravity had a more pronounced effect on the transition from oscillatory to turbulent flow.

Compared to the effort on float-zone configurations, fewer studies have been done on square or cylindrical container configurations. Lee[13] conducted a normal gravity experimental study in a modified two-dimensional square cavity. One side wall was heated and the other one was maintained at room temperature. It was found that beyond a critical temperature difference between the side walls, an oscillatory flow phenomenon occurred. The conclusion was made that the oscillatory flow was caused by a Kelvin-Helmholtz type instability in the shear layer. In contrast to the square container, thermocapillary flow in a cylindrical container was also studied by Lee[14] at normal gravity with a heating wire placed along the center axis. Oscillatory flow was observed in this configuration and it was concluded that the oscillation was caused by a coupling of the flow and the surface (capillary) waves.

Several models or mechanisms have been proposed to predict the onset of oscillations for "float-zone configurations". Chun's[15] proposed model is that oscillations start if the maximum steady state heat flux occurs at the zero axial temperature gradient location on the interface. The origin of the oscillatory Marangoni instability was identified as a travelling wave of temperature perturbations on the free surface around the circumference of the floating zone. According to this model, the critical Marangoni number for the onset of oscillatory flow depends only on the aspect ratio (regardless of the size of the floating zone) for a typical fluid. To better characterize the onset phenomenon, a model by Ostrach[16] states that there are two conditions to be satisfied in order for oscillations to begin. The first is that the critical Marangoni number must be exceeded and the second is that the critical value of the S-parameter (Capillary number/Prandtl number) must also be exceeded. Ostrach's model suggests that surface deformation (the S-parameter) plays a decisive role in the onset of oscillation.

In the present investigation, the flow configuration (shown in Fig. 1) is based on a cylindrical container filled with silicone oil. The temperature

gradient is established by directing a CO_2 laser on to the center of the free surface. The objectives of the present paper are to conduct ground-based experiments to measure the onset conditions of oscillatory flows, to formulate linear stability analysis to predict the onset conditions, and to characterize the onset of oscillatory thermocapillary flows using appropriate system parameters.

According to the previous research findings based on the floating zone configuration, for a typical fluid, the onset of flow oscillation can not be characterized by only one system parameter such as the aspect ratio (e.g., Chun's [15] model). To better characterize the onset conditions of flow oscillations, a modified dynamic Bond number (in addition to the aspect ratio) is proposed (Section IV) in this paper. It is assumed that gravity always plays a role in the Marangoni instability due to the buoyancy force and the influence on the surface deformation.

The modified dynamic Bond number (Bo_{md}) here is defined as

$$Bo_{md} \equiv \frac{Ra^{r_1}}{Ma} Ca^{r_2}$$
$$= (\frac{\rho g \beta \Delta T H^3}{\nu \alpha})^{r_1} (\frac{\gamma \Delta T R}{\mu \alpha})^{-1} (\frac{\gamma \Delta T}{\sigma})^{r_2} \quad (1)$$

where Ra is the Rayleigh number, Ca is the Capillary number, H is the liquid height, R is the chamber radius, σ is the surface tension between silicone oil and air, $\gamma = -\frac{d\sigma}{dT}$, ρ is the density, α is the thermal diffusivity, ν is the kinematic viscosity, β is the thermal expansion coefficient, g is the gravity level, and $\Delta T = \frac{Q}{2\pi H k}$. Q is the total laser power and k is the thermal conductivity of silicone oil. The definition of ΔT is obtained by equating the input laser power to the total heat loss to the cooling water through the side wall. It is noted that the liquid height is chosen as the length scale for the Rayleigh number. This is due to the fact that, at normal gravity conditions, stratified layers can be clearly observed when the liquid layer gets thicker (larger H). It is believed that the stratified layers tend to stabilize the flow and delay the onset of oscillations. Perhaps a more pronounced effect of buoyancy force on the onset of oscillations can be seen with the present definition of the Rayleigh number.

In order for Bo_{md} to be a system parameter, the total exponential power for ΔT has to be zero. Thus the ΔT_c (or Q_c, the critical laser power) only appears in the critical Marangoni number as an output of the experiment. The above condition results in $r_2 = 1 - r_1$. For a single fluid, if the ratio of the laser beam diameter to the chamber diameter (r_{lc}) is fixed, the only variables in the system

are the gravity level, the chamber diameter, and the chamber height (three degrees of freedom). When the dimensions (diameter and height) of the chamber are selected, experiments conducted at various gravity levels will determine r_1. According to the definition of Bo_{md},

$$Bo_{md} \propto g^{r_1} \cdot H^{3r_1-1}(\frac{H}{R})^{-1}$$

Ideally, one could fix the aspect ratio ($Ar \equiv \frac{H}{R}$) and vary the size of the container until same critical Marangoni numbers are found at normal and micro-gravity levels. If the Bo_{md} is the appropriate nondimensional number for characterizing the onset conditions of the oscillatory flows, the r_1 can be determined and experimental data will be well correlated.

Currently, since almost no microgravity experimental data are available, the data in this paper will be presented using $r_1 = 1$ for simplicity (i.e., $Bo_{md} = \frac{Ra}{Ma}$).

II. Experimental Apparatus and Procedure

The apparatus used for the present experiment is shown in Fig. 2. It consists of: a cylindrical copper test chamber which contains the test fluid (2 cs. silicone oil) and has an adjustable Teflon bottom; a CO_2 laser system which serve as the radiant energy source to establish a temperature gradient and thus a surface tension gradient on the fluid surface which causes fluid movement; a Ronchi imaging system focused on the the fluid surface to insure leveling of the surface; an infrared imager to measure the temperature distribution on the fluid surface; a controlled water bath to provide a constant chamber wall temperature; thermisters embedded in the test chamber to record the wall temperature; alaser power meter; and direct data acquisition hardware. The test apparatus was assembled on an automatically-leveling optical table in order to eliminate any vibrations.

All experiments were conducted with a Gaussian distribution of laser beam intensity directed normal to the fluid surface and a beam ratio (the ratio of the laser beam diameter to chamber diameter) equal to 0.2. The chamber wall temperature was kept constant at 20° C. The parameters that were varied in the experiments are the aspect ratio, defined as $Ar = \frac{H}{R}$, where H is the fluid height and R is the chamber radius; and the dynamic Bond number, which is the ratio of the Rayleigh number to the Marangoni number, and is defined as

$Bo_{md} = \frac{\rho g \beta H^3}{\gamma R}$. In the present experiments, there are five chambers of various diameters (0.5, 1.0, 1.2, 2.0, 3.0 cm). The bottom wall of the test chambers are adjustable to accommodate various aspect ratios. Tests were conducted for constant aspect ratio and constant dynamic Bond number cases. The test matrix is as follows:

Constant Ar Cases: 0.5, 0.67, 0.8, 1.0, 1.2, 1.5, 2.0

Constant Bo_{md} Cases: 0.17, 0.34, 0.7, 1.0, 2.0

The thermodynamic and transport properties for 2 cs. silicone oil are listed below.

$$\lambda = 0.109 \; \tfrac{W}{m \cdot K}; \quad \gamma = 8.5 \times 10^{-5} \; \tfrac{N}{m};$$
$$\nu = 2.0 \times 10^{-6} \; \tfrac{m^2}{s}; \quad \rho = 872 \; \tfrac{Kg}{m^3};$$
$$\alpha = 7.27 \times 10^{-8} \; \tfrac{m^2}{s}; \quad \beta = 1.17 \times 10^{-3} \; \tfrac{1}{K}$$

All of the electronic equipment was allowed to come to thermal equilibrium before the experiment were conducted. The laser was directed onto the fluid surface and a steady axisymmetric thermocapillary flow is developed. The laser power was then gradually increased in small increments until the flow became unstable and oscillatory. At the critical point for the onset of oscillatory motion, determined from the infrared image and/or the Ronchi imaging system, the laser power and the maximum temperature at the center of the fluid were measured. The experiment was then conducted starting from an oscillating fluid and the laser power was gradually decreased until oscillations ceased. Each test case was performed ten times and the average of these values was used to calculate the critical Marangoni number. Using the definition of ΔT in Eq. (1), the Marangoni number is defined as

$$Ma \equiv \frac{\gamma QR}{2\pi \mu \alpha k H} \qquad (2)$$

III. Modeling and Numerical Analysis

To fully understand the surface tension driven flow instability, a theoretical investigation has to be conducted in parallel with the experimental study. Such analytical or numerical solutions to the problem can provide more detailed information which could help analyze and explain the measured data.

All theoretical studies on the stability limit for STDC were based on the float-zone configuration. No formal investigations have been performed for the flow configuration used in the present study. In the category of linear stability study on a float zone, neutral curves for hydrothermal waves with an assumed velocity profile at the basic state have been

presented by Smith and Davis[17]. In the second part of the article,[18] they include the mechanism of free surface waves. However, their results are valid only for an infinite layer and do not compare well with experimental data. This is due to the fact that the effect of finite boundaries strongly alters the stability limit. To remedy this deficiency, Neitzel et al.[19] applied the energy-stability theory to investigate the stability properties of thermocapillary convection in a float zone. In their study, the flow velocity at the basic state is obtained by solving the Navier-Stokes equations for incompressible flow. The calculated critical Marangoni numbers as a function of aspect ratio are in resonable agreement with measured data[4], but the free surface deformation effect is not included. Lai et al.[20] have shown the importance of free surface deformation on the onset of oscillatory flow. They concluded that the time lag between velocity and temperature due to the surface deformation controls the onset of oscillation. However, their conclusion was drawn without any consideration of the effect of hydrodynamic instability. Hence, a stability analysis with a full account of hydrothermal waves and free surface waves in a finite domain is necessary to advance the understanding of the problem. A linear stability analysis is proposed in this section. The solutions for the basic state will be obtained using a numerical method by solving the Navier-Stokes equations with free surface deformation.

The evolution of disturbances in STDC is governed by the incompressible Navier-Stokes equations with the Boussinesq approximation:

$$\nabla \cdot \vec{V} = 0 \qquad (3)$$

$$\frac{\partial \vec{V}}{\partial t} + (\vec{V} \cdot \nabla)\vec{V} = -\frac{1}{\rho_o}\nabla p - \nabla \times \left[\nu(\nabla \times \vec{V})\right]$$
$$+ \nabla \left[2\nu\nabla \cdot \vec{V}\right] + \beta(T - T_o)\vec{g} \quad (4)$$

$$\frac{\partial T}{\partial t} + (\vec{V} \cdot \nabla)T = \nabla \cdot (\alpha\nabla T) + \frac{1}{\rho_o c_p}\left[\frac{\partial p}{\partial t} + (\vec{V} \cdot \nabla)p\right] \quad (5)$$

where $\vec{V}$ is the velocity vector, ρ_o is the density at a reference temperature T_o, p is the static pressure, T is the temperature, c_p is the specific heat at constant pressure, and $\vec{g}$ is the gravity vector.

In this paper, we formulate the incompressible stability problem in cylindrical coordinates for the present configuration. The total field can be decomposed into a mean value and a perturbation quantity:

$$\phi = \bar{\phi} + \phi' \quad \text{and} \quad \phi = (p, u, v, w, T)^T \qquad (6)$$

where u is the velocity component in the radial direction, v is the velocity component in the tangential direction, and w is the velocity component in the axial direction.

Following the linear theory, we assume that the disturbance vector ϕ for an instability wave with an azimuthal wave number m can be expressed as

$$\phi'_{(r,\theta,z,t)} = \Psi_{(r,z)}e^{im\theta - \lambda t} \qquad (7)$$

where λ is the eigenvalue of the system and Ψ is the "shape function" vector given by

$$\Psi = (\hat{p}, \hat{u}, \hat{v}, \hat{w}, \hat{T})^T \qquad (8)$$

It is noted that a harmonic solution is assumed in the θ direction with a wavenumber m. This is because in the ground-based experiment, the oscillatory flow exhibits standing-wave structure in the azimuthal direction. Based on this phenomenon, it is assumed that the onset of flow oscillations is mainly triggered by the growth of azimuthal disturbance. With the formulation in Eq. (7), the system of equations is reduced to a two-dimensional form and more efficient numerical calculations can be carried out. For linear stability analysis, a single disturbance mode (m) is considered.

Substituting Eq. (6) into Eqs. (3)-(5), subtracting the perturbation equation from the governing equations corresponding to the steady mean flow, linearizing the perturbation euation, and using Eqs. (8)-(9) give the following equations for the shape function

$$\hat{A}\frac{\partial \Psi}{\partial r} + \hat{C}\frac{\partial \Psi}{\partial z} + \hat{D}\Psi = V_{rr}\frac{\partial^2 \Psi}{\partial r^2} + V_{rz}\frac{\partial^2 \Psi}{\partial r\partial z} + V_{zz}\frac{\partial^2 \Psi}{\partial z^2}$$
$$(9)$$

where the vectors $\hat{A}$, $\hat{C}$, and $\hat{D}$ are defined as

$$\hat{A} \equiv A - imV_{r\theta}$$

$$\hat{C} \equiv B - imV_{z\theta}$$

$$D \equiv -\lambda\Gamma + D + imB + m^2V_{\theta\theta}$$

Matrices Γ, A, B, C, D, V_{rr}, $V_{r\theta}$, V_{rz}, $V_{\theta\theta}$, $V_{\theta z}$, and V_{zz} are Jacobians of the corresponding total flux vectors. For linearized perturbation equations, they contain only mean flow quantities. The mean flow quantities are obtained by solving the steady state Navier-Stokes equations in the (r, z) coordinate system numerically.[21] The eigenvalue problem given by Eq. (9) can then be solved by following the technique of Malik.[22,23] The solutions gives the neutral stability curve at which γ is a purely imaginary number.

60

IV. Discussion of Results

Based on the test matrix given in Section II, the critical Marangoni numbers have been measured for each test condition in which the onset of flow oscillation occurs. Figure 3 shows the measured critical Marangoni number (Ma_c) versus dynamic Bond number (Bo_{md}) at various aspect ratios. In general, the Ma_c increases with Bo_{md}. This can be attributed to the stabilization effect of the stratified layer caused by gravity. According to Fig. 3, for each aspect ratio (Ar), there seems to be an asymptotic limit of Bo_{md} beyond which there is no onset of oscillation. The effect of Ar on the onset of oscillations can be seen in Fig. 4. For small aspect ratios, while the effect of the stratified layer is reduced, the bottom wall starts to play a dominant role in the onset of oscillations. Due to the wall damping, a higher laser power is needed to make the fluid unstable. As shown in Fig. 4, the critical Marangoni numbers increase sharply when aspect ratios are lower than 0.5. It seems that there exists a lower limit of Ar below which there is no onset of oscillations. In Fig. 4, it can be seen that when Ar is greater than 0.8, the critical Marangoni number approaches a constant and becomes insensitive to the dynamic Bond number. This might suggest that for a deep layer, the characteristics of the onset of oscillations on earth are quite close to those in the microgravity environment.

In the present study, the onset of oscillations is characterized using two system parameters: Ar and Bo_{md}. A stability map can be generated as shown Fig. 5. In the test matrix, there are a number of cases at which no onset of oscillations can be observed. These points can roughly determine the domain of instability. It is noted that in a part these nonocsillating cases, the laser power was so high such that significant evaporation of the silicone oil occurred. This might have altered the characteristics of the onset of oscillatory flows.

V. Conclusion

A series of ground-based experiments have been conducted to measure the onset conditions of the oscillations of Marangoni flows based on 2 cs. silicone oil in a cylindrical container heated with CO_2 laser. For a single fluid, in addition to the aspect ratio, a modified dynamic Bond number (a combination of capillary and traditional dynamic Bond number) is proposed to correlate the experimental data. Results obtained from ground-based experiments show that for each aspect ratio there seems to

be an asymptotic limit for the dynamic Bond number beyond which no flow oscillations could occur. On the other hand, for each dynamic Bond number, a lower limit of the aspect ratio seems to exist for the onset of flow oscillations.

References

1. B'enard, H., *Rev. Gev. Sci. Pure Appl.*, vol. 11, pp.1261-1271, 1309-1328, 1990.

2. Koschmieder, E. L., and Pallas, S. G., *Int. J. Heat Mass Transfer*, vol. 22, pp. 535-546, 1974.

3. Davis, S. H., "Thermal Capillary Instabilities," *J. Ann. Rev. Fluid Mech.*, vol. 19, pp. 403-435, 1987.

4. Velten, R., Schwabe, D., and Scharmann, A., "The Periodic Instability of Thermocapillary Convection in Cylindrical Liquid," *Phys. Fluids A*, vol. 3, No. 2, pp. 267-279, 1991.

5. Ostrach, S., Kamotani, Y., and Lai, C. L., "Oscillatory Thermocapillary Flows," *Phys. Chem. Hydro.*, vol. 6, No. 5/6, pp. 585-599, 1985.

6. Monti, R., and Fortezza, R., "Oscillatory Marangoni Flow in a Floating Zone: Design of a Telescience Experiment for Texus 23," Proceedings of the 7th European Symposium on Materials and Fluid Sciences in Microgravity, pp. 285-289, 1989.

7. Schwabe, A. and Scharmann, A., "Measurements of the Critical Marangoni Number of the Laminar Oscillatory Transition of Thermocapillry Convection in Floating Zones," ESA SP-222, p. 281, 1984.

8. Napolitano, L. G., Monti, R., and Russo, G., "Some Results of the Marangoni Free Convection Experiment," ESA SP-222, p. 15, 1984.

9. Vargas, M., Ostrach, S., and Kamotani, Y., "Surface Tension Driven Convection in a Simulated Floating Zone Configuration," M. S. Thesis, Dept. of Mech. and Serospace Engr., Case Western University, 1982.

10. Velten, R., Schwabe, D., and Scharmann, A., "Gravity-Dependence of the Instability of Surface-Tension Driven FLow in Floating Zones," ESA SP-295, p. 271, 1989

11. Velten, R., Schwabe, D., and Scharmann, A., "The Periodic Instability of Thermocapillary Convection in Cylindrical Liquid Bridges," *Phys. Fluids*, A3, p. 267, 1990.

12. Chun, C. H., "Verification of Turbulence Developing from the Oscillatory Marangoni Convection in a Liquid Column," ESA SP-222, p.271, 1984.

13. Lee, K., "An Experimental Study of Combined Natural and Thermocapillary Convection in a Rectangular Container," M. S. Thesis, Dept. of Mech. and Aerospace Engr., Case Western Reserve University, 1986.

14. Lee, J. H., "An Experimental Study of Thermocapillary Convection in a Cylindrical Container," M. S. Thesis, Dept. of Mech. and Aerospace Engr., Case Western Reserve University, 1990.

15. Chun, C. H., "Experiments on Steady and Oscillatory Temperature Distribution in a Floating Zone Due to the Marangoni Convection," Acta Astronautica, 7, p. 479, 1980.

16. Ostrach, S. and Kamotani, Y., "Recent Developments in Oscillatory Thermocapillary Flows," AIAA/IKI Microgravity Science, Conference Proceedings, p. 25, 1991.

17. Smith, M., and Davis S., "Instabilities of Dynamic Thermocapillary Liquid Layers, Part 1. Convective Instabilities," *J. Fluid Mech.*, vol. 132, pp. 119-144, 1983.

18. Smith, M., and Davis S., "Instabilities of Dynamic Thermocapillary Liquid Layers, Part 2. Surface-Wave Instabilities," *J. Fluid Mech.*, vol. 132, pp. 145-162, 1983.

19. Neitzel, G. P., Law, C. C., Jankowski, D. F., and Mittelmann, H. D., "Stability and Instability of Thermocapillary Convection in Models of Float-Zone Crystal Growth," *AIAA J.*, pp. 57-65, 1991.

20. Lai, C. L., Ostrach, S., Kamotani, Y., "The Role of Free-Surface Deformation in Unsteady Thermocapillary Flow," Japan Heat Transfer Joint Seminar, San Diego, California, September 17-20, 1985.

21. Hsieh, K.-C., and Pline, A. D.,"A Comprehensive Numerical Study of Surface Tension Driven Convection with Free Surface Deformation," AIAA Paper No. 91-1306, 26th Thermophysics Conference, June, 1991.

22. Malik, M. R.,"A Numerical Methods for Hypersonic Boundary Layer Stability," *J. Computational Physics*, Vol. 86, No. 2, pp. 376-413, 1990.

23. Malik, M. R., Chuang, S., and Hussaini, M. Y.,"Accurate Numerical Solution of Compress-ible Linear Stability Equations," *ZAMP*, Vol. 33, No. 2, 189., 1982.
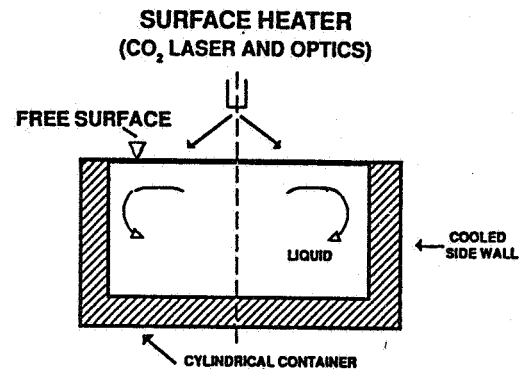
Fig. 1 Schematic Diagram for Flow Configuration
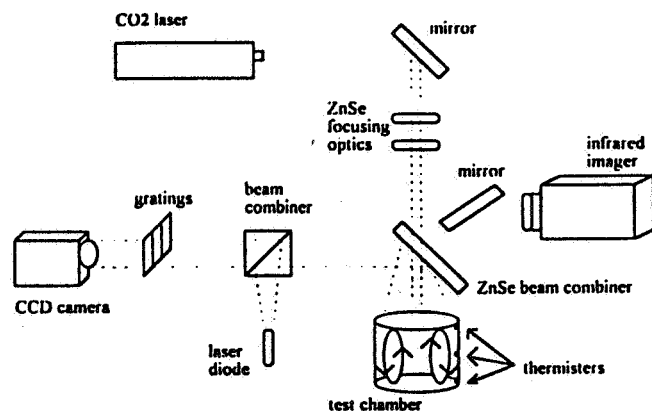
Fig. 2 Schematic Diagram for Experimental Setup
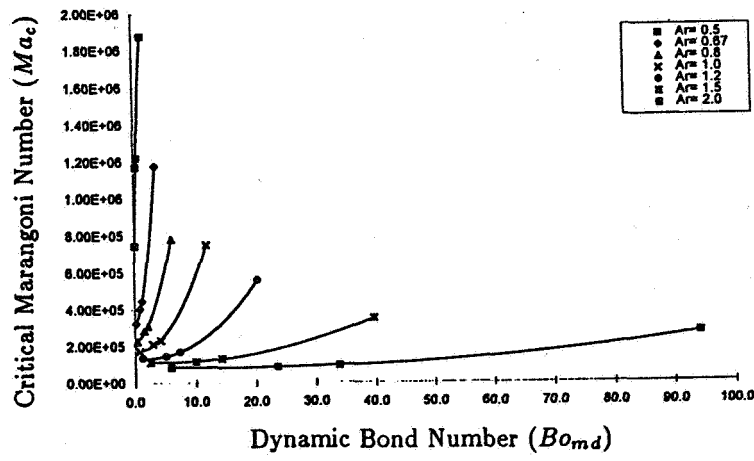
Fig. 3 Measured Critical Marangoni Number versus Dynamic Bond Number for Various Aspect Ratios
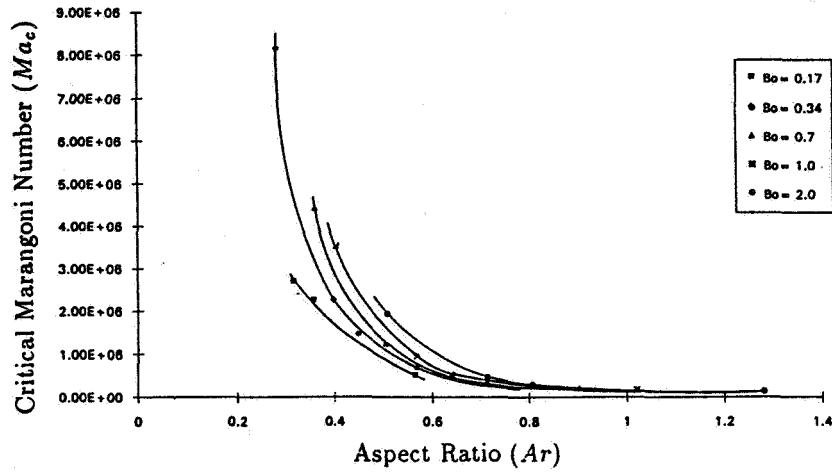
Fig. 4 Measured Critical Marangoni Number versus Aspect Ratio for Constant-Dynamic-Bond-Number Cases
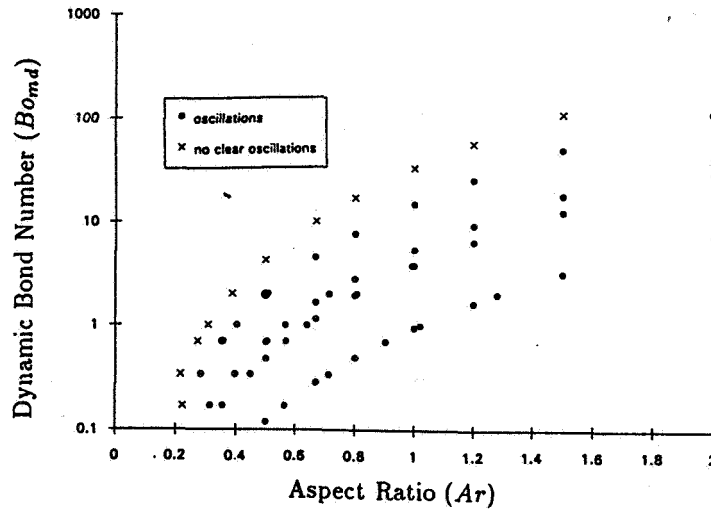
Fig. 5 Flow Instability Map Determined from Ground-Based Experiments

MULTILAYER FLUID DYNAMICS OF IMMISCIBLE LIQUIDS

Jean N. Koster
University of Colorado
Dept. Aerospace Engineering Sciences
Boulder, Colorado 80309-0429

ABSTRACT

A comprehensive analytical, numerical and experimental study of convective flow in multilayer immiscible liquids has been performed. Studies include transparent high Prandtl number liquids as well as opaque low Prandtl metallic melts. A new radioscopic flow visualization has been developed for the latter studies.

INTRODUCTION

The study of thermal convection in a double layer system of immiscible liquids is inspired by the development of liquid encapsulated crystal growth techniques for producing mono-crystalline electronic materials. Encapsulation of the electronic melt is used to control the melt's stoichiometry when the melt contains a volatile component. The encapsulant, typically a liquid glass, also has the potential for reducing or even eliminating convective flow in the melt. Convective flow in the melt, especially time-dependent flow, can lead to undesirable inhomogeneities in the solidified material. To reduce buoyancy driven thermal convection in the melt by taking advantage of the reduced gravity environment aboard a spacecraft, space based processing of GaAs with the liquid encapsulated float zone processing technique has been proposed.

Fluid dynamics of the melt float zone during the solidification process poses a formidable problem involving the transport of mass and heat along with phase change in one layer. To make the problem manageable we focus on simplified model situations. We consider the following basic multiple layer fluid dynamical systems [1-14]:

I) High Prandtl number fluids
    a) Natural convection featuring a liquid/liquid interface and a free upper surface
    b) Rayleigh-Bénard convection featuring one interface
II) Low Prandtl number fluids
    a) Development of a radioscopic flow visualization capability
    b) Single/double layer natural convection with solidification

The multi-layer problem is characterized by mechanical and thermal coupling across liquid/liquid interfaces. The liquid layers are mechanically coupled via transfer of momentum across the interfaces. Transfer of momentum results from the continuity of interface tangential velocity and balance of shear stress across the interface. Together these two conditions comprise the 'no-slip' condition at a liquid-liquid interface. Thermal coupling is achieved through continuity of temperature at the interface and the balance of heat transfer across the interface. It is these coupling conditions that distinguish the multi-layer problem from the single layer problem.

We also present results from an analytical study of thermocapillary flow in a horizontal liquid layer encapsulated by two immiscible liquids, featuring two liquid/liquid interfaces (*Figure 1*). The three layers are confined in a shallow rectangular cavity which is differentially heated. The differential heating produces a temperature gradient parallel to the two interfaces. These investigations are in support of a space flight experiment, to be performed aboard the International Microgravity Laboratory IML-2.

Recently, radioscopic techniques have been presented as viable methods to track liquid metal flows, melt/gas interfaces, and melt/crystal interfaces [15-23]. The potential of radioscopic techniques for fluid dynamics and solidification studies has been well delineated by these studies.

We report on new radioscopic studies on melting and solidification of mono-component gallium under natural convection conditions. The effect of natural convective flow on the shape of the melt front is discussed. This work seeks further understanding of liquid encapsulated convection flows by analytically and numerically modeling convective flows in encapsulated gallium layers as preparation to experiments planned in the near future. Our main emphasis is the velocity and density fields in both layers which will be the primary data in the forthcoming experiments.

Since X-ray absorption is a function of material density, it was proposed that the difference in absorption from the hot and cold liquids could provide sufficient variation in intensity levels to be detected by the radioscopic image processing system. The percent density difference which must be detected for visualization of constant density fields in liquid gallium with an applied temperature difference of 8° C is calculated to be about $\Delta\rho = 0.2\%$.

NUMERICAL SIMULATION AND ANALYTICAL STUDIES

The multilayer fluid systems are numerically simulated using the commercial finite-element computer code FIDAP. Simulation of the experimental system is restricted to a 2-D model. The natural convection cases were extensively studied with asymptotic methods.

Rayleigh-Bénard convection is considered to further analyze the coupling between immiscible liquids (*Figure 2*). By visualizing the temperature field in double layers confined in a narrow slot, we have observed the two modes of viscous and thermal coupling near the onset of convection, and beyond. Generally, the observations are found to be in remarkable agreement with 2-D numerical simulations. The experiments also showed that onset of convection was in the form of steady flow. Oscillatory convection at onset was not detected from the thermocouple signals.

Analytical and numerical models have been compared for flows in encapsulated gallium melts. The analytical model is a useful tool for quickly obtaining a basic understanding of the general flow field and assessing the underlying physics. The obtained data will serve as a basis for liquid metal flow studies in a layer of gallium encapsulated by glycerol. Liquid encapsulation of gallium reduces the flow velocities to the level of a rigidly contained gallium layer. Flow velocities in the viscous encapsulant are negligibly small. The

liquid encapsulant acts essentially as a solid; the flow velocity at the interface is close to zero. The superiority of glass lining of ampoules and encapsulation comes with the absence of corrosion of electronic melts, control of volatiles, and barrier to contaminants in the surrounding atmosphere.

Thermocapillary convection is studied analytically in a two-dimensional layer of GaAs which is symmetrically encapsulated by liquid B_2O_3. In a space based reduced gravity environment thermal convection is primarily due to thermocapillary stresses at free surfaces and interfaces. The free surface tension gradient of B_2O_3 is parameterized and its influence along with the influence of varying encapsulant layer thickness on flow in the GaAs melt is investigated. The results are compared with those for rigidly contained encapsulant layers. The free surface and the interface are considered to be deformable. The analytical model is benchmarked with a numerical simulation which confirms the validity and accuracy of the model.

Within the bounds of validity of the analytical model, it is found that thermocapillary flow in the GaAs melt can be significantly controlled by the encapsulant liquid. A 'near-halt-condition' or 'quasi-no-flow' condition in the melt can be achieved if the ratio of the free surface tension gradient (of B_2O_3) to the interface tension gradient (of B_2O_3/GaAs) is around 2.3. Experimental data on the surface tension gradient of boron oxide, when available, will show how closely B_2O_3 encapsulation approaches the theoretically required surface tension gradient ratio for a no-flow condition. A thin encapsulant layer is found to be also helpful in reducing the flow in the melt layer. Also, it is observed that a free outer encapsulant surface is more effective in reducing convective flow in the electronic melt layer than a liquid glass lined ampoule with rigid containment.

Preliminary studies were done to model effects of density inversion on the flow pattern in convective situations. It is well known that some fluids exhibit a density inversion behavior in a certain temperature range. A common example is water which possess a maximum density at 3.98°C at standard conditions. Others include liquid helium in the range of temperature about 2.178 K and the pseudobinary alloy $Hg_{1-x}Cd_xTe$ in the range of temperature 1028 K. The single layer studies are currently extended to double liquid layers with density inversion occurring in the lower layer.

EXPERIMENTS

Experiments are performed in a two-layer system, such as 10 cSt silicone oil over a fluorinert FC-70 liquid. Other silicone oils and fluorinerts are also used. Both the natural convection cases and the Rayleigh-Bénard cases are of interest.

The flow field is visualized with the aid of tracer particles suspended in the fluids. A streakline, if the exposure time is not very long, depicts the local velocity vector at the particle location. Velocity measurements are performed with a Laser Doppler Velocimetry (LDV) system and particle displacement tracking velocimetry (PDTV). Real time holographic interferometry is used to obtain the temperature field. In addition to the visualization of the flow field, we also measured the surface tension of the two liquids under investigation, and

the interface tension between them as a function of temperature. A radioscopic facility has been developed to visualize melting and solidification of opaque metals. The system consists of a modified non-destructive testing facility with 160 kV tungsten X-ray source, image intensifier, image acquisition and processing system, temperature data acquisition system, and heaters and controllers.

Figure 3 shows a visualization of melting gallium under natural convection. The lighter portion represents the solid gallium. Liquid is visualized by the dark area. Because solid gallium has a 3% lower density than liquid gallium, the solid is more transparent to X-rays. As the absorption is proportional to the density, density changes are visualized as intensity changes. Using background subtraction image processing techniques, the small density change can be visualized as a black and white transition with a steep linear gray scale covering the 3% density change across the interface line. This high resolution permits visualization of corrugated interfaces as a function of time.

The method has now been improved to permit coarse visualization of the density fields within liquid gallium. When a fluid is differentially heated, the density of the fluid varies as a function of temperature. Since X-ray absorption is a function of material density, the difference in absorption from the hot and cold liquids provides sufficient variation in intensity levels to be detected by the radioscopic image processing system. The resolution of 0.2% density change has been achieved to date (*Figure 4*). It is confirmed that natural convection has a major influence on the shape of the solid/liquid interface.

A vertical Bridgman furnace is currently in the final stages of development. Visualization of density fields, solidification fronts and flow patterns in InSb are planned for the near future. Further exploratory studies were made for natural convection in encapsulated liquids undergoing solidification, and with liquids that exhibit miscibility gaps.

CONCLUSION

A comprehensive study has been made on the convective fluid dynamics of multiple immiscible liquid layers. Thermal coupling and viscous coupling have been demonstrated in several cases. Oscillatory coupling has not been observed so far. It is found that the argument of interface contamination has been used too deliberately in the past. New measuring techniques have been developed to study liquid metals fluid dynamics. Flow patterns and density fields can now be observed in opaque melts.

ACKNOWLEDGEMENTS

REFERENCES

1. Fontaine, J.P., Koster, J.N., and Sani, R.L., "Thermocapillary effects in a shallow cavity filled with high Prandtl number fluids," *Ann. Chim. Fr.*, **17**, 1992, 377-388.

2. Prakash, A., Fujita, D., and Koster, J.N., "Surface tension and buoyancy effects on a free-free layer," *European Journal of Mechanics B/Fluids,* **12** (1), 1993, 15-29.

3. Tong, W., and Koster, J.N., "Coupling of natural convection flow across a vertical density inversion interface," Wärme- und Stoffübertragung, **28**, 1993, 471-479.

4. Doi,T., and Koster, J.N., "Thermocapillary convection in two immiscible liquid layers with free surface," *Physics of Fluids A: Fluid Dynamics,* **5**(8), 1993, 1914-1927.

5. Prakash, A., and Koster, J.N., "Natural and thermocapillary convection in three layers," *European Journal of Mechanics B/Fluids*, **12**(5), 1993, 635-655.

6. Tong, W., and Koster, J.N., "Natural convection of water in a rectangular cavity including density inversion," *Int. J. Heat Fluid Flow*, **14**(4), 1993, 366-375.

7. Tong, W., and Koster, J.N., "Penetrative convection in sublayer of water including density inversion," *Wärme- und Stoffübertragung,* **29**, 1993, 37-49.

8. Tong, W., and Koster, J.N., "Density Inversion Effect on Transient Natural Convection in a Rectangular Enclosure," *Int. J. Heat Mass Transfer,* **37**, 1994, 927-938.

9. Prakash, A., and Koster, J.N.,"Convection in multiple layers of immiscible liquids in a shallow cavity - Part I: Natural convection," *Int. J. Multiph. Flow*, 1994, in print.

10. Prakash, A., and Koster, J.N.,"Convection in multiple layers of immiscible liquids in a shallow cavity - Part II: Steady thermocapillary convection," *Int. J. Multiphase Flow*, 1994, in print.

11. Prakash, A., Koster, J.N., "Thermocapillary Convection in Three Immiscible Liquid Layers," *Microgravity Q.*, 1994, in print.

12. Burkersroda C.v., Prakash, A., and Koster, J.N. "Interfacial Tension between Fluorinerts and Silicone Oils," *Microgravity Q.,* 1994, in print.

13. Campbell, T.A., and Koster, J.N., "Visualization of Liquid/Solid Interface Morphologies in Gallium Subject to Natural Convection," *J. Crys.Growth,* 1994, in print.

14. Pool, R.E., and Koster, J.N., "Visualization of Density Fields in Liquid Metals," *Int. Jl. Heat Mass Transfer,* 1994, in print.

15. F.P. Chiaramonte, G. Foerster, D.J. Gotti, E.S. Neumann, J.C. Johnston, and K.J. De Witt, AIAA 92-0845, (1992).

16. K. Kakimoto, M. Eguchi, H. Watanabe, and T. Hibiya, J. Crystal Growth, 88 (1988), pp. 365-370.

17. K. Kakimoto, M. Eguchi, H. Watanabe, and T. Hibiya, J. Crystal Growth, 91 (1988), pp. 509-514.

18. K. Kakimoto, M. Eguchi, H. Watanabe, and T. Hibiya, J. Crystal Growth, 99 (1990), pp. 665-669.

19. K. Kakimoto, M. Eguchi, and T. Hibiya, J. Crystal Growth, 112 (1991), pp. 819-823.

20. J.A. Hubert, A.L. Fripp, and C.S. Welch, AIAA 93-0475, (1993).

21. P.G. Barber, R.K. Crouch, A.L. Fripp, W.J. Debnam, R.F. Berry, and R. Simchick, J. Crystal Growth, 74, (1986), pp. 228-230.

22. A.L. Fripp, W.J. Debnam, G.W. Woodell, R.T. Simchick, S.K. Sorokach, and P.G. Barber, Crystal Growth in Space and Related Optical Diagnostics, J.D. Trolinger & R.B. Lal, Eds., Proc. SPIE, 1557, (1991), pp. 235-244.

23. R.T. Simchick, S.Sorokach, A.L. Fripp, W.J. Debnam, R.F. Berry, and P.G. Barber, Advances in X-Ray Analysis, 35 (1992), pp. 1295-1300.
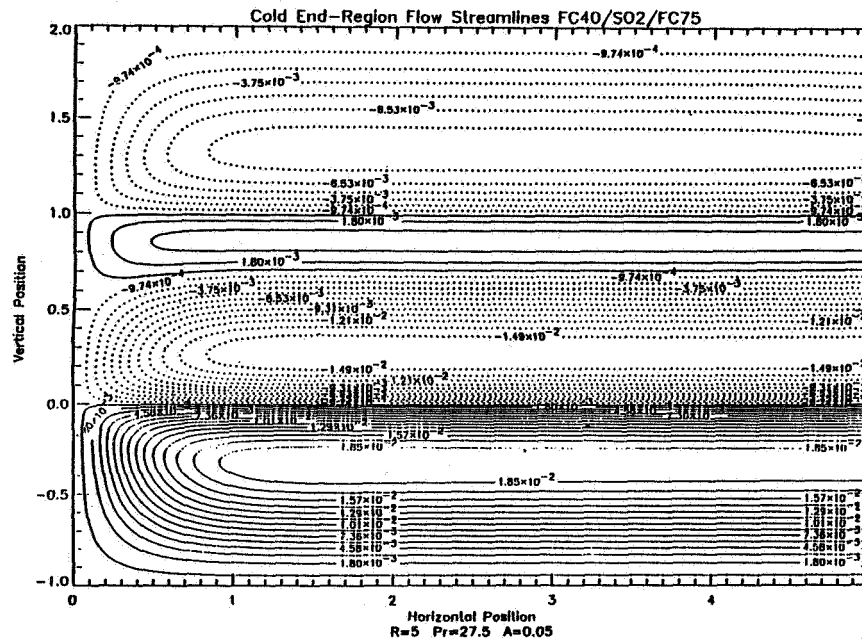
Figure 1: Spaceflight configuration: FC-40 /SO-2/FC-75
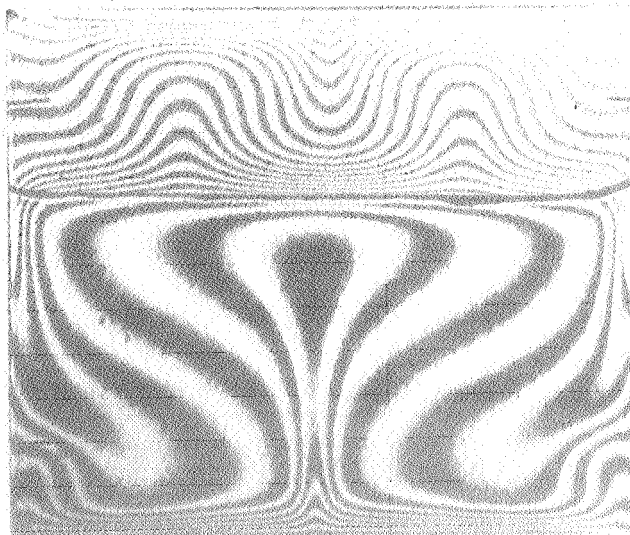
Figure 2 Silicone oil 100 cSt / Ethylene Glycol, $\Delta T = 12$ K

Time (minutes)
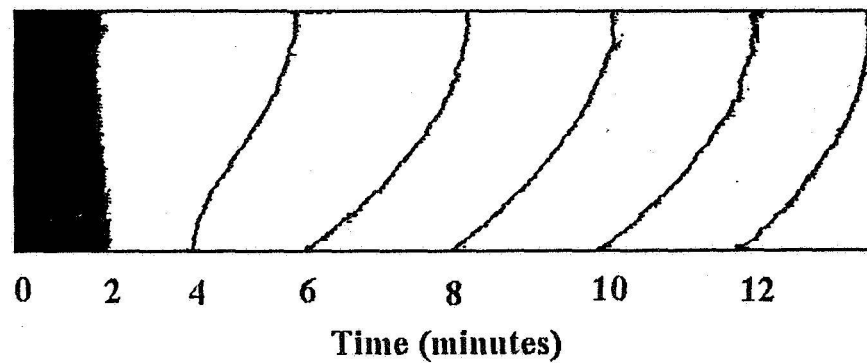
Figure 3: Natural convection in liquid gallium. Advancing melting front as a function of time. Grashof number $Gr = 1.1 \times 10^6$
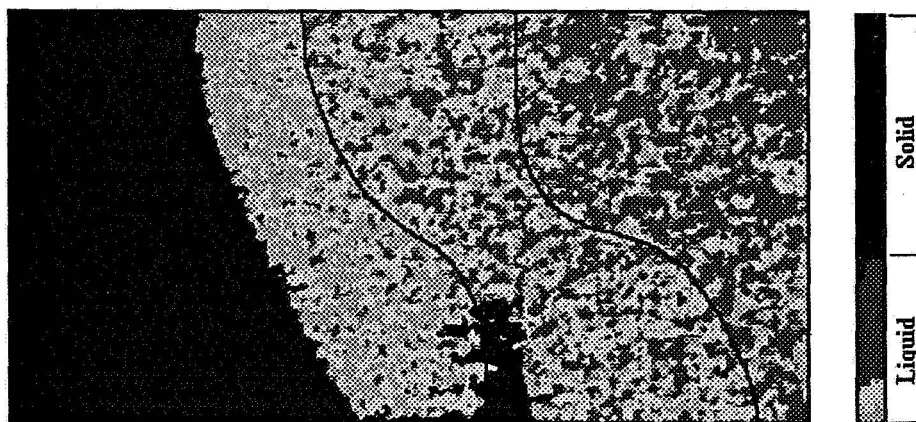
Figure 4: Isodensity fields in 1.25 cm layer of liquid Gallium subject to natural convection and solidification.

Interfacial Phenomena

Dynamics and Statics of Nonaxisymmetric and Symmetric Liquid Bridges

J. Iwan D. Alexander, Andrew H. Resnick, William F. Kaukler and Yiqiang Zhang
Center for Microgravity and Materials Research
University of Alabama in Huntsville
Huntsville, Alabama 35899

Project summary and objectives

This program of theoretical and experimental ground-based research focuses on the understanding of the dynamics and stability limits of nonaxisymmetric and symmetric liquid bridges. There are three basic objectives: First, to determine the stability limits of nonaxisymmetric liquid bridges held between non-coaxial parallel disks, Second, to examine the dynamics of nonaxisymmetric bridges and nonaxisymmetric oscillations of initially axisymmetric bridges. The third objective is to experimentally investigate the vibration sensitivity of liquid bridges under terrestrial and low gravity conditions. Some of these experiments will require a low gravity environment and the ground-based research will culminate in a definitive flight experiment.

Motivation

The motivation for this work arises from several areas:

-Axisymmetric liquid bridge stability and dynamics have been the subject of numerous theoretical and experimental investigations, while nonaxisymmetric bridges have received less attention.

- The dynamics of liquid bridges (both axisymmetric and nonaxisymmetric), particularly the breakage of bridges and the sensitivity of bridges to vibration, are of particular importance for practical aspects of fluids handling in microgravity.

-Apart from purely fluid dynamic interests, liquid bridge stability is an important factor in determining the stability of molten liquid zones associated with floating zone crystal growth experiments, as well as model floating zone systems designed to study related thermocapillary flow phenomena.

- Finally, space experiments involving the study of zone vibration and response of liquid bridges to uncontrolled g-jitter are a suitable test of the need for vibration isolation techniques for experiments which will operate using liquid bridge configurations. Whether the bridges are melts or lower temperature liquids, the problem of rupture or breakage in response to spacecraft vibration (or g-jitter) is an important consideration for experiment design (e.g., the type of isolation, allowable zone slenderness, etc.)

Experimental Work

Experiments are conducted in a neutral-buoyancy or Plateau tank. The bridges are held between rigid supports which allow for rotation and lateral and vertical translation. Each support can be independently vibrated at frequencies less than 10 Hz. Bridge injection is automated with simultaneous recording of precise volume data. We use two imaging methods. Video images are obtained from two orthogonal cameras. In addition, a high quality Fourier transform imaging system for edge detection is being developed and the basic system assembled is now ready.

The important physical parameters are the aspect ratio of the bridge, the liquid volume and the static and dynamic Bond numbers. The liquid volume and the slenderness (aspect ratio) of the bridge depend on the precision with which lengths can be determined. The disk widths are known to within 10 μm. The length of the bridge is set by the positioning device and can be determined with a precision of 1-2 μm. Thus, for bridges of 2.5 cm length the slenderness, $\Lambda = L/2R_0$, can be determined to within $\pm$ 0.04%. Volume can be measured with a precision of 0.1 mm^3 and an accuracy of 0.1%. For the Bond number, the main error sources arise in the density and surface tension. The surface tension causes the largest error and density limits the magnitude of the smallest obtainable Bond number. The liquid bath is a methanol-water solution. Variation of the methanol concentration changes the density difference between the Dow Corning 200$^{\circledR}$ silicone oil bridge and the bath. At 83% water concentration a condition of neutral buoyancy is obtained. The accuracy of our density measurements is currently 5 parts in 10^4.

Interfacial tension measurements were made using the drop weight technique [1,2]. The results are shown in Fig. 1. The interfacial tension of the silicone oil-solution interface ranges from a

low of 2.645 dyne cm^{-1} (100% methanol) to a high of 60.48 dyne cm^{-1} (100% water). We note that care must be taken in the vicinity of the neutral buoyancy point where the data diverge. This occurs because as neutral buoyancy is approached, the drop size increases exponentially, with a corresponding increase in drop-time. We extrapolated through the neutral buoyancy point using a cubic polynomial cubic fit to the data that yielded an interfacial tension at neutral buoyancy of 48.7 dyn cm^{-1}.

Experiments have been carried out in three areas.
a) Stability limits, symmetric and nonsymmetric breaking behavior of initially axisymmetric bridges.
b) Lateral shearing, squeezing and force measurements.
c) Vibration dynamics and breaking behavior.

Experimental Results

Figures 2-6 show examples of selected results for static and dynamic conditions. In all cases the images have been grabbed from video. In Figs. 2, 5 and 6, the half-illumination shows a dark background to the left of the bridge. The left side of the bridge is bright and shows a distorted view of the square background grid. The right side of the bridge is dark and its boundary contrasts with the bright background. In order to test our experimental set-up we repeated the work of Slobozhanin (see ref. [3]). In particular, we concentrated on the nonaxisymmetric loss of stability of initially axisymmetric bridges. The breaking of a static bridge is shown in Fig.2. (Note the long drawn-out neck prior to breaking and the satellite bubble that remains following the breakup). In some cases (see also Russo and Steen [4]) stability was lost to stable nonaxisymmetric rotund bridges. In other cases the bridge lost stability and broke nonaxisymmetrically (see Fig. 3.). This occurs near the transition point separating axisymmetric from nonaxisymmetric instability. The distance between the 1 cm diameter disks is 2.525 cm. Figure 4 shows shearing and squeezed-shearing configurations. Such experiments were also carried out for bridge configurations where the lower support disk was replaced by a disk attached to a cantilever arm. This allowed us to measure the interplay between the various forces applied to the lower disk.

The effects of vibration and oscillation are also being studied. Figure 5 shows laterally oscillating bridges. In Fig. 5a), the distance between the 1cm diameter disks is 2.525 cm. The upper disk moves at 1 Hz with a 0.25 cm amplitude. Figure 5b) shows a sequence with lateral motion of the upper disk with a frequency of 1 Hz and an amplitude of 0.1 cm. Note the difference in the deformation modes. Figure 6 shows a bridge oscillated laterally at 1 Hz and vertically (both disks) at 1.2 Hz. The bottom disk is rotating at 1rps. A "c-mode" is excited and interferes with an axisymmetric mode caused by the vertical oscillation.

Theory and numerical simulation

Dynamic stability of long axisymmetric bridges

A review of the literature related to liquid bridges can be found in [5]. Over the last twenty years many different studies have been carried out. Most of these papers are only concerned with static stability limits. Only a few attempts have been made to analyze the influence of the dynamics of the liquid bridge [5-12]. These efforts have been centered more in the dynamics itself than in its influence on the stability limits.

The theoretical work described is this section is part of a joint study carried out at the CMMR and at LAMF in Madrid. The study focuses on the effect of vibration on the stability limits of bridges and how vibration modifies the static stability boundaries [1]. It has been demonstrated in [7] that near the static stability limit of cylindrical liquid bridges there is a self-similar solution for the dynamics of the liquid bridge. Their analysis is based on a one-dimensional model in which the axial velocity is assumed to be dependent on the axial coordinate z and the time t, but not on the radial coordinate r . (This hypothesis is valid provided the slenderness is large enough [6]). Within the validity range of this analysis the variation with time of the interface deformation is given by Duffing's equation [14]. In addition to the Duffing equation model, we have been using the 1D-model of Zhang and Alexander [9]. Both models are in good qualitative agreement for the parameter range investigated so far. The results of the study indicate that depending on the nature of the axial vibration the bridge may be stabilized or destabilized relative to the static stability margin.

At the static stability margin the effective dimensionless potential energy ξ of the liquid bridge, which accounts for both gravity field and surface energies, in self-similar variables is

$$\xi = -\frac{1}{2}m\alpha^2 - \frac{1}{4}\alpha^4 - \beta\alpha, \tag{1}$$

where α is the amplitude of the periodic forcing, β is the effective Bond number and m is ± 1 (depending on whether the volume is greater or less than the volume of an equivalent right circular cylinder). Equilibrium shapes are given by

$$\frac{d\xi}{d\alpha} = -m\alpha - \alpha^3 - \beta = 0. \tag{2}$$

Eq. (2) has one real root if $m = +1$, which is unstable ($d^2\xi/d\alpha^2 < 0$), and three real roots, $\alpha_1 > \alpha_2 > \alpha_3$, in the case $m = -1$. The two extreme roots, α_1 and α_3, correspond to unstable equilibrium shapes. The middle one is stable. Thus, the stability margin will be the difference between the energy of the unstable equilibrium shapes and of the stable one, $\Delta\xi = \xi_{unstable} - \xi_{stable}$. This behavior is summarized in Fig. 7, The stability margin is defined by the smallest value, $\Delta\xi = \Delta\xi_1$ and is proportional to the square of the distance to the stability limit. The stability margin represents a limit to the minimum energy needed to break the liquid bridge. This means that the response of the liquid bridge will depend on the energy of the perturbation. The liquid bridge will remain stable if the energy is smaller than the corresponding stability margin and could be unstable if the energy increases. In this last case, the evolution of the liquid bridge depends on how the perturbation is imposed and on how the energy is dissipated by viscosity. Now consider the forced oscillation of the liquid bridge in gravitationless conditions ($\beta = 0$, $b \neq 0$). In that case $\alpha_2 = 0$ and $\alpha_1 = -\alpha_3 = 1$, so that $\Delta\xi = 1/4$. The time variation of the interface is

$$\alpha_{\theta\theta} + \gamma\alpha_\theta + \alpha - \alpha^3 = b\cos(\Omega\theta + \varphi), \tag{3}$$

which, assuming steady oscillations are reached, can be integrated in a first approximation [11] obtaining $\alpha = a\cos\Omega\theta$, where the amplitude a is related to viscosity, γ, and the amplitude of the perturbation, b, and to the frequency of the perturbation, Ω, through the equation

$$a^2\left(1-\Omega^2 - \frac{3}{4}a^2\right)^2 + \gamma^2\Omega^2 a^2 = b^2. \tag{4}$$

Within this approximation the oscillation of the liquid bridge is easily visualized by plotting the liquid bridge evolution in the phase space (deformation-velocity-energy diagram), as shown in Fig. 8. Note that, since we are considering an evolution, kinetic energy must be also taken into account, so that at every point of the phase space the energy will be the sum of the potential energy plus the kinetic energy:

$$\xi = \frac{1}{2}\alpha^2 - \frac{1}{4}\alpha^4 + \frac{1}{2}\alpha_\theta^2. \tag{5}$$

Two different oscillations of the liquid bridge, with amplitude $a < 1$, are shown in Fig. 8. One corresponds to $\Omega < 1$, the other to $\Omega > 1$. For the $\Omega > 1$ case, the static stability margin is exceeded ($\Delta\xi = 1/4$) but the configuration remains stable. The liquid bridge will be unstable when $a = 1$, This yields

$$\gamma^2 = \Omega^{-2}\left[b^2 - \left(\frac{1}{4} - \Omega^2\right)^2\right] \tag{6}$$

Once b and Ω are fixed, the liquid bridge evolution will be stable if the viscosity of the liquid is greater than the value resulting from (10). Otherwise it will be unstable. Results obtained by numerical integration of (3) are shown in Fig. 9. Each one of the curves b = constant represents the corresponding dynamic stability limit. Points on the right of a given curve are stable (high viscosity, γ) whereas those of the left side (low γ) are unstable. Note that, once γ and b are fixed there can be multiple values of Ω that lead to instability.

Numerical modelling of nonaxisymmetric bridges

We have developed a numerical code to deal with the vibration dynamics of axisymmetric and nonaxisymmetric bridges. For the nonaxisymmetric cases the code is currently limited because our mapping technique does not allow a full range of contact angles. The code can still be used for slender nonaxisymmetric bridges, however. The code has been checked against a previously developed axisymmetric code developed by us and against the work of Chen [15] who examined the effects of an inclined gravity vector on liquid bridge shapes. Our results for the effect of inclination angle on the minimum stable volume for fixed Bond number and aspect ratio are shown in Figs. 10-12. The results show that, for a fixed Bond number, inclining the gravity vector to the bridge axis results in a decrease in the miminum stable volume.

Summary

We have presented selected examples of our ongoing work, We have made progress in several areas especially in the area of bridge vibration dynamics and nonaxisymmetric behavior. Particularly interesting is a novel technique for measuring the changing force on one of the discs as the bridge characteristics are varied. This gives additional insight into the behavior of deforming and breaking bridges. During the next eighteen months we plan to complete a study of nonaxisymmetric breaking of axisymmetric bridges under static and dynamic conditions, a study of the static stability of bridges held between noncoaxial parallel disks and to have made significant progress into the study of vibrating bridges and the question of dynamic stability of bridges.

References

[1] M.C. Wilkinson and M.P. Aronson, Applicability of the drop-weight technique to the determination of the surface tensions of liquid metals, J. Chem. Soc., Faraday Trans., I, **69**, 474 (1973).

[2] J.M. Andreas, E.A. Hauser, and W.B. Tucker, Boundary tension by pendant drops, J. Phys. Chem., **42**, 1001 (1938)

[3] L. A. Slobozhanin and J.M. Perales, Stability of liquid bridges between equal disks in an axial gravity field, Phys. Fluids A, 5 (1993) 1305..

[4] M.J. Russo and P.H. Steen, Instability of rotund capillary bridges to general disturbances: Theory and experiment, J. Colloid Int. Sci., 113 (1986) 154.

[5] J.M. Perales, and J. Meseguer, Theoretical and experimental study of the vibration of axisymmetric viscous liquid bridges, Phys. Fluids A 4 (1992) 1110.

[6] Meseguer, J., The breaking of axisymmetric slender liquid bridges, J. Fluid Mech. 130, 123-151(1983).

[7] D. Rivas, and J. Meseguer, One dimensional, self-similar solution of the dynamics of axisymmetric slender liquid bridges, J. Fluid Mech. 138, (1984) 417.

[8] A. Sanz, J. López-Díez, Non-axisymmetric oscillations of liquid bridges, J. Fluid Mech. 205 (1989) 503.

[9] Y.Q. Zhang and J.I.D. Alexander, Sensitivity of liquid bridges to axial vibration, Physics of Fluids, A 2 (1990) 1966-1974.

[10] D. Langbein, Oscillations of finite liquid columns, Microgravity Sci. Technol. 5 (1992) 73.

[11] R.M.S.M. Schulkes, Nonlinear liquid bridge dynamics, in ESA SP-333, Vol. 1 (ESA Publ. Div., ESTEC, Noordwijk 1992) 61.

[12] J.M. Vega, and J Perales, Almost cylindrical isorotating liquid bridges for small Bond numbers, in ESA SP-191, (ESA Publ. Div., ESTEC, Noordwijk 1992), 247.

[13] J. Meseguer, M.A. Gonzalez and J.I.D. Alexander, Dynamic stability of long axisymmetric bridges, Microgravity Science and Technology, to be published.

[14] J.J. Stoker, Nonlinear vibrations, Vol. II (Interscience, 1966).

[15] H. Chen and M.Z. Saghir, Nonaxisymmetric equilibrium shapes of the liquid bridge, Microgr. Sci. Technol., 7 (1994) 12.
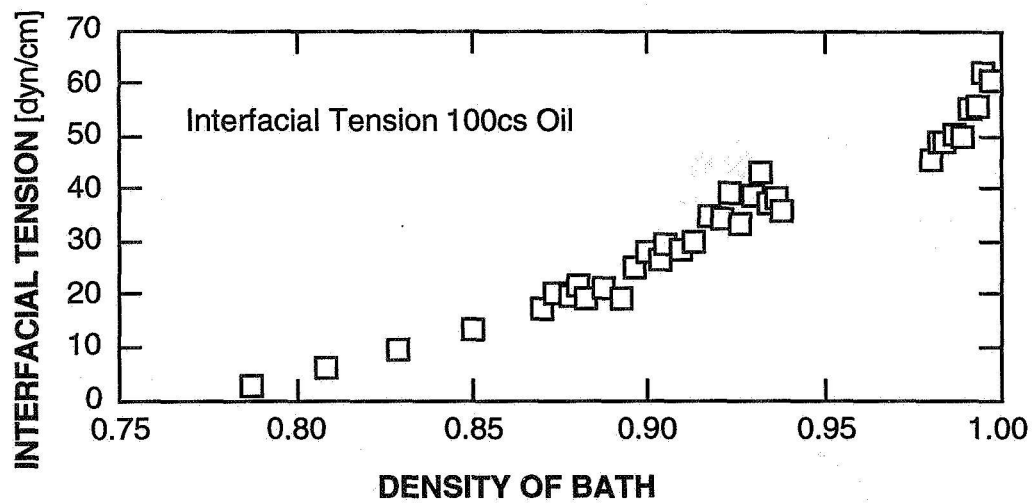
Fig. 1. Interfacial tension of Dow Corning 200 fluid-methanol/water interface as a function of methanol concentration.
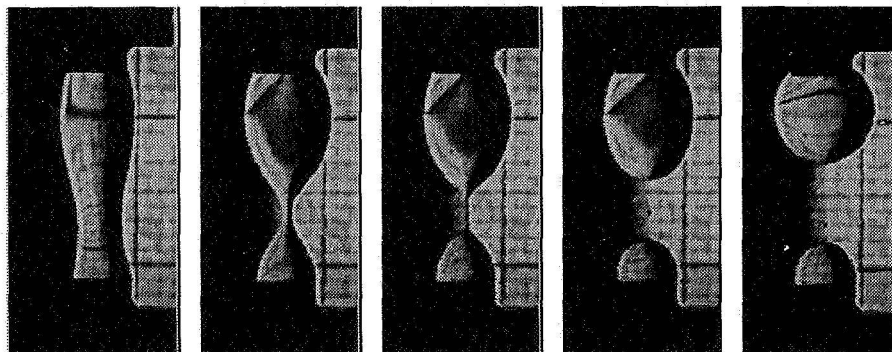
Fig. 2. Axisymmetric breaking of liquid bridge.
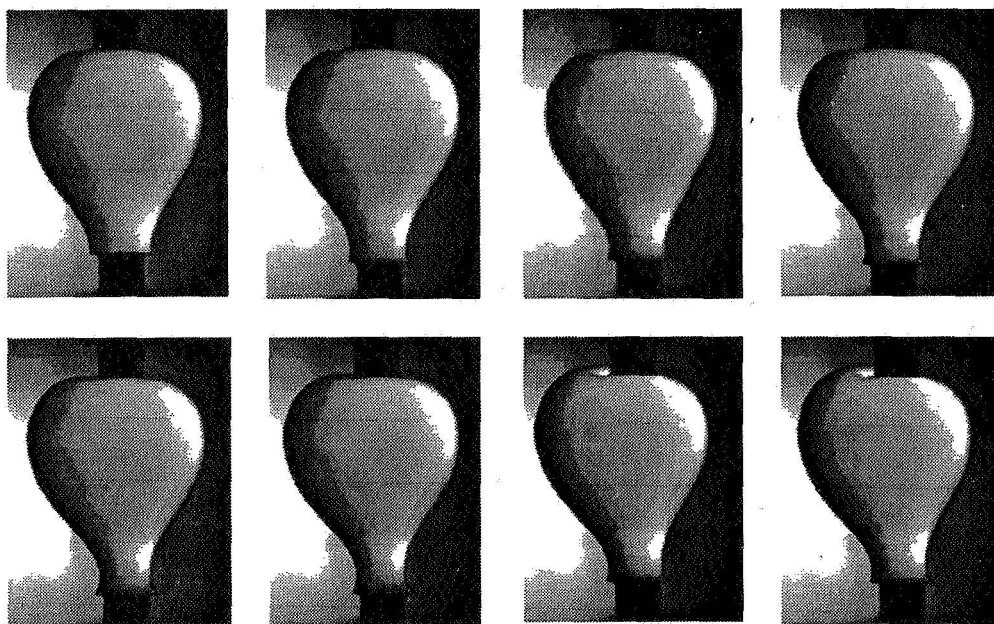
Fig. 3. Nonaxisymmetric loss of stability of an initially axisymmetric bridge. The aspect ratio and relative volume at breaking are 3.25 and 4.23, respectively. The Bond number, Bo, is 0.1.
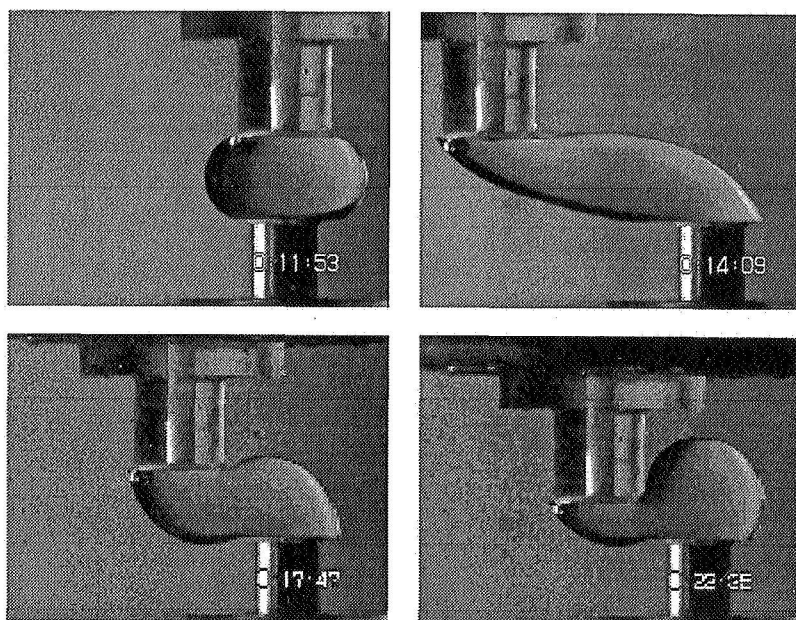
Fig. 4.   Shearing and squeezing of liquid bridges.
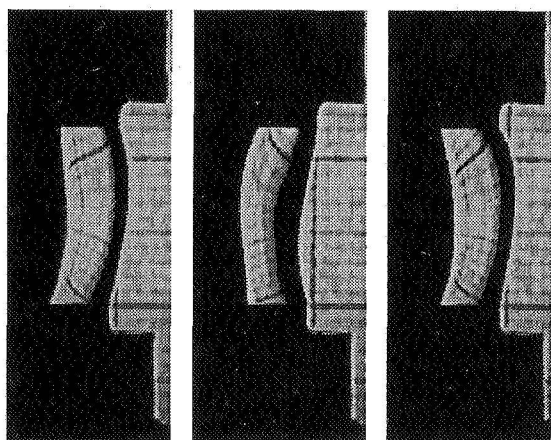
Fig 5a. Lateral oscillation at 1 Hz, 0.25 cm amplitude.
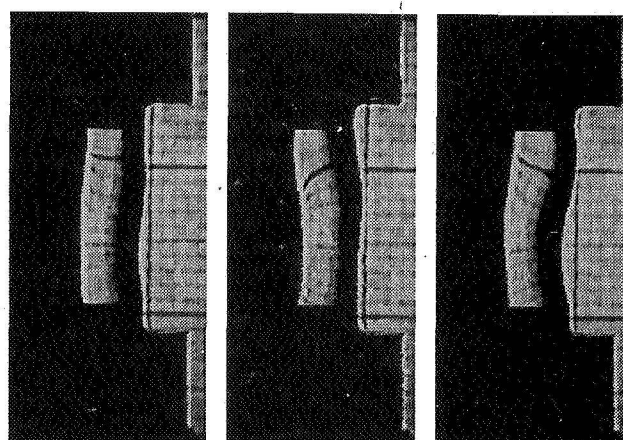
Fig. 5b.   Lateral oscillation at 1 Hz, 0.1 cm amplitude.
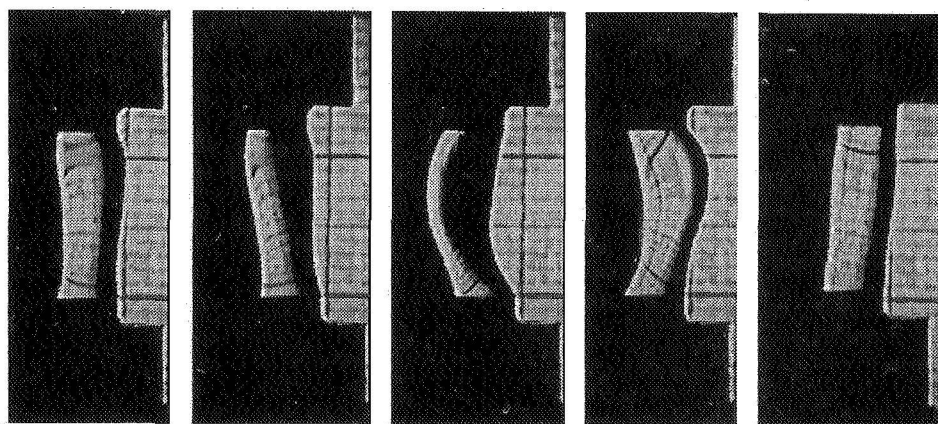
Fig. 6.   Rotation (lower disk) at 1 rps, lateral oscillation (upper disk) at 1 Hz, amplitude 0.4 cm, vertical oscillation (both disks) at 1.2 Hz.
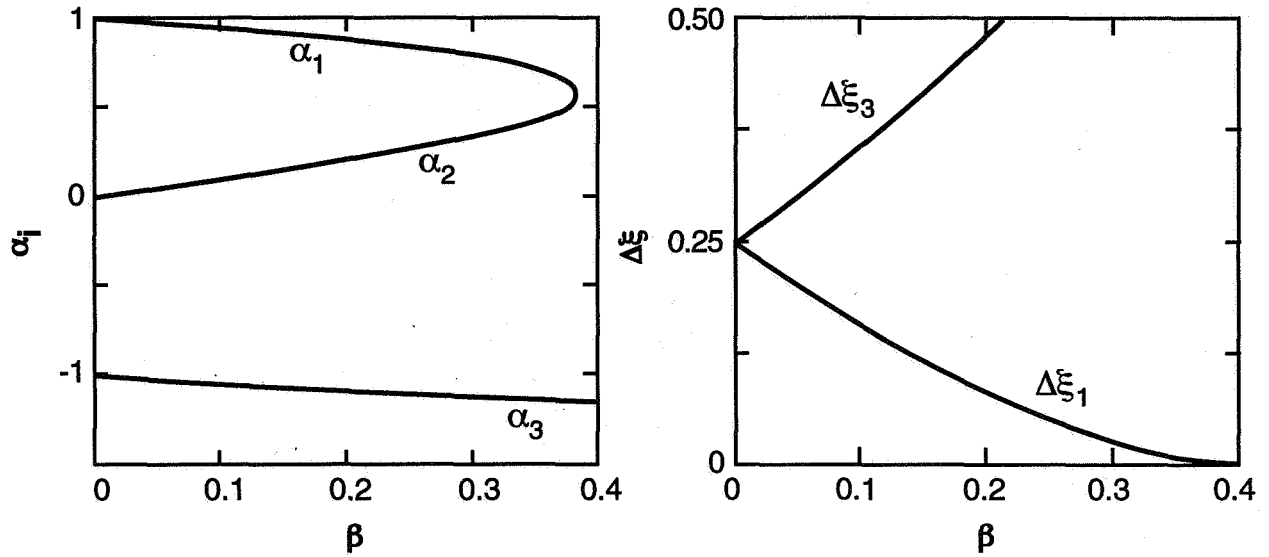
Fig. 7. Variation of the roots, α_i, (of eq. (2)) and the energy difference $\Delta\xi_i$ with the Bond number β.
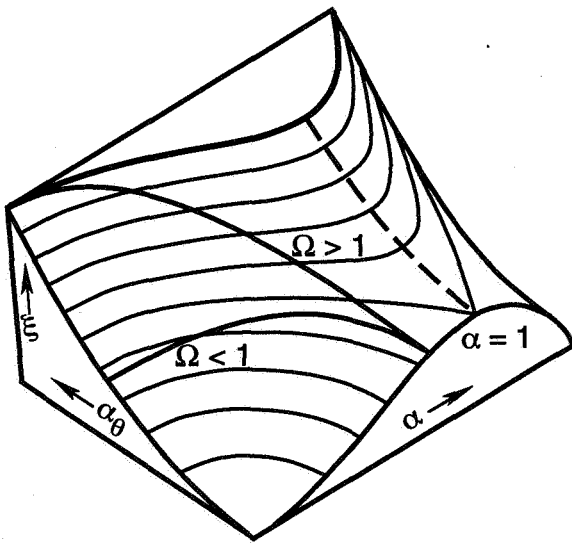
Fig. 8. Phase space of the forced oscillations of a liquid bridge according to eq. (5). Two evolutions are represented, $\Omega > 1$ and $\Omega < 1$, where Ω is the frequency of the forcing.
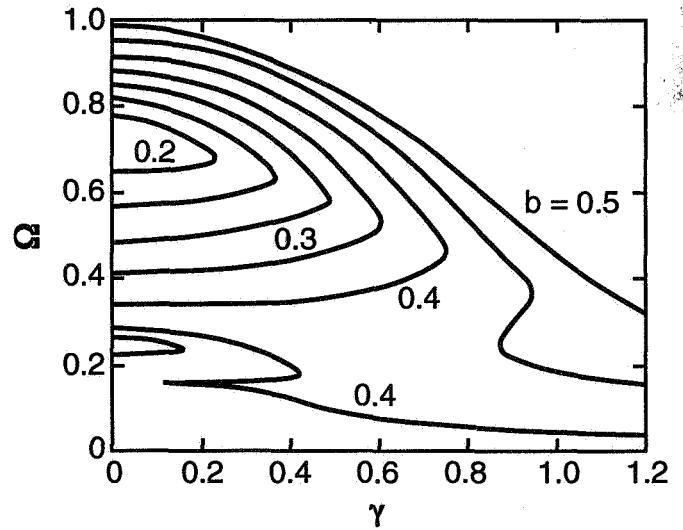
Fig. 9. Stability diagram in self-similar variables as given by eq. (6). Points on the left of each curve $b = $ constant are unstable for this value of b, whereas those lying on the right are stable.

81
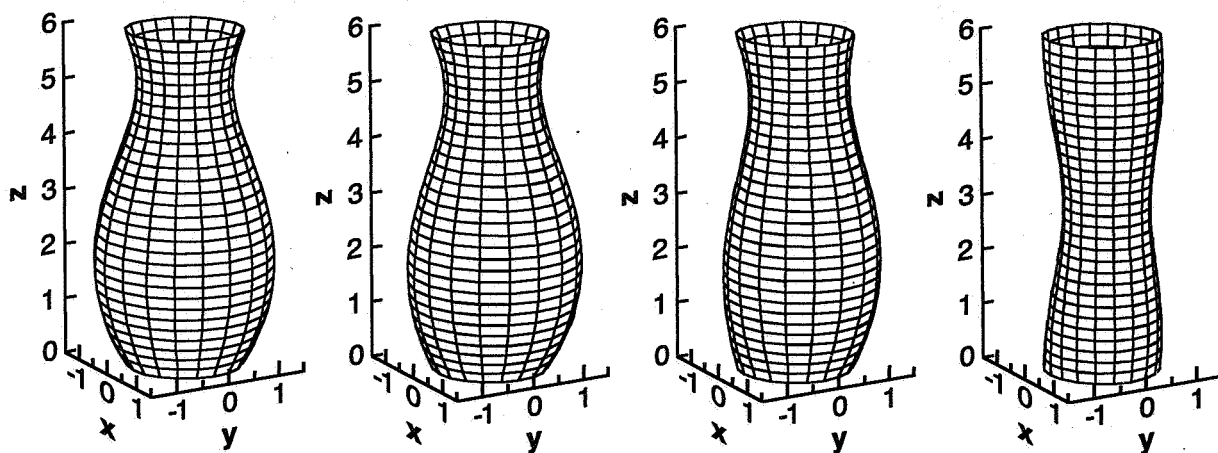
Fig. 10. Bridge profiles prior to breaking for a non-axial gravity vector. L/2r = 3, Bo = 0.05, for inclinations of a) 0, b) 30, c) 60 and d) 90 degrees, resectively.
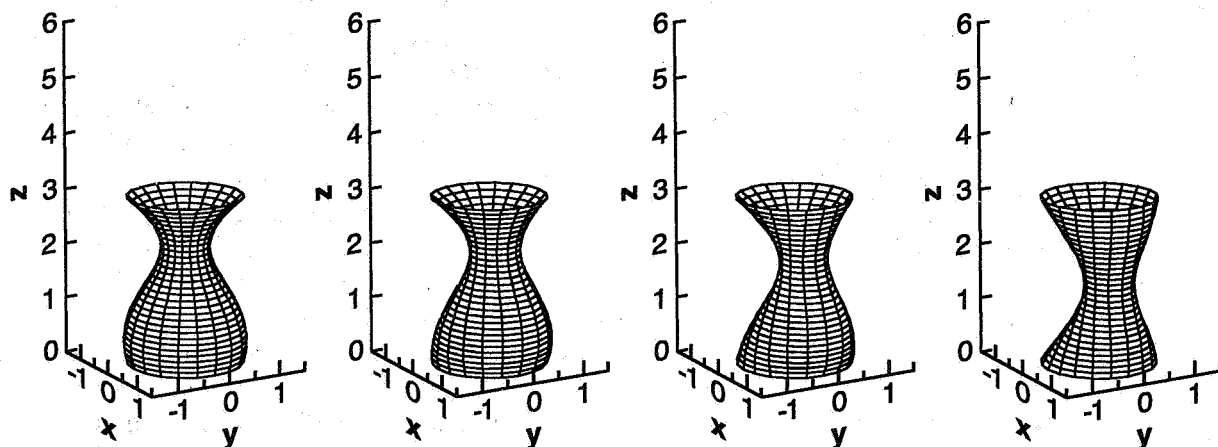
Fig. 11. Bridge profiles prior to breaking for a non-axial gravity vector. L/2r = 1.5, Bo = 0.5, for inclinations of a) 0, b) 30, c) 60 and d) 90 degrees, resectively.
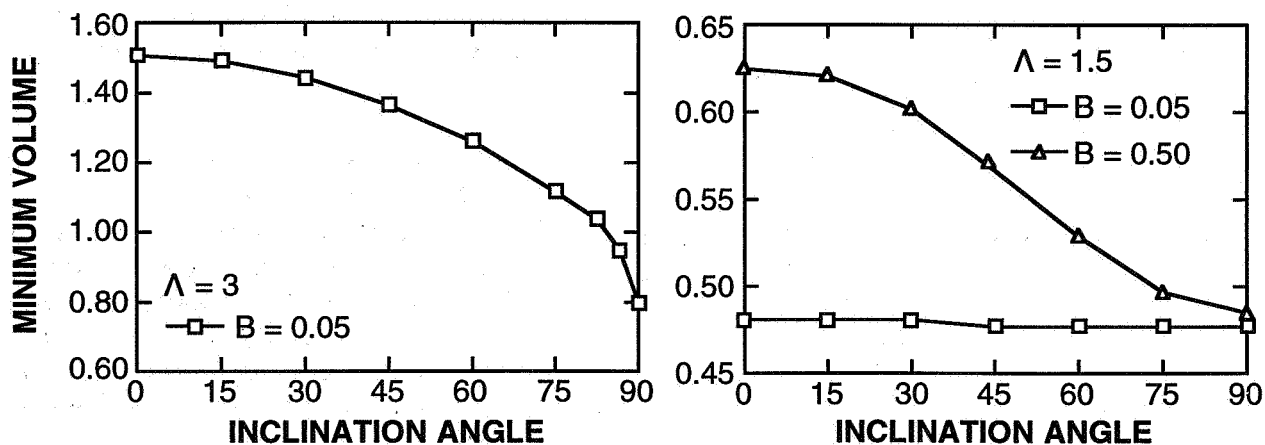
Fig. 12. Effect of inclination angle on the minimum stable volume at fixed Bo and aspect ratio.

EQUILIBRIUM FLUID INTERFACE BEHAVIOR UNDER LOW- AND ZERO-GRAVITY CONDITIONS

Paul Concus
Lawrence Berkeley Laboratory and Department of Mathematics
University of California
Berkeley, CA 94720

Robert Finn
Department of Mathematics
Stanford University
Stanford, CA 94305

INTRODUCTION

We describe here some of our recent mathematical work, which forms a basis for the Interface Configuration Experiment scheduled for USML-2. The work relates to the design of apparatus that exploits microgravity conditions for accurate determination of contact angle. The underlying motivation for the procedures rests on a discontinuous dependence of the capillary free surface interface S on the contact angle γ, in a cylindrical capillary tube whose section (base) Ω contains a protruding corner with opening angle 2α, see Figure 1. Specifically, in a gravity-free environment, Ω can be chosen so that, for all sufficiently large fluid volume, the height of S is uniquely determined as a (single-valued) function $u(x,y)$ entirely covering the base; the height u is bounded over Ω, uniformly in γ throughout the range $|\gamma - \frac{\pi}{2}| \leq \alpha$, while for $|\gamma - \frac{\pi}{2}| > \alpha$ the fluid will necessarily move to the corner and uncover the base, rising to infinity (or falling to negative infinity) at the vertex, regardless of volume. Background details and historical discussion are given in [1], [2], [3]. We mention here only that procedures based on the phenomenon promise excellent accuracy when γ is close to $\pi/2$ but may be subject to experimental error when γ is close to zero (or π), as the "singular" part of the domain over which the fluid accumulates (or disappears) when a critical angle γ_0 is crossed then becomes very small and may be difficult to observe. In what follows, we ignore the trivial case $\gamma = \pi/2$ (planar free surface interface), to simplify the discussion.

CANONICAL PROBOSCIS VESSELS

As a way to overcome the experimental difficulty, "canonical proboscis" sections Ω were introduced in [4]. These domains consist of a circular arc attached symmetrically to a (symmetric) pair of curves described by

$$x = \sqrt{R_0^2 - y^2} + R_0 \sin\gamma_0 \ln \frac{\sqrt{R_0^2 - y^2}\cos\gamma_0 - y\sin\gamma_0}{R_0 + y\cos\gamma_0 + \sqrt{R_0^2 - y^2}\sin\gamma_0} + C, \qquad (1)$$

and meeting at a point P on the x-axis, see Figure 2. Here R_0, as well as the particular points of attachment, may be chosen arbitrarily. The case $\gamma_0 < \pi/2$ is illustrated; the supplementary one $\gamma_0 > \pi/2$ is reduced to that one on replacing the height u by its negative. We discuss here only the case $\gamma_0 < \pi/2$ in what follows. The (continuum of) circular arcs Γ_0 are all horizontal translates of a given such arc, of radius R_0 and with center on the x-axis, and the curves (1) have the property that they meet all the arcs Γ_0 in the constant angle γ_0. If the radius ρ of the circular boundary arc can be chosen in such a way that

$$|\Sigma| R_0 \cos\gamma_0 = |\Omega|, \qquad (2)$$

C-2

C
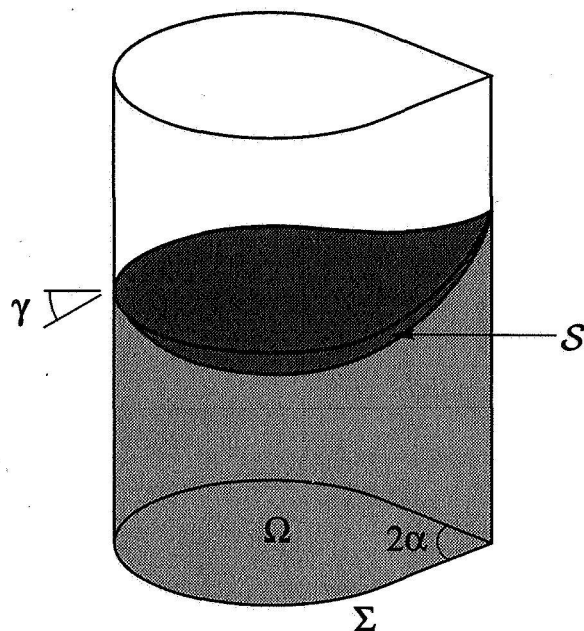
Figure 1. *Capillary surface in cylindrical tube with protruding corner in section.*
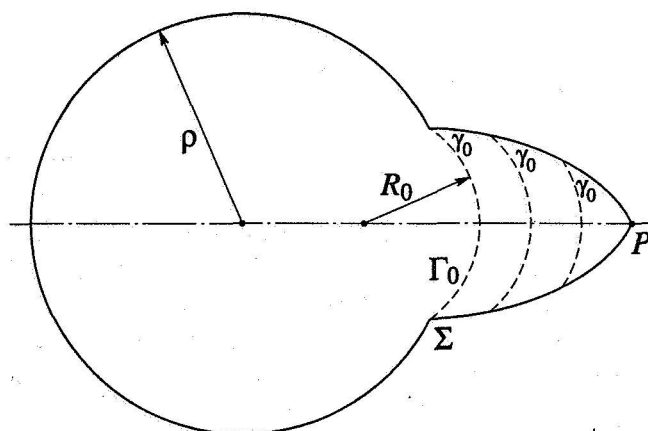
Figure 2. *Proboscis domain showing three members of the continuum of extremal arcs.*

then the arcs Γ_0 become extremals for a "subsidiary" variational problem ([5], see also [2, Chap. 6], [3]) determined by the functional

$$\Phi \equiv |\Gamma| - |\Sigma^*| \cos\gamma + \frac{|\Sigma|}{|\Omega|} |\Omega^*| \cos\gamma . \tag{3}$$

defined over piecewise smooth arcs Γ, see Figure 3. ($|\Sigma|$ and $|\Omega|$ denote respectively the length of Σ and area of Ω.) It can be shown [5], [2] that every extremal for Φ is a subarc of a semicircle of radius R_0, with center on the side of Γ exterior to Ω^*, and that it meets Σ in angles $\geq \gamma_0$ on the side of Γ within Ω^*, and $\geq \pi - \gamma_0$ on the other side of Γ (and thus in angle γ_0 within Ω^* whenever the intersection point is a smooth point of Σ). It is remarkable that whenever (2) holds, $\Phi = 0$ for every Ω^* that is cut off in the proboscis by one of the arcs Γ_0; see [4] and the references cited there.

In [4], a value for ρ was obtained empirically from (2) in a range of configurations, and it was conjectured that the angle γ_0 on which the construction is based would be critical for the geometry.
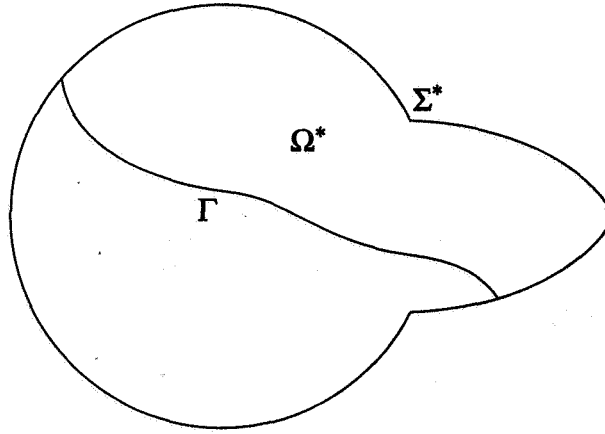
Figure 3. *Admissible configuration for variational problem.*

That is, a solution of the Young-Laplace capillary free-surface equation [2, Chap. 1]

$$\operatorname{div} Tu = \frac{|\Sigma|}{|\Omega|} \cos\gamma \quad \text{in } \Omega,$$

$$\nu \cdot Tu = \cos\gamma \quad \text{on } \Sigma,$$

where

$$Tu \equiv \frac{\nabla u}{\sqrt{1 + |\nabla u|^2}}$$

and ν is the exterior unit normal on Σ, should exist in Ω if and only if $\left|\gamma - \frac{\pi}{2}\right| < \left|\gamma_0 - \frac{\pi}{2}\right|$. Additionally, the surface height should approach infinity as $\left|\gamma - \frac{\pi}{2}\right| \nearrow \left|\gamma_0 - \frac{\pi}{2}\right|$, exactly in the region swept out by the arcs Γ_0. And if upper and lower bounds for ρ can be found, independent of γ and of the points of attachment of the circular arc portion of the boundary, then the section Ω can be designed so as to be contained in a fixed rectangle and so that the "singular" Ω_0^* contains another fixed rectangle, for all choices of γ bounded away from $\pi/2$. If γ is close to $\pi/2$ then previously applied techniques for determining contact angle in corner domains with planar walls are effective, see [6, p.136]. Thus, the experimental apparatus can be built so as to remain bounded in size, and so that the observed singular behavior occurs over a fixed rectangle, for all eventual measurements in the range of γ for which the previous techniques do not apply well.

For the above conjectures, which form the basis of our proposed procedure and for which the mathematical underpinnings were proved only partially in [4], complete mathematical proofs have been obtained. Specifically, it is shown in [7]:

Theorem 1. *For any γ_0 in the range $0 \le \gamma_0 < \pi/2$ and for any point of attachment, there exists a unique solution ρ of (2) as an unbranched continuation of the unique value $\rho = 2R_0 \cos\gamma_0$ obtained when the point of attachment is at P, and there holds $R_0 \cos\gamma_0 \le \rho \le 2R_0$.*

Theorem 2. *Let ρ be determined as in Theorem 1 for a proboscis domain Ω, and let Γ be a subarc in Ω of a semicircle of radius R_0. Let Ω_0^* be the portion of Ω cut out by Γ on the side exterior to its center. Then $\Phi[\Omega_0^*; \gamma_0] \ge 0$, equality holding if and only if Γ is one of the extremal arcs indicated in Figure 2.*

The stated geometrical properties of Ω follow from Theorem 1, from the relation $2\alpha = \pi - 2\gamma_0$ for the angle 2α formed at P, and from the convexity properties of the curves (1) that are considered. Using general results established in [5] and in [2, Chap. 6], Theorem 2 establishes that γ_0 is the

85

| .450e+01 |
| .405e+01 |
| .360e+01 |
| .315e+01 |
| .270e+01 |
| .225e+01 |
| .180e+01 |
| .135e+01 |
| .900e+00 |
| .450e+00 |
| .000e+00 |
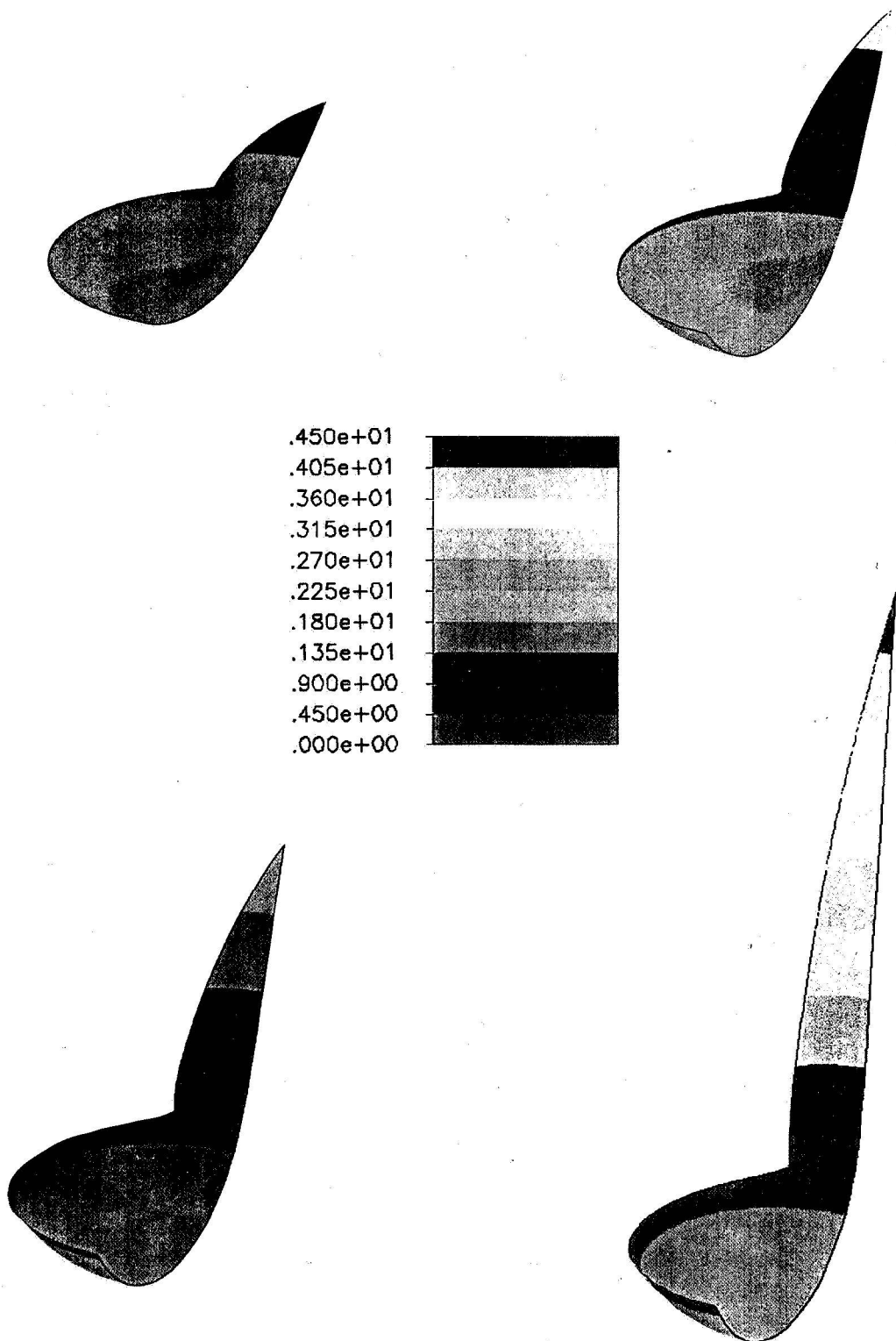
Figure 4. *Equilibrium interfaces, proboscis domain;* $\gamma = 60°, 40°, 35°, 31°$; $\gamma_0 = 30°$.

critical angle and also that there are no "extraneous" extremals, that is, the proboscis domain swept out by the extremal arcs Γ indicated in Figure 2 is exactly the domain in which the fluid height will rise unboundedly as $\left|\gamma - \frac{\pi}{2}\right| \nearrow \left|\gamma_0 - \frac{\pi}{2}\right|$.

Figure 4 is taken from [8] and shows results of computer calculations for a particular proboscis domain with $\rho = 1$ and proboscis length approximately 2/3, for four contact angles γ decreasing to the critical $\gamma_0 = 30°$. The individual figures show projections of the three dimensional surfaces, cut along the plane of symmetry, with height above the center of the circular arc portion indicated according to the scale of shadings shown. It is seen that although the fluid rise in the corner is not discontinuous as occurs for a planar wedge, the rise height in the proboscis is relatively modest until γ becomes very close to γ_0, and then becomes extremely rapid (at $\gamma = \gamma_0$ the rise height would be infinite). The proximity of γ to γ_0 could thus be readily evidenced by sensors close to the vertex, near the top of a container of carefully selected height. The method appears to open a prospect for contact angle measurements more accurate than can be obtained with presently available methods. The experiment for testing the proposed procedure on board the forthcoming USML-2 Space Shuttle flight is being designed and fabricated in collaboration with M. Weislogel of NASA Lewis Research Center. It is planned to use video cameras for recording the fluid behavior. The fabricated test containers will have two diametrically opposed canonical proboscis extensions to a circular cylinder, instead of just the one shown in Figure 2. These extensions will correspond to differing critical contact angles, to allow bracketing of the determined contact angle value.

CONCLUSION

The mathematical underpinnings have been completed for design of the canonical proboscis vessels for the USML-2 Interface Configuration Experiment. Testing of the mathematical results, in the presence of physical effects not included in the idealized Young-Laplace mathematical theory, such as those associated with contact-line resistance and inaccuracies in fabricating the vessels, awaits completion of the design and fabrication of the vessels and commencement of the experiment.

ACKNOWLEDGMENTS

REFERENCES

1. R. Finn: *On the contact angle in capillarity.* Proc. Third Intl. Coll. Diff. Eqns., Plovdiv, VSP, Zeist, 1993, 55–62.

2. R. Finn: *"Equilibrium Capillary Surfaces".* Springer-Verlag, New York, 1986. Russian translation (with Appendix by H.C. Wente) Mir Publishers, 1988.

3. P. Concus and R. Finn: *Dichotomous behavior of capillary surfaces in zero gravity.* Microgravity Sci. Technol. 3 (1990) 87–92; Errata, 3 (1991) 230.

4. B. Fischer, R. Finn: *Non-existence theorems and measurement of capillary contact angle.* Zeit. Anal. Anwend. 12 (1993) 405–423.

5. R. Finn: *A subsidiary variational problem and existence criteria for capillary surfaces.* J. reine angew. Math. 353 (1984) 196–214.

6. P. Concus, R. Finn, M. Weislogel: *Drop tower experiments for capillary surfaces in an exotic container.* AIAA J. 30 (1992) 134–137.

7. R. Finn, T. Leise: *On the canonical proboscis.* Zeit. Anal. Anwend., to appear.

8. P. Concus, R. Finn, F. Zabihi: *On canonical cylinder sections for accurate determination of contact angle in microgravity.* In: *"Fluid Mechanics Phenomena in Microgravity",* AMD Vol. 154, Amer. Soc. Mech. Engineers (ed.: D. A. Singer and M. M. Weislogel) New York, 1992, 125–131.

THE BREAKUP OF A LIQUID JET AT MICROGRAVITY

S.P. Lin and A. Honohan
Department of Mechanical and Aeronautical Engineering
Clarkson University, Potsdam, NY 13699

ABSTRACT

The parameter ranges in which a viscous liquid jet emanating into a viscous gas will breakup in three different modes are calculated. The three modes of jet breakup are: Rayleigh mode of capillary pinching, Taylor mode of atomization, and the absolute instability mode. The aparatus designed for elucidating these three different modes of instability is described. Some preliminary results of the ongoing ground based experiments will be reported.

INTRODUCTION

We investigate the stability of core-annular flow with respect to spatially growing disturbances. Spatially growing disturbances are especially relevant to the atomization process which utilizes the amplification of disturbances as they are convected downstream to generate small droplets. Atomization is a process used in various industrial, applications which include fuel sprays, fire suppressing, and advanced material processing. The atomization process must be carried out outside of the Rayleigh regime [1] of jet breakup by capillary pinching. It must also avoid absolute instability [2,3]. The liquid core-gas annular flow of two viscous fluids is shown to be capable of exhibiting either absolute or convective instability depending on the specific values of flow parameters involved. The relevant parameters are the Weber number, the Reynolds number, the Froude number, the density ratio, the viscosity ratio, and the radius ratio. The type of instability depends most sensitively on We and Re. The critical Weber number below which the flow is convectively unstable and above which the flow is absolutely unstable, is obtained as a function of the Reynolds number of the given remaining parameters. There are two modes of convective instability. The Rayleigh mode of convective instability caused by capillary pinching and the Taylor mode of atomization caused by interfacial stress fluctuation. The Taylor mode instability is shown to change over to the Rayleigh mode when the Froude number is increased beyond a certain value with the rest of flow parameters fixed. The practical implication of this is that the atomization processes widely used on earth in a given parameter range may fail to produce droplets smaller than the jet thickness at microgravity. This is due to the reduction in the interfacial stress fluctuation in the liquid core-gas annular flow at microgravity. Thus we are given an opportunity to explore the fundamental dynamics of interface at microgravity. The experiment described herein is aiming at elucidating these theoretical concepts. Moreover, the experiment will enable us to ascertain the notion of absolute instability which is predicted in various theories neglecting the gravity.

STABILITY ANALYSIS

Consider the stability of a cylindrical liquid jet of density ρ_1 flowing vertically downward in the direction of gravitational acceleration g. The jet is surrounded by a gas of density ρ_2 occupying the annular space between the jet and the inner wall of a vertical pipe of radius R_2.

The liquid and gas flows have the same pressure gradient in the jet flow direction. Hence the pressure drop across the liquid-gas interface at any cross section is constant along the axial direction. This pressure difference is balanced exactly by the surface tension force per unit surface area of the liquid cylinder of constant radius R_1 which is also the radius of curvature. This basic flow which satisfies exactly the Navier-Stokes equations can be written as [4]

$$W_1(r) = -1 + \frac{Nr^2}{[N-(1-\ell^2)]}\left\{1 - \frac{1-Q}{4N}\frac{Re}{Fr}[2\ln\ell + (1-\ell^2)]\right\},$$

$$W_2(r) = \frac{(\ell^2 - r^2)}{[N-(1-\ell^2)]}\left\{1 - \frac{(1-Q)}{4N}\frac{Re}{Fr}[2\ln\ell + (1-\ell^2)]\right\}$$

$$+ \frac{(1-Q)}{4N}\frac{Re}{Fr}[\ell^2 - r^2 - 2\ln(\frac{\ell}{r})]$$

$$N = \frac{\mu_2}{\mu_1}, \quad \ell = \frac{R_2}{R_1}, \quad Q = \frac{\rho_2}{\rho_1}$$

where the subscript 1 or 2 stands for the liquid or the gas phase respectively, r is the radial distance normalized with R_1, $W(r)$ is the axial velocity distribution, μ is the dynamic viscosity, ρ is the density, and W_o is the maximum jet velocity, Re $\equiv$ Reynolds number $= \rho_1 W_o R_1/\mu_1$, and Fr $\equiv$ Froude number $= W_o^2/gr_1$,

The axisymmetric normal mode disturbance is governed by the well known Orr-Sommerfeld equation in each phase. The solutions of the governing equations in the liquid and the gas phases are represented respectively by truncated series of two complete sets of orthogonal functions. These sets of functions satisfy the boundary conditions of zero radial velocity along the jet axis and on the inner wall of the vertical pipe. The other boundary conditions to be satisfied include the vanishing of tangential components of velocity at the pipe wall and the five conditions at the liquid-gas interface. The interfacial conditions are: balance of normal and tangential components of interfacial forces, continuity of normal and tangential velocity components, and a kinematic condition which relates the total time rate of displacement of the interface to the radial component of velocity. In addition to the five parameters introduced in the description of the basic state, there is an additional flow parameter appearing in this system. This additional parameter is the Weber number.

$$We = S/\rho_1 W_o^2 R_1,$$

which arises from the normal force balance at the interface. The Weber number represents the

90

ratio of the surface tension force to the inertia force. For a given set of flow parameters, the set of homoegneous equations possess a non-trivial solution only for certain characteristic frequencies ω and wave numbers k of the normal mode disturbance. ω and k must satisfy the condition that the determinant of the coefficient matrix of the above system vanishes. This yields the characteristic equation given by equation (21) of Lin and Ibrahim [4]. The normal mode disturbances involve an exponential factor exp(ikz + ωt), where t is the time and z is the axial distance measured in the opposite direction of the liquid flow. Both k and ω are complex, i.e. $k = k_r + ik_i$, and $\omega = \omega_r + i\omega_i$. Hence $k_i > 0$ gives the spatial growth rate of disturbances convected as a group in the downstream direction. $\omega_r > 0$ gives the temporal growth rate of unstable disturbances. k_r is the real wave number which is inversely proportional to the wave length. ω_i is the natural frequency of oscillation of the normal mode disturbance. The group velocity of the disturbance is given by $-\partial\omega_i/\partial k_r$. In the temporal formulation k is treated as real.

To determine the spatial amplification rate of convectively unstable disturbances for a given set of parameters, we put $\omega_r = 0$ and assign different values to ω_i in the characteristic equations. k_r and k_i are then solved from the real and imaginary parts of the characteristic equation. The subrountines CGEDI and DNSQ in the SLATEC library are utilized to effect the solution. The set of points (k_r, k_i) for various values of ω_i determine the spatial amplification curve $\omega_r = 0$. The numerical results are reported elsewhere. The main findings are already summarized in the introduction and will not be repeated here.

EXPERIMENTS

The liquid jet is produced using the pressure vessel shown in Figure 1. Prior to the experiment the vessel is filled with liquid and compressed gas. The pressure inside the vessel is monitored with a pressure gauge at the top of the cylinder. To start the flow of liquid, a remotely operated solenoid valve is opened. The pressure difference between the inside of the vessel and the surrounding air forces the liquid through a nozzle connected to the solenoid valve. Different jet velocities can be obtained by varying the internal pressure of the vessel. This design was chosen over several alternatives because of its versatility. This single vessel will be capable of producing jets which exhibit all three modes of jet breakup, namely Rayleigh mode, Taylor mode and absolutely unstable mode. Table 1 delineates some estimated operating parameters for each mode. An estimation of the expected intact length of the jet is also presented in Table 1.
Currently the design is limited by the solenoid valve to a maximum pressure of 60 psig. The same pressure vessel, with a different solenoid valve can be used at pressures up to about 150 psig. This operating pressure is sufficient to span much of the parameter range for Rayleigh mode and absolutely unstable mode, with Taylor mode requiring higher pressures.

Other components of the apparatus include a piezoelectric device, camera, and light source. A piezoelectric device, with the proper electronics, may be used in order to introduce disturbances of various frequencies into the liquid jet. The camera and light source will be used to record the stability characteristics. All of these components, including the pressure vessel, are contained within a single steel frame with dimensions of 50 cm x 25 cm x 76 cm.

One g experiments are currently being carried out at Clarkson University. Preliminary results for the one g tests will be presented. The apparatus was designed so that it could be used for drop tower testing with a minimum amount of modification.

ACKNOWLEDGEMENTS

REFERENCES

[1]S.P. Lin and Z.W. Lian, AIAA Journal 28, (1990), 120.

[2]S.J. Leib and M.E. Goldstein, Phys. Fluids 29, (1986), 952.

[3]S.P. Lin adn Z.W. Lian, Phys. Fluids A 1, (1989), 490.

[4]S.P. Lin and E.A. Ibrahim, J. Fluid Mech. 218, (1991), 641.

Table 1: Parameter Ranges for Liquid Jet Experiments

for a nozzle diameter of 0.5 mm

Absolute Instability

Fluid	U (m/s)	Reynolds Number (R)	Weber Number (We)	Density Ratio (Q)	Intact Length (cm)	Pressure (psig)
SAE 10 Oil	1.08	2.27	0.135	0.00134	1.5	26
SAE 10 Oil	0.54	1.14	0.538	0.00134	0.7	13
SAE 30 Oil	1.07	0.85	0.133	0.00134	3.0	69
SAE 30 Oil	0.53	0.42	0.544	0.00134	1.5	34
SAE 30 Oil	0.15	0.12	6.79	0.00134	-	9.5
Water	0.75	190	0.500	0.0013	0.2	0.2
Water	0.47	118	1.300	0.0013	0.1	0.1
Water	0.15	37	13.00	0.0013	-	0.04
Ethanol	0.85	140	0.16	0.0016	-	0.02

Rayleigh Mode Instability

Fluid	U (m/s)	Reynolds Number (R)	Weber Number (We)	Density Ratio (Q)	Intact Length (cm)	Pressure (psig)
SAE 10 Oil	10.83	22.8	0.00134	0.00134	25	272
SAE 10 Oil	3.423	7.20	0.0134	0.00134	10	84
SAE 30 Oil	10.67	8.44	0.00134	0.00134	2.0	680
SAE 30 Oil	3.375	2.67	0.0134	0.00134	5.0	220
Water	14.88	3720	0.0013	0.0013	3.8	23
Water	4.71	1170	0.013	0.0013	1.3	3.1
Ethanol	8.50	1398	0.0016	0.0016	2.5	7.5

Taylor Mode Instability

Fluid	U (m/s)	Reynolds Number (R)	Weber Number (We)	Density Ratio (Q)	Pressure (psig)
Water	148.8	74400	0.00013	0.0013	3000
Water	105.2	52600	0.00026	0.0013	1300
Water	74.4	37200	0.00052	0.0013	680
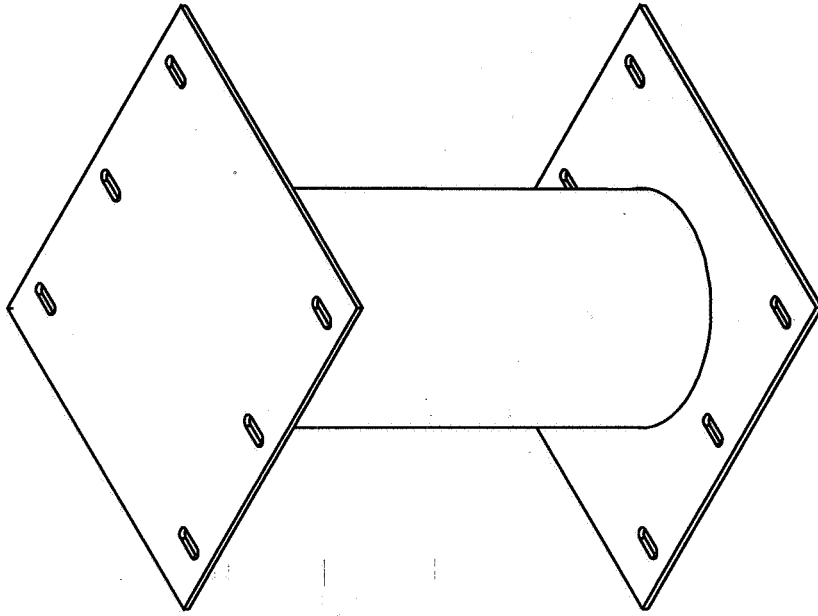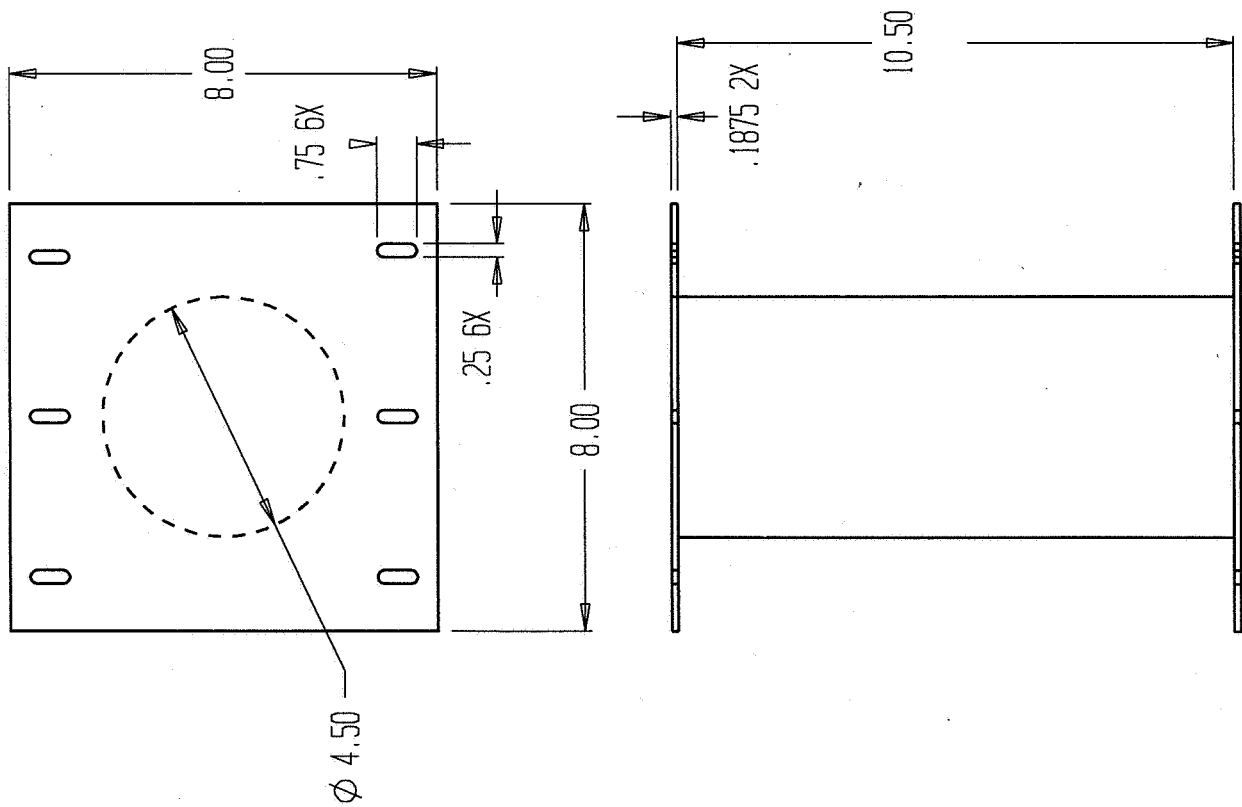
Figure 1: Pressure Vessel Design

Cylinder Thickness = 0.25"
All Dimensions in inches
Material – low carbon steel

8.00

.75 6X

.25 6X

8.00

Ø 4.50

.1875 2X

10.50

MICROSCALE HYDRODYNAMICS NEAR MOVING CONTACT LINES

S. Garoff, Q. Chen, E. Ramé, K.R. Willson
Department of Physics
Carnegie Mellon University
Pittsburgh, PA 15213

ABSTRACT

The hydrodynamics governing the fluid motions on a microscopic scale near moving contact lines are different from those governing motion far from the contact line. We explore these unique hydrodynamics by detailed measurement of the shape of a fluid meniscus very close to a moving contact line. The validity of present models of the hydrodynamics near moving contact lines as well as the dynamic wetting characteristics of a family of polymer liquids are discussed.

INTRODUCTION

Wetting and spreading of two immiscible liquids or a liquid and a gas across a solid surface are ubiquitous in nature and technology. In the reduced gravity of space, the behavior of multi-phase fluid systems can be greatly influenced, if not dominated, by forces associated with surface tension and the wetting characteristics of the system. The wetting of a surface is described by the shape of the fluid-fluid (liquid-liquid or liquid-gas) interface as it approaches the solid surface. The contact angle is often used to specify this shape near the solid surface and acts as a boundary condition to the differential equation describing the fluid-fluid interface shape. For static wetting, the correct determination of the contact angle hinges on the extrapolation of the hydrostatic shape of the macroscopic fluid body to the solid surface. The dynamic case is much more complex. Dynamic forces cause the stress field in the fluid and the curvature of the interface to increase as the contact line is approached.[1,2] This rapid increase of the interface curvature, called "viscous bending", makes it difficult to specify a contact angle in a manner similar to that used in statics.

To properly describe the moving contact line, one must alleviate the divergence of the stress field and interface curvature predicted when the hydrodynamics which successfully describes motion of a single fluid past a wall is applied up to the contact line. This is done by assuming that a small region near the contact line is governed by different hydrodynamics, such as allowing slip of the fluid past the solid surface. At present, we use a model consisting of an approximate expression for the shape of the fluid-vapor interface obtained by the method of

matched asymptotic expansions in three regions: (1) an inner region very near the contact line where the classical hydrodynamics break down, (2) an intermediate region further from the contact line which is controlled by the balance of viscous and surface tension forces and is governed by classical hydrodynamics, and (3) an outer region far from the contact line which is controlled by the balance of surface tension forces and gravity and is dominated by the macroscopic geometry of the fluid body.[3] The final description of the interface shape to order 1 in the capillary number Ca ($Ca = \mu U / \gamma$ where μ is the viscosity, U is the contact line speed and γ is the surface tension) is:

$$\theta \sim g^{-1}[g(\omega_0) + Ca \ln (\tfrac{r}{a})] + f_0(\tfrac{r}{a}, \tfrac{R_t}{a}, \omega_0) - \omega_0 \qquad (1)$$

where
$$g(x) \equiv \int_0^x \frac{\rho - \sin \rho \cos \rho}{2 \sin \rho} d\rho \; ,$$

r is the distance from the contact line, θ the slope of interface, a is the capillary length, f_0 is the outer interface shape for a static meniscus rising on a tube of radius R_t immersed vertically into a fluid bath in our experiments, and ω_0 is the single fitting parameter and characterizes the dynamic wetting of a materials system. The first term in equation 1, representing the interface shape in the intermediate region, and the value of ω_0 form the correct, dynamic contact angle boundary condition for the moving contact line problem.

EXPERIMENTAL TECHNIQUE AND RESULTS

To experimentally probe the physics governing moving contact lines, we carefully measure the fluid-vapor interface shape very near a moving contact line.[4] Using videomicroscopy and digital image analysis, the local slope of the meniscus on the outside of a large diameter tube is determined from $10\mu m$ to $400\mu m$ from the contact line. Critical design and alignment of the optical system are essential to minimize systematic error in measuring the interface shape. Our system is calibrated by comparison to the known shape of static menisci.

To date, our studies have focused on the spreading of a class of polymer liquids, polydimethylsiloxanes (PDMS), on clean Pyrex.[4,5] We have found that equation 1 correctly describes the interface shape for $Ca < 0.1$ (see figure 1) and that the predicted form of the interface shape in the intermediate region forms a geometry-independent boundary condition for the macroscopic interface shape in the outer region. Our results show that the asymptotic behavior of any model proposed to describe the unique hydrodynamics occurring in the inner region near the contact line must be of the form $Ca \ln(r)$. For $Ca > 0.2$, our measurements show systematic deviations from the model (see figure 2). These deviations are localized to a region near the contact line. The size of this region expands as Ca increases.

In a study of hydroxyl- and methyl-terminated PDMS, we have found that dynamic wetting is very sensitive to the details of the fluid-surface interaction.[5] Strong interactions of the fluid molecules and the surface enhance this sensitivity, and it is larger than the sensitivity to molecular weight. The Ca dependence of the parameter ω_0, which describes dynamic wetting, is indistinguishable for methyl-terminated PDMS fluids which range over an order of magnitude in viscosity and are spreading over Pyrex surfaces with slightly varying surface chemistries (see figure 3). In contrast, the hydroxyl-terminated PDMS fluids which have a more chemically active end termination show distinct differences in their dynamic wetting depending on the precise chemical conditions on the Pyrex surface (see figure 4). These experiments show that the interaction between the polymer chain and the surface strongly affect the inner scale hydrodynamics.

Understanding the fundamental physics and chemistry governing moving contact lines and dynamic contact angles demands measuring properties free from the contamination of the specific macroscopic geometry of the experiment. In low gravity, the region where the geometry-free viscous forces dominate geometry-dependent forces expands. This region increases by over an order of magnitude from a fraction of the capillary length (a = 1.5mm) on earth to a fraction of the experimental container (5cm) in low gravity. Thus, while optical systems detect only a small fraction of the geometry-free region in terrestrial gravity, they probe long extents of the region in low gravity. Thus, microgravity studies will be an important tool in future explorations of the geometry-free properties of moving contact lines.

REFERENCES
1. C. Huh and L.E. Scriven, J. Coll. Interf. Sci., 35 (1971) 85.
2. E.B. Dussan V. and S.H. Davis, J. Fluid Mech., 65 (1974) 17.
3. E.B. Dussan V., E. Ramé and S. Garoff, J. Fluid Mech., 230 (1991) 97.
4. J.A. Marsh, S. Garoff and E.B. Dussan V., Phys. Rev. Lett., 70 (1993) 2778.
5. K.R. Willson and S. Garoff, accepted for publication in Colloids and Surfaces.
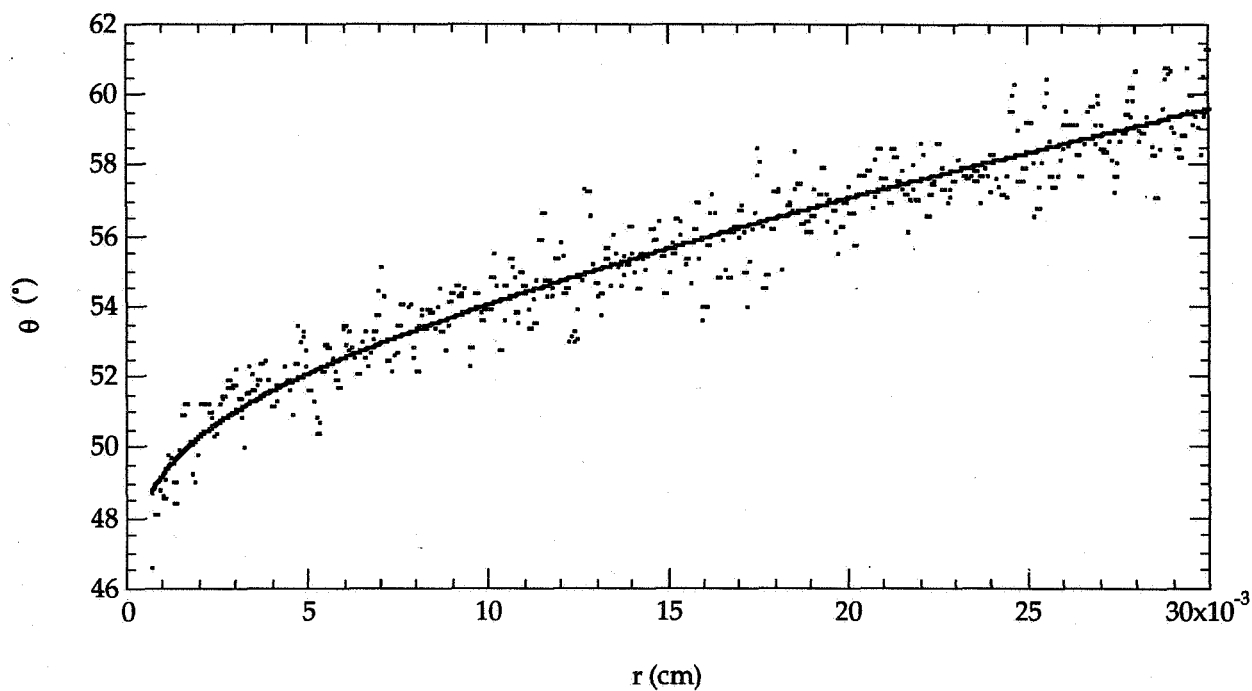
Figure 1. Interface shape data and fit at $Ca = 0.005$.
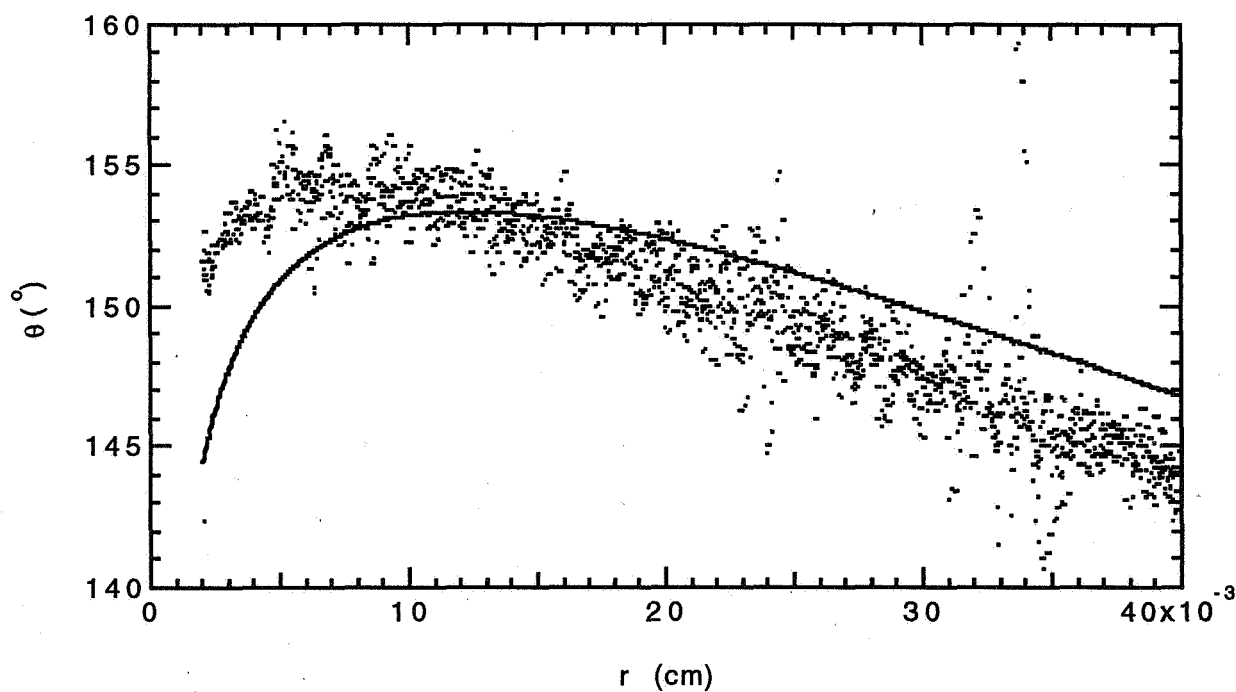
Figure 2. Interface shape data and fit at Ca= 0.46.
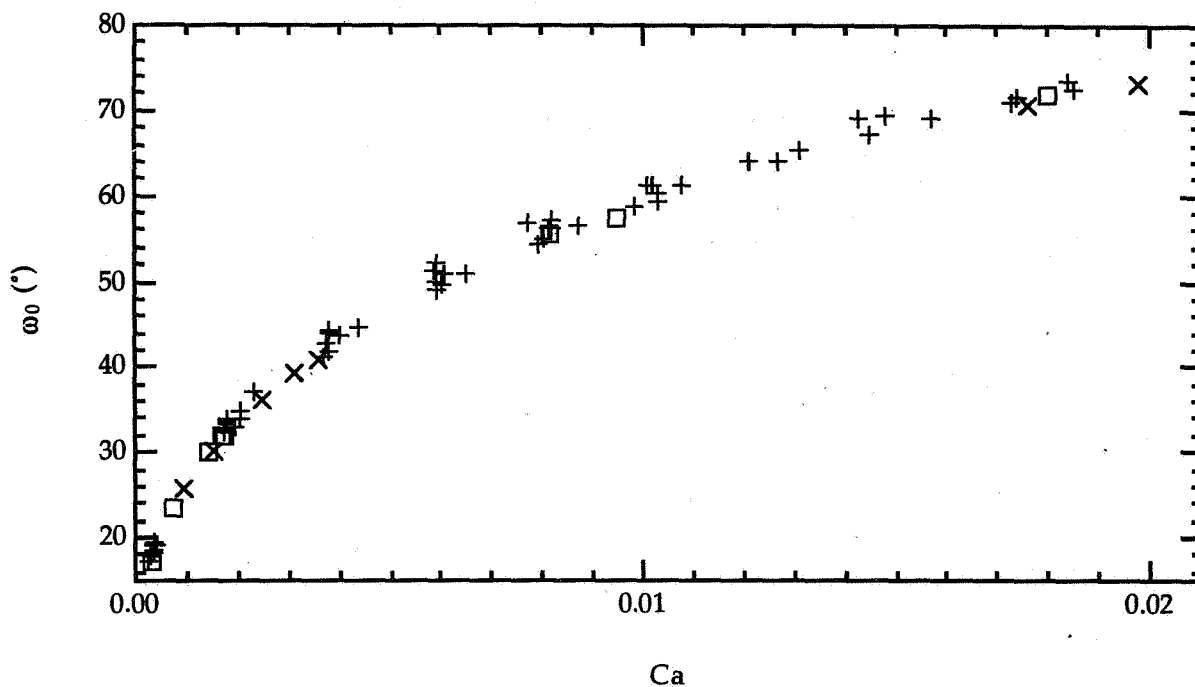
Figure 3. ω_0 vs. Ca for methyl-terminated PDMS of different viscosities on various Pyrex surfaces. (+ : 10poise, ☐ :50poise, x : 100poise)
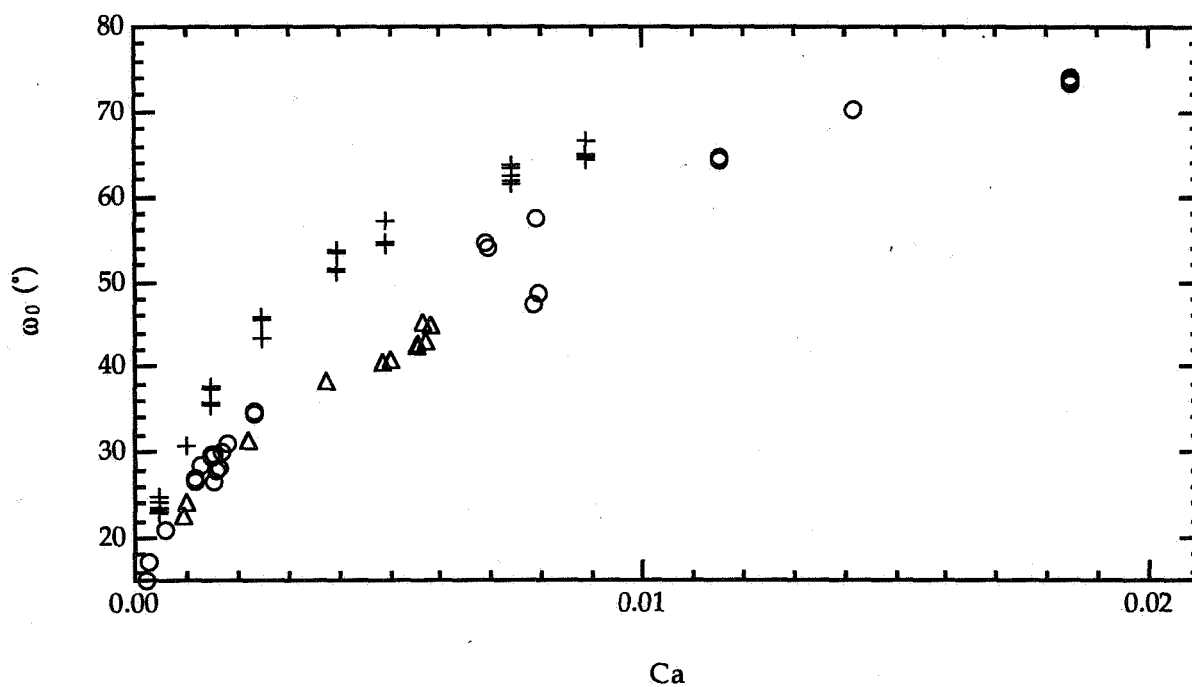
Figure 4. ω_0 vs. Ca for hydroxyl-terminated PDMS of different viscosities on various Pyrex surfaces. (+ : 10poise, O :45poise, Δ: 160poise)

PHASE SEGREGATION DUE TO SIMULTANEOUS MIGRATION AND COALESCENCE

Robert H. Davis, Hua Wang, and Debra Hawker
Department of Chemical Engineering
University of Colorado
Boulder, Colorado 80309-0424

ABSTRACT

Ground-based modeling and experiments have been performed on the interaction and coalescence of drops leading to macroscopic phase separation. The focus has been on gravity-induced motion, with research also initiated on thermocapillary motion of drops. The drop size distribution initially shifts toward larger drops with time due to coalescence, and then back towards smaller drops due to the larger drops preferentially settling out. As a consequence, the phase separation rate initially increases with time and then decreases.

INTRODUCTION

Dispersions of drops of one fluid in a second, immiscible fluid are frequently encountered in industrial and natural processes such as extraction, rain-drop growth, food and beverage processing, and the formation of liquid-phase-miscibility-gap materials. In the absence of stirring or bulk motion, dispersed drops of different sizes may undergo relative motion under the action of gravity. The larger drops migrate more rapidly and catch up to the smaller drops in their path, leading to possible contact and coalescence. In a finite sample, drop migration and coalescence generally result in an inhomogeneous dispersion with phase separation. In extraction, this is the desired result; the two phases must separate subsequent to mixing for the partitioned component to be recovered. A counter-example is the processing of liquid-phase-miscibility-gap metals, for which the desired product is a composite material with fine particles of one metal uniformly dispersed in a matrix of the other. Low-gravity environments suppress buoyancy-driven droplet motion, but coalescence and phase separation may still occur due to thermocapillary effects [1].

Gravity sedimentation of particles in the absence of coalescence or aggregation has been studied extensively [2]. Similarly, coalescence of drops in spatially uniform dispersions in the absence of phase separation has been modeled extensively [3-6]. A notable example of simultaneous sedimentation and coalescence is the study of Reddy, Melik & Fogler [7]. They noted that the probability size distribution shifts toward larger drops when coalescence dominates, toward smaller particles when sedimentation dominates, and initially toward larger drops and subsequently toward small drops when both mechanisms are important.

In the current work, we predict the macroscopic phase separation and drop-size distributions for buoyancy-driven sedimentation and coalescence of immiscible dispersions of drops by solving the general population dynamics equations with both time-dependence and spatial-dependence retained, and incorporating a mass balance on the drops arriving at the moving interface. Preliminary experiments on two-phase systems are also presented. Comparison work has been performed on drop coalescence due to Brownian diffusion and thermocapillary effects, with the focus to-date on spatially uniform dispersions [5,6,8].

THEORY

We consider a dilute dispersion of spherical drops of viscosity μ' and density ρ' dispersed in an immiscible fluid of viscosity μ and density ρ. The drops are considered to be nonBrownian, but not so large that inertial effects or deformation are important. For common liquids, these conditions are met for drops with diameters of 2-100 μm [9].

The typical problem of interest is illustrated in Fig. 1. The initial condition (Fig. 1a) is a uniform suspension of droplets of one fluid dispersed in a second, immiscible liquid. After mixing is stopped, the drops begin to rise due to buoyancy (assuming, for illustrative purposes, that $\rho' < \rho$). As the drops reach the top of the container, they coalesce into an overlying, segregated layer of the dispersed-phase fluid (Fig. 1b). This layer grows with time (Fig. 1c) until all of the dispersed drops have coalesced into it (Fig. 1d). The problem is complicated by the possibility that the drops also collide and coalesce with each other as they rise, and, because the larger drops move faster and leave the smaller ones behind, the drop size distribution varies with both time and position.

The temporal and spatial evolutions of the drop size distribution are studied by using population dynamics equations:

$$\frac{\partial n_i}{\partial t} + \frac{\partial (u_i n_i)}{\partial z} = \frac{1}{2} \sum_{j=1}^{i-1} J_{j(i-j)} - \sum_{j=1}^{N} J_{ij} \ , \quad i = 1, 2, ... N \ , \tag{1}$$

where n_i is the number of drops per unit volume in the discrete size category i, u_i is the Stokes' settling velocity of drops of size i, t is time, z is the direction of drop migration (vertical, as defined in Fig. 1), J_{ij} is the rate of collisions per unit volume of size i drops with size j drops, and N is the total number of size categories. The first term on the right-hand-side of Eq. (1) is the rate of formation of size i drops by collision of two smaller drops, and the second term is the rate of loss of size i drops due to their collisions to form larger drops. The collision rate between drops in size category i (larger drops) and the size category j (smaller drops) may be expressed as [9]:

$$J_{ij} = n_i n_j \pi (a_i + a_j)^2 \mid u_i - u_j \mid E_{ij} \ , \tag{2}$$

where a_i and a_j are the large and small drop radii, respectively, and E_{ij} is the collision efficiency. The collision efficiency equals unity when the drops move independently until colliding; values of E_{ij} differing from unity are given previously [9] and account for hydrodynamic forces which cause the drops to move around one another and the attractive forces which pull them together.

The rate at which the lighter phase grows at the top of the vessel due to droplets reaching this phase is determined by a mass balance:

$$-A \frac{dh_u}{dt} = \sum_{i=1}^{N} A \left(u_i - \frac{dh_u}{dt} \right) n_i V_i \ , \tag{3}$$

where the left-hand-side is the rate of accumulation of the upper phase and the right-hand-side is the flux of drops into the upper phase, A is the cross-sectional area of the container, $V_i = \frac{4}{3}\pi a_i^3$ is the volume of a drop of size i, and $\phi = \sum_{i=1}^{N} V_i n_i$ is the total volume fraction of droplets in the suspension just below the upper interface at $z = h_u(t)$. The initial condition is $h_u = H$ at $t = 0$.

The population dynamics equations were nondimensionalized and then solved using the Lax-Wendroff finite-difference method [10]. The numerical methods used in the modeling involve logarithmic discretization of drop spectra into N categories which have equal spacing in the logarithm of droplet mass or volume, and the mass or volume of a droplet within each discrete category doubles every fourth category [3]. The initial size distributions, assumed uniform for $0 \leq z \leq H$, were chosen to be normal distributions on a number basis, as specified by the number-averaged drop radius, a_o, and the standard deviation, σ, of drop radii. In dimensionless form, normal distributions are characterized by a single dimensionless parameter, $\hat{\sigma} = \sigma/a_o$. The dimensionless parameters which affect the macroscopic behavior of a dispersion include the viscosity ratio, $\hat{\mu} = \mu'/\mu$, the dimensionless standard deviation of radii in the initial distribution, $\hat{\sigma} = \sigma/a_o$, the initial volume fraction, ϕ_o, and the time scale ratio, $N_\tau \equiv \tau_s/\tau_c = 3\phi_o H/4a_o$, where $\tau_s = H/u_o$ is the characteristic settling time for drop with velocity u_o and radius a_o to travel the length of the container, and $\tau_c = 4a_o/(3\phi_o u_o)$ is the characteristic coalescence time.

102

Figure 2 shows the evolution of the average radius (defined in [5] as the radius of a drop having the mass-averaged volume) versus time at the container midpoint for a dispersion having $\hat{\sigma} = 0.2$, $\hat{\mu} = 0.1$, and different values of N_r. It is seen that the average droplet radius initially increases with time due to coalescence; after the larger drops sediment out of the dispersion, the average radius began to decrease.

The variation of the droplet volume fraction with dimensionless position at different times is shown in Fig. 3 for a dispersion with $\hat{\mu} = 0.1$, $\hat{\sigma} = 0.2$, and $N_r=20$. The volume fraction in the lower regions of the container decreases rapidly with time as the drops rise. For short times, the volume fraction in the upper regions of the dispersion is the same as the initial volume fraction. This is because droplets which rise out of a control volume at the top of dispersion are replaced at an equal rate by droplets moving into the control volume. With time increasing, however, larger drops rise out of the dispersion, and the volume fraction at any height in the dispersion system is significantly less than the initial volume fraction.

Typical results for the gravitational phase separation rate are shown in Fig. 4 for a dispersion having $\hat{\mu} = 0.1$, $\hat{\sigma} = 0.1$ (dashed lines), $\hat{\sigma} = 0.2$ (solid lines), $\phi_o=0.05$, and different N_r. When $N_r=0$, no coalescence occurs. Phase separation then takes place at a constant rate until the largest drops rise out of the dispersion, after which the phase separation rate monotonically decreases due to fewer and smaller drops arriving at the phase interface. When $N_r > 0$, the phase separation rate initially increases, because coalescence leads to larger drops with faster rise rates. Once these drops rise out of suspension, however, the phase separation rate reaches a maximum and then decreases as only smaller drops remain. Note that relatively large values of $N_r \geq O(10)$ are necessary for coalescence to significantly affect the phase separation process. This is because typical collision efficiencies are $O(10^{-1})$ for dispersions with $\hat{\mu} = 0.1$ [9].

EXPERIMENTS

Experiments to observe and measure drop coalescence and phase segregation due to gravity sedimentation have been initiated with two phase systems: 1,2-propanediol drops in dibutyl sebacate, and an aqueous biphase mixture containing 1% dextran (MW = 500) and 6.5% polyethylene glycol (PEG, MW = 8000) by weight. The experiments were carried out in an optical cuvette of 1 cm × 1 cm cross-section, with heights up to 20 cm. Before transferring the two phases to the cuvette, vortexing was performed twice for one minute each. This resulted in a range of drop diameters of approximately 5-30 μm. The height of the segregated minority phase was followed as a function of time using a videomicroscope connected to a video recorder and a personal computer containing Global Lab Image analysis software by Data Translation. For the aqueous biphase system, samples at various heights were taken using inserted syringes and analyzed for the volume fraction of the droplet phase.

The experimental results are in qualitative agreement with the theory; quantitative comparison has not yet been made. Figure 5 shows a plot of the height of the segregated droplet phase, normalized by the final height it achieves after complete separation, versus time for two values of the total height of the 1,2-propanediol/dibutyl sebacate dispersion: $H = 10$ cm and $H = 14.5$ cm. In both cases, a sigmoidal-shaped curve is observed, as expected. The initial phase separation rate is slow because of the small drop sizes and velocities; it then speeds up as coalescence occurs to yield larger drops, and then it decreases again as the large drops settle out of the dispersion. As predicted from Fig. 4, the phase separation is faster for the taller dispersion (N_r greater) because there is more opportunity for coalescence. At a given position, the observed drop size increased initially due to coalescence and then decreases due to sedimentation of the larger drops, as predicted in Fig. 2, but quantitative analysis of the drop size distributions has not yet been performed.

Similar results have been obtained with the aqueous biphasic system. Figure 6 shows the volume percent of minority phase versus distance from the bottom of the cuvette for a total minority phase volume percent of 6.5% and total height of the dispersion of $H = 17$ cm. Note that the minority, dextran-rich phase is more dense than the continuous, PEG-rich phase, and so the droplets settle downward. Similar to the behavior predicted in Fig. 3, the droplet volume fraction is uniform and equal to its initial value for short times and

then decreases with time. The decrease occurs first in the upper portion of the container, due to droplets settling downward.

CONCLUSIONS

Quantitative predictions of the temporal and spatial evolutions of the drop size distributions and macroscopic phase separation rates in droplet dispersions due to buoyancy-driven motion are presented. Droplet coalescence significantly increases the phase separation rate initially, and then the phase separation rate decreases after the larger drops are removed from the dispersion. The predicted trends are verified by experiments.

ACKNOWLEDGMENTS

REFERENCES

1. Bergman, A., Fredriksson, H., & Shahani, H., The effect of gravity and temperature gradients on precipitation in immiscible alloys. *J. Mat. Sci.* **23** (1988) 1573-1579.

2. Davis, R.H. & Acrivos, A. Sedimentation of noncolloidal particles at low Reynolds numbers. *Ann. Rev. Fluid Mech.* **17** (1985) 91-118.

3. Rogers, J.R. & Davis, R.H. Modeling of collision and coalescence of droplets in microgravity processing of Zn-Bi immiscible alloys. *Metallurgical Trans.* **21A** (1990) 59-98.

4. Satrape, J.V. Interactions and collisions of bubbles in thermocapillary motion. *Phys. Fluids A* **4** (1992) 1883-1900.

5. Wang, H. & Davis, R.H. Droplet growth due to Brownian, gravitational, or thermocapillary motion and coalescence in dilute dispersions *J. Colloid Interface. Sci.* **159** (1993) 108-118.

6. Zhang, X., Wang, H. & Davis, R.H. Collective effects of temperature and gravity on droplet coalescence *Physics of Fluids A* **5** (1993) 1602-1613.

7. Reddy, S.R., Melik, D.H. & Fogler, H.S. Emulsion stability-theoretical studies on simultaneous flocculation and creaming. *J. Colloid Interface Sci.* **82** (1981) 116-127.

8. Zhang, X. & Davis, R.H. The collision rate of small drops due to thermocapillary migration *J. Colloid Interface Sci.* **152** (1992) 548-561.

9. Zhang, X. & Davis, R.H. The collisions of small drops due to Brownian and gravitational motion *J. Fluid Mech.* **230** (1991) 479-504.

10. Lax, P.D. & Wendroff, B. 1960 Systems of conservation laws. *Comm. Pure Appl. Meth.* **13** (1960) 217-237.
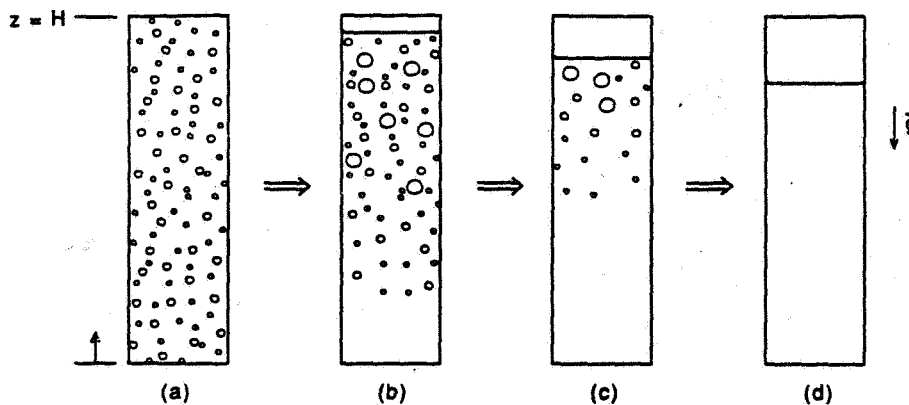
Fig. 1–Schematic of the time evolution of the phase separation process due to the simultaneous migration and coalescence of rising drops or bubbles.
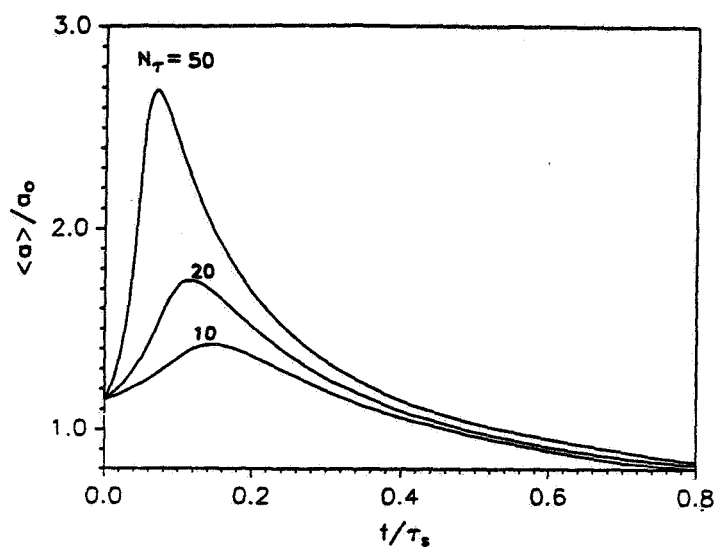
Fig. 2–Predicted time evolution of the average drop radius at $z/H = 0.5$ for a dispersion having $\hat{\mu}$=0.1 and $\hat{\sigma}$=0.2.
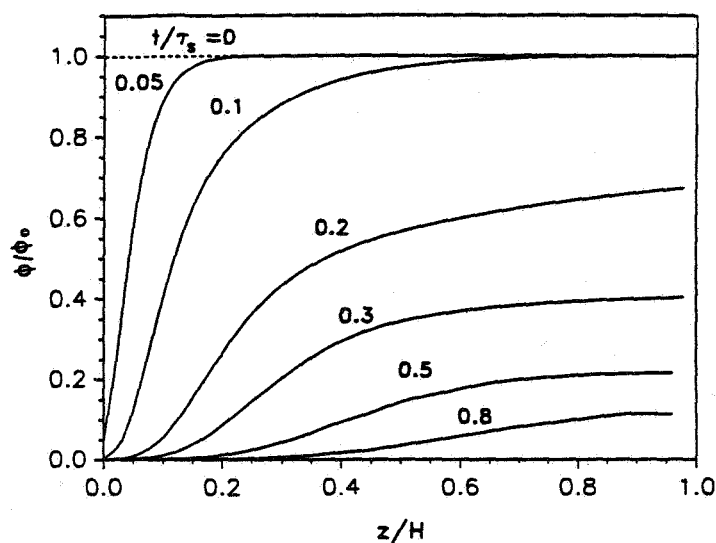
Fig. 3–Predicted variation of volume fraction with position at different times for a dispersion having $\hat{\mu} = 0.1$, $\hat{\sigma} = 0.2$, and $N_\tau = 20$.
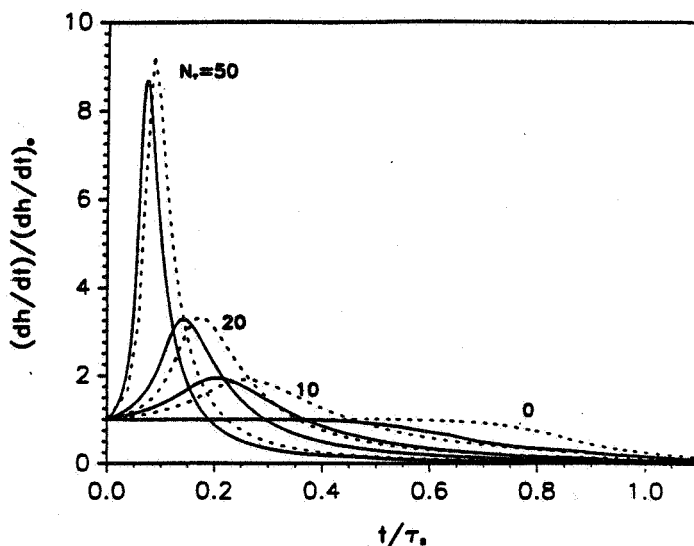
Fig. 4–Predicted rate of phase separation versus time for a dispersion having $\hat{\mu} = 0.1$, $\hat{\sigma} = 0.2$ (solid lines), $\hat{\sigma} = 0.1$ (dashed lines), $\phi_o = 0.05$ and different N_τ in a container of finite depth.
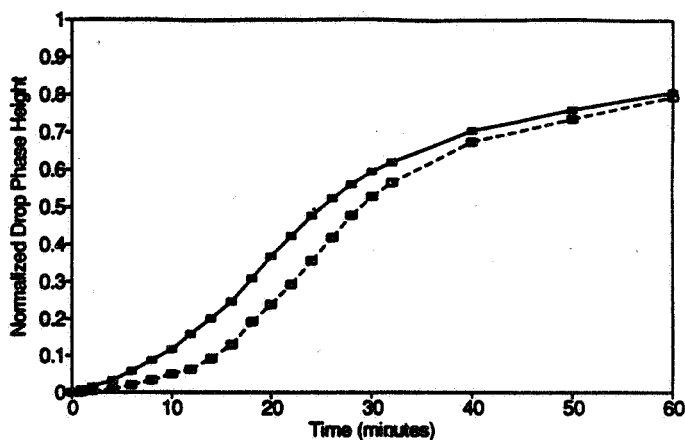
Fig. 5–Measured height of segregated minority phase (normalized by final height) versus time for 1,2-propanediol drops at $\phi_o = 0.034$ in dibutyl sebacate with $H=10$ cm (open squares) and $H = 14.5$ cm (closed squares).
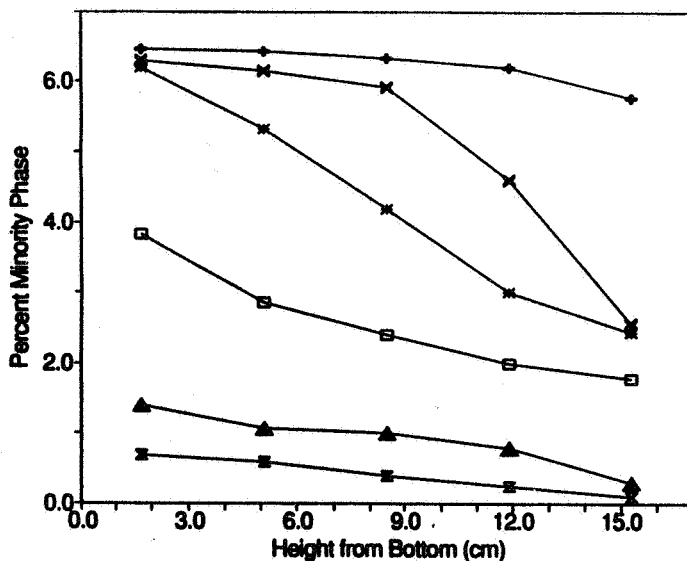
Fig. 6–Volume percentage of dispersed phase versus distance from the bottom of the curvette for dextran-rich drops at $\phi_o = 0.065$ in PEG-rich continuous phase with $H = 17$ cm at $t = 15$, 30, 45, 60, 120, and 240 min (top to bottom).

Influence of Flow on Interface Shape Stability in Low Gravity

Paul H. Steen (PI)
School of Chemical Engineering
Cornell University
Ithaca, NY 14853

Science objectives

1)Understand the influence in low gravity of flow on interface shape. For example, document and control the influence of axial flow on the Plateau-Rayleigh instability of a liquid bridge.

2)Extend the ground-based density-matching technique of low gravity simulation to situations with flow; that is, develop Plateau chamber experiments for which flow can be controlled.

Relevance of science and potential applications

Containerless containment of liquids by surface tension has broad importance in low gravity. For space vehicles, the behavior of liquid/gas interfaces is crucial to successful liquid management systems. In microgravity science, free interfaces are exploited in various applications. Examples include float-zone crystal growth, phase separation near the critical point of liquid mixtures (spinoidal decomposition) and quenching of miscibility gap molten metal alloys. In some cases, it is desired to stabilize the capillary instability while in others it is desired to induce capillary breakup. In all cases, understanding the stability of interface shape in the presence of liquid motion is central.

Research approach

Both analytical/numerical and experimental approaches are employed.

Stability analyses include linear and nonlinear techniques. The linear stability approach has been used to analyze the shape stability of a cylindrical interface containing axial shear flows, both isothermally- and thermocapillary-driven[1, 2]. Computational feasibility currently limits this approach to base states that are separable flows, effectively, the axial-infinite interfaces. It is now well-known that infinite cylindrical interfaces can be stabilized[3, 4, 5]. For finite interfaces an alternative approach is needed. In the limit of no motion, minima of the free-energy functional are obtained using the calculus of variations supplemented by numerical branch-tracing[6]. For weak motion (creeping flow), we extended this approach below using a modified functional. Near the singularity represented by the Plateau-Rayleigh limit, bifurcation theory using Liapunov-Schmidt reduction is a natural tool for the solution of the appropriate nonlinear Euler-Lagrange equation. All these analytical/numerical tools lend themselves to understanding the physics of stability in terms of simple competition mechanisms.

As for the experimental approach, a dynamic Plateau chamber has been built and is used to study liquid bridges held captive by rod-ends and embedded in a controlled surrounding flow. Theory has guided the experiments to a particular window in parameter space. Such guidance is crucial since interesting stabilization effects occur over narrow parameter ranges for this problem.

Science results

The stability of liquid bridges of finite extent near the Plateau-Rayleigh length is the main subject of this report. The bridge is sheared axially by embedding it in a pipe flow. Finite amplitude deviations from cylindrical shape are accounted for by a nonlinear theory. The predictions so far are limited to small deviations from no flow, no gravity, and the Plateau-Rayleigh limit. They explain the experimental observation of a slight stabilization to lengths *beyond* the Plateau-Rayleigh limit.

The schematic of the experimental configuration is shown in figure 1. The bridge liquid attaches to each rod end with a cicular contact-line of radius r_o. A smaller diameter rod (radius r_i) connects the two end rods. This annular geometry influences the pressure at the interface when the bridge liquid is in motion. In the absence of motion, the interface shape and its stability are controlled by dimensionless bridge length L, volume $\overline{V}$, and the gravity to surface tension strength B (Bond number). The strength of gravity is controlled by the density imbalance $\Delta\rho$ (bridge - surrounding liquid). In the absence of motion the connecting rod plays no role. By controlling the flow rate of the external liquid, between the outer tube wall (radius r_t) and the interface, traction at the interface transmits motion to bridge liquid. In summary, with motion, the shape and stability of the interface depend on a dimensionless flow rate C (capillary number), two radius ratios and the viscosity ratio in addition to the three parameters that determine shapes and stability under static conditions.

Upward flow is driven by a pressure gradient that opposes the hydrostatic gradient of a heavy bridge. This is the interesting case. In one protocol, B and C are fixed and the bridge length is quasistatically increased maintaining a cylindrical volume ($\overline{V} = 1$). Breakup is recorded at length L_c. The experiment is repeated for a different C. The symbols in figure 2 show the results. The opposing effects of gravity and flow are evident: a maximun length occurs near $B = C$. Flow effectively cancels density imbalance. The solid curve is the destabilization by gravity (theory) from the Plateau-Rayleigh limit ($L_c = 2\pi$) in the absence of motion ($C = 0$). Unexplained is the apparent stabilization to length *greater* than 2π.

A different experimental protocol fixes the bridge length for given B. A volume is chosen and the flow rate C is increased/decreased until breakup occurs. Figure 3 show these results. The data are connected by a solid line representing interpolation (dotted indicates extrapolation). Note that as the bridge length approaches 2π the effects of flow on breakup become nonlinear and, indeed for $L = 6.099$, there is apparently an 'island' of stability for cylindrical volumes: bridges exist in the presence of flow that would otherwise breakup. Details of these experiments are found in[7, 8, 9].

The nonlinear analysis is based on a model that accounts for the external flow by imposing a shear stress τ on the interface of surface tension σ. The dissipation of this single phase configuration with deformable interface is minimized. The normal stress balance is a modified Young-Laplace equation and also corresponds to the nonlinear Euler-Lagrange equation of a modified functional. Solutions of the nonlinear equation with their stabilities are obtained by Liapunov-Schmidt reduction using bifurcation theory. Perturbation parameters measure deviations from no flow, no gravity and the Plateau-Rayleigh limit. The following dimensionless groups arise (cylindrical volume is assumed):

$$\overline{C} = \tau r_o / \sigma \tag{1}$$

$$B = r_o^2 \Delta\rho g / \sigma \tag{2}$$

$$A = (r_o - r_i)/r_o \tag{3}$$

$$\lambda = L/(2\pi r_o) - 1. \tag{4}$$

λ is treated as the primary bifurcation parameter. $\gamma = (\overline{C}, B)$ are the perturbation unfolding parameters. In the equlibrium state ($\gamma = 0$), the Young-Laplace equation is recovered which has a linear operator with null space ϕ spanned by $\sin(k\pi x)$. The bifurcation diagram shows a subcritical pitchfork structure. The nontrivial branch near the singular point takes the form:

$$\epsilon\phi + w(x). \tag{5}$$

$w(x)$ is in the complement of the null space and is $o(\epsilon)$. The bifurcation equation is $g = 0$ and the universal unfolding is

$$g = -\frac{\lambda\epsilon}{2} - \frac{3\epsilon^3}{32} + (\overline{C}p - B) + \overline{C}q\epsilon^2, \tag{6}$$

$$C = \overline{C}p(A) \tag{7}$$

Details of the analysis and the form of functions $p(A)$ and $q(A)$ are given elsewhere[10]. The classical subcritical pitchfork is recovered for no flow and no gravity ($C = B = 0$). For gravity ($B \neq 0$) and no flow ($C = 0$) the perturbation results of[11] are recovered. The presence of creeping flow without gravity is always destabilizing ($B = 0, C \neq 0$). Thus, the physics at work here is different from that in the infinite cylinder where inertial effects are responsible for stabilizing pressures. There, finite Reynolds number flows can can stabilize without gravity[1]. Our main result is the perturbed bifurcation structure with flow and gravity for $B = C$. This case shows somewhat surprisingly that even though each of two effects is separately destabilizing, together they can stabilize. The maximum stability limit is plotted in figure 4 ($A = 0.5$) as a function of imposed shear and gravity imbalance. We see that the destabilizing effect of gravity can be overcome by the pressure field induced by the shear flow. In the operating regime where the stability limit is extended beyond 2π, the liquid column does not have a perfect cylindrical shape. The predictions of figure 4 are to be compared to the data of figure 2.

Theory (additional results from the past year − periferal to the above disscusion)

1) Stability (instability) of a static bridge equilibrium ($B = 0$) is immediate once the family of equilibria to which it belongs is identified; direct calculation of the second variation is circumvented[6].
2) All known families of static bridge equilibria ($B = 0$) are ultimately connected and thereby inherit their states of instability (number of unstable modes) ultimately from the stability of the sphere[6].

Experiment(additional results from the past year − periferal to the above disscusion)

3) A comparison of pairs of relatively immiscible liquids suitable for use in a dynamic Plateau chamber with density balance within 10^{-4} g/cm^3 has been presented. Pure water and the isomeric system of 2-, 3- and 4-fluorotoluene is one preferred pair. Pure water and the homologous system of chlorocyclohexane and chlorocyclopentene is another[12].
4) Further observation and analysis of the collapse of the soap-film bridge have been performed. The soap-film collapse is viewed as a prototype collapse.

Research plan

Theory

The nonlinear analysis presented above is limited by the single phase assumption of the model. Moreover, even with the model, there is limited validity in amplitude ϵ, length deviation λ and C and B. We shall attempt to remove these limitations. Another goal is to make precise the relationship between our approach and that of energy stability theory (with linking parameters).

Experiment

Further tests of stabilization guided by the new theoretical results are planned. Exploratory experiments will probe the influence of a time-dependent driving flow on the stability limit of bridges, and the coalesence of droplets in the presence of flow.

Conclusion

We have shown in theory and in experiment that shear can stabilize a finite liquid column beyond the Plateau-Rayleigh limit, among other results. Surpriseingly, a slight density imbalance is required. Two imperfections (density and flow) conspire to stabilize even though each on its own destabilizes. Apparently, only lengths slightly longer than the Plateau-Rayleigh length are achievable.

References

[1] M.J. Russo and Steen P.H., "Shear Stabilization of the Capillary Breakup of a Cylindrical Interface," Phys. Fluids A, *1* (1989) 1926-1937.

[2] H.A. Dijkstra and Steen P.H., " Thermocapillary Stabilization of the Capillary Breakup of an Annular Film of Liquid," J. Fluid Mech., *229* (1991) 205-228.

[3] T. W. F. Russel and Charles M.E. "The Effect of the less Viscous liquid in the Laminar Flow of Two immisicible Liquids," Can. J. Chem. Engng., *39* (1959) 18-24.

[4] A.L. Frenkel, Babachin A.J., Levich B.G., Shlang T., and Sivashinsky G.I., " Annular Flows Can Keep Unstable Films from Breakup: Nonlinear Saturation of Capillary Instability," J. Colloid Interface Sci., *115* (1987) 225-133.

[5] H.H Hu, Lundgren T.S. and Joseph D.D., "Stability of Core-annular Flow with a Small Viscosity Ratio," Phys Fluid A, *2* (1990) 1945-1954.

[6] B. J. Lowry and Steen P. H.,"Capillary Surfaces: Stability from Families of Equilibria with Application to the Liquid Bridge," Proc. Roy. Soc. A, accepted.

[7] B.J. Lowry, Ph.D. Dissertation, Cornell University, Ithaca NY, 1994.

[8] B.J. Lowry and Steen P.H.,"Stabilization of an Axisymmetric Liquid Bridge by Viscous Flow," Int. J. Multiphase Flow, *20(2)* (1994) ···

[9] B. J. Lowry and Steen P. H.,"Flow-influenced Stabilization of Liquid Columns in a Dynamic Plateau Chamber," AIAA Paper 93-0255 (1993).

[10] Y. J. Chen and Steen P. H.,"Influence of Flow on Interface Shape Stability," Proceedings of the 14th IMACS World Congress, Atlanta, GA, July 1994.

[11] J.M.Vega and J.M.Pearles,"Almost Cylindrical Isorotating Liquid Bridges for Small Bond Numbers," *ESA SP-191* (1983) 247.

[12] B. J. Lowry and Steen P. H.,"On the Density Matching of Liquid using Plateau's Method," AIAA Paper 94-0832 (1994)
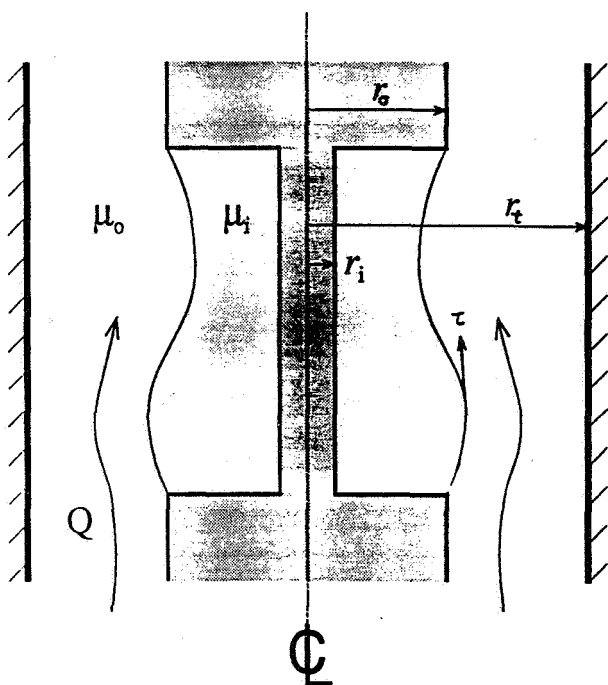
Figure 1 Definition sketch of the experiment.
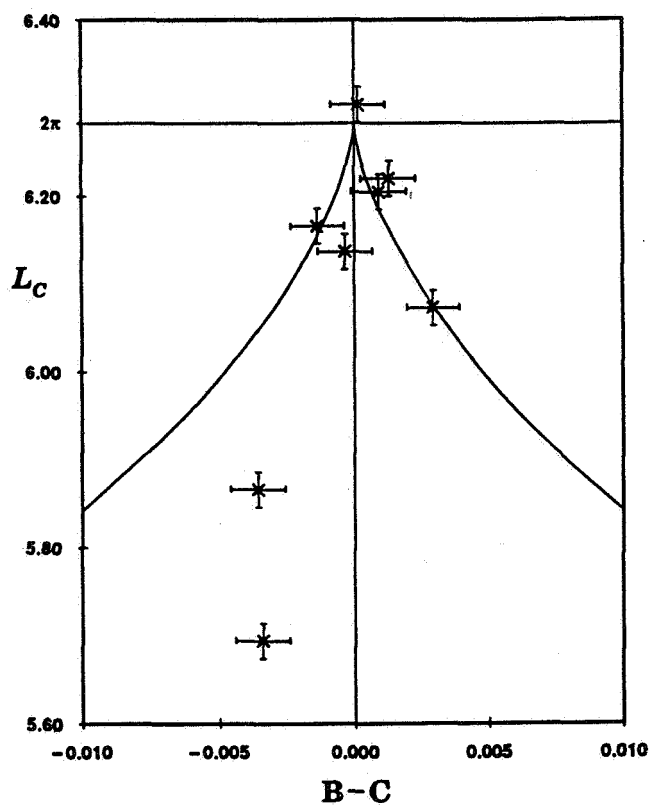
Figure 2 – detail of L_C(B – C) peak for $\bar{V} = 1.00 \pm 0.02$ and B = 0.0029 with comparison to static L_C(B) curve (80% 4-FT, 20% 2-FT, $r_t = 2.130 r_o$)
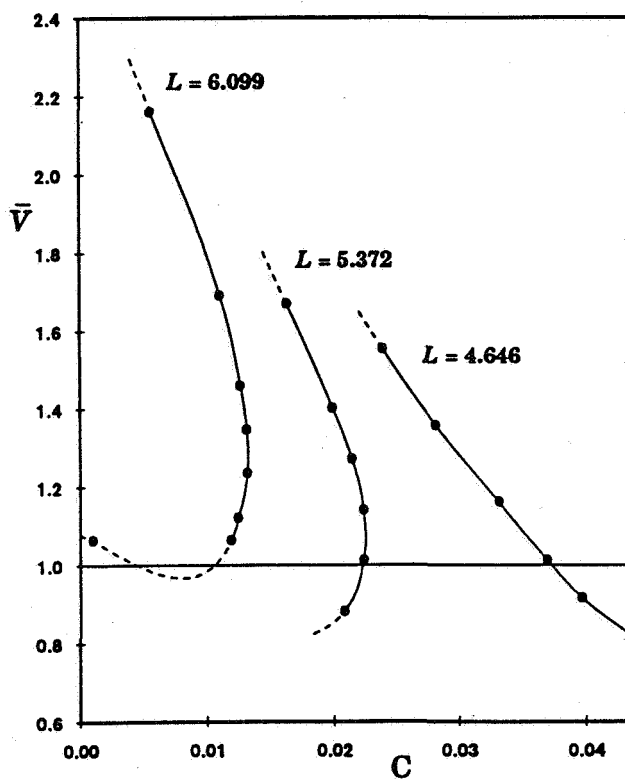
Figure 3 — liquid bridge stability limits in terms of volume and capillary number with B = 0.0080 ± 0.0005 (80% 4-FT, 20% 2-FT, T = 19.95°C, r_i = 0.532r_o , r_t = 2.130r_o)
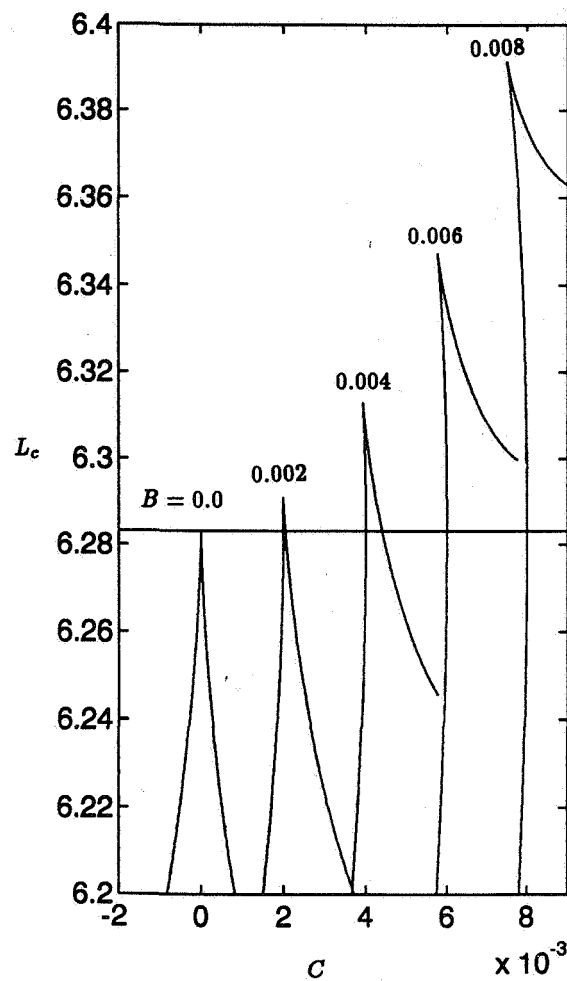
Figure 4 Critical length L_c of bridge versus C
$A = 0.5$

WETTING AND SPREADING AT THE MOLECULAR SCALE

Joel Koplik
Benjamin Levich Institute and Department of Physics
City College of the City University of New York, New York, NY 10031

Jayanth R. Banavar
Department of Physics and Materials Research Laboratory
Pennsylvania State University, University Park, PA 16802

ABSTRACT

We have studied the microscopic aspects of the spreading of liquid drops on a solid surface by molecular dynamics simulations of coexisting three–phase Lennard–Jones systems of liquid, vapor and solid. We consider both spherically symmetric atoms and chain-like molecules, and a range of interaction strengths. As the attraction between liquid and solid increases we observe a smooth transition in spreading regimes, from partial to complete to terraced wetting. In the terraced case, where distinct monomolecular layers spread with different velocities, the layers are ordered but not solid, with qualitative behavior resembling recent experimental findings, but with interesting differences in the spreading *rate*.

INTRODUCTION

The spreading of liquids on solid surfaces has lately received considerable attention, due to its crucial role in materials processing and its ubiquity in zero-gravity environments, as well as the fascinating scientific issues which arise. Wetting has long been studied both theoretically and experimentally [1-3], and many features are well understood within the context of the continuum equations augmented with van der Waals forces. However a number of significant microscopic issues are unresolved, such as the precise boundary condition appropriate to a moving contact line and the dynamics of contact angle hysteresis, and for such problems molecular scale calculations can provide invaluable information. Previous work has examined the contact line problem [4], showing that the no-slip boundary condition breaks down in regions of unusually high stress, and several calculations in progress address the effects of heterogeneities and hysteresis, but here we will consider the somewhat related ill-understood phenomenon of "terraced wetting." It has been observed, using interferometric techniques [5], that certain polymeric liquids spread on atomically smooth substrates in the form of distinct monomolecular layers of nanometer thickness, which extend laterally over millimeter distances to completely wet the solid. Such films are too thin for a lubrication analysis to be applicable, and only heuristic alternative models based on Langevin dynamics or two-dimensional liquid layers are available. This situation motivated us [6] to conduct molecular dynamics (MD) simulations of spreading, based on the atomic scale motion of the constituent atoms. While we are restricted to small drops, whose initial radius is only about 10 atomic sizes, our results complement the experiments by providing detailed three-dimensional information about the spreading dynamics.

SIMULATION METHOD

In an MD computer simulation [7], one places atoms in a region of space with random initial velocities corresponding to the desired temperature, and integrates Newton's equations of motion. The force on any one atom is due to interactions with the others, and we consider Lennard-Jones potentials of the form

$$V(r) = \frac{\beta}{r^6} \left(\frac{1}{r^6} - \alpha \right) ,$$

where the coefficients are related to the conventional Lennard-Jones energy and distance parameters ϵ and σ via $\alpha = \sigma^{-6}$ and $\beta = 4\epsilon\sigma^{12}$, respectively. The fluid subsystem is used as reference, with all distances expressed in terms of $\sigma \equiv \sigma_{ff}$, mass in terms of m_f, and times in terms of $\tau \equiv (m_f \sigma_{ff}^2/\epsilon_{ff})^{1/2}$. The parameter $\alpha \equiv \alpha_{fs}$, the strength of the attraction between fluid and solid molecules, is varied from 1.0 to 1.4 to produce different wetting regimes, and ϵ_{ff} is kept at 1. For the solid-solid interactions we choose $\epsilon_{ss} = 50$ and $\sigma_{ss} = 2^{-1/6}d$, where $d = \sqrt{2}$ is the lattice constant, so that the equilibrium position of the solid particles is also the minimum of the potential. The mass of the solid particles is $5m_f$. The potentials of fluid-fluid interactions and fluid-solid interactions are cut off at $2.5\sigma_{ff}$ and $2.5\sigma_{fs}$ respectively, and the potential of solid-solid interactions is cut off at $1.8\sigma_{ss}$.

The "computational protocol" in our simulations is to consider 4000 fluid particles confined to a cube of side $L = 60\sigma$, with the boundaries at $z = 0$ and $z = L$ are replaced by a solid wall made of 5 layers of fcc solid, totalling 9000 molecules, with the (100) surface exposed to the fluid. The solid is thick enough to prevent a direct interaction between the fluid particles on either side, and the remaining directions have periodic boundary conditions imposed. The equations of motion are integrated using the Beeman algorithm [7], with a time step 0.005τ. The entire system is equilibrated at $T = 0.7$ with $\alpha = 0$ and $\beta_{fs} = 1$. The drop has then a roughly spherical shape of radius 10σ, surrounded by a cloud of vapor. The center of the drop is gradually moved to 16σ above the solid surface by time $t = 35$, whereupon the fluid-solid interactions attract the drop, leading to contact and subsequent spreading. The middle layer of the solid is kept at constant temperature $T = 0.7$ by rescaling of the velocities of the particles in that layer, in analogy to a laboratory experiment where the solid substrate is kept at a constant temperature. The computation ends when the drop attains a steady state, or reaches the edges of the simulation box.

One difference betwen the present simulations and laboratory experiments is that the solid-liquid interaction cuts off at a fixed distance, whereas a realistic long-range van der Waals potential, arising from a superposition of many layers of r^{-6} interaction, behaves approximately as r^{-3} [8]. In order to check that the partial wetting is not due to this cutoff, we ran a simulation with an extended fluid-solid interaction. This extra potential had the form $k/(z - z_0)^3$ for z (the coordinate normal to the solid surface) greater than the cutoff, with the constants k and r_0 determined by the continuity of the potential there. We compared the final states with and without this extended potential for $\alpha = 1.0$ and did not see any qualitative changes.

We will also consider simple polyatomic molecules, made by introducing an attractive confining potential between adjoining atoms along a chain, e.g., $V_{12}(r) \sim r^{+12} + r^{+6}$. If non-adjoining atoms retain a Lennard–Jones attraction, the resulting molecule is compact rather

114

than elongated, while appropriate repulsive or orientational potentials may be introduced to maintain a long chain. At the expense of further computational effort, other MD practitioners often work with realistic specific materials.

MONATOMIC FLUIDS

First we consider the spreading of a simple monatomic fluid, such as Argon, where the Lennard–Jones potential above is quatitatively valid. We studied a range of solid-liquid interaction strengths from $\alpha = 1.0$ to 1.4, in steps of 0.1. For values $\alpha \leq 1.1$ we observed partial wetting, in which the drop reached a stable shape, while for $\alpha \geq 1.2$ the drop continues to spread up to the boundaries of the simulation box. In Fig. 1(a,b,c) we illustrate the three types of behavior seen by showing the final states for $\alpha = 1.1$, 1.2, and 1.4, respectively. The points in the figures are the centers of the fluid molecules, where the three-dimensional system has been projected onto the two-dimensional surface of the box. Note that the vapor density decreases as α increases, due to the condensation of vapor molecules onto the solid wall, and in Fig. 1(c) a condensed layer of regularly spaced molecules, commensurate with the solid structure, lies on the surface. There *appear* to be fewer molecules as α increases, but this illusion is caused by the enhanced ordering in the fluid. In Fig. 1(a) a true steady state is reached, with a well-defined contact angle. In contrast, in Fig. 1(b) the spreading is slow but does not terminate. Even at $t = 885$ the height of the drop is still decreasing while the particle "reservoir" in the bulk of the drop is nearly depleted – this case corresponds to complete wetting. In Fig. 1(c), the spreading is complete, and the drop evolves into two distinct molecular layers; we consider this case in detail.

The time evolution of a terraced spreading drop is shown in Fig. 2, in the form of snapshots of the profile at various stages, with the final state given in Fig. 1(c). At $t = 140$, several liquid layers have formed, rather more prominently than in the $\alpha = 1.1$ case, say, but layering in liquids near solid surfaces is not in itself unusual [8]. At $t = 240$ however, it is evident that the first two layers spread faster than the bulk of the drop, and that the first layer spreads faster than the second. Furthermore, a clear step-like structure has formed. At $t = 340$ the spreading of the first layer continues, while the motion of the second layer has nearly come to a stop. At later times $t = 440$ and 540 the first layer continues to move outward while depleting the central bulk of the drop.

The structures of the first and second layers in terraced spreading are quite strongly ordered. The particles form a defective hexagonal lattice, with stronger ordering in the first layer than the second, and within each layer the inner part is more ordered than the outer part. As the boundary of the layer moves outward, vacancies are created both in the interior and at the edge. When such plots are examined as a function of time, one sees that the vacancies in the first layer provide the likely sites for the particles to move in from above. Although ordered, the layers are by no means solid: since an MD simulations provides detailed information on the molecular motion, we have studied the intra-layer and inter-layer movement of particles in detail. Histograms of the horizontal and vertical displacements have a generally diffusive shape, with the trend that particles near the center of the first layer are most constrained, while the outer parts of the drop move most readily. In contrast to some theoretical models of terraced spreading, the conclusion here is that, except for perhaps the inner ring of the first layer, the liquid is not at all rigid or impenetrable.

115

For comparison with experiment, it is useful to quantify the rate of spreading of the drop. Fig. 3 shows the evolution of the average radii of the first and second layers as a function of time. Evidently, a reasonable fit is $R^2(t) = C \log t + D$, with $C \approx 430$ and 272 for the first and second layers, respectively. Similar behavior is found for the other values of α where complete wetting occurs, with the same functional form and different values for the constants. This relation disagrees with the $R^2 \sim t$ behavior found in laboratory experiments with non-volatile liquids [5] ("dry spreading"). One might suspect that the discrepancy is related to the fact that the condensation of vapor ahead of the drop reduces the degree of attraction of liquid to the surface. On the other hand, in this case the condensed vapor forms a distinct layer of fairly regular lattice, clearly separated from the spreading liquid, whereas only when α is smaller does the condensate mix with the drop. Another possible source of disagreement is the comparatively small number of molecules in the simulation. A laboratory drop has an enormous reservoir of molecules in its center available for continued spreading, whereas we have nearly exhausted the supply. Note however that the eventual leveling off of R^2 for the second layer resembles a simple finite-size effect, and suggests that a larger drop would continue to spread at the same rate. Indeed, a single run on a larger system, with 9000 fluid molecules and a maximum radius of 30, gives results consistent with those described above.

CHAIN MOLECULES

To further explore the differences between simulation and experiment in the growth rate of the layers, we have considered fluids made of more complicated molecules, by the simple device of combining Lennard–Jones atoms into chains. If the above simulations are repeated with diatomic dumbbell molecules, we see no significant difference in the spreading behavior – at large enough solid-liquid attraction the spreading is again in the form of sharp layers, whose growth rate is still $R^2 \sim \log t$. In this case however, the liquid's volatility is considerably reduced so that the spreading is "dry", without an adsorbed vapor layer on the substrate. For longer chains, however, the results do change in the direction of experiment. In work in progress [6], we have studied the spreading of chains of length 8; note that because of the Lennard–Jones attraction between non-adjacent atoms, the molecules are compact rather than elongated, and not at all entangled. Our preliminary results for this system give terraced spreading with a growth rate $R^2 \sim t^{0.8}$. At the extreme, other workers [9] have conducted MD simulations in which the substrate is a plane whose potential varies only with the normal distance, which can be thought of as the limit of molecule (or monomer) size much larger than the solid lattice spacing. Here one finds diffusive behavior, $R^2 \sim t$, in agreement with laboratory observation. We are now studying the case of length-16 chains, to elucidate the crossover behavior.

An intuitive picture of the results is as follows. The strong solid–liquid interaction draws fluid molecules to the solid, and the free energy is minimized by an ordered structure with well-defined layers, in which as many fluid atoms as possible are in positions favored by the periodic lattice potential. The temperature is still above melting, so the liquid atoms can diffuse between and within the layers, and layer growth involves vacancy creation and filling. If the fluid molecules are small, it is easy for most or all of their constitutent atoms to find the preferred sites, and the growth is slow and sub-diffusive, in analogy to diffusion in the presence of traps. When the molecule size increases, steric and thermal effects make

it difficult for a significant fraction of the atoms to simultaneously be in preferred sites, so that the pinning effect is less effective and the growth is faster.

CONCLUSIONS

In summary, we have carried out systematic molecular dynamics studies of drop spreading on a solid surface. We observe that fairly modest variations in the strength of the solid-liquid attraction potential lead to qualitatively different wetting regimes, each with a laboratory counterpart. We have focused on the novel terraced spreading case, where our results give the internal dynamical structure for this spreading regime, and where we have shown that the rate of spreading depends on the size and nature of the fluid molecules.

More generally, we have indicated how molecular simulation can complement theory and experiment, by providing otherwise unavailable small-scale information about the internal dynamics of a system, by providing "clean" results free of theoretical bias of laboratory contamination, and by allowing one to systematically vary significant parameters in a many-body problem and compute the consequences. In other related work in progress, we are exploring the relation between the presence of structural and chemical surface heterogeneity and contact line hysteresis. Here again, we can control the substrate's properties in complete detail, vary the fluid both in molecular size and in its Newtonian *vs.* non-Newtonian behavior, and observe the resulting dynamics at high resolution. We hope to help clarify these important issues in wetting as well.

REFERENCES

1. E. B. Dussan V., *Ann. Rev. Fluid Mech.* **11**, 371 (1979).

2. P. G. de Gennes, *Rev. Mod. Phys.* **57**, 827 (1985).

3. L. Leger and J. F. Joanny, *Rep. Prog. Phys.* **55**, 431 (1992).

4. J. Koplik, J. R. Banavar and J. F. Willemsen, *Phys. Fluids A* **1**, 784 (1989); P. A. Thompson and M. O. Robbins, *Phys. Rev. Lett.* **63**, 766 (1989).

5. F. Heslot, N. Fraysse and A. M. Cazabat, *Nature* **338**, 640 (1989); N. Fraysse et al., *J. Colloid Int. Sci.* **158**, 27 (1993).

6. J.-x. Yang, J. Koplik and J. R. Banavar, *Phys. Rev. Lett* **67**, 3539 (1991); *Phys. Rev. A* **46**, 7738 (1992); J. De Coninck, U. D'Ortona, J. Koplik and J. R. Banavar, in preparation (1994).

7. M. P. Allen and D. J. Tildesley, *Computer Simulation of Liquids*, Oxford (1987); see also J. Koplik and J. R. Banavar, *Ann. Rev. Fluid Mech.* **27**, in press (1995).

8. J. N. Israelachvili, *Intermolecular and Surface Forces*, Academic, 1985.

9. J. A. Niemenen, D. B. Abraham, M. Karttunen and K. Kaski, *Phys. Rev. Lett.* **69**, 124 (1992).
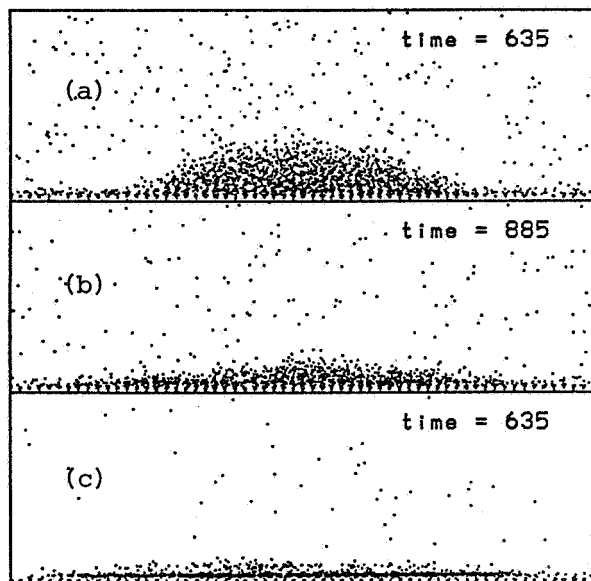
1. The final states of spreading observed for (a) $\alpha = 1.1$ at $t = 635\tau$, (b) $\alpha = 1.2$ at $t = 885\tau$, and (c) $\alpha = 1.4$ at $t = 635\tau$. The points represent the centers of molecules in three-dimensions, projected onto the front plane.

2. Time evolution of complete terraced wetting at $\alpha = 1.4$. The format is as in Fig. 1.

3. Dependance of drop radius on time for $\alpha = 1.4$, for the first (squares) and the second (circles) layers.

118

STOCHASTIC MODEL OF THE RESIDUAL ACCELERATION ENVIRONMENT IN MICROGRAVITY

Jorge Viñals
Supercomputer Computations Research Institute
Florida State University
Tallahassee FL 32306-4052

ABSTRACT

We describe a theoretical investigation of the effects that stochastic residual accelerations (g-jitter) on-board spacecraft can have on experiments conducted in a microgravity environment. We first introduce a stochastic model of the residual acceleration field, and develop a numerical algorithm to solve the equations governing fluid flow that allow for a stochastic body force. We next summarize our studies of two generic situations: stochastic parametric resonance and the onset of convective flow induced by a fluctuating acceleration field.

STOCHASTIC MODEL OF G-JITTER

We have introduced a stochastic model to describe in quantitative detail the effect of the high frequency components of the residual accelerations onboard spacecraft (often called g-jitter) on fluid motion. Each Cartesian component of the residual acceleration field $\vec{g}(t)$ is modeled as a Gaussian narrow band noise characterized by three independent parameters: its intensity $< g^2 >$, a dominant frequency Ω, and a characteristic spectral width τ^{-1}. The autocorrelation function of g-jitter is defined by

$$< g(t)g(t') >=< g^2 > e^{-|t-t'|/\tau} \cos \Omega(t - t').$$ (1)

The power spectrum for this autocorrelation function is,

$$P(\omega) = \frac{1}{2\pi} < g^2 > \tau \left(\frac{1}{1 + \tau^2(\Omega + \omega)^2} + \frac{1}{1 + \tau^2(\Omega - \omega)^2} \right).$$ (2)

For very small τ, $g(t)$ tends to white noise. For very large values of τ, each realization of $g(t)$ is a periodic function of angular frequency Ω. Up to statistical moments of second order, each realization of narrow band noise can be viewed as a temporal sequence of periodic functions of angular frequency Ω with amplitude and phase that remain constant only for a finite amount of time (τ on average). At random intervals new values of the amplitude and phase are drawn from prescribed distributions. This model is based on the following mechanism underlying the residual acceleration field: one particular natural frequency of vibration of the spacecraft structure (Ω) is excited by some mechanical disturbance inside the spacecraft, the excitation being of random amplitude and taking place at a sequence of unknown (and essentially random) instants of time. The power spectrum of such a process is the Lorentzian function given by Eq. (2), centered at $\omega = \Omega$, and of width $1/\tau$. This power spectrum has been shown to provide a reasonable fit to actual power spectra measured during the various microgravity missions, as illustrated in Fig. 1.

The values of the three parameters that define narrow band noise can be estimated from acceleration data measured onboard spacecraft. For example, from acceleration data from Spacelab 3 [1], we find $\sqrt{< g^2 >} \simeq 6 \times 10^{-4} g_E$, where g_E is the intensity of the Earth's gravitational field, $\Omega/2\pi \simeq 11 Hz$, and $\tau \simeq 0.16s$. Therefore $\Omega\tau \simeq 11$, which is an intermediate value between the white noise and deterministic limits. Of course, different values will be obtained when data from different missions are analyzed, but the values given seem to be fairly typical [2].

Finally, and from a theoretical standpoint, narrow band noise provides a convenient way of interpolating between monochromatic noise (akin to the traditional studies involving a deterministic and periodic gravitational field), and white noise (in which no frequency component is preferred). In the limit $\Omega\tau \to 0$ with $D =< g^2 > \tau$ finite, narrow band noise reduces to white noise of intensity D; whereas, for $\Omega\tau \to \infty$ with $< g^2 >$ finite, monochromatic noise is recovered.
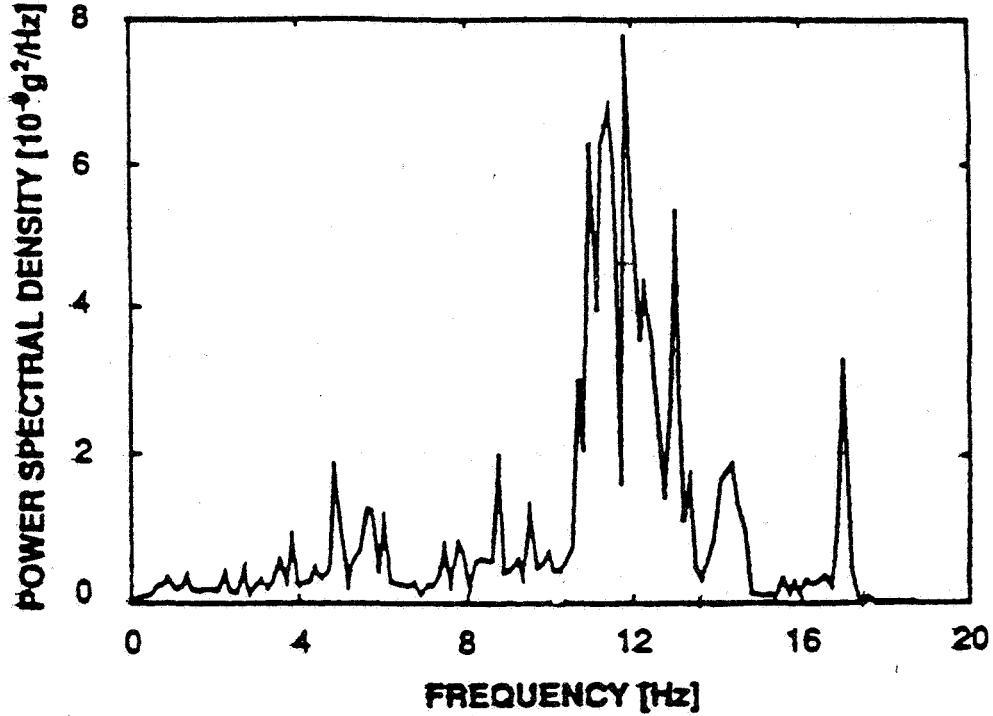
Figure 1: Power spectral density of a representative time window aboard Spacelab 3, [1]. The thick solid curve is the power spectrum given in Eq. (2) with the values of the parameters given in the text.

Numerical algorithm to generate narrow band noise

A realistic analysis of the effect of g-jitter on fluid flow will ultimately involve complex systems and geometries. It has therefore been necessary to develop a numerical algorithm that is able to simulate narrow band noise, and a method to integrate stochastic differential equations which contain this type of noise. We have first developed such a scheme to integrate the ordinary differential equation describing the motion of the parametric oscillator driven by narrow band noise [3]. The method developed is explicit and second order in time, and treats the stochastic contribution exactly.

Briefly, the equation to be solved is first expanded in powers of Δt, with Δt being the time step used in the numerical calculation. There appear terms of the form,

$$\Gamma_1(t, \Delta t) = \int_t^{t+\Delta t} dt' g(t'), \qquad \Gamma_2(t, \Delta t) = \int_t^{t+\Delta t} dt' \int_t^{t'} dt'' g(t''). \tag{3}$$

The number of multiple integrals of $g(t)$ equals the highest order in Δt retained in the discretization of the differential equation. The key point of the algorithm is that the integrals need not be done for each particular realization of the noise and iteration of the time stepping procedure. Instead, the variables $\Gamma_1(t, \Delta t)$ and $\Gamma_2(t, \Delta t)$ are themselves random variables with correlations that can be calculated exactly as a function of the parameters of the original noise and the time step Δt. Thus, during the numerical integration of the equation, a standard random number generator is used to sample directly the random variables Γ_1 and Γ_2 without ever explicitly specifying $g(t)$.

Finally, and in contrast with the case of a deterministic $g(t)$, the integration of the fluid equations has to be performed for an ensemble of realizations of $g(t)$, and the results averaged over the ensemble. Unfortunately, this adds considerably to the computational effort required.

120

STOCHASTIC PARAMETRIC RESONANCE

The response of an entire class of systems to a time dependent gravitational field can be described as parametric resonance. In simple cases, parametric resonance is modeled by the Mathieu equation for the most unstable mode of the system. The particular case that we have focussed on concerns the linear response of the free surface of an incompressible fluid subjected to a random effective gravity (parametric surface waves). In this case, each spatial Fourier component of the surface displacement satisfies the damped Mathieu equation [4]. Other examples of parametric resonance include Rayleigh-Bénard [5] and thermosolutal convection [6], both in an oscillatory gravitational field.

We have studied by analytical and numerical means the stability of the solutions of the parametric oscillator (Mathieu equation) when the driving force is a narrow band noise. Stability has been defined with respect to the second order statistical moments of the oscillator coordinate because of their relation to the energy of the oscillations. The neutral stability curve (Fig. 2) has been obtained analytically in the limit of low frequencies, and close to subharmonic resonance. An interpolation formula with no adjustable parameters has been derived that reduces to the two asymptotic forms in the two limits discussed. The main assumption underlying the interpolation formula is that, even in the stochastic case, the dominant response of a surface mode of natural frequency ω is subharmonic resonance, and its stability is determined by the intensity of the driving noise at 2ω. The approximation is seen to break down in the limit $\Omega\tau \gg 1$, but is found to be in agreement with the results of numerical computations up to $\Omega\tau \sim 30$. The values of $\Omega\tau$ estimated for g-jitter lie well within this range of validity.

The effects of varying the width of the noise spectrum on the stability of the parametric oscillator can be summarized as follows: In the region close to white noise ($\tau \simeq 0$), the noise intensity is determined by the parameter $D = \langle g^2 \rangle \tau$. The effect of increasing the correlation time τ while keeping D constant is in the direction of increasing stability. The same general conclusion is found to apply for $\Omega \neq 0$. We interpret this result to be a consequence of decreasing the intensity of the power spectrum at the corresponding subharmonic resonant frequency. In the opposite limit, $\Omega\tau \gg 1$, the strength of the external driving force is given by $\langle g^2 \rangle$, which is proportional to the area beneath the power spectrum. In this case, the broadening of the spectrum (decreasing τ) at constant $\langle g^2 \rangle$ has a stabilizing effect on the frequency at subharmonic resonance. This is interpreted as a lack of efficiency in exciting the resonance when the noise effectively spans a larger range of frequencies and cannot persist at resonance for very long times. The same trends would apply to a system which only has a discrete set of natural frequencies.

CONVECTION DRIVEN BY A FLUCTUATING GRAVITATIONAL FIELD

This research addresses the mechanical response of a fluid in which a smooth density gradient exists due, perhaps, to an imposed temperature of composition gradient. In this case, a fluctuating effective gravitational field may induce a number of convective instabilities due to its random value and orientation. The configuration studied is that of cavity flow in a "laterally" heated container [7]. The base state is a quiescent state in a two dimensional square geometry of side L, with an initial uniform temperature gradient along the x direction. We assume that the equation of state of the fluid is given by $\rho = \rho_0 [1 + \alpha(T - T_0)]$, where ρ is the mass density of the fluid at temperature T, ρ_0 is a reference density at some temperature T_0, and α is the thermal expansion coefficient. At $t = 0$, a time dependent gravitational field is turned on. The component of the gravitational field which is parallel to the initial density gradient is much too weak to trigger any fluid motion, although it will contribute to the flow once the fluid is set in motion. We have chosen to neglect this component in our initial study. On the other hand, components of the gravitational field perpendicular to the initial density gradient do not have to exceed a finite threshold in order to induce convection. In this case the quiescent state is not stationary. However, the facts that the actual values taken by the effective gravity are relatively small, and average to zero, raise the question of whether a significant convective flow can be generated, and how it may depend on the parameters of g-jitter.

Approximate analytic solutions to the flow field have been found in the limit in which the temperature field in the cavity is not appreciably distorted by the flow. In this limit of negligible heat transport, one focuses on the mechanical response of the fluid to the fluctuating acceleration field. We have been able to isolate a few important characteristics of cavity flow that result entirely from the stochastic nature of the acceleration field, and that would not have been obtained under a strictly periodic gravity modulation.
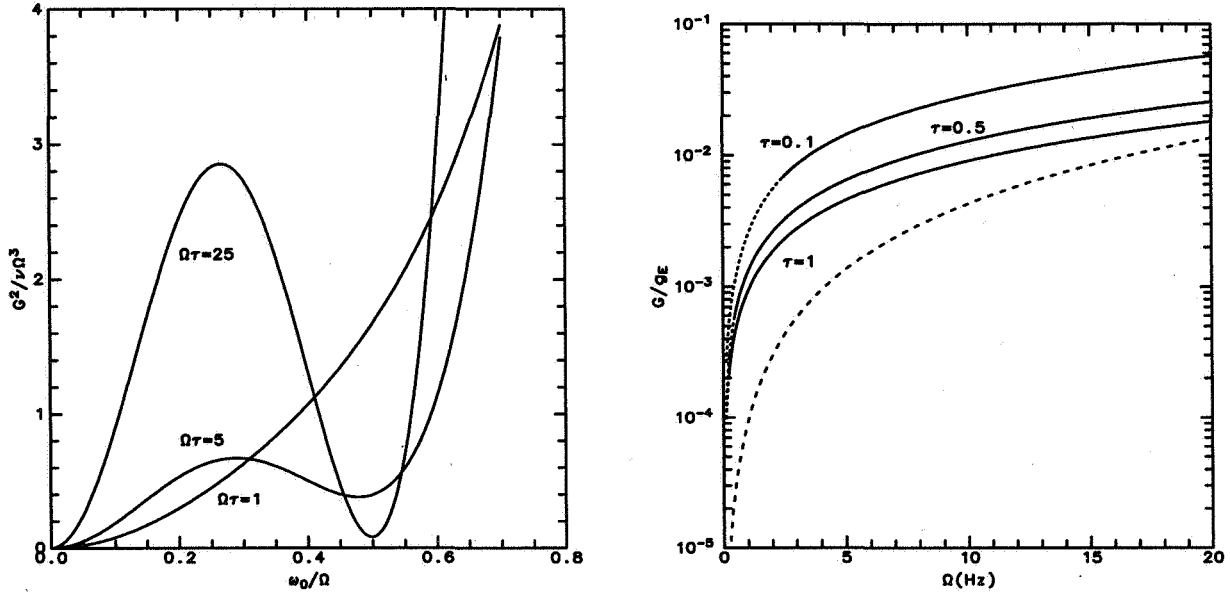
Figure 2: (Left) Stability boundaries for the second moments of a free fluid surface. The figure shows the dimensionless mean squared fluctuations in gravitational acceleration versus the dimensionless frequency of the surface modes. The intensity of the fluctuations in the gravitational field is given by $G^2 = \langle g(t)^2 \rangle$. Different curves show the stability boundaries for various values of the dimensionless correlation time $\Omega\tau$. (Right) Estimate of tolerable levels of g-jitter for instability of a planar water-air surface at room temperature. We show the normalized root mean squared g-jitter for instability as a function of the characteristic frequency of the driving noise (g_E is the intensity of the gravitational field on the Earth's surface). Three different correlation times are shown, as indicated in the figure. The dashed line is the stability curve for the Mathieu equation for the same driving frequency (deterministic case).

Although the imposed acceleration field, and hence the vorticity, average to zero, the vorticity itself can be described by a random walk in time. Specifically, at short times $t < \tau$, the mean square vorticity at the center of the cavity $\langle \xi^2 \rangle$ oscillates with angular frequency Ω, the characteristic frequency of the noise. The amplitude of the oscillatory component decays exponentially with a decay rate $1/\tau$. For $t \gg \tau$, $\langle \xi^2 \rangle$ increases linearly in time according to,

$$\langle \xi^2 \rangle \propto \langle g^2 \rangle \tau \left(\frac{\alpha \Delta T}{L} \right)^2 \frac{t}{1 + (\Omega\tau)^2}, \tag{4}$$

where ΔT is the imposed temperature difference across the cavity. This growth will not continue indefinitely, and $\langle \xi^2 \rangle$ is expected to saturate at a finite value due to viscous dissipation at the walls. The time required to reach saturation, and the maximum value of $\langle \xi^2 \rangle$ attained, are currently under investigation.

Another important consequence of our result is that there is fluid motion regardless of the value of the characteristic frequency Ω. It is often stated in the literature that the main effects of g-jitter on fluid motion are caused by those frequency components of the jitter that are close to inverse characteristic times of the process under study. The case of cavity flow provides a clear counterexample to that rule.

Numerical study of cavity flow

In order to study more realistic situations, a numerical algorithm to study cavity flow in two dimensions under the action of a fluctuating gravitational field has been developed [8]. We have solved the Navier-Stokes
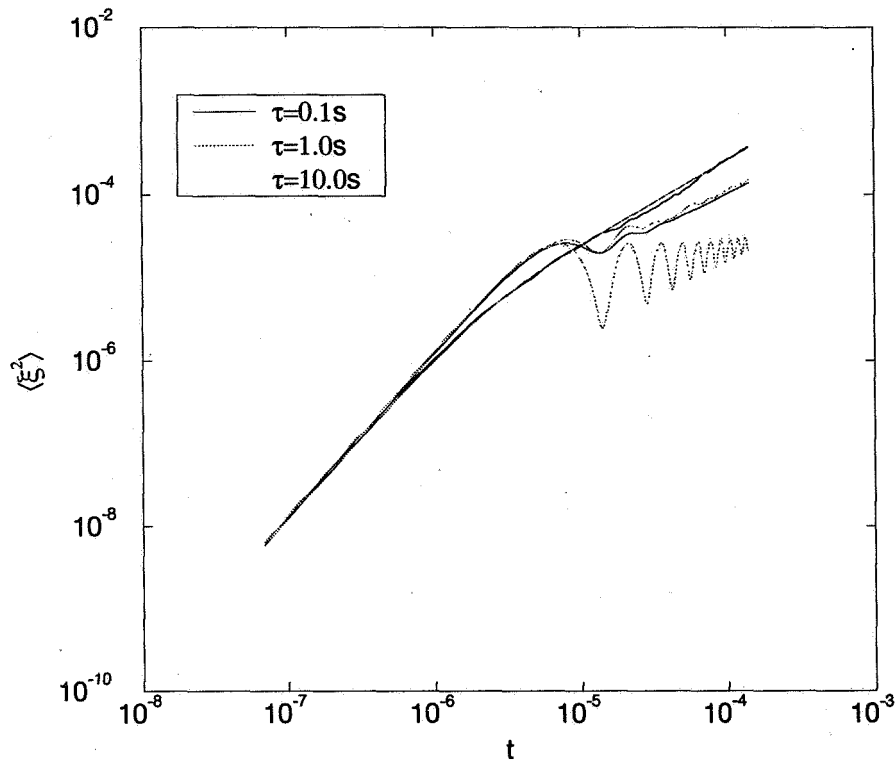
Figure 3: Second moment of the vorticity as a function of time for $\Omega/2\pi = 1Hz$ and (from top to bottom) $\tau = 0.1s, 1s$ and $10s$. The curves shown are the results of both analytic and numerical calculations. The numerical results are averages over 300 independent realizations of the random noise.

equation in the Boussinesq approximation by using a stream function-vorticity formulation. A Forward Time-Centered Space method is used which is first order accurate in time, and second order in space. The small Rayleigh numbers (appropriate for typical microgravity conditions) and the relatively large Prandtl numbers used in our calculations place us well within the range of stability of the technique when purely deterministic functions are involved. The Poisson equation that relates the stream function and the vorticity has been solved by a Successive Over Relaxation technique.

We have thus far explored values of the parameters within the range of validity of the analytic predictions described above. Due to the gentleness of the flow, our calculations are performed on a small, evenly spaced grid. The results for the mean square vorticity at the center of the cavity are shown in Fig. 3 (the numerical results are averages over three hundred independent realizations of the random function). The mean squared vorticity obtained numerically is in excellent agreement with the analytic calculations.

CONCLUSIONS

A stochastic model of the residual acceleration environment onboard spacecraft has been introduced. Not only does it provide a realistic description of the acceleration environment, but it also allows to smoothly interpolate between two well known limits: the white noise limit and the deterministic limit (a periodically modulated gravitational field). Two generic situations have been studied by both analytic and numerical means: a fluid system with a sharp density discontinuity (e.g., an interface separating two immiscible fluids or two coexisting phases of different density), and a system with a smooth density gradient due, perhaps, to

an imposed temperature or composition gradient.

We have first concentrated on the response of an interface separating two regions of different density to a fluctuating acceleration field. Two main conclusions have emerged from our study. First, an external driving force with a broad frequency spectrum leads to parametric resonance in a wide frequency range. The resonant behavior is *not* given by the superposition of the resonances produced by each of the frequency components because of the nonlinear coupling between the external force and the oscillator coordinate. Second, the resonant behavior of the second moments (or the energy) is in general *weaker* than the resonance that would result from any of the frequency components alone.

In the case of a smooth density gradient, the component of the gravitational field which is parallel to the initial density gradient is much too weak to trigger any fluid motion in typical microgravity conditions (although it will contribute to the flow once the fluid is set in motion). The perpendicular component, however, does induce fluid flow with an amplitude that grows sublinearly in time: the flow field itself averages to zero but its mean squared value grows linearly with time (until viscous effects lead to saturation).

ACKNOWLEDGMENTS

References

[1] J.I.D. Alexander, Microgravity Sci. Technol. **3**, 52 (1990).

[2] G.L. Martin, C.R. Baugher and F.H. Henderson, "Summary report of mission acceleration measurements, STS-50", Acceleration Characterization and Analysis Project, NASA (1992).

[3] W. Zhang, J. Casademunt and J. Viñals, "Study of the parametric oscillator driven by narrow band noise to model the response of a fluid surface to time-dependent accelerations", Phys. Fluids A **5**, 3147 (1993).

[4] J. Casademunt, W. Zhang, J. Viñals and R.F. Sekerka, "Stability of a fluid surface in a microgravity environment", AIAA J. **31**, 2027 (1993).

[5] A.A. Wheeler, G.B. McFadden, B.T. Murray and S.R. Coriell, "Convective stability in the Rayleigh-Bénard and directional solidification problems: high-frequency gravity modulation", Phys. Fluids A **3**, 2847 (1991).

[6] B.V. Saunders, B.T. Murray, G.B. McFadden, S.R. Coriell and A.A. Wheeler, "The effect of gravity modulation on thermosolutal convection in an infinite layer of fluid", Phys. Fluids A **4**, 1176 (1992).

[7] J. Casademunt and J. Viñals, "Convection induced by a fluctuating acceleration field", in *Fluid Mechanics in Microgravity*, D.A. Siginer, R.L. Thomson and L.M. Trefethen, Eds., (ASME, New York, 1993), p. 133.

[8] J.R. Thomson, J. Casademunt and J. Viñals, "Cavity flow induced by a fluctuating acceleration field", Phys. Fluids, preprint.

Drops and Bubbles

NONLINEAR DYNAMICS OF DROPS AND BUBBLES
AND CHAOTIC PHENOMENA

E.H. Trinh[2], L.G. Leal[1], Z.C. Feng[3], and R.G. Holt[2]

[1]Chemical and Nuclear Engineering Department,University of California at Santa Barbara
[2]Jet Propulsion Laboratory, California Institute of Technology
[3]Mechanical Engineering Department, Massachusetts Institute of Technology

ABSTRACT

Nonlinear phenomena associated with the dynamics of free drops and bubbles are investigated analytically, numerically and experimentally. Although newly developed levitation and measurement techniques have been implemented, the full experimental validation of theoretical predictions has been hindered by interfering artifacts associated with levitation in the Earth gravitational field. The low gravity environment of orbital space flight has been shown to provide a more quiescent environment which can be utilized to better match the idealized theoretical conditions. The research effort described in this paper is a closely coupled collaboration between predictive and guiding theoretical activities and a unique experimental program involving the ultrasonic and electrostatic levitation of single droplets and bubbles. The goal is to develop and to validate methods based on nonlinear dynamics for the understanding of the large amplitude oscillatory response of single drops and bubbles to both isotropic and asymmetric pressure stimuli. The first specific area of interest has been the resonant coupling between volume and shape oscillatory modes of isolated gas or vapor bubbles in a liquid host. The result of a multiple time-scale asymptotic treatment, combined with domain perturbation and bifurcation methods, has been the prediction of resonant and near-resonant coupling between volume and shape modes leading to stable as well as chaotic oscillations. Experimental investigations of the large amplitude shape oscillation modes of centimeter-size single bubbles trapped in water at 1 G and under reduced hydrostatic pressure, have suggested the possibility of a low gravity experiment to study the direct coupling between these low frequency shape modes and the volume pulsation, sound-radiating mode. The second subject of interest has involved numerical modeling, using the boundary integral method, of the large amplitude shape oscillations of charged and uncharged drops in the presence of a static or time-varying electric field. Theoretically predicted non linearity in the resonant frequency of the fundamental quadrupole mode has been verified by the accompanying experimental studies. Additional phenomena such as hysteresis in the frequency response of ultrasonically levitated droplets in the presence of a time varying electric field, and mode coupling in the oscillations of ultrasonically modulated droplets, have also been uncovered. One of the results of this ground-based research has been the identification and characterization of phenomena strictly associated with the influence of the gravitational field. This has also allowed us to identify the specific requirements for potential microgravity investigations yielding new information not obtainable on Earth.

I. INTRODUCTION

The application of the methods of nonlinear dynamics to the problem of the oscillatory behavior of single drops and bubbles has provided a new, more integrated framework for the analysis of the very diverse phenomena that are observed over a wide range of experimental parameters. It also underscores the similarities as well as the fundamental differences found in the large amplitude dynamics of drops and bubbles. A resurgence of interest in this area has taken place in recent years due to a combination of circumstances involving the development of improved numerical techniques, the introduction of novel experimental methods based on single particle levitation, and the recognition of a number of new application areas. The opportunities offered for experimentation in low gravity and the accompanying institutional support have also greatly contributed to the recent advances in this discipline. The ability to observe and to quantitatively measure the dynamical variables associated with the motion of isolated drops and bubbles has added, and will continue to add, to the data base that is necessary to induce new theoretical effort, as well as to compare with existing predictions.

Models for acoustically driven spherical gas bubbles in water have been analyzed at resonance conditions with the methods of chaos physics [1,2] to reveal a recurrent pattern in the bifurcation sets characteristic of period doubling cascades to chaos. Direct experimental evidence of chaotic radial oscillations has, however, not yet been obtained[3]. On the other hand, periodic, quasiperiodic, and chaotic light emission from sonoluminescing bubbles has been experimentally discovered [4]. Interest in the coupling between the low frequency shape oscillatory modes with the radial sound emitting oscillations of bubbles in water has arisen due to the possibility of previously unrecognized contributions to ambient sea noise, for example from gas bubbles entrained in breaking waves, as suggested by Longuet-Higgins [5,6]. Although experimental evidence for sound radiation from bubbles generated from the impact of droplets on a free liquid surface exists [7,8], no verification of the direct excitation of radial bubble oscillation from shape modes has yet been provided. Prior theoretical treatments of the radial to shape mode coupling [9,10] have yielded evidence for chaotic bubble oscillations through a period doubling sequence (reference 9), and for an inviscid fluid through a homoclinic orbit (reference 10). The recently developed capability of ultrasonically trapping centimeter-size bubbles in water and of inducing large amplitude higher mode number shape oscillations [11,12], has been used to investigate the shape to radial mode coupling mechanism. The first part of this paper describes the theoretical and experimental studies motivated by the definition of a potential low gravity experiment that is aimed at the direct observation of this coupling.

Large amplitude shape oscillations of single drops have been extensively investigated in recent years through theoretical as well as experimental means. Early experimental results in the linear and nonlinear regions of oscillating drops [13] were motivated by the results of numerical studies using marker and cell techniques [14] as well as by the upcoming performance of a low gravity flight experiment [15]. Subsequent numerical treatments of nonlinear drop shape oscillations have considered the stability and mode coupling of inviscid electrically uncharged [16], as well as charged drops [17]. More recent finite element treatments of the dynamics of freely suspended drops have been provided by Lundgren and Mansour [18] and Basaran [19] among others. The presence of a steady and time varying electric field has also been studied by Feng and Beard [20] and Kang [21]. Inviscid and low viscosity liquid behavior have thus been numerically simulated, and some limited experimental evidence for nonlinear behavior of droplets acoustically levitated in a liquid host was provided by Trinh and Wang[22], and for drops in a gas by Becker et al.[23] and Trinh et al.[24]. Additional experimental data have been gathered in low gravity using acoustically positioned drops during a fourteen-day Space Shuttle mission in 1992. In the second part of this paper, we describe a numerical study using boundary integral methods which deals with the shape and oscillations of a free drop in the presence of a constant as well as time-varying electric field. Recent experimental results obtained with the use of a hybrid ultrasonic-electrostatic drop levitator will also be discussed.

Before dealing with the nonlinear dynamics of free bubbles and drops, we will present some of the recent findings obtained from microgravity experiments. The purpose of this short summary is the identification of the principal differences between Earth-based and orbit-based experimental conditions.

II. SOME RESULTS OF LOW GRAVITY BUBBLE AND DROP EXPERIMENTS

A.Drop experiments in microgravity.

A set of experiments on USML-1 dealt with the equilibrium shape of rotating free drops. Similar acoustic levitation and rotation methods were used in Earth-based and Spacelab experiments. Because of the static distortion, unavoidable with uncharged levitated drops in 1 G, theoretical predictions could not be verified. The onset of bifurcation was always measured at lower rotation rate than predicted. A parametric study with the value of the static distortion as the variable showed that the measured bifurcation point decreases with increasing oblate static deformation [25]. As shown in figure 1, the removal of this static shape distortion in the space experiment allowed the verification of the theoretical prediction.

B. Bubble oscillations in low gravity.

A small ultrasonic device for bubble dynamics studies was flown aboard the Space Shuttle during the USML-1 Spacelab mission in 1992. One of the main results was the verification of the drastic reduction in

static shape distortion and the elimination of capillary wave excitation at the bubble surface by the ultrasonic wave. As figure 2 indicates, the results of the measurement of the fundamental mode frequency for large bubbles in 1 G deviates from the theoretically expected values. Measurement in low gravity removes this discrepancy for both the fundamental and the next higher mode. Thus, the most obvious manifestation of the interfering effects of the positioning and manipulating ultrasonic field found in 1 G is eliminated because the intensity of this field is greatly reduced in microgravity.

III. NONLINEAR BUBBLE OSCILLATIONS

A. Theoretical Studies.

The problem of an isolated bubble of near spherical shape in a liquid of small viscosity has been treated in the framework of potential flow with a thin boundary layer near the bubble surface. An *asymptotic method* combining domain perturbation and multiple time-scale techniques was used to derive the governing equations and boundary conditions at successive orders of approximation. A slow time scale for the resonant interaction between radial and shape mode was defined, and dynamical equations were derived for the amplitude functions of the interacting oscillatory modes for resonant and near-resonant conditions. The specific cases of interest for this initial study were the two-to-one (and the one-to-one) resonance interactions where the frequency of the radial mode was twice (or equal to) that of an interacting high order shape mode.

In an earlier study [10] the stability of initially perturbed and radially oscillating bubbles in an *inviscid* liquid was analyzed via an examination of the solution trajectories for the radial mode and one nearly resonant shape mode in an equivalent planar representation. For the *two-to-one case*, it was shown that for a radial deformation exceeding a given threshold, a homoclinic orbit emanates from a fixed point corresponding to purely radial oscillations. This implies the possibility for producing chaotic dynamics upon the introduction of a time-varying pressure perturbation. The addition of a weak viscous effect requires that this forcing function be large enough to overcome the dissipation. For higher viscosity systems, the dynamics become more complicated [26]. It was established, however, that a continuous energy exchange takes place between the resonant radial and shape modes on a long time scale. Whenever two-to-one resonance conditions are achieved (higher oscillation amplitude is reached) this process is accelerated.

In a subsequent study [27], the effect of viscosity was introduced in addition to time-dependent isotropic and non-isotropic (asymmetric) pressure perturbations. Bifurcation analysis of the amplitude equations for the two types of oscillatory modes reveals that for a sufficiently large amplitude in the volume mode, the onset of instability may lead to chaotic oscillations in both volume and shape modes. It was found, however, that a critical degree of detuning between the volume and shape resonance was required for chaos to occur. If an asymmetric pressure perturbation directly forces the shape oscillations, chaos was found to occur even for exact resonance; no detuning was required. Figure 3 reproduces a schematic description of the bifurcation sets, projected on the plane of the asymmetric drive amplitude (Δ_n) and the drive frequency detuning (σ). Here σ is the nondimensional parameter expressing the difference between the frequency of the pressure perturbation and the frequency of the shape mode resonant with the volume mode. The regions with one fixed point correspond to stable oscillation of the coupled shape and volume modes at fixed amplitude. In regions with larger σ, the amplitude of the radial mode is typically smaller than the shape mode. However, if we traverse the diagram at a constant $\Delta_n \sim 3$, and decreasing values of σ, the needle-like regions correspond to a saddle-node bifurcation across which the solution changes to one with a much stronger radial mode. Within the needle, two steady solutions coexist - one with the amplitudes of the radial and shape modes much stronger than the other. Finally, within the parabolic region around $\sigma = o$, the amplitudes of the shape and volume modes are *time modulated* -with the dynamics being either periodic on a slow time scale, or chaotic depending upon the specific values of Δ_n and σ.

B. Experimental Studies.

Usually, investigation of nonlinear bubble dynamics is carried out with ultrasonic methods consisting of trapping a single sub-critical bubble at a pressure antinode in a standing wave. As the bubble grows and reaches critical size, the carrier frequency of the standing wave matches the resonant volume mode frequency,

and the bubble oscillates at high amplitude. The pressure perturbations are therefore quasi-isotropic, and the volume mode is always driven first. On the other hand, the theoretical work described above, suggests that energy exchange can also take place in the reverse direction: from the shape to the volume mode. We have explored this alternate path to study the mode coupling problem, although we also intend to pursue the study of this problem via the direct excitation of the volume mode.

In order to satisfy the matching of the resonance conditions for centimeter-size bubbles, one must reduce the hydrostatic pressure in order to lower the volume mode resonance frequency to match a resonant shape mode of sufficiently low order to reduce viscous dissipation and to achieve significant oscillation amplitude. Using an apparatus described in references 11 and 12 placed in a vacuum chamber, we have been able to trap 0.5 cm diameter bubbles in 1 G at an ambient pressure down to 0.25 atmosphere. We have also verified that modulation of the ultrasonic standing wave allows the excitation of shape modes up to order 6 with *macroscopic* oscillation amplitude. The Earth's gravitational field prevents us from trapping a bubble of such a size at a lower ambient pressure due to the onset of cavitation in the host fluid.

The microgravity environment allows a significant relaxation in these experimental constraints by greatly reducing the necessary power to position a single bubble of 1 cm in diameter. The hydrostatic pressure can be further lowered, and a match between the volume mode frequency and twice the frequency of a shape mode of order 4 or 5 can be easily obtained. Thus the excitation of the fifth shape mode at a frequency of 138 Hz and at 0.045 atmosphere hydrostatic pressure should allow the observation of the radial mode excitation at 276 Hz when a 0.5 cm air bubble is trapped in water.

IV. LARGE AMPLITUDE SHAPE OSCILLATIONS OF CHARGED AND UNCHARGED DROPS IN AN ELECTRIC FIELD

A. Theoretical Studies.

Using a spheroidal approximation for the equilibrium drop shape, an initial investigation of the dependence of drop oscillation frequencies on the presence of electric charges or of an electric field was carried out [21]. Predictions of the resonant frequency changes due to mean drop deformation, of the effects of resonant coupling between time-periodic oscillations in the electric field and the drop shape, and of the conditions for transition to chaotic oscillations of the drop shape have been obtained for a conducting drop in a time-dependent electric field.

A more recent numerical treatment using the boundary element method [28] has investigated the variations of the fundamental shape mode resonance frequency for charged and uncharged drops as function of the electric field strength and the drop charge. The results agree with those of Feng and Beard [20] for small values of the electric field strength, but differ at the higher values. The variations of the resonance frequency on the amplitude of shape oscillations has also been calculated. Additional calculations involving the effects of a sinusoidal time-varying electric field was also obtained. Some of these results can readily be compared with the experimental data described below.

B. Experimental Studies.

The dynamics of ultrasonically levitated drops in the presence of a static and/or time varying electric field have been investigated in order to quantify the effect of a static field on the oscillation frequencies, the effects of a static shape distortion on the resonances of the droplet, the dynamic response of the drop to a sinusoidal time-varying E field, and the effect of charges on the drop dynamics. The advantage of a hybrid levitation system is the partial decoupling of the electric field and the levitation function, thus allowing the measurement of the influence of the E field in the absence of surface charges.

Figure 4 reproduces experimental data for the measurement of the resonance frequency of the fundamental mode of shape oscillation as a function of amplitude for *driven* oscillations. The decreasing trend is in agreement with the theoretical results described above. In this case, the oscillations are driven by a sinusoidal varying electric field. The drop is ultrasonically levitated, and has an oblate spheroidal equilibrium shape.

Figure 5 reproduces experimental data for the response of a drop to a frequency sweep in the increasing and decreasing frequency direction. Hysteresis is clearly present for significant oscillation amplitude.

V. SUMMARY

Theoretical treatments of the resonant volume to shape oscillations mode coupling has provided strong evidence for the possibility of direct energy transfer under specific circumstances. The experimental effort has demonstrated the capability of exciting higher order shape modes at a reduced hydrostatic pressure, and parameters for a low gravity investigation have been delineated. Direct comparison between a numerical model and experimental results for the dynamics of levitated charged and uncharged drops in a static and time varying electric field has been possible. Hysteresis has been uncovered in the frequency response of droplets modulated by a sinusoidal varying electric field.

ACKNOWLEDGMENTS

REFERENCES

1. W. Lauterborn and U. Parlitz, J. Acoust. Soc. Am. **84**, 1975 (1988)

2. U. Parlitz, V. English, C. Scheffczyk, and W. Lauterborn, J. Acoust. Soc. Am. **88**, 1061 (1990)

3. R.G. Holt and L.A. Crum, J. Acoust. Soc. Am. **91**, 1924 (1992)

4. R.G. Holt, D. F. Gaitan, A.A. Atchley, and J. Holzfuss, Phys. Rev. Lett. **72**, 1376 (1994)

5. M.S. Longuet-Higgins, J. Fluid Mech. **201**, 525 and J. Fluid Mech. **201**, 543 (1989)

6. J. Ffowcs-Williams and Y.P. Guo, J. Fluid Mech. **224**, 507 (1991)

7. H.C. Pumphrey and L.A. Crum, J. Acoust. Soc. Am. **87**, 142 (1990)

8. J.S. Stroud and P.L. Marston, J. Acoust. Soc. Am. **94**, 2788 (1993)

9. C.C. Mei and X. Zhou, J. Fluid Mech. **229**, 29 (1991)

10. Z.C. Feng and L.G. Leal, Phys. Fluids A **5**, 826 (1993)

11. T.J. Asaki, P.L. Marston, and E.H. Trinh, J. Acoust. Soc. Am. **93**, 706 (1993)

12. R.G. Holt and E.H. Trinh, J. Acoust. Soc. **95**, vol.5, Pt.2, 2398 (1994) (A)

13. E. Trinh, A. Zwern, and T.G. Wang, J. Fluid Mech. **115**, 453 (1982), and E. Trinh and T.G. Wang, J. Fluid Mech. **122**, 315 (1982)

14. G.B. Foote, J. Comp. Phys. **11**, 507 (1973)

15. T.G. Wang, M. Saffren, and D.D. Elleman,'Drop Dynamics in Space", in Materials Sciences in Space with Applications to Space Processing, L. Steg Editor, AIAA, New York (1977)

16. R. Natarajan and R.A. Brown, Proc. Roy. Soc. **A410**, 209 (1987)

17. J.A. Tsamopoulos and R.A. Brown, J. Fluid Mech. **147**, 373 (1984)

18. T.S. Lundgren and N.N. Mansour, J. Fluid Mech. **194**, 479 (1988)

19. O.A. Basaran, J. Fluid Mech. **241**, 169 (1992)

20. J.Q. Feng and K.V. Beard, Proc. R. Soc. Lond. **A430**, 133 (1990), J. Fluid Mech. **222**, 417 (1991), and J. Fluid Mech. **227**, 429 (1991)

21. I.S. Kang, "Dynamics of a conducting drop in an electric field", to appear in J. Fluid Mech.

22. E. Trinh and T.G. Wang,"Large amplitude drop shape oscillations",Proceedings of the Second International Colloquium on Drops and Bubbles", D.H. Le Croisette Editor, JPL Publication 82-7, 143 (1982)

23. E. Becker, W.J. Hiller and T.A. Kowalewski, J. Fluid Mech. **258**, 191 (1994)

24. E.H. Trinh, J. Robey, A. Arce, and M. Gaspar, Mat. Res. Soc. Symp. Proc. **87**, 57 (1987)

25.E.H. Trinh and E. Leung, Am. Inst. of Aeronautics and Astronautics paper **90-0315** (1990), and A. Biswas, E. Leung, and E.H. Trinh, J. Acoust. Soc. Am. **90**, 1502 (1991)

26. N. McDougald, PhD thesis UCSB (in preparation)

27. Z.C. Feng and L.G. Leal, "Bifurcation and chaos in shape and volume oscillations of a periodically driven bubble with two-to-one internal resonance", to be published

28. Z.C. Feng and L.G. Leal, "Numerical simulation of the dynamics of an electrostatically levitated drop", in preparation
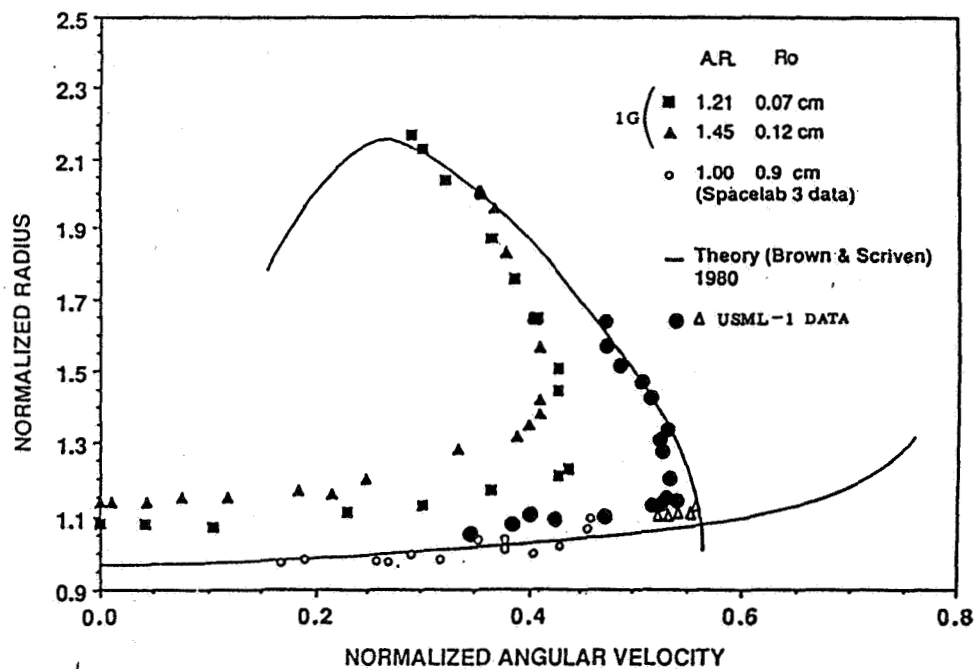
Figure 1.

Comparison of ground-based results for the measurement of the bifurcation point for the equilibrium shape of rotating free drops. Measurement in 1G involves statically distorted drops while the conditions of microgravity allows experimenting with no shape distortion.
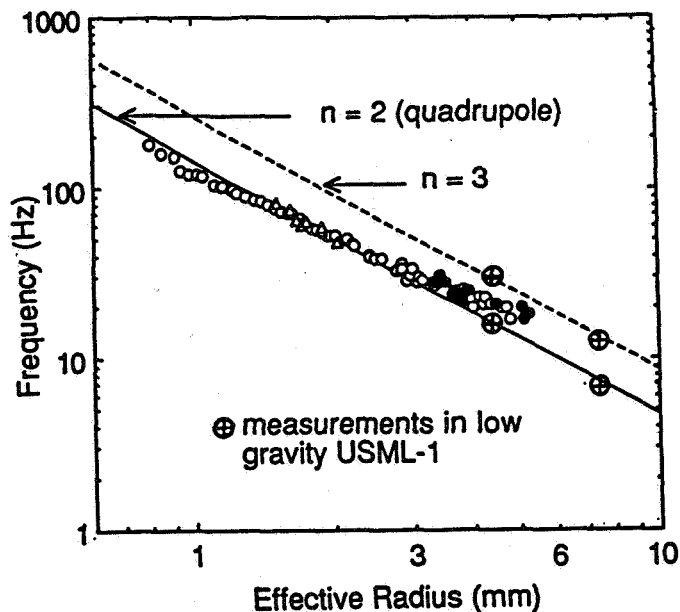
Figure 2.

Comparison of ground-based and microgravity data for the resonant mode frequencies of a free bubble. The data are from P.L. Marston, E.H. Trinh, J. Depew, and T.J Asaki, IUTAM Symposium Proceedings (1993)
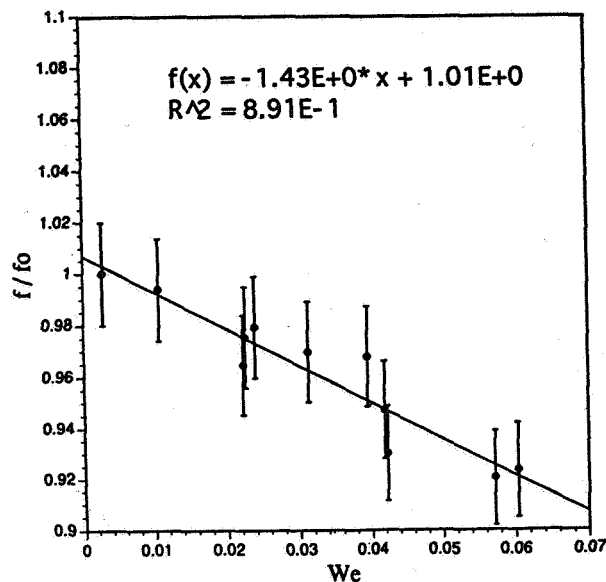
Figure 4.

Experimental results of the measurement of the frequency shift as a function of the driving electric field amplitude. The drops are ultrasonically levitated and electrically shape modulated. The Weber number We is proportional to the square of the electric field magnitude.
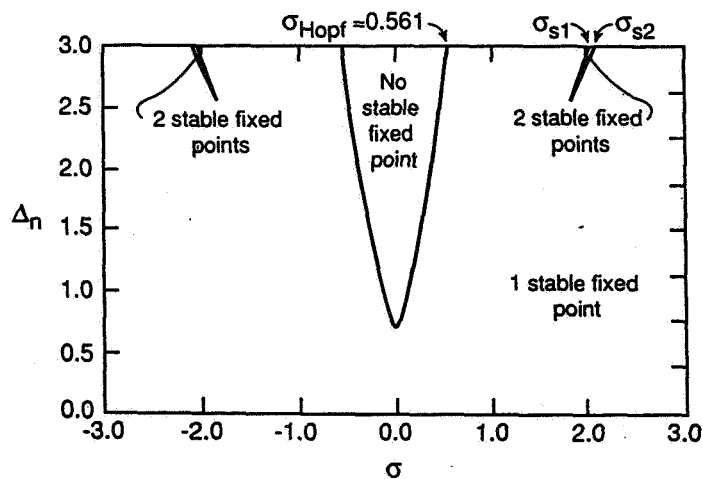
Figure 3.

Bifurcation sets in the frequency (σ) and perturbation amplitude (Δ_n) space.
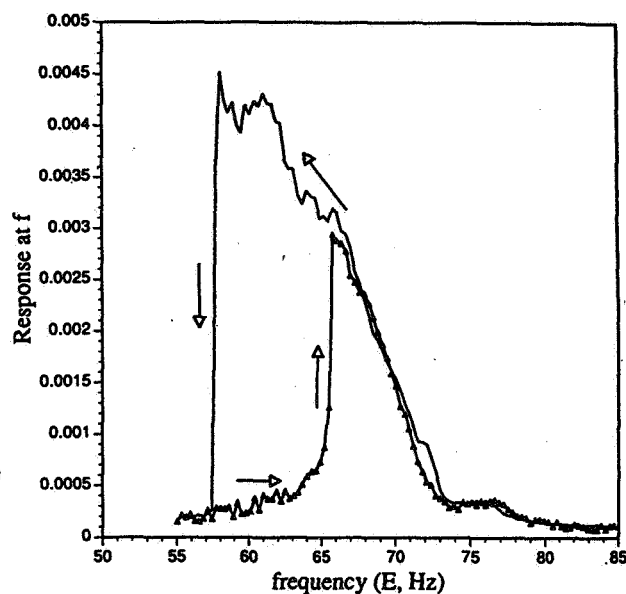
Figure 5.

Experimental evidence for hysteresis in the frequency response of levitated drop driven by a sinusoidal time-varying electric field. The sense of the arrows shows the frequency sweep direction.

133

COMPUTATIONS OF DROP COLLISION AND COALESCENCE

Grétar Tryggvason, Damir Juric, Mohammed H.R. Nobari, and Selman Nas
Department of Mechanical Engineering
The University of Michigan
Ann Arbor, Michigan 48109

ABSTRACT

Computations of drops collisions and coalescence are presented. The computations are made possible by a recently developed finite difference/front tracking technique that allows direct solutions of the Navier-Stokes equations for a multi-fluid system with complex, unsteady internal boundaries. This method has been used to examine the boundaries between the various collision modes for drops of equal size and two examples, one of a "reflective" collision and another of a "grazing" collision is shown. For drops of unequal size, coalescence can result in considerable mixing between the fluid from the small and the large drop. This problem is discussed and one example showed. In many cases it is necessary to account also for heat transfer along with the fluid mechanics. We show two preliminary results where we are using extensions of the method to simulate such problem. One example shows pattern formation among many drops moving due to thermal migration, the other shows unstable evolution of a solidification front.

INTRODUCTION

The presence of a free surface that is not constrained to be more or less flat due to the action of gravity is perhaps the most important aspect of fluid flow in microgravity. The absence of gravity generally makes surface tension effects important at much larger length scales than we are used to on earth. The large amplitude surface motion possible when gravity is small or absent is generally highly nonlinear and thus difficult to analyze by conventional means. Such surface motion is, nevertheless, to be expected in microgravity environment and it is necessary to understand it to be able predict its motion, or avoid it if necessary. Experiments in microgravity are at best expensive, and usually difficult as well. It is therefore desirable to be able to predict the evolution numerically. Such numerical simulations can, occasionally, replace experiments information that can not be measured. In other cases numerical simulations can complement experiments and aid in the design of experiments.

Numerical simulations of free surface flows have remained one of the frontiers of computational fluid dynamics since the beginning of large scale computations of fluid flow. For an early work on drop collision, see ref. 3. Progress has however been much slower than for homogeneous flows and numerical simulations have not played the same role in multi-fluid and multiphase research as they have done for turbulence research, for example. Recently, however, a number of investigators have made considerable progress and this paper reviews briefly our effort in this area of relevance to microgravity fluid physics. We start by a description of the numerical methodology, since it is critical to the success of our work, and then review a few applications.

NUMERICAL METHOD

The numerical method is a hybrid between so called front capturing methods where a sharp front is resolved on a stationary grid and front tracking methods where the interface is followed by separate computational elements. We use a stationary regular grid for the fluid flow, just as front capturing methods, but track the interface by a separate grid of lower dimension. This grid is usually referred to as a front. However, unlike front tracking methods, we do not treat each phase separately, but work with the Navier-Stokes equations for the whole flow field. In a conservative form those are:

$$\frac{\partial \rho \overline{u}}{\partial t} + \nabla \cdot \rho \overline{u}\overline{u} = -\nabla p + \overline{f} + \nabla \cdot \mu \left(\nabla \overline{u} + \nabla \overline{u}^T \right) + \int_F F_s \delta \left(\overline{x} - \overline{x}_f \right) da$$

Here, $\overline{u}$ is the velocity vector, p the pressure, and ρ and μ are the discontinuous density and viscosity fields, respectively. $\overline{f}$ is a body force that can be used to initiate the motion. The surface tension forces, F_σ act only on the interface between the fluid and appears in the current formulation multiplied by a three-dimensional delta function, δ. The integral is over the entire front.

It is important to note that this equation contain no approximations beyond those in the usual Navier-Stokes equations. In particular, it contains implicitly the proper stress conditions for the fluid interface. The above equation is discretized on a staggered grid using second order second order centered finite differences for the spatial derivatives and a second order time integration scheme for most of our computations. For short simulations, first and second order give very comparable results, but for long time simulations the higher order is a must. To monitor the accuracy we check, among other quantities, how well we conserve mass. While the finite difference method has good conservation properties, the front tracking is not inherently conservative. By using second order time integration and sufficiently fine resolution we always find that mass is well conserved. The momentum equation is supplemented by an equation of mass conservation, which for incompressible flows is simply

$$\nabla \cdot \bar{u} = 0$$

Combining this equation with the momentum equation leads to an elliptic equation for the pressure. Unlike the pressure equation for homogeneous flows, here it is nonseparable and fast methods used extensively for homogeneous flows (FISHPACK, for example) are not applicable. We used a simple SOR for many of our early computations (in the so-called Black and Red form for computations on the CRAY), but now a multigrid package (MUDPACK from NCAR) is used for most of our computations. Since the density and the viscosity are different for the different fluids, it is necessary to track the evolution of these fields by solving the equations of state which simply specify that each fluid particle retains it original density and viscosity:

$$\frac{\partial \rho}{\partial t} + \bar{u} \cdot \nabla \rho = 0; \quad \frac{\partial \mu}{\partial t} + \bar{u} \cdot \nabla \mu = 0$$

In our front tracking code we do not solve these equations in this form, but use the front to determine the value at each grid point. This can be achieved efficiently by distributing the density gradient (or the jump) onto the grid and then reconstructing the density from its gradient. This allows two interfaces to lie close to each other so the gradient cancel. Usually it is only necessary to reset the density and viscosity of grid points next to the front.

The surface tension force, which is computed from the front configuration is, perhaps, the most difficult part of the algorithm. Therefore, we have spent considerable time on that and explored various alternatives. The current algorithm, which appear to be very satisfactory, is based on computing directly the force on each element by

$$\bar{F}_\sigma = \oint_{elem} \sigma \bar{n} \times \bar{t} ds$$

where $\bar{t}$ is a tangent to the boundary of the surface element, $\bar{n}$ is the surface normal, and σ is the surface tension coefficient. By computing the surface tension forces this way, we explicitly enforce that the integral over any portion of the surface gives the right value, and for closed surfaces, in particular, we enforce that the integral of surface tension forces is zero. This is particularly important for long time simulations where a failure to enforce this constrain can lead to unphysical motion of bubbles and drops.

Since the boundary between the fluids (the front) usually undergoes considerable deformation during each run, it is necessary to modify the surface mesh dynamically during the course of the computations. The surface mesh is an unstructured grid consisting of points that are linked by elements. Both the points and the elements are arranged in a linked list, so it is relatively easy to change the structure of the front, including adding and deleting points and elements. Topological changes, such as when bubbles coalesce or drops break in two can also be accomplished by minimum effort. This is usually considered a major difficulty in implementing methods that explicitly track the front, but we have shown that with the right data structure these tasks become relatively straight forward. Although topology changes are easily done from a programming point of view, the physics is far from trivial. In reality, drops bounce off each other if the time when the drops are close is shorter than the time it takes to drain the film. Usually the film becomes very thin before it breaks and it would require excessive grid refinement to resolve the draining fully. At the moment we are dealing with this issue in a rather *ad hoc* way by simply changing the topology of the front at a prescribed time. However, considerable analytical work has been done on film draining and rupturing and we are currently exploring the possibility of combining such a model with our simulations.

Although by no means new, the formulation of two (or more) fluid problems in terms of one equation for the whole flow field is somewhat unusual. Furthermore, even though it is a rigorous approach, it is not immediately obvious that it will lead to an efficient computational method. We have therefore conducted extensive validation tests, not only to check the implementation, but also to assess its accuracy. We have compared the code with analytical solutions where available, such as the linear oscillations of a drop and the propagation of waves, with other computational work such as the simulations of Leal and coworkers (see, e.g. ref. X) and experimental results. The actual resolution requirement varies with the parameters of the problem. High Reynolds numbers, for example, generally require finer resolution than lower ones, as in other numerical calculations. We have also found that for problems where the surface tension varies, such as for contaminated bubbles and drops moving by thermal migration

we generally require finer resolution than for flows where the surface tension is constant. However, in all cases have we found that the methods converges rapidly under grid refinement, and in those cases where we have has other solutions we have found excellent agreement, even for modest resolutions. Examples of these validations are contained in various papers and dissertations, see ref. 5-9, 11, and 12.

RESULTS

We have investigated the head-on collisions of two drops in detail by axisymmetric computations and also done several fully three dimensional calculations of off-axis collisions. Figure 1 shows the head on collision of two drops from ref. 9. To move the drops toward each other we apply a body force on each drop that is turned off once the drops have reached the desired velocity and before the drops collide. In this case, the drop Weber number, $\rho d U^2 / \sigma$, and the Reynolds number, $\rho U d / \mu$, are 115 and 185, respectively. As the drops collide, they deform and once they are close enough, the film between them is ruptured so the drops coalesce into one drop. The kinetic energy is converted into surface tension energy as the drop is deformed into a disk-like shape, and once the it is nearly stationary the process is reversed and surface tension pulls the drop back into a spherical shape. In this particular case, the initial kinetic energy is sufficiently high and the dissipation sufficiently low that the drop actually splits into three. This evolution is observed experimentally, see ref. 2 and 4, for example, and is called reflective collision. For lower initial energy the drops do not separate again, but remain one. We have investigated the boundary between reflective collision and coalescing collisions (when the drops permanently become one drop) and found good agreement with experimental observations. For collisions close to the boundary there is a slight sensitivity to the exact time of rupture, but away from the boundary the evolution is not affected by the exact rupture time.

When the drops do not approach each other along the same axis, the evolution is fully three-dimensional. If the off-axis distance is small, the evolution is similar to a head on collision, but if the distance is large a new collision mode, usually called grazing collision, becomes possible. Figure 2 shows such a collision. The drops are initially accelerated toward each other by a body force. This force is turned off once the drops have reached the desired velocity and before they collide. As the drops collide, they deform, and once the film of ambient fluid between them is thin enough it is ruptured and the drops allowed to coalesce. If the offset is small, the coalescence is permanent for the Reynolds and Weber numbers used here, but when the offset is large, as is the case in figure 2, the drops tear apart again. We have compared the boundaries between permanent coalescence and grazing with experimental observations and find excellent agreement [see ref. 7 and 8 for details]. Both the axisymmetric and the three-dimensional computations have shed considerable light on the collision process and the role played by losses of surface tension energy during the actual coalescence when the thin film between the drops is ruptured.

Another problem that we have investigated in some detail is the coalescence and subsequent mixing of two, initially stationary drops of unequal size. This study was motivated by experiments conducted by Anilkumar, Lee and Wang (ref. 1) who brought two drops together slowly and made a video recording of the evolution after the film between them ruptures and surface tension forces pull the small drop into the larger one. For high viscosity drops the motion is quickly dissipated and the fluid from the small drop remains near the point where the drops touched. For lower viscosity, however, the fluid from the small drop is injected much more violently into the larger one, forming a jet that often reaches across the larger drop. In general, the penetration depth depends on the nondimensional viscosity and the size ratio of the drops, since for two drops of the same size, no jet formation occurs by symmetry. This problem requires a careful resolution of inertia, viscous and surface tension effects. We have investigated this problem in some detail and provided a reasonably complete picture of how the evolution depends on the parameters of the problem. Figure 3 shows the process. The initial configuration is shown on the left and the final configuration is on the right.

As the multi-fluid problem has been brought under control, we have moved toward more complex physics. A problem of a long standing interest to the microgravity community is the thermal migration of bubbles and drops. Here, two complications arise. First, we must solve for the temperature field and second, surface tension is now no longer a constant but depends on the temperature. We have dealt with variable surface tension before for problems involving surface active materials (or surfactants) so the added complication here is only the heat transfer part. Figure 4 shows a few frames from a two-dimensional calculation of the motion of six drops in a temperature gradient. The drop surface and isothermals are shown. The top and bottom boundaries are rigid walls at constant temperature, but the horizontal boundaries are periodic. The evolution seen here is typical for many drops at these parameter values. The drops line up across the channel until there is not room for more. The rest then forms a new line. If there are not

enough drops to fit across the channel, the drops position themselves as far apart from each other as possible. Preliminary simulations of fully three-dimensional drops indicate that the interactions are much weaker in three-dimensions, but we have not conducted a systematic study yet.

For material processing and thermal management the fluid mechanics is often, if not always going to be accompanied by phase changes. In preparation for simulations of fluid systems undergoing a change of phase such as during boiling or solidification, we have developed a method based on the same single domain formulation used for the fluid flow for solidification. Up to now we have only simulated solidification and figure 5 shows an example where an initially undercooled melt solidifies. We are currently combining this methodology with our fluid dynamics method.

CONCLUSIONS

We have discussed our development of numerical method suitable for the predictions of free surface flows in microgravity and the application of these methods to several problems. These applications have already lead to a better understanding of some aspects of drop collisions and coalescence and also demonstrate the versatility of the method. Overall, it seems reasonable to state that the fluid problem is under good control with the exception of how to handle the rupture of thin films. Our current *ad hoc* strategy seems to work well in some cases, but it is highly desirable to have a more general way of determining when the film ruptures. We believe that the rupture time is the most important information needed, and that for a large class of problems the details of the post rupture motion, including the formation of small drops can be safely ignored. In most cases the fluid motion is only a part of the process of interest and heat transfer and phase change must be dealt with in order to establish the understanding needed for a complete predictive capability. We have taken preliminary steps in this direction and examined the thermal migration of drops and solidification.

ACKNOWLEDGMENTS

REFERENCES

1. A.V. Anilkumar, C.P. Lee, and T.G. Wang. Surface-Tension-Induced Mixing Following Coalescence of Initially Stationary Drops. Phys. Fluids A. 3 (1991), 2587-2591.

2. N. Ashgriz and J.Y. Poo. Coalescence and separation in binary collisions of liquid drops. J. Fluid Mech. 221 (1990), 183-204.

3. G.B. Foote. The Water Drop Rebound Problem: Dynamics of Collision. J. Atmos. Sci. 32 (1975), 390-402.

4. Y.J. Jiang, A. Umemura, and C.K. Law. An experimental investigation on the collision behavior of hydrocarbon droplets. J. Fluid Mech. 234 (1992), 171-190.

5 Y.-J. Jan. Ph.D. Thesis, Computational Studies of Surfactant Effect on Bubble and Drop Dynamics. The University of Michigan, 1993.

6. S. Nas and G. Tryggvason. Computational Investigation of the Thermal Migration of Bubbles and Drops. In *AMD 174/FED 175 Fluid Mechanics Phenomena in Microgravity*, Ed. Siginer, Thompson and Trefethen. 1993 ASME Winter Annual Meeting.

7 M.R. Nobari. Ph.D. Thesis, Numerical Simulation of Oscillation, Collision, and Coalescence of Drops. The University of Michigan, 1993, 155 pages.

8. M.R.H. Nobari and G. Tryggvason. AIAA 94-0835 Numerical Simulations of Drop Collisions.

9. M.R.H. Nobari, Y.-J. Jan, and G. Tryggvason. Head-on collision of drops—A numerical investigation. ICOMP-93-45, NASA TM 106394.

10. G. Ryskin and L. G. Leal. Numerical solution of free-boundary problems in fluid mechanics. Part 1-3. J. Fluid Mech 148 (1984), 1-43.

11. S.O. Unverdi and G. Tryggvason. A Front Tracking Method for Viscous Incompressible Flows. J. Comput. Phys., 100 (1992) 25-37.

12. S.O. Unverdi and G. Tryggvason. Multifluid flows. Physica D 60 (1992) 70-83.
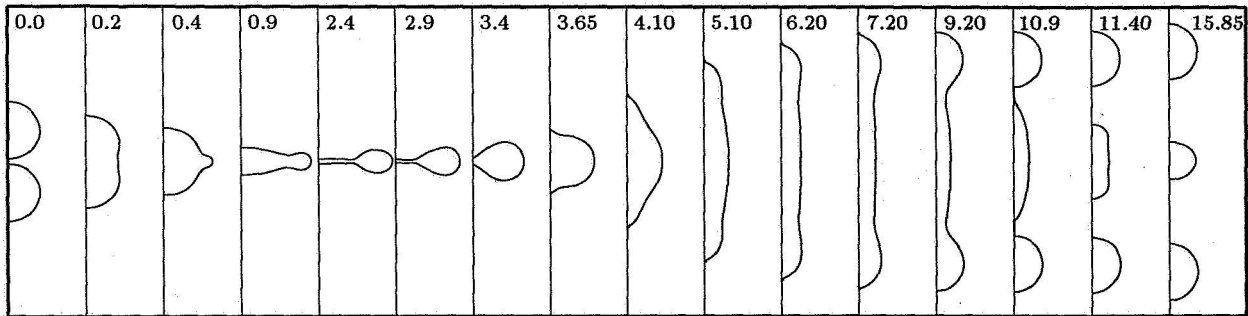
Figure 1. The head on collision of two drops computed by an axisymmetric version of our method. Here We=115 and Re=185. The drops are sufficiently energetic so they break up again after initial coalescence.
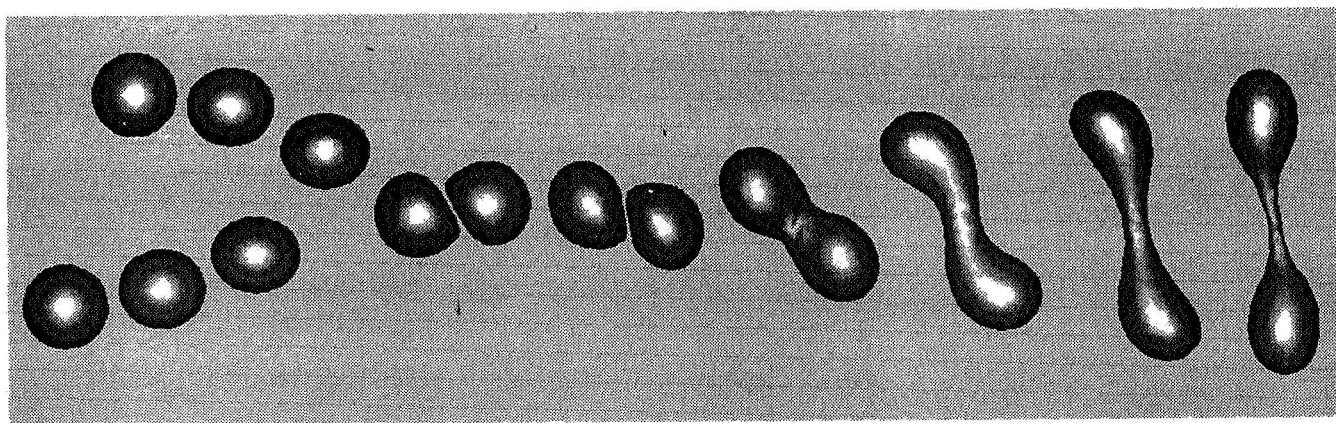
Figure 2. Fully three-dimensional grazing collision of two drops. Here, We = 23 and Re = 68. The line along which each drops moves are separated by 0.825 drop diameters.
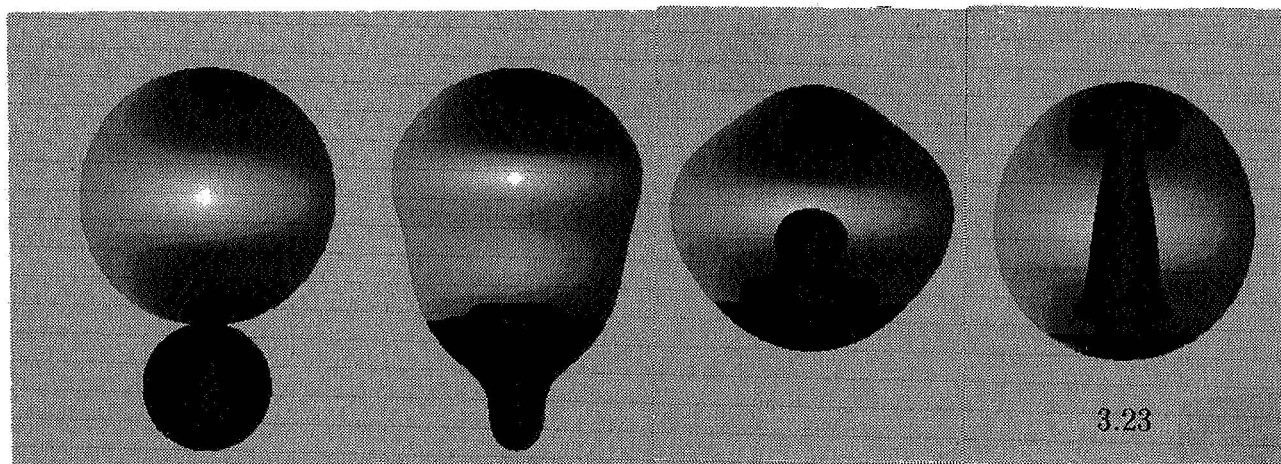
Figure 3. Coalescence and mixing of two stationary drops of unequal size.
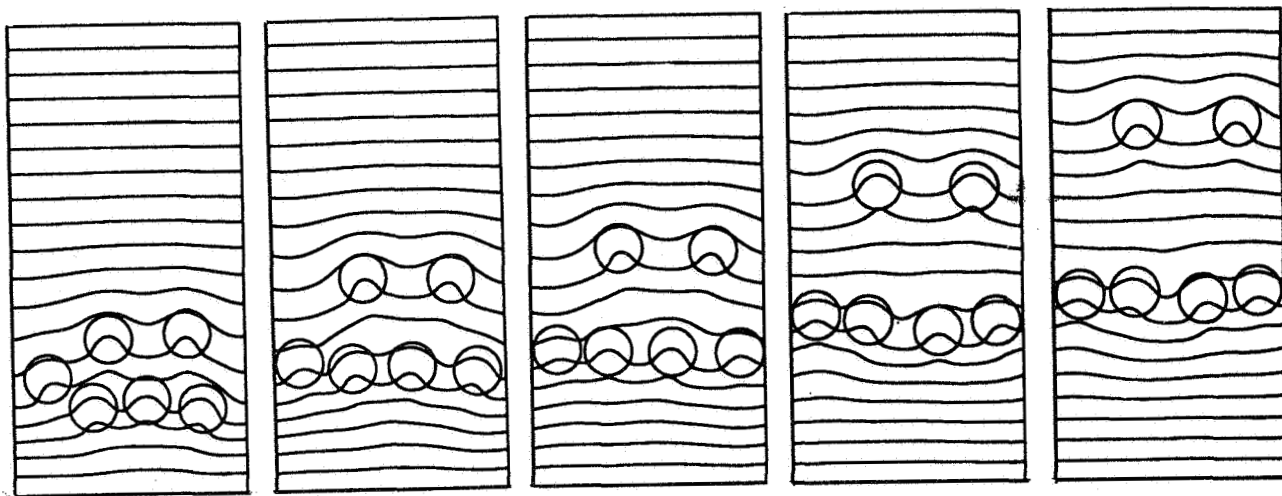
Figure 4. The thermal migration of several two-dimensional drops. The initial conditions are to the left. The drops and the isotherms are shown.
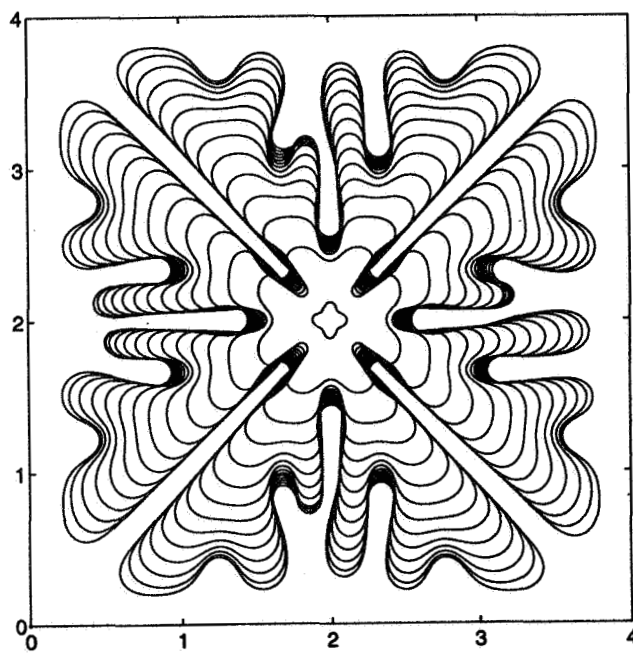
Figure 5. The evolution of an unstable solidification front. The front is shown at several times as it advances into the undercooled melt.

A REALISTIC MODEL OF EVAPORATION FOR A LIQUID DROPLET

An-Ti Chai
NASA Lewis Research Center
Cleveland, OH 44135

V. S. Arpaci
Department of Mechanical Engineering
and Applied Mechanics
University of Michigan
Ann Arbor, MI 48109

An intuitive delineation along with dimensional considerations and experimental evidences are presented to show that in a general case, the evaporation of a liquid droplet undergoes three regimes through the process. Initially, the heat transfer inside the evaporating droplet is conduction controlled; then, in the second stage, convective heat transfer may take over; finally, the convections subside, and the process returns to conduction controlled mode.

Consider a simple sphere of liquid droplet undergoing the evaporation process. According to the well known Maxwell's theory, the rate of evaporation can be described by the linear D-square law of quasi-steady droplet evaporation [1]:

$$-\frac{dm}{dt}=-4\pi r^2 D_{df}\frac{dc}{dr}$$

or

$$-\frac{dD^2}{dt}=8\frac{D_{df}}{\rho}(c_d-c_\infty)$$

where m, r, D_{df}, c, D, and ρ represent mass, radius, diffusion coefficient, concentration, droplet diameter, and liquid density, respectively. The subscript d refers to a location at the droplet surface, and subscript ∞, a distant point or simply the ambient.

If one takes a closer look at the evaporation process, it is not difficult to realize that the classical D-square law of Maxwell does not really describe the whole process. Consider a free-floating liquid drop whose surface temperature decreases as the liquid evaporates. As the process continues, a radial

temperature gradient builds up at the free surface until the critical Marangoni number is exceeded. Then the onset of instability induces thermocapillary convective flows, which in turn speed up the evaporation. The convective flows will subside when the interior of the droplet reaches a certain equilibrium temperature, and the process will return to the conduction controlled mode.

Based on the above reasoning, the entire evaporation process can be more realistically described as follows. In the initial stage, a droplet evaporates essentially according to the D-square law and is depicted as regime I in Fig. 1. As the evaporation continues, the faster heat loss through evaporation exceeds the heat supplied through conduction and a radial temperature gradient begins to develop at the surface. Meanwhile, the Marangoni number of the droplet near the surface increases with the temperature gradient build-up. When the Marangoni number reaches its critical value, the onset of (Marangoni instability induced) convective flow commences, and this is the beginning of regime II. The convective flow effects faster heat transfer to the evaporating surface, which should result in a significant increase in the evaporation rate. Eventually, the interior temperature of the liquid drop reaches a lower (than the ambient) equilibrium value, which can not maintain the radial temperature gradient for sustaining the convective flows. At this point, the convective flow motion subsides and the process enters into the final stage of regime III. In the final stage, the liquid drop continues its evaporation at the rate sustained by the heat input from its ambient environment (excluding radiative heating), which is conduction controlled as in regime I. The process continues until the droplet evaporates completely.

While buoyancy-driven fluid problems related to spherical geometry instability have been treated to a considerable extent in the literature, the thermocapillary instability of spherical geometry has been almost completely overlooked except for the recent work of Cloot and Lebon [2] who deal with the mathematical aspects of thin spherical shell configuration, and Arpaci, Selamet, and Chai who take into consideration some physical aspects of the problem, paying special attention to realistic boundary conditions and surfactant effects [3]. To help establish the validity of the intuitive reasoning to have thermocapillary instability involved in the droplet evaporation process, the following dimensional arguments are in order.

Consider an interface momentum balance of a curved surface which is affected by the presence of surfactant

$$F_S(1-\beta) \sim F_V(1-R)$$

where F_S and F_V respectively denote surface tension and viscosity forces, and β and R the effect of surfactant and that of spherical curvature respectively on the cartesian Laplacian. The inertial contribution is neglected for infinitesimal instability considerations.

The thermal energy balance at the interface is

$$Q_H \sim Q_K(1+B),$$

where Q_H and Q_K respectively denote heat from enthalpy flow and conduction, and B denotes the Biot number (heat loss from the interface). Explicitly,

$$F_S \sim \Delta\sigma l, F_V \sim \mu Vl, Q_H \sim \rho c_p VTl^2, Q_K \sim kTl,$$

and the equations of momentum and energy balance lead to

$$\frac{F_S(1-\beta)}{F_V(1-R)} = \frac{\Delta\sigma(1-\beta)}{\mu V(1-R)}, \quad \frac{Q_H}{Q_K(1+B)} = \frac{\rho c_p Vl}{k(1+B)}$$

In the above expressions, σ, μ, ρ, c_p, and k have their conventional meanings of surface tension, viscosity, density, specific heat, and conductivity, respectively. For surface tension-driven flow, the flow velocity V is a dependent variable. Consequently, the above two expressions cannot be used as ultimate dimensionless numbers characterizing these flows. However, the combination of them in a way which eliminates the velocity V yields

$$\frac{F_S(1-\beta)}{F_V(1-R)} \frac{Q_H}{Q_K(1+B)} = \frac{1-\beta}{(1+B)(1-R)} Ma_{\beta,B,R}$$

where

$$Ma = \frac{|\Delta\sigma|l}{\mu\alpha}$$

is the usual definition of Marangoni number, l a characteristic length(liquid layer thickness), and $\alpha = k/\rho c_p$ is the thermal

143

diffusivity.

Now consider the case for a simple, clean and flat liquid layer. Similar arguments lead to

$$\frac{F_S}{F_V}\frac{Q_H}{Q_K}=Ma$$

Consequently, the critical Marangoni number for a liquid droplet, relative to Ma_c for a simple, clean and flat liquid layer, can be written as

$$(Ma_{\beta,B,R})_c=\frac{(1+B)\ (1-R)}{1-\beta}\ Ma_c$$

which suggests that the heat transfer and surfactant delay, and the curvature hastens the onset of instability.

For evaporating droplets, latent heat enthalpy flow Q_2 needs to be taken into consideration in addition to the sensible heat of Q_H. Here

$$\frac{Q_H}{Q_2}\sim\frac{c_p\Delta T}{h_{fg}}=Ja$$

is the Jacob number, with h_{fg}, the latent heat. Thus for evaporating droplets, the Marangoni number needs to be replaced by

$$Ma\,(1+\frac{1}{Ja})\ .$$

The critical Marangoni number for the onset of surface tension-driven convection in a thin layer of fluid, according to Pearson's study [4], is $Ma_c = 80$. Experiments carried out by Apollo 17 crew, however, gave an order of magnitude higher Ma_c in the range of 400 - 2,600 [5,6]. Various reasons have been cited to account for the difference, but no conclusive argument has been made.

To the best of our knowledge, similar studies for the case of an evaporating liquid droplet do not exist. The curvature is

144

expected to decrease the critical Marangoni number. However, a preliminary calculation has shown that the Marangoni number could reach as high as up to 10^4 for a water or methanol droplet with a radius of 1 mm, evaporating in a relatively mild (ambient temperature) environment. A Marangoni number of such a magnitude clearly indicates that the surface tension-driven convection can be expected in the evaporating droplets targeted for this study.

Ideally, accurate measurements of droplet evaporation can be performed in space using the Drop Physics Module or the Fluids Module on board the USML (United States Microgravity Laboratory), which we have already proposed to do. However, before we get the opportunity to conduct the space experiments, we are able to report here the ground-based experimental evidences (some photos were presented as poster exhibits at the VIIIth European Symposium on Materials and Fluid Sciences in Microgravity, Bruxelles, Belgium, April 13-16, 1992[7]) that unequivocally demonstrate the feasibility of conducting the experiments in space and the validity of the new model for droplet evaporation.

In order to minimize buoyancy effects and droplet deformation due to weight, we limited our sample size to approximately 1.5-1.75 mm in diameter. The sample droplet, prepared and injected at room temperature, is suspended with a wire loop inside an evaporation chamber. A sheet (approximately 0.2 mm thick) of laser light is used to illuminate a cross section of the sample; two variable intensity spot lights are used for general illumination. Flow visualization is accomplished with an Olympus microscope equipped with zoom body mechanism (7.5-64x), video and still cameras. Aluminum powder of 1 micron size is used as tracing particles. The presence of the wire loop causes a slight rotation in the bulk fluid, and the uneven heating of the loop by the illuminating light could also disturb the flow patterns. However, these undesirable effects are not as detrimental so far as our qualitative data is concerned. The flow patterns induced by thermocapillary instability can be unequivocally identified.

For evaporating liquids, we tested distilled water, methanol, acetone, and low viscosity silicon oil (Dow Corning 200 fluid, 0.65 cs). Water has been notoriously known for its suppression of surface tension-driven flows because the large dipole moment of its molecules attracts contaminations on the free surface. We certainly experienced considerable difficulty with water to induce any appreciable flows driven by surface tension forces. The volatile acetone makes it hard to obtain flow patterns steady enough for one to take photo pictures. Methanol and the 0.65 silicon oil both behave consistently well.

Figure 2(a) shows a water droplet evaporating in normal atmospheric pressure. There is no apparent internal flow of any

kind. Methanol droplets in a vapor saturated environment and a methanol droplet in the brief quasi-stationary evaporation mode (prior to the onset of instability induced convective flows) can also be represented by Fig. 2(a). Figure 2(b) shows a fairly symmetric convective flow pattern developed in an evaporating methanol (or 0.65 cs silicone oil) droplet seconds after the process gets started. However, after considerable evaporation, the temperature of the droplet decreases significantly and can no longer sustain the thermocapillary convection; the convective flows die down and the evaporation returns to conduction controlled mode. Figure 2(c) clearly shows that this is the case.

For reference and comparison, we painted a wire loop black and used it to suspend a sample droplet. Upon illumination with the sheet of laser light, the point where light intersects the loop obviously absorbed enough light to create a local warm spot, hence a surface temperature gradient on the sample droplet. The vigorous bulk flow motion exhibited in Fig. 3 was generated precisely in this manner.

REFERENCES

1. Fuchs, N. A. Evaporation and Droplet Growth in Gaseous Media, Pergamon Press, New York, 1959

2. Cloot, A. and Lebon, G. Marangoni Convection in a Rotating Spherical Geometry, Phys. Fluids A **2** (4), 525-529, 1990

3. Arpaci, V. S., Selamet, E. and Chai, A. T., Thermocapillary Instability of Spherical Shells, HTD-Vol. 180, Fundamentals of Forced and Mixed Convection and Transport Phenomena ASME 1991

4. Pearson, J. R. A., On Convection Cells Induced by Surface Tension, J. Fluid Mech. **4**, 489-501, 1958

5. Grodzka, P. G. and Bannister, T. C., Heat Flow and Convection Demonstration Experiments Aboard Apollo 14, Science **176**, 506-508, 1972

6. Grodzka, P. G. and Bannister, T. C., Heat Flow and Convection Demonstration Experiments Aboard Apollo 17, Science, **187**, 165-167, 1975

7. Chai, A. T., Rashidnia, N., and Arpaci, V. S., Marangoni Instability Induced Convection in an Evaporating Liquid Droplet, Proceedings of the VIIIth European Symposium on Materials and Fluid Sciences in Microgravity, Brussels, Belgium, 12-16 April 1992, 187-192, ESA SP-333 (August 1992)
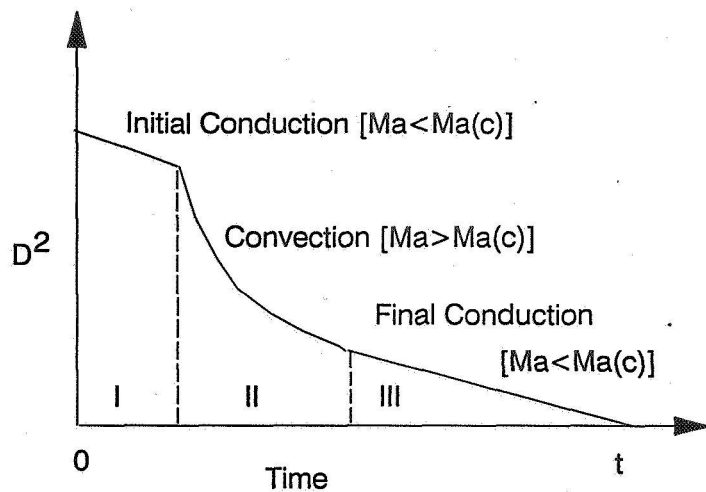
Figure 1. Three regimes of droplet evaporation

(a)

(b)
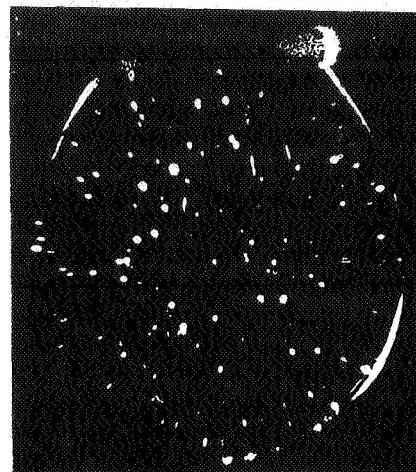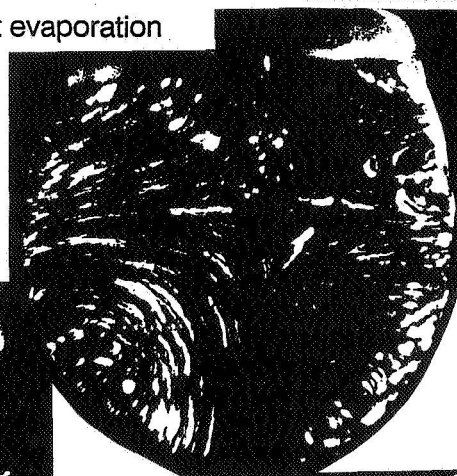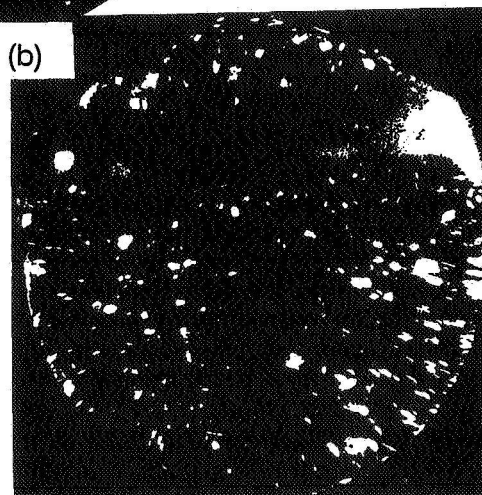
Figure 3. A pattern of strong bulk flow motion generated by an imposed surface temperature gradient.

(c)

Figure 2. Laser sheet light illuminated cross section of an evaporating droplet (a) in regime I (b) in regime II, (c) in regime III.

THERMOCAPILLARY MOTION OF DEFORMABLE DROPS

Hossein Haj-Hariri and Qingping Shi
Department of Mechanical, Aerospace, and Nuclear Engineering
University of Virginia
Charlottesville, VA 22903, USA

Ali Borhan
Department of Chemical Engineering
The Pennsylvania State University
University Park, PA 16802, USA

ABSTRACT

The thermocapillary motion of initially spherical drops/bubbles driven by a constant temperature gradient in an unbounded liquid medium is simulated numerically. Effects of convection of momentum and energy, as well as shape deformations, are addressed. The method used is based on interface tracking on a base cartesian grid, and uses a smeared color or indicator function for the determination of the surface topology. Quad-tree adaptive refinement of the cartesian grid is implemented to enhance the fidelity of the surface tracking. It is shown that convection of energy results in a slowing of the drop, as the isotherms get wrapped around the front of the drop. Convection of momentum results in a slowdown if the drop has a lower density than the exterior phase. Shape deformations resulting from inertial effects affect the migration velocity. The physical results obtained are in agreement with the existing literature. Furthermore, remarks are made on the sensitivity of the calculated solutions to the smearing of the fluid properties. Analysis and simulations show that the migration velocity depends very strongly on the smearing of the interfacial force whereas it is rather insensitive to the smearing of other properties, hence the adaptive grid.

INTRODUCTION

Recently there has been considerable interest in the development of methods for the numerical simulation of flows involving sharp fluid-fluid interfaces. The common feature of the more successful of these methods is the replacement of the concentrated interfacial forces by a smeared body force. The discontinuous variations of other fluid properties across such interfaces are treated similarly. Therefore the multi-fluid problems with concentrated forces reduce to single-fluid ones with smoothly-varying properties, subject to appropriate distributions of body forces. The obvious advantage is the simplification of the topology of the problem and the requisite numerical grid for the discretization of the equations governing the flow. This nontrivial simplification is the direct result of smearing of the properties and the interfacial forces. Some notable early contributions are those by Hirt and Nichols [1], Peskin [2], Brackbill et al. [3], followed recently by Tryggvason et al. [4], Haj-Hariri et al. [5], and Sheth and Pozrikidis [6].

The motion of drops and bubbles in a fluid medium is of fundamental importance in many natural physical processes as well as a host of industrial activities. Drops or bubbles floating in a fluid can be moved by a large number of 'weak' forces including gravity, which is normally the dominant mechanism of drop motion on earth, and interfacial tension gradients which can play a major role under microgravity conditions where sedimentation and gravity-driven convection are largely eliminated. Interfacial tension gradients induced at the surface of a drop or bubble through variations of temperature, surfactant concentration, or surface charge distribution give rise to unbalanced tangential stresses which result in fluid motion (cf. [7]).

Most of the work on the motion of drops due to interfacial tension gradients is relatively recent, as summarized in the review article by Subramanian [8]. The majority of the analytical and numerical investigations assume a fixed spherical shape for the migrating drop. This is an appropriate assumption only in the limit of large interfacial tension with small variations on the surface of the drop. The validity of this assumption is highly questionable in the presence of the convective transport of momentum and energy, as well as for droplet motion in the vicinity of solid boundaries (e.g. container walls). It is the purpose of this work –and others like it– to develop a sufficiently general numerical technique for simulating deformable drops, so that effects such as inertia, heat convection, and container walls can be modeled.

The thermocapillary migration of droplets was first demonstrated by Young et al. [9], who derived the following expression for the migration velocity of a spherical drop of radius a in a constant temperature gradient, $\mathbf{G}$, within an unbounded fluid medium:

$$\mathbf{U}_{YGB} = b\mathbf{G},\qquad(1)$$

where b is a function of the dimensional parameters, whose form is given in the above reference, and is not an issue here. Equation (1) is valid for negligible values of the Reynolds and Marangoni numbers, i.e. in the absence of convection of momentum and energy. From a practical viewpoint, however, a wide range of values of these parameters can be encountered in space applications, depending on the physical properties of the fluids involved. Moreover, in practical applications, bubbles and drops interact with each other as well as with neighboring surfaces comprising the container walls. This has motivated a series of theoretical analyses which have led to considerable progress in predicting the thermocapillary migration velocity of drops at nonzero values of Re and Ma, as well as in the vicinity of other surfaces. Szymczyk and Siekmann [10] obtained numerical solutions of the equations governing thermocapillary motion of a spherical gas bubble for $Re \leq 100$ and $Ma \leq 1000$, while Balasubramaniam and Lavery [11] performed similar calculations for up to $Re = 2000$ and $Ma = 1000$. The results of these studies show the scaled thermocapillary velocity to be a decreasing function of Marangoni number at fixed Reynolds number.

Whereas a large range of values of Re and Ma have been explored numerically for the thermocapillary motion of a spherical gas bubble, similar studies for the case of liquid drops have been mostly analytical in nature, using perturbation techniques which limit the utility of the results to a much smaller range of Re and Ma. Moreover, most of the numerical calculations to date have assumed a *fixed spherical shape* for the drop. This limits the usefulness of the large Reynolds number results from these studies since, typically, drops and bubbles in common fluids deform substantially when moving at large Reynolds numbers. Some analyses have accounted for small deformations of the drop from a spherical shape (e.g. Haj-Hariri et al. [12]). However, the results of these asymptotic analyses are limited to a small range of the governing parameters. Since the terminal velocity of a drop can be strongly affected by its shape, drop deformations must be taken into account.

In this work the large-Marangoni-number thermocapillary migration of deformable drops and bubbles is studied using the method described below. The results are compared with analyses and other comptuations where possible. The advantage of the present method is that a deforming drop can be studied just as easily as a non-deforming one. Also the case of high-Reynolds-number thermocapillary migration of a deformable drop is studied. There is complete agreement with the trends predicted by Haj-Hariri et al. [12].

MODELING TECHNIQUE

Consider the incompressible, axisymmetric thermocapillary migration of a deformable drop in an infinite domain in the absence of container walls. The great difficulty in treating this problem lies in the *a'priori* unknown location of the drop surface. The variations in temperature complicate matters further because of the intimate coupling between the evolving temperature distribution and the unknown drop shape. We account for this explicit coupling by introducing the idea of continuum modeling of the interface between the drop and the surrounding phase. The so-called Continuum Surface Force (CSF) model –originally developed by Brackbill et al. [3]– allows the shape of the drop or bubble to be determined as part of the numerical solution without any additional effort.

The basic idea of the CSF technique consists of replacing all surface properties by corresponding volume properties defined over a volume obtained by *smearing* the interface S. This is done using a passive-scalar color function C having distinctly different constant values in the two phases. We incorporate temperature-induced variation of interfacial tension into the CSF model and modify it to allow for the simultaneous solution of the momentum and energy equations. An important observation is that the CSF method fails to work for problems involving migration because the tangential component of surface velocities wash the color function away from the interface and result in the loss of integrity of the surface after some time. As a remedy, the interface $C = 0.5$, instead of the entire color function field, is advected by the flow. The color function is then redistributed based on the new interface location. This is similar to the surface-tracking procedure of Unverdi and Trygvasson [4], with the added advantage of grid refinement. Moreover, we suspect that

the calcualtion of surface curvatures in three dimensions will be more economical using the color function instead of a direct calculation.

As such, the stress jump, $\mathbf{f}$, across $\mathcal{S}$, is given by

$$\mathbf{f} = \frac{1}{Ca}\left[\left(\frac{\partial\sigma}{\partial T}\right)(\mathbf{I} - \mathbf{nn})\cdot\nabla T - \sigma\mathbf{n}\nabla\cdot\mathbf{n}\right]. \tag{2}$$

where $\mathbf{n} = -\nabla C/|\nabla C|$. The surface force per unit interfacial area is then replaced by its volume-distributed counterpart, $\mathbf{F}$, where

$$\mathbf{F} = \mathbf{f}|\nabla C|, \tag{3}$$

and $|\nabla C|$ plays the role of a smeared delta function. Thus, a single grid can be generated without regard for the actual shape of the drop. Following each solution iteration, the color function is propagated passively in the computed velocity field, and the deformed shape of the drop is determined. Clearly, the degree of smearing is directly related to the resolution of the grid being used.

GOVERNING EQUATIONS AND SOLUTION STRATEGY

Including the smeared body force $\mathbf{F}$, expressed by Eq. (3), the dimensionless momentum equation in the presence of interfacial tension becomes,

$$\frac{\partial\mathbf{u}}{\partial t} + \mathbf{u}\cdot\nabla\mathbf{u} = \frac{1}{\bar{\rho}Re}[-\nabla p + \mathbf{F} + \nabla\cdot(\mu\nabla\mathbf{u})]. \tag{4}$$

The solution of the flow problem also requires a knowledge of mass and temperature distributions. The mathematical description of the system is then completed by the addition of the dimensionless continuity and energy equations :

$$\nabla\cdot\mathbf{u} = 0, \tag{5}$$

$$\frac{\partial T}{\partial t} + \mathbf{u}\cdot\nabla T = \frac{1}{Ma}\nabla\cdot(\bar{\alpha}\nabla T), \tag{6}$$

where an overbar denotes the single-phase extension of the physical properties. The variables in the dimensionless equations above are based on the following characteristic scales,

$$U^* = \frac{-\sigma_T G a}{\mu_{ex}} \quad T^* = G a \quad t^* = \frac{a}{U^*} \quad P^* = \frac{\mu_{ex} U^*}{a} \quad F^* = \frac{\mu_{ex} U^*}{a^2}. \tag{7}$$

The dimensionless parameters are the Reynolds, capillary, and Marangoni numbers :

$$Re = \frac{-\sigma_T G a^2}{\mu_{ex}\nu_{ex}} \quad Ca = \frac{-\sigma_T G a}{\sigma_0} \quad Ma = \frac{-\sigma_T G a^2}{\mu_{ex}\alpha_{ex}}, \tag{8}$$

where σ_o is the interfacial tension at some reference temperature for the drop, and $\rho, \mu,$ and α are the density, viscosity, and thermal diffusivities of the appropriate phases, respectively.

The basic numerical algorithm for the solution of Eqs. (4)–(6) is the splitting method consisting of two steps. The first step is the calculation of an intermediate velocity field resulting from the convection and diffusion of momentum as well as the tangential component of the body force. The second step requires the solution of a poisson equation for the pressure to enforce incompressibility. The only explicit step is the updating of the interface and the redistribution of the color.

SENSITIVITY TO SMEARING: ADAPTIVE GRID REFINEMENT

The method described above is not at its best if it is implemented with inadequate resolution. This was shown by Haj-Hariri et al. [13] wherein an analytically tractable model problem was employed to illustrate

151

the effect of the smearing of the fluid properties and the interfacial force on some global variables of the problem, in particular the interfacial velocity (analogous to the migration velocity here). This study indicated a much stronger dependence of the solution on the smearing of the interfacial forces as opposed to that of the other fluid properties. Therefore there is a vital need for enhanced resolution.

One way to improve the resolution is to use a refined mesh over the interface region. However the use of the refined grid in the region away from the interface is unwise because the physical variables have no appreciable variations in that region. The adaptive local grid-refinement (quad-tree method) proves ideal for this purpose. With the use of local grid-refinement, the computer storage requirements are reduced and a desired accuracy is achieved on a near-optimal mesh. An important consideration in adaptive schemes is the data structure. The data structure used is a quad-tree structure −"father" cells are refined by division into four "son" cells. In this study, whether a cartesian grid cell needs to be refined depends on the gradient of the color function C, hence requiring grid refinement only in the vicinity of the interface. Furthermore, a smooth transition from large cells to small cells is ensured by prohibiting more than a one-level difference between adjacent cells.

NUMERICAL RESULTS

Marangoni-number effects

As a test of the numerical method detailed above, the thermocapillary migration of a spherical drop (bubble) with negligible Reynolds and capillary numbers was simulated. The vanishing of these two parameters results in a nondeforming drop (bubble) shape. The effect of energy convection (Marangoni number) on the migration velocity is presented in Figs. 1 and 2. Figure 1 corresponds to the migration of a gas bubble and replicates the work of Balasubramaniam and Lavery [11]. The dimensionless migration velocity for a gas bubble in the limit of vanishing Marangoni number is found from Eq. (1) to be 0.5. The increase in the convection of energy results in the wrapping of the isotherms about the drop and reduction of the driving force and migration velocity (cf. Shi et al. [5]). The migration velocity for this simulation is normalized by its value at $Ma = 0$ and presented in Fig. 1. The results are virtually identical to those of Balasubramaniam and Lavery [11] for Marangoni numbers less than 100. For higher values of Ma the migration velocity asymptotes to 0.255, very close to 0.235, the value predicted analytically by Balasubramaniam [14]. Results from other analyses of the same problem, in the absence of any deformations, are presented in table ??.

If the gas bubble is replaced by a liquid drop (with $\rho = 0.6\rho_{ex}$), then for moderate values of Marangoni number the effect on the migration velocity is minimal. The migration velocity for the drop is lower than that for the gas bubble at all values of Ma. In particular, at $Ma = 0$, Eq. (1) predicts a value of 0.23 as opposed to 0.5 for a gas bubble.

Reynolds-number effects

In order to allow for deformations, the capillary number was increased to unity. Increasing the Marangoni number alone does not seem to lead to any substantial deformations at $Re = 0$. Hence, we consider instead the effects of the convection of momentum by letting $Re = 1$. The drop phase has density, viscosity, and thermal conductivity ratios of 0.6, 0.7, and 0.1, respectively. The migration velocity for such a drop, in the limit of vanishing Re and Ca, is given by Eq. (1) as 0.232. The perturbation analysis of Haj-Hariri et al. [12] predicts a reduction of the migration velocity, as well as an oblate-spheroidal deformed shape. Both of these trends are confirmed by the simulations. The deformed shape is presented in terms of contours of the color function in Fig. 3. Figure 4 contains the final adapted grid for this computation. The calculated migration velocity of the deformed drop is 0.180. To assess the contribution of the shape deformation to the change in the migration velocity, the same simulation was performed while constraining the drop shape to remain spherical. The reduction in the migration velocity was now 40% less, at 0.203. Therefore, the role of deformations is very important and there is a need for powerful simulation methods that allow the shape of the drop to change.

CONCLUSIONS

The model presented above extends previous investigations of the thermocapillary motion of drops by removing the assumption of a fixed spherical drop shape and accounting for the convective transport of momentum and energy, thereby generating more realistic solutions to this problem. The continuum modeling of free interface combined with local grid-refinement provide a powerful tool for studying thermocapillary motions of two- and three-dimensional deformable drops. The method eliminates the need for interface tracking and reconstruction, and does not impose any restrictions on the number, complexity, or dynamic evolution of free interfaces. The deformation of a drop in thermocapillary migration at high values of Re and Ma can affect its migration velocity in a manner not predicted by perturbation analysis or fixed-shape simulations. In fact, the above results indicate that an increase in the convective transport of momentum and energy can lead to drop deformations which, in turn, dramatically affect the thermocapillary migration velocity.

ACKNOWLEDGEMENTS

REFERENCES

[1] C. W. Hirt and B. D. Nichols. Volume of fluid (vof) method for the dynamics of free boundaries. *J. Comp. Phys.*, 39:201–225, 1981.

[2] C. S. Peskin. Numerical analysis of blood flow in the heart. *J. Comp. Phys.*, 25:220–252, 1977.

[3] J. U. Brackbill, D. B. Kothe, and C. Zemach. A continuum method for modeling surface tension. *J. Comp. Phys.*, 100:335, 1992.

[4] S. O. Unverdi and G. Tryggvason. A front-tracking method for viscous, incompressible, multi-fluid flows. *J. Comp. Phys.*, 100:25–37, 1992.

[5] Q. Shi, H. Haj-Hairiri, and A. Borhan. Thermocapillary motion of deformable drops. *Bull. Am. Phys. Soc.*, 38(12):2309, 1993.

[6] K. Sheth and C. Pozrikidis. Immersed boundary method for two-phase flows. *Bull. Am. Phys. Soc.*, 38(12):2291, 1993.

[7] V. G. Levich. *Physicochemical Hydrodynamics*. Prentice-Hall, Inc., 1962.

[8] R. S. Subramanian. Transport processes in bubbles, drops and particles. In R. P. Chhabra and D. DeKee, editors, *Transport processes in bubbles, drops, and particles*. Hemisphere Publishing Corporation, New York, 1990.

[9] N. O. Young, J. S. Goldstein, and M. J. Block. The motion of bubbles in a vertical temperature gradient. *J. Fluid Mech.*, 6:350–356, 1959.

[10] J. A. Szymczyk and J. Siekmann. Numerical calculation of the thermocapillary motion of a bubble under microgravity. *Chem. Eng. Commun.*, 69:129–147, 1988.

[11] R. Blasubramaniam and J. E. Lavery. Numerical simulation of thermocapillary bubble migration under microgravity for large reynolds and marangoni numbers. *Num. Heat Transfer*, 16:175–187, 1989.

[12] H. Haj-Hariri, A. Nadim, and A. Borhan. Effect of inertia on the thermocapillary velocity of a drop. *J. Colloid Interface Sci.*, 140:277–286, 1990.

[13] H. Haj-Hariri, Q. Shi, and A. Borhan. Effect of local property semaring on global variables : Implication for numerical simulations. *Phys. Fluids A*, 1994. in print.

[14] R. Blasubramaniam. Thermocapillary bubble migration for large marangoni numbers. Contractor Report 179628, NASA, May 1987.
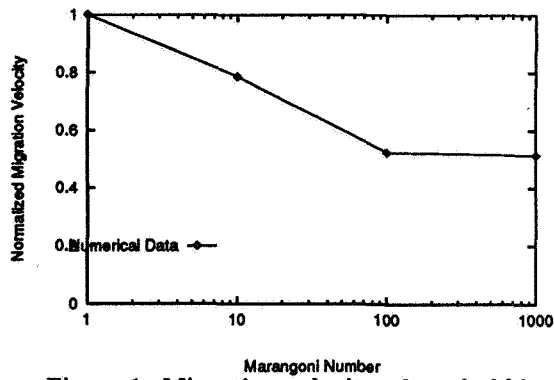
Figure 1: Migration velocity of gas bubble
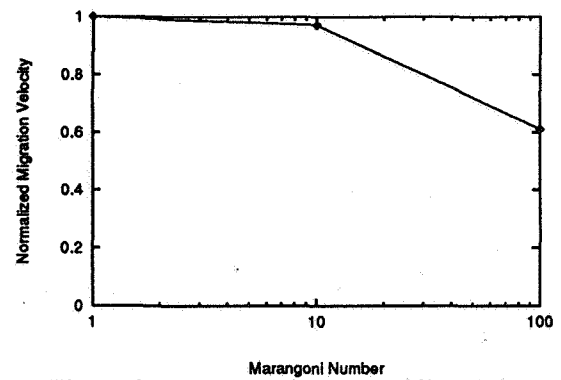
Figure 2: Migration velocity of liquid drop

References	Ma		
	10	100	1000
Shankar & Subramanian '88	0.74	0.50	0.36
Balasubramaniam & Lavery '89	0.75	0.49	0.34
Balasubramaniam '88			0.47
Szymczyk & Siekmann '88	0.73	0.48	
Present Work	0.77	0.52	0.51
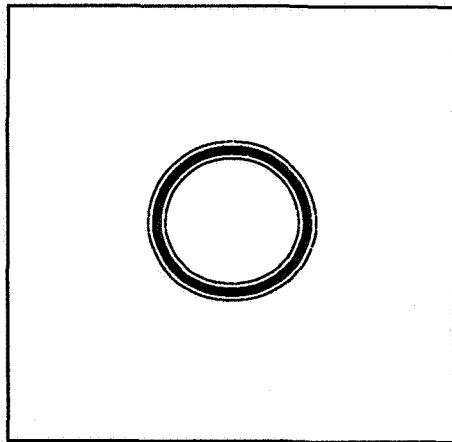
Figure 3: Deformed-drop color contours
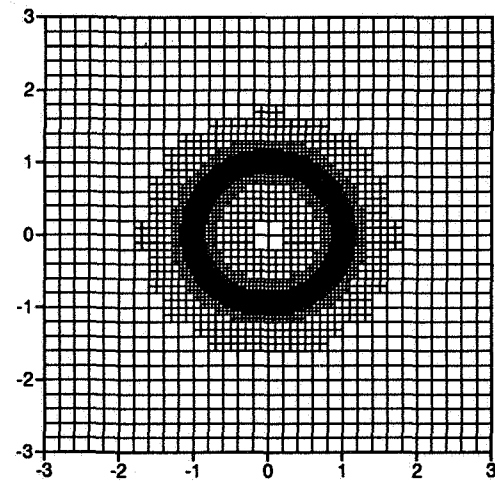
Figure 4: Deformed-drop adapted grid

GROUND BASED STUDIES OF THERMOCAPILLARY FLOWS IN LEVITATED DROPS

Satwindar Singh Sadhal
Department of Mechanical Engineering
University of Southern California
Los Angeles, CA 90089-1453

Eugene H. Trinh
Jet Propulsion Laboratory
4800 Oak Grove Drive
Pasadena, CA 91109

ABSTRACT: Analytical studies along with ground-based experiments are presently being carried out in connection with thermocapillary phenomena associated with drops and bubbles in a containerless environment. The effort here focuses on the thermal and the fluid phenomena associated with the local heating of acoustically levitated drops, both at 1-g and at low-g. In particular, the Marangoni effect on drops under conditions of local spot-heating and other types of heating are being studied.

With the experiments conducted to date, fairly stable acoustic levitation of drops has been achieved and successful flow visualization by light scattering from smoke particles has been carried out. The results include situations with and without heating. As a preliminary qualitative interpretation of these experimental results, we consider the external flow pattern as a superposition of three discrete circulation cells operating on different spatial scales. The observations of the flow fields also indicate the existence of a steady state torque induced by the streaming flows.

The theoretical studies have been concentrated on the analysis of streaming flows in a gaseous medium with the presence of a spherical particle undergoing periodic heating. A matched asymptotic analysis was carried out for small parameters derived from approximations in the high frequency range. The heating frequency being 'in tune' with the acoustic frequency results in a nonzero time-averaged thermal field. This leads to a steady heat flow across the equatorial plane of the sphere.

INTRODUCTION

The potential for advancing fundamental understanding of liquid undercooling phenomena with containerless experimentation is well recognized. In particular, at zero-g, a liquid can remain undisturbed and experience deep undercooling. This high degree of undercooling can promote certain types of crystal growth and at the same type provide homogeneity of the product. In this regard, there is a strong interest in understanding the basic thermodynamics of such processes as well as in the measurement of properties such as thermal conductivity and thermal diffusivity.

In the absence of gravity, the principal effect of heating is the variation of interfacial tension. This generates a tangential stress at the interface and leads to liquid motion, which is also known as the Marangoni effect. Since this type of motion is characterized by the strength of the stimulus as well as the fluid mechanical and the thermophysical properties of the sample, an observation of the thermally driven motion can be used to infer these material properties. For such an interpretation, a successful predictive model is required to go along with the experimental studies.

OBJECTIVES

The principal objectives consist of fundamental studies concerning the fluid mechanics of acoustically levitated drops with thermally driven motion. The long term goal is to obtain a better understanding of the thermodynamics of undercooled liquids and also to measure their thermophysical properties. For thermal measurements, the idea of levitating a liquid drop in an acoustic field, and spot-heating it over a small fraction of its area by a laser beam has been explored. By carrying out the measurements of the thermocapillary effects of such heating, it is possible to infer the thermal properties of the sample by theoretical analysis corresponding to the experiments.

Analytical Part

Under the current program for ground-based studies, analytical models of acoustically levitated drops with thermal interaction are being developed. These models deal with the unexplored aspects of convective transport that arise due to the interference by the acoustic field on the drops. Thus, for many cases in ground based studies, the drops are deformed to spheroidal shapes and call for new analytical studies on the thermoacoustics of such systems.

Numerical and perturbation solutions for the combined thermal and acoustic fields are being developed with the final aim of having a comprehensive model that would work in conjunction with the experiments. This requires the solution to the Navier-Stokes equations together with the energy equation. The analysis, while providing the interpretation of experimental data, will also be useful for the assessment of the necessity and the feasibility of a space experiment.

Experimental Part

The experimental problem of interest is the thermal response of a spot-heated levitated drop in a convective gas flow of varying intensity. The ultimate objective is to quantitatively determine the transient and steady-state temperature distribution on the drop surface as a function of time, sample physical properties, geometry, and of the input radiant energy. Although the final goal will be to carry out an experiment in microgravity, the current project is limited to ground-based investigations using proven experimental techniques in order to verify and to correlate with the theoretical work. Also included in the goals is the development of experimental methods for a potential future microgravity investigation.

SIGNIFICANCE

As discussed in the Introduction, containerless processing is useful for deep undercooling which facilitates the production of certain types of crystals with a high degree of uniformity. The ongoing research will provide fundamental understanding of the Marangoni flows associated with localized heating of levitated drops. In addition, a comprehensive theoretical and experimental system is being developed for the thermodynamic measurement and analysis of materials in containerless environments. For ground based studies where there is interference from the acoustic field, a rigorous numerical model will provide significant new information about the behavior of these complex systems. The new work on compound drops will play a fundamental role for a zero-g space experiment. Most importantly, the model development along with the experimental studies will represent fundamental groundwork for the measurement of thermophysical properties of undercooled liquids.

RESEARCH APPROACH

Analysis

The relevant problems can be mathematically described by the Navier-Stokes equations and the energy equation in a coordinate system suitable for the spherical or the spheroidal geometries. With a defined acoustic field and a quantified heat source, approximate analytical methods and numerical methods will be employed.

Asymptotic Methods: The perturbation expansions are useful when a small parameter can be identified. The various approximations being used are discussed below:

1. Weak acoustic field:
   In this case, forced convection is negligible and thermally driven transport dominates. This

includes Marangoni convection along with heat conduction.

2. Low Marangoni number:
   With Ma $\ll$ 1, along with a weak acoustic field, the heat flow is conduction dominated. Such an analysis has been conducted for spot-heated spherical drops by Sadhal, Trinh & Wagner [1]. Presently, the analysis has been extended to oblate spheroids with axisymmetric spot heating.

3. High frequency acoustic field:
   In a high frequency field, as is the case for ultrasonic levitation, various large and small dimensionless parameters have been identified. In particular, $\varepsilon = U_0/a\omega \ll 1$ along with $M^{-1} \ll 1$, where $M^2 = a^2\omega/\nu$, serve as suitable perturbation parameters. Here, U_0 is the velocity amplitude, ω is the frequency, ν is the kinematic viscosity and a is the particle length scale.

   For application to the case of steady streaming motion around a rigid sphere of radius a, a standing acoustic field with a velocity distribution of the form, $U_\infty \cos(\omega\tau^*)\sin(2\pi z^*/\lambda)$ is considered. With the long wavelength approximation, $a\omega/c \ll 1$, and with the sphere positioned in the vicinity of the maximum wave velocity, the flow field in the distant neighborhood of the sphere can be assumed to be $U_\infty \cos(\omega\tau^*)$.

Numerical Methods: Outside the range of the above approximations, numerical treatment is necessary. In fact, even for the perturbation methods used, some cases of asymptotic matching have required numerical procedures. Finite difference techniques would be suitable for full numerical treatment of the Navier-Stokes and the energy equations.

For situations involving spheroidal drops, the numerical analysis in the relevant curvilinear coordinate systems would be quite appropriate. The success of this approach in heat conduction problems has lent considerable credence to such methods for the current investigation.

Experiments

In 1-g, ultrasonic and electrostatic levitators are being used in order to provide the levitation capability. The schematic description of the electrostatic-acoustic hybrid levitator is given in Figure 1. Oblate spheroidal *uncharged* drops up to about 8 mm in diameter can be levitated ultrasonically and the shape can be adjusted to nearly spherical by adjusting the static electric field. With electrostatic levitation of charged drops, their static shape can be adjusted from oblate to prolate depending on the magnitude of the charge and that of the electric field. In addition to providing a nearly spherical levitated drop, the hybrid system will be used to better control the rotational state of the sample.

At present, pure acoustic levitation experiments with flow visualization inside and outside the drop are being conducted. The principal components of the apparatus are the ultrasonic prestressed transducer-reflector combination and sheet illumination. The vertical ultrasonic standing wave is generated between the transducer radiating face and the opposed reflector which presents a concave axially symmetric curved surface to the incoming wave. The levitation region is enclosed in a transparent chamber and the flow visualization is carried out by means of light scattering on tracer particles from a 5 mW unpolarized He-Ne beam. For the external flow, the tracer particles are generated by burning incense sticks or cotton ropes, and have sizes ranging from 0.1 to 1.0 μm. For the internal flow, suspended reflecting flakes are used.

The major difficulty in 1-g is with the adjustment of the ultrasonic field in order to cancel out any residual solid-body or differential rotation of the drop so as to resolve the inner thermocapillary

flows. Partial success has been achieved in the area of rotation control. Residual drop rotation rate of less than less than 0.1 rps can be obtained for short periods of about 30 sec, interrupted by random slow rotation periods with velocities up to 0.5-1.0 rps. Empirical adjustments of the levitator and the drop parameters can provide long duration periods with very low rotation rate (less than 0.5 rps). This rotation problem is very much reduced in low gravity, as observed during KC-135 tests.

RESULTS

Analysis

A detailed analysis has been carried out to examine the process of convective heat transfer due to acoustic streaming induced by a sound field about an isolated sphere which is subject to time-periodic temperature fluctuations. The important feature of interest in the present study is the energy transport phenomenon emanating from the time-independent contribution of the convective term due to the interactions of the thermal oscillations with the acoustic field.

With the approximations as listed under Research Approach, for sufficiently large frequencies, a thin Stokes layer region on the surface of the sphere constitutes the inner solution for the flow field which is then matched with a suitable outer solution. The temperature field in the fluid is induced by thermal oscillations which, for the purposes of simplicity, are taken to be harmonic (at a single frequency) and of the form, $T_\infty + (\Delta T)_a \cos(\omega \tau^* + \gamma)$, with $(\Delta T)_a \ll T_\infty$. Since the acoustic field of frequency ω is taken to be 'tuned' with the thermal field, the interaction of the thermal oscillations and the acoustic field results in a nonzero time averaged steady convective transport of heat in the fluid. This is the principal effect being investigated in this study, with attention restricted to gases with $\text{Pr} = O(1)$. For large streaming Reynolds numbers, $R_s = U_\infty^2/\omega\nu$, the matching of the inner Stokes layer with the outer field is through a thicker outer boundary layer.

The thermal disturbance is scaled in nondimensional form as the boundary condition, $\phi = \cos(\tau + \gamma)$, where $\tau = \omega\tau^*$ is the dimensionless time. With $\varepsilon \ll 1$ and $M \gg 1$, the procedures for inner and outer expansions, similar to Riley [2] and Gopinath [3] that have been used for fluid flow, are applicable for the energy equation. The major new result is the temperature field around the sphere which, in the inner region, has the perturbed form, $\Phi = \Phi_0 + \varepsilon(\Phi_{1s} + \Phi_{1u}) + \ldots$, where the subscripts u and s refer to the unsteady and the time-averaged steady components, respectively. The calculations in the inner region together with matching in the outer thicker boundary layer region yield

$$\Phi_0 = e^{-\eta\sqrt{\text{Pr}}} \cos(\tau + \gamma - \eta\sqrt{\text{Pr}}) \tag{1}$$

$$\Phi_{1s} = \frac{3\mu}{2} e^{-\eta\sqrt{\text{Pr}}} \left[\sqrt{\text{Pr}}\,(1-\eta)\cos(\gamma - \eta\sqrt{\text{Pr}}) - (2 + \eta\sqrt{\text{Pr}})\sin(\gamma - \eta\sqrt{\text{Pr}}) \right. \tag{2}$$

$$+ \left. \frac{\text{Pr}\sqrt{\text{Pr}}}{(1+\text{Pr})^2} e^{-\eta} \left\{ (1-\text{Pr})\cos(\gamma + \eta - \eta\sqrt{\text{Pr}}) + 2\sqrt{\text{Pr}}\,\sin(\gamma + \eta - \eta\sqrt{\text{Pr}}) \right\} \right] + \mu\,\Phi_{1\infty}(\text{Pr}, \gamma),$$

where

$$\Phi_{1\infty}(\text{Pr}, \gamma) = \frac{3}{2}\frac{\sqrt{9\text{Pr}+4}}{(1+\text{Pr})}\sin(\gamma - \gamma_0) \quad \text{with} \quad \tan\gamma_0 = \frac{\sqrt{\text{Pr}}(1+3\text{Pr})}{2(1+2\text{Pr})}, \quad \text{and} \quad \eta = (r-1)\frac{M}{\sqrt{2}}. \tag{3}$$

Together with this steady temperature field, there is a corresponding heat flux at the surface of the sphere, leading to an average Nusselt number across each hemisphere,

$$\frac{\text{Nu}_i}{\sqrt{R_s}} = \int_0^1 \left(-\frac{\partial\Phi_{1s}}{\partial\eta}\right)_{\eta=0} d\mu = -\frac{3}{2}\sin(\gamma_1 + \pi/4)\sin(\gamma - \gamma_1) \quad \text{with} \quad \tan\gamma_1 = \frac{\sqrt{\text{Pr}}-1}{\sqrt{\text{Pr}}+1}. \tag{4}$$

Experiments

Empty Chamber: According to the experimental results, a reflector with a smaller radius of curvature causes streaming to be directed towards the driver along the axis of symmetry, while the larger radius of curvature will generate flow in the opposite direction. It may be possible that with velocity antinodes more sharply defined closer to the reflector with a smaller radius, downward flow may be preferred. More investigation, however, is needed.

Isothermal Levitation: In Figure 2, a photograph of the video images of the streaming flow fields around a levitated liquid shell at 37 kHz is given. An axially symmetric vortex attached to the upper part of the sample can be faintly seen. Increasing the sound pressure causes flattening of the sample together with increasing the size of the secondary vortex. With the primary streaming field in the downward direction, the flow direction in the secondary vortex in the region along the central axis is away from sample. On the lower side of this vortex, it is towards the sample. The position of the vortex is on the upstream side of the sample which is opposite to the case of a simple flow past a sphere at intermediate Reynolds number. A satisfactory explanation is not immediately available.

In the case of a drop (as opposed to a shell), a sound pressure of 165 dB is required for levitation ($R_s = 460$). The secondary vortex is displaced to the lower half of the sample on the downstream side. Close inspection of the levitated drop reveals a solid body rotation at about 1 rps, with its axis perpendicular to the axis of the acoustic field. There is no available explanation for this residual torque which is clearly non-axisymmetric.

Heated Samples: A qualitative measurement of the effect of an acoustic standing wave on the temperature of a steadily heated thermistor gives an appreciation of the enhancement of the convective heat transfer from the sample to the environment. The main additional contribution to the flow field is the free convection which exhibits itself by splitting the lower set of eddies, stretching of the outermost eddy, and vortex shedding upon oscillation of the acoustic field, as seen in Figure 3.

CONCLUSION

The analytical and experimental studies of drops in an acoustic field have led to several new results. These are briefly summarized here.

1. The main results of the theoretical developments consist of the interaction of the acoustic field with the 'tuned' thermal oscillations of a spherical particle. In the case of a simple sinusoidal variation of the surface temperature of the sphere, there is net steady time-averaged temperature distribution and a corresponding heat flow across the equatorial plane of the sphere.

2. With levitated samples, flow visualization experiments have shown that the primary circulation in the acoustic field combines with the secondary streaming attached to the samples. The vortices generated by the presence of the sample have spatial dimensions on the scale of the sample size. At low sound pressures, the flow patterns can be represented by the simple superposition of the primary and the secondary flows. However, at high pressures, the interaction of the flows is not so straightforward.

3. A heated sample in an acoustic field experiences substantial cooling by the flow around the particle. This is found to be in qualitative agreement with the theoretical studies of Gopinath & Mills [4].

REFERENCES

1. S. S. Sadhal, E. H. Trinh & P. Wagner, *Fluid Mechanics Phenomena in Microgravity*, ASME Publication No. AMD-Vol. 154 / FED-Vol. 142, (1992) 105–110.

2. N. Riley., *Quart. J. Mech. Appl. Math.*, **19** (1966) 461–472.

3. A. Gopinath., *Quart. J. Mech. Appl. Math.* **46** (1993) 501–520.

4. A. Gopinath & A. F. Mills., *J. Heat Transfer*, **115** (1993). 332–341.
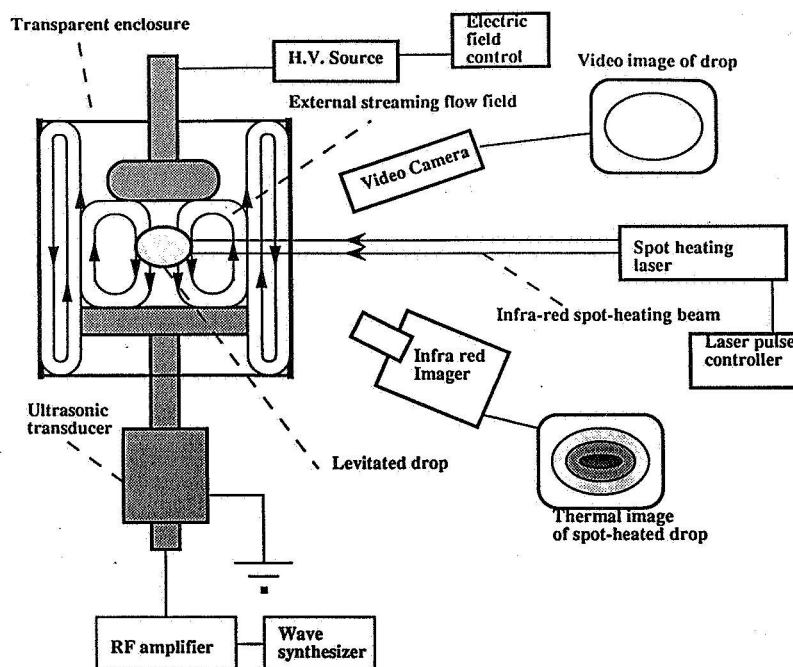
FIGURE 1: Schematic description of an electrostatic-acoustic hybrid experimental apparatus for the study of spot-heated levitated liquids.
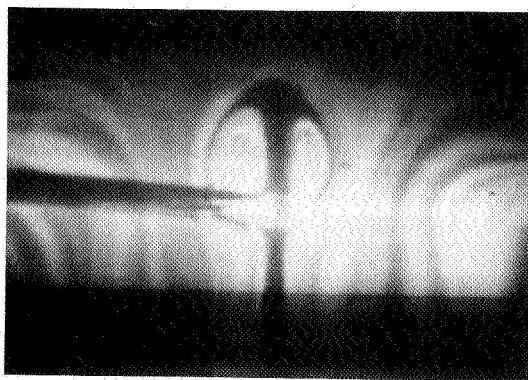
FIGURE 2: Flow visualization of streaming past a levitated liquid shell.
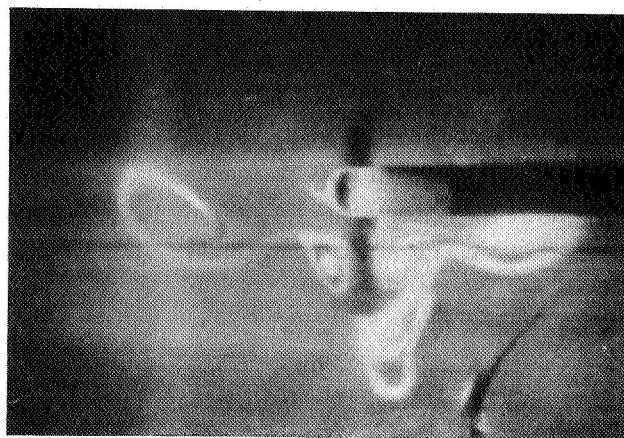
FIGURE 3: Flow field around a heated thermistor in 1-g.

THERMOCAPILLARY MIGRATION AND INTERACTIONS OF BUBBLES AND DROPS

R. Shankar Subramanian
Box 5705
Clarkson University
Potsdam, New York 13699-5705

and

R. Balasubramaniam
NASA Lewis Research Center
Cleveland, Ohio 44135

ABSTRACT

Results from ground-based theoretical and experimental research on the motion of bubbles and drops in a temperature gradient are described and a brief account is given of plans for a flight experiment scheduled in 1994.

INTRODUCTION

When a drop or bubble is placed in another fluid and subjected to the action of a temperature gradient, the drop will move. Such motion is a direct consequence of the variation of interfacial tension with temperature which leads to a thermocapillary stress at the interface between the drop and the continuous phase. Because of this stress, the state of rest in the two fluids adjoining the interface is not tenable. The ensuing motion of the fluids usually leads to a propulsion of the drop, labelled "thermocapillary migration," in the general direction of the warmer fluid. A variation of the composition of species on the interface also can lead to such capillary stresses and drop movement. However, a uniform temperature gradient is more straightforward to establish and maintain when compared to a similar composition gradient. Therefore, virtually all existing experimental research on this subject has focused on thermocapillary migration. The literature on both experimental and theoretical research in this field upto approximately 1989 has been adequately reviewed by Wozniak et al. [1] and Subramanian [2].

The movement of suspended objects such as drops and bubbles is relevant to situations that are likely to arise in low gravity experiments. Liquid drops might be encountered during the formation and solidification of alloys, and in separation processes such as extraction that might be used in long duration space voyages for recycling purposes. Also, a dispersion of vapor bubbles might be encountered in heat transfer fluids used in spacecraft which undergo phase change. Gas bubbles may be encountered in crystallization where dissolved gases are rejected at the interface and also in separation processes such as gas absorption. In most applications, it is likely that a collection of drops or bubbles would be involved in which the individual members will influence the motion of each other, and also possibly coalesce leading to changes in size distributions over time.

RATIONALE FOR EXPERIMENTS

The objective of this research effort is to develop an understanding of the thermocapillary migration and interactions of drops and bubbles from first principles. Both theoretical predictions and experimental observations are necessary to achieve this objective. Predictions from idealized models alone are inadequate for the following reasons.

1. The interface between two fluids is sometimes contaminated by substances which are surface active in the system. Such materials, commonly called surfactants, are specific to each pair of fluids. They adsorb on the interface because this lowers the free energy of the system. However, because of motion along the interface, it is possible to develop and sustain gradients of surfactant

concentration on the interface. This produces a capillary stress which generally tends to oppose that due to the applied temperature gradient. Because of the difficulty in measuring the relevant physical properties of surfactant systems such as adsorption constants and surface diffusion coefficients, it is very difficult to construct precise models of the behavior of systems containing surfactants even when the surface active substance is a known entity. More commonly, trace amounts of a variety of impurities in the chemicals can act as surfactants and this makes the task of modeling even more onerous. Using a simplistic model, Nallani and Subramanian [3] have had some success in describing the behavior of one system (methanol drops in silicone oil) which appeared to contain surfactants. However, this cannot always be done.

2. Even when the system is clean, the fluid in which the drop is submerged is enclosed in a container. In principle, unsteady interactions of the migrating drops with container walls can be modeled even permitting significant convective transport effects and shape deformation, but the computational problem can be substantial. It is useful to obtain experimental data so that the correctness of predictions from models can be independently verified. For similar reasons, experimental data needs to be acquired on pairs of drops. Such pairwise interactions are usually used in modeling systems of multiple drops.

In view of the above, we have been conducting an experimental program on the ground for over a decade to study aspects of thermocapillary migration that one can examine while the system is subject to the earth's gravitational field. Since free convection in the continuous phase is a potential source of problems in interpreting the data, vertical temperature gradients are best to use. The presence of buoyant convection and gravity driven motion of the suspended bubbles or drops places severe restrictions on the length scales of systems that can be studied. This limits the values of two important dimensionless groups that influence the speed of the drops, namely the Reynolds number and the Marangoni number, that can be obtained in ground-based experiments. The Marangoni number is a Péclet number defined using a reference velocity that is appropriate for thermocapillary motion. In addition to the speed of the objects, their shapes are of interest. In this case, the Capillary number plays a significant role in low Reynolds number problems in affecting the shapes of drops and hence their speed, and the Weber number would play a similar role when inertia is important. To conserve space, definitions are not given here, but they are well-known and can be obtained from textbooks on fluid mechanics.

IML-2 FLIGHT EXPERIMENTS

Due to the restrictions introduced by gravity, we are planning to conduct experiments in summer 1994 on the IML-2 mission of the Space Shuttle. The experiments will be performed in the Bubble, Drop, and Particle Unit (BDPU) which is an apparatus designed and built in Europe under the auspices of the European Space Agency. Our plans are to establish temperature gradients in a silicone oil contained in a rectangular cell which is 60 mm long and 45 x 45 mm in cross section. In separate cells, gas bubbles and liquid drops will be injected and their motion photographed. The radii of the bubbles as well as the temperature gradients used will be varied systematically in the experiments so as to cover as wide a range of the Marangoni number as possible. The Reynolds number will be on the order of unity in these experiments. Predictions of the behavior of spherical bubbles for a wide range of Marangoni and Reynolds numbers have been given by Balasubramaniam and Lavery [4]. Also, recently we have obtained asymptotic results for the limit of large values of the Marangoni number both in the low Reynolds number limit and in the limit of potential flow [5, 6]. These predictions will be tested in the IML-2 experiments. Here, we present some recent results from the ground-based research and point out certain interesting aspects of interaction problems.

162

GROUND-BASED RESEARCH

Experimental Apparatus and Procedure

The ground-based experiments were conducted in a test cell schematically shown in Figure 1. The heart of the apparatus is a rectangular region bounded above and below by two aluminum blocks which can be maintained at desired temperatures, thus establishing a vertical temperature gradient in the fluid contained in the enclosure. The side walls are made of teflon and equipped with double glass windows for viewing and lighting purposes. Septums are mounted in the wall to permit insertion of very fine glass capillaries which can be used to inject small bubbles or drops. The procedure consists of filling the cell with the desired continuous phase liquid and establishing an appropriate temperature gradient, followed by the insertion of one or more bubbles or drops. The entire process of injection and migration is recorded using a video camera mounted on a microscope. The video tape is later analyzed frame by frame to obtain information on drop/bubble sizes and velocities.

Results and Discussion

Using this test cell, Srividya [7] performed experiments on fluorinert FC-75 drops in a Dow-Corning DC-200 series silicone oil of nominal viscosity 50 cs contained in the test cell. FC-75 is more dense than the silicone oil, and an upward temperature gradient was used so that the thermocapillary effect would retard the downward settling of the drops. Conditions were set such that the drops, in the region of observation, experienced an average temperature of either 20° C or 40° C. Data were obtained on drops ranging in radius from 60 to 150 μm and in upward temperature gradients ranging from 4 to 11 K/mm. In separate experiments, the temperature field in the cell was measured in the region where the drops migrated and was confirmed to be linear. Also, the residual free convection in the cell was characterized in experiments using tracers and the magnitudes were found to be within the measurement uncertainty of the drop velocities. The Reynolds number in the experiments were less than 0.015.

The data obtained at an average temperature of 40°C are shown in Figure 2. As anticipated, the drops settled at velocities predicted by the standard Hadamard-Rybczynski model for low Reynolds number motion under isothermal conditions. Under the action of an upward temperature gradient, they settled at lower speeds, with the overall reduction being enhanced for larger temperature gradients. The data collapse onto a single straight line when the thermocapillary contribution to the velocity is extracted and plotted against the product of the applied temperature gradient and radius. The slope of this straight line can be used to infer the rate of change of the interfacial tension with temperature which was determined to be $-0.0397mN/(m.K)$. This value is somewhat higher than the value of $-0.03041mN/(m.K)$ obtained from a series of interfacial tension measurements made at different temperatures ranging from $5-65°C$. However, both values are subject to experimental uncertainty. The static measurements suffer from an inability to maintain perfectly still conditions in the liquids and the actual interfacial tension values are only good to approximately 0.1 mN/m. On the other hand, the migration experiments were performed under conditions wherein the Péclet number was as large as 5. The theory used to fit the data assumes the Péclet number to be negligible.

In another series of experiments in a similar cell [8] pairs of air bubbles were injected into a DC-200 silicone oil of nominal viscosity 1000 cs to observe interaction effects both under isothermal conditions and in the presence of a downward temperature gradient. In the non-isothermal runs, care was taken to maintain the Rayleigh number substantially below the critical value at which cellular convection would be triggered. In separate experiments, the magnitude of the residual convection in the liquid was characterized and found to be well within the uncertainty of the velocities measured. Convective transport of both energy and momentum was negligible in the experiments.

Under these conditions, the results for bubble velocities were found to be generally consistent with predictions from theoretical models. Sometimes, the experiments produced counter-intuitive observations; for example, when a large bubble and a small bubble are present in a downward temperature gradient that is sufficient to force the large bubble downward, the small bubble is seen to move upward! If the small bubble were isolated, it would move downward quite rapidly under these conditions. The reason is a substantial upward draft caused by the large bubble even though it is moving downward; this is a consequence of the Stokeslet contribution to the flow around this bubble. The velocity field around an isolated bubble moving under these conditions is a superposition of a Stokeslet and a potential dipole from the gravity and thermocapillary contributions respectively.

While Fluorinert-silicone oil form a a suitable candidate pair for flight experiments, the large density differnce between them precludes interaction experiments on the ground under conditions when convective energy transport is important. Therefore, we have identified the pair diethyl maleate - propanediol as a candidate for ground-based experiments. Preliminary experiments on isolated drops show confirmation of the expected scalings at negligible Reynolds and Péclet number. Experiments on pairs are planned in the coming year.

Wei and Subramanian [9] have solved the problem of multi-bubble interactions under conditions of negligible Reynolds and Péclet number using the method of boundary collocation. Space limitations prohibit us from presenting these results in full detail here, and only interesting samples are provided. In Figure 3 the streamlines in a laboratory reference frame are displayed for motion induced by two bubbles which are migrating in a large body of fluid. The flow patterns corresponding to the thermocapillary migration problem are contrasted with those for body force driven motion. The differences are striking. In the axisymmetric case, a separated reverse flow wake is observed. By reversing the order of the large and small bubbles, it is possible to produce a flow pattern in which this reverse flow region occurs in front of the migrating pair. In the asymmetric case (wherein the line of centers is normal to the temperature gradient), to the right of the migrating bubble pair, fluid from far away is drawn toward the bubbles and thrown outward. These interesting flow patterns arise from the nature of the driving force in thermocapillary migration which is the temperature gradient field on the surfaces of the bubbles. In the case of an isolated bubble under similar conditions, the temperature field, arising from the solution of Laplace's equation in the fluid, is the first Legendre Polynomial in the cosine of the polar angle. The resulting flow is a potential dipole which possesses fore-aft symmetry. When higher Legendre modes are excited by breaking the symmetry of this situation, complex flow patterns arise as a consequence of the superposition of relatively simple multicellular flows driven by the pure Legendre modes. Additional discussion can be found in [9].

Results for the velocities of the individual bubbles in a pair were calculated by the boundary collocation method and compared with predictions from the method of reflections. Also, limited results were calculated for a chain of three bubbles whose centers lie on a straight line which is either parallel or perpendicular to the applied temperature gradient. In this case, a pairwise-additive approximation using the reflections solution was constructed. The approximations perform very well when the bubbles are far apart, but begin to depart from the correct solution when the distance of separation between the bubble surfaces is less than approximately one-half the radius of the larger bubble in the pair. Further details are given in [9].

It is important to emphasize that the above calculations in the case of more than one bubble are limited to the linear problem wherein convective transport effects are neglected altogether and several other simplifying assumptions are made. There is a need for theoretical predictions to be made

permitting significant convective transport effects and also accommodating shape deformations.

CONCLUDING REMARKS

In the future, this research will continue in the direction of experiments on systems involving more than one drop (or bubble) interacting with each other and possibly with the boundaries of the system. A good beginning would be to work with a pair of such objects introduced at appropriate well-defined locations in the test cell after a temperature gradient has been established. On the ground, one is restricted to investigating a very small range of parameters in the thermocapillary migration problem because of the complicating effects of gravity on the motion of the drops. Therefore, it will be necessary to perform experiments under reduced gravity conditions in order to fully explore a good range of parameters in this problem. It would be more diffcult to perform studies of the actual approach and coalescence of drops since coalescence is usually a very rapid process. However, it is envisioned that as the study matures, attempts to explore coalescence will be undertaken.

ACKNOWLEDGMENTS

References

[1] G. Wozniak, J. Siekmann, and J. Srulijes, Z. Flugwiss. Weltraumforsch, **12** (1988) 137-144.

[2] R.S. Subramanian, "The motion of bubbles and drops in reduced gravity," in *Transport Processes in Drops, Bubbles, and Particles*, (R. Chhabra and D. Dekee, Eds.), Hemisphere, 1992, pp. 1-41.

[3] M. Nallani and R.S. Subramanian, J. Colloid Interface Sci., **157** (1993) 24-31.

[4] R. Balasubramaniam and J.E. Lavery, Numerical Heat Transfer A, **16** (1989), 175-187.

[5] R. Balasubramaniam, "Thermocapillary Bubble Migration – Solution of the Energy Equation for Potential-Flow Approximated Velocity Fields," International Association for Mathematics and Computers in Simulation Symposium, Bangalore, India, December 1992.

[6] R. Balasubramaniam and R.S. Subramanian, "Thermocapillary Bubble Migration – Thermal Boundary Layers for Large Marangoni Numbers," submitted for publication, Journal of Fluid Mechanics, August 1993.

[7] C.V. Srividya, "Migration of Fluorinert FC-75 Drops in a Silicone Oil in a Vertical Temperature Gradient," M.S. Thesis in Chemical Engineering, Clarkson University, 1993.

[8] H. Wei and R.S. Subramanian, "Interactions between two bubbles under isothermal conditions and in a downward temperature gradient," submitted to Phys. Fluids A, 1994.

[9] H. Wei and R.S. Subramanian, Phys. Fluids A, **5** (1993) 1583-1595.
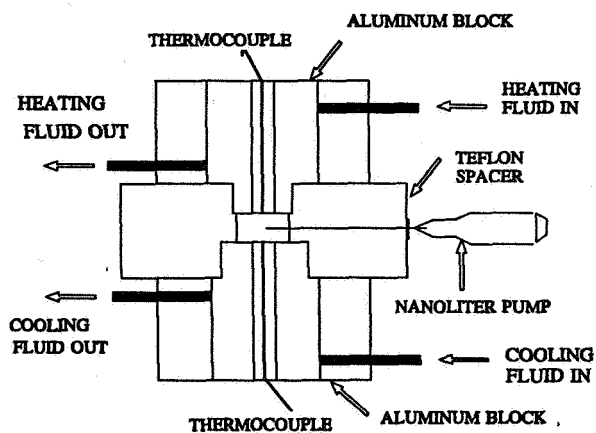
Figure 1. Sketch of Test Cell
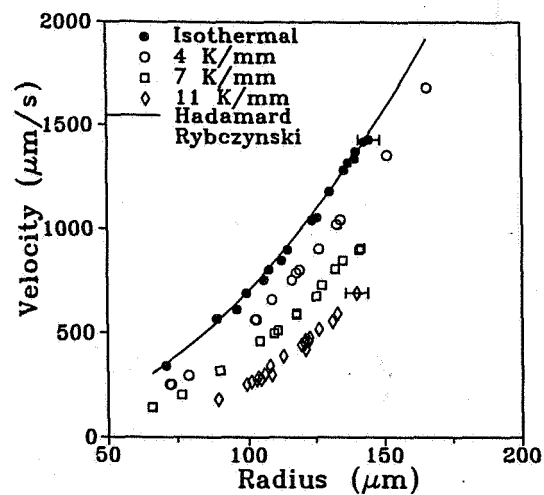
Figure 2. Downward velocity of Fluorinert FC-75 drops in a Dow-Corning DC-200 series silicone oil of nominal viscosity 50 cs
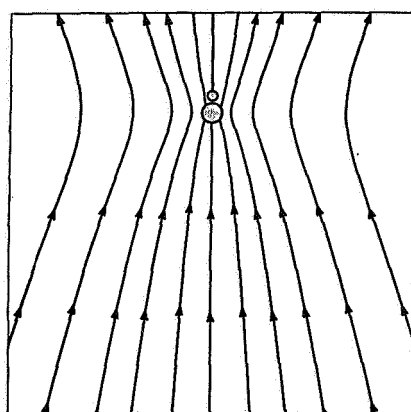
Body Force Driven Motion
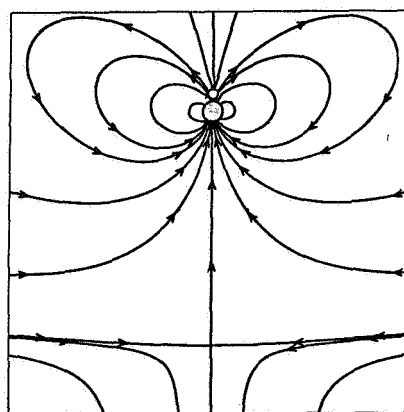
Thermocapillary Migration

(a)
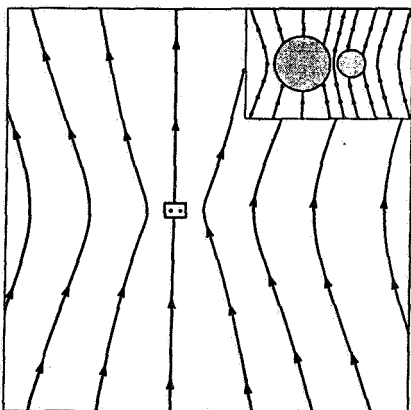
Body Force Driven Motion
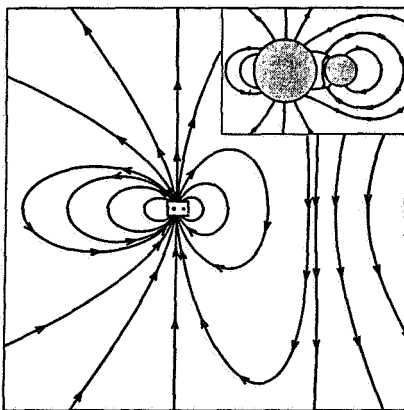
Thermocapillary Migration

(b)

Figure 3. Streamlines in a laboratory reference frame for flow generated by a pair of non-identical bubbles undergoing body force driven motion or thermo-capillary migration. (a) axisymmetric case – a meridian section is shown. (b) asymmetric case – a section in a symmetry plane is shown. Velocity normal to this plane is zero.

166

Uniform Hydrogen Fuel Layers for Inertial Fusion Targets by Microgravity

P. B. Parks and R. L. Fagaly

General Atomics, P. O. Box 85608, San Diego, California
92186-9784

Abstract

A critical concern in the fabrication of targets for inertial confinement fusion (ICF) is ensuring that the hydrogenic (D_2 or DT) fuel layer maintains spherical symmetry. Solid layered targets have structural integrity, but lack the needed surface smoothness. Liquid targets are inherently smooth, but suffer from gravitationally induced sagging. One method to reduce the effective gravitational field environment is freefall insertion into the target chamber. Another method to counterbalance the gravitational force is to use an applied magnetic field combined with a gradient field to induce a magnetic dipole force on the liquid fuel layer. Based on time dependent calculations of the dynamics of the liquid fuel layer in microgravity environments, we show that it may be possible to produce a liquid layered ICF target that satisfies both smoothness and symmetry requirements.

Introduction

In the Inertial Confinement Fusion (ICF) concept,[1] multiple high power laser or ion beams are focused on a small spherical target containing condensed hydrogen fuel. The intense pressure generated by the incident beams cause the target to implode to high density (~1000x liquid density) and temperature (>100 million K) with the subsequent release of thermonuclear energy. For ICF to be economically attractive, the gain (thermonuclear energy out divided by beam driver energy in) must be large enough to overcome driver inefficiencies.

The ultimate goal of ICF research is the development of an Inertial Fusion Energy Power Plant.[2] Such a plant would most likely utilize a 2 ~ 5 MJ driver with a 500 MJ yield/target (gain >100). Using a 5-10 Hz shot rate, this would produce 1000 MW electrical power. With reasonable progress, a demonstration inertial fusion power plant could be expected to be operational in 2020 ~ 2030.

Cryogenic targets planned for ICF experiments are in the form of a liquid or solid hydrogen fuel layer which coats the inner surface of a low-Z (e.g., polystyrene) microballoon. The region interior to the fuel layer (the "bubble") contains low pressure hydrogen gas at the vapor pressure of the liquid or solid fuel layer.

Fig. 1. Liquid layer in a spherical shell. a is the radius of the vapor bubble, a_1 the amplitude of the $\ell = 1$ harmonic, b is the inner radius of the shell and c is the outer radius of the shell.

A critical concern in the fabrication of these targets is ensuring that the hydrogenic fuel layer maintains smooth, spherically symmetric uniformity with peak-to-valley variations on the 1000Å scale. Non-uniform or rough surfaces in the target or fuel can instigate Rayleigh-Taylor instabilities.[3] These instabilities can grow—allowing the cold condensed fuel to mix with the inner hot gaseous region and damp out the fusion reaction. To prevent Rayleigh-Taylor growth, the smoothness of the (plastic) shell surface must be less than 500Å.

Solid fuel layers have the advantage of being able to support the condensed hydrogen fuel layer naturally. However, surface smoothness is a problem. To date, no solid layering technique has been able to produce a smooth inner layer at the 1000Å level. Because of surface tension, liquid

fuel layers will have a smooth inner surface. However, an unacceptable departure from uniformity arises by gravity-induced sagging of the liquid. Hence, the layer thickness will vary from thin at top to thick at bottom (Fig. 1).

There are almost a dozen suggested layering methods for both liquid and solid fuel layers. For example fast refreeze, beta-decay heating,[4] thermally induced gradients using helium gas jets,[5] graded intensity laser beams,[6] and microwave plasma heating.[7] The beta-layering technique is a volumetric heating process which relies on tritium beta-decay to produce a uniform layer, hence it is only good for DT layers. Thermal gradient methods induce dynamic circulating flow patterns in liquid fuels. The fuel can be distributed around inside the capsule by adjusting the temperature profile to produce a uniform thick layer. Only beta-layering has demonstrated 100 μm thick fuel layers. The best beta-layered surface to date has a surface roughness on 2 μm, an order of magnitude larger than desired.

Plastic foams[8] can be used to trap liquid fuel. The foam density must be low (< 30 mg/cc) to minimize the amount of higher Z materials (the carbon in the plastic). The foam cell size must also be small (≤ 1 μm) to minimize surface irregularities. If the volume of the liquid significantly exceeds the volume of the foam pores (overfilled), thick overfill layers will sag due to gravity. Thin overfilled layers (< 1 μm) may conform to irregularities commensurate with the foam cell size.[9] A rough estimate of the minimum overfill thickness to avoid surface imprinting (and Rayleigh-Taylor instabilities) would be about three times the foam cell size.

Microgravity Methods

There are two microgravity layering methods that have the potential to produce adequate liquid targets. These methods work by reducing the gravitational force, preventing the liquid layer from slumping to the bottom of the target.

One method for reducing the gravitational force is to use the simple freefall method. In the absence of other forces, surface tension will drive the inner surface of the liquid to a spherical shape. AS will be shown, short range forces will center the bubble after an appropriate damping time. Unfortunately, for an ordinary liquid layer, the damping times are much longer than a typical ~1 second drop time. However, if we consider an overfilled foam target with a thin ~1 μm liquid layer, by virtue of its smaller inertia, the thin liquid layer will approach a stable, more symmetric, equilibrium in a relatively short time.

The other technique[10,11] uses an applied magnetic field to support the liquid fuel layer against gravity. The method proposed here makes use of the diamagnetic nature of hydrogen. The magnetic dipole force per unit volume is $\chi \, B \cdot \nabla B / \mu_0$. Balancing this against the gravitational force per unit volume $F_g = \rho g$ yields the required product of field strength with field gradient:

$$B \frac{\partial \vec{B}}{\partial z} = \frac{\mu_o \, \rho \, \vec{g}}{\chi}$$

(1)

Taking $\chi = -2.2 \times 10^{-6}$ (SI), $\rho = 200$ kg/m^3, $g = 9.8$ m/sec^2, one obtains 1.12×10^3 T^2/m or 11.2 T^2/cm for deuterium, a value achievable with commercially available superconducting magnets.

In the following we investigate the degree of symmetry attained by each of the two layering methods described above, i.e., the concentricity of the inner surface of the liquid fuel layer and examine the time-dependent motion of the liquid fuel layer. A more complete version of the

analysis presented here is given in ref. 11. We first note that the amplitudes of the perturbations on the inner fuel layer are extremely small compared to the radius of the target so that a perturbative approach is warranted.

Assuming axial symmetry, we can then describe the radial coordinate of the inner surface of the liquid fuel layer, $r_s(\theta,t)$, by expanding it in Legendre polynomials:

$$r_s(\theta,t) = a_0(t) + \sum_{\ell=1}^{\infty} a_\ell(t)\, P_\ell \cos \theta \qquad (2)$$

where t is time, θ is the polar angle in a spherical polar coordinate system (Fig. 1), and a_ℓ is the perturbation amplitude of the ℓth spherical harmonic ($a_\ell \ll a_0 \leq b < c$). In the case of overfilled foam targets, b is replaced by d, the inner radius of the foam layer. This method of decomposition of surface nonuniformities (as well as absorbed laser energy and pressure nonuniformities) into spherical harmonics, is traditionally used in target performance and fusion gain calculations.

We study the liquid fuel layer beginning with the energy equation:

$$\frac{\partial}{\partial t}(E + P_{gm} + P_\gamma + P_{LV}) + \dot{Q}_{vis} = 0 \qquad (3)$$

with E being the kinetic energy of the whole layer, $\dot{Q}_{vis}$ is the viscous dissipation rate, and the three potential energies considered here being P_{gm}, the potential energy in the combined gravitational and applied B-fields or net gravitational field in the case of freefall, P_γ the free energy stored in the liquid/vapor interfacial surface, and P_{LV} is the potential energy stored in the long range attractive forces between the molecules of the liquid fuel layer and the outer shell or foam matrix. Since all the molecules are neutral and non-polar, only the potential associated with the London-Van der Waals force is relevant. Each of these components can be analyzed separately. By using the orthogonal properties of the Legendre polynomial, all the terms in Eq. 3 can be reduced to functions of the mode amplitudes.

The surface tension energy at the liquid/vapor interface (with constant surface tension γ) can be written as:

$$P_\gamma = 2\pi\gamma \sum_{\ell=1}^{\infty} (\ell-1)(\ell+2)(2\ell+1)^{-1} a_\ell^2 \qquad (4)$$

It is noteworthy that the first $\ell = 1$ mode results in no change of the surface area or its potential energy, P_γ. This simply means that the interior "vapor bubble" can undergo a vertical shift without changing its liquid/vapor surface area; accordingly, surface tension forces alone cannot counterbalance the gravitational forces. A similar conclusion was reached in Ref. 12 using the extended Young-Laplace equation of capillarity.

The other energy terms depend on the velocity perturbations within the fluid layer. Assuming incompressible and irrotational flow, the velocity field is represented by $\vec{v} = -\nabla\phi$. The volume integrals can then be converted to surface integrals, viz:

$$E = \frac{1}{2}\rho \int \phi \,\nabla\phi \cdot \hat{n}\, dS \qquad\qquad \dot{P}_{gm} = \int \Phi_{gm}\, \vec{v}\cdot \hat{n}\, dS \qquad (5a, b)$$

$$\dot{P}_{LV} = \int \Phi_{LV}\, \vec{v}\cdot \hat{n}\, dS \qquad\qquad \dot{Q}_{vis} = \eta \int \nabla v^2 \cdot \hat{n}\, dS \qquad (6a, b)$$

169

where $\hat{n}$ is the surface normal,

$$\hat{n} = \frac{\nabla (r - r_s)}{|\nabla (r - r_s)|} \quad \approx -\hat{r}_u - \frac{\hat{\theta}_u}{r} \sum_{\ell = 1}^{\infty} a_\ell(t) \, (1 - \mu^2)^{1/2} \, P_\ell'(\mu) \tag{7}$$

where $P_\ell'(\mu) = dP_\ell / d\mu$, η is the viscosity of the liquid fuel, and $\Phi_{gm} = U_g + U_m$ is the combined gravitational and magnetic dipole potentials per unit volume; $U_g = \rho g z$, $U_m = |\chi| \vec{B} \cdot \vec{B} / 2\mu_o$.

The attractive interaction energy between a liquid hydrogen molecule and a shell (or foam) molecule is due to the long range dipole-induced dipole interaction for non-polar molecules such as glass or plastic. In the electrostatic ($c \rightarrow \infty$ limit), the interaction potential obeys the London-Van der Waals inverse sixth power law formula. However, since the dipole moments of the individual atoms are fluctuating at a frequency characteristic of the electronic motions ω_0, there will be a time between the fluctuating dipole that radiated the electromagnetic field and the reradiated field when it arrives back at the fluctuation and interacts with it. When the distance between two molecules, d, is such that the propagation time d/c exceeds the fluctuation period $\sim 2\pi/\omega_0$, the "retardation effect" is significant and reduces the range of the Van der Waals forces.[13] The retardation effect can be quantified by multiplying the Van der Waals interaction energy between the molecules with the empirical expression $f(p) \approx 2.45 \, p^{-1} - 2.17 \, p^{-2} + 0.59 \, p^{-3}$, where $p = \omega_0 d/c$.

The total interaction energy between a single liquid molecule of mass m at position $\vec{r}$ and the entire plastic sphere (or foam) layer is given by the pairwise approximation.[13] With $d = |\vec{r}' - \vec{r}|$ this is:

$$\Phi_{LV}(\vec{r}) = \frac{N^{eff} B^{eff}}{m} \int_{volume\ of\ shell\ (foam)} \frac{d^3 r' \, f(p)}{|\vec{r}' - \vec{r}|^6} \tag{8}$$

and B^{eff} is the effective London constant defined through the weighted product for foam-filled fuel layers as $N^{eff} B^{eff} = B_s N_s \, (1 - f_{void}) + B_H N_H \, f_{void}$, where N_s is the number density of the solid (s) portion (the plastic shell) and N_H is the number density of the liquid isotope (H) filling the void, with f_{void} being the volume void fraction, typically $f_{void} = 0.95$.

The equilibrium amplitude of the first mode, a_1^{eq}, results from a balance between the net vertical force and the strength of the London-Van der Waals force. The layer concentricity a_1^{eq}/a is then given by

$$\frac{a_1^{eq}}{a} = \frac{-3 \, a \, c^3 \, m \, \varepsilon \, g}{4 \, \pi \, N^{eff} B^{eff}} \left[x \, \tilde{\phi}'(x) + E_1(x) \, \tilde{\phi}(x) \right]_{x = a/b}^{-1} \tag{9}$$

where $\tilde{\phi}'(x)$ is the derivative of $\tilde{\phi}(x) = \Phi_{LV} \times 3 \, m \, c^3 / 4 \pi \, N^{eff} B^{eff}$ with respect to $x = r/b$. This result can also be obtained by setting the time derivatives $\dot{a}_1$ and $\ddot{a}_1$ to zero in Eq. (3).

For freefall (assuming no turbulence or vibration), surface tension drives the higher order equilibrium amplitudes to zero. In the case of magnetic field assisted microgravity for which $B \cdot \nabla B$ has small non-vertical components, these higher order amplitudes, a_ℓ^{eq}/a, are proportional to $a^2 \gamma^{-1} (a/L)^{\ell-1}$ where L is the scale length of the magnetic field gradient. Fortunately, the higher order modes are less than 0.01% if $L \geq 5$ cm and $a \approx c \sim 500 \mu m$.

C-3
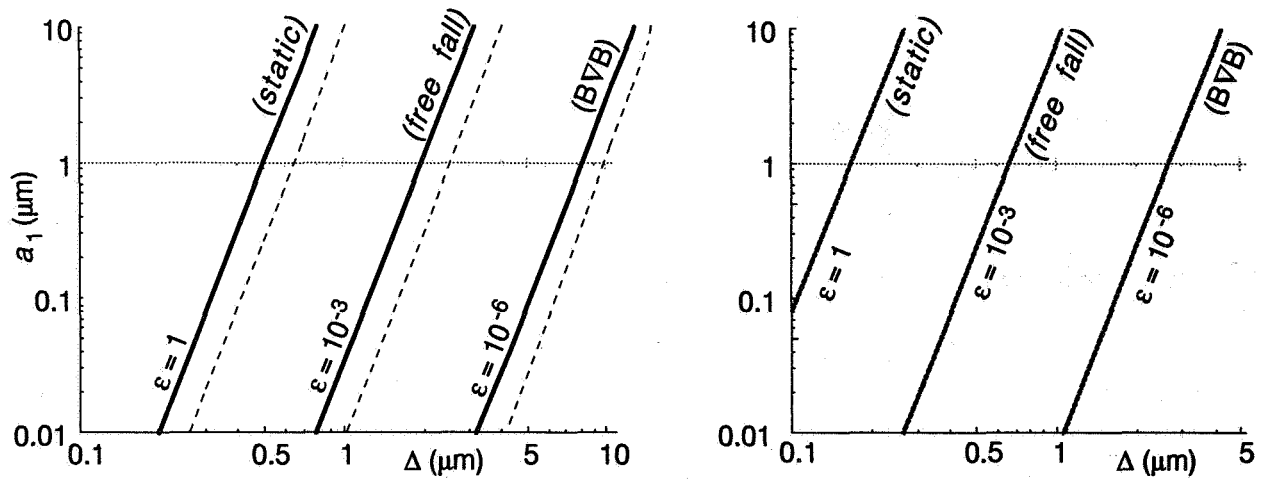
Fig. 2a a_1^{eq} for hollow plastic shells: the solid line is for a 1 000 μm dia., the dashed line a 250 μm dia.

Fig. 2b a_1^{eq} for a 100 μm thick foam shell having a density of 50 mg/cc ($f_{void} = 0.95$).

As can be seen (Fig. 2a), a_1^{eq} is directly proportional to the reduced gravitational field, εg. Its dependence on the thickness of the liquid layer, $a_1^{eq} \sim \Delta^5$ comes from taking the limit as $\Delta/a \ll 1$ in Eq. (9).

Fig 2b. shows that a 1 mm diameter overfilled foam target can support a liquid layer ~0.2 μm thick in a 1 g environment. For a given nonconcentricity, $\Delta \sim \varepsilon^{-1/5}$; for $a_1^{eq}/a = 1\%$, $\Delta \sim 0.7$ μm for $\varepsilon = 10^{-3}$ (free fall) and ~3 μm for $\varepsilon = 10^{-6}$ (B·∇B).
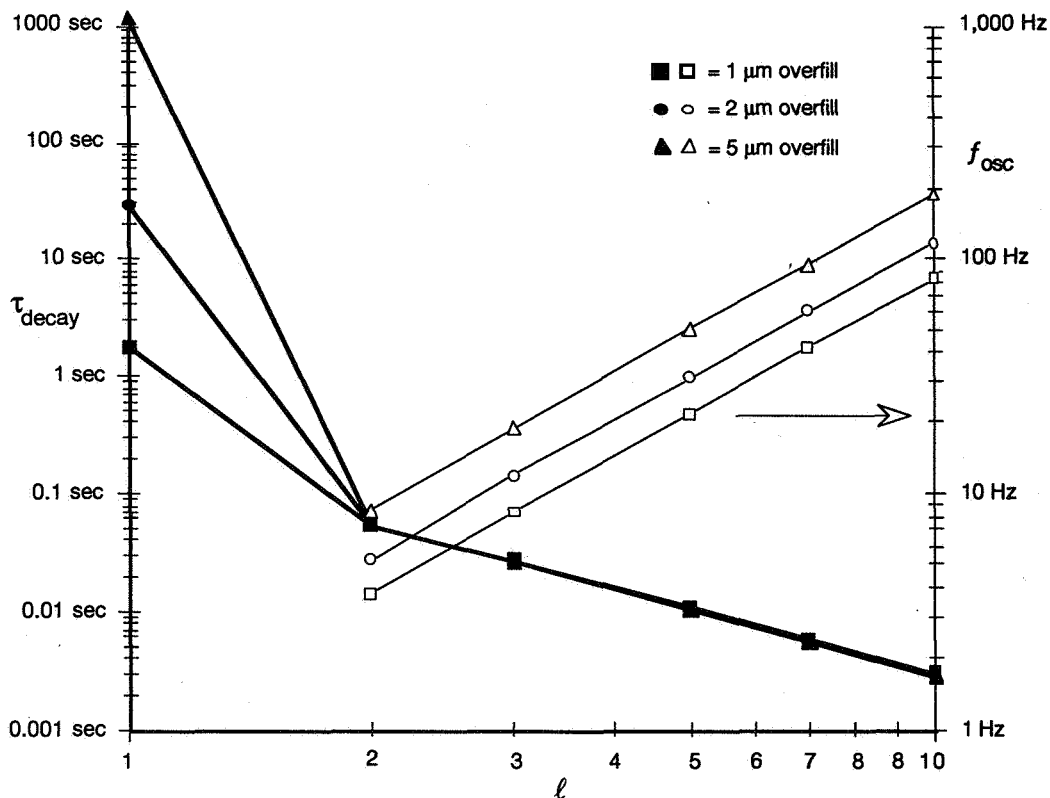
Fig. 3 Time constants and oscillation frequencies as a function of mode number for an overfilled foam target.

171

Figure 3 displays the time constants as a function of liquid fuel layer thickness Δ for a large shell ($c = 500 \, \mu m$) with an ordinary liquid D_2 layer in conditions typical of B·∇B experiment (10^{-6} g) and an overfilled foam target in freefall and stationary situations (10^{-3} g and 1 g). The long damping times for the $\ell = 1$ modes are due to the extremely weak Van der Waals[14] attractive forces between the liquid and the plastic shell or foam material.

In the case of the overfilled foam layers, the decay times for all modes can be short enough to consider the simple freefall method, where drop times from height h, $t_{drop} = (2h/g)^{1/2}$, can be manifestly longer (nearly 1 sec for a 2 meter drop).

Conclusions

Symmetric cryogenic targets are critical for inertial confinement fusion. To date, no layering method has demonstrated the needed symmetry and surface smoothness. Microgravity techniques may achieve the required symmetry, but development is needed. Specifically we need to measure the London-Van der Waals Forces between liquid deuterium and plastic and observe the actual time dependent behavior of liquid layers in microgravity environments. This should lead to an accurate model of the liquid layer interaction that will allow the ICF community to design present and future ICF targets.

References

1. J. D. Lindl, R. L. McCrory, And E. M. Cambell, *Physics Today*, September 1992, p. 32.

2. W. J. Hogan, R. Bangerter and G. L. Kulcinski,September 1992, p. 42.

3. S. G. Glendinning, S. V. Weber, S. Dixit, M. A. Henesian. J. D. Kilkenny, H. T. Powell, R. J. Wallace, J. P. Knauer and C. P. Verdon, *Bull. Am. Phys. Soc.*, **37**, 1470 (1992).

4. J. K. Hoffer and L. R. Foreman, *Phys. Rev. Lett.*, **60**, 1310 (1988).

5. K. Kim, B. J. Smoot, R. L. Woerner, and C. D. Hendricks, *Appl. Phys. Lett.*, **34**, 282 (1979).

6. V. Varadarajan, K. Kim, and T. P. Bernat, *J. Vac. Sci. Technol. A* , **5**, 2750 (1987).

7. S. Denus, W. Muniak, and E. Woryna, *Laser Part. Beams*, **7**, 15 (1989).

8. R. A. Sacks & D. H. Darling, *Nuclear Fusion*, **27**, 447 (1987).

9. C. Hendricks, W. J. Schafer Associates, Livermore, CA, Private communication

10. Arnold Honig at Syracuse University, Private communication

11. C. G. Paine and G. M. Seidel, *Rev. Sci. Instrum.*, **62**, 3022 (1991).

12. P .B. Parks and R.L. Fagaly, "Field–assisted Microgravity for ICF Target Fuel Layering", submitted to *Journal of Applied Physics*

13. R. J. Hunter, Foundations of Colloid Science, Vol. I, Ch. 4, (Clarendon Press, Oxford, 1986)

14. L. S. Mok, K. Kim, and T. P. Bernat, *Phys.Fluids* , **28**, 1227 (1985).

Solidification

CONVECTION AND MORPHOLOGICAL STABILITY DURING DIRECTIONAL SOLIDIFICATION

S. R. Coriell, A. A. Chernov, B. T. Murray, and G. B. McFadden

National Institute of Standards and Technology

Gaithersburg, MD 20899 USA

ABSTRACT

For growth of a vicinal face at constant velocity, the effect of anisotropic interface kinetics on morphological stability is calculated for a binary alloy. The dependence of the interface kinetic coefficient on crystallographic orientation is based on the motion and density of steps. Anisotropic kinetics give rise to traveling waves along the crystal-melt interface, and can lead to a significant enhancement of morphological stability. The stability enhancement increases as the orientation approaches a singular orientation and as the solidification velocity increases. Shear flows interact with the traveling waves and, depending on the direction of the flow, may either stabilize or destabilize the interface. Specific calculations are carried out for germanium-silicon alloys.

INTRODUCTION

During the directional solidification of a binary alloy solute inhomogeneities can arise from both fluid flow and morphological instability. In microgravity buoyancy-driven fluid flow is reduced, and experiments to study the evolution of morphological patterns without the interference of fluid flow may be possible. We are carrying out theoretical studies of the interaction of fluid flow with the crystal-melt interface [1-3]. Included in this research are: (1) calculations of cellular morphologies in the absence of fluid flow; (2) evaluation of the Seebeck voltage for cellular interfaces as a method for monitoring interface morphology in metallic alloys; (3) linear stability analyses of coupled interfacial and convective instabilities; (4) calculations of the effects of time-dependent gravitational accelerations (g-jitter) on fluid flow during directional solidification. This ground based research will focus on providing theoretical interpretation and guidance for a series of space experiments to be carried out by J. J. Favier, R. Abbaschian, and colleagues on tin-bismuth alloys using the MEPHISTO apparatus and by K. Leonartz and colleagues on succinonitrile-acetone alloys. Bismuth typically grows from the melt with facets, and in this paper we will describe recent studies of morphological stability when the interface attachment kinetics is highly anisotropic.

During solidification of a binary alloy, the crystal-melt interface may become morphologically unstable [4, 5] leading to cellular or dendritic growth. Here, we consider the effect of anisotropy of interface kinetics on morphological instability during growth of a binary alloy at constant velocity. We treat growth in a direction near a singular orientation, and use a model of kinetic anisotropy based on step motion. The effect of anisotropy of surface tension and interface kinetics has previously been treated [6] in a quasi-static approximation to the diffusion field; kinetic anisotropy gave rise to traveling waves along the crystal-melt interface. In this article, we keep the full time-dependence of the diffusion field and show that the traveling waves resulting from kinetic anisotropy can provide a significant enhancement of morphological stability, especially for orientations near the singular orientation and for large growth velocities. We have recently obtained similar results for constant velocity growth from a supersaturated solution [7].

In solution growth, it is well known that a solution flowing above a vicinal face of a crystal has a strong influence on morphological stability [8-10]. If the flow is opposite to the direction of the step motion, there is a stabilization of the interface with respect to step bunching. In the absence of a shear flow, there is an apparent flow of liquid opposite to the step motion (in a reference frame attached to the moving steps) and this stabilizes the interface, preventing step bunching and the formation of macrosteps [7].

For melt growth, interface stability near a vicinal face was the subject of an earlier treatment by Yuferev [11] in which he concluded that interface stability is enhanced for very small deviations from the singular orientation. Also, Kolesnikova and Yuferev [12] have carried out weakly nonlinear calculations in the frozen temperature approximation, i.e., equal thermal properties and vanishing latent heat. A strong interaction

175

between a shear flow parallel to the crystal-melt interface and anisotropy of kinetics has recently been found [10].

In this article, we carry out a linear treatment of interface stability during constant velocity solidification of a binary alloy. We allow for an interface kinetic coefficient that depends on the crystallographic orientation of the crystal-melt interface. We carry out specific calculations for germanium-silicon alloys for orientations in the vicinity of a singular orientation, which occur in this alloy [13].

THEORY

We consider directional solidification of a binary alloy at constant velocity $\bar{V}$ in the z-direction and treat the morphological stability of an initially planar crystal-melt interface. We choose an (x, y, z) coordinate system (moving with the macroscopically planar interface) such that the crystal-melt interface is described by $z = h(x, t)$, where t is the time. Further, we consider a two-dimensional problem and assume that all quantities are independent of the y-coordinate.

The temperature fields, $T_L(x, z, t)$ and $T_S(x, z, t)$, in the melt and crystal and the solute field in the melt, $C_L(x, z, t)$, satisfy the partial differential equations

$$\frac{\partial T_L}{\partial t} = \kappa_L \nabla^2 T_L + \bar{V} \frac{\partial T_L}{\partial z}, \tag{1}$$

$$\frac{\partial T_S}{\partial t} = \kappa_S \nabla^2 T_S + \bar{V} \frac{\partial T_S}{\partial z}, \tag{2}$$

and,

$$\frac{\partial C_L}{\partial t} = D \nabla^2 C_L + \bar{V} \frac{\partial C_L}{\partial z}, \tag{3}$$

where κ_L and κ_S are the thermal diffusivities in the melt and crystal, respectively, and D is the solute diffusivity; we neglect diffusion in the solid. We also assume that there is no fluid flow in the melt and that the thermophysical properties are independent of temperature and solute concentration. These transport equations and assumptions are most appropriate for dilute alloys.

The boundary conditions at the crystal-melt interface are

$$(\mathbf{V} \cdot \mathbf{n})(1 - k)C_L = -D \nabla C_L \cdot \mathbf{n}, \tag{4}$$

$$L_v(\mathbf{V} \cdot \mathbf{n}) = (k_S \nabla T_S - k_L \nabla T_L) \cdot \mathbf{n}, \tag{5}$$

$$T_S = T_L, \tag{6}$$

$$\mathbf{V} \cdot \mathbf{n} = \beta(p)(T_e - T_L), \tag{7}$$

where

$$T_e = T_M + mC_L - T_M \Gamma \mathcal{K}, \tag{8}$$

V is the solidification velocity vector, n is the unit normal to the interface, k is the segregation coefficient, L_v is the latent heat per unit volume, k_S and k_L are the thermal conductivities of crystal and melt, respectively, $\beta(p)$ is the kinetic coefficient, T_M is the melting point, m is the liquidus slope, $\Gamma = \gamma/L_v$, γ is the surface tension, and $\mathcal{K}$ is the mean curvature of the crystal-melt interface. We will assume that $\beta(p) = \beta_{st}|p|$, with $p \equiv \tan\theta$, where θ measures the deviation of the interface from a singular orientation. We will denote the orientation of the planar interface relative to the singular orientation by $\bar{p}$, and consider that $\bar{p} > 0$. We fix the far-field boundary conditions by specifying the bulk alloy concentration C_∞ and the temperature gradient in the melt at the crystal-melt interface. We will perform stability calculations for germanium-silicon alloys; the required properties are given in reference [14].

In [7, 10, 14] the morphological stability of a solid-liquid vicinal interface is treated using linearized theory in two dimensions. The perturbation to the planar interface ($z = 0$) with crystallographic orientation $\bar{p}$ has the form

$$z \propto \exp(\sigma t + i k_x x). \tag{9}$$

Here k_x is the wavenumber and σ is the complex temporal factor,

$$\sigma = \sigma_r + i\sigma_i. \tag{10}$$

The interface is unstable if $\sigma_r > 0$. The dispersion relation for σ as a function of k_x can be obtained analytically. In the thermal steady-state approximation, i.e., $\kappa_L \to \infty$ and $\kappa_S \to \infty$, it reduces to

$$\sigma/\bar{V} = \{-\bar{G} - T_M\Gamma k_x^2 + ik_x\bar{V}/(\beta_{st}\bar{p}^2) + mG_c[\alpha - \bar{V}/D]/[\alpha - (1-k)\bar{V}/D]\}$$

$$\{L_v\bar{V}/(2\bar{k}k_x) + (\bar{V}/\beta_{st}\bar{p}) + mG_c/[\alpha - (1-k)\bar{V}/D]\}^{-1}, \tag{11}$$

where

$$\alpha = (\bar{V}/2D) + \sqrt{(\bar{V}/2D)^2 + k_x^2 + (\sigma/D)}, \tag{12}$$

$\bar{G} = (k_SG_S + k_LG_L)/(2\bar{k})$, and $\bar{k} = (k_S + k_L)/2$. In a previous treatment [6] of the effect of anisotropic kinetics on morphological stability, a quasi-static approximation was made for the diffusion field which is equivalent to setting $\sigma = 0$ in the definition of α. In this limit, the above expression agrees with eq. (13) of reference [6]. The dispersion relation can be written as a cubic polynomial with complex coefficients in the variable $\alpha - (\bar{V}/2D)$; this has the advantage that all roots of the nonlinear equation can be determined. In the thermal steady-state approximation, we have numerically solved the cubic polynomial to determine the stability conditions. We have also numerically solved the ordinary differential equations as a boundary value problem to determine the stability conditions; this does not require the thermal steady-state approximation.

RESULTS

The dispersion relationship $\sigma_r = \sigma_r(\bar{V}, \bar{G}, c_\infty, \bar{p}, k_x)$ includes, as independent parameters, the normal growth rate $\bar{V}$, the temperature gradient $\bar{G}$, the impurity concentration c_∞ and the slope $\bar{p}$; stability requires that $\sigma_r < 0$ for all values of k_x. In principle, the slope, $\bar{p}$, may be fixed independently of the other processing variables by cutting the crystal to prepare an initial interface; however, only very small deviations (less than a tenth of a degree) from a singular interface make sense because large deviations are indistinguishable from a rough interface. Even such a prepared interface may be replaced (wedged out) by the nearest singular face in the course of sufficiently long growth. Under the typical conditions of faceted growth, the vicinal slope $\bar{p}$ on a facet is, like $\bar{V}$, dependent on supercooling and is determined either by a dislocation step source or by two-dimensional nucleation on the most supercooled region of the facet. In these cases, the slope $\bar{p}$ is a function of the growth rate $\bar{V}$ which is determined by the conditions of crystal pulling (Czochralski) or crucible movement through a temperature gradient (Bridgman and related techniques). In the following, we consider stability conditions for both an independently given slope and for a slope determined by $\bar{V}$, i.e., $\bar{p} = \bar{p}(\bar{V})$, for dislocation assisted growth and for growth by two-dimensional nucleation.

Figure 1 presents the real part of the temporal factor σ, i.e., σ_r, as a function of the wavenumber k_x in dimensionless form for the processing conditions $\bar{V} = 10$ μm/s, $G_L = 50$ K/cm, and $C_\infty = 5$ at%. The upper plot with $\bar{p} = 0.002$ is for isotropic kinetics. The lower two plots are for anisotropic kinetics with $\bar{p} = 0.002$ and 0.0015. Stabilization due to anisotropy is evident. Also, for $\bar{p} < 0.0015$ the interface becomes absolutely stable, i.e., stable against perturbations for all k_x. Stability at $Dk_x/\bar{V} < 5$ is common to all the curves; in this region of k_x the perturbation wavelength $2\pi/k_x > D/\bar{V}$, i.e., the diffusion boundary layer follows the perturbed interface and thus there is less driving force for instability. The steep drop in σ_r at high wavenumbers is associated with capillary stabilization, while the kinetic stabilization determines the overall level of σ_r at lower k_x and thus the height of the maximum.

We suppose that the unperturbed slope $\bar{p}$ is determined by a screw dislocation with the elementary Burger's vector intersecting the face under consideration. We also assume that the supercooling, ΔT, and thus the value of $\bar{p}$, along the face is constant with ΔT given by $\bar{V}/(\beta_{st}\bar{p})$. Letting γ_{st} be the linear energy of a step, the growth rate of the face is given by [15]

$$\bar{V} = \frac{h^2 L_v \beta_{st}\Delta T^2}{19\gamma_{st}T_M} \tag{13}$$

and the slope is

$$\bar{p} = [h^2 L_v \bar{V}/(19\gamma_{st}T_M\beta_{st})]^{\frac{1}{2}} \tag{14}$$

177

where h is the step height. It was shown by Voronkov [15] that the step fluctuations at the melting point decrease the step free energy for (111) Si and Ge by a factor of three or four; therefore, for the linear stability calculations for Ge, we assume that $\gamma_{st} = \gamma h/4$.

If the crystal face is free of screw dislocations or the supercooling is so high that step generation by two-dimensional nucleation is more effective than by the dislocation mechanism, the growth rate is [16]

$$\bar{V} = h(\bar{v}^2 J)^{\frac{1}{3}} \tag{15}$$

where the nucleation rate J (cm^{-2} s) is obtained from

$$J = [hk_B T_M^2 \Delta T/(\omega^2 L_v)]^{\frac{1}{2}} q\beta_{st} \exp[-\pi h\gamma^2/(k_B \Delta T L_v)]. \tag{16}$$

Here q is the density of surface sites on which nucleation is possible, ω is the atomic volume, and k_B is Boltzmann's constant. Thus, the growth rate is

$$\bar{V} = (h^7 q^2/\omega)^{\frac{1}{6}} \beta_{st} \Delta T^{\frac{5}{6}} [k_B T_M^2/(\omega L_v)]^{\frac{1}{6}} \exp[-\pi h\gamma^2/(3k_B \Delta T L_v)]. \tag{17}$$

and the slope $\bar{p}$ is given by

$$\bar{p} = h(J/\bar{v})^{\frac{1}{3}} = (h^7 q^2/\omega)^{\frac{1}{6}} \frac{[k_B T^2/(\omega L_v)]^{\frac{1}{6}}}{\Delta T^{\frac{1}{6}}} \exp[-\pi h\gamma^2/(3k_B \Delta T L_v)]. \tag{18}$$

Thus eq. (17) and eq. (18) give the dependence $\bar{p}(\bar{V})$ in parametric form with ΔT the parameter. In evaluating these expressions, we make the approximation that $h^7 q^2/\omega = 1$.

In Fig. 2, we present a stability diagram in terms of the critical solute concentration as a function of the ratio of the liquid temperature gradient and the growth velocity for $G_L = 50$ K/cm. The interface is stable to small perturbations for concentrations lying below the given curves. The calculations have been carried out by numerically solving the differential equations. The solid curve is the Mullins and Sekerka [4] result which for isotropic kinetics does not depend on the kinetic coefficient [6]. The dashed and dotted curves are calculated from the present model of anisotropic kinetics with $\bar{p} = 0.01$ and 0.001, respectively. Anisotropic kinetics causes a substantial enhancement of the region of stability.

The remaining two curves in Fig. 2 are for dislocation and two-dimensional nucleation controlled growth for which $\bar{p}$ is a function of velocity. For the dislocation controlled growth, $\bar{V} = 8.7 \times 10^4 \bar{p}^2$ cm/s. In the case of two-dimensional nucleation, eq. (17) and eq. (18) have been evaluated numerically to obtain $\bar{V}$ as a function of $\bar{p}$.

We note that as $\bar{p}$ becomes small, the concentration at the onset of instability becomes very large where other effects, which we have not taken into account, such as fluid flow and the concentration dependence of the distribution coefficient, liquidus slope, and diffusion coefficient, may be important. However, it is clear from the results that as a singular orientation is approached, anisotropic kinetics has a large stabilizing effect.

As $\bar{p}$ becomes very small or $\bar{V}$ becomes very large, the thermal steady-state approximation is no longer valid. For example, in the thermal steady-state approximation, for $\bar{p} = 0.001$ and $\bar{V} = 0.001$ and 0.01 cm/s, the critical concentrations are 7.8847 and 5.4579 at%, respectively; whereas the numerical values are 7.8852 and 7.6689 at%. Thus for $\bar{p} = 0.001$, the thermal steady-state approximation underestimates the critical concentration. The thermal steady-state approximation fails because the wavespeed is sufficiently large that k_x^2 is no longer much greater than σ_i/κ_S.

Near a singular orientation, due to anisotropy the value of $T_M\Gamma$ may be much less than the value used in our calculations [14]; therefore, we have also carried out a few calculations with $T_M\Gamma$ reduced by a factor of 100. For $\bar{p} = 0.001$ and $\bar{V}$ ranging from 0.001 to 0.1 cm/s, the critical concentrations are essentially unchanged. Similarly, for dislocation controlled growth, the results for the critical concentrations are again unchanged. Thus, in the strongly kinetically controlled regime the value of the capillary constant is unimportant. Capillarity is still important at large wavenumbers, but in the kinetically controlled regime the onset of instability occurs at relatively small wavenumbers.

CONCLUSIONS

In the calculations described above, we have assumed that the melt is stagnant. It is well known that fluid flow can alter the conditions for stability [10, 17]. For an ideal fluid and anisotropic kinetics, Chernov [10] has shown that a flow parallel to the interface and opposite in direction to the step motion stabilizes the interface while a flow in the direction of the step motion destabilizes the interface. We are carrying out numerical calculations of the linear stability of a crystal-melt interface in the presence of a parallel shear flow. The method is similar to that previously used for isotropic kinetics [18]; in addition, we have developed a pseudospectral algorithm to treat the problem. Qualitatively, the results are in agreement with Chernov [10] for an ideal fluid.

References

[1] B. V. Saunders, B. T. Murray, G. B. McFadden, S. R. Coriell, and A. A. Wheeler, Phys. Fluids A4 (1992) 1176-1189.

[2] B. T. Murray, S. R. Coriell, G. B. McFadden, A. A. Wheeler, and B. V. Saunders, J. Crystal Growth 129 (1993) 70-80.

[3] R. J. Braun, G. B. McFadden, B. T. Murray, S. R. Coriell, M. E. Glicksman, and M. E. Selleck, Phys. Fluids A5 (1993) 1891-1903.

[4] W. W. Mullins and R. F. Sekerka, J. Appl. Phys. 35 (1964) 444-451.

[5] S. R. Coriell and G. B. McFadden, in D. T. J. Hurle (ed.) Handbook of Crystal Growth 1 Fundamentals, Part B: Transport and Stability, North-Holland, Amsterdam, 1993 pp. 785-857.

[6] S. R. Coriell and R. F. Sekerka, J. Crystal Growth 34 (1976) 157-163.

[7] A. A. Chernov, S. R. Coriell, and B. T. Murray, J. Crystal Growth 132 (1993) 405-413.

[8] A. A. Chernov and T. Nishinaga, in Morphology of Crystals, Ed. I. Sunagawa (Terra, Tokyo, 1987) pp. 207-267.

[9] A. A. Chernov, Contemp. Phys. 30 (1989) 251-276.

[10] A. A. Chernov, J. Crystal Growth 118 (1992) 333-347.

[11] V. S. Yuferev, Phys. Chem. Mech. of Surfaces 2 (1985) 1916-1925.

[12] E. A. Kolesnikova and V. S. Yuferev, Soviet Phys.-Cryst. 34 (1989) 7-10.

[13] J. P. Dismukes and L. Ekstrom, Met. Trans. 233 (1965) 672-680.

[14] S. R. Coriell, B. T. Murray and A. A. Chernov, J. Cryst. Growth (1994) in press.

[15] V. V. Voronkov, Sov. Phys. Cryst. 17 (1973) 807-813.

[16] A. A. Chernov, *Modern Crystallography III. Crystal Growth*, Springer Ser. Sol. St., vol. 36 (Springer, Berlin, 1984).

[17] S. H. Davis, in D. T. J. Hurle (ed.) Handbook of Crystal Growth 1 Fundamentals, Part B: Transport and Stability, North-Holland, Amsterdam, 1993 p. 859-897.

[18] S. R. Coriell, G. B. McFadden, R. F. Boisvert, and R. F. Sekerka, J. Crystal Growth 69 (1984) 15-22.
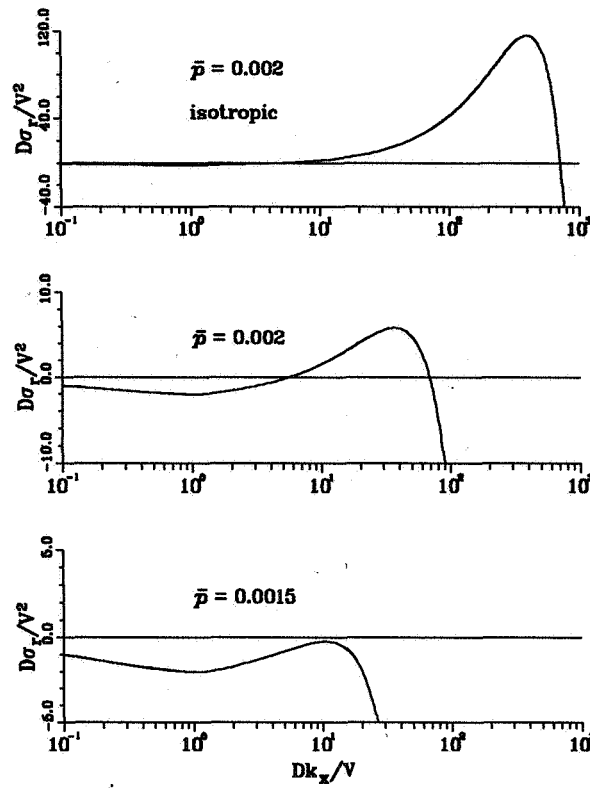
Figure 1: The real part of the temporal growth rate as a function of the spatial wavenumber for three values of the crystallographic orientation with respect to the growth direction for $\bar{p} = 0.002$ and 0.0015. The upper plot is for isotropic kinetics, while the two lower plots are for anisotropic kinetics.
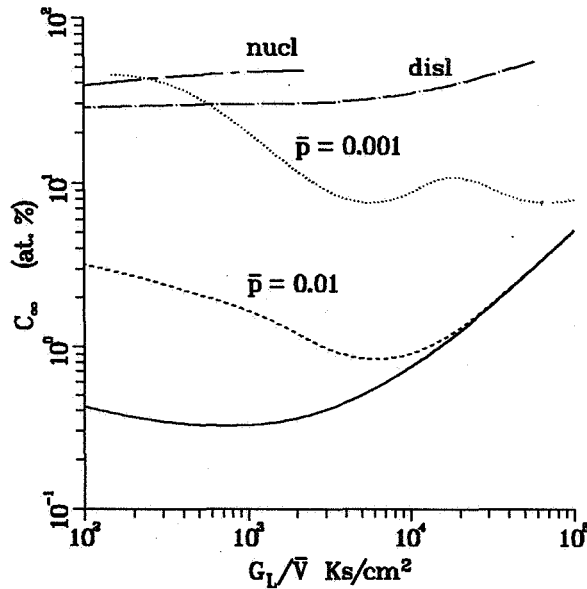
Figure 2: The silicon concentration at the onset of instability during directional solidification of germanium-silicon alloys as a function of the liquid temperature gradient divided by the growth rate with $G_L = 50$ K/cm. The interface is morphologically stable for concentration values below the curves. The solid curve is based on the Mullins and Sekerka theory with isotropic kinetics; the remaining curves are for anisotropic kinetics. The dashed and dotted curves correspond to $\bar{p} = 0.01$ and 0.001, respectively. The curves labeled "nucl" and "disl" correspond to nucleation and dislocation controlled growth for which $\bar{p}$ is a function of $\bar{V}$.

SHEAR STABILIZATION OF SOLIDIFICATION FRONTS

S.H. Davis and T.P. Schulze
Northwestern University
Department of Engineering Sciences and Applied Mathematics
Evanston, IL 60208

ABSTRACT

A linear-stability analysis is performed on the interface formed during the directional solidification of a dilute binary alloy in the presence of a time-periodic flow. In general, the flow is generated by the elliptical motion of the crystal parallel to the interface. The presence of the flow can either stabilize or destabilize the system relative to the case without flow with the result depending on the frequency and amplitude of the oscillations as well as the properties of the material. In particular, we find that the morphological instability present in the absence of flow can be entirely suppressed with respect to disturbances of the same frequency as the oscillation.

INTRODUCTION

The manufacturing of crystals with uniform material properties is frequently hampered by the presence of morphological instabilities during the solidification of multi-component materials. These nonuniformities result from an interaction between surface morphology and the concentration gradients created by solute rejection. In order to eliminate these nonuniformities, it is necessary to suppress the instability. In the context of directional solidification, this can be done by producing materials with sufficiently low solute concentration, or by controlling the speed of the solidification front[1].

When it is undesirable to operate within these restricted ranges of parameters, some other method of stabilization is necessary. In the 1960's, Hurle suggested that flow in the melt, either forced or resulting from natural convection, might be used to stabilize the interface. Since then, a number of studies have investigated the effect of various flows on morphological stability.

Delves[2] studied solidification into a Blasius boundary layer, using a parallel-flow approximation. Coriell, McFadden, Boisvert and Sekerka[3] investigated solidification into a plane Couette flow. Forth and Wheeler[4] and Hobbs and Metzener[5] investigated solidification into a parallel flow with the asymptotic suction profile. McFadden, Coreill, and Alexander[6] and Brattkus and Davis[7] looked at solidification into a stagnation point flow. Brattkus and Davis[8] also looked at solidification over a rotating disc. Merchant and Davis[9] studied solidification into a temporally modulated stagnation point flow, and Schulze and Davis[10] considered solidification into a compressed Stokes boundary layer (CSL). For a more extensive review of the role of convection in solidification see Davis [11].

Here, we follow up on the work studying solidification into a CSL. This flow can be generated by oscillating the crystal parallel to the interface.

GOVERNING EQUATIONS

We consider the directional solidification of a dilute binary mixture at constant speed V. We choose a coordinate system with x-axis located at the mean position of the crystal interface, moving with the front, and a z-axis that is fixed in the laboratory frame of reference. The equations governing the system in the fluid region are the Navier-Stokes, continuity, and solute diffusion equations:

$$\Omega \mathbf{u}_t + \epsilon \mathbf{u} \cdot \nabla \mathbf{u} - \mathbf{u}_z = -\nabla p + S \nabla^2 \mathbf{u} \tag{2.1}$$

$$\nabla \cdot \mathbf{u} = 0 \tag{2.2}$$

$$\Omega C_t + \epsilon \mathbf{u} \cdot \nabla C - C_z = \nabla^2 C \tag{2.3}$$

$$T = z. \tag{2.4}$$

To simplify the analysis, we neglect latent heat and density changes, and we assume equal densities and thermal properties between the two phases. We also assume that heat diffuses much faster

than solute, and, in this limit, the temperature field is fixed and depends linearly on the vertical coordinate—the frozen temperature approximation [12]. We begin by considering the problem in two dimensions.

We have nondimensionalized the equations by scaling the fluid velocity with the amplitude of the crystal oscillations U; the spatial coordinates with the diffusion boundary layer thickness D/V, where D is the solute diffusivity; time with the frequency of the crystal oscillations ω; and the temperature and solute concentrations using the product of the diffusion boundary layer thickness and their respective gradients at the interface.

The nondimensional parameters that appear in the equations and boundary conditions are the morphological number M, the surface energy parameter Γ, the Schmidt number S, the nondimensional frequency Ω, the segregation coefficient k, and a parameter measuring the amplitude of the lateral oscillations ϵ.

$$M = \frac{mVC_\infty(1 - 1/k)}{GD} \tag{2.5}$$

$$\Gamma = \frac{T_m \gamma V}{DL_V mC_\infty(1 - 1/k)} \tag{2.6}$$

$$S = \frac{\nu}{D} \tag{2.7}$$

$$\Omega = \frac{\omega D}{V^2} \tag{2.8}$$

$$\epsilon = \frac{U}{V} \tag{2.9}$$

Here m is the liquidus slope in the phase diagram of the binary mixture, C_∞ is the far-field solute concentration, G is the thermal gradient, T_m is the melting temperature of the solvent, γ is the surface free energy, L_V is the latent heat per unit volume, and ν is the kinematic viscosity.

The interfacial conditions, evaluated at $z = h(x, y, t)$ are as follows:

$$u = \cos t \tag{2.10}$$

$$w = 0 \tag{2.11}$$

$$C = M^{-1}h - 2\Gamma H \tag{2.12}$$

$$[1 + \Omega h_t + \epsilon \cos t \, h_x][1 + (k-1)C] = C_z - C_x h_x, \tag{2.13}$$

where H is the mean curvature of the interface.

The basic state for this system takes the form

$$\bar{u} = e^{-Bz}\cos(t - Az) \tag{2.14}$$

$$\bar{w} = 0 \tag{2.15}$$

$$\bar{C} = 1 - e^{-z} \tag{2.16}$$

$$\bar{h} = 0, \tag{2.17}$$

where A and B are known real constants that depend on the Schmidt number and forcing frequency.

To analyse the response of this state to infinitesimal perturbations, we disturb each of these quantities, and separate the disturbances into normal modes of the form

$$\phi = \bar{\phi} + \hat{\phi}(z,t)e^{i\alpha x}e^{\sigma t} + c.c. \tag{2.18}$$

Here we are seeking time-periodic eigenfunctions with the same period as the basic state, and σ is the Floquet exponent. If the real part of σ is not zero, then the disturbances will experience a net growth or decay over one period.

Routine algebraic manipulations result in two linearized disturbance equations for the solute concentration and vertical component of the velocity.

182

SMALL AMPLITUDE OSCILLATIONS

In this section we find conditions on the morphological number M such that the system is neutrally stable in the limit of small forcing, $\epsilon \to 0$. In this limit, we find that $\sigma = 0$ on the neutral curve, and we expand the inverse morphological number as

$$M^{-1} = M_0 + \epsilon^2 M_2 + \ldots, \tag{3.19}$$

where M_0 corresponds to the no-flow, or Mullins and Sekerka, result.

In Figure 1 we plot the correction to the no-flow result for the CSL as a function of the disturbance wavenumber for various forcing frequencies. If $M_2 < 0$ for a given wavenumber, a disturbance with that wavenumber will be stabilized relative to the case with no flow. Notice that for $\Omega = 1$ all finite wavelengths are stabilized. The Schmidt number and segregation coefficient have been chosen to represent a lead-tin alloy for all of the figures in this paper.

In Figure 2 we map out the regions of the α-Ω plane where the flow has a stabilizing influence on the interface ($M_2 < 0$). Notice that there is a range of frequencies for which all finite wavenumbers are stabilized. We refer to this as a *window of stabilization*.

It turns out that the CSL is only able to stabilize in two dimensions. In three dimensions, only disturbances with wavevectors aligned with the parallel flow will be stabilized while those with wavevectors perpendicular to the flow are unaffected—thus the flow acts as a pattern selection mechanism only.

SMALL AMPLITUDE NONPLANAR OSCILLATIONS

Motivated by the work of Kelly and Hu[13] on Benard convection, we attempt to extend the stabilizing influence of the CSL to three dimensions by considering the influence of nonplanar oscillations. Specifically, we consider the effect of adding a second oscillation perpendicular to the first which has the same frequency, but may differ in amplitude and phase. This corresponds to translating the crystal in elliptical orbits parallel to the interface.

For the correction due to a weak flow, we get

$$M_2 = [(cos\,\theta + \lambda cos\,\gamma sin\,\theta)^2 + \lambda^2 sin^2\theta sin^2\gamma]M_2^{(2D)}, \tag{4.20}$$

where $M_2^{(2D)}$ is the result for oscillations in one direction only (CSL), θ is the angle that the disturbance wave vector makes with the x-axis, λ is the amplitude ratio of the oscillations, and γ is the phase difference between the oscillations.

If the two oscillations are either perfectly in or out of phase (corresponding to a phase angle that is an integral multiple of π), there will be some θ_c for which the correction to the no-flow result, M_2, is zero. This means that the flow will be able to destabilize the interface if $M_2^{(2D)} > 0$, but acts only as a pattern selection mechanism if $M_2^{(2D)} < 0$, with disturbances oriented at the angle θ_c being the least stable. This is a degenerate case corresponding to a single oscillation along an axis lying in the x-y plane. The result is therefore equivalent to that for the CSL.

When the phase between the oscillations, γ, is not a multiple of π, the factor appearing in front of $M_2^{(2D)}$ is positive, and it is possible to stabilize an arbitrary three-dimensional disturbance provided $M_2^{(2D)} < 0$. Thus the ability of the nonplanar oscillations to stabilize the interface is predicted by the results for the CSL, and the window of stabilization is the same for both cases.

The maximum stabilization occurs when the phase angle is $\pi/2$, with the stabilization being greater along whichever axis has the largest amplitude oscillations. If the amplitude ratio, λ, is one, there will be no preferred direction for cell orientation.

FINITE AMPLITUDE OSCILLATIONS

In the previous section we showed that some degree of stabilization can be achieved by using small-amplitude nonplanar oscillations with a frequency lying within a given range. In this section we show that the Mullins and Sekerka interfacial mode can be entirely suppressed if these oscillations have sufficiently large amplitude.

Following the method used by Hall[14] for the Stokes layer, we find an exact solution for our system in the form of a Fourier series in time. We then truncate this series to produce numerical results.

In Figure 3 we plot M^{-1} versus α for a forcing frequency $\Omega = 10$, which lies within the window of stabilization, and we see that by taking epsilon sufficiently large we can force the neutral curve below the x-axis. In Figure 4 we plot M^{-1} versus ϵ for the same frequency and with the wavenumber fixed at the critical value for the instability in the absence of flow. Notice that when ϵ exceeds about 60, the instability is completely supressed.

CONCLUSION

We have found that nonplanar oscillations of the crystal during directional solidification can be used to entirely suppress the Mullins and Sekerka instability provided the frequency of these oscillations is within a given range and that their amplitude is sufficiently large. We have found that this window of stabilization persists for a wide range of material parameters and operating conditions.

We have searched for other modes of instability, especially subharmonics, but have not located any. If there are no other modes of instability, the modulation proposed here may provide a practical means for stabilizing the interface during directional solidification.

References

1 Mullins, W.W. and Sekerka, R.F., *J. Appl. Phys.* **35** (1964) 444.

2 Delves, R.T., *J. Cryst. Growth* **8** (1971) 3.

3 Coriell, S.F., McFadden, G.B., Boisvert, R.F. and Sekerka, R.F., *J. Cryst. Growth* **69** (1984) 15.

4 Forth, S.A. and Wheeler, A.A., *J. Fluid Mech.* **202** (1989) 339.

5 Hobbs, A.K. and Metzener, P., *J. Cryst. Growth* **112** (1991) 539.

6 McFadden, G.B., Coriell, S.R. and Alexander, J.I.D., *Commun. Pure Appl. Math.* **41** (1988) 683.

7 Brattkus, K. and Davis, S.H., *J. Cryst. Growth* **87** (1988) 385.

8 Brattkus, K. and Davis, S.H., *J. Cryst. Growth* **89** (1988) 423.

9 Merchant, G.J. and Davis, S.H., *J. Cryst. Growth* **96** (1989) 737.

10 Schulze, T.P. and Davis, S.H., *J. Cryst. Growth* (in press).

11 Davis, S.H., in *Handbook of Crystal Growth*, edited by D.T.J. Hurle, North-Holland (1993).

12 Langer, J.S. *Rev. Mod. Phys.* **52** (1980) 1.

13 Kelly, R.E. and Hu, H.-C., *J. Fluid Mech.* **249** (1993) 373.

14 Hall, P., *Proc. Roy. Soc. Lond. A.* **359** (1978) 151.
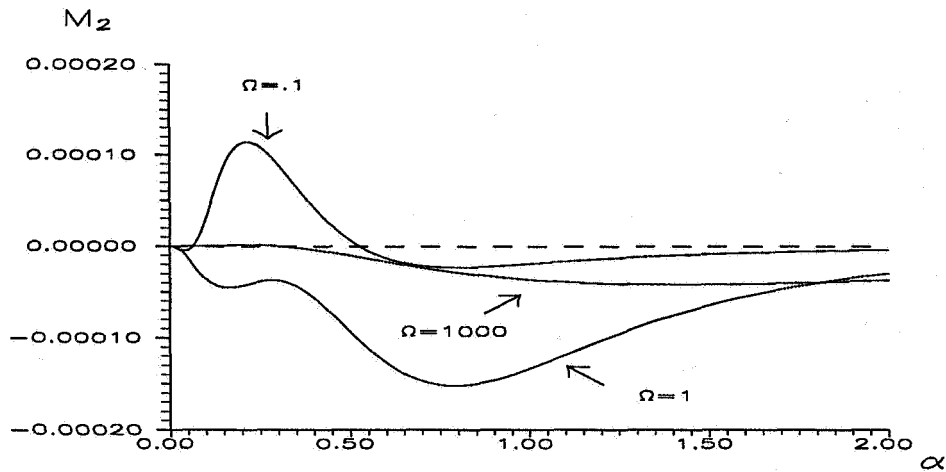
Figure 1: M_2 vs. α for $S = 81.0$, $k = 0.3$ and various Ω. M_2 is independent of Γ. When M_2 is above the x-axis, the influence of the flow is destabilizing, and when M_2 is below the x-axis, the influence of the flow is stabilizing. As $\Omega \to \infty$, $M_2 \to 0$, and as $\Omega \to 0$, M_2 approaches a steady state. Note that for $\Omega = 1$ the flow is stabilizing for all wavenumbers.
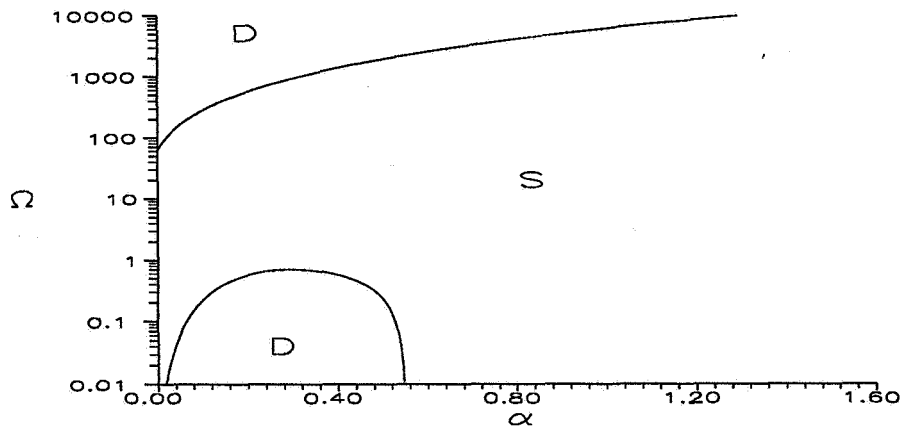
Figure 2: **Directional solidification into Stokes layer:** Regions of the α-Ω plane where the flow stabilizes (S) or destabilizes (D) the interface relative to the case without flow. $S = 81.0$ and $k = 0.3$; result is independent of Γ.
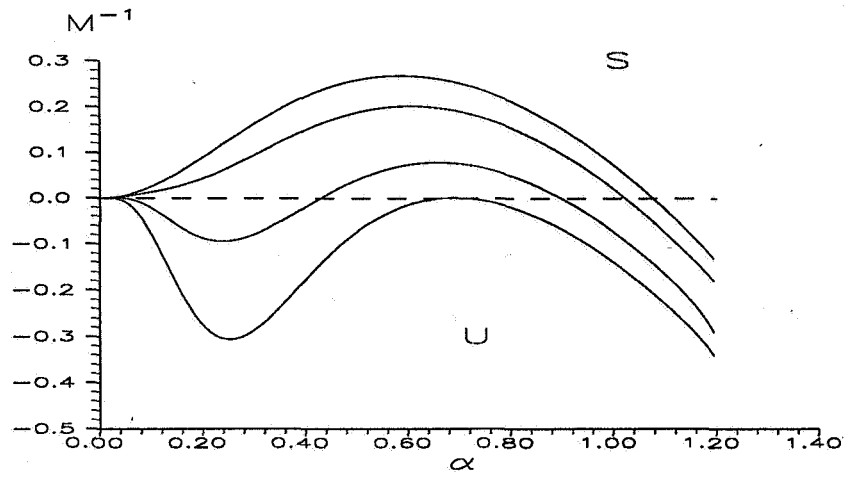
Figure 3: M^{-1} vs. α for $k = 0.3$, $S = 81.0$, $\Omega = 10.0$, and $\epsilon = \{0, 20, 40, 60\}$. As ϵ is increased the flow stabilizes the interface, and for $\epsilon \approx 60$ the Mullins and Sekerka interfacial instability is entirely suppressed.
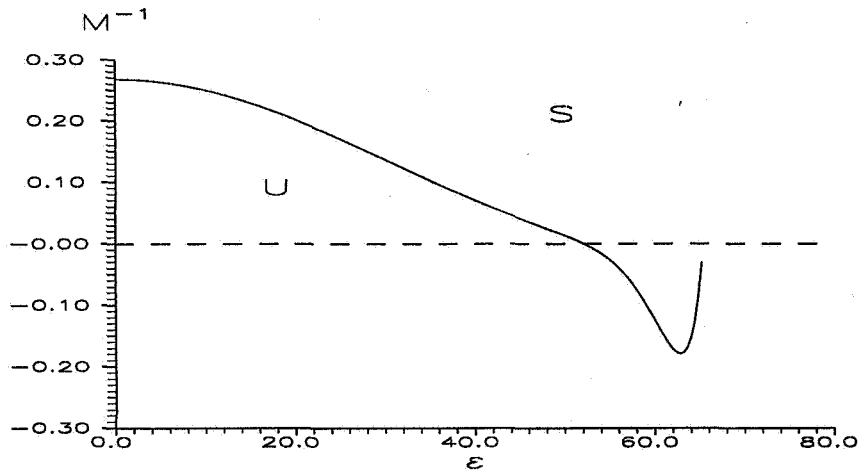
Figure 4: M^{-1} vs. ϵ for $k = 0.3$, $S = 81.0$, $\Omega = 10.0$, and α fixed at the critical value for the no-flow system. Notice that the stabilizing trend begins to reverse if the amplitude of the flow oscillations is too great.

186

CRYSTAL GROWTH AND FLUID MECHANICS PROBLEMS IN DIRECTIONAL SOLIDIFICATION

P.I.: S. Tanveer

Co-P.I.s: G.R. Baker & M. R. Foster

Ohio State University, Columbus, OH 43210

1. SCIENTIFIC OBJECTIVES:

Broadly speaking, our efforts have been concentrated in two aspects of directional solidification:

A. A more complete theoretical understanding of convection effects in a Bridgman apparatus.

B. A clear understanding of scalings of various features of dendritic crystal growth in the sensitive limit of small capillary effects.

For studies that fall within class A, the principal objectives are as follows:

(A1.) Derive analytical formulas for segregation, interfacial shape and fluid velocities in mathematically amenable asymptotic limits.

(A2.) Numerically verify and extend asymptotic results to other ranges of parameter space with a view to a broader physical understanding of the general trends.

With respect to studies that fall within class B, the principal objectives include answering the following questions about dendritic crystal growth:

(B1.) Are there unsteady dendrite solutions in 2-D to the completely nonlinear time evolving equations in the small surface tension limit with only a locally steady tip region with well defined tip radius and velocity? Is anistropy in surface tension necessary for the existence of such solutions as it is for a true steady state needle crystal? How does the size of such a local region depend on capillary effects, anisotropy and undercooling?

(B2.) How do the different control parameters affect the nonlinear amplification of tip noise and dendritic side branch coarsening?

2. SCIENTIFIC AND TECHNOLOGICAL RELEVANCE

The vertical Bridgman apparatus (Fig. 1) is used in the directional solidification of a molten binary alloy. The desired crystal for technological applications (as in semi-conductors) is the one with minimal compositional variations (i.e. minimal segregation) and crystalline defects. However, due to significant heat flux through the sides of Bridgman device that is necessary to avoid constitutional supercooling, differences in fluid densities occur that results in convection at any Rayleigh number. Convection without sufficiently vigorous and uniform mixing leads to a significant radial segregation. A clear understanding of the dependence of segregation and interface deformation on the numerous non-dimensional parameters is likely to lead to improved design and control of this industrially relevant process.

Prior theoretical work [see Brown[1] for a review], mostly numerical, has significantly furthered our understanding of the Bridgman problem; nonetheless, without explicit analytical formulas, it is difficult to get a general idea of the trends in various regions of the parameter space. We overcome this problem by deriving explicit formulas in some asymptotic ranges. This is complimented by numerical calculations

187

to determine the practical range of validity of the asymptotic results as well as to extend the suggested scaling dependences to other ranges of parameter space.

Dendritic crystal growth is an important problem in pattern formation [see References [2-4] for reviews]. In the simplest case, one is interested in the growth of a pure needle crystal in an undercooled melt. It is also arises in the context of directional solidification when the drawing speed exceeds some critical value that determines a "cell to dendrite transition". In this case, the growth is controlled by solutal diffusion rather than thermal. Nonetheless, the equations are similar to that in a pure needle crystal growth. Appearance of dendritic structures in directional solification leads to undesirable striations of solute rich material in the crystal. Further understanding of the basic process of dendritic crystal growth can be both scientifically and technologically rewarding.

By answering question (B1) without the limitations of an assumed steady state, linear stability or a linear WKB wave packet analysis, we address directly the controversy between the premises of "microscopic solvability"[2,3] and other theories[5,6] that rely on the equivalent of a "marginal stability" hypothesis made originally by Langer & Muller-Krumbaar. It is to be noted that inclusion of surface tension anisotropy is crucial in the first case but not so for the other. Further, our analytical approach provides us with important scale information in the small capillary limit, where increasingly small scales need to be resolved in any traditional method of numerical computation. An analytical understanding of the parameter dependence of noise amplification and side branch coarsening is also important since it is likely, to influence ways of controlling this process.

3. RESEARCH APPROACH

3a. Bridgman Problem

Using a standard quasi-steady assumption, analytical calculations have so far been carried out in the limit when fluid velocities and interfacial deformation are small enough to permit linearization of the Navier-Stokes equation and the interfacial matching condition (about a planar interface). This assumption can formally be justified in the limit of small horizontal heat transfer; nonetheless, our analysis of the equations suggests that the actual expressions for radial segregation at the interface and interface deformation may actually transcend this limitation. Further, with a no-stress boundary condition on the side walls, a convenient radial expansion in terms of a Bessel function representation reduces the problem to an eighth order ordinary differential equation in the melt that is coupled with two second order equations in the crystal through the interfacial conditions. The resulting equations are further analyzed using standard WKB techniques in the two cases of (i) large thermal Rayleigh number R_T in a thermally stable configuration and (ii) large solutal Rayleigh number R_c in a solutally stable configuration.

Further, a numerical code based on a finite difference scheme has been developed to solve the coupled heat-mass transfer and fluid equations with a no-slip as well as no-stress sidewall boundary conditions in order to compare and contrast the two cases and determine the range of validity of the large R_T or $|R_c|$ asymptotics. We also wish to explore the possibility that the complicated dependence of segregation and interfacial deformation on the seventeen nondimensional parameters can be largely understood in terms of only a few lumped parameters that are in turn functions of other parameters, as suggested by the asymptotic results. A systematic bifurcation study of the possible steady states is also planned.

3b. Dendrite Problem

With a one sided diffusion model of the growth of a pure dendrite, but with no assumption about a quasi-stationary field, we have so far looked at two opposite limits: (i) small undercooling when the Peclet

number based on tip radius and velocity of a dendrite is small and (ii) large undercooling when Peclet number based on tip radius and velocity tends to infinity.

i. Small Peclet number limit

In the small Peclet number limit, various regions of an initially near parabolic dendrite are identified where different equations have to be solved to follow the dynamics of disturbances initiated near the tip. Not unexpectedly, there is an $O(1)$ region near the tip where the diffusion problem reduces to a Laplacian.

In this order $O(1)$ region near the tip, the dynamics for $O(1)$ times is studied by using a conformal mapping function $z(\zeta, t)$ that maps the upper half ζ plane to the physical (z) domain. The complex dynamics of the analytically continued $z(\zeta, t)$ is studied in $Im \ \zeta \ < \ 0$ with a view to understanding the asymptotic behavior of the dynamics for sufficiently small but nonzero capillary effects. This unusual procedure of extending the domain to the complex unphysical ζ plane is a mathematical convenience and allows for a perturbative investigation of small capillary effects on the otherwise ill-posed zero surface tension dynamics. Further, in this formulation, one can mimic small noise by introducing a statistical ensemble of complex singularities that correspond to the same initial interface within some presribed error. By studying the dynamics of singularities as they come close to the real ζ axis and cause large interfacial distortions, one can understand and identify robust features of this highly sensitive dynamics and determine the dependence on capillary effects, anisotropy and Peclet number.

The analysis of disturbance in the $O(1)$ tip region of the dendrite is complimented by analysis of the solutions in other regions of the semi-infinite dendrite, where a Laplacian approximation for the field is invalid. Study of such solutions is relevant to side branch coarsening when tip noise advects and amplifies along the sides of a dendrite to a sufficiently large distance from the tip.

ii. Large Peclet number limit

In this case, a boundary layer analysis is possible for disturbances of some distinguished length scale and size superposed on a near parabolic initial dendrite. The resulting pair of nonlinear partial differential equations involving one space and time variable is studied.

4. DISCUSSION OF RESULTS

4a. Bridgman Problem

For the Bridgman problem, we have derived explicit analytical formula for for radial segregation and interfacial slope in the (i) asymptotic limit of large thermal Rayleigh number[7] R_T and (ii) large solutal Rayleigh number[8] $|R_c|$.

Here, we will only present results for case (i). Rather than give the more general formulas, that is a little too complicated to describe in this few pages, we describe the the special case obtained under additional assumptions that the vertical height is much larger than the cylinder radius and that the diffusion in the solid is negligible. The expression for radial segregation is of the form

$$\frac{\partial c_s}{\partial r}(r, \ z_0) \ \sim \ \sum_{n=1}^{\infty} A_n J_1(\lambda_n r) \left[1 - \frac{\delta_2}{\lambda_n}\right] e^{-\lambda_n(z_0 - z_I)}. \tag{1}$$

In the above formula, $c_s(r, z)$ is the solute concentration in the solid at a point with cylindrical coordinates (r, z). Further, λ_n is the n-th zero of the Bessel function $J_1(x)$ not including $x = 0$, A_n and δ_2 are functions of other nondimensional parameters. In deriving formulae (1), it was implicitly assumed that the solutal Peclet number $<< \ R_T^{1/6}$ and that the $z_{II} - z_0$ and $z_0 - z_I$ are of the same order. Also, in (1), gravity enters into the formula through an $R_T^{-1/6}$ scaling of A_n. The interfacial slope is also given by an expression

similar to (1). We also have scaling information on the size of fluid velocities in different regions of the Bridgman apparatus.

While Brattkus & Davis[9] have analyzed a two dimensional version of this problem in the past, their results have been derived in the absence of a thermally insulated so called adiabatic zone, i.e. $z_{II} = z_0 = z_I$ in the notation of Fig. 1. Indeed, the effect of this insulation zone leads us to both important quantiative as well as qualitative differences with their results. In (1), the small scale components radial segregation and interfacial deformation, i.e. coefficients of $J_1(\lambda_n r)$ for large n, is exponentially quenched by factors of $e^{-\lambda_n(z_0 - z_I)}$. This quenching is absent without an insulation zone. Also, if the insulation zone thickness is comparable or much larger than the cylinder radius then an overwhelming part of the contribution in the summation in (1) and similar summation for the slope comes from the first term, implying that each of these quantities will have a $J_1(\lambda_1 r)$ radial dependence. In that case, the Coriell-Sererka hypothesis[10] on the proportionality of radial segregation and interfacial slope is approximately true, though the constant of proportionality is different from what they derived with no fluid motion. Further, in this case, a most interesting aspect of this result is the result that radial segregation and interfacial deformation can each be reduced very significantly by choosing $\delta_2 = \lambda_1 = 3.83$. Physically, the nondimensional parameter δ_2 is the logarithmic derivative of the horizontal heat loss with respect to z, evaluated in the limit of approaching $z = z_I$ from below. Recall that z is the vertical distance from the base of the cylinder scaled by the cylinder radius, while $z = z_I$ is the location of the lower edge of the insulation zone. Thus, to the extent these asymptotic results hold, we have a prediction on optimal growth condition.

We have also carried out some independent numerical verification of our analytic results. There was one point of concern to us – use of an unphysical no-stress boundary conditions at the cylinder side walls, rather than a no slip condition. Fortunately, numerical results[11] with no-stress and no-slip side wall conditions, so far obtained for the linearized 2-D problem, show that in the large thermal Rayleigh number regime, there is very little difference between the two with regards to our central results.

Further, the numerical results are found to be consistent with the asymptotic scaling relations, though precise quantitative comparison was not possible due to resolution difficulties at very large Rayleigh number. However, the optimal analytically predicted condition adapted to the 2-D geometry, $\delta_2 = \pi$, appears to hold quite well for moderately large thermal Rayleigh number, well within the limits of accurate computation. As δ_2 increases past this value, the interface shape changes from being concave to convex towards the melt.

b. Dendrite problem

In the large Peclet number limit, a system of nonlinear hyperbolic equations is found to describe[12] the temporal development of disturbances of some distinguished spatial scales and sizes; this develop "shock" in finite time when the lateral diffusion becomes important.

In the small Peclet number limit[13], the equations in the $O(1)$ region around the tip has been analyzed. Exact solutions describing both tip splitting and side branching have been found when surface tension effects are completely ignored (Figs. 2 and 3). These correspond to moving pole singularities of $z_\zeta(\zeta, t)$ in the unphysical region $Im\ \zeta < 0$. As these singularities move towards the real ζ axis without actually hitting it in finite time, we obtain the different stages of the evolution shown in the figures. Generally, it has been established that every initial singularity (not just poles) of z_ζ in $Im\ \zeta < 0$ has a component of motion towards the real domain. This result is analogous to what was obtained for the Hele-Shaw case[14]. For a class of initial conditions containing singularities that do not impinge $Im\ \zeta = 0$ in finite time, asymptotic analysis reveals that for a long time, the zero surface tension dynamics is the leading order behavior of the actual solution for small nonzero surface tension. However, these class of initial conditions

is a small subclass of the general class of initial conditions that will generically contain singularities and zeros of z_ζ that impinge the the real ζ axis in finite time, causing a cusp or a corner or some other singularity in the interfacial shape. Fig. 4 shows the effect of a zero impinging the real ζ axis at $\zeta = 0$. At about the time when singularities would have otherwise appeared on the interface, capillary effects have to be accounted for. The analytical and numerical evidence[15] obtained by performing an inner equation analysis for the related Hele-Shaw problem suggests that singularity formation is impeded by the effect of surface tension; however for isotropic surface tension, narrow structures formed by the approach of a complex singularity cannot settle down to a steady state; instead it appears to fatten out before tip splitting. This process regenerates itself as other singularities, initially further out in the complex plane approach the real ζ axis. However, with a nonconstant surface tension parameter d_0 modelling anisotropy with minimal surface tension axes aligned appropriately, a cusp or corner formation event for zero surface tension presages a rapid evolution over an inner scale for small but nonzero d_0. The inner solution settles to a local steady state with tip radius and velocity determined from a steady state dendrite theory[2,3]. The dendrite tip corresponds to only a small region on the real ζ axis which, unlike isotropic surface tension case, does not expand with time. Further approach of complex singularities towards the real ζ axis leads to side branching. Some features of our results have qualitative consistency with direct numerical simulation of anistropic Hele-Shaw dynamics[17] or that of a dendrite[18]. However, our perturbative approach gives essential scaling information that is difficult to establish otherwise.

REFERENCES

1. R. A. Brown, (1988), *AICHE J.* **34**, 881.
2. D. Kessler, J. Koplik & H. Levine, Advances in Physics, 37, 255 (1988).
3. P. Pelce, Dynamics of Curved Fronts, Academic Press, NY 1988.
4. W. Kurz & R. Trivedi, Acta Metall. Mater. 38, 1 (1990).
5. E. Coutsias & H. Segur, In "Asymptotics Beyond All orders", NATO ARW Proceedings (Ed. Segur et al), Plenum, 1991.
6. J.J. Xu, Phys. Rev. A, 43, 930 (1991).
7. S. Tanveer (1994), To appear in the Phys. Fluids A (June, '94).
8. S. Tanveer (1994), In preparation.
9. K. Brattkus & S.H. Davis, (1988), *Journal of Crystal Growth* **91**, 538-556.
10. S. R. Coriell, & R.F. Sererka, (1979), J.Crystal Growth 46, 479.
11. G. Koester, G.R. Baker (1994), In preparation.
12. M.R. Foster (1994), In preparation.
13. M. Kunka, M.R. Foster & S. Tanveer (1994), In preparation.
14. S. Tanveer, Phil. Trans. R. Soc. London A, 343, 155 (1993).
15. V. Hakim, M. Siegel & S. Tanveer (1994), In preparation.
16. R. Almgren, W.S. Dai & V. Hakim, Phys. Rev. Lett., 1994.

17. Saito, G. Goldbeckwood & H. Muller-Krumbaar, Phys. Rev. A 38, 2148 (1988),

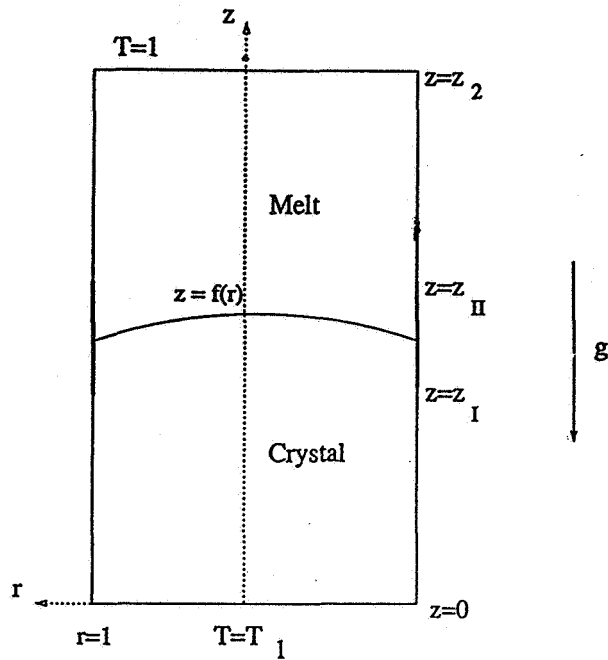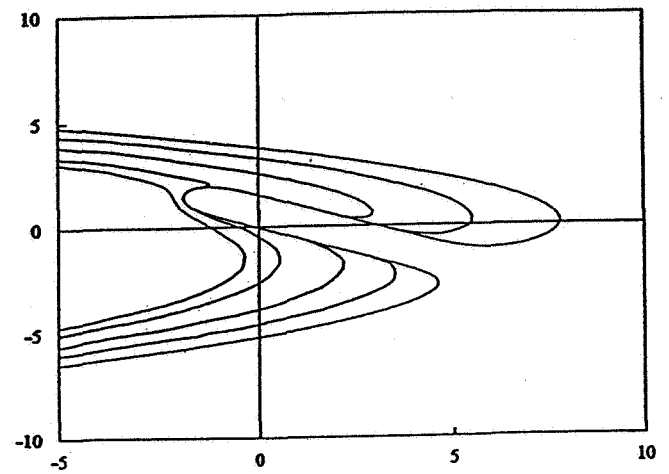Fig. 1: Sketch of Bridgman device
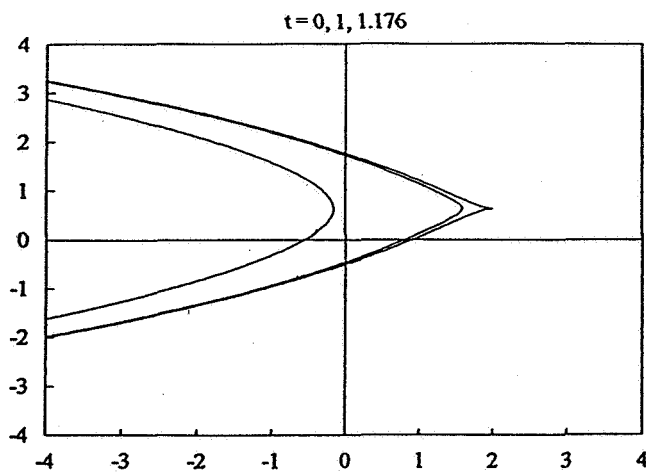

Fig. 2: Evolving tip splitting $d_0 = 0$ needle crystal

$t = 0, 1, 1.176$

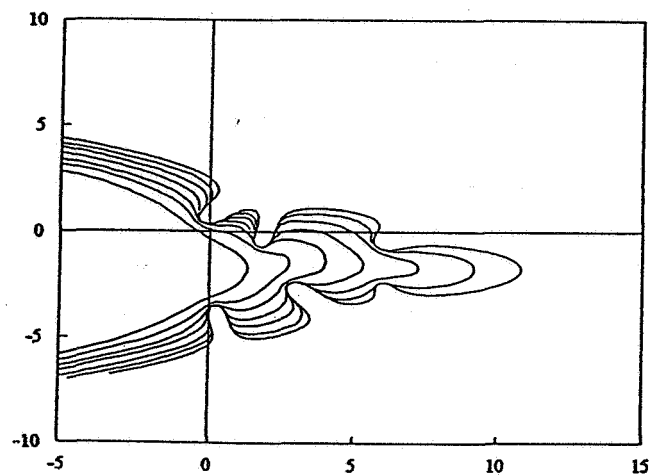Fig. 4: Cusp formation in $d_0 = 0$ evolution

Fig. 3: Evolving side branching $d_0 = 0$ needle crystal

192

INTERACTIONS BETWEEN SOLIDIFICATION AND COMPOSITIONAL CONVECTION IN MUSHY LAYERS

M. Grae Worster
Institute of Theoretical Geophysics
Department of Applied Mathematics and Theoretical Physics
Silver Street, Cambridge CB3 9EW, ENGLAND

INTRODUCTION

Mushy layers are ubiquitous during the solidification of alloys. They are regions of mixed phase wherein solid crystals are bathed in the melt from which they grew. The matrix of crystals forms a porous medium through which the melt can flow, driven either by external forces or by its own buoyancy in a gravitational field. Buoyancy-driven convection of the melt depends both on temperature gradients, which are necessary for solidification, and on compositional gradients, which are generated as certain components of the alloy are preferentially incorporated in the solid phase and the remaining components are expelled into the melt. In fully liquid regions, the combined action of temperature and concentration on the density of the liquid can cause various forms of double-diffusive convection. However, in the interior of mushy regions the temperature and concentration are thermodynamically coupled so only single-diffusive convection can occur. Typically, the effect of composition on the buoyancy of the melt is much greater than the effect of temperature, and thus convection in mushy layers is driven primarily by the compositional gradients within them.

It has long been recognized that compositional convection within mushy layers can become focused into narrow channels, called 'chimneys', which are identified as 'freckles' in completely solidified castings. Freckles destroy the structural and compositional uniformity of a casting, in most cases rendering the casting useless. There has consequently been much interest in determining the conditions under which chimneys will form during casting and in determining ways in which their formation might be suppressed.

Chimneys and the associated compositional convection have been observed in many laboratory experiments in which aqueous solutions of ammonium chloride were cooled and solidified from below [1–3], and freckles that are visually similar to the ammonium-chloride chimneys have been observed in experimental castings of lead–tin alloys solidified from below [4]. In both these systems, the light component of the alloy is rejected during solidification so that the interstitial melt in the mushy layer is less dense than the un-solidified melt above it and can therefore rise convectively out of the mushy layer.

The rising interstitial liquid is relatively dilute, having come from colder regions of the mushy layer, where the liquidus concentration is lower, and can dissolve the crystal matrix through which it flows. This is the fundamental process by which chimneys are formed. It is a nonlinear process that requires the convective velocities to be sufficiently large, so fully fledged chimneys might be avoided by means that weaken the flow. Better still would be to prevent convection altogether, since even weak convection will cause lateral, compositional inhomogeneities in castings. This report outlines three studies that examine the onset of convection within mushy layers.
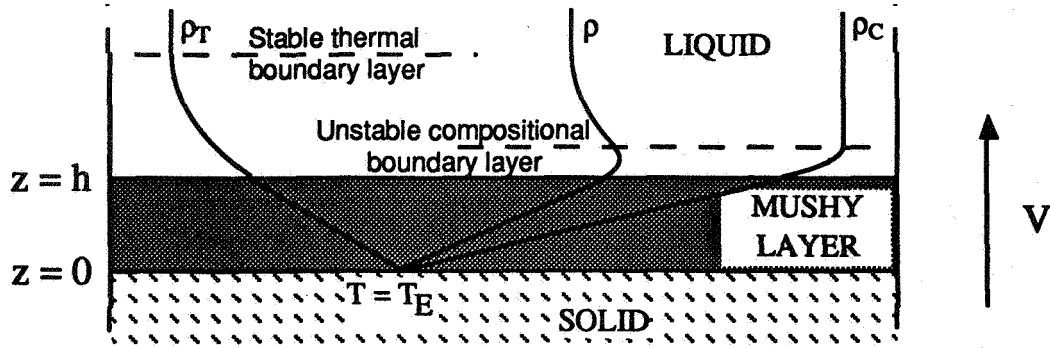
Figure 1. A schematic diagram showing the steady upwards solidification of an alloy at speed V. The steady density field ρ is indicated. It is the resultant of the density fields ρ_T due to the temperature gradient and ρ_C due to the compositional gradient.

LINEAR STABILITY ANALYSIS

A convenient system for mathematical analysis is one in which the alloy is solidifying at a constant rate V, as shown in figure 1. In a frame of reference moving at the solidification rate, governing equations for the mushy layer are

$$\left(\frac{\partial\theta}{\partial t} - \frac{\partial\theta}{\partial z}\right) + \mathbf{U}.\nabla\theta = \nabla^2\theta + S\left(\frac{\partial\phi}{\partial t} - \frac{\partial\phi}{\partial z}\right), \tag{1}$$

$$(1-\phi)\left(\frac{\partial\theta}{\partial t} - \frac{\partial\theta}{\partial z}\right) + \mathbf{U}.\nabla\theta = (\theta - \mathcal{C})\left(\frac{\partial\phi}{\partial t} - \frac{\partial\phi}{\partial z}\right), \tag{2}$$

$$\nabla.\mathbf{U} = 0, \tag{3}$$

$$\frac{\mathbf{U}}{\Pi(\phi)} = -R_m(\nabla p + \theta\hat{z}), \tag{4}$$

where

$$\theta = \frac{T - T_L(C_0)}{T_L(C_0) - T_E} = \frac{C - C_0}{C_0 - C_E}, \tag{5a, b}$$

represents both the temperature T and the concentration C in the mushy layer, ϕ is the solid fraction, and $\mathbf{U}$ is the fluid velocity. In these equations, lengths have been scaled with the thermal diffusion length $H = \kappa/V$, time with κ/V^2 and fluid velocities with V, where κ is the thermal diffusivity. These equations are augmented by the buoyancy-driven Navier-Stokes equations and diffusion-advection equations for heat and solute in the fully liquid region, as well as various boundary and interfacial conditions [5].

The important dimensionless parameters governing the evolution of mushy layers are the Stefan number S and a compositonal ratio $\mathcal{C}$, gvien by

$$S = \frac{L}{c(T_L(C_0) - T_E)} \quad \text{and} \quad \mathcal{C} = \frac{C_s - C_0}{C_0 - C_E}, \tag{6a, b}$$

where c and L are the specific heat and latent heat respectively,and a parameter θ_∞, which can be interpreted either as the dimensionless far-field temperature in the liquid or as the temperature gradient at the mush–liquid interface in the basic, steady state. Compositonal convection is determined principally by the Rayleigh numbers

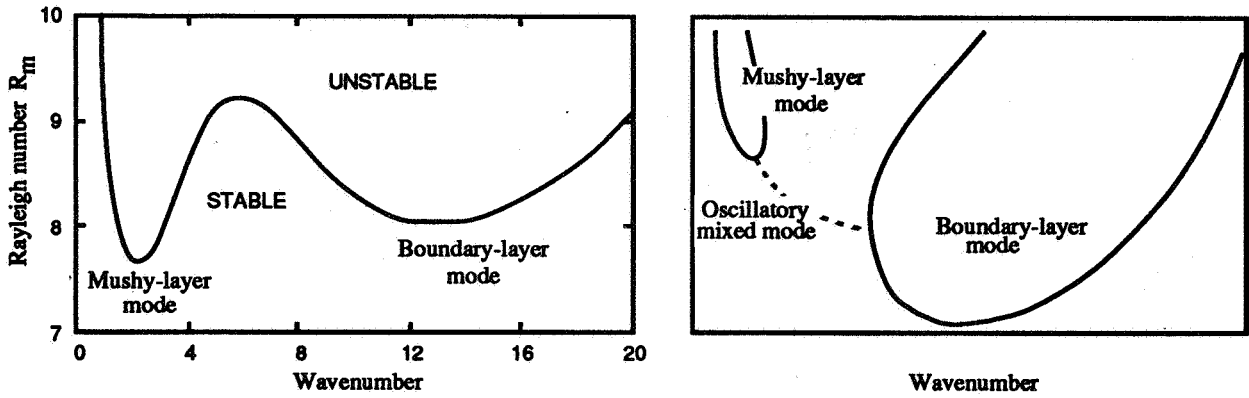$$R_m = \frac{\beta(C_0 - C_E)g\,\Pi^* H}{\kappa\nu}, \tag{7}$$

194

Figure 2. (a) A marginal stability curve for convection within and above a mushy layer [6] when the stabilizing thermal buoyancy is neglected. Parameter values were chosen so that the two modes of instability would occur at about the same Rayleigh number. Either mode can, in principle, be the most unstable. (b) A sketch of a typical marginal stability curve once thermal buoyancy is included in the analysis [8]. Parameter values are chosen such that the boundary-layer mode occurs well before the mushy-layer mode, which is the situation in most experiments.

which measures the strength of buoyancy relative to the resistance to flow in the mushy layer and $R_{\delta C} = \epsilon^3 \mathcal{H} R_m$, which is a compositional Rayleigh number based on the buoyancy and dimensions of a compositional boundary layer above and adjacent to the mush–liquid interface. The physical parameters entering these expressions are the solutal expansion coefficient β, the acceleration due to gravity g, the kinematic viscosity of the liquid ν and a characteristic permeability of the mushy layer Π^*. The dimensionless parameter $\epsilon = D/\kappa$, where D is the compositional diffusivity, is typically very small, while the mobility ratio $\mathcal{H} = H^2/\Pi^*$ is typically very large.

The governing equations have a steady solution with no flow [5–7]. The density field associated with this steady state is illustrated in figure 1. Most of the unstable buoyancy occurs within the mushy layer, where the fluid is relatively immobile. There is a thin, unstable compositional boundary layer above the mushy layer, where the fluid is relatively mobile. A linear stability analysis [6] shows that these two unstable regions give rise to two modes of compositonal convection: a mushy-layer mode and a boundary-layer mode (figure 2a). Either mode can in principle be the most unstable, though experimental evidence suggests that the boundary-layer mode usually occurs first. The linear-stability analysis has recently been extended [8] to include the stabilizing thermal buoyancy in the liquid region. The thermal buoyancy can cause the two steady modes to disconnect via an oscillatory mode of convection (figure 2b) that is presumably related to internal gravity waves in the stably-stratified liquid region. The stability of a transient basic state in which the mushy layer is growing away from a cooled boundary has also been analysed using a quasi-static approximation [9].

Influenced by experiments [10] in which chimneys were initiated by sucking fluid from the boundary layer with a pipette and by the experimental observation that convection emanating from the boundary layer usually preceeds chimneys, some argue that chimneys are caused by convection in the liquid region (i.e. the boundary-layer mode) eroding the layer from above. It is more plausible, in my opinion, that chimneys are formed by the mushy-layer mode of convection eroding the layer from within. However, since the boundary-layer mode is seen to occur first in experiments, it is important to investigate what influence this mode has on the mushy layer and to ask whether the stability analysis of a quiescent state has any relevance to chimney-forming convection in the mushy layer.

The boundary-layer mode of convection has characteristic length scales that are much smaller than the overall dimensions of the mushy layer and the characteristic length scale of the mushy-layer mode. Emms & Fowler [9] exploited this fact and homogenized a model of fully developed convection above the mushy layer to determine spatially averaged boundary conditions at the mush–liquid interface. One of the results of their analysis is that pre-existing convection above the mushy layer has little influence on the onset of convection within the mushy layer. However, as described in the next section, the story is different once non-equilibrium effects are taken into account.

INTERFACIAL UNDERCOOLING

The temperature of solidifying phase boundaries is below the equilibrium freezing (liquidus) temperature. Further undercooling at a mush–liquid interface is caused by the curvature of the dendrite tips and constitutional effects associated with the compositional boundary layer. Usually such departures from equilibrium are small and can safely be neglected in macroscopic models of alloy solidification. However, it has been shown that interfacial undercooling can have large, global consequences when coupled with convection of the liquid region [11].

Huppert & Hallworth [12] conducted experiments in which they observed that the occurence of chimneys in ammonium-chloride mushy layers could be delayed by the addition of small quantites of copper sulphate to the solution. In an attempt to explain these observations, Worster & Kerr [13] measured the undercooling at the mush–liquid interface in similar experiments. They found that the level of undercooling increased with the rate of solidification and with the level of contamination by copper sulphate. They incorporated this empirical information into a macroscopic model of the solidifying system in which the liquid region is assumed to be convecting vigorously (the boundary-layer mode) while the mushy layer is stagnant.

In accord with the experimental results [12], the mathematical model [13] predicts that, as the level of interfacial undercooling increases, the mushy layer grows more slowly, the solid fraction of the mushy layer increases and the composition of the liquid region evolves more rapidly. These are all consequences of the fact that the strength of compositional convection in the liquid region increases as the level of undercooling increases. The resultant increase in solute flux causes the solid fraction to increase and the liquid region to evolve more rapidly. The increase in heat flux and the increase in release of latent heat cause the mushy layer to grow more slowly. These three effects all combine to cause the Rayleigh number associated with the mushy layer to increase more slowly, and can cause the Rayleigh number eventually to decrease (figure 3a). The appropriate Rayleigh number is given in (7), with H being the height of the mushy layer, $C_0 - C_E$ being replaced by the compositional difference across the mushy layer, and with Π^* being evaluated in terms of the mean solid fraction according to an expression for a regular array of cylinders [3].

The height of the mushy layer when the Rayleigh number is predicted to have reached various fixed values is shown in figure 3b. On the same figure, data [12] of the heights of the mushy layer when chimneys were first observed are shown. Comparison between the data and the theoretical predictions lends some support to the idea that chimneys occur once a critical Rayleigh number (*for the mushy layer mode*) is exceeded and that compositional convection in the liquid region, in concert with interfacial undercooling, can significantly alter the propensity of the mushy layer to form chimneys.
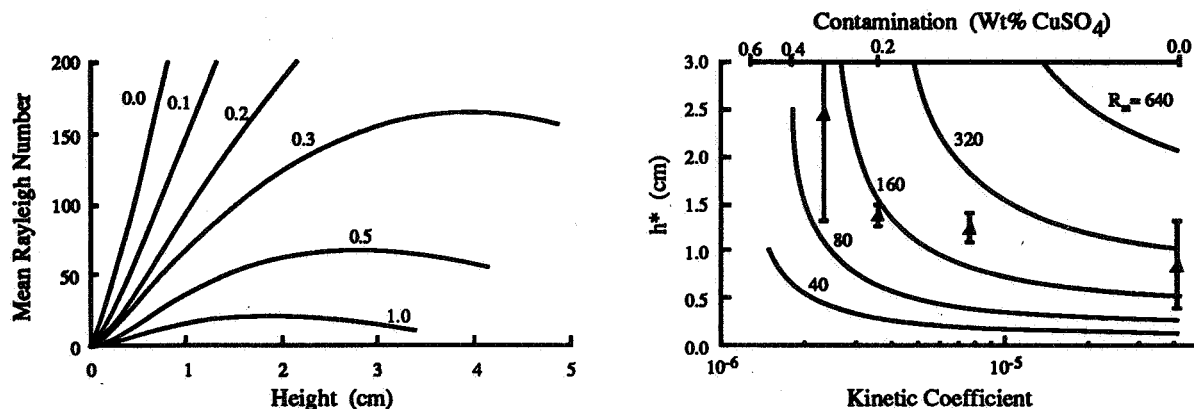
Figure 3. (a) Predicted values of the mean Rayleigh number of the mushy layer as functions of the depth of the layer, as it evolves while vigorous compositional convection driven by interfacial undercooling occurs in the liquid region. The numbers on the curves correspond to different levels of undercooling. The Rayleigh number reaches a maximum, which decreases as the level of undercooling increases. (b) The critical height at which given values of the Rayleigh number (indicated by the numbers on the curves) are first reached as function of the kinetic coefficient, which measures the level of undercooling.

NONLINEAR BIFURCATIONS

Linear stability analyses determine the critical Rayleigh number R_c above which the solidifying system is unstable to infinitesimal disturbances. However, it has long been suspected that the bifurcation from quiescent to convecting states is sub-critical, i.e. that steady convecting states (perhaps giving rise to chimneys) exist at Rayleigh numbers less than R_c. In this case, linear stability analyses may give inadequate indication of the conditions required to avoid chimney-forming convection.

This suspicion was confirmed using a small-amplitude analysis of the mushy-layer mode of convection [14]. Use was made of a 'near-eutectic' approximation of the governing equations [15] which is achieved in the asymptotic limit $C \to \infty$, $\theta_\infty \to \infty$, with $C/\theta_\infty = O(1)$. Effects of latent heat can be additionally retained in the analysis if the distinguished limit $S/C = O(1)$ is taken [9]. This limit reduces the equations for a mushy layer to those of a non-reacting porous medium of constant permeability. Effects fundamental to the character of mushy layers, namely the coupling between the temperature and concentration, and the dependence of permeability on the solid fraction, can then be introduced as perturbations to the simpler system.

It was discovered [14] that the bifurcation to convective rolls could be either super-critical (as shown in figure 4a) or sub-critical depending on the magnitude of $d\Pi/d\phi$, and that the bifurcation to convection with a hexagonal planform is trans-critical, with the backward branch corresponding to upflow in the centres of the hexagons. The form of the trans-criticality that was found is due to nonlinear perturbations to the permeability of the mushy layer.

Trans-critical hexagonal convection may also result from asymmetries of the basic-state density field and solid fraction. These effects may cause the backward branch of the trans-critical bifurcation to correspond to downflow in the centres of the hexagons (figure 4b), in agreement with experimental observations [16]. If this is the case, then a judicious choice of control parameters may eliminate the backwards branch altogether and render the system globally more stable to chimney-forming convection. An analysis of this extended system, including the determination of
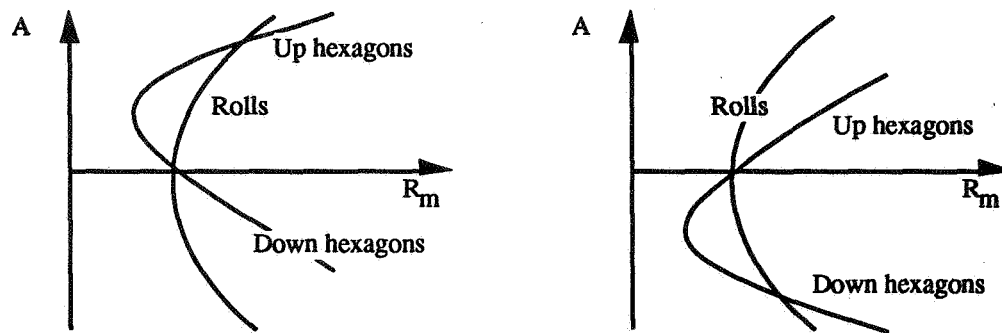
197

Figure 4. Schematic, nonlinear bifurcation diagrams showing the amplitude of steady, convecting states as functions of the Rayleigh number. (a) Trans-critical bifurcation to hexagons, with the backward branch corresponding to upflow in their centres, has been found by [14] as a consequence of nonlinear perturbations to the permeability of the mushy layer. (b) Asymmetries in the quiescent state may lead to the backward branch corresponding to downflow in the centres of the hexagons.

the stability characteristics of the nonlinear solutions is currently being undertaken.

CONCLUSIONS

Linear stability analyses indicate that there are two modes of compositional convection that can occur during the solidification of a binary alloy from below: a boundary-layer mode of very short wavelength compared with the depth of the mushy layer; and a mushy-layer mode that is most likely to be responsible for the formation of chimneys. Vigorous convection in the liquid region (originating as the boundary-layer mode) can couple with interfacial undercooling at the mush-liquid interface and reduce the liklihood of chimneys forming in the mushy layer. A nonlinear analysis of convection interior to a mushy layer, currently under way, promises to yield conditions under which the solidifying system is globally more stable to the formation of chimneys.

REFERENCES

1. Copley, S.M., Giamei, A.F., Johnson, S.M. & Hornbecker, M.F. (1970) *IMA J. Appl. Maths* **35**, 159–174.
2. Chen, F. & Chen, C.F. (1991) *J. Fluid Mech.* **227** 567–586.
3. Tait, S. & Jaupart, C. (1992) *J. Geophys. Res.* **97**(B5) 6735–6756.
4. Sample, A.K. & Hellawell, A. (1984) *Metallurgical Transactions A* **15A**, 2163–2173.
5. Worster, M.G. (1991) *J. Fluid Mech.* **224**, 335–359.
6. Worster, M.G. (1992) *J. Fluid Mech.* **237**, 649–669.
7. Hills, R.N., Loper, D.E. & Roberts, P.H. (1983) *Q. J. Mech. Appl. Maths* **36**, 505–539.
8. Chen, F., Lu, J.W. & Yang, T.L. (1994) *J. Fluid Mech.* (in press).
9. Emms, P. & Fowler, A.C. (1993) *J. Fluid Mech.* **262**, 111–139.
10. Hellawell, A. (1987) In *Structure and Dynamics of Partially Solidified Systems* (ed. D.E. Loper), pp. 3–22. NATO ASI Series. Martinus Nijhoff.
11. Kerr, R.C., Woods, A.W., Worster, M.G. & Huppert, H.E. (1990a) *Nature* **340**, 357–362.
12. Huppert, H.E. & Hallworth, M.A. (1993) *J. Cryst. Growth* **130**, 495–506.
13. Worster, M.G. & Kerr, R.C. (1994) *J. Fluid Mech.* **269**, 23–44.
14. Amberg, G. & Homsy, G.M. (1993) *J. Fluid Mech.* **252**, 79–98.
15. Fowler, A.C. (1985) *IMA J. Appl. Maths* **35**, 159–174.
16. Tait, S., Jahrling & Jaupart, C. (1992) *Nature* **359**, 406–359.

Phase Transitions

TURBIDITY OF A BINARY FLUID MIXTURE: DETERMINING η

Donald T. Jacobs
Physics Department
The College of Wooster
Wooster, Ohio 44691

ABSTRACT

A ground based (1-g) experiment is in progress that will measure the turbidity of a density-matched, binary fluid mixture extremely close to the critical point. By covering the range of reduced temperatures $t \equiv (T\text{-}T_c) / T_c$ from 10^{-8} to 10^{-2}, the turbidity measurements will allow the critical exponent η to be determined. No experiment has determined a value of the critical exponent η, yet its value is significant to theorists in critical phenomena. Interpreting the turbidity correctly is important if future NASA flight experiments use turbidity as an indirect measurement of relative temperature in shuttle experiments on critical phenomena in fluids.

INTRODUCTION

Although critical phenomena have been investigated for 100 years, it has only been in the last 20 years that comprehensive, quantitative models have begun to appear.[1,2] These models provided a framework for the observations made on a multitude of physical systems which had similar behavior near a critical point. The numerous theoretical extensions and experimental verifications which followed have provided a wealth of information but by no means has the understanding of critical points become complete. Numerous predictions remain untested or inadequately confirmed. One significant exponent prediction has still eluded experimental verification: the value of Fisher's "elusive exponent η", which was predicted in order to explain light scattering measurements at small angles. An enhanced experimental technique is described that determines a value for η by measuring the total light being scattered (called the turbidity), in a density matched, binary fluid mixture of methanol and cyclohexane. In addition, the experiment will provide an important ground-based control for one aspect of an experiment on a recent shuttle mission: the ZENO project.

Since the correlation length is very large near the critical point compared to the molecular size, the behavior of a system is not determined by the type of gas but by its critical properties. It is these critical properties that have universal descriptors. For example, the correlation length ξ diverges close to the critical point as a power law $\xi = \xi_0 t^{-\nu}$ where $t \equiv (T - T_c)/T_c$, ξ_0 is the amplitude describing the correlation length far from the critical temperature T_c, and ν is a universal critical exponent ($\nu \simeq 0.64$). Not only will the critical exponents be the same for all gases near their critical point but also for many other thermodynamic systems that have a critical point (second-order phase transition). One example is a binary fluid mixture–two components which are partially miscible below a certain temperature and completely miscible above.

The development of renormalization group theory from earlier concepts of scaling and universality provided a theoretical framework for distinguishing systems, predicting critical exponent relations, approximating values for critical exponents, and obtaining amplitude relations. The current consensus is that liquid–gas systems, ferromagnets, and binary liquid mixtures all

belong to the same universality class—n=1 (spin dimension), d=3 (spatial dimension) which corresponds to the three-dimensional Ising model. Despite this dramatic success, there are still fundamental gaps in our knowledge of these systems. The critical exponent η has a small predicted value ($\eta \approx 0.03$) which has made its measurement extremely difficult. It is one of the last exponents to lack direct experimental verification.

PREVIOUS WORK

Michael Fisher[3] first proposed the critical exponent η to describe how the correlation function behaves at T_c. Recent field theoretic analysis and partial differential approximants give the following values for γ, ν and η:

γ	ν	η	Source
1.238 ± 0.003	0.631 ± 0.003	0.038 ± 0.014	Nickel[4]
1.241 ± 0.002	0.630 ± 0.0015	0.031 ± 0.004	LeGuillou and Zinn-Justin[5]
1.2378 ± 0.0006	0.6312 ± 0.0003	0.0375 ± 0.0005	George and Rehr[6]

In the words of George and Rehr, who used partial differential approximants, "η ... show(s) significant discrepancies with respect to the field-theoretic results" of reference 5.

While the theoretical predictions may not agree within their quoted uncertainty, the experimental situation is even less well-known. Three principal techniques have been used to look for η and they all involve scattering phenomena using either x-rays, neutrons, or light. Tracy and McCoy examined the experimental results before 1975 and concluded[7] that "no experiment to date unambiguously and directly establishes that the critical exponent η is greater than zero." At the same time, Cannell[8] published a measurement of SF_6 which found $\eta = 0.03 \pm 0.03$. A high precision, angular light scattering experiment on the liquid mixture 3-methylpentane and nitroethane concluded[9] that $\eta = 0.017 \pm 0.015$; "we cannot prove on the basis of the experimental data alone that η must be finite." Even the most recent x-ray scattering measurement,[10] done on the liquid mixture perfluoromethylcyclohexane and n-heptane finds $\eta = 0.03 \pm 0.03$. Turbidity measurements[11] have without exception assumed $\eta = 0$ because data could not be taken sufficiently close to the critical point to warrant inclusion.

TURBIDITY

A binary fluid mixture exhibiting an upper consolute point will be one phase, homogeneous, and essentially clear when the mixture is well above its critical consolute temperature T_c. The constant transmitted light intensity at these temperatures is referred to as I_0. As the temperature of the fluids approaches T_c, concentration fluctuations, "droplets," begin to form and cause the transmitted light intensity I to be reduced. The total incremental intensity of light scattered per unit length is defined as the turbidity τ. The turbidity is dependent upon the transmitted light intensities I and I_0 by

$$\tau = L^{-1} \ln(I_0 / I)$$

where L is the optical path length. The turbidity is related to critical phenomena by assuming Ornstein-Zernike scattering[12,13] and has different forms if η is or is not zero. The effect of η can

best be illustrated by a plot of turbidity τ versus reduced temperature t (see Figure 1). Having $\eta \neq 0$ is expected to result in lower turbidity values at small reduced temperatures (close to the critical point), but identical turbidity values as when $\eta = 0$ when at large reduced temperatures. An advantage of measuring the turbidity is that all three critical exponents ν, γ and η appear explicitly in the theoretical expressions. While the scaling relation $\gamma = (2 - \eta)\nu$ can be invoked to reduce the number of adjustable parameters needed to fit the data, it does not have to be and some of the analysis will be devoted to determining all three exponents.

EXPERIMENT

The binary fluid mixture to be measured in this experiment is methanol and cyclohexane. These fluids combine similar densities ($\Delta\rho/\bar{\rho} = 0.016$) which minimizes the effect of gravity, with quite different refractive indices which allows significant light scattering near the critical point. This system has also been studied extensively with published measurements of the turbidity, viscosity, surface wetting, dynamic light scattering, coexistence curve, and excess molar volume. The critical composition is 29.0% by weight methanol with a critical temperature of about 45°C, depending on the amount of water present.

The thermostat is an onion-layer design with low thermal mass stages for (relatively) fast changes in temperature. When properly controlled, such an enclosure is capable of maintaining temperatures to within ± 10 μK at room temperatures ($t \approx 3 \times 10^{-8}$). The temperature is sensed by stable, calibrated Thermometrics thermistors. Each stage will be controlled with a thermistor and heater allowing a feed-back network using external electronics. The outer stages can use a digital control network where the resistance of each thermistor is measured by a precision digital voltmeter and reported to a computer which determines the correct voltage to be applied to that stage's heater. The cell will be controlled using an AC bridge with a lock-in amplifier as a null-detector coupled to a PID controller in order to achieve the desired precision in temperature control ($t \sim 10^{-8}$).

The cell design is a cylindrical cell with BK-7 optical windows enclosing the fluid mixture, which is sealed with Kalrez o-rings. The optical path length would be a fixed value of 2.0 mm. This length would allow adequate resolution at $t \sim 10^{-3}$ yet also give good resolution at small reduced temperatures ($t \sim 10^{-8}$).

The turbidity is determined from the transmitted light intensity I when the fluids are close to T_c compared to the transmitted intensity I_0 when the fluids are well into the one-phase region.

To obtain η, we use an optical system capable of measuring the turbidity with a resolution that can distinguish between the various theoretical predictions. With the small path length cell, the most stringent measurements will be at temperatures far from the critical temperature where the light scattering is weak. The ($\pm 2\%$) fluctuations in a 3mW, polarized HeNe laser is reduced by passing the beam through a laser power amplitude stabilizer before being split with one part passing through the fluids and the other part traveling around the thermostat to provide a reference intensity. A light chopper is used to sample the two beams at different frequencies. The light not scattered from the fluids in the cell passes through a pinhole before the beams are directed through a diffuser and a 632.8nm bandpass filter before striking photodiode detectors. The voltages are measured using lock-in amplifiers tuned to the chopper frequencies. The thermostat, laser, power controller, and photodetector are placed on an optical table to minimize vibration and noise. Fig. 2 illustrates the optical system.

The interfacing software (writen in LabVIEW) accesses the instruments via a GPIB and allows the computer to set the lock-in amplifiers and then measure the light intensities and room temperature over long periods of time. Early problems with room temperature drift and vibration of the light intensity have been solved and the stability of the intensity ratio of the two beams is less than 0.1% over a long period of time (40 hours as shown in Fig. 3). This stability and resolution are quite adequate for the turbidity measurement in progress.

CONCLUSION

This turbidity experiment should provide the best determination of the exponents ν, γ and η, and amplitudes ξ_0 and χ_0. This research will be the investigation of the critical exponent η, on whose value the theorists cannot agree, and whose effect the experimentalists have been unable to definitively detect. The experiment outlined should provide the first evidence of a non-zero η and perhaps resolve which theoretical value is correct. This experiment also provides a good proving ground for the acquisition and analysis of turbidity data similar to that obtained in the shuttle experiment ZENO. Finally, a rigorous understanding of the turbidity very close to the critical point may allow its use as a temperature probe in future shuttle experiments on near-critical fluids, or at the very least, as a definitive indicator of the critical point.

REFERENCES

1 . S. C. Greer, *Acc. Chem. Res.* 11, 427 (1978); G. Ahlers, *Rev. Mod. Phys.* 52, 489 (1981).

2 . S.C. Greer and M.R. Moldover, *Ann. Rev. Phys. Chem.* 32, 233 (1981); A. Kumar, H.R. Krishnamur, and E.S.R. Gopal, *Phys. Rep.* (Netherlands) 98, 57 (1983).

3. M.E. Fisher, *J. Math. Phys.* 5, 944 (1964).

4. B.G. Nickel in *Phase Transitions-Cargese 1980*, ed. by M. Levy, J.C. LeGuillou, and J. Zinn-Justin (Plenum, New York, 1981), p. 291.

5. J.C. LeGuillou and J. Zinn-Justin, *Phys. Rev. B* 21, 3976 (1980).

6. M.J. George and J.J. Rehr, *Phys. Rev. Lett.* 53, 2063 (1984).

7. C.A. Tracy and B.M. McCoy, *Phys. Rev. B* 12, 368 (1975).

8. D.S. Cannell, *Phys. Rev. A* 12, 225 (1975).

9. R.F. Chang, H. Burstyn, and J.V. Sengers, *Phys. Rev. A* 19, 866 (1979).

10. Y. Izumi, *Phys. Rev. A* 39, 5826 (1989)

11. D.T. Jacobs, *Phys. Rev. A* 33, 2605 (1986); R.B. Kopelman, R.W. Gammon, and M.R. Moldover, *Phys. Rev. A* 29, 2048 (1984); C. Houessou *et al.*, *Phys. Rev. A* 32, 1818 (1985)

12. V.G. Puglielli and N.C. Ford, Jr., *Phys. Rev. Lett.* 25, 243 (1970).

13. P. Calmettes, I. Lagues, and C. Laj, *Phys. Rev. Lett.* 28, 478 (1972).
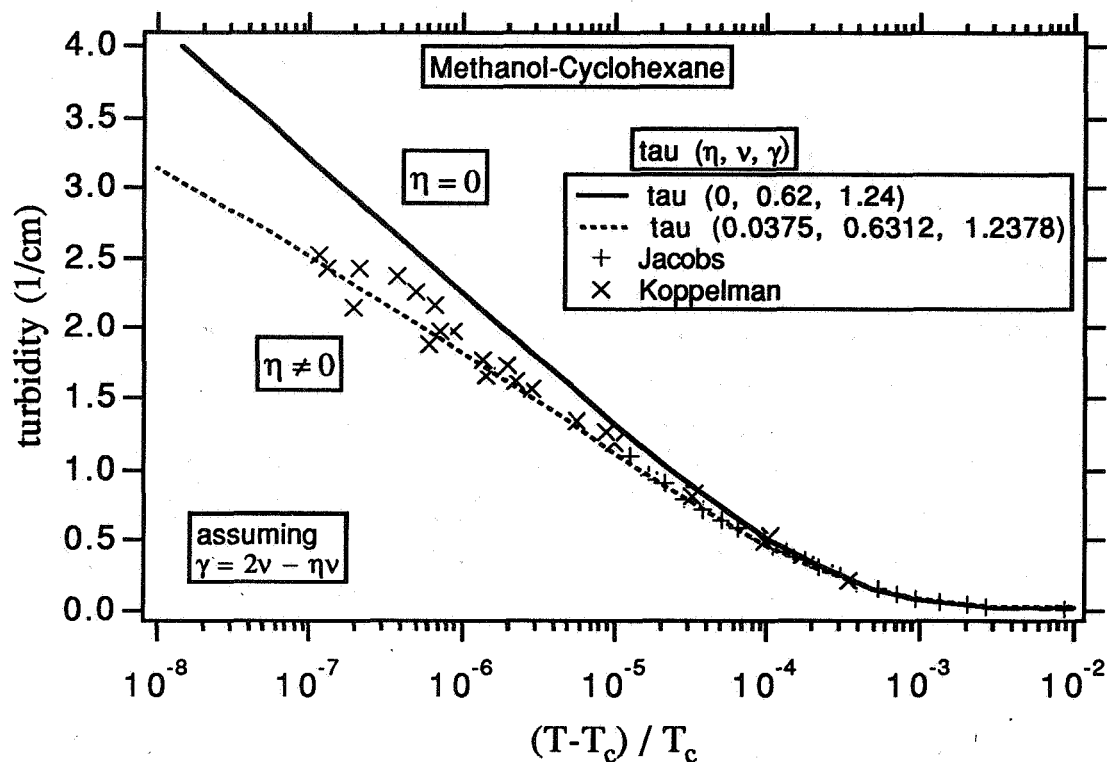
Fig. 1. Theory and published data for the turbidity of Methanol-Cyclohexane. The upper (solid) line is the theoretical curve when the critical exponent $\eta = 0$, while the lower (dashed) curve assumes it is 0.0375. The data are from reference 11 and are more consistent with $\eta \neq 0$, but a value of η can not be determined from the existing data.
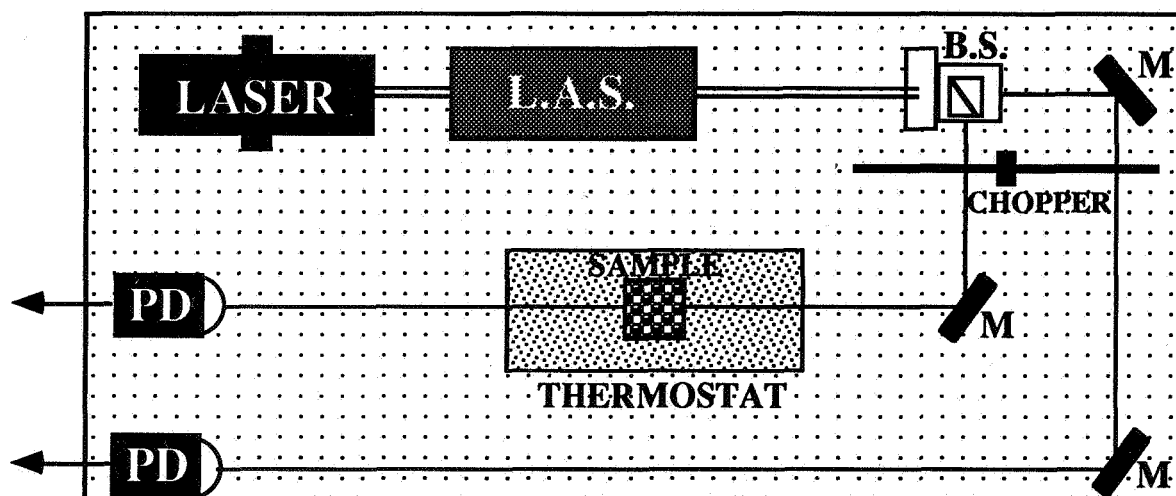
Fig. 2. Optical schematic. The laser beam passes through a laser amplitude stabilizer (L.A.S.) before striking the beamsplitter (B.S.). Each beam is chopped at a different frequency. The photodiodes (PD) detect the light and provide a signal to lock-in amplifiers whose reference frequency is locked to the chopper.

Fig. 3. Measured ratio of laser.light intensities through air using photodiodes and lockin-amplifiers when the two beams of Fig. 2 are chopped. This demonstrates the techniques' stability and resolution.

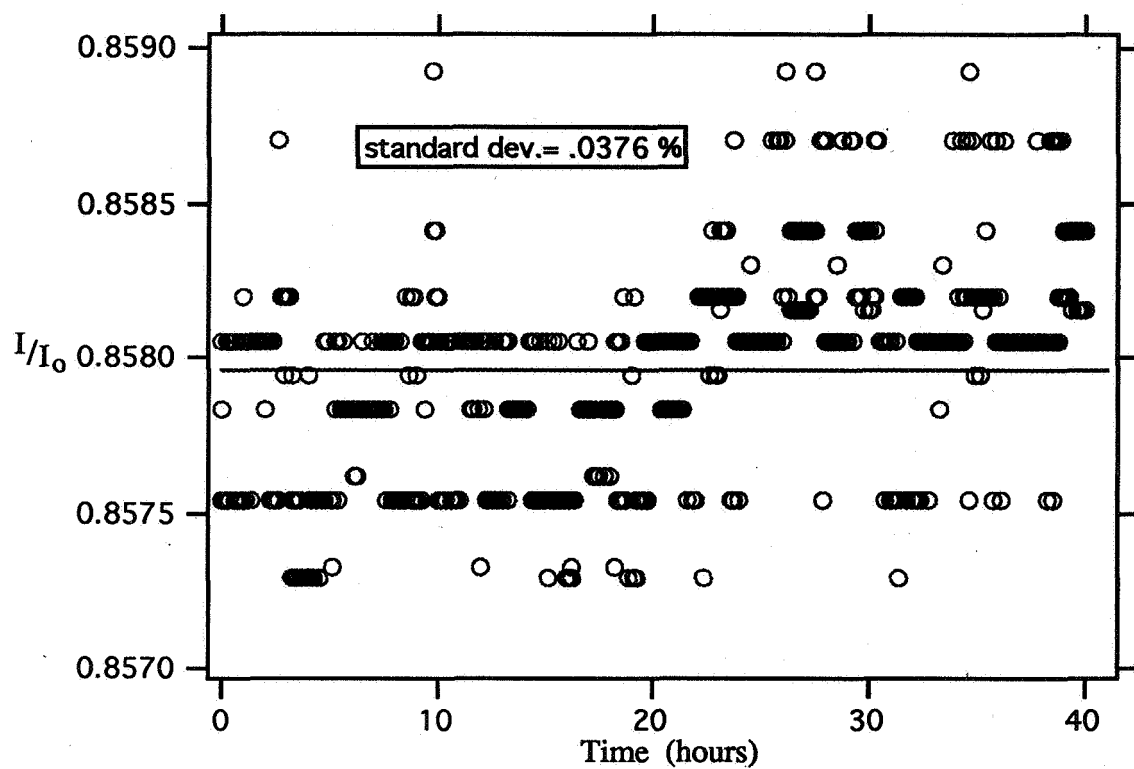# A COARSE GRAINED APPROACH TO THERMOCAPILLARITY EFFECTS IN BINARY SYSTEMS

Jorge Llambías, Aritomo Shinozaki and David Jasnow
Department of Physics and Astronomy
University of Pittsburgh
Pittsburgh, PA 15260

ABSTRACT

An coarse-grained approach to thermocapillarity effects in binary fluid systems is discussed along with example numerical results.

1. INTRODUCTION

Coarse grained models have played an important role in developing a theoretical understanding of a variety of dynamical phenomena. Particularly important examples include the elucidation of universality classes in critical dynamics [1], developments in nucleation theory [2], and the kinetics of phase separation and spinodal decomposition [3]. There has been considerable success in developing "minimal" models which correctly predict the essential, universal features of a variety of non-equilibrium growth processes while at the same time exhibiting computational efficiency. A particularly successful example is the modeling of the coarsening during microphase separation in diblock copolymer melts. [4]

There are many problems in which the interest is in phenomena occurring on length scales from the correlation length on up to "macroscopic" scales. The coarse grained approach is ideally suited for this, and can be supplemented by, for example, molecular dynamics for dealing with phenomena on shorter scales.

In this brief paper we present a coarse grained model for the study of a variety of thermocapillarity effects in binary systems which should provide a correct description even far from equilibrium, e.g., for deep quenches such as one considers in typical spinodal decomposition phase separation experiments. As examples we show preliminary results of numerical integrations of the appropriate dynamical equations for phase separation in a temperature gradient, both in a "solid" and liquid system and with the temperature either as a passively imposed or fluctuating field. We comment on the new features introduced by the temperature variations in comparison to the related isothermal phenomena.

2. OVERVIEW

The full problem of interest contains the essential features of a binary system over a range of parameters which allows both miscibility and phase coexistence. Here we consider the case of a conserved order parameter (such as the concentration of one of the species) coupling to a conserved energy density as well as to the fluid velocity field. The basic ideas at the macroscopic level are discussed, for example, by Landau and Lifshitz [5]. At an appropriate point features of a coarse grained free energy are introduced which then specifies the model.

Our general aim is to express the equations of motion for a phase separating, two component fluid. The new ingredient for a binary system is the (conserved) order parameter ϕ, corresponding to the concentration, and its associated chemical potential, μ. Along with a conservation equation

for the total density there is an additional conservation

$$\rho \left(\frac{\partial \phi}{\partial t} + \mathbf{v} \cdot \vec{\nabla} \phi \right) = -\vec{\nabla} \cdot \mathbf{j}_c \tag{1}$$

where $\mathbf{j}_c$ is an as yet undetermined concentration flux. As discussed below, the specifics of the coarse grained modeling will determine $\mathbf{j}_c$. The "mode-coupling" advective term in Eq. (1) represents an important coupling in the studies of critical dynamics.

The energy and entropy equations, which are developed in detail in Ref. [5], require a heat current, also to be specified. For the energy equation one may introduce an enthalpy $w(s, p, \phi)$ with s and p the entropy and the pressure, and

$$dw = T ds + (1/\rho) dp + \mu d\phi \quad , \tag{2}$$

leading to

$$\vec{\nabla} p = \rho \vec{\nabla} w - \rho T \vec{\nabla} s - \rho \mu \vec{\nabla} \phi \quad . \tag{3}$$

This is an important equation since it contains the corresponding mode coupling between concentration fluctuations and the velocity field. Since $\vec{\nabla} p$ enters the Navier-Stokes equation, one finds the additional driving force for velocity field, $\mu \vec{\nabla} \phi$.

Details of the thermodynamic analysis are standard, and the reader may refer to Ref. [5]. In particular, the energy or entropy equation is turned into an equation for the temperature field via $ds = \frac{\partial s}{\partial T} dT + \frac{\partial s}{\partial \phi} d\phi$ and using the equation of motion for ϕ [5].

We point out here a few features relevant to the specific models which follow. The entropy production, as discussed in Ref. [5] can be made positive using the constitutive equations for concentration and heat currents

$$\mathbf{j}_c = -\alpha \vec{\nabla} \mu - \beta \vec{\nabla} T \tag{4}$$

$$\mathbf{j}_q = (\mu + \beta T / \alpha) \mathbf{j}_c - \kappa \vec{\nabla} T \quad , \tag{5}$$

if κ, $\alpha > 0$. The kinetic coefficient β, related to the Soret effect, can play a role in the ensuing dynamics.

Within this approach there remains the question of specifying the thermodynamic functions. In particular one must specify the chemical potential to describe the system and obtain the relevant currents. It is here that the particular choice of coarse grained free energy is made. Note that the interesting behavior resides in the dynamics of the order parameter ϕ and that the total density can be taken as constant. Hence, one can effectively ignore any density fluctuations and consider the fluid as incompressible. In doing so, the pressure gradient entering the Navier-Stokes equation as in Eq. (3), introduces the enthalpy, which will essentially be determined as part of the solution to guarantee incompressibility.

For our purposes here it is sufficient to specify a free energy density of the form [6]

$$F(\phi, T) = f(\phi, T) + \frac{1}{2} R^2 (\vec{\nabla} \phi)^2 \tag{6}$$

where $f(\phi, T)$ represents the local free energy. The parameter R is taken as a constant, but the phenomenology certainly admits functional dependence on ϕ and T. The chemical potential, energy density and entropy all follow, closing the equations.

3. EXAMPLES

We turn now to some applications of the general system of equations, beginning first with simplifications.

(i) Conserved order parameter with temperature gradient

There are thermocapillarity effects, or, perhaps more precisely, effects driven by the interfacial free energy, even in the absence of velocity fields, i.e., in purely diffusive systems. One may think of phase separation in a "solid" or an extremely viscous fluid. Furthermore one may imagine heat diffusion to be much more rapid than concentration diffusion. The model considered corresponds in the critical dynamics context to Model B [1] in the presence of an imposed temperature gradient. This is interesting in that the model is the usually accepted one to describe phase separation, but the coupling of the temperature field to the order parameter is very weak if the two phases are made symmetric. One takes the local free energy of the form $f(\phi, T) = \frac{1}{2}r(T)\phi^2 + \frac{1}{4}u\phi^4$ leading to the chemical potential of the form

$$\mu = -R^2\nabla^2\phi + r(T)\phi + u\phi^3 \tag{7}$$

where $r(T) = r_1(T/T_0 - 1)$. Here T_0 is a reference temperature (playing the role of the value at criticality), and r_1 and u are positive constants. The phase boundary in this symmetric model lies at $\mu = 0$. An additional term on the right of Eq. (7) can be added to introduce a latent heat, which will become more important when temperature is included as an active, fluctuating variable. This model reasonably describes a binary system; there are coexisting phases at sufficiently low temperature, and the surface tension is naturally a function of temperature, vanishing in this mean field model as $|T - T_0|^{3/2}$ as $T \to T_0-$. Considerable effort has gone into studying phase separation kinetics and domain growth starting typically from a high temperature configuration and quenching to a uniform temperature below T_0. [3]

Since it is being assumed that thermal conductivity is relatively large, we impose a constant temperature gradient $T = T_l(1 + \gamma x)$ where x measures distance from one side of the sample and $T_l = T(x = 0) < T_0$. The dynamics of the model are then described in suitably dimensionless form by the system

$$\frac{\partial \phi}{\partial t} = \nabla^2 \mu \tag{8}$$

$$\mu = -\nabla^2\phi - (1 - \gamma x)\phi + \phi^3 \tag{9}$$

In this equation we have neglected the potential dependence of the kinetic coefficient, α, on the order parameter, which dependence is important in studying driven diffusive systems. [7] This point will be reconsidered elsewhere.

Simulations of the system (9) are carried out with large space and time steps which nonetheless are sufficient to reveal the essential features. We have studied the dynamics of phase separation in two dimensions. As noted, temperature couples weakly to this process, favoring neither phase. For example, the asymptotic domain growth exponent is not changed by changing the quench temperature of a homogeneous system, but the amplitude of the growth law is modified. Hence it is important to know whether in a temperature gradient one merely observes ordinary phase separation in each temperature "slice." As will be reported in more detail elsewhere, the temperature gradient induces an anisotropy in the system, with characteristic lengths along the gradient growing more slowly than perpendicular to the gradient. This is an effect of the transport current in the phase separating system.

The system has been specifically chosen to be completely symmetric in the two bulk phases. In a temperature gradient, motion of a domain (or bubble) of one phase in the background of the other is due to the contribution to the free energy of the domain walls, which is temperature-dependent. The total free energy is reduced when the domain drifts to the high temperature side. However, recall that the only dynamics included in the model so far are those of order parameter diffusion, hence the process can be quite slow. Sample motion of a droplet is shown in Fig. 1. By considering slab geometry, which should yield the essential features of a droplet or domain, one can show that for small gradients the drift velocity is proportional to the temperature gradient γ, while the spreading of the drop is a higher order effect. This analysis, including the analytic treatment of the response of a "ϕ^4-kink" to a temperature gradient, will be presented elsewhere.

(ii) Conserved order parameter and coupled slow mode

The next stage of complexity couples the conserved order parameter (concentration) to a slow, conserved mode like an energy density or other density. For our fluid, the natural example is a heat mode. Such a model corresponds to "Model D" in the study of critical dynamics [8]. As far as critical dynamics are concerned, the conserved dynamics of the order parameter degrees of freedom are not affected by coupling to an additional slow mode. [8] However for deep quenches, and for domain migration in a temperature gradient, it is interesting to consider the effect of the slow heat mode. Our interest will be to detect differences due to finite thermal conductivity, and, for example, to a Soret effect.

To this end we consider the general treatment sketched in the Overview, but for the moment drop all fluid velocity terms. There is a conserved energy density following from a free energy density as in Eq. (6) with the same local part as above. The entropy density follows from $S = -\frac{\partial F}{\partial T}$, while the chemical potential follows from $\mu = \delta/\delta\phi \int F d^d x$ as in Eq. (9).

As an example we show in Fig. 2 the phase separation patterns starting from a high temperature initial condition to a state with a temperature ramp. The overall average order parameter is chosen off-critical, but the left-hand part of the system should be in the unstable regime. Phase separation via spinodal decomposition is affected by the Soret effect (and particularly its relative sign) causing a concentration gradient to advance from the wall. Essentially this is a kinetic finite-size effect. Analysis of the features of this process will be presented elsewhere.

(iii) Imposed temperature gradient and velocity coupling

Now we turn to the full problem which includes the fluid velocity fields, i.e., finite viscosity. In Fig. 3 a sample phase separation sequence is shown. The qualitative change in domain dynamics with the inclusion of velocity fields and the finite system size is significant, as expected. One observes, for example, "boundary forcing" induced by the boundary conditions, and its effect on the dynamics. The full time sequence clearly shows the merging of domains. Detailed analysis including the behavior of separate temperature "slices" to determine anisotropic behavior in domain growth will also be discussed elsewhere.

4. CONCLUDING REMARKS

We have presented here a brief description of modeling in which thermocapillarity effects can be studied at the coarse-grained level. Features such as phase separation kinetics, droplet migration and flow in binary fluid systems can be studied with the aim of extracting universal features. Several specific examples have been provided to demonstrate the range of phenomena that can be considered in this fashion.

REFERENCES

[1] P. C. Hohenberg and B. I. Halperin, Rev. Mod. Phys. *49*, 435 (1977)

[2] J. S. Langer, Ann. Phys. (N.Y.) *54*, 258 (1969)

[3] See, e.g., A. Shinozaki and Y. Oono, Phys. Rev. E *48*, 2622 (1993) and references cited therein.

[4] Y. Oono and M. Bahiana, Phys. Rev. Lett. *61*, 1109 (1988)

[5] L. Landau and I. M. Lifshitz, *Fluid Mechanics*, second edition (Pergamon, New York, 1987)

[6] H. W. Alt and I. Pawlow, Physica D *59*, 389 (1992).

[7] C. Yeung, T. Rogers, A. Hernandez-Machado and D. Jasnow, J. Stat. Phys. *66* 1141 (1992).

[8] B. I. Halperin, P. C. Hohenberg and S.-K. Ma, Phys. Rev. B *10*, 139 (1974).

FIGURE CAPTIONS

1. Migration of droplet of one phase in background of other in an imposed temperature gradient. Diffusion only, no hydrodynamics.

2. Phase separation in a temperature gradient. Finite size of system combinbed with Soret term affect the phase separation kinetics.

3. Phase separation in imposed temperature gradient, with hydrodynamic coupling.
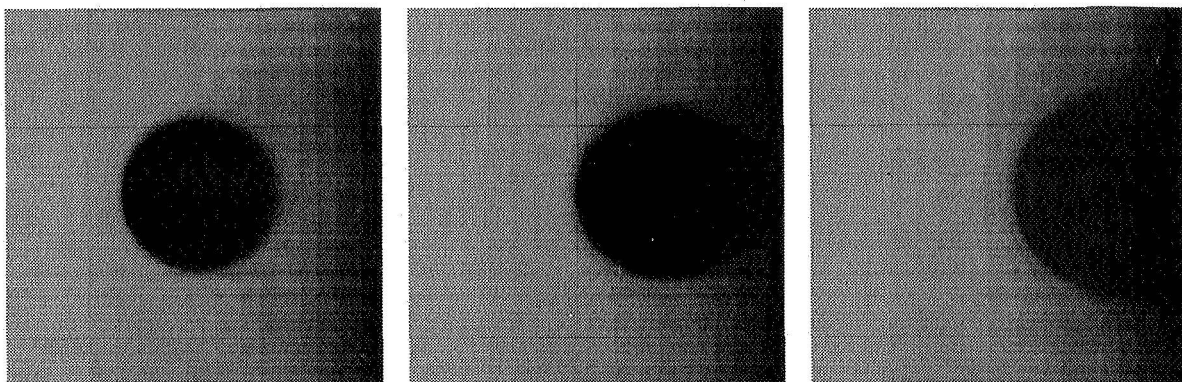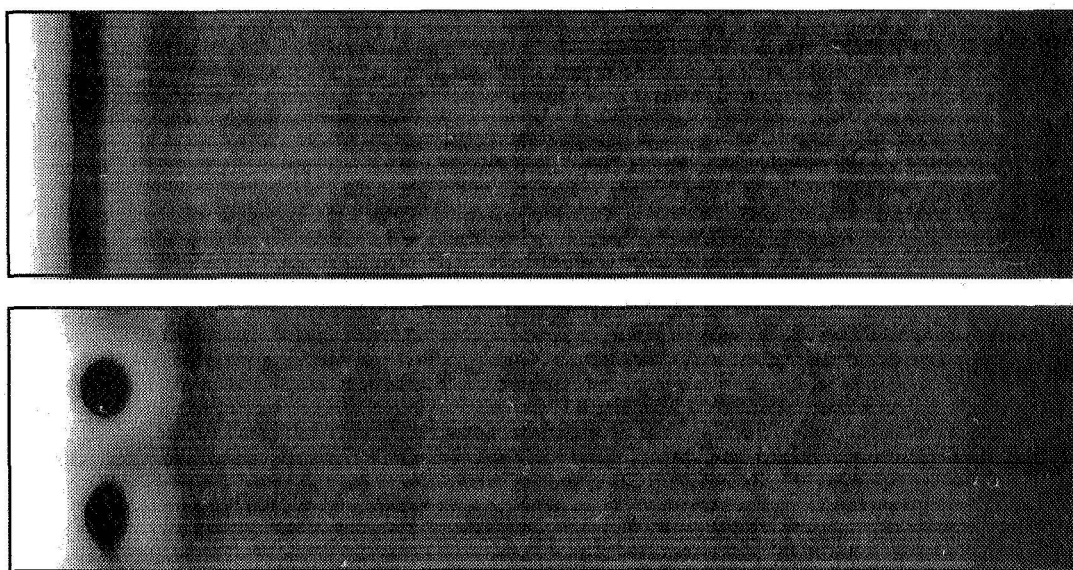
Figure 1

Figure 2

Figure 3

HELIUM II SLOSH IN LOW GRAVITY

Graham O. Ross
Lockheed Palo Alto Research Laboratory
Research & Development Division
Lockheed Missiles and Space Company, Inc.
Palo Alto, California 94304-1187

ABSTRACT

This paper describes the status and plans for the work being performed under NASA NRA contract NASW-4803 so that members of the Microgravity Fluid Dynamics Discipline Working Group are aware of this program. The contract is a cross-disciplinary research program and is administered under the Low Temperature Microgravity Research Program at the Jet Propulsion Laboratory.

The purpose of the project is to perform low-gravity verification experiments on the slosh behavior of He II to use in the development of a CFD model that incorporates the two-fluid physics of He II. The two-fluid code predicts a different fluid motion response in low-gravity environment from that predicted by a single-fluid model, while the 1g response is identical for the both types of model.

INTRODUCTION

The motion of helium II in the low-gravity environment of an orbiting satellite is of critical importance for the design of the satellite attitude and translation control systems. Space vehicle designers are particularly interested in the frequency of oscillation and damping rate of the fundamental slosh mode as well as the cross-axis coupling, if any, induced by rotation of the satellite. There is concern and uncertainty about the potential for persistent fluid slosh motion due to the absence of viscosity in the superfluid component of helium II.

CFD CODE DEVELOPMENT

A superfluid helium (SFHe) simulation has been developed based on the commercial CFD code FLOW-3D from Flow Science in Los Alamos, NM. The SFHe code incorporates Landau's two-fluid model, a critical-velocity threshold, mutual friction between the two fluid components and a new method of reconciling the motion of the two independent components at the free surface.

Two-Fluid Model

The SFHe model calculates independent fluid velocities and cell fluid contents for the normal and superfluid components of the helium II. At each time step, the motion of each component is calculated separately, with allowance for mutual friction as described later. The total pressure in the void and fluid is allocated to the components

based on their relative proportions. Calculations for each component's motion are based on its partial pressure, while output pressures are a summation of the two.

The time step process calculates an intermediate explicit estimate of the new velocity $\tilde{u}^{n+1}$ using the Navier-Stokes equation without the pressure term. The pressure term is incorporated in the second step of the process, where the cell pressures at the new time are adjusted in an iterative loop to force the divergence to zero for each full cell in the tank. This converts the $\tilde{u}^{n+1}$ velocity estimate to a final value u^{n+1} at the t+1 time step.

Critical Velocity

The empirical equation described by Van Sciver (1986) and Putterman (1974)

$$v_c \approx d^{-1/4} \quad \text{(cgs)}$$

is used to calculate the critical velocity above which the two components interact through mutual friction. This formula is based on the flow of the helium II through a small circular or rectangular tube; as such, it is really a one-dimensional flow field under study. In this simulation, the critical velocity is determined by the smallest separation distance between surfaces in the vicinity of the cell. This threshold value is then compared to the magnitude of the total velocity vector, ignoring the relative orientation of the flow to the surface. This avoids discontinuities in the linking of the components based on small variations in flow direction.

Mutual Friction

The formulation proposed by Gorter and Mellink (1949)

$$\vec{F}_{sn} = A\, \rho_s\, \rho_n\, v_{sn}^2 \left(\vec{v}_s - \vec{v}_n\right)$$

is used to calculate the amount of coupling between the two components when the differential velocities exceed the critical velocity. Again, as in the case of the critical velocity, the experimental work in this area has been done with small one-dimensional apparatus. In the three-dimensional model, the mutual friction force in each orthogonal direction is calculated using the normal and superfluid component velocities in that direction alone. This avoids the pitfall of having the mutual friction accelerate the fluid in one direction because of a high velocity value in a perpendicular direction.

Motion of Free Surface

One of the concerns unique to this type of simulation is calculating the position of the free surface of the fluid. The interaction of the normal and superfluid components at the free surface is not well understood and there were no models of free surface behavior found in the literature. The general consensus seems to be that the free surface should assume an intermediate position between the shapes predicted for a pure

normal fluid and a frictionless superfluid. Figure 2 shows a thought experiment where a rotating bucket of helium has the normal fluid in solid-body rotation while the superfluid has not spun up and is stationary. In this condition, the equilibrium shape of the surface for each component is different but the two-fluid model requires a common surface for both components.

As shown in figure 1, the SFHe simulation independently calculates the new surface position of each component for each time step and then calculates a weighted-average of the two positions based on the relative proportions of the components. This enforces the requirement of a single common interface while allowing the two components to flow as required by their independent velocity fields. This weighted averaging is not a conservative operation, since the component velocities in the affected cells are not adjusted after the fluid content is changed, but this is consistent with the experimental behavior observed by Mehl and Zimmermann (1968) and Reppy and Depatie (1964).

1-G VERIFICATION TESTS WITH JPL SFHE DEWAR

A series of ground slosh experiments was performed by the author at JPL using their SFHe dewar shown in figure 3 as a verification of the code in 1-g. The dewar was moved laterally to create a slosh wave oscillating in the plane of the test cell and the slosh amplitude decay curve was calculated An exponential curve has been fitted to the combined results of tests at common temperature and fill levels as shown in figure 4 for the runs at 1.7 K. The two-fluid model predicts a slosh frequency (2.63-2.86 Hz) and damping rate (-0.0110 and -0.0114 at 1.7 K) that is identical to that of a single-fluid CFD code; both types of model match the experimental results (2.45-2.77 Hz for all cases and -0.0115 at 1.7 K) within 5 percent. Figure 5 shows the experimental damping coefficient test results for the various temperatures and fill ratios tested. The lack of significant differences between the predictions of the two-fluid and the single-fluid models in either frequency or damping suggests that the 1-g acceleration field is far more influential than the friction or surface tension effects that are unique to the two-fluid model.

LOW-G SLOSH PREDICTIONS FOR GP-B DEWAR

One of the aspects of fluid response studied in the internal project was the impulse response of a large rotating tank that is partially filled with liquid helium. For the purpose of the computer runs, the dimensions and fluid temperature of the Gravity Probe-B dewar were used. The fluid velocity field and the overall force are plotted for both the single-fluid simulation and the two-fluid SFHe model.

Contrary to the results of the CFD simulations in 1g, zero gravity simulations show marked differences in the fluid motion predicted by the single-fluid and two-fluid models. Figures 6 & 7 show the fluid velocity fields 160 seconds after the application of a lateral impulse to the GP-B dewar while it is rotating at 1 rpm. The single-fluid model predicts an symmetrical oscillating flow field while the two-fluid model predicts that the fluid converts to a rotating velocity field with the fluid flowing against the direction

of rotation of the tank in inertial space. In addition, the two components show a difference in their directions of flow.

PLANNED LOW-G EXPERIMENTAL WORK TO BE PERFORMED UNDER NASW-4803

Based on the 1-g experiments and the low-gravity simulations performed to date, it is necessary to perform low-gravity experiments to be able to verify the performance of the SFHe simulation. This contract was awarded to build a SFHe dewar and perform slosh experiments on the KC-135. The dewar that I used for the ground tests was previously used to perform slosh experiments on the KC-135; JPL is in the process of refurbishing the dewar and its support equipment package. The current plan is to build a new SFHe test cell from Lexan with stainless steel tubes support tubes and retrofit this into the existing dewar. Development tests are currently being performed to develop a method of sealing the Lexan-to-steel interface.

CONCLUSIONS

This work is still in its equipment development phase. I am working closely with Peter Mason and Bob Chave at JPL to coordinate the equipment design and integration. It may be possible to perform the first KC-135 experiments this summer.

REFERENCES
Gorter, C.J. and J.H. Mellink. (1949) On the irreversible processes in liquid helium II. *Physica* vol. 15, nos. 3-4, pp. 285-304

McCarty, J.L. and D.G. Stephens. (1960) *Investigation of the natural frequencies of fluids in spherical and cylindrical tanks.* NASA Technical Note D-252, referenced in NASA SP-106.

Mehl, J.B. and W. Zimmermann, Jr. (1968) Flow of superfluid helium in a porous media. *The Physical Review,* vol. 167, no. 1, pp. 214-229.

Putterman, S.J. (1974) *Superfluid Hydrodynamics,* North-Holland Publishing Co.

Reppy, J.D. and D. Depatie. (1964) Persistent currents in superfluid helium. *Physical Review Letters,* vol. 12, pp. 187-189.

Van Sciver, S.W. (1986) *Helium Cryogenics,* Plenum Press.
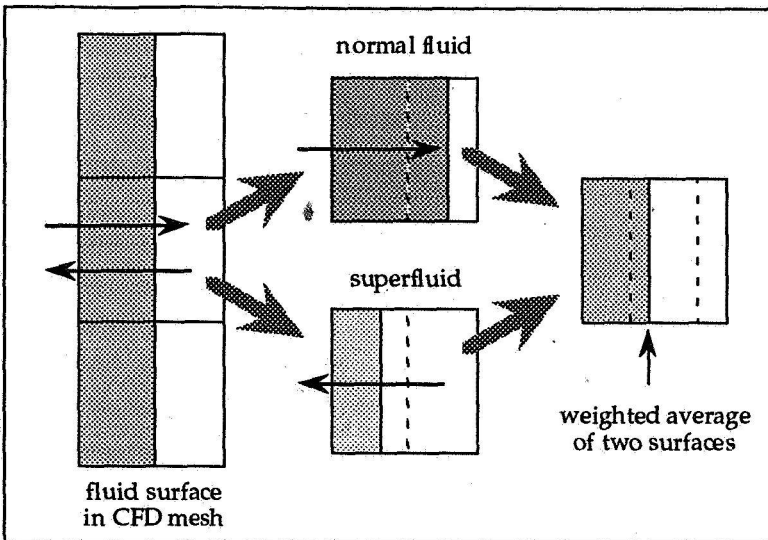
Motion of He II Components at Surface
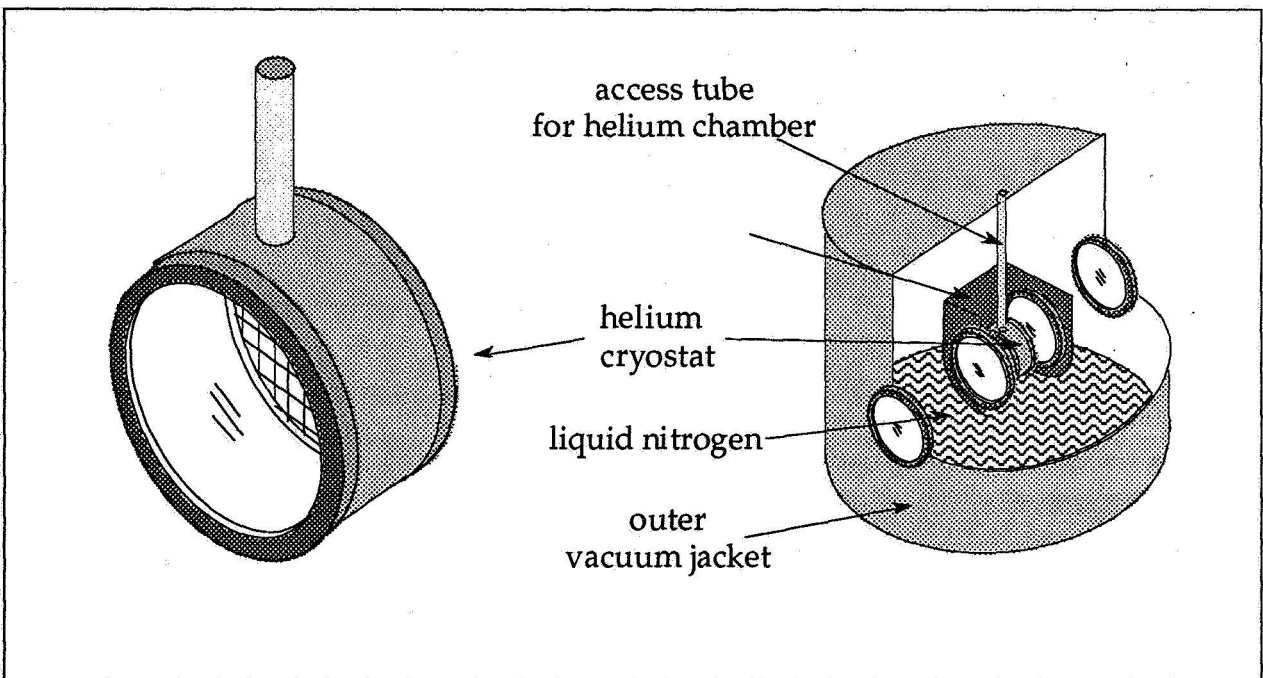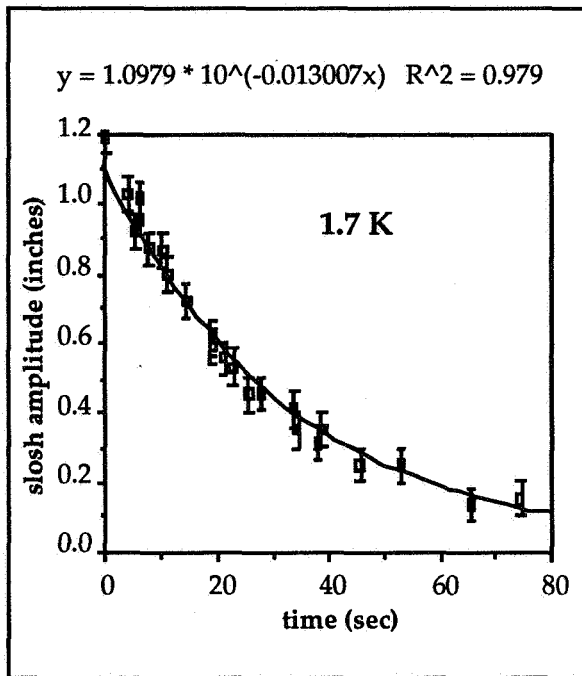Figure 1
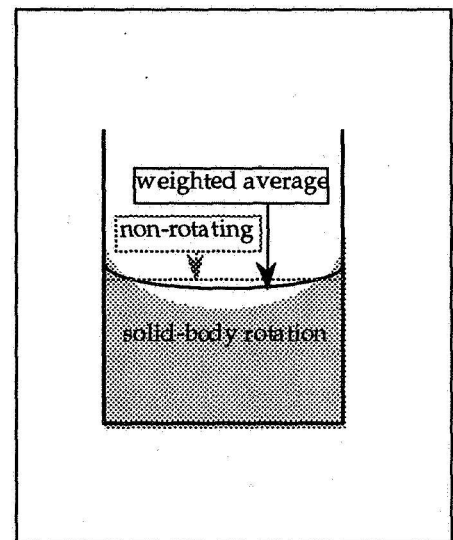
Rotating Bucket of He II
Figure 2

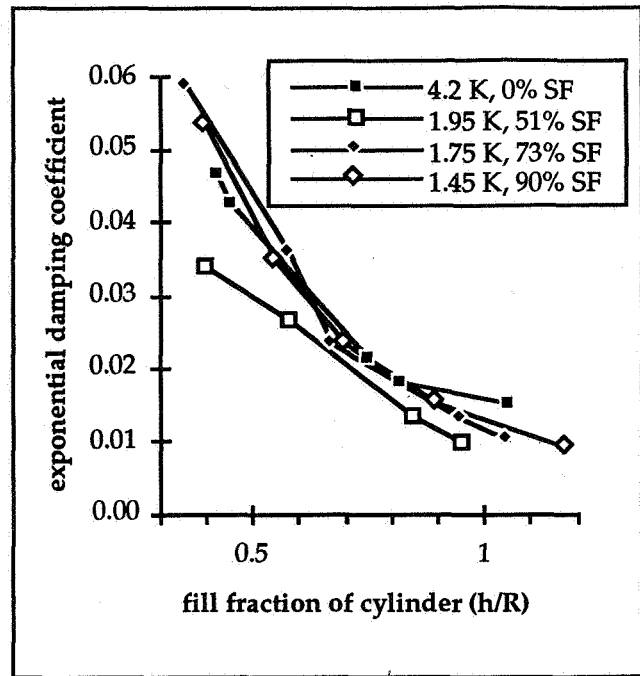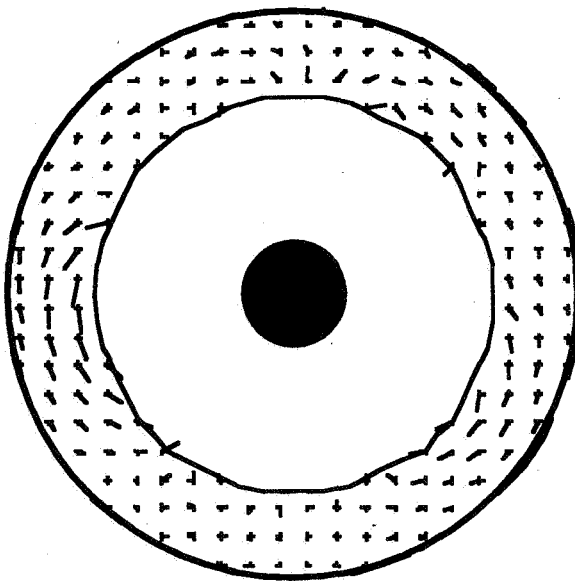Figure 3   JPL He II Dewar

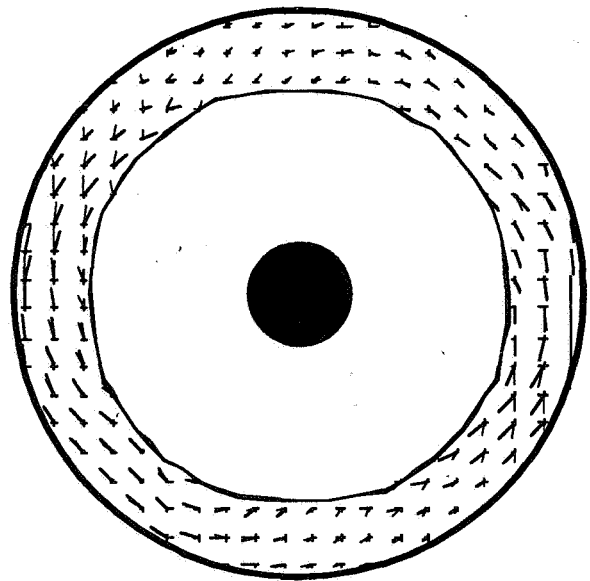$y = 1.0979 * 10^{\wedge}(-0.013007x)$ $R^{\wedge}2 = 0.979$

1.7 K Raw Data and Fitted Curve
Figure 4

Damping Coefficients in JPL Dewar
Figure 5

Fluid Velocity Field in Single-Fluid Model
Figure 6

Fluid Velocity Field in Two-Fluid Model
Figure 7

Multiphase Flow/ Heat Transfer

STUDY OF TWO-PHASE FLOW AND HEAT TRANSFER IN REDUCED GRAVITIES

Davood Abdollahian
S. Levy, Inc.
Campbell, California 95008

Fred Barez
San Jose State University
San Jose, California 95123

ABSTRACT

Design of the two-phase flow systems which are anticipated to be utilized in future spacecraft thermal management systems requires a knowledge of two-phase flow and heat transfer parameters in reduced gravities. A program has been initiated by NASA to design a two-phase test loop and perform a series of experiments to generate the data for the Critical Heat Flux (CHF) and onset of instability under reduced gravities. In addition to low gravity airplane trajectory testing, the experimental program consists of a set of laboratory tests with vertical upflow and downflow configurations. Modularity is considered in the design of this experiment and the test loop is instrumented to provide data for two-phase pressure drop and flow regime behavior. Since the program is in the final stages of the design and construction task, this article is intended to discuss the phenomenon, design approach, and the description of the test loop.

INTRODUCTION

Design of two-phase systems for operation in reduced gravities requires a knowledge of two-phase flow and heat transfer in microgravity and high acceleration environments. In addition to the primary two-phase flow parameters, several criteria, including heat transfer boundaries and instability mechanisms, are expected to be strongly dependent on the acceleration levels. Unlike pool boiling, which has been studied extensively under high and low accelerations, very little work has been done on understanding and modeling two-phase flow. The recent and ongoing efforts have mainly concentrated on generating the data and developing models for two-phase pressure drop, flow regime transition, and two-phase heat transfer coefficients

Two-phase systems are generally designed for operation under the nucleate boiling regime in order to utilize the high heat transfer characteristics of two-phase flow. Operation of these systems beyond the critical heat flux may lead to a sudden jump in the surface temperature due to reduction in the heat transfer coefficient (film boiling regime). This temperature is usually above the melting point of many materials; the maximum surface heat flux is also called the limit of stable burnout. In many practical situations, two-phase components fail at heat fluxes well below the limit of stable burnout. This is due to hydrodynamic instabilities which result in sudden reductions in flow and burnout at smaller heat fluxes. Knowledge of stable burnout limit and the onset of hydrodynamic instability is crucial for operation of any two-phase loop. At this stage, it is generally concluded that considerably more data, preferably under long duration steady-state conditions, is needed to complete and confirm the design approaches for application to reduced gravities.

Background

There are a number of mechanisms which lead to hydrodynamic instability. Some of these mechanisms are not important for the systems designed for operation at earth gravity, but are believed to be significant for reduced gravity operation. Instabilities resulting from the interaction of the system components and the characteristic of two-phase flow are particularly important for systems operating under a forced convective mode of heat transfer. These include excursive, oscillatory, parallel channel, and density wave instabilities.

Excursive and Oscillatory Instabilities. Excursive or Ledinegg instability is the simplest form of hydrodynamic instability in forced convective systems. It occurs under operating conditions which result in an increase in two-phase pressure drop with decreasing flow rate. For an imposed external pressure drop under such conditions, operation at more than one flow rate is possible. Small disturbances may lead to a shift from one flow rate to another (usually lower) in a non-recurring manner and burnout may occur.

Pressure drop-flow rate characteristics of two-phase channels occasionally follow an "S" shaped behavior as shown in Figure 1. Operation in the negative slope part of this system may lead to excursive instability. If a dynamic feedback mechanism exists, it can also lead to an oscillatory behavior. An oscillation will occur if the slope of the pressure drop-flow rate characteristic is more negative than the imposed external supply system. In a constant head supply system (zero slope) as shown in Figure 1, operation at points 1 and 3 would be stable while operation at point 2 would be unstable (slope of the system characteristic is more negative than supply slope). Physically, if the flow rate at point 2 is slightly decreased along (A), the external system is supplying less pressure drop than is required to maintain the flow and the flow rate will be decreased until point 3 is reached.
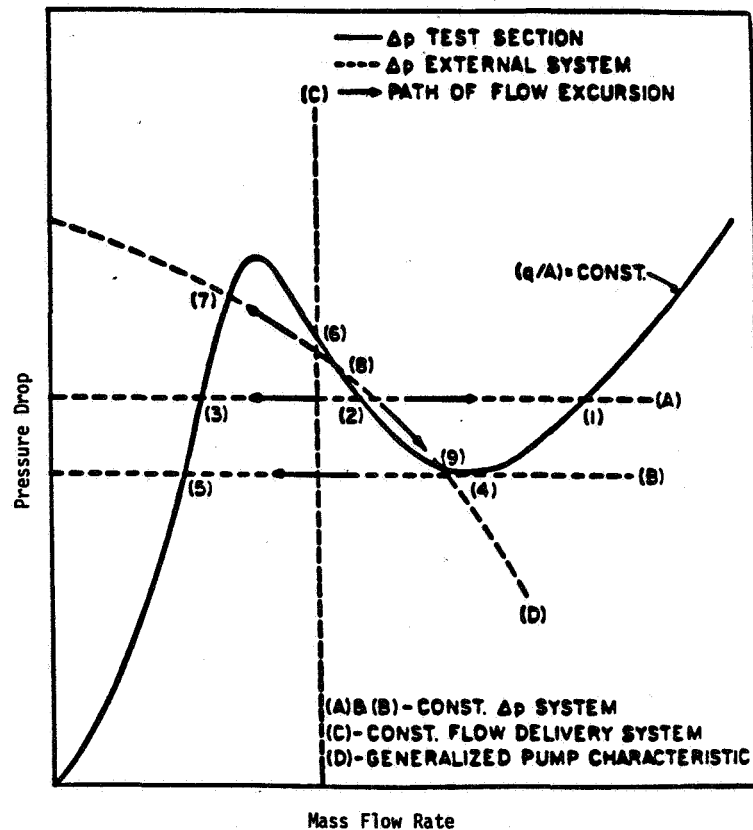

Figure 1. Graphical Interpretation of Excursive Instability

Parallel Channel Instabilities. When several two-phase channels are used in parallel, the variations in the flow rate through one channel do not affect the overall pressure drop. This situation is similar to imposing a constant pressure drop across a single channel which is prone to excursive instability. In such cases, severe maldistribution of flow could occur which would lead to burnout.

Density Wave Instability. The most common form of instability encountered in industrial systems at earth gravity is density wave oscillation. This mechanism is due to multiple feedback between the flow rate, vapor generation rate, and ΔP within the boiling channel. Small perturbations in the flow will result in pressure fluctuations in the single-phase portion of the channel. This in turn will result in void and therefore pressure fluctuations of the opposite sign in the two-phase region. With the right timing, the perturbations may acquire appropriate phases and become self-sustained.

For a given heat flux, the maximum and minimum of the pressure drop-flow rate characteristic depend on the particular system. A boiling channel with vertical upflow can operate into the negative slope region before becoming unstable. However, the same channel with downward flow will become unstable at the onset of subcooled void generation, which is very close to the minimum point. High accelerations ($g > g_0$) in the direction of the flow would be even more severe than downward flow since the bubbles will be swept upstream with higher velocities.

Generally, systems should be designed to avoid operation in the negative slope region completely. This is particularly important when several channels with multivalued characteristics operate in parallel. Due to the imposed constant pressure across the channels, severe flow maldistribution may result which could lead to unstable behavior and burnout. At earth gravity, this situation is usually avoided by orificing the flow at the entrance so that single-phase pressure drop is comparable to two-phase pressure drop. Orificing will shift the minimum to lower flow rates and lower negative slopes, therefore stabilizing the system. Two-phase systems for spacecraft applications may not be able to afford such large pressure drops (orifice or throttling valve) in the loop to stabilize the flow.

For a given flow rate, the negative slope region depends on the void distribution and the two-phase pressure drop. It is known that for the same conditions, two-phase pressure drops under reduced gravities are larger than at earth gravity. This would mean a steeper negative slope which could result in burnout at lower flow rates (or for a given flow rate burnout at a lower heat flux).

DESCRIPTION OF THE TEST LOOP

A test loop is designed for generating data for the critical heat flux (stable burnout) and the onset of two-phase flow instability under reduced gravity conditions. The schematic of the test loop is shown in Figure 2. The test system is packaged on two learjet racks and will be used to perform a series of normal gravity laboratory tests with vertical upflow and downflow configurations as well as airplane trajectory tests. For the laboratory tests, most of the components with the exception of the test section, will be mounted on the racks. This will avoid rotating and tilting the racks with flow direction.

The test apparatus is a closed loop consisting of a magnetically coupled gear pump, a bladder type accumulator, a preheater section, a heated and an adiabatic test section, a flow visualization section, and a tube-in-tube condenser. A bypass leg across the test section path is provided for flow/pressure control as well as imposing a fixed pressure drop across the test section. The heated section, shown in Figure 3, consists of a 5/16 inch OD stainless steel tube with nickel-chromium heater wire wrapped over a 14 inch length of its mid-section. A high temperature bonding material is used to electrically insulate the heater

wire from the test section and the outside environment. This material is magnesium oxide based and has a high thermal conductivity which results in excellent heat transfer and nearly uniform heating of the test section. Measured test section surface temperatures will be used to sense sudden rise in the wall temperature which indicate CHF or drop in flow rate due to instabilities. Ribbon type thermocouples are used to monitor the wall temperature in gaps between the wires and at the end of the heated section. One of these thermocouples is directly connected to a temperature controller and is used for safety purposes. Upon sensing a large temperature rise, the heater power is shut down, solenoid SV2 is closed, and SV3 is opened to flood the test section path.

The adiabatic section is two feet long and intended for two-phase pressure drop measurements over a region where the vapor phase content is known and does not change with distance. This section has the same diameter as the heated section and is thermally isolated from it with a Teflon flange. Differential pressures across two sections of the adiabatic tube will be measured and recorded. A purge system is provided which will run subcooled Freon through the sense lines prior to pressure measurements.

Freon 114 is selected as the working fluid due to its low heat of vaporization which results in lower power requirements than other refrigerants. The test variables are power level, flow rate, and system pressure. The range of variation of these parameters are:

Flow Rate: 0.05 - 1.5 GPM

Power Level: 300 - 1000 Watts

Pressure: 35 - 60 psi

The measurements include fluid temperature and pressure, surface temperature of the test section, flow rate, and pressure drop across the adiabatic section. Turbine flow meters are used to measure the total flow rate and the flow rate in the test section leg. Flush mounted flow through thermocouples will be used to monitor the fluid temperature.

The condenser is a single pass tube-in-tube design which uses standard tube fittings for the end connections. It consists of a 40 inch long 1/2 inch diameter inner tube and 3/4 inch diameter outer tube. Pumped ice water is used as the heat rejection source.

The data acquisition and control system consists of a 486 PC, a high speed multifunction I/O board, and a 32 channel analog input multiplexer/amplifier. Labview for Windows is used for data acquisition and control. The software is used to control the experiment electrical loads, provide for calibration of the experiment inputs, and display/record the experiment inputs.

The user interface panel is mouse driven and consists of a set of indicators and controls. The manual controls include pump activation, heater enable button, pressure sense line purge control, test section flood button, data recording control, emergency stop, and software stop.

Modularity of the test loop was one of the criteria in design and selection of the components. This loop can serve as a test bed for generating data for other two-phase flow parameters as well as evaluating the performance of loop components.

Test Procedure

Two sets of tests are planned for the laboratory experiments which are aimed at investigating the effect of gravity on the onset of instability and the critical heat flux. Onset of unstable behavior will be studied by generating the pressure drop/flow characteristic of the system. These tests will be performed by measuring the pressure drop across a given length of the test section while the flow rate is reduced until unstable pressure fluctuations are observed or a sudden drop in flow rate is sensed. The pressure drop across the test section leg will be fixed by the bypass line. The critical heat flux tests will be carried out by gradually increasing the heat input to the test section until a surge in wall temperature is observed. At several heat input settings, the system will be brought to steady state to generate pressure drop data in the adiabatic section.
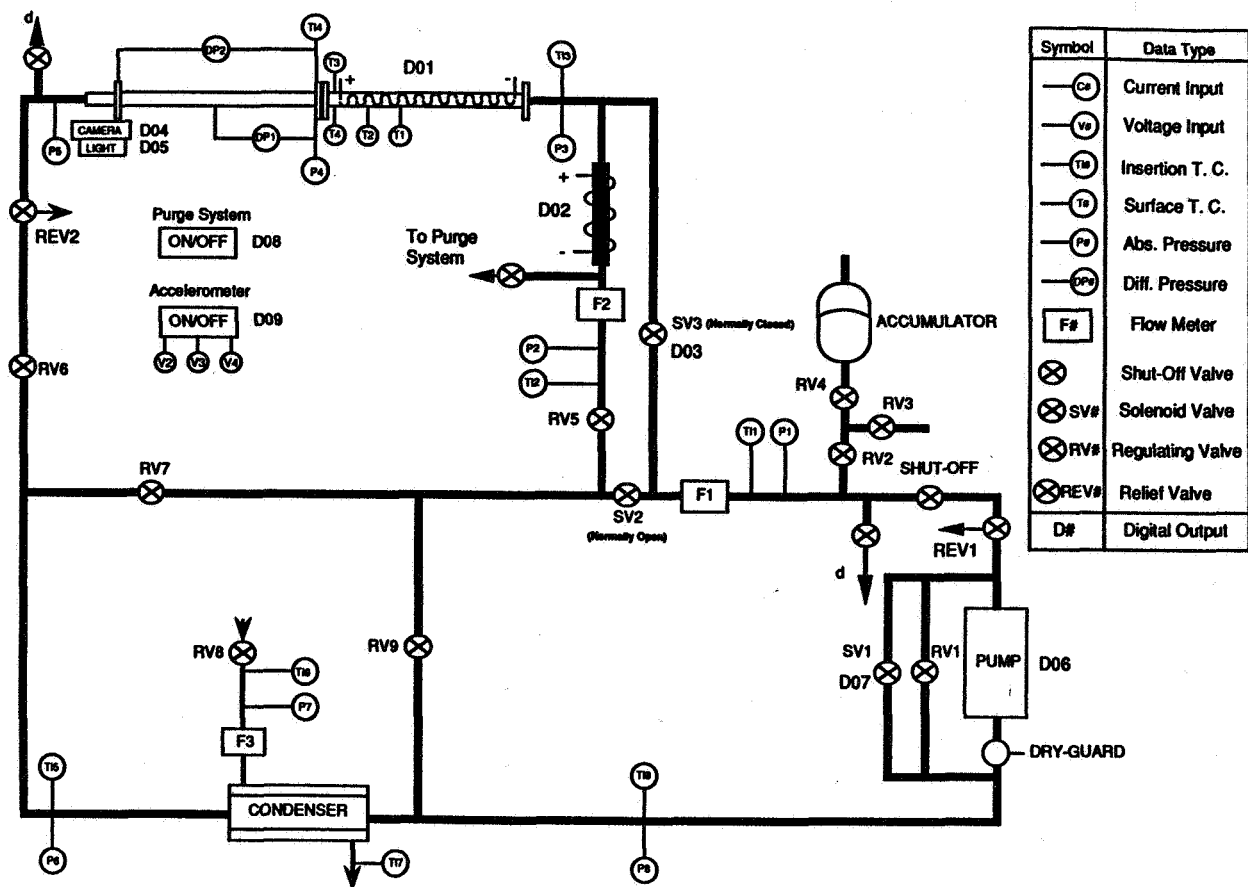
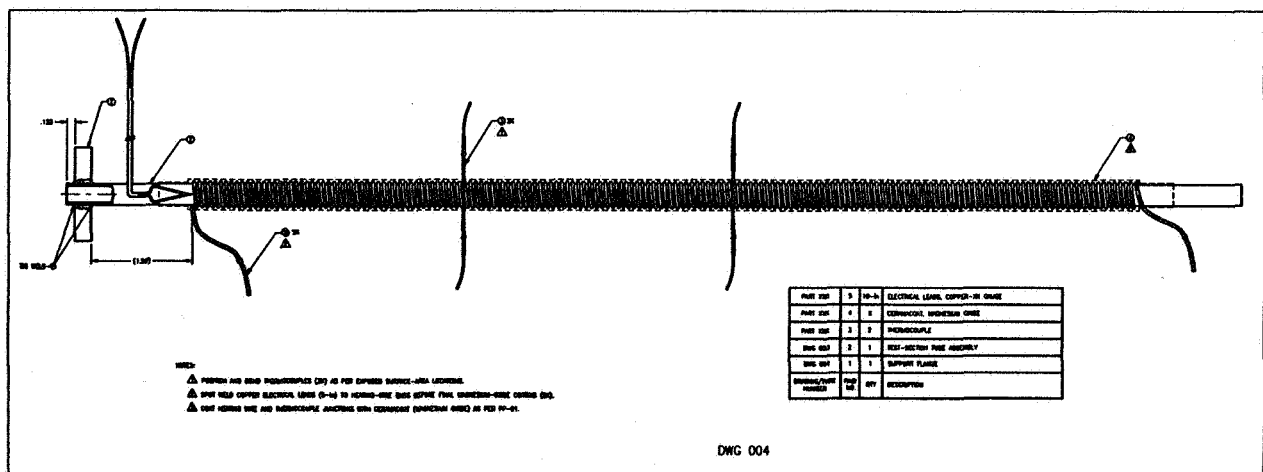| Symbol	Data Type
Ca	Current Input
Va	Voltage Input
Ta	Insertion T. C.
Ts	Surface T. C.
Pa	Abs. Pressure
DPa	Diff. Pressure
F#	Flow Meter
⊗	Shut-Off Valve
SV#	Solenoid Valve
RV#	Regulating Valve
REV#	Relief Valve
D#	Digital Output

Figure 2. Flow Schematic of the Test Loop

DWG 004

Figure 3 - Heated Test Section

CHARACTERIZATION OF ANNULAR TWO-PHASE GAS-LIQUID FLOWS IN MICROGRAVITY

W. Scott Bousman
Department of Chemical Engineering
University of Houston
Houston, Texas 77204-4792

John B. McQuillen
National Aeronautics and Space Administration
Lewis Research Center
Cleveland, Ohio 44135

ABSTRACT

A series of two-phase gas-liquid flow experiments were developed to study annular flows in microgravity using the NASA Lewis Learjet. A test section was built to measure the liquid film thickness around the perimeter of the tube permitting the three dimensional nature of the gas-liquid interface to be observed. A second test section was used to measure the film thickness, pressure drop and wall shear stress in annular microgravity two-phase flows. Three liquids were studied to determine the effects of liquid viscosity and surface tension. The results of this study provide insight into the wave characteristics, pressure drop and droplet entrainment in microgravity annular flows.

INTRODUCTION

Two-phase gas-liquid flows are expected to occur in a wide variety of future space operations including: efficient, lightweight thermal transport systems on large spacecraft, storage and transfer of cryogenic propellants, two-phase power cycles and space nuclear power systems [1]. The lack of buoyancy between liquid and gas phases in the microgravity environment causes two-phase flows to behave differently than those on earth. Thus, in order to reliably design and operate gas-liquid flow systems in the microgravity environment, models which account for the behavior encountered in microgravity must be developed.

Microgravity gas-liquid flows distribute themselves into several distinct flow patterns depending on the flow rates of liquid and gas and fluid physical properties as described in Bousman and Dukler, 1993 [2]. Several studies have shown that the annular flow pattern, in which most of the liquid is in the form of a liquid film distributed around the inside perimeter of a pipe surrounding a core of gas and entrained droplets, encompasses most of the gas and liquid flow rate parameter space of interest in the previously mentioned applications [1,2,3]. Annular flow is the most prevalent flow pattern encountered in earth-based industrial applications as well.

Numerous studies of annular flow have shown that it is the rough, wavy gas-liquid interface which accounts for much of the greatly-enhanced momentum, heat and mass transfer effects observed [4]. Models based on flat or periodically wavy liquid films are completely inadequate. In order to develop realistic models of annular flow in the microgravity environment, the characteristics of the gas-liquid interface must be better understood. This work presents the initial results of an on-going experimental study of microgravity annular flows at the NASA Lewis Research Center.

EXPERIMENTAL APPARATUS

The facilities and experimental apparatus used in this study are described in more detail in Bousman and Dukler, 1994 [5]. Microgravity two-phase flow experiments are conducted on the NASA Lewis Learjet which can produce 20-25 second periods of microgravity (0 ± 0.02 g) by following a Keplerian trajectory [6]. A flow loop provides metered quantities of gas and liquid to an annular mixer. The two-phase mixture flows through a development section and into an instrumented test section.

Based on experience gained from previous flow pattern mapping studies, two test sections were constructed to provide the measurements needed to characterize annular flow. The first section consists of a 1.27 cm ID acrylic tube equipped with five parallel wire film thickness conductance probes. The first four probes are offset $60°$ angularly and

5 mm axially while the fifth probe is oriented the same as the first but located 5 cm downstream. The second test section is a 1.27 cm ID acrylic tube equipped with parallel wire probes to measure both film thickness and void fraction, two pressure transducers to measure the pressure drop in the system and a flush mounted hot-film wall shear stress probe. All signals were acquired at 1 kHz to provide sufficient resolution of the waves. In addition, high speed (400 frame/s) photography allowed for direct flow visualization. Three liquids were used in this study so that the effect of liquid physical properties could be determined: water ($\mu = 1$ cP, $\sigma = 70$ dyne/cm), 50-50 wt% water-glycerin ($\mu = 6$ cP, $\sigma = 63$ dyne/cm) and water-Zonyl FSP (a DuPont fluorosurfactant) ($\mu = 1$ cP, $\sigma = 20$ dyne/cm).

RESULTS AND CONCLUSIONS

The general character of annular two phase flows in microgravity was studied using the five probe test section described above. A typical time trace of air-water annular flow in microgravity is shown in Figure 1. The measurement taken by the first four probes around the perimeter of the tube clearly shows that the waves are ring-like in nature. While the wave shape around the perimeter is irregular, the mean values of the film thicknesses measured by the probes are equal within the error of the measurement. Comparing the measurements of the first and fifth probe, which are both oriented along the bottom of the tube but separated axially by 5 cm, shows that the waves are continuously evolving in shape. Wave splitting and recombination events are frequently observed in these traces. The wave celerity measurements, computed by cross correlating the signals, show that the waves are moving in a narrow range of velocities.

The effect of the liquid physical properties is shown in Figure 2 where three film thickness time traces are presented at the same gas and liquid superficial velocities. Comparing the air-water and air-water/glycerin traces shows that increasing the liquid viscosity leads to a film which contains larger, rougher disturbance waves. The air-water/glycerin trace contains little smooth substrate film between disturbance waves. The effect of liquid surface tension is seen by comparing the air-water and air-water/Zonyl traces in Figure 2. These show that decreasing the surface tension produces an annular film which contains smoother, smaller disturbance waves with larger regions of smooth substrate film in between the disturbance waves. The frequency of disturbance waves in the water experiments is greater than that of either of the other two liquids. These observations are typical of runs in this study with superficial gas and liquid velocities in the range of 5-25 m/s and 0.07- 0.5 m/s respectively.

Since results from five probe test section showed the microgravity annular films to be axisymmetric in a mean sense, the remaining annular studies used the second test section which contained only one film thickness probe. The mean film thickness of air-water annular flows taken over the entire parameter space studied is shown in Figure 3 as a function of gas and liquid superficial velocities. As expected, the film thickness decreases with decreasing liquid superficial velocity but also decreases with increasing gas superficial velocity. The air-water/glycerin results showed the same trend but the mean values were 20-30% greater than those of the air-water experiments. The air-water/Zonyl experiments also showed a similar trend but mean film thickness values were 40-50% lower than the air-water values. Qualitatively, the experiments show that the wave amplitude decreases relative to the substrate thickness as the superficial gas velocity increases, leading to the reduction in mean film thickness shown. This can be quantified by computing the ratio of the standard deviation to mean film thickness as is shown for the air-water runs in Figure 4. The plot shows that this ratio is essentially independent of superficial liquid velocity but a strong function of the superficial gas velocity. It should be noted that the results are also nearly independent of liquid properties since results which are nearly identical to Figure 4 are obtained for both of the other liquids tested.

The mean pressure drops measured in the experiments are shown in Figure 5 for the air-water and air-water/glycerin experiments as well as the pressure drop for single phase gas flow computed from the Blasius correlation. The air-water/Zonyl runs are not shown because they are essentially identical to those measured for air-water. Figure 5 shows that there is a 5-15 fold increase of the gas flow pressure drop due to the presence of the liquid film. The small reduction in cross-sectional area in the pipe due to the presence of the liquid cannot account for this large change and clearly it is the waves which are responsible for the large increase in pressure drop. Figure 5 also shows that the pressure drop in the air-water/glycerin system is 15-25% greater than that in the air-water system. This is consistent with the higher amplitude disturbance waves on the air-water/glycerin liquid films as was shown in Figure 2.

A more detailed understanding of the annular flow pressure drop is possible if the total pressure drop is separated into its component parts as detailed by Fore, 1993 [7]. A force balance on the annular film yields

$$\frac{-\Delta P}{L} = \frac{4}{D} \tau_w + \frac{4}{D} g \, \rho_L \, \overline{h} + g \rho_{GC} \frac{(D-2\overline{h})^2}{D^2} + A_E \tag{1}$$

where τ_w is the mean wall shear stress and A_E is the body force due to droplet entrainment and deposition. The second and third terms in (1) are the hydrostatic heads of the liquid film and the gas core and are negligible in microgravity. The remaining terms are contributions to the total pressure drop due to wall friction and entrainment/deposition;

$$\frac{\Delta P_T}{L} = \frac{\Delta P_{WF}}{L} + \frac{\Delta P_E}{L} \tag{2}$$

The pressure drop due to wall friction is computed from the wall shear stress measurements and Eq. (1). The rate of entrainment cannot be measured in the short microgravity periods available in ground-based microgravity facilities. The fraction of the total pressure drop attributed to wall friction is shown for air-water in Figure 6. As shown, the fraction approaches 100% for low flow rates suggesting that entrainment is nearly absent at low gas rates. As the gas rate increases, the fraction decreases achieving a minimum value of less than 40% and suggesting that the rate of entrainment is large at these gas velocities. The fraction is expected to trend back towards 100% at still higher gas velocities since the waves, and therefore entrainment of droplets from the crest of the waves, are significantly suppressed at velocities higher than 50 m/s at normal gravity. Limitations on the aircraft flow loop prevented this from being tested directly. The results indicate slightly less entrainment for the air-water/glycerin system but considerably more for the air-water/Zonyl with only 20% of the total pressure drop attributed to wall friction at the highest gas velocities. The increase in entrainment, coupled with a decrease in wave amplitude, may explain why the mean pressure drop is nearly the same as in the air-water experiments even though the waves are smaller for the air-water/Zonyl runs.

ACKNOWLEDGEMENTS

REFERENCES

1. Dukler, A.E., Fabre, J., McQuillen, J.B. and Vernon, R., "Gas-Liquid Flow at Microgravity Conditions: Flow Patterns and Their Transitions", *International Journal of Multiphase Flow*, **14**, 4, 1988, pp. 389-400.

2. Bousman, W.S. and Dukler, A.E., "Studies of Gas-Liquid Flow in Microgravity: Void Fraction, Pressure Drop and Flow Patterns", Proceedings of the 1993 ASME Winter Meeting, New Orleans, 1993.

3. Zhao, L. and Rezkallah, K.S., "Gas-Liquid Flow Patterns at Microgravity Conditions", *International Journal of Multiphase Flow*, 19,5, 1993, pp. 751-763.

4. Dukler, A.E., "The Role of Waves in Two-Phase Flow: Some New Understandings", *Chemical Engineering Education*, Awards Lecture 1976.

5. Bousman, W.S. and Dukler, A.E., "Ground Based Studies of Gas-Liquid Flows in Microgravity Using Learjet Trajectories", Proceedings of the 32nd AIAA Winter Meeting, Reno, 1994.

6. Lekan, J., "Microgravity Research in NASA Ground Based Facilities", NASA Technical Memorandum 101397, 1989.

7. Fore, L.B., Droplet Entrainment in Vertical Gas-Liquid Annular Flow, Ph.D. Dissertation, University of Houston, December, 1993.
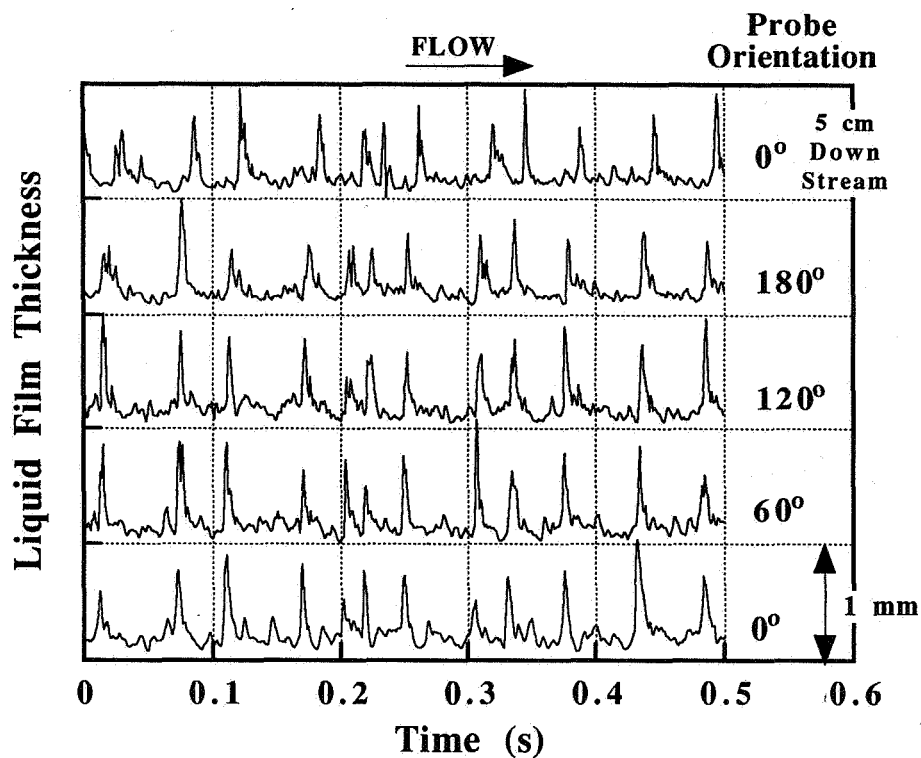
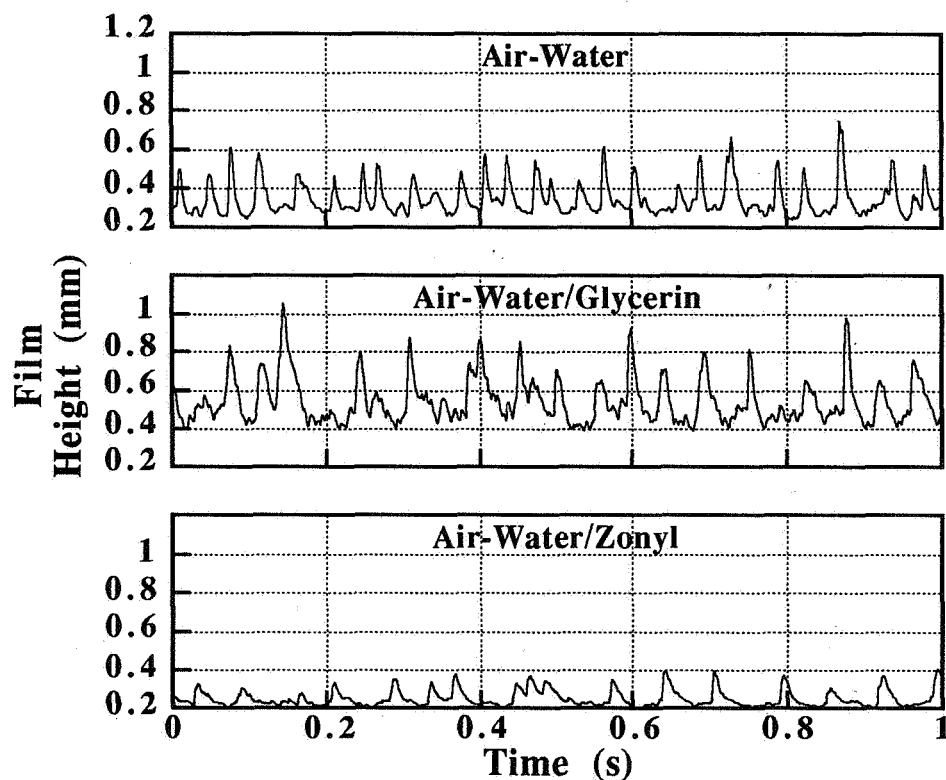Figure 1 Circumferential Distribution of an Annular Film in Microgravity

Figure 2 Film Thickness Time Traces of Annular Flow at Ugs = 25 m/s, Uls = 0.1 m/s
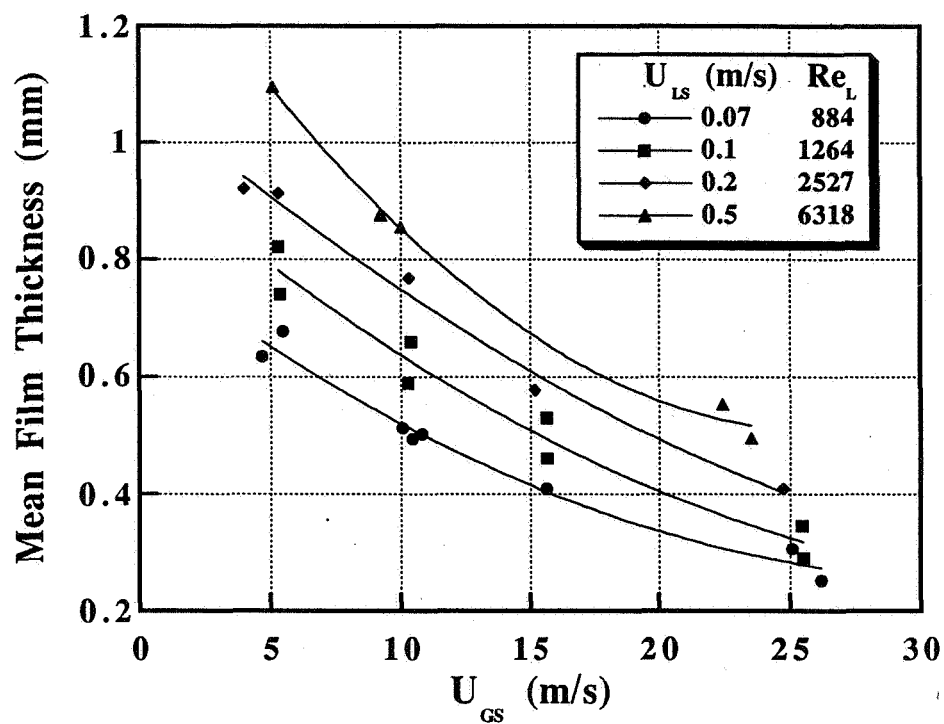for Air-Water, Air-Water/Glycerin and Air-Water/Zonyl

Figure 3   Mean Film Thickness in Microgravity Air-Water Annular Flow
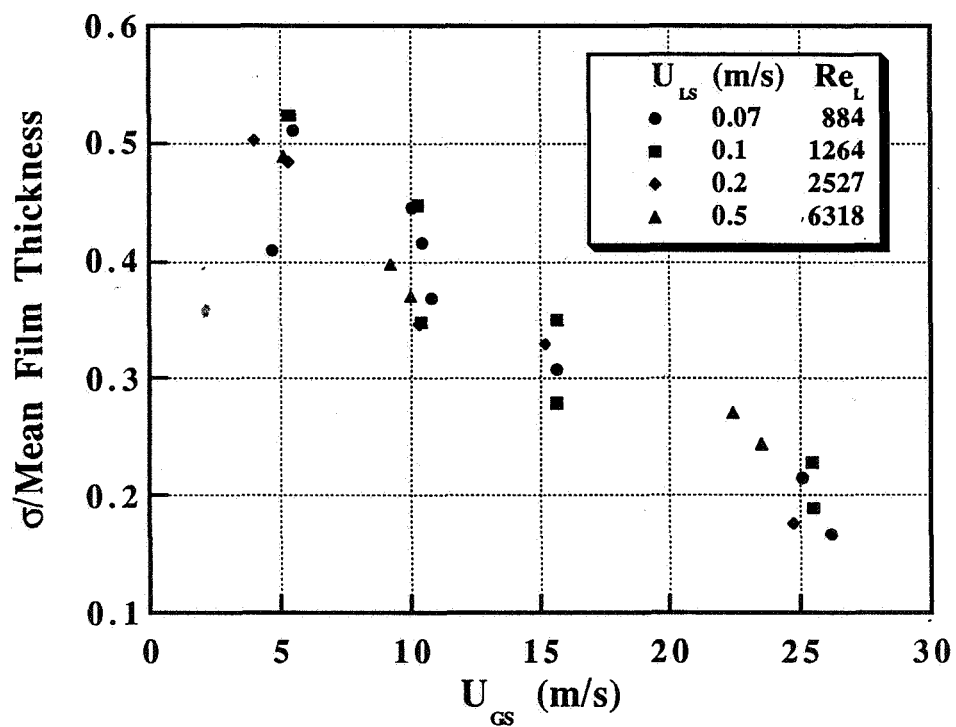

Figure 4   Ratio of Standard Deviation to Mean Film Thickness for
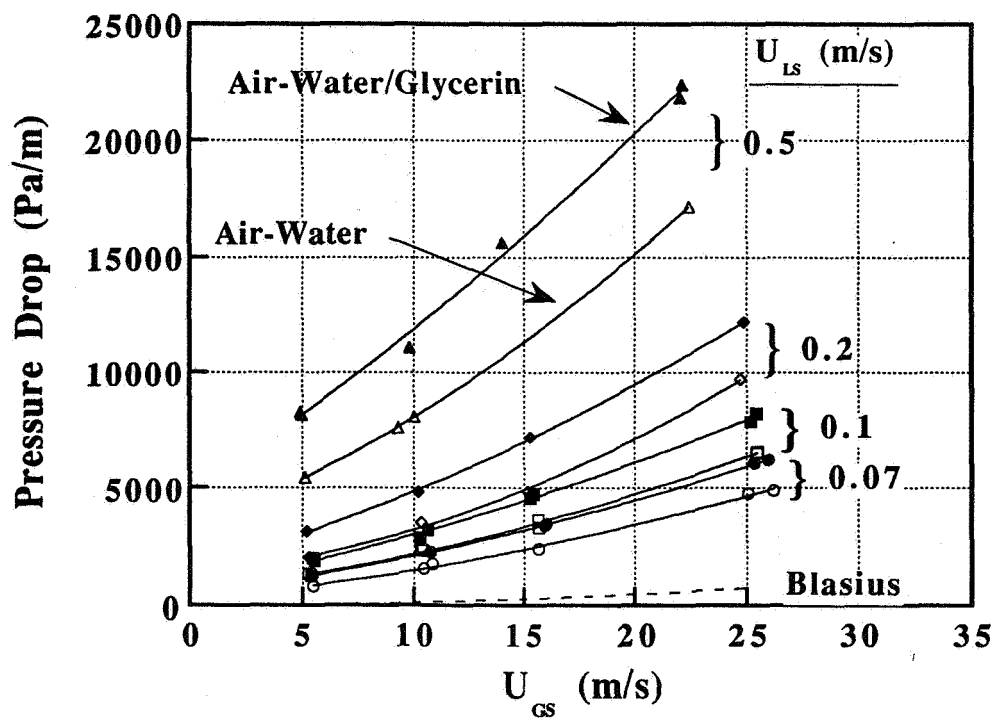Microgravity Air-Water Annular Flow

Figure 5   Pressure Drop for Annular Flow in Microgravity, 1.27 cm ID Tube
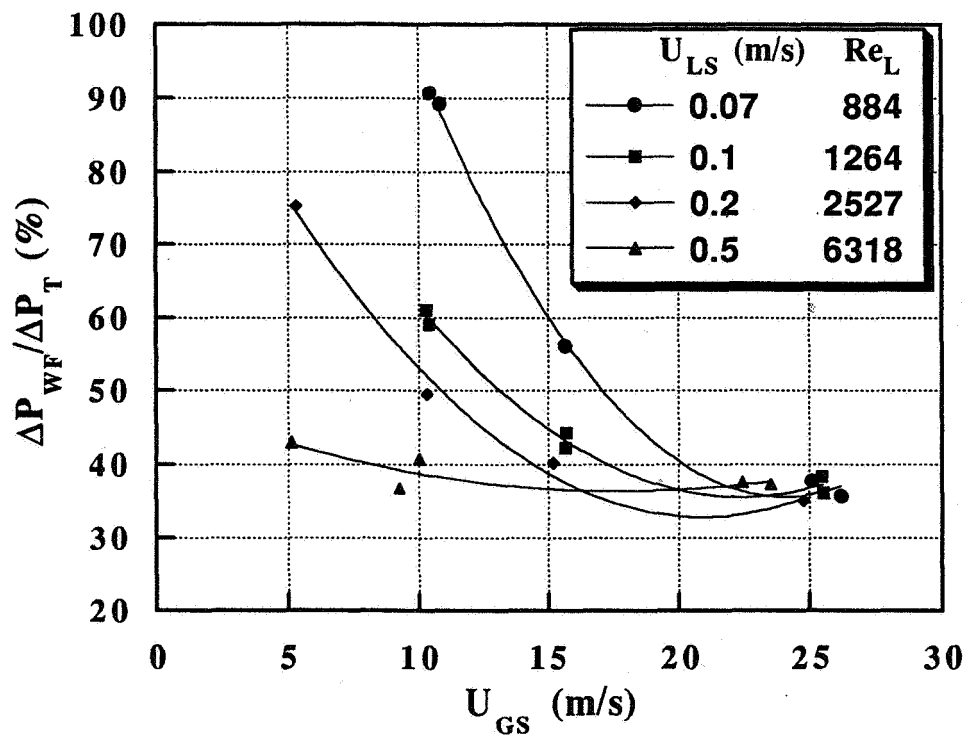

Figure 6   Fraction of Total Pressure Drop Due to Wall Friction, Air-Water, 1.27 cm ID Tube

ANALYSIS OF PHASE DISTRIBUTION PHENOMENA
IN MICROGRAVITY ENVIRONMENTS

Richard Lahey, Jr.
Fabian Bonetto
Center for Multiphase Research
Rensselaer Polytechnic Institute
Troy, NY 12180-3590

INTRODUCTION

In the past one of NASA's primary emphasis has been on identifying single and multiphase flow experiments which can produce new discoveries that are not possible except in a microgravity environment. While such experiments are obviously of great scientific interest, they do not necessarily provide NASA with the ability to use multiphase processes for power production and/or utilization in space.

The purpose of the research presented in this paper is to demonstrate the ability of multidimensional two-fluid models for bubbly two-phase flow to accurately predict lateral phase distribution phenomena in microgravity environments. If successful, this research should provide NASA with mechanistically-based analytical methods which can be used for multiphase space system design and evaluation, and should be the basis for future shuttle experiments for model verification.

DISCUSSION

During the last decade mechanistically-based multidimensional two-fluid models have been developed and successfully applied to the prediction of bubbly two-phase flows. It appears that these models should also work in microgravity environments, however this still needs to be verified.

To this end experiments are being conducted within Rensselaer's Center for Multiphase Research (CMR). In particular, microgravity conditions have been simulated using neutral buoyant polystyrene spheres, and future experiments will be performed in which neutral buoyant oil droplets are immersed in flowing water.

The purpose of this paper is to present the progress to date in the analytical modeling of dispersed flows and to present the solid/fluid data which has been taken to support these modeling efforts.

We will begin by summarizing the multidimensional two-fluid model and then will present the solid/fluid data which has been acquired in this program.

ANALYSIS

The analysis of multidimensional two-phase flow can be done using two-fluid models and associated computational fluid dynamic (CFD) numerical evaluation algorithms (eg, PHOENICS or FLOW3D). For example, the evaluation of adiabatic bubbly two-phase flows are governed by the two-fluid conservation equations for mass and momentum. These balance equations can be derived using ensemble averaging techniques [Lahey & Drew, 1992].

TWO-PHASE FLOW BALANCE EQUATIONS

The three dimensional balance equations for adiabatic two-phase flow are:

Mass Conservation

$$\frac{\partial [\alpha_k \rho_k]}{\partial t} + \nabla \cdot [\alpha_k \rho_k \underline{v}_k] = 0 \tag{1}$$

where α_k is the volume fraction, ρ_k is the density, and $\underline{v}_k$ is the average velocity of phase-k, respectively.

Momentum Conservation

$$\frac{\partial [\alpha_k \rho_k \underline{v}_k]}{\partial t} + \nabla \cdot [\alpha_k \rho_k \underline{v}_k \underline{v}_k] = -\nabla [\alpha_k p_k] + \nabla \left[\alpha_k \left(\underline{\underline{\tau}}_k + \underline{\underline{\tau}}_k^{Re} \right) \right] + \alpha_k \rho_k \underline{g} + \underline{M}_k \tag{2}$$

233

where $\underline{M}_k$ is the interfacial force density, p_k is the static pressure, $\underline{\tau}_k$ is the viscous stress tensor, and $\underline{\tau}_k^{Re}$ is the Reynolds stress on phase-k, respectively.

The interfacial jump condition for momentum is:

$$\underline{M}_v + \underline{M}_\ell = \underline{m}_i^\sigma \tag{3}$$

where, m_i^σ is the interfacial momentum source density due to surface tension effects (eg, Marangoni forces).

CLOSURE

For dispersed spherical particles (eg, bubbles), we may use the interfacial transfers developed by Park [1992]. It is conventional to partition the interfacial force density $(\underline{M}_k)$ into drag (d) and nondrag (nd) components:

$$\underline{M}_v = \underline{M}_v^{(d)} + \underline{M}_v^{(nd)}. \tag{4}$$

We assume the following form of the interfacial drag law:

$$\underline{M}_\ell^{(d)} = -\underline{M}_v^{(d)} = \frac{1}{8}\rho_\ell C_D |\underline{v}_r|\underline{v}_r A_i''' \tag{5}$$

where, $\underline{v}_r = \underline{v}_v - \underline{v}_\ell$, and for spherical monodispersed bubbles, $A_i''' = 6\alpha_v / D_b$ is the interfacial area density of the interface between the continuous phase and the dispersed bubbles. Assuming the validity of inviscid flow theory for the continuous phase the non-drag interfacial force density for the continuous phase is, using cell-model averaging techniques [Park, 1992], [Lopez de Bertodano, 1992]:

$$\underline{M}_\ell^{(nd)} = -\underline{M}_v^{(nd)} = -p_{\ell_i}\nabla\alpha_v + \alpha_v\rho_\ell C_{vm}\underline{a}_{vm} + \alpha_v\rho_\ell C_1\underline{v}_r\cdot\nabla\underline{v}_r + \alpha_v\rho_\ell C_2\left[\underline{v}_r\cdot(\nabla\underline{v}_r^T) + (\nabla\cdot\underline{v}_r)\underline{v}_r\right]$$

$$+ b_s\rho_\ell\underline{v}_r\cdot\underline{v}_r\nabla\alpha_v + a_s\rho_\ell\underline{v}_r\cdot\nabla\alpha_v\underline{v}_r + \alpha_v\rho_\ell C_{rot}\underline{v}_r\times\nabla\times\underline{v}_v + \alpha_v\rho_\ell C_L\underline{v}_r\times\nabla\times\underline{v}_\ell \tag{6}$$

Also, for a spherical dispersed phase the interfacial force required to have the bubbles maintain a spherical shape is [Park, 1992]:

$$\underline{m}_i^s = \nabla\cdot[\alpha_v\underline{\sigma}_s] = \nabla\cdot\left[\alpha_v\rho_\ell\left(\hat{a}_s\underline{v}_r\underline{v}_r + \hat{b}_s\underline{v}_r\cdot\underline{v}_r\underline{I}\right)\right] \tag{7}$$

Also, for the interfacial averaged-pressure, we have [Park, 1992]:

$$p_{\ell_i} = p_\ell + C_p\rho_\ell|\underline{v}_r|^2 \tag{8}$$

For bubbly two-phase flows the total Reynolds stress tensor for the continuous liquid phase is given by superposition as,

$$\underline{\tau}_\ell^{Re} = \underline{\tau}_{\ell(BI)}^{Re} + \underline{\tau}_{\ell(SI)}^{Re} \tag{9}$$

where, for bubbly two-phase flows the bubble-induced shear stress is given by cell-model averaging [Lopez de Bertodano, 1992] as:

$$\alpha_\ell\underline{\tau}_{\ell(BI)}^{Re} = -\alpha_v\rho_\ell\left[a_\ell\underline{v}_r\underline{v}_r + b_\ell\underline{v}_r\cdot\underline{v}_r\underline{I}\right] \tag{10}$$

We note that $\underline{\tau}_{\ell(SI)}^{Re}$ is the shear-induced Reynolds stress which may come from a classical k-ε model and an algebraic stress law [Rodi, 1984].

For the inertial coupling of all dispersed/continuous phase interactions we have [Park, 1992]:

$$C_{vm} = C_L + C_{rot} = \frac{1}{2}, C_L = C_{rot} = \frac{1}{4}, C_1 = \frac{5}{4},$$
$$C_2 = -\frac{9}{20}, a_s = \hat{a}_s = -\frac{9}{20}, b_s = \hat{b}_s = \frac{3}{20}, C_p = \frac{1}{4}, a_\ell = -\frac{1}{20}, b_\ell = -\frac{3}{20}. \tag{11}$$

It is significant to note that there are no arbitrary constants in the two-fluid model, however data on the interfacial drag coefficient, C_D, and the lateral lift coefficient, C_L, indicate that they should be a function of Reynolds number.

MODEL ASSESSMENT

The two-fluid model given in Eqs. (1)-(11) has been assessed against a wide variety of terrestrial air/water bubbly flow data.

Figure-1 shows a comparison of the two-fluid model with the air/water bubbly upflow void fraction data of Serizawa [1974]. Good agreement can be seen. Figure-2 shows that the turbulence model being used does a good job of predicting the measured nonisotropic turbulent structure of Serizawa. Similarly, Figure-3 shows that the model predicts Serizawa's two-phase Reynolds stress data and that, unlike fully developed single-phase flow (ie, $j_v = 0$), the two-phase Reynolds stress distribution is not linear in the radial direction (since the radial void distribution is not linear).

Figure-4 is very exciting because it shows that the same multidimensional two-fluid model which was used to predict Serizawa's bubbly upflow data is able to predict the air/water bubbly downflow data of Wang et al [1987]. Notice the lateral phase distribution in Figure-4 is completely different from Figure-1. This is due to the fact that the lateral lift force changes sign for downflows since the effect of buoyancy causes the relative velocity to change sign.

Figures-5&6 are perhaps the most impressive comparisons of all, since they show that the same multidimensional two-fluid model is also able to predict the lateral phase and velocity distribution in complex geometry conduits (ie, vertical air/water bubbly upflows in an isosceles triangular test section).

These data comparisons clearly indicate that the multidimensional two-fluid model given in Eqs. (1)-(11) is able to predict a wide range of adiabatic bubbly flow data taken on earth. Moreover, since this model is based on first principles it should also be able to predict lateral phase distribution for bubbly flows in microgravity experiments.

EXPERIMENTS

In order to simulate microgravity bubbly flow data, a experiment has been performed using approximately 2 mm diameter expanded polystyrene spheres immersed in water. The specific gravity of these spheres was 1.03, thus they were essentially neutral buoyant.

Figure-7 is a schematic of the test loop. Figure-8 shows a schematic of the novel ventri-type phase separation device which was developed and used to avoid damage to the dispersed particles. Figure-9 is a schematic of the horizontal test section and the DANTEC three-dimensional laser Doppler anemometer (LDA) system which was used. It can be noted that the fiber optic laser transmitter/receiver heads were submerged in water and the tubular test section was constructed of fluorinated ethylene propylene (FEP) which has about the same index of refraction as water, thus no corrections for laser beam refraction were necessary.

Figure-10 presents the measured particle volume fraction distribution. These data were corrected for beam interruptions, etc. using the method of Alajbegović, et al [1994]. It should be noted when these data were integrated across the cross-section they agreed to within ±1% with the corresponding global volume fraction data, which were taken using quick closing valves (Figure-11).

Figures-12 & 13 show the Reynolds stress data for the dispersed particles and the continuous liquid phase (water), respectively, and figures-14 & 15 show data for the axial velocity fluctuations of the particles and the water, respectively. It can be seen that both data sets yield similar results.

Figure-16 gives data on the mean axial velocity of the particles and the liquid phase, respectively. It can be seen that these data are symmetric (as they should be for neutral buoyant particles) and that the relative velocity is negligible, as would be expected for bubbly flow in a microgravity environment. Hence, except for interfacial boundary condition differences between a bubble and a solid sphere, these data comprise an excellent basis for the assessment of the two-fluid model for use in microgravity environments.

MODEL ASSESSMENT

Figures-17 show good agreement between the multidimensional two-fluid model presented in Eqs. (1)-(11) and the solid/fluid data discussed herein.

Interestingly, it appears that the two-fluid model predictions agree better with the uncorrected particle volume fraction data than the corrected data. It is not completely clear at this time why this occurs, however the data correction method

which we used [Alajbegović et al, 1994] implicitly assumes that the dispersed particles are opaque, while the actual particles were translucent, thus it is likely that the data correction applied was inappropriate. This issue will require further study and the results of this study will be reported subsequently.

Nevertheless, it appears that the essential physics of lateral phase separation is captured by the two-fluid model, and thus it should be appropriate for microgravity environments.

Since solid particles satisfy the no slip condition at their surface while vapor bubbles and liquid droplets do not, a series of experiments using neutral buoyant oil droplets immersed in water will also be performed and the two-fluid model will also be assessed against these data. An oil/water loop, shown schematically in Figure-18, has been designed and built and system shakedown is under way.

SUMMARY & CONCLUSIONS

It has been shown that a mechanistically-based, multidimensional two-fluid model has been developed, and that it is capable of predicting a wide range of terrestrial bubbly flow data.

An experiment has been performed in which detailed multidimensional measurements have been made for turbulent solid/fluid flows which simulate bubbly flows in a microgravity environment (ie, the spherical particles used had essentially the same density as water and thus the buoyancy term was eliminated).

Initial comparisons between the solid/fluid data and the multidimensional two-fluid model showed good agreement and imply the validity of this model for microgravity environments.

REFERENCES

Alajbegović, A., Assad, A., Bonetto, F. and Lahey, R.T., Jr., "Phase Distribution and Turbulence Structure for Solid/Fluid Upflow in a Pipe," Approved for publication, *Int. J. Multiphase Flow*, 1994.

Lahey, R.T., Jr. and Drew, D.A., "On the Development of Multidimensional Two-Fluid Models for Vapor/Liquid Two-Phase Flows," *Chem. Eng. Comm.*, Vol-118, 1992.

Lopez de Bertodano, M., "Turbulent Bubbly Two-Phase Flow in a Triangular Duct," Ph.D. Thesis, Nuclear Engineering & Science, Rensselaer Polytechnic Institute, Troy, NY, 1992.

Park, J-W., "Void Wave Propagation in Two-Phase Flow," Ph.D. Thesis, Nuclear Engineering & Science, Rensselaer Polytechnic Institute, Troy, NY, 1992.

Serizawa, A., "Fluid-Dynamic Characteristics of Two-Phase Flow," Ph.D. Thesis, University of Kyoto, Japan, 1974.

Wang, S.K., Lee, S.J., Lahey, R.T., Jr. and Jones, O.C., Jr., "3-D Turbulence Structure and Phase Distribution Measurements in Bubbly Two-Phase Flows," *Int. J. Multiphase Flow*, Vol-13, No. 3, 1987.
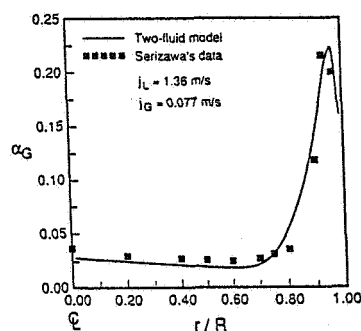
Figure-1 Comparison with Serizawa's data [1986]: void fraction distribution ($C_L = 0.1$)
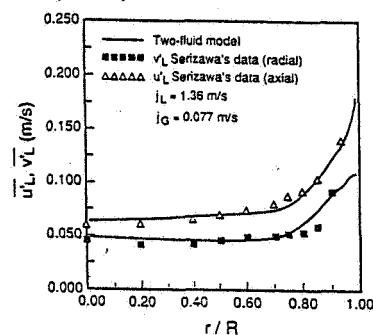

Figure-2 Comparison with Serizawa's data [1986]: velocity fluctuation distributions ($C_L = 0.1$)
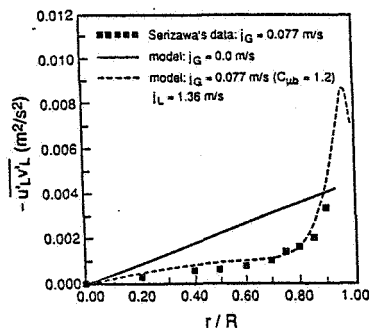

Figure-3 Comparison with Serizawa's data [1986]: Reynolds stress distribution ($C_L = 0.1$)

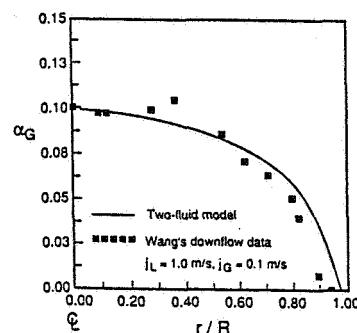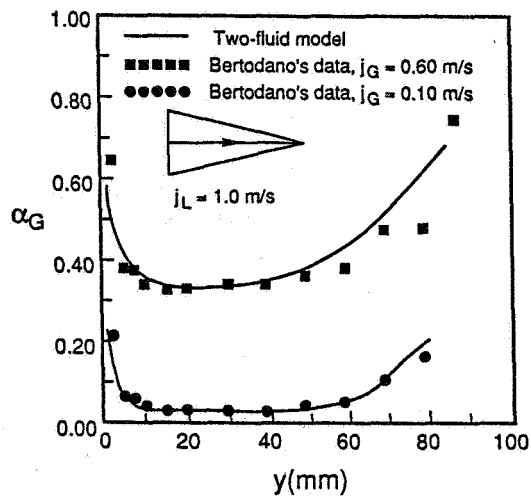Figure-4 Comparison with Wang's downflow data [1986]: void fraction distribution ($C_L = 0.1$)

Figure-5 Comparison with Lopez de Bertodano's data [1992]: void fraction distribution ($C_L = 0.1$)
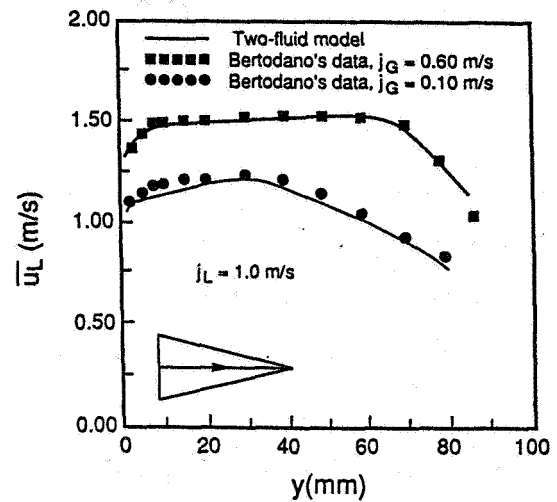
Figure-6 Comparison with Lopez de Bertodano's data [1992]: average axial velocity distribution ($C_L = 0.1$)

Schematic solid-liquid loop
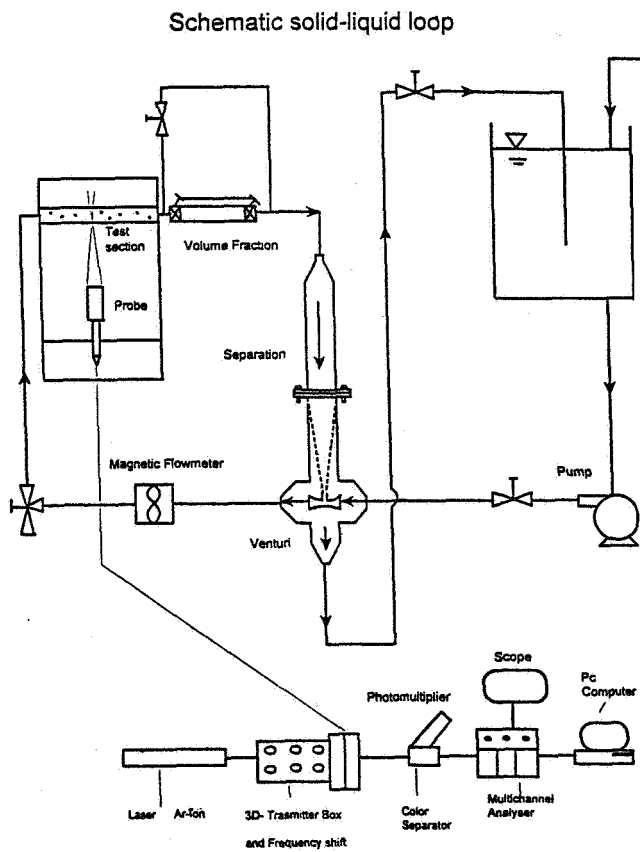
Figure 7 Schematic solid-liquid loop
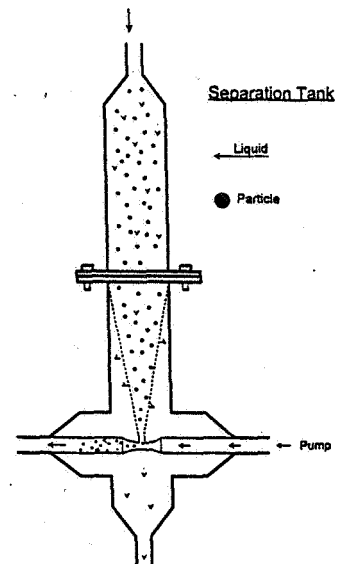
Figure-8 Separation tank

237
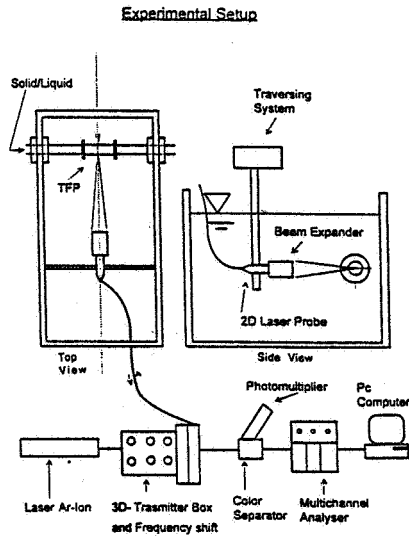
Figure-9 Experimental Setup
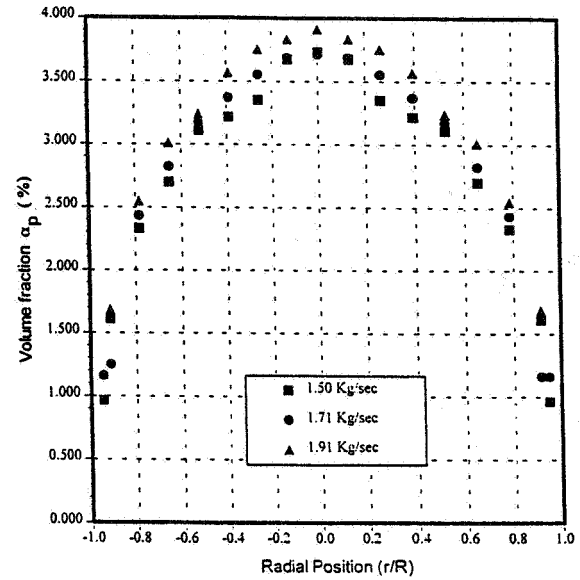
Figure-10 Measurement of local volume fraction of polystyrene particles with density equal to 1030 Kg/m^3

→ Particle and liquid
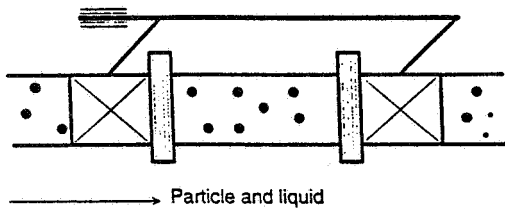
Figure-11 Quick Closing Valves

Figure-12 Particle Reynolds stress for polystyrene particles with density equal to 1030 Kg/m^3

Figure-13 Liquid Reynolds stress for polystyrene particles with density equal to 1030 Kg/m^3

238
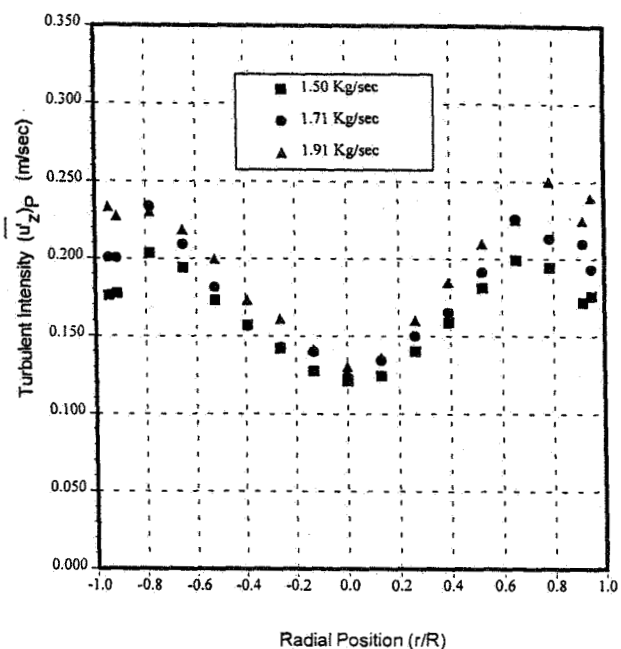
Figure-14 Particle axial turbulence fluctuations for polystyrene particles with density equal to 1030 Kg/m^3

Figure-15 Liquid turbulence fluctuations for polystyrene particles with density equal to 1030 Kg/m^3

Figure-16 Average axial velocity for polystyrene particles with density equal to 1030 Kg/m^3

Figure-17a Predictions of neutral buoyant particle volume void fraction data

Figure-17b Prediction of mean velocity profiles

Figure-18 Oil/Water Loop

240

EXPERIMENTAL AND THEORETICAL STUDIES OF REWETTING OF UNHEATED/HEATED GROOVED PLATES

S. H. Chan
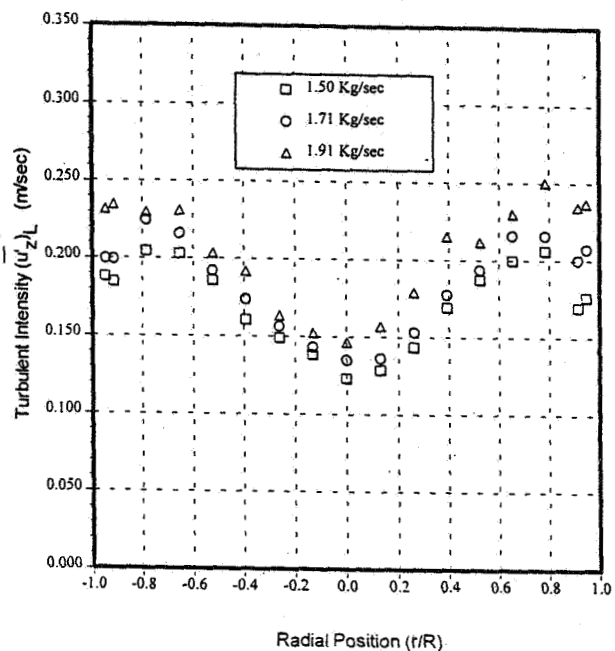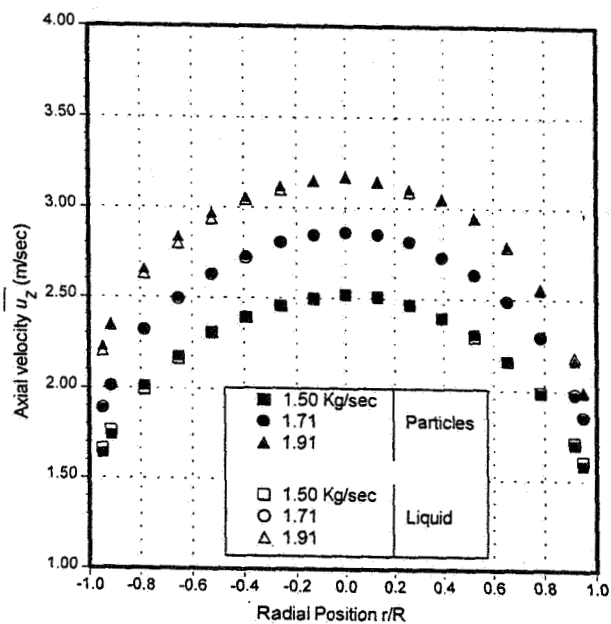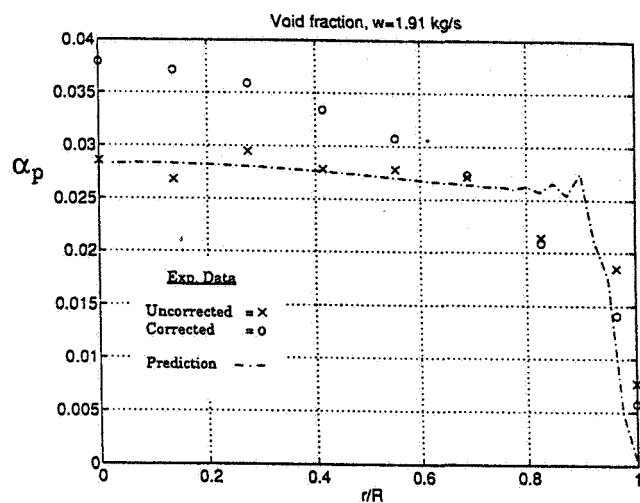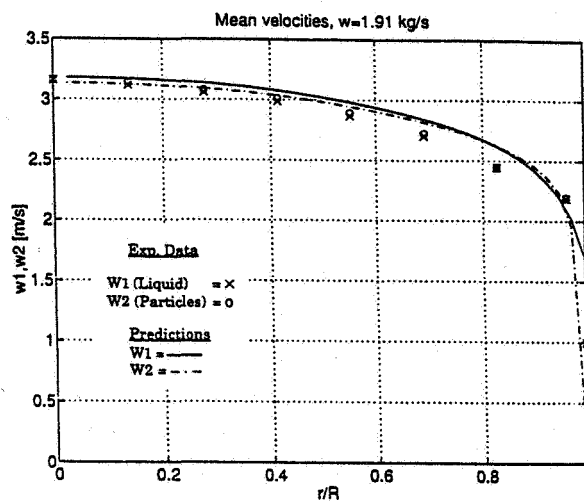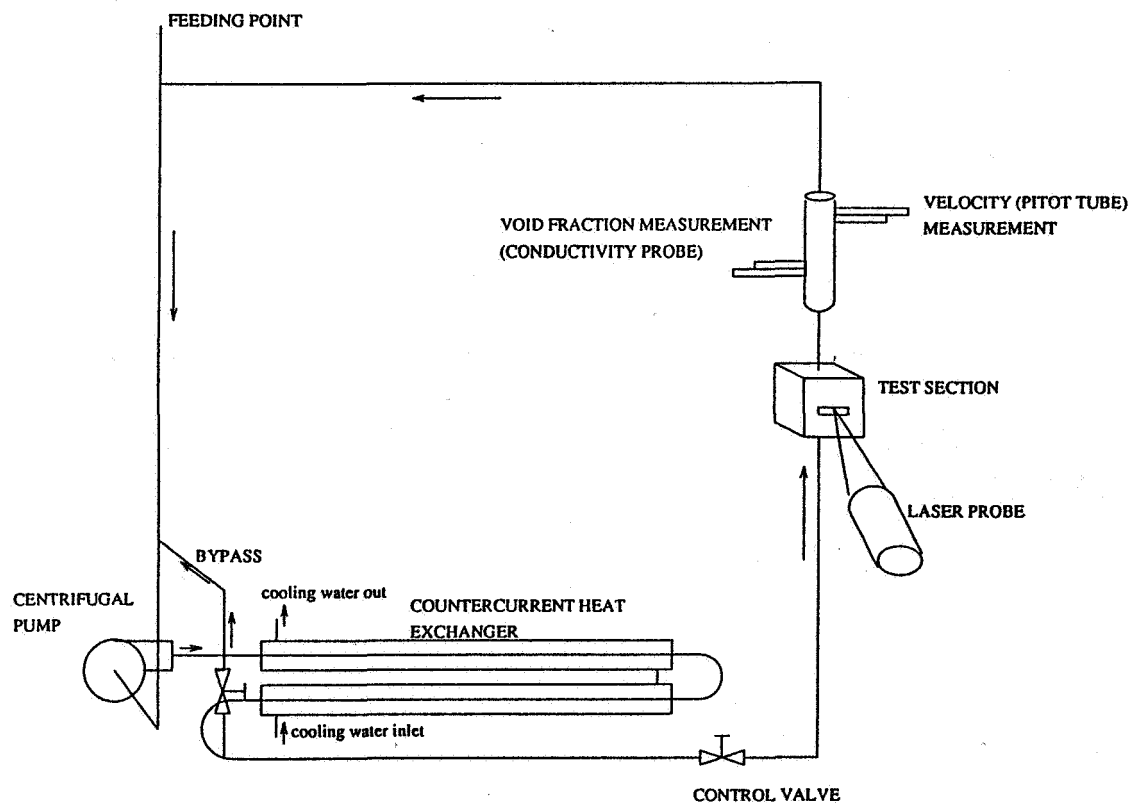
Department of Mechanical Engineering
University of Wisconsin-Milwaukee, Milwaukee, WI 53201

ABSTRACT

Theoretical and experimental investigations of the rewetting characteristics of thin liquid films over unheated and heated grooved plates were performed. Studied factors which affected the rewetting characteristics of the plate were mass flow rate of the rewetting liquid on the plate, the orientation of the plate (face up, face down or inclined) and smooth/groove surface conditions. The initial plate temperature was also varied, with experiments being performed between room temperature and 150 °C. It was found that the rewetting velocity increased with the initial plate temperature. But when the temperature was increased further above the Leidenfrost temperature (liquid front temperature), the rewetting velocity decreases with the initial plate temperature. Hydrodynamically controlled and conductively controlled rewetting models were presented to explain and to predict the rewetting characteristics in these two distinct regions. Also found was a higher rewetting velocity when the grooved plate was placed in the face up orientation than in the face down orientation.

INTRODUCTION

Rewetting of the heated surface of a monogroove heat pipe is an important issue in the design of space station radiators since the dry-out of coolant in the surface grooves due to thermal overload leads to the failure of the heat rejection system of the space station.

The present work investigated both experimentally and theoretically the rewetting on a heated, grooved plate to simulate rewetting of the circumferentical grooves in the inner surface of of a monogroove heat pipe. A wide range of conditions was studied to reveal rewetting characteristics of the grooved plate.

REWETTING OF UNHEATED GROOVED PLATE

<u>Experiment</u>   Experiments were first conducted at the room temperature to study how the rewetting of an unheated, grooved plate was affected by the plate orientation and the mass flow rate of working liquid supplied to the plate. The experimental setup at the room temperature condition consists of a liquid supply system with an adjustable flow rate, a test section (containing the grooved plate) and a video recording system with high resolution frame by frame playback capability. The working liquid (2-propanol) is delivered to the test section by the liquid supply system and is driven within the grooves by surface tension. The grooved plate is fashioned from a sheet of oxygen-free copper and is chemically cleaned after every experimental run. Experimental runs are recorded with a Super-VHS-C camcorder. The tape is played back on the S-VHS VCR frame by frame to determine the position of the liquid front vs time (1/30 second per frame).

<u>Results and Discussion</u>   The supplied liquid flow rate effects on transient wicking

length and wetting velocity are shown in Fig.3. Three flow rates were used: $\dot{m} = 15$, 41 and 48 ml/min. The lowest flow rate was found to provide an inadequate amount of working fluid to rewet the plate. It was also found that at higher flow rate (41 ml/min or higher), increasing the flow rate had no effect on the rewetting of the plate. After this finding, the unheated tests were performed at the flow rate of 48 ml/min, and the heated tests at 31 ml/min. The prediction based on the hydrodynamically controlled model to be presented later is also shown in Fig.3. The comparison between the face up and face down cases (i.e. the horizontal grooved surface facing upward and downward, respectively) is shown in Fig.4. It was found that the rewetting velocity in the face up case is larger than that in the face down case. This is probably because the surface tension force in the face up case is larger than that of the face down case.

REWETTING OF HEATED GROOVED PLATE

<u>Experiment</u>   The experimental apparatus consists of following components [Fig.2]: liquid supply system with an adjustable flow rate, an experimental platform which contains a grooved plate with embedded thermocouples evenly spaced along the bottom in the groove direction, a data acquisition system with multiplexer to simultaneously read and recored the signals from the thermocouples, a heater with a temperature controller for maintaining a constant heater temperature, a traveling thermocouple sensor used to measure temperatures along the top of the plate, a video recording system capable of recording and playing back high resolution pictures frame by frame, and a signal light to synchronize the computer data acquisition with the video.

The plate was chemically cleaned, and then heated at one end to the desired initial temperature. The video camera was activated, and a signal light was turned off to indicate the commencement of computer data acquisition. The working fluid was then introduced to the plate, and the rewetting process was recorded. If desired, surface temperatures were also measured using a traveling thermocouple. The traveling thermocouple was useful for determining the temperature of the liquid front, as well as for gauging the accuracy or serviceability of the embedded thermocouples. When working with 2-propanol extreme care should be taken to insure adequate insulation, ventilation and fire safety.

Rewetting experiments were conducted at various initial temperatures of the heated, grooved plates and with plates in the face up and face down orientations.

<u>Results and Discussion</u>   Experiments were performed at several plate temperatures in both the face up and face down orientations. Confirmation of the flow rate effect was also performed, as the fluid delivery system is such that there is overflow from the end of the plate. Thus only fluid carried by capillary action rewets the plate. It was determined that through a range of flow rates there was a constant velocity with which the fluid would travel as discussed above. However if the flow rate was too high a hydraulic effect would be present. It should be noted that this flow rate will vary from plate to plate, as it is determined by the groove geometry and the number of grooves wetted.

The heated plate case which is presented is one in which the initial plate temperature is above 110 °C. The face up (Fig.6) and face down (Fig.7) orientations are compared. The figures are in two formats. At the top there is a contour plot depicting the temperature in relation to time and location. Below the surface plots are the temperature profiles along

the length of the plate shown in 10 second intervals except the top two profiles which are 2.5 seconds apart. In both formats the location of the fluid front, which was obtained from study of the video, is superimposed.

Following the fluid front for the face up case (Fig.6), it is seen that the front travels between the 95°C and the 100°C contour lines and eventually stagnates at around 110 mm.

Following the fluid front for the face down case (Fig.7), the front crosses several contour lines and stagnates around 70 mm. It should be noted that during the face up (Fig.6) experiment, the thermocouple located at 80 mm malfunctioned. This resulted in the obvious contour and profile anomalies in the figures at the 80mm position.

The dramatic difference between the temperatures profiles in the face up and face down cases indicates a vapor diffusion layer effect. The 2-propanol vapor is more dense than air, and hence forms over the face up plate a vapor layer, through which vapor must diffuse through. This layer is not present in the face down case thus allowing for convection to dominate the heat transfer.

THEORY

In the rewetting process of monogroove heat pipe, it is important to predict the liquid advancing velocity. If the initial plate temperature is less than the Leidenfrost temperature, the advancing liquid is believed to be driven by a capillary force. The liquid advancing velocity is hydrodynamically controlled by the balance of surface tension force, friction force, gravitational force and the acceleration term as described by

$$\frac{\sigma}{R}A_1 = \tau_w A_w + mgsin\alpha + m\frac{du}{dt} \tag{1}$$

where R is the characteristic capillary radius, σ the surface tension, m the total mass of liquid in the grooves, A_1 the liquid cross section area, α the inclination angle of the plate, u the liquid front mean velocity, A_w the wetted wall area, and $\tau_w = f\rho u^2/8$ shear stress where f=64/Re_{Dh}. The initial condition for above equation is: u=0 when t=0.

To simplify the problem, R is assumed to be constant and equal to half of the groove width, which is equivalent to a contact angle of zero. From Fig.4, it can be seen that the prediction is in good agreement with the experimental data. For the face down case, the use of same capillary radius seems to overestimate the driving force. Since the rewetting velocity of the unheated plate in the face down position is slower than in the face up position, the effective capillary radius or contact angle may be affected by plate orientation. Therefore the groove plate was placed in various inclinations and the mean wicking length at the face down orientation was found to be slightly shorter than the face up position as shown in Fig.1. Thus the difference in the prediction between the face up and face down positions is nondiscernable when R is changed slightly, as shown in Fig.4.

For the plate with initial temperatures above the Leidenfrost temperature, the rewetting velocity is conduction controlled[1]. The plate temperature is determined by solving the conduction equation,

$$\frac{\partial\theta}{\partial\tau} = \frac{\partial^2\theta}{\partial\eta^2} - B\theta \tag{2}$$

The initial condition is: $\tau = 0,$ $\theta(\eta,0) = \theta_0(\eta)$ and

243

the boundary conditions are: $\theta(0,\tau) = \theta_1(\tau)$, $\qquad \theta(\eta_{L1}, \tau) = 1$ $\qquad$ for wet region

$\qquad\qquad\qquad\qquad \theta(\eta_{L1}, \tau) = 1$, $\qquad \theta(\eta_L, \tau) = \theta_2(\tau)$ $\qquad$ for dry region

In the above, $\theta_0(\eta)$, $\theta_1(\tau)$ and $\theta_2(\tau)$ are specified by the experimental conditions. By using the variable space method [2], the equation (2) becomes:

$$\frac{d\theta}{d\tau}\Big|_n = \frac{\partial \theta_n}{\partial \eta} \frac{d\eta_{L1}}{d\tau} \frac{\eta_n}{\eta_{L1}} + \frac{\partial^2 \theta_n}{\partial \eta^2} - B\theta_n \qquad for \quad 0 < \eta < \eta_{L1}$$

$$\frac{d\theta}{d\tau}\Big|_n = \frac{\partial \theta_n}{\partial \eta} \frac{d\eta_{L1}}{d\tau} \frac{\eta_L - \eta_n}{\eta_L - \eta_{L1}} + \frac{\partial^2 \theta_n}{\partial \eta^2} \qquad for \quad \eta_{L1} < \eta < \eta_L$$

(3)

where η_{L1} is a non-dimensional distance of the liquid front and is determined by matching following condition:

$$\frac{\partial \theta}{\partial \eta}\Big|_{dry} = \frac{\partial \theta}{\partial \eta}\Big|_{wet}$$

(4)

Numerical calculation of eq.(3) was performed simultaneously for both the wet region and dry region. From the calculation it is found that the value of the liquid front temperature is very important for the heat conduction controlled model. In the current calculation, an experimental value of $95°C$ has been used to calculate liquid moving velocity and temperature profile. The predicted rewetting distance and plate temperature profiles are compared with experimental data as shown in Fig.5 and 6B.

CONCLUSION

This study reports experimental results of rewetting of heated and unheated, grooved plates. Theoretical models were presented to explain and predict the rewetting behavior. The following conclusions can be reached: (i) With sufficient supply of liquid flow rate, the advancing liquid front velocity is insensitive to the variation of the supplied liquid flow rate, since the liquid is driven by surface tension. (ii) The rewetting of the plate is hydrodynamically controlled when the initial plate temperature is lower than the Leidenfrost temperature. However, it becomes conduction-controlled when the initial plate temperature exceeds the Leidenfrost temperature. (iii) The rewetting speed in the face down case is slower than that in the face up case probably due to different capillary radius (contact angle).

ACKNOWLEDGEMENT

REFERENCES

[1]. S.H.Chan and W.Zhang, J. of Heat Transfer, Vol.116 (1994), 171-179.

[2]. W.D.Murray and F.Landis, J. of Heat Transfer, Vol.81 (1959), 106-112.
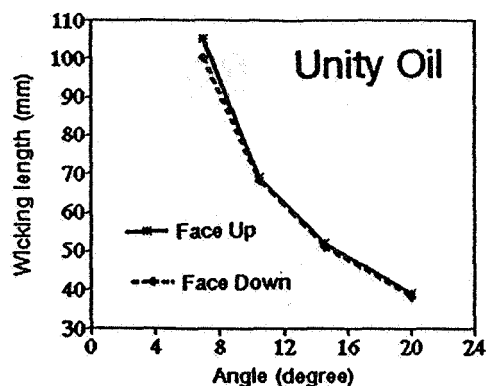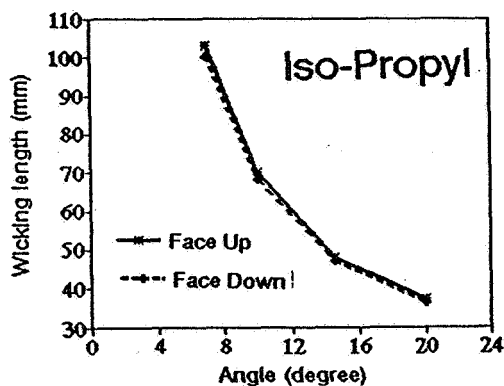
Fig.1 Wicking length L vs inclination angle α
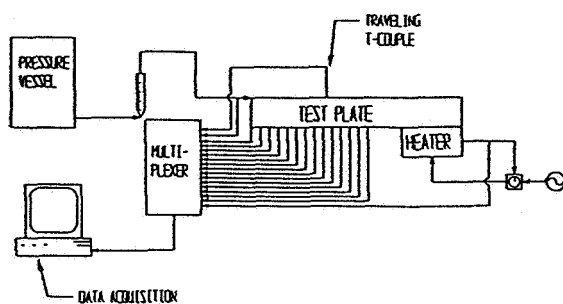
Fig.2 Schematic diagram of experiment setup
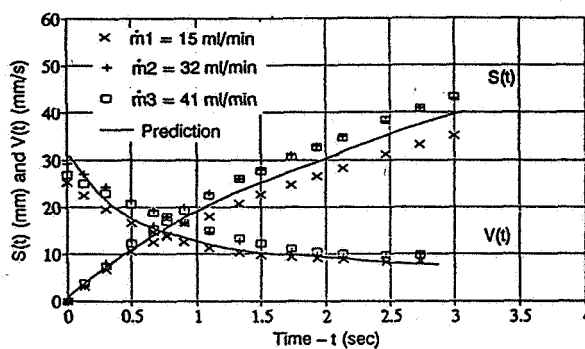
Fig.3 Mass flow rate effects on wicking distance and liquid front velocity
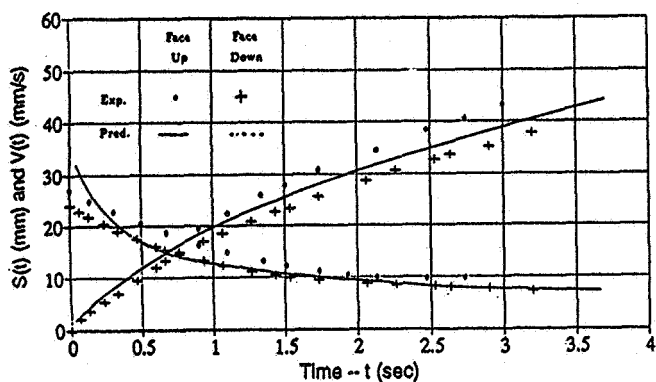
Fig.4 Predicted and experimental results of liquid front location and velocity on unheated plate under the face up and face down positions
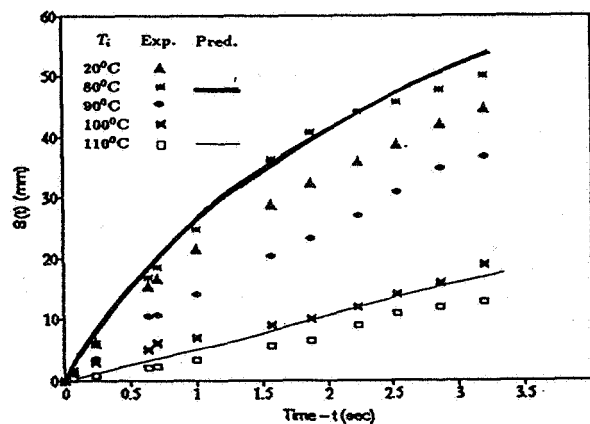
Fig.5 Predicted and experimental rewetting distance on heated groove plate with different initial plate temperatures

245
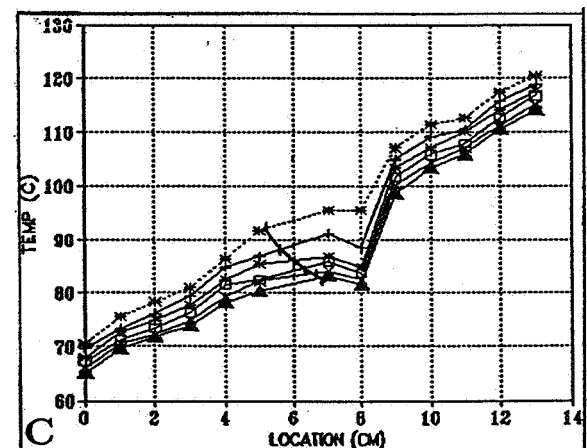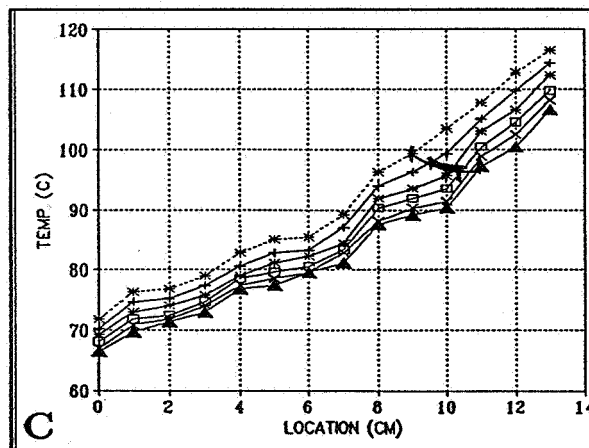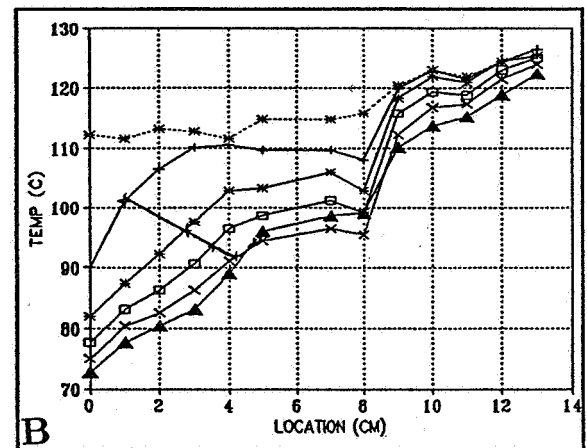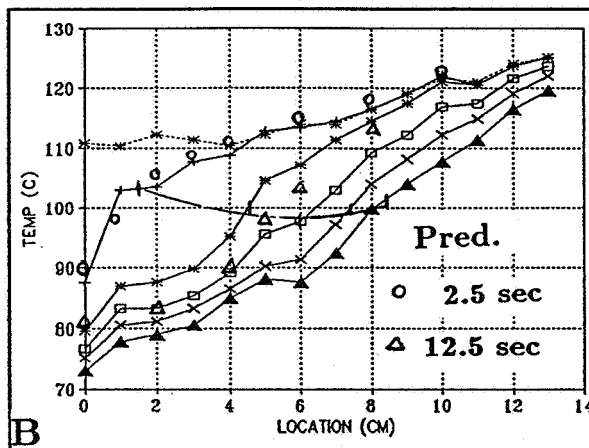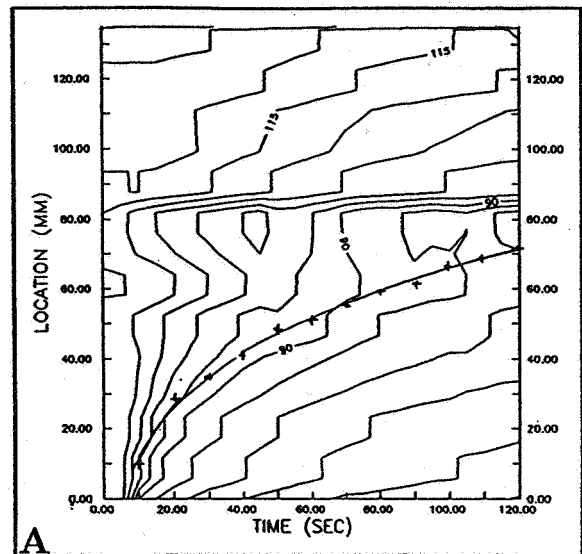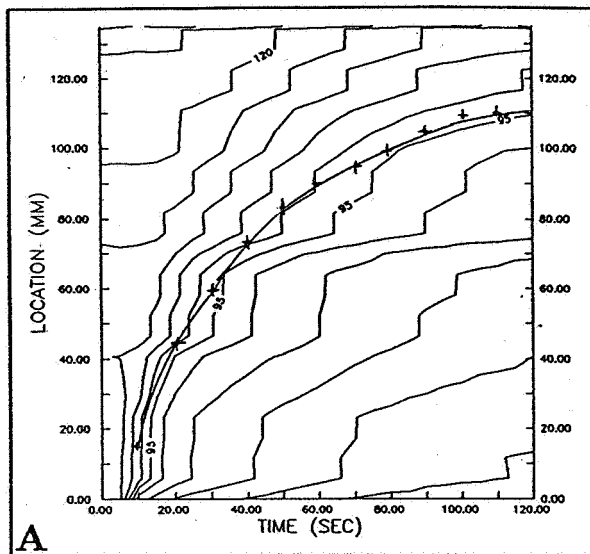
Fig.6 Temperature profiles for the face
up case at $T_i > 110°C$

Fig.7 Temperature profiles for the face
down case at $T_i > 110°C$

EFFECTS OF THERMOCAPILLARITY ON AN EVAPORATING EXTENDED MENISCUS IN MICROGRAVITY

K. P. Hallinan and Q. He
University of Dayton
Department of Mechanical and Aerospace Engineering
Dayton, OH 45469-0210

ABSTRACT

An analytical investigation of the effects of thermocapillarity on the flow field within and heat transfer from the extended meniscus region of a heated meniscus which is re-supplied by capillarity is presented. Microgravity conditions are considered. The analysis shows that even for extremely small temperature differences between the wall and the vapor (< 1 mK) thermocapillary stresses at the liquid-vapor interface due to a non-uniform interfacial temperature drastically alters the flow field. At the same time, these stresses were shown to have only a slight effect on the heat transfer from the extended meniscus but increasing with an increasing temperature difference. Additionally, thermocapillary effects were shown to be sensitive to pore size. A criterion was established from a scaling analysis identifying the conditions necessary for thermocapillarity to affect the operation of capillary-pumped heat transport devices in microgravity. A critical Marangoni number and corresponding critical temperature difference between wall and vapor were identified.

INTRODUCTION

Evaporation from curved menisci is observed in a variety of heat transport devices which rely upon nucleate boiling or capillary phase-change, such as heat pipes, sweat coolers, grooved evaporators, and other enhanced heat transfer surface devices. Capillary phase-change devices (heat pipes and capillary-pumped loops or CPL's) have much promise for high heat transport applications in space. Reliance upon capillarity for the transport of liquid to where energy can be dissipated via evaporation offers outstanding potential for the thermal control of high heat flux devices in low gravity environments. The passive means of fluid transport also precludes the need for mechanically pumping liquid from one location to another. The heat transfer enhancement realized with phase change over pure convection also affords the potential for substantial weight and power savings.

Evaporation of a nearly perfectly wetting liquid in a pore, groove, or capillary due to heat input has received little attention at the microscale. Recent theoretical work, however, has identified the extended meniscus region for wetting liquids as where the maximal evaporation flux is present at least when the wall's thermal conductivity is much greater than the liquid [1,2]. In fact, over distances on the order of microns, the evaporative flux goes from zero to a maximum value and then decreases rapidly as the film thickens and therefore the thermal resistance increases. As a consequence, the liquid-vapor interfacial temperature gradients (shear stresses) are likely most severe in the extended meniscus. However, the previous analytical work has neglected the resulting thermocapillary stresses. It is hypothesized that these stresses can choke the flow into and/or be responsible for destabilizing the extended meniscus. The practical implication relative to the operation of capillary-pumped heat transport devices in microgravity is that if the thermocapillary stresses at the near contact line region are important, they may result ultimately in the deprime of the evaporator wick, such has commonly occurred in practice [3].

Identification of the conditions which lead to interfacial instabilities and the subsequent observation of the evolution of instabilities in microgravity, should they arise, are vital. In space, capillary-pumped heat transport devices have not performed as expected [3]. Whereas in 1-g body forces are always present to stabilize such instabilities, their absence in low-g dictates that evaporating menisci are inherently more

unstable. If the evolution of instabilities in low-g ultimately leads to the dry-out of the pores within heat pipes and CPL's, then an understanding of the conditions leading to their onset may allow designers of such devices the opportunity to design around such a failure mode. This present research ultimately aims to investigate the effects of the thermocapillarity on the stability of the extended meniscus.

MODEL

A model is developed to assess the importance of thermocapillary stresses in the thin film portion of a meniscus within a circular or grooved pore geometry. The disjoining pressure gradient theory is used to describe the flow in the thin film region of the meniscus. The governing system of equations is developed through application of conservation laws.

In developing the model, the following assumptions are used: (1) $\mu_v \ll \mu_l \Rightarrow$ viscous stresses on the vapor side are neglected; (2) the effect of the circumferential curvature is negligible; (3) a Gibbs approximation for both the liquid-vapor and liquid-solid interface is assumed; (4) small Bond number $\Rightarrow$ microgravity; (5) the liquid is perfectly wetting and non-polar; and (6) the thin film evaporative flux equation, developed by Brown et al. [4] is used.

Boundary conditions include no-slip and impermeability at the wall, as well as the conservation of mass, momentum and energy at the liquid-vapor interface.

SCALING ANALYSIS

The governing equations and boundary conditions are scaled in a manner analogous to Burelbach, Bankoff, and Davis [5] except in the specification of lengthscales appropriate for the x and y directions (respectively the coordinates parallel and normal to the wall). A reasonable lengthscale in the vertical direction is the film thickness, h_0, which defines a balance between the capillary pressure terms and the disjoining pressure terms in the extended meniscus. The bulk meniscus curvature, K, which in the thin film where the slope is small is approximately equal to h_{xx}. This term can be scaled as h_0/x_0^2 or $1/R$. Thus, the balance between capillary pressure and disjoining pressure terms yields:

$$\frac{\bar{A}}{h_0^3} = \frac{\sigma_{lv}}{R} \qquad \Longrightarrow \qquad h_0 = \left\{ \frac{\bar{A}R}{\sigma_{lv}} \right\}^{1/3}$$

where $\bar{A}$ is the modified Hamaker constant, σ_{lv} is the surface tension, and R is the radius of the pore or groove. Likewise, the x-scale is chosen such that it effectively defines the length of the extended meniscus, obtained again by balancing the capillary pressure and disjoining pressure terms.

$$\sigma_{lv} \frac{h_0}{x_0^2} \sim \frac{\bar{A}}{h_0^3} \qquad \Longrightarrow \qquad x_0 = \left\{ \frac{\sigma_{lv} h_0^4}{\bar{A}} \right\}^{1/2}$$

Viscous scales for time, velocity, and pressure are selected to respectively be h_0^2/ν, ν/h_0, and $\rho\nu^2/h_0^2$, where ν is the kinematic viscosity. Temperature differences are scaled by $T_w - T_v$. Finally, the mass flux is scaled with $k\Delta T/h_0 h_{lv}$.

A regular perturbation method was utilized to simplify the analysis of the resulting non-dimensional governing system. The characteristic slope, $X = h_0/x_0$, was chosen as the perturbation parameter. The following zeroth order system is derived for the change in film thickness with time,

$$h_{0_\tau} = -Ej_0 + \left\{ P_{0_\xi} \frac{h_0^3}{3} - MaPr^{-1} \left[(j_0 h_0)_\xi + j_0 h_{0_\xi} \right] \frac{h_0^2}{2} \right\}_\xi \tag{1}$$

where

$$P_{0_\xi} = -Sh_{0_{\xi\xi\xi}} + 3\hat{\Pi} \frac{h_{0_\xi}}{h_0^4} \tag{2}$$

and $E = k\Delta T/\rho\nu h_{l\nu} \Rightarrow$ evaporation number, $j_0 \Rightarrow$ dimensionless evaporative flux, $Ma = \gamma\Delta T h_0^2/\rho\nu k x_0 \Rightarrow$ Marangoni number, $Pr = \mu c_p/k \Rightarrow$ Prandtl number, $S = \sigma_{l\nu,0} h_0/\rho\nu^2 X^2 \Rightarrow$ dimensionless curvature, and $\hat{\Pi} = A/12\pi\rho\nu^2 h_0 \Rightarrow$ dimensionless disjoining pressure.

This equation is an extremely non-linear differential equation and can only be solved numerically.

NUMERICAL APPROACH

A series of numerical experiments were conducted for quasi-steady conditions, i.e., where the liquid evaporating from the extended meniscus is continually replenished and the meniscus is fixed in space ($\partial_\tau = 0$). The boundary conditions used for solving equation (1) were chosen in both the meniscus and adsorbed film regions. Since the capillary number, $Ca = \mu_0 u_0/\sigma_{l\nu}$, associated with the bulk meniscus flows is small, as described by Hallinan et al. [6], the apparent contact angle is assumed to be unchanged dynamically. Therefore, the bulk meniscus curvature does not change relative to the equilibrium meniscus curvature. This assumption dictates that in meniscus region, i.e. at $\xi \to \infty$, the curvature is $K_m = 1/R$. In the adsorbed film region, where there is no evaporation, the thin film thickness, h_0, can be calculated [4]. The slope, curvature and third derivative of the film thickness are also zero in the adsorbed film region. But the application of these boundary conditions leads to a trivial solution of equation(1) for steady state of constant film thickness. In order to get a nontrivial solution, a very small perturbation, $\Delta h = 10^{-5} h_0$, is applied to the adsorbed film thickness. The third derivative is set to zero, the second derivative is found by letting evaporative flux go to zero, and the slope is chosen such that the curvature of the extended meniscus matches that of bulk meniscus at $\xi \to \infty$.

NUMERICAL RESULTS

The basic goals of this study are to identify the role of the thermocapillary stresses on the flow field and the heat transfer from the extended meniscus. Results are presented for pentane as the working fluid at a temperature of 20 °C for a pore size of 10 cm. Such a pore size is considered because of its likely use in a future space flight experiment. Differences in temperature between the wall and the vapor in the range from $10^{-5} - 10^{-2}$ °C are considered with the corresponding Marangoni numbers ranging from $10^{-7} - 10^{-5}$. Numerical results obtained by considering thermocapillary effects are compared to those obtained neglecting their contribution, i.e. for Ma=0.

Thermocapillary effects for the range of Marangoni numbers studied were shown to have little effect on the film profile. Of significance, however, was their effect on the velocity profile. As ΔT increases, as shown in Fig. 1, the length of the film decreases considerably. Thus, because ΔT characterizes the maximum temperature difference along the film, if the film shortens in length, the interfacial temperature gradients are magnified.

Thermocapillary effects on the velocity profile are shown to be important even when ΔT or the Marangoni number is extremely small. Ignoring thermocapillary effects, the velocity profiles for a ΔT of 0.002 K are shown in Fig. 2(a), where the maximum velocity appears at the liquid-vapor interface. Accounting for the thermocapillary effects, the velocity profile changes even for the very small ΔT considered. Figure 2(b) demonstrates that the maximum velocity is no longer at the liquid-vapor interface after a certain distance away from the adsorbed film region. As ΔT is increased further, reversed flows, which are counter the model's assumptions, are predicted.

Figure 3, which provides a plot of the local evaporative flux versus axial distance, shows that for small ΔT the thermocapillary effects on heat transfer are hardly noticeable for the cases considered. But when ΔT is increased, e.g., $\Delta T = 0.02 K$, $Ma = 2.6e\text{-}5$, the evaporative flux does decrease. The Marangoni effects therefore can affect the heat transfer primarily near the peak evaporative flux, where temperature gradients are most severe.

ESTIMATE OF THE IMPORTANCE OF THERMOCAPILLARITY

The previous numerical results showed quantitatively that the effects of thermocapillarity on the flow and temperature fields were important even for extremely small differences in temperature between the assumed isothermal wall and the vapor (< 1 mK). In fact, for Marangoni numbers greater than 10^{-5} the numerical solution was observed to lead to reversed flows or thermocapillary flows on the surface, which is inconsistent with the approximations inherent to using the lubrication approximation. That a *critical* Marangoni number on this order of magnitude possibly produces reversed flow in the extended meniscus is not surprising, especially upon close consideration of the equation for the film profile shown in equation (1). Apparent from inspection of this equation is that when the terms involving the Marangoni number become on the same order of magnitude as the driving pressure terms, either the meniscus will recede due to thermocapillarity forces or it will recede due to the inability of the bulk flow to replenish the evaporation from the extended meniscus.

Scaling arguments can therefore be used to estimate a critical Marangoni number. Assuming the terms associated with the driving pressure can be scaled by $\hat{\Pi}$, and j_0 scales as approximately 1 for low evaporative thermal resistance, and all terms involving h can be assumed already to be on the order of 1, then the critical Marangoni number can be estimated to be:

$$Ma_c/Pr = \hat{\Pi} - E$$

In this expression for Ma_c, $\hat{\Pi}$ effectively describes the potential available in the film which must minimally overcome the thermocapillary force acting on the film, while still being capable of replenishing the flow of liquid which evaporates from the film. The significance of the evaporation number, E, is that it increases as ΔT increases. Thus it provides a measure of the total evaporation from the extended meniscus. Therefore, not surprisingly, as the evaporative flux increases the critical Marangoni number decreases. For the test conditions considered in the numerical solution, only a small ΔT of 0.035K is required for this condition to be satisfied.

Interestingly this relationship for the critical Marangoni number reveals a slight sensitivity to pore size. Using the lengthscales described earlier for the characteristic length and thickness of the film (x_0 and h_0), for example, the critical Marangoni number and associated ΔT for a pore size of 10 μm is respectively, 9.671E-4 and 0.754 K.

CONCLUSIONS

Thermocapillary stresses at the liquid-vapor interface within an evaporating extended meniscus have been shown to significantly affect the flow field within the extended meniscus even when the extended meniscus heat transport is very small. It is also clear that their effect is first felt on the velocity field near the liquid-vapor interface, and as ΔT increases they begin to affect the heat transport as the interfacial thermocapillary stresses near the same order of magnitude as the shear stresses at the wall. When this occurs, the available potential to drive the liquid into the extended meniscus must overcome both forces, and thus, for $T_w - T_v$ fixed, thermocapillary effects will choke the flow into the extended meniscus. Finally, a scaling analysis was used to develop an expression for the critical Marangoni number which defines the condition where the disjoining pressure potential is roughly balanced by the thermocapillary force acting over the entire film. For such a condition, it is reasonable to expect that flow into the extended meniscus would be entirely choked, and if evaporation occurs, the meniscus would recede.

ACKNOWLEDGMENTS

References

[1] Holm, F. W. and Goplen, S. P., "Heat Transfer in the meniscus Thin-Film Transition Region," *J. Heat Transfer,* Vol. 101, 1979, pp. 543-546.

[2] Stephan, P. C. and Busse, C. A., "Theoretical Study of an Evaporating Meniscus in a Triangular Groove," 7th Int.. Heat Pipe Conf., Minsk, USSR, 1990.

[3] Ku, J., "Overview of Capillary Pumped Loop Technology," presented at 1993 National Heat Transfer Conference, Atlanta, Georgia.

[4] Brown, J. R., Hallinan, K. P., Chebaro, H. C., Chang, W. S., 1993, "Review of Heat Transfer from Stable Evaporating Thin Films in the Neighborhood of a Contact Line," presented at 1993 National Heat Transfer Conference, Atlanta, Georgia.

[5] Burelbach, J. P., Bankoff, S. G., and Davis, S. H., 1988, "Nonlinear Stability of Evaporating / Condensing Liquid Films," J. Fluid Mech., Vol. 195, pp. 463-494.

[6] Hallinan, K. P., Chebaro, H. C., Kim, S.J., and Chang, W.S., 1994, "Evaporation from an Extended Meniscus for Non-isothermal Conditions," accepted for publication in *J. of Thermophysics and Heat Transfer.*
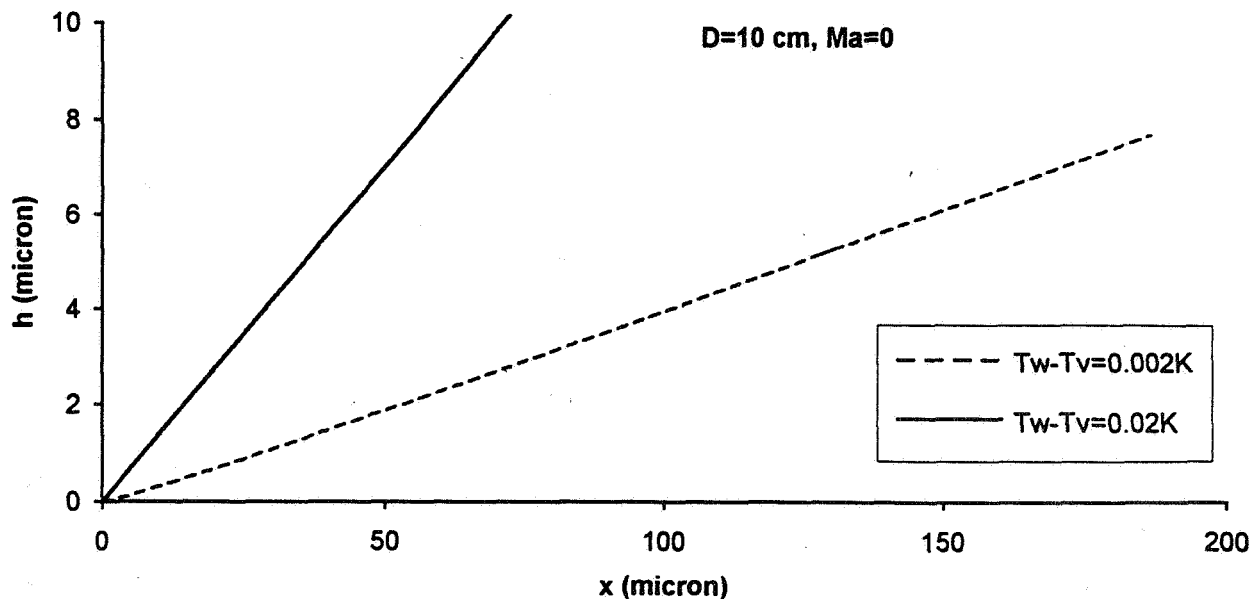
Figure 1: Extended meniscus profile for pore of radius 5 cm with Ma = 0
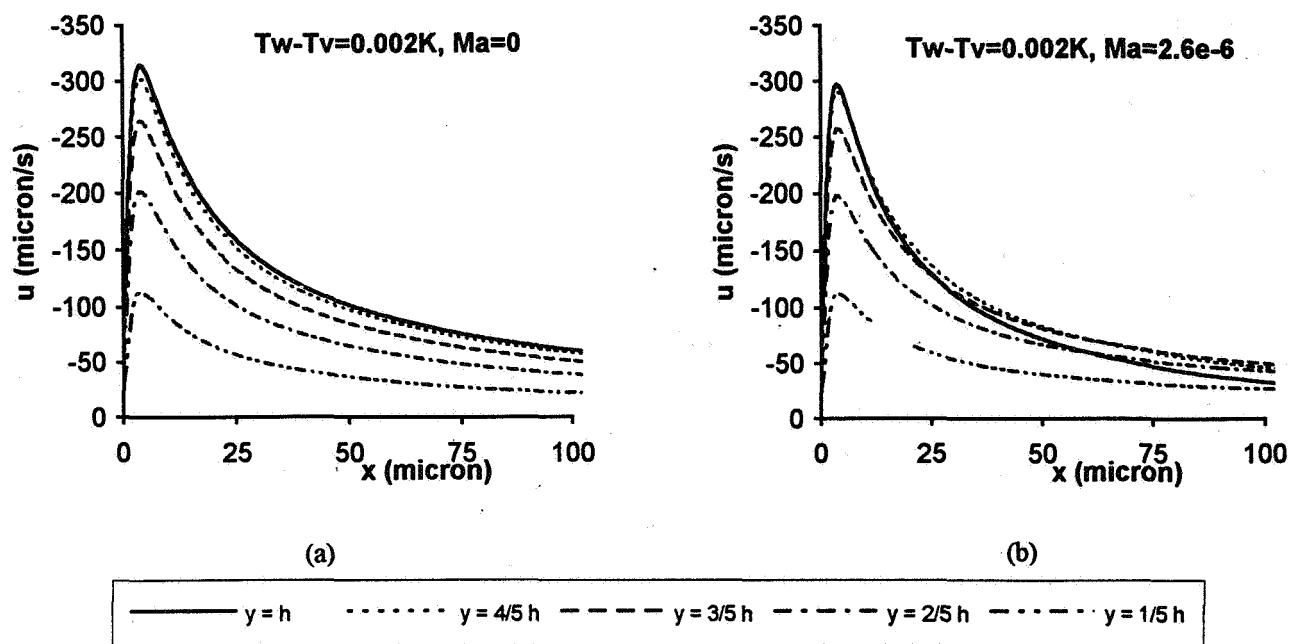
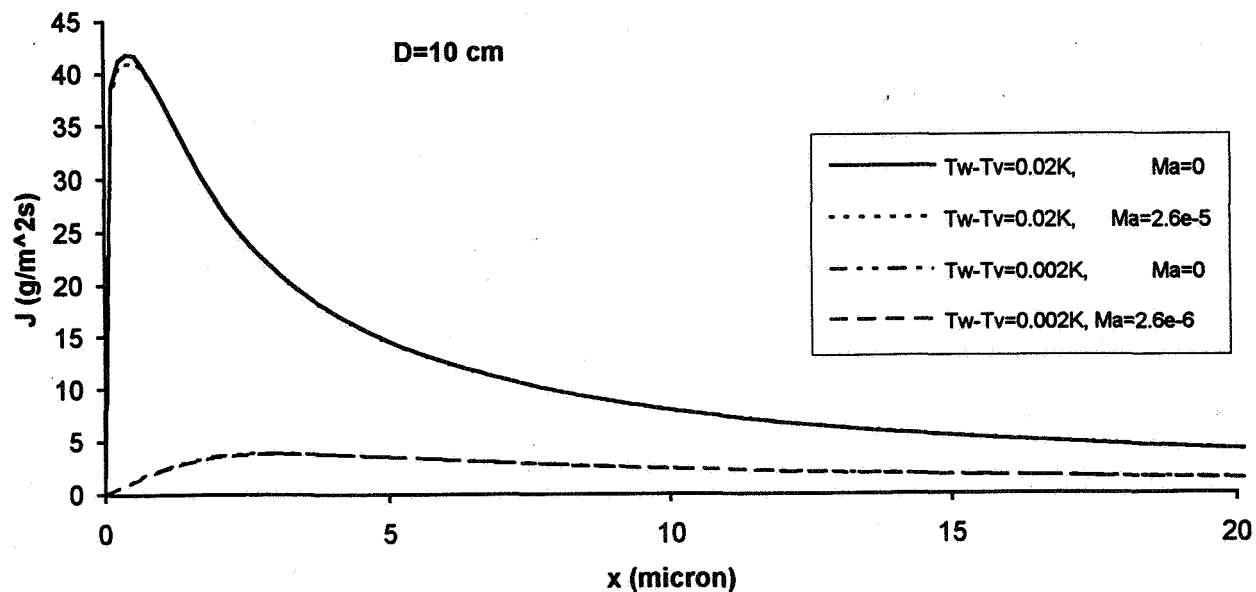Figure 2: Velocity profile for pore of radius 5 cm with Ma = 0

Figure 3: Axial evaporative flux for pore of radius 5 cm

INTERFACIAL FORCE FIELD CHARACTERIZATION OF A CONSTRAINED VAPOR BUBBLE THERMOSYPHON USING IAI

Sunando DasGupta, Joel L. Plawsky and Peter C. Wayner, Jr.
The Isermann Department of Chemical Engineering
Rensselaer Polytechnic Institute,
Troy, NY 12180-3590

ABSTRACT

The isothermal profiles of the extended meniscus in a quartz cuvette were measured in a gravitational field using IAI (image analyzing interferometer) which is based on computer enhanced video microscopy of the naturally occurring interference fringes. The experimental results for heptane and pentane menisci were analyzed using the extended Young-Laplace Equation. These isothermal results characterized the interfacial force field *in-situ* at the start of the heat transfer experiments by quantifying the dispersion constant for the specific liquid-solid system. The experimentally obtained values of the disjoining pressures and the dispersion constants are compared to that predicted from the DLP theory and good agreements are obtained. The measurements are critical to the subsequent non-isothermal experiments because one of the major variables in the heat sink capability of the CVBT is the dispersion constant. In all previous studies of micro heat pipes the value of the dispersion constant has been "guesstimated". The major advantages of the current glass cell is the ability to view the extended meniscus at all times. Experimentally, we find that the extended Young-Laplace Equation is an excellent model for the force field at the solid-liquid-vapor interfaces.

INTRODUCTION

When the gravitational body force is essentially removed, the shape of a constrained liquid volume with a free interface changes dramatically to reflect the new force field. The resulting equilibrium shape under microgravity conditions depends on the intermolecular force field which changes rapidly in the vicinity of the liquid-vapor and liquid-solid interfaces. Under non-equilibrium conditions, microgravity fluid dynamics and change of phase heat transfer are a function of further changes in the shape of the fluid volume from its equilibrium shape. Therefore, in small systems, the shape dependent interfacial intermolecular force field can be used to control fluid flow and heat transfer [1, 2]. The initial equilibrium liquid film shape is controlled by fixing the container shape, the liquid and solid substrate surface properties, and the volume of the liquid.

In particular, we are concerned with the experimental study of the generic constrained vapor bubble thermosyphon (CVBT) system presented in Fig. 1. For a completely wetting system, the liquid will coat all the walls of the chamber. For a finite contact angle system, some of the walls will have only a small amount of adsorbed vapor which changes the surface properties of the solid-vapor surface. Liquid will fill a portion of the corners in both cases. If temperature at End (2) is higher than End (1), because of an external heat source and sink, energy flows from End (2) to End (1) by conduction in the walls and by an evaporation, vapor flow and condensation mechanism. The condensate flows from End (1) to End (2) because of the intermolecular force field which is a function of the film profile. A CVBT with a very small cross section has been called a micro heat pipe.

There is a "pressure jump" at the liquid-vapor interface, due to the anisotropic stress tensor near interfaces. For many years, the classical Young-Laplace equation of capillarity has been successfully used to describe the pressure jump at a curved liquid-vapor interface [3, 1, 4, 5, 6, 7, 8, 9]. An example of its use to describe the fluid dynamics in a micro heat pipe is given in a publication by Wu and Peterson [10]. In this case, the pressure jump is a function of the liquid-vapor surface tension and the interfacial radius of curvature. Recently Khrustalev and Faghri [11] and Swanson and Peterson [12] have used this type of model to analyze a micro heat pipe. Swanson and Herdt [13] have used the three dimensional augmented Young-laplace equation to develop a mathematical model describing the evaporating meniscus in a capillary tube. However, near the liquid-solid interface, additional changes in the stress field within the liquid occur because of changes in the intermolecular force field due to solid molecules replacing liquid molecules. These long range van der Waals forces have been found to be extremely important in that they lead to the concept of an extended evaporating meniscus [1, 2]. In a completely wetting system, a thin adsorbed film extends for a long distance beyond the classical equilibrium meniscus [14]. The thin film controls the important processes of spreading and wetting. It forms a thin liquid bridge between the "classical menisci" formed in the corners of the chamber presented in Fig. 1. Herein, we present the initial experimental results of a study of the three dimensional extended meniscus in a configuration of general importance to the microgravity environment : the constrained vapor bubble thermosyphon.

The effects of both the liquid-vapor and liquid-solid interfaces on the effective pressure jump at the liquid-vapor interface of the extended two dimensional meniscus have been modeled using the following augmented Young-Laplace equation. Here P_l is the liquid pressure, P_v is the vapor pressure, $\bar{A}$ is the Hamaker constant (negative for a completely wetting liquid), B is the retarded dispersion constant for thicker films, $\delta(x)$ is the film thickness, K is the curvature and σ is the surface tension. The first term on the right hand side of Eq. (1) is called the disjoining pressure, Π, and it represents the change in the body force on the liquid due to the long range van der Waals forces between the liquid and solid over a narrow range of thicknesses.

$$P_l - P_v = \frac{B}{\delta^n} - \sigma K$$

$$\frac{B}{\delta^n} = \frac{B}{\delta^4} = -\Pi \quad \delta \geq 40nm \quad ; \quad \frac{B}{\delta^n} = \frac{\bar{A}}{\delta^3} = -\Pi \quad \delta \leq 20nm$$

(1)

According to Eq. (1), the effective pressure in the liquid is reduced below that in the vapor by both capillarity and disjoining pressure in a completely wetting system. This leads to a reduction in the vapor pressure. However, the vapor pressure reduction can be offset by a temperature increase to obtain the vapor bubble thermosyphon presented in Fig. 1. The chemical potential field is a function of the temperature and the effective liquid pressure which is a function of the shape of the liquid film. Therefore, the process is understood by measuring the temperature field and the liquid film shape.

THEORY

The augmented Young-Laplace equation can be written for a point in the thicker portion of the meniscus, where the disjoining pressure effects are negligible and for another point where both effects are present. For the isothermal non-evaporating (Q=0) cases considered here the liquid pressure will remain the same, irrespective of the position.

$$\sigma K - \frac{B}{\delta^4} = \sigma K_\infty \quad , \quad Q = 0$$

(2)

We note that the curvature at the thicker portion of the meniscus (K_∞) is nearly constant [15]. In Eq. (2), the curvature at the liquid-vapor interface (K) can be expressed in the following form.

$$K = \frac{\frac{d^2\delta}{dx^2}}{[1 + (\frac{d\delta}{dx})^2]^{3/2}}$$

(3)

Using a simplified form of curvature, which is valid only if the square of the slope is small compared to one, Eq. (2) can be written in the following way.

$$\sigma \frac{d^2\delta}{dx^2} - \frac{B}{\delta^4} = \sigma K_\infty$$

(4)

For the isothermal experiments reported in this study the value of the maximum slope is 0.15 and hence using the simplified form of curvature is justified. The following variables are introduced next to modify Eq. (4) to obtain Eq. (6).

$$\eta = \frac{\delta}{\delta_0} \quad Z = x (\frac{K_\infty}{\delta_0})^{1/2}$$

(5)

$$\frac{d^2\eta}{dZ^2} + (\frac{-B}{\sigma K_\infty \delta_0^4}) \frac{1}{\eta^4} = 1$$

(6)

Eqs 2 - 6 are valid for an <u>equilibrium situation</u> with no evaporation or condensation. A dimensionless variable, α, is defined next.

$$\alpha^4 = \frac{-B}{\sigma K_\infty \delta_0^4}$$

(7)

Eq. (6) can now be written as

$$\frac{d^2\eta}{dZ^2} = 1 - \frac{\alpha^4}{\eta^4} \tag{8}$$

For the equilibrium case, Q=0 and α=1. Any values of α other than unity will signify deviation from the equilibrium situation. The experimental section of the paper and the subsequent discussion will present two experimental cases, which were very close to equilibrium. The results will demonstrate the utility of the model and the evaluation of the values of α. After multiplying both sides of Eq. (8) by 2dη/dZ and integrating (C_1 is the constant of integration),

$$\left(\frac{d\eta}{dZ}\right)^2 = 2\eta + \frac{2}{3}\frac{\alpha^4}{\eta^3} + C_1 \tag{9}$$

The boundary condition used for the completely wetting case is

$$For \quad \eta = \alpha \quad \frac{d^2\eta}{dZ^2} = 0 = \frac{d\eta}{dZ} \tag{10}$$

We note that this can be viewed as an artificial boundary condition for a non-equilibrium system for which $\alpha > 1$. The utility of the extended model is demonstrated below.

Using the boundary condition, the slope of the meniscus can be expressed as

$$\frac{d\delta}{dx} = - \left(K_\infty \delta_0 \right)^{1/2} \sqrt{2\eta + \frac{2}{3}\frac{\alpha^4}{\eta^3} - \frac{8}{3}\alpha} \tag{11}$$

Hence if the curvature at the thicker end of the meniscus, K_∞, along with B, δ_0 and σ are known, the slope of the meniscus can be directly calculated as a function of the film thickness, using only the augmented Young-Laplace equation. The minus sign in Eq. (11) is indicative of the fact that for the reference frame selected, the meniscus slope should always be negative (film thickness decreases as distance increases).

Herein we compare the slope of the meniscus obtained by numerical analysis of the experimental data for a system with unknown values of Hamaker constant (or dispersion constant, depending on the adsorbed film thickness) and the slope predicted by the augmented Young-Laplace equation (Eq. 11). The slope predicted by Eq. (11) is a function of α and the α corresponding to the closest match between these two slopes is selected to determine the value of the dispersion constant for the CVBT, in situ, for our isothermal experiments, as will be apparent in the next sections. Finally we compare the experimentally obtained values of the dispersion constants and the disjoining pressures with the predictions from the DLP theory for our experimental system.

EXPERIMENTAL

A schematic diagram of the cell and the experimental set up is shown in Fig. 2. The cell was essentially a small cuvette, made of quartz to facilitate optical observation and measurement of the liquid meniscus. The prototype cell was square (3mm x 3mm inside) in cross section, as is the case with the actual CVBT. The actual CVBT being made is slightly more complicated to facilitate the cleaning (it has a vacuum port, a pure test liquid feed port) and it is made of a special high refractive index glass to enhance the contrast for optical measurements. The present study was conducted as a precursor to the non-isothermal CVBT experiments, mainly to develop the method for accurately measuring the liquid film thickness profile and to estimate the dispersion constant, in situ, at the start of the experiment. The isothermal results characterize the interfacial force field and the information are critical to the operation and the heat sink capability of the CVBT.

The film thickness profile at the corners of the experimental cell was measured using IAI - image analyzing interferometry. Interference phenomena were used to determine the profile of the capillary meniscus in the thickness range $\delta \geq 0.1\mu m$. A detailed description of the IAI techniques and hardware were presented in [15,16]. The cell was partially filled up with the liquid and placed on the microscope stage. The whole assembly was tilted with respect to the horizontal at two different angles in the two settings used in this study. The system was left to equilibrate with the surroundings for 3 hours before taking any data. An optical interference pattern representing the thickness profile was readily observed (Fig. 3). The pictures of the interference patterns formed at the corners of the cell at two specific points (A and B, as shown in Fig. 2) for each angle setting were captured in the image processor. From each image a plot of the pixel grey value versus distance was extracted. The grey value at each pixel was a measure of the reflectivity. As is evident from Fig. 3, the reflectivity underwent a cyclic change with

increase in film thickness. The computer program scanned the peaks and valleys and filtered the noise from the real peaks/valleys. It then interpolated peak/valley envelopes and by analyzing the relative reflectivity of any pixel with respect to these (dark and light pixel envelopes), determined a film thickness at every pixel [16]. The fact that the extended capillary meniscus merged smoothly to an adsorbed flat film was utilized to estimate the adsorbed film thickness from the grey value data and the peak/valley envelopes. The estimated error in measuring the adsorbed film thickness was ±0.5nm-1.0nm for the thickness range studied herein.

Figure 4 is an example of the measured film thickness profiles with heptane as the test liquid. The picture was for a specific angle. In an isothermal system of spreading liquid on an inclined solid substrate the curvature should remain constant in the region where dispersion forces can be neglected. So the film profile in this range approximated a parabola and a plot of $\delta^{1/2}$ vs x was a straight line. As can be seen form Fig. 4, $\delta^{1/2}$ vs x was nearly a straight line in all the cases, showing the proximity of the cases to isothermality. On the other hand it is clear that the thickness profile at point B was steeper than in point A as a result of higher hydrostatic pressures and subsequent higher curvatures. We also observed that an increase in angle resulted in an increase in the film curvature. Plotting $\delta^{1/2}$ vs x, therefore, clearly illustrates the sensitivity of the film thickness shape to externally imposed conditions. This will not be obvious from a plot of δ versus x. Next we address the significance of the film thickness profile measurements.

RESULTS AND DISCUSSION

Figure 5 is a representative picture of the close match between the experimental slope and the slope obtained by the solution of the augmented Young-Laplace equation. The triangles represent the slope at every tenth point obtained by data analysis, whereas the solid line represents the solution of the augmented Young-Laplace equation for the specific value of α. Table 1 summarizes the results for pentane in the small cell inclined at two different angles. Similar results were also obtained for heptane. The values of the dispersion constant for the solid-liquid-vapor system are presented in Table 1. They are calculated from the known values of α corresponding to the minimum error. The values of B for each liquid are reasonably close to each other. We also calculated the dispersion force and the values of B from the DLP theory for quartz-pentane-vapor and quartz-heptane-vapor systems. To calculate the dispersion force from the DLP theory, the same methodology as described in [8, 17] was used. The dielectric functions of the liquids and quartz are obtained from spectroscopic optical data as described by [18]. The results are presented in Table 2 and in Fig. 6. Figure 6 is a plot of the disjoining pressure as a function of the film thickness for heptane wetting on quartz. The solid line is from DLP theory [19], whereas the symbols are from the experiments. Since the dispersion forces for the two alkanes on quartz, as predicted by the DLP theory, are about the same, the experimental data for the pentane-quartz-vapor system are also plotted on the same graph. Both Table 2 and Fig. 6 clearly demonstrate that our experimentally obtained values of B and the disjoining pressures are very close to that predicted from the exact DLP theory.

Table 1 : Selected characteristics of pentane meniscus

	Angle of Inclination = 5.67°				Angle of Inclination = 9.92°			
	δ_0 (nm)	$K_\infty \times 10^{-3}$ (m^{-1})	α	B (J m)	δ_0 (nm)	$K_\infty \times 10^{-3}$ (m^{-1})	α	B (J m)
Point A	22.0	2.512	1.12	1.43×10^{-29}	19.0	3.044	1.04	0.72×10^{-29}
Point B	20.0	3.147	1.04	0.91×10^{-29}	20.0	4.186	1.12	1.63×10^{-29}

Table 2 : Experimental and theoretically calculated values of B(δ) for pentane and heptane on quartz

	n-pentane				n-heptane		
Angle (°)	δ_0 (nm)	B_{expt} (Jm)	B_{DLP} (Jm)	Angle (°)	δ_0 (nm)	B_{expt} (Jm)	B_{DLP} (Jm)
5.67	22.0	1.43×10^{-29}	1.65×10^{-29}	6.24	24.0	2.60×10^{-29}	1.76×10^{-29}
	20.0	0.91×10^{-29}	1.57×10^{-29}		23.0	1.57×10^{-29}	1.73×10^{-29}
9.92	19.0	0.72×10^{-29}	1.53×10^{-29}	9.92	23.0	2.41×10^{-29}	1.73×10^{-29}
	20.0	1.63×10^{-29}	1.57×10^{-29}		22.0	2.71×10^{-29}	1.69×10^{-29}

Similar results were obtained by Gee [17] from adsorption studies of n-alkanes on quartz for high disjoining pressure regimes ($\delta \leq 40$Å) and by Blake [20], who measured the disjoining pressure as a function of film thickness for n-octane and

n-decane on α-alumina. Blake's techniques demonstrated that Lifshitz theory correctly predicts the results in the low disjoining pressure regimes (δ was between 250Å and 800Å), whereas our present study is concerned with adsorbed film thicknesses of about 200Å. For completeness, we also note that recent studies [21, 22] indicate some limitations of the DLP theory in predicting the interactions in very thin liquid films (below 20Å) and suggest that structural effects are present in some adsorbed films at room temperature, provided the substrates are smooth and homogeneous.

The most important point of the present study is that the dispersion constants for a CVBT (micro heat pipe) system were evaluated in situ at the start of the experiments. This is a definite improvement over previous studies of micro heat pipes where little attention was given to the values of dispersion constants. These constants characterize the interfacial force field and are profoundly important in the basic understanding of the operation and performance of a micro heat pipe. For example, it has been shown that the contact line region in an extended evaporating meniscus, where the intermolecular force effects are important, plays a critical role in the overall heat transfer and liquid flow [1, 14, 12, 23, 24]. Hence our isothermal measurements are critical to the subsequent non-isothermal experiments.

CONCLUSIONS

1. The use of an IAI in conjunction with a CVBT in a gravitational field under isothermal conditions was demonstrated.
2. Procedures to measure the dispersion constant in-situ for the vapor-liquid-solid system were developed.
3. Good agreement between theoretical and experimental values of the dispersion constant was obtained.

ACKNOWLEDGEMENTS

REFERENCES

1. Potash, M., Jr. and Wayner, P.C., Jr., Int. J. Heat Mass Transfer, 15 (1972) 1851-1863.
2. Wayner, P.C., Jr., Kao, Y.K., and LaCroix, L.V., Int. J. Heat Mass Transfer, 19 (1976) 487-492.
3. Derjaguin and Kussakov, Acta Physicochim URSS, 10 (1939) 25.
4. Derjaguin, B.V., and Churaev, N.V., Colloid J. USSR, 38 (1976) 438-448.
5. Teletzke, G. F., Scriven, L. E., and Davis, H. T., Chem. Eng. Comm., 55 (1987) 41-81.
6. Renk, F., Wayner, P.C., Jr., and Homsy, G.M., J. of Colloid and Interface Sci., 67 (1978) 408-414.
7. Moosman, S. and Homsy, S.M., J. of Colloid and Interface Sci., 73 (1980) 212-223.
8. Truong, J.G. and Wayner, Jr., P.C., J. Chem. Phys., 87, (1987) 4180-4188.
9. DasGupta, S., Schonberg, J. A., Kim., I., Y., and Wayner, P. C. Jr., J. Colloid Interface Sci., 157 (1993) 332-342.
10. Wu, D. and Peterson, G. P., J. Thermophysics, 5 (1991) 129-134.
11. Khrustalev, D., and Faghri, A., Proceedings of National Heat Transfer Conference, Atlanta, GA 1993.
12. Swanson, L. W., and Peterson, G. P., Proceedings of the 1993 National Heat Transfer Conference, Atlanta, GA 1993.
13. Swanson and Herdt, J. Heat Transfer, 114 (1992) 434-441.
14. Wayner, Jr., P.C., Colloids and Surfaces, 52 (1991) 71-84.
15. DasGupta, S., Schonberg, J. A., and Wayner, P. C., Jr., J. Heat Transfer, 115 (1993) 201-208.
16. DasGupta, S., Sujanani, M., and Wayner, P.C., Jr., Proc. of the 2nd World Conference on Experimental Heat Transfer, Fluid Mechanics and Thermodynamics, Keffer, J. F. et al. ed., Elsevier Science Publishing Co. Inc., New York, 1991, pp. 361-368.
17. Gee, M.L., Healy, T.W., and White, L.R., J. Colloid Interface Sci., 131(1) (1989) 18-23.
18. Hough, D. B, and White, L. R., Adv. Colloid Interface Sci., 14 (1980) 3-41.
19. Dzyaloshinskii, I. E., Lifshitz, E. M., and Pitaevskii, L. P., Ad. Phys., 10 (1961) 165-209.
20. Blake, T. D., J. Chem. Soc., Faraday Trans. 1, 71 (1975) 192-208.
21. Beaglehole, D., Radlinska, E. Z., Ninham, B. W., and H. K. Christenson, Phys. Rev. Lett., 66(16) (1991) 2084-2087.
22. Beaglehole, D., and H. K. Christenson, J. Phys. Chem., 96 (1992) 3395-3403.
23. Stephan, P.C. and Busse, C.A., Int. J. Heat Mass Transfer, 35 (1992) 383-391.
24. Schonberg, J. A., DasGupta, S., and Wayner, P. C., Aerospace Heat Exchanger Technology 1993, R. K. Shah and A. Hashemi (Eds.), Elsevier Science Publishers B. V., 1993 pp. 239-254.

C-4.

$$P_v = P_l + \sigma K + \frac{(-B)}{\delta^h}$$

VAPOR

VAPOR FLOW

LIQUID FLOW

SOLID BARRIER

LIQUID FILM, THICKNESS = $\delta(x,\theta)$

VAPOR

① v_1 (a)   (b)   (c) v_2 ②

CONDENSATION   EVAPORATION

$T_2 > T_1$

$P_{v2} > P_{v1} > P_{l1} > P_{l2} < P_{v2}$

Fig. 1 CVBT Concept.

M MICROSCOPE

VC CCD CAMERA

IPM IMAGE PROCESSING
      MICROCOMPUTER

VR VCR

FCG FRAME CODE
        GENERATOR

FCG

V
R

IPM

VC

M

QUARTZ CELL, 3mmx3mm INSIDE

MICROSCOPE STAGE

ANGLE OF
INCLINATION

Fig. 2 Schematic Diagram of the Experimental Set-up.

90 µm
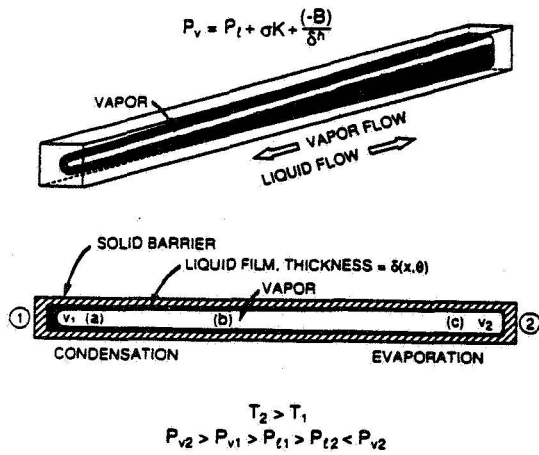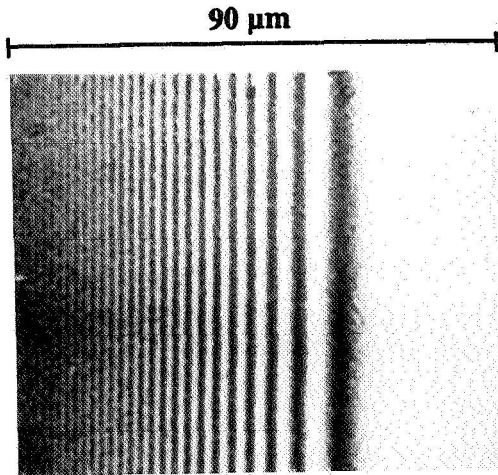
Fig. 3 Interference Fringes for Pentane on Quartz.

FILM THICKNESS PROFILES

Liquid : Heptane

Angle of Inclination : 6.24

$\Delta Z = 2.17 \times 10^{-3}$ m

——— Point A

- - - - Point B

$\delta^{1/2}$, $(\mu m)^{1/2}$

DISTANCE (µm)
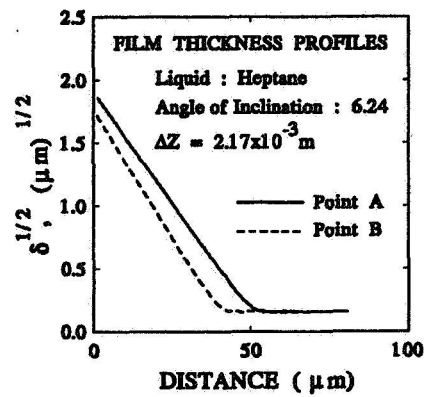
Fig. 4 Film Thickness Profiles of Heptane at Different
Positions for an Inclination Angle of 6.24°.

COMPARISON OF SLOPES
EXPERIMENTS AND THEORY

Liquid : Heptane
Point A
Angle = 9.92

$\alpha = 1.13$

——— Data Analysis

▲ ▲ ▲ Aug. Y - L Eqn.

- SLOPE

δ (µm)
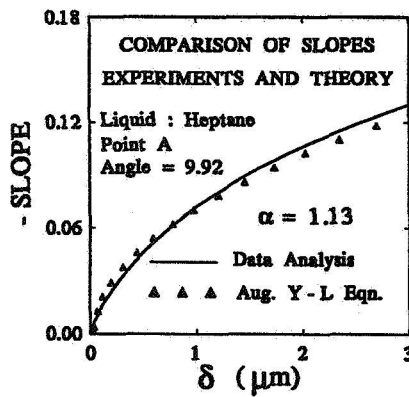
Fig. 5 Comparison of the Experimental Slope and the slope
from the Augmented Young-Laplace Equation (Eq. 11).

——— DLP THEORY

EXPERIMENTS

■ PENTANE

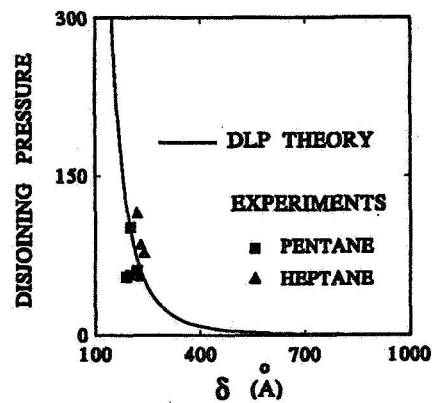▲ HEPTANE

DISJOINING PRESSURE

δ (A)

Fig. 6 Comparison of the Experiments and DLP Theory
for the Adsorption of Pentane and Heptane on Quartz.

258

BUBBLE DYNAMICS, TWO-PHASE FLOW, AND BOILING HEAT TRANSFER IN A MICROGRAVITY ENVIRONMENT

Jacob N. Chung
Department of Mechanical and Materials Engineering
Washington State University
Pullman, WA 99164-2920

ABSTRACT

The two-phase bubbly flow and boiling heat transfer in microgravity represents a substantial challenge to scientists and engineers and yet there is an urgent need to seek fundamental understanding in this area for future spacecraft design and space missions. At Washington State University, we have successfully designed, built and tested a 2.1 second drop tower with an innovative airbag deceleration system. Microgravity boiling experiments performed in our 0.6 second Drop Tower produced data and flow visualizations that agree with published results and also provide some new understanding concerning flow boiling and microgravity bubble behavior. On the analytical and numerical work, the edge effects of finite divergent electrode plates on the forces experienced by bubbles were investigated. Boiling in a concentric cylinder under microgravity and an electric field was numerically predicted. We also completed a feasibility study for microgravity boiling in an acoustic field.

INTRODUCTION

The thermo-fluid dynamics of two-phase system in microgravity encompass a wide range of complex phenomena that are not well enough understood for engineering design to proceed. Yet there is an urgent need to explore these phenomena for future spacecraft design and space mission. Predicting the two-phase flow and boiling heat transfer phenomena under a microgravity environment requires a thorough understanding of a multitude of fundamental physical processes including bubble dynamics, fluid dynamics, heat transfer, and interfacial transport. Significant gains in microgravity boiling science may result from investigating both the complexities of these phenomena in isolation and when acting in consort.

The current research concentrates on the bubble nucleation, bubble dynamics and heat transfer mechanism under microgravity. Specifically, we intend to study the transport mechanisms when the dominance of buoyancy force is replacd by a velocity shear force, an electro-magnetic force or an acoustical force under the microgravity condition.

EXPERIMENTATION

A. WSU 0.6 Second and 2.1 Second Drop Towers

The original purpose of the 0.6 second drop tower was to serve as a 1/4 scale model for the design and construction of the "WSU 2.1 Second Drop Tower." However, with proper planning, it was able to accommodate short time microgravity experiments and has been used extensively as a testing facility for new ideas and experimental designs. The drop distance of this drop tower is 2.13 meters tall which provides a drop time of 0.6 second. The dimensions of the airbag are 45.72 cm x 45.72 cm x 91.44 cm. The maximum deceleration level of the experiment is approximately 3g's. The low gravity level was calculated to be approximately 10^{-3} g. The WSU 0.6 second Airbag Drop Tower consists of three major parts: a release-retrieve mechanism, a drag shield, and a airbag deceleration system. Figure 1 shows an overall view of the drop tower.

An empty elevator shaft located in Eastlic Hall on the Washington State University campus was converted to a 2.1 second drop tower facility. The use of a drag shield combined with an innovative airbag deceleration system, and a tapered pin release mechanism provides low gravitational acceleration ($\sim 10^{-4}$g), very low impact deceleration (~ 15g), and low release vibrations ($\sim \pm 5$g). Its ability to drop an experiment from a variable height sets it apart from any other drop tower in the world today, and can provide a 1.2 second drop with as little as 5-8g deceleration. A typical g-level history curve for a full 2.1 second drop is shown in figure 2. This can be compared to a deceleration level of 70g as reported for the obsolete sand box system at the NASA Lewis Research Center.

The drop tower was designed with a combined release-retrieve mechanism that can drop a 317 kg load (181 kg drag shield, 136 kg experiment) from any height up to 22 meters and remotely retrieve the experiment within 10 minutes. An innovative airbag deceleration system uses a 1.82 x 2.13 x 3.66m airbag to create the required 20,000 to 35,000 Newton force required to decelerate the experiment after its fall and subsequent 74 km/hr impact. The drop tower was designed to accept the standard experimental "rigs" that are presently used at the NASA Lewis Research Center, making their experiments compatible with our tower. A user-friendly, Windows-based drop and data acquisition program (PULSE) was written to control the entire drop tower operation. This software allows complete control over the release mechanism, and up to 11 other pieces of equipment. This program is also capable of collecting data on 7 input channels, provides simple control over all data acquisition requirements, immediately plots a control curve for each channel used, calculates means and standard deviations for each channel, can write the data to a file or can copy the data directly to the clip board for use in a widows based program. This drop tower's low cost of construction and operation, relative ease of fabrication, and ability to be completely controlled by one person from the drop level makes it ideal for the university environment and for the research at hand. Figure 3 shows an overall view of the drop tower (not to scale).

B. Preliminary Experimental Results

We have performed pool and flow boiling experiments in the 0.6 second drop tower. The results of the transient boiling experiment show that for a short period of time, when the heat flux is relatively low and the subcooling level remains relatively high, the heat transfer is enhanced in microgravity. At a high enough heat flux, however, dryout would happen almost immediately under microgravity condition and cause the heat transfer to decrease. These results are in good agreement with the study by Merte, Lee, and Ervin [1]. We also found that the increase in heat flux would decrease as the total heat flux becomes higher. At the highest heat flux of 8 W/cm^2 dryout occurred and it actually decreased the heat transfer. Figure 4 presents a sample of these results with comparisions to the the work of Merte, Lee, and Ervin [1].

In the comparison between experiments of the same heat flux level with and without forced flow, the low heat flux cases (2.88 W/cm^2) result in an increased heat flux with the flow (7.7cm/s). With the medium heat flux (4.17 w/cm^2), the flow does not affect the heat flux very much. With the high heat flux (5.95 w/cm^2), there was some evidence that the flow field prevents dryout, however, the short times involved limited our insight. In the short time available only the higher heat fluxs have enough time to cause dryout, and if more time were available the dryout might have also been observed for the medium heat flux. However, this probably would not be the case for the low heat flux as the bubbles were immediately removed by the flow field as discussed below. The results in the highest heat flux (8 W/cm^2) experiment show dryout occurred in less than 0.1 second after the drop and the heat flux decreased dramatically.

The flow visualization study shows that with a low heat flux, the vapor bubbles are carried by the flow and roll across the heater surface. With a higher heat flux the forced flow provided by the system does not seem to overcome the surface tension. The forced flow therefore does not remove the vapor bubbles from the surface for these higher heat flux cases.

The increase in heat flux under microgravity may be attributed to:
1. The surface tension effects at the liquid-vapor-solid interface causing rewetting to occur and maintaining the nucleate boiling [1].
2. More fresh liquid is available at the heater surface as a result of the liquid inertia which continues to bring the fresh liquid toward the heater surface while the induced upward flow of liquid is stopped when the bubbles do not rise off the heater surface.
3. The thinning of the superheated microlayer.
4. The increase in microlayer evaporation rate resulting from the sliding of the vapor bubble caused by the forced flow [2].
5. The sliding of the vapor bubbles causing agitation on the surface, which creates more nucleation sites and therefore enhances the nucleate boiling.

The results of the current study showed good agreement with previous reports and provided a better understanding for future research. Figure 5 provides typical flow visualization photographs.

NUMERICAL AND ANALYTICAL ANALYSIS

A. Electric Field

On the numerical and analytical side, we have investigated the edge effects of a finite plate on the dielectrophoretic force experienced by a gas bubble in a dielectric fluid. We also looked into the bubble growth and dynamics in a concentric cylinder under an electric field.

The dielectrophoretic force on a spherical bubble in an electric field is given as

$$F_{DEP} = 2\pi R^3 \varepsilon_l \left(\frac{\varepsilon_v - \varepsilon_l}{\varepsilon_v + 2\varepsilon_l} \right) \nabla |E|^2 \qquad (1)$$

and for the divergent plates

$$\nabla |E|^2 = \frac{-2}{r^3} \left(\frac{\partial V}{\partial \phi} \right)^2 \qquad (2)$$

Where R is the radius of the bubble, E is the strength of the electric field, ε_l and ε_v are the dielectric permittivity for the liquid and vapor phase respectively, and ϕ and r are the angular and radial coordinate, respectively. For two divergent infinite plate electrodes with voltages V and -V respectively, the following is obtained:

$$\nabla |E|^2 = \left(\frac{-2V^2}{r^3 \theta^2} \right) \quad , \quad F_{DEP} = -4\pi R^3 \varepsilon_l \left(\frac{\varepsilon_v - \varepsilon_l}{\varepsilon_v + 2\varepsilon_l} \right) \left(\frac{V^2}{r^3 \theta^2} \right) \hat{r} \qquad (3),(4)$$

Where r is the distance from the fictitious plate intersection and θ is the angle between the two plates.

For finite plates, the general expression for the voltage at any point is:

$$V(r) = \iint_S \frac{\rho(r')ds'}{4\pi\varepsilon_o |r - r'|} \qquad (5)$$

Where S is the surface of object over which charge exists, $\rho(r)$ is the charge density at position r, ε is the dielectric permittivity of the medium between the plates and $|r - r'|$ is the distance between r' and r. The charge density is not known priori to begin with for the finite plates. However, with the voltage on the plates known, the moment method was employed to solve the integral equations for the charge density. The voltage at each point allows the calculation of the electric field and gradients of the electric field. This is the final information which is needed in order to find the dielectrophoretic force.

Figure 6 presents the DEP force over the entire calculated area for both finite and infinite cases and for a test fluid of R-113. In these plots z = 0 corresponds to the center of the plate and z=1.9 corresponds to the edge of the plate. Also the plots are for $\phi = 0$ (center of the plates).

Because of its higher practical application value, microgravity boiling in a concentric cylinder was investigated by numerical simulations. The simulation covers the bubble growth, bubble detachment from the heater surface and bubble dynamics and movement in an electric field after detachment. The bubble growth starts from the isobaric stage where the heat transfer is the governing mechanism. The bubble is assumed to remain in the shape of a segmented sphere with a constant contact angle. The heat for bubble growth is supplied by the heater surface through a conduction thermal boundary layer to reach the bubble. The detachment is based on a criterion proposed by Fritz [3],

$$Bo^{1/2} = 0.0208\phi \qquad (6)$$

Where

$$Bo = \frac{g(\rho_l - \rho_v)d_d^2}{\sigma} \quad \text{is the Bond Number} \qquad (7)$$

In the above φ is the contact angle, σ is the surface tension coefficient g is the gravitation acceleration, ρ_l and ρ_v are the densities for the liquid and vapor respectively and d_d is the bubble detachment diameter. After detachment, the bubble dynamics and movement are tracked by the following equation of motion for the bubble:

$$(M + M')\frac{d\mathbf{U}}{dt} = \frac{1}{32}C_D\rho_l^2\pi R^2 U^2\mathbf{e}_U + \frac{3}{8}\sqrt{\pi\rho_l\mu_l}R^2\int_0^1\frac{\mathbf{U}}{\sqrt{t-t'}}dt' + 2\pi R^3\varepsilon_1\frac{\varepsilon_2-\varepsilon_1}{\varepsilon_2+2\varepsilon_1}\nabla E + M\mathbf{g} \quad (8)$$

In the above equation, M is the mass of the bubble, M' is the added mass due to the acceleration of the surrounding fluid, which is approximated as half of M, C_D is the drag coefficient, μ_l is the fluid viscosity, and R is the bubble radius. The first term on the right-hand-side is the drag force, Basset force is the second term, the dielectrophoretic force is represented by the third term and the gravitational force is shown in the last term. The numerical method employed to obtain the dielectric force is similar to that for the divergent plates and therefore will not be repeated here. Results for water and R-113 are included in Figure 7.

B. Acoustic Field

A lot more work is still needed in order to really understand all of the physics of how acoustic radiation pressure can be applied in moving vapor bubbles. To this date we have numerically derived all the factors that are required in the the design of a working experiment. With a simple static force balance of buoyancy, surface tension, and radiation force we have shown that an acoustic force produced by a high intensity ultrasonic horn can move vapor bubbles off a heater surface. Finally, an acoustic boiling chamber has been designed based on the numerical calculations. This chamber will form one module of the Enhanced Pool and Flowing Boiling Experiment (EPFBE-1) presently being built for the 2.1 second drop tower. Experiments are planned for summer 1994. The components of interest are the rectangular resonant acoustic chamber, the high intensity ultrasonic horn, and a nicrome wire with working fluid FC-72.

ACKNOWLEDGMENTS

REFERENCES

1. H. Merte, Jr., H.S. Lee, and J.S. Ervin, Transient Nucleate Pool Boiling in Microgravity - Some Initial Results, Int. Symp. Microgravity Science and Applications, Paper J-5, 1993.

2. Tsung-Chang, G. and Bankoff, S.G., On the Mechanism of Forced-Convection Subcooled Nucleate Boiling, J. Heat Transfer, Vol. 112, pp. 213-218, 1990.

3. Fritz, W. Maximum Volume of Vapor Bubbles, Physik Zeitschr, Vol. 36, pp. 379-384, 1935.
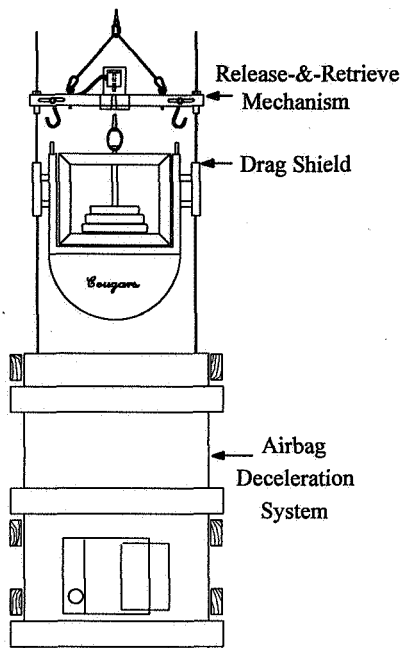
Figure 1 - 0.6 Second Microgravity
Drop Tower
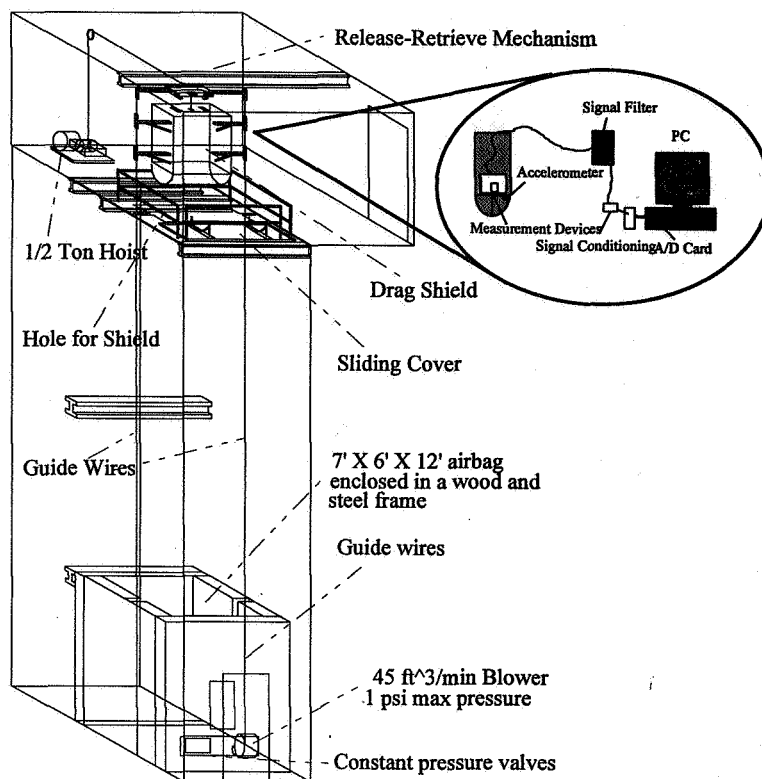
Figure 3 - Overall View of WSU 2.1
Second Drop Tower
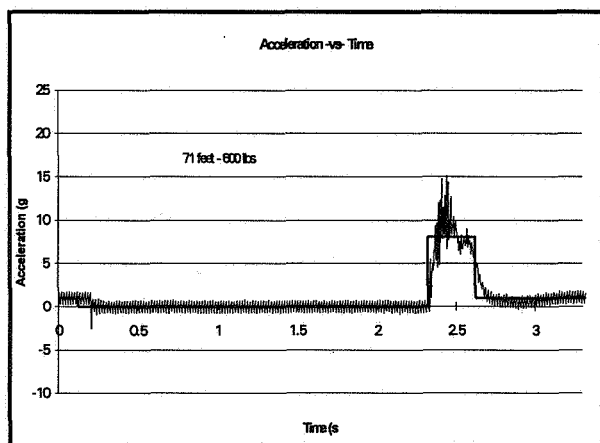
Firgure 2 - G-level History Curve
Acceleration -vs- Time
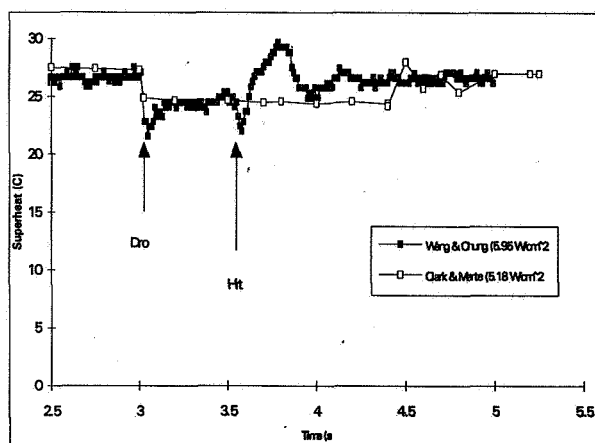
Figure 4 - Heater Surface Superheat
Pool Boiling - R-113

7.6 W/cm^2 - Microgravity boiling with and without flow
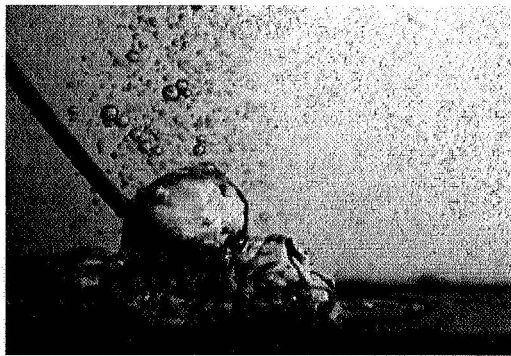
Time = 0.567 sec
Velocity = 0 cm/s
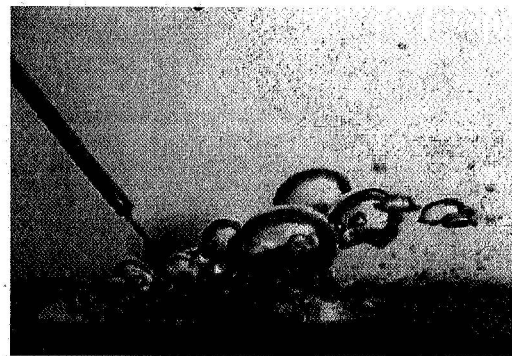
Time = 0.567 sec
Velocity = 7.7 cm/s

2.8 W/cm^2 - Microgravity boiling with and without flow
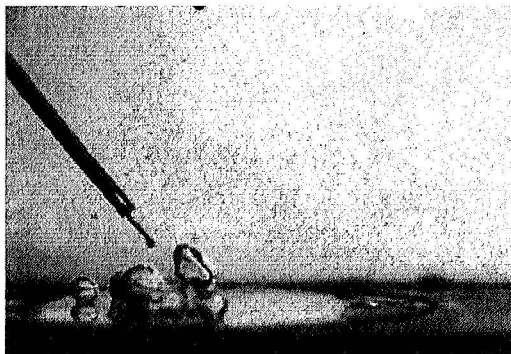
Time = 0.567 sec
Velocity = 0 cm/s
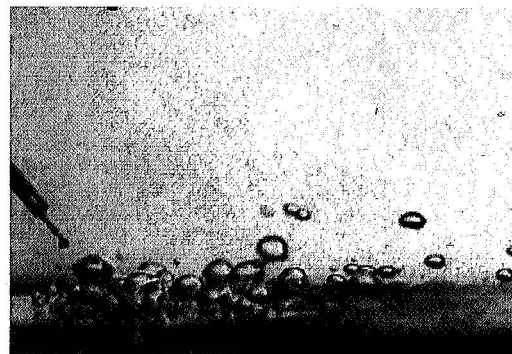
Time = 0.567 sec
Velocity = 7.7 cm/s

Figure 5 - Microgravity Boiling Flow Visualization photographs
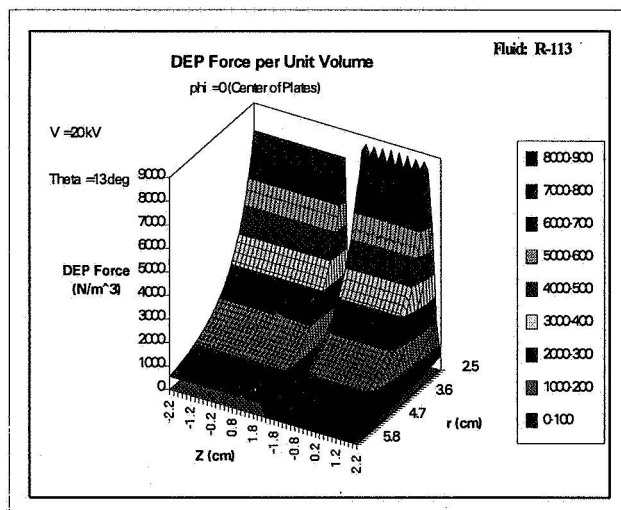
**Figure 6 - DEP Force per Unit
Volume Across Finite Plate
and Infinite Plate**
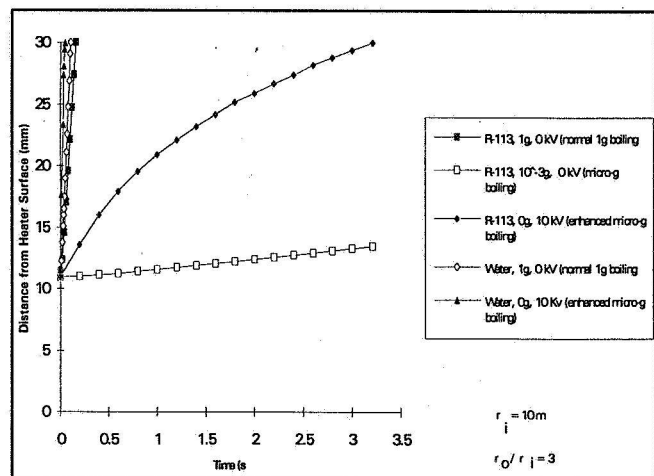
Figure 7 - Bubble Motion After Detachment

Pool and Flow Boiling in Variable and Microgravity

Herman Merte, Jr.
Professor of Mechanical Engineering
The University of Michigan
Ann Arbor, Michigan

INTRODUCTION

As is well known, boiling is an effective mode of heat transfer in that high heat flux levels are possible with relatively small temperature differences. Its optimal application requires that the process be adequately understood. A measure of the understanding of any physical event lies in the ability to predict its behavior in terms of the relevant parameters. Despite many years of research the predictability of boiling is currently possible only for quite specialized circumstances, e.g., the critical heat flux and film boiling for the pool boiling case, and then only with special geometries.

Variable gravity down to microgravity provides the opportunity to test this understanding, but possibly more important, by changing the dimensional and time scales involved permits more detailed observations of elements involved in the boiling process, and perhaps discloses phenomena heretofore unknown.

The focus here is on nucleate boiling although, as will be demonstrated below, under certain circumstances in microgravity it can take place concurrently with the dryout process. In the presence of earth gravity or forced convection effects, the latter process is usually referred to as film boiling. However, no vapor film as such forms with pool boiling in microgravity, only dryout. Initial results are presented here for pool boiling in microgravity, and were made possible at such an early date by the availability of the Get-Away-Specials (GAS).

Also presented here are some results of ground testing of a flow loop for the study of low velocity boiling, eventually to take place also in microgravity. In the interim, variable buoyancy normal to the heater surface is achieved by rotation of the entire loop relative to earth gravity. Of course, this is at the expense of varying the buoyancy parallel to the heater surface. Two questions which must be resolved early in the study of flow boiling in microgravity are (1) the lower limits of liquid flow velocity where buoyancy effects become significant to the boiling process (2) the effect of lower liquid flow velocities on the Critical Heat Flux when buoyancy is removed. Results of initial efforts in these directions are presented, albeit restricted currently to the ever present earth gravity.

POOL BOILING

Before a nucleate pool boiling system can attain the steady periodic behavior normally observed in a gravity field, where buoyancy is the predominant vapor removal mechanism, the process must pass through a transient phase. Where the buoyancy is drastically reduced, as in microgravity, the process is anticipated to be inherently transient unless some special circumstances can be provided to maintain a subcooled bulk liquid domain. Absent this, the elements of transient boiling possible are:

(a)   Conduction
(b)   Onset of natural convection
(c)   Nucleation
(d)   Vapor bubble growth/collapse
(e)   Departure
(f)   Motion following departure

In the transient pool boiling experiments conducted in the microgravity of space in the GAS on the shuttle STS-47, only elements (a), (c) and (d) were present and are considered here. The heater surface used is rectangular in shape, 1.91 cm by 3.81 cm (0.75 × 1.5 inches), consisting of a 400 Angstrom thick semi-transparent gold film sputtered on a quartz substrate, and serves simultaneously as a heater and a resistance thermometer. Viewing is provided simultaneously from the underside and side of the heater surface. Degassed R-113 with a normal boiling point of 47.2°C (117°F) was used as the working fluid. The subcooling level was controlled by varying the system

pressure, which was maintained constant to within ± 690 N/m² (± 0.1 psi) during any particular test. The experimental technique followed is described in ref. (1).

Measurement of the mean heater surface resistance, and hence temperature, was obtained at 10 Hz, and permitted the computation of heat transfer by conduction to the substrate, and to the fluid, from which a mean heat transfer coefficient was determined.

Figures 1 and 2 present the measured heater surface temperature and heat transfer coefficients for 2 of the 9 tests conducted. It is noted that a quasi-steady process exists for this subcooled case during the some 75 seconds of active boiling, although a tendency toward a decrease exists at the end. The 9 tests which constitute the matrix of test conditions are shown in Table 1. The behavior at earth gravity obtained following the space flight are compared with that in microgravity. Boiling in microgravity under these conditions, with a relatively large flat heater surface, appears quite unstable.

The heater surface superheat at the moment of nucleation are plotted in Fig. 3 as a function of heat flux with subcooling as a parameter for the identical system in microgravity, and post-and pre-flight. A rather anomalous behavior is noted in that the heater surface superheat required to nucleate the fluid is a maximum at the intermediate heat flux level. A similar behavior occurred with a different system in the STS-57. The maximum is also noted when the system is operated inverted in earth gravity. In ground based testing reported in ref. (2), nucleation at a/g = -1 occurred at heater surface superheats of approximately 10°C at heat flux levels varying from 50 w/cm² at a subcooling of 11°C to 22 w/cm² with a saturated liquid. These are consistent with extrapolations to the right in Fig. 3. Future space experiments are proposed to explore heat flux levels down to 0.5 w/cm², which would extrapolate Fig. 3 to the left.

It is observed in Fig. 2, which applies for the lowest level of heat flux and virtually saturated liquid, that a correspondence exists between decreases in the mean surface temperature and increases in the mean heat transfer coefficient. This is not unexpected, since the latter is determined from the former. Upon viewing the motion pictures taken through the heating surface from the underside it was noted also that a decrease in the mean heat transfer coefficient corresponded to a distinct increase in the heater surface dryout area. Provision was made for the measurement of the fractional dry area of each frame of the 16 mm film, and examples are given in Fig. 4 for Run No. 9 in Fig. 2. Fig. 4a is for the region of 61.5 — 67.5 seconds, in which the surface is rewetting, while Fig. 4b is for the region of 80.5 — 85.5 seconds, in which the surface is drying out again. These behaviors are apparently random, and are the subject for further proposed microgravity experiments at lower levels of heat flux and higher levels of bulk liquid subcooling.

If the assumption is made that the heat transfer to the fluid in the dry portion of the heater surface can be neglected, and that the heat transfer coefficient over the remaining wetted portion of the heater surface is approximately uniform, then this latter quantity can be determined by dividing the overall mean heat transfer coefficient by the fractional wetted area. These results are also plotted in Figs. 4a and 4b, and show that the microgravity boiling heat transfer coefficients are virtually the same during the rewetting and dryout phases, 1250 and 1200 w/cm²C, respectively. Each data point in Fig. 4 corresponds to a single frame, taken at 10 pps, and the oscillations are a reality in the physical process. The rather large excursions in the boiling heat transfer coefficients early in Fig. 4a and late in Fig. 4b are a consequence of the inherent relatively large uncertainty in measurement of the fractional wet area at low levels of wetting, and should be disregarded.

FLOW BOILING

A schematic of the low velocity forced convection boiling loop for proposed studies with R-113 in microgravity is shown in Fig. 5, with a more detailed view of the test section in Fig. 6. Velocities can be varied from 0.5 cm/s to 32 cm/s by pump speed control combined with changes in test section height, from 2.54 cm (1 inch) to 0.318 cm (0.125 inch). The use of a flow loop permits the study of boiling under steady conditions as well as under transients, as in the prior described pool boiling studies, and thus can accommodate the use of more massive metallic surfaces which, while more representative of engineering surfaces, also introduce complications associated with heat capacity effects. The flow loop proper occupies a volume of about 1.22 × .61 × .46 m (48 × 24 × 18 inches).

Although up to 6 heater surfaces can be accommodated simultaneously, a maximum of 3 is anticipated, with the remaining ports used for visualization. In addition to the gold film on quartz substrate heaters described previously, two flat metallic substrate heaters are used, with the same dimensions as the gold film heaters, but with maximum heat flux capabilities to 15 w/cm^2 and 75 w/cm^2. The latter heater is used for Critical Heat Flux studies with R-113, and has a larger uncertainty in the heat flux measurement at the lower levels of heat flux, below about 20 w/cm^2. System pressure, fluid temperature at the test section inlet, and flow rate controls are completely automated. More details on the flow loop and heater surfaces are available in refs. (3) and (4).

Fig. 7 is a sample result from ref. (5), showing how buoyancy influences the boiling heat transfer behavior at a low level of velocity of 4.1 cm/s. In single phase mixed convection heat transfer both buoyancy and imposed bulk liquid flow provide the mechanisms for fluid motion, where the relative significance of these is characterized by the Richardson number. For dealing with the combined effects of buoyancy and imposed bulk liquid flow with boiling, a "two-phase Richardson number" is developed in ref. (5) and (6), and is shown as the lower curve in Fig. 8 as a function of N_d, the product of the Weber and square of the Froude numbers. Also included as the upper curve in Fig. 8 is the square of the velocity ratio of Siegel (ref. 7), used to describe the rise velocity relative to a fluid flowing vertically. Tentative bounds are included in Fig. 8 for inertial and buoyant dominated domains, based as yet on limited experimental data. It is anticipated that experimentation proposed for parabolic flights in aircraft will provide additional data for bracketing more closely the relative influences of buoyancy and inertial effects.

Figs. 9 and 10, from ref. (4), show measurements of the Critical Heat Flux (CHF) at relatively low and high velocities, respectively, with R-113 at various orientations of the flat heater surface relative to the buoyancy vector. The angle $\theta = 0$ applies to the horizontal upward facing orientation. The CHF is normalized relative to a pool boiling correlation of ref. (1), q_{co}, which includes the influence of bulk liquid subcooling. The curves labeled "model" in Figs. 9 and 10 are for pool boiling modified by multiplying by the square root of θ over the interval of 90 to 270 deg., and arise from equating buoyancy and drag forces in the inverted positions where the vapor bubbles are held against the heater surface as they slide. The model is described in ref. (4).

The onset of forced convection effects become quite distinctive between Figs. 9 and 10, and it can be anticipated that the CHF will become independent of θ at sufficiently large velocities. Plans are underway to increase the maximum velocity attainable to about 60 cm/s. It can also be anticipated that the behavior of the CHF will take on quite another character in microgravity, where buoyancy effects become totally negligible. The only forces remaining then are momentum (or inertia) of the bulk liquid flow and surface tension, both liquid-vapor and liquid-vapor-solid. These can be expected to influence not only the CHF (or dryout - more likely), but the departure sizes of the vapor bubbles as well.

REFERENCES

1. Ervin, J. S., Merte, H., Jr., Keller, R. B., Kirk, K., "Transient Pool Boiling in Microgravity," Int. J. Heat Mass Trans., 35, March, 1992, pp. 659-674.
2. Ervin, J. S., Merte, H. , Jr., "A Fundamental Study of Nucleate Pool Boiling under Microgravity," Final Report to NASA Lewis Research Center on NASA Grant NAG3-663, Report No. UM-MEAM-91-08. August, 1991.
3. Kirk, K. M., Merte, H., Jr., Keller, R. B., "Low Velocity Nucleate Flow boiling at Various Orientations," ASME Symposium-Fluid Mechanics Phenomena in Microgravity, Ed. by D. A. Siginer and M. M. Weislogal, AMD - Vol. 154/FED - Vol. 142. 1992.
4. Brusstar, M. J., Merte, H., Jr., "Effects of Buoyancy on the Critical Heat Flux in Forced Convection," AIAA J. Thermophysics and Heat Transfer, 8, April - June, 1994, pp. 322-328.
5. Kirk, K. M., Merte, H. Jr., "A Study of the Relative Effects of Buoyancy and Liquid Momentum in Forced Convection Nucleate Boiling," Final Report to NASA Lewis Research Center on NASA Grant NAG3-1310, Report No. UM-MEAM-92-06. November, 1992.
6. Kirk, K. M., Merte, H., Jr., "A Mixed Natural/Forced Convection Nucleate Boiling Heat Transfer Criteria," Proceedings of 10th International heat Transfer Conference, Aug. 14-18, 1994, Brighton, U.K.
7. Siegel, R., "Effect of Reduced Gravity on Heat Transfer," Advances in Heat Transfer, eds. James P. Hartnett and Thomas F. Irvine, Vol. 4, pp. 200-205.
8. Ivey, H. J., Morris, D. J., "On the Relevance of the Vapour-Liquid Exchange Mechanism for Subcooled Boiling Heat Transfer at High Pressure," UKAEA, AEEW-R-137, 1962.
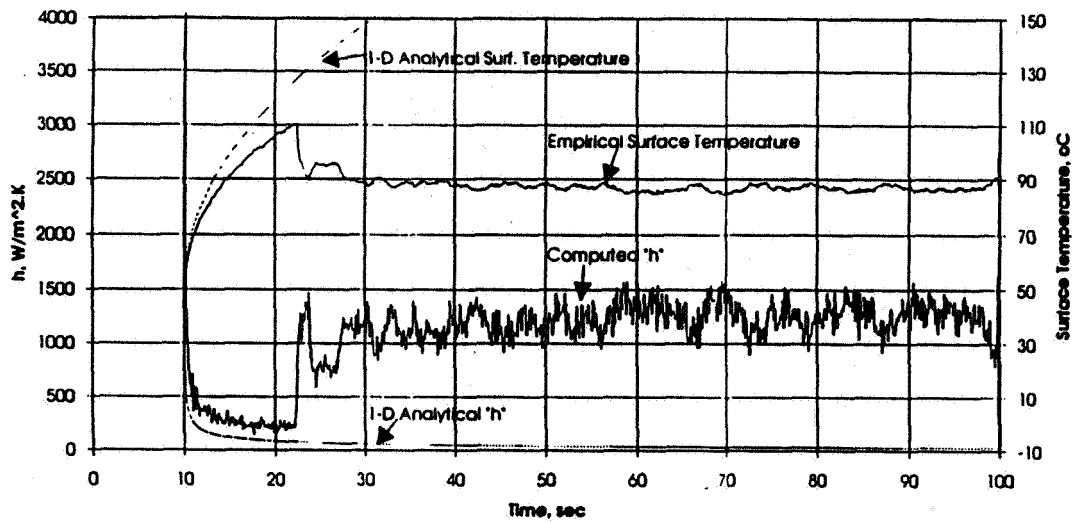
Figure 1.   Mean heater surface temperature and heat transfer coefficient.   R-113.   PBE Prototype.   STS-47.   Run No. 2. $q_T'' = 3.6$ w/cm^2. $\Delta T_{sub} = 11.9°C$. $T_{sat} = 61.1°C$.
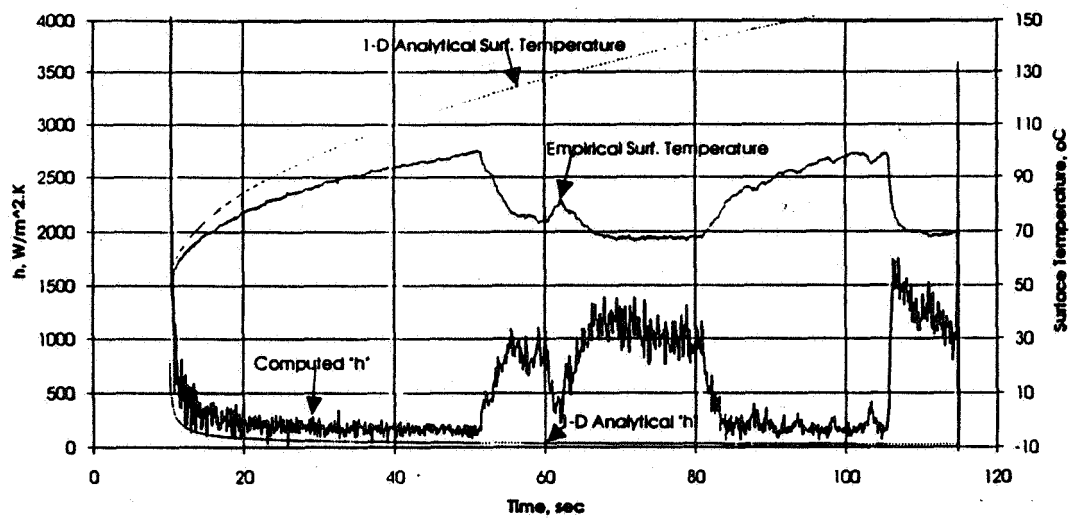
Figure 2.   Mean heater surface temperature and heat transfer coefficient.   R-113.   PBE Prototype.   STS-47.   Run No. 9. $q_T'' = 1.8$ w/cm^2. $\Delta T_{sub} = 0.2°C$. $T_{sat} = 49.4°C$.

Run No.	q'' w/cm^2 Approx.	ΔT_{sub} °C Approx.	$\bar{h}$ w/m^{2}K a/g = +1 Post Flight 11/4/92	$\bar{h}$ w/m^{2}K a/g ≅ 10^{-5} STS-47
1	7.0	10.7	2500 Nucleate Boiling	700 Dry Out
2	3.6	11.5	1300 Nucleate Boiling	1250** Steady State + Oscillating
3	1.8	11.0	450 (350)* Non-Boiling Convection	1100 → 600 Steady State → Dry Out
4	7.0	2.7	2300 Nucleate Boiling	200 Dry Out
5	3.6	2.8	550 (430)* Non-Boiling Convection	400 → 200 Increased Dry Out
6	1.8	2.8	550 (350)* Non-Boiling Convection	1150 Steady State + Oscillating (Rewet)
7	7.0	0.6	2300 Nucleate Boiling	200 Dry Out
8	3.5	0.4	600 (400)* Non-Boiling Convection	300 → 200 Increased Dry Out
9	1.8	0.2	500 (350)* Non-Boiling Convection	1100 → 200** Steady State + Dry Out & Rewet

* Computed from natural convection correlation: $Nu = 0.15 \times Ra^{1/3}$
** Detailed results following.

Table 1.   Comparison of measured mean heat transfer coefficients for PBE Prototype between a/g = +1 and STS-47 space flight.
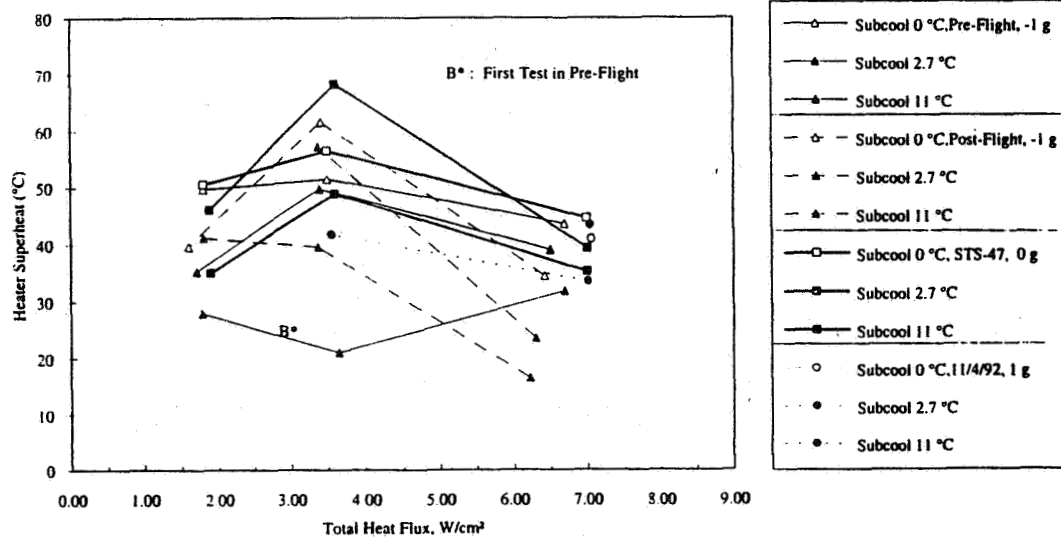
Figure 3.   Heater surface superheat at nucleation for PBE Prototype System for a/g = ± 1 and STS-47 space flight.
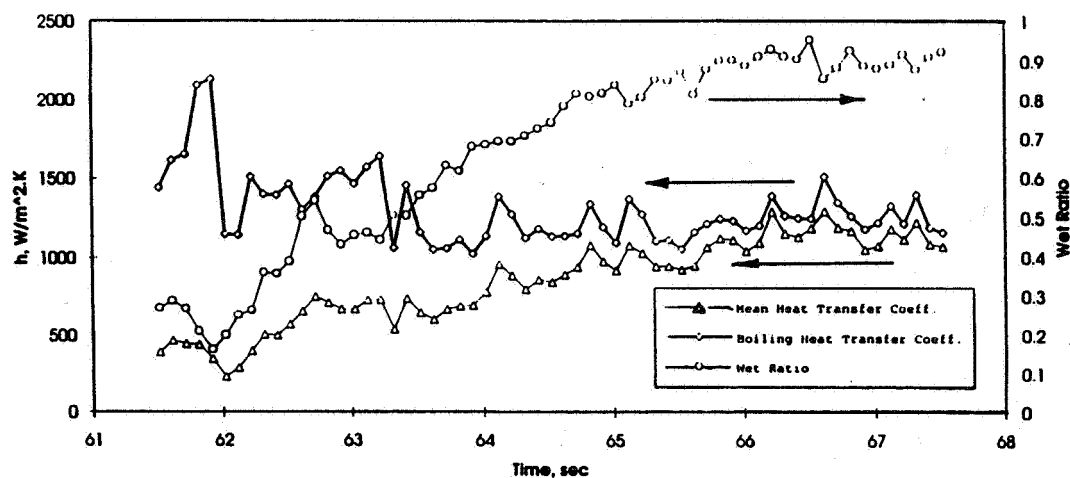
a. Rewetting portion of Figure 2. 61.5 — 67.5 sec.
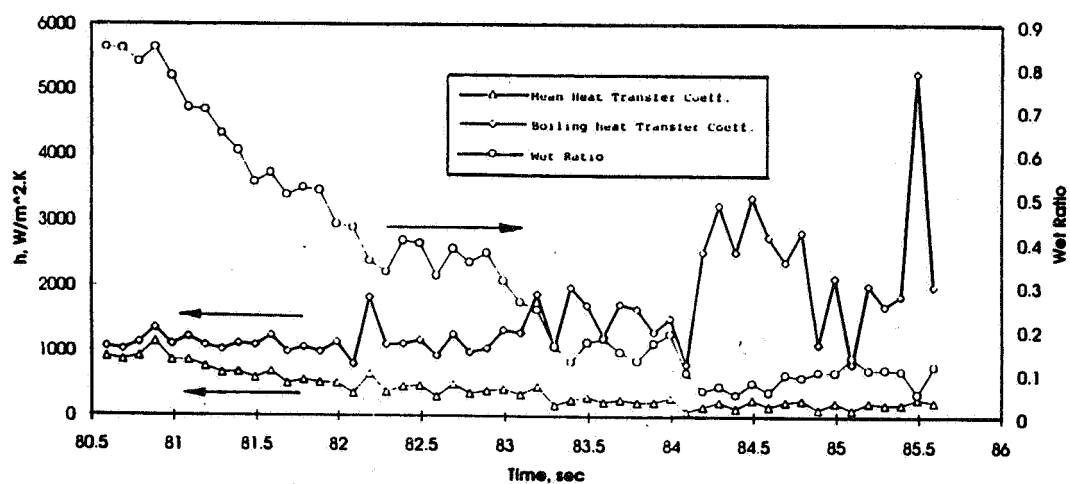
b. Dryout portion of Figure 2. 80.5 — 85.5 sec.

Figure 4. Fractional wetted area — nucleate boiling heat transfer coefficient — mean heat transfer coefficient with rewetting and dryout. PBE Prototype. STS-47. Run No. 9. $q_T'' = 1.8$ w/cm^2. $\Delta T_{sub} = 0.2°C$. $T_{sat} = 49.4°C$.
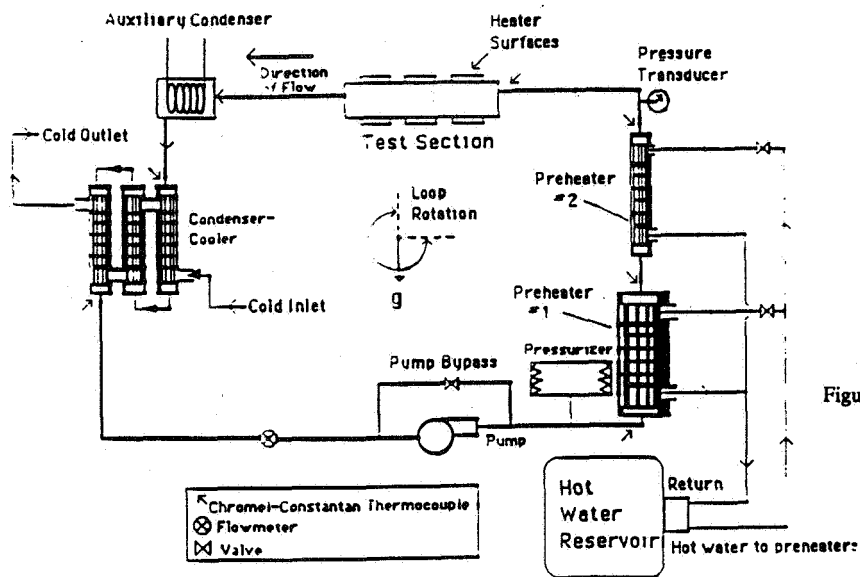
Figure 5. Low velocity boiling loop for variable orientation and low gravity.
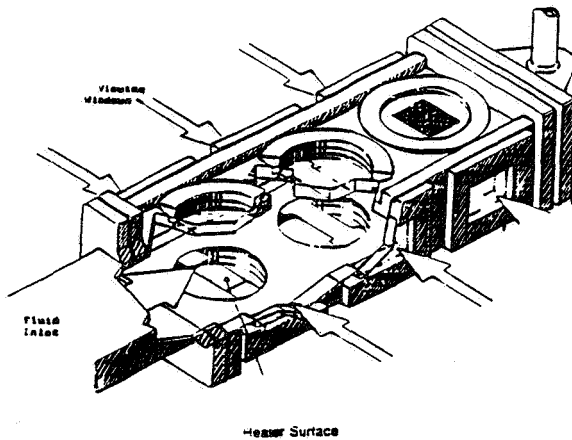
Figure 6. Test section. Flow area = 10.80 cm (4.25 in.) wide × 0.318, 1.27 or 2.54 cm (0.125, 0.50 or 1.0 in.) high.
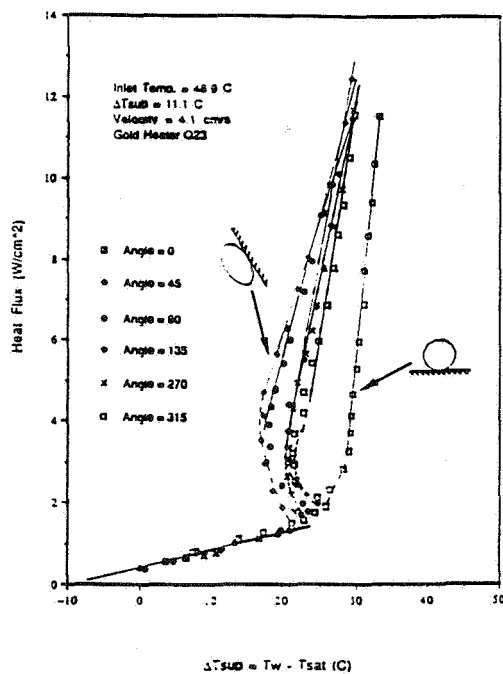
Figure 7. Heat flux vs heater surface superheat at various orientations. Test Section inlet temperature = 48.9°C. ΔT_{sub} = 11.1°C. Velocity = 4.1 cm/sec. Gold film heater on quartz.

271
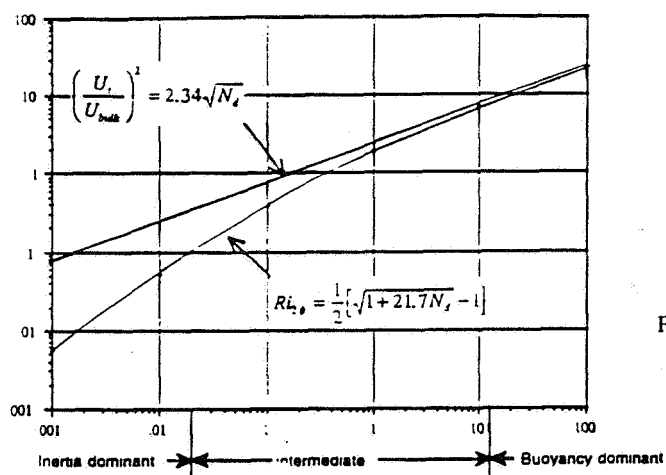
Figure 8. Flow effects relative to buoyancy with boiling.

$$N_i = \frac{g\Delta\rho\sigma}{\rho_i U^4}$$

Inlet conditions:
U = 8.5 cm/s, Re = 6000
T. S. Height = 12.7 mm
Tin = 50.8 deg. C

Subcooling:

O   2.8 deg. C
△   5.6 deg. C
□   11.1 deg. C
——   Model

(uncertainties indicated by error bars)
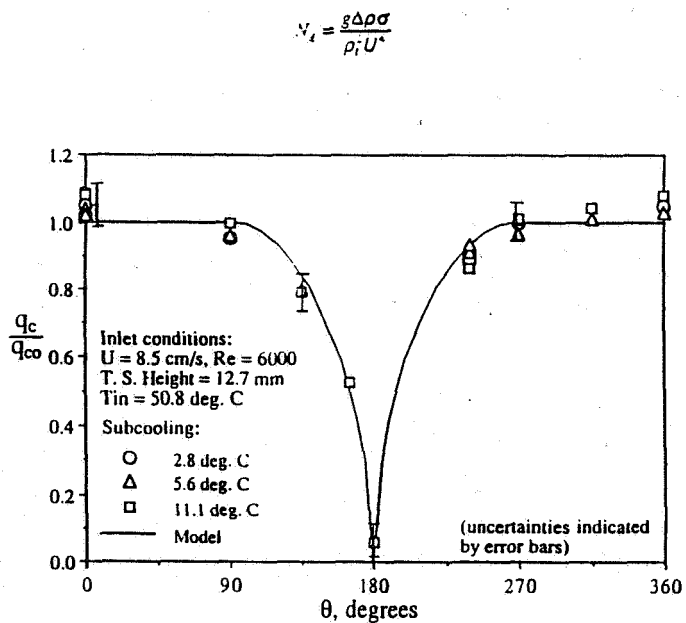
Figure 9. Critical Heat Flux at various orientations with low velocity (8.5 cm/s). R-113.

Inlet Conditions:
U = 35 cm/s, Re = 6500
T. S. Height = 3.2 mm
Tin = 50.8 deg. C

Subcooling:
O   5.6 deg. C
△   11.1 deg. C
□   22.2 deg. C
- - - Model

(uncertainties indicated by error bars)

Figure 10. Critical Heat Flux at Various orientations with relatively high velocity. (35 cm/s). R-113).

272

TRANSPORT PHENOMENA IN STRATIFIED MULTI-FLUID FLOW IN THE PRESENCE AND ABSENCE OF GRAVITY

Norman Chigier, Min Xu and David Squarer
Carnegie Mellon University
5000 Forbes Avenue
Pittsburgh, Pennsylvania 15213

Nasser Rashidnia
NYMA Inc
NASA Lewis MS 500-102
Microgravity Fluids Branch
Cleveland, Ohio 44135

ABSTRACT

An experiment is being conducted to study the effects of buoyancy on planar stratified flows. A wind tunnel has been designed and constructed to generate planar flows with separate heating for the top and bottom planar air jets emerging from slot nozzles separated by an insulating splitter plate. The objective is to generate planar jet flows with well defined and well controlled velocity and temperature profiles. Magnitudes of velocity and temperature will be varied separately in each flow for both laminar and turbulent flow conditions. Both stably and unstably stratified flows will be studied by changing the temperature distributions in each air stream. This paper reports on the design of the apparatus and initial measurements of velocity and turbulence made by laser Doppler velocimetry.

INTRODUCTION

Transport processes in multi-fluids in the presence and absence of gravity have been studied by numerous researchers. However, most of the previous studies considered the initiation of flow convection and diffusion in a small contained fluid volume that is initially at rest [1,2,3]. The objective of the present study is to investigate the turbulent mixing in stably or unstably stratified flow in the presence and absence of gravity, thereby defining and isolating the effect of buoyance on turbulent mixing.

Under conditions of gravity, stratified shear flows will be stable or unstable depending on the sign of the vertical density gradient, and turbulence will be damped 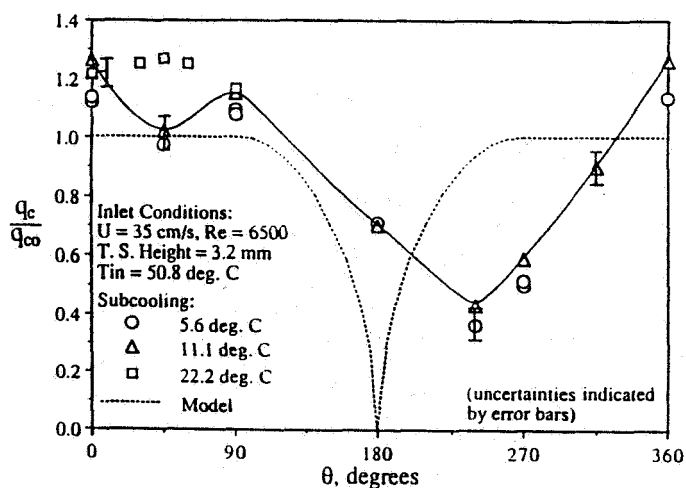in stably stratified flow, but will be generated by unstably stratified flow [4]. This research describes experiments, in an earth-based test facility, which are planned to be followed up by similar tests under microgravity conditions, and at a range of fluid velocities at which buoyancy and inertia forces are of the same order of magnitude. These experiments with variable buoyancy, forced flows, and gravity conditions, will provide the capability to isolate the effects of buoyancy in stable and unstable stratified shear flows. The turbulence characteristics are determined by laser Doppler velocimetry (LDV), including mean and fluctuating velocity components, Reynolds shear stress, and the temperature field using thermocouples. Particular attention was devoted to designing and constructing a low speed wind tunnel which can generate approximately uniform velocity and temperature profiles in two separate flow streams, that mix downstream from the exit of a two-dimensional nozzle. The earth-based wind tunnel was designated as a "once through" system, whereas the space-based test facility will include a recirculating flow and a cooler, in order to be compatible with the shuttle environment. The establishment of the desired boundary conditions at the wind tunnel exit was accomplished by passing the flowing air through two separate electric heaters, a series of grids, and a converging nozzle, while thermally insulating the two air streams from each other by means of an insulating splitter plate, which is gradually tapered towards the exit.

The overall objectives of this research are:
- To use the reduced gravity environment to improve the understanding of the fundamental physical processes of mixing between layers of fluid of different density and velocity.
- To separate the effects of molecular and turbulent diffusion from gravitational forces during the mixing of two fluid layers.
- To determine the influence of orientation on mixing under gravity and non-gravity conditions.
- To identify non-dimensional parameters that govern the physical phenomena.
- To outline a second phase to this study, in which a dispersed phase will be added to the same flow field.

The understanding of mixing in stratified flows which may be caused by temperature or concentration gradients is important for the understanding of different physical phenomena. This fundamental flow phenomena is encountered in numerous engineering applications in the earth's gravitational field. In atmospheric physics, temperature gradients are the important driving forces which often determine the air quality in urban areas. Thermal stratification in the oceans has long been recognized as a potential energy source which could be exploited. Air and water pollution are often determined by plume hydrodynamics which can be defined by the physics of stratified flow [4].

This research will provide information that will contribute to the basic understanding of the changes in mixing between flowing fluids of different density, as gravity is reduced to zero, and thereby will help minimize any undesirable effects which may result in any of the above listed applications.

DESIGN OF THE EXPERIMENT

In order to study the fundamental physical processes of mixing between layers of shear flows with density gradients, it is necessary to have well established and defined initial flow conditions. To simplify the problem of multiple layers in real flows, a wind tunnel has been constructed in which two co-flowing air streams generated from separated systems make contact in parallel at the edge of a splitter plate. Initially the velocity and density profiles in each flow should be approximately uniform so that there is a sharp step-wise change in velocity and density at the initial interface between the two streams. Uniform velocity profiles can be achieved by convergent nozzles with large contraction ratios. The accelerating flow through the nozzle provides near-uniform velocity distributions. The splitter plate between the flows needs to be thin so that the bluff body interface at the end of the splitter plate is so small that it has a negligible impact on the step change in velocity between the streams. Initial density differences between the two air streams are generated by heating one stream for mixing with the other unheated stream. The upper flow will be heated for stable stratification, while the lower flow will be heated for unstable stratification. Adiabatic conditions of the heated stream before exiting the nozzle are required for achieving initial step-wise density profiles. Therefore, the insulating property and the geometry of the splitter plate which separates the two flows are important concerns in the design.

A low velocity wind tunnel-type facility has been designed and constructed for the experiments conducted under earth-based gravity conditions. Figure 1 shows a 3-D schematic of the experimental apparatus. It consists of two completely separated air systems with a splitter plate sandwiched in between. Each system has the following sections: a first diffuser, an electrical heater, a second diffuser, a honeycomb flow straightener and six mesh screens, and a convergent nozzle. The nozzle only converges in one direction to form a rectangular exit with an aspect ratio of 20. The shape and the dimensions of the nozzle exits are shown in Fig. 2. Two air streams are separated by the splitter plate. Both exits have the same dimensions of 12.7 mm(0.5") in height and 254 mm (10") in width. Each exit cross sectional area is 3225.8 mm^2.

The flow contraction ratio and the convergent shape are crucial factors in wind tunnel designs, for eliminating flow disturbances and flow separation from the walls. Based on many successful previous applications, the following convergent equations suggested by Rouse and Hassan were selected for this apparatus. The explanation of symbols in the equations is given in Fig.3.

$0 \leq x \leq x_i$:

$$\frac{R}{D/2} = \frac{D_s}{D} - (\frac{D_s}{D} - 1)\frac{(x/L_1)^3}{(x_i/L_1)^2} \qquad (1)$$

$x_i \leq x \leq L_1$:

$$\frac{R}{D/2} = 1 + (\frac{D_s}{D} - 1)\frac{(1-x/L_1)^3}{(1-x_i/L_1)^2} \qquad (2)$$

$x_i/D_s = 0.3$, $(D_s/D)^2 = 12.009$, $L_1/D_s = 1.2$

Substituting the nozzle exit dimensions in the above equations, gives

$0 \leq x \leq 91.44mm$: $\qquad$ $R = 152.4 - 4.568 \times 10^{-5} x^3 mm$ $\qquad\qquad$ (3)

$91.44mm \leq x \leq 365.76mm$: $\quad$ $R = 12.7 + 5.076 \times 10^{-6}(365.76-x)^3 mm$ $\qquad$ (4)

$D_s = 12D = 24H = 304.8mm$ (12")

$x_i = 0.3D_s = 91.44mm$ (3.6")

$L_1 = 1.2D_s = 365.76mm$ (14.4")

Aluminum sheets were cut and welded together to form the upper and lower nozzles, which were clamped together, separated by an insulating sharp edged splitter plate with a convergent angle of 2° (Fig. 1). Flanges were welded to the inlet of the nozzles, and connected with the flanges of the honeycomb and mesh screens section. The aluminum honeycomb consists of many small, straight hexagonal tunnels (about 5mm opening width), for straightening the flows and minimizing the velocity fluctuations in the vertical direction. Five stainless steel mesh screens (1.13 mm opening width, 50.7% open area), were installed upstream from the honeycomb, and one downstream from the honeycomb. The velocity fluctuations in the axial direction are reduced by passing through these screens. This section is designed so that the relative positions of each screen and the honeycomb can be easily adjusted, and the number of screens can be increased or decreased, for better flow conditioning.

In order to obtain a step-wise initial density gradient in the two co-flowing air streams, either the upper or the lower flow needs to be heated, depending on the sign of the gradient. Two electrical coil type heaters and a control system were specially designed and manufactured for this purpose. Each heater has a maximum power of 15 kW (45 Amps, 240 Volts, 3 phase) which is sufficient to heat an air flow of 80 CFM to 200°C. Equipped with a precise controlling system, the heater can operate over a wide range of flow conditions. An air flow of less than 1 CFM can be heated to 50°C within a few minutes. Figure 4 shows the internal structure of the apparatus, air supply systems and the heater control system. The air

temperature downstream of the heater is detected by a thermocouple and fed back to a digital temperature controller which generates a corresponding 4~20 mAmps command signal to a zero-cross distributive SCR (silicon controlled rectifier) heater power controller. The instantaneous power supplied to the heater is properly adjusted according to the command signal so that the flow temperature can be stabilized at the preset temperature within a short period.

As mentioned previously, the insulating property and the thickness of the splitter plate plays a crucial role in the design. To establish the ideal step-wise velocity and temperature profiles results in contradictory requirements for the splitter plate. A thin and smooth plate will improve the velocity profile but will distort the temperature profile due to increase in heat conduction through the plate. As a compromise, a special design of gradually reducing the plate thickness was selected, as shown in Fig. 4. Marinite-I was chosen as the plate material for its excellent thermal insulating property and high structural strength. Its thermal conductivity and thermal expansion coefficient are 0.12 W/(m°K) at 205°C (0.81 Btu-in/ft^2,hr,°F) and 4.14 x10^{-6} 1/°K (2.3 x10^{-6} in/in/°F), respectively. The thickness of the plate gradually reduces from 50.8 mm (2") at the heater section to 0.508 mm (0.02") at the nozzle exits. A simple one-dimensional heat transfer model was used to predict the approximate heat flux through the splitter plate. Figure 5 shows the calculated local heat flux from the heated flow (200°C) to the unheated flow (20°C). Inside the nozzle, the substantial decrease of the plate thickness and the increase in the flow velocity due to contraction, results in considerable increase in the local heat flux, which impacts on the temperature profile.

RESULTS

The initial flow conditions for both air streams were measured at the nozzle exits. A 2 component LDV system was used to measure the axial and vertical components of the air flow velocities and velocity fluctuations. A TSI six jets atomiser provides micron size Propylene Glycol droplets which were used as seeding particles mixed in the air flows for velocity measurements. Figure 6 shows the results of the initial axial mean velocity profiles as a function of horizontal position y and vertical position z, while the maximum velocity was kept at 1 m/s. These profiles show very good similarity between upper and lower jets with maximum velocity at the center of each jet and zero velocity at the splitter plate and the top and bottom walls. The profiles are almost identical between y/H= -8 and y/H=8 which demonstrates the extent of two dimensionality of the flow system. The wall effects are also seen near the side walls.

Figure 7 shows the axial mean velocity profile at the center of the 2-D nozzle (y=0) when the maximum flow velocity u_m varies from 1m/s to 5m/s. For the flow velocity of 1m/s, since it is a laminar flow, the boundary layer is thick and the profile is parabolic. As the velocity increases, the boundary layer thickness is reduced, and the profile becomes flatter. At u_m=5m/s, the flow is turbulent, and the profile approaches a plug flow. However, in all the cases, boundary layers with high velocity gradients exist near the splitter plate surfaces due to the wall effects, which hinder the generation of sharp step-wise profiles.

Vertical mean velocity and velocity fluctuations were measured simultaneously with the axial velocity using LDV. Figure 8 shows the results at the center point of the jet (y=0, z=6.35mm) as a function the axial mean velocity u. The vertical mean velocity v and velocity fluctuations u' and v' increase with the flow velocity, but their magnitudes are only a few percent of u. The stream lines at the nozzle exit are smooth and horizontal. The axial rms velocity u' is approximately twice the vertical rms velocity v' at the nozzle exit for all the flow conditions.

The flow velocities and fluctuations at different downstream distances were also measured and are shown in Fig. 9 and 10. As the jet spreads downstream, the axial mean velocity profile widens and relaxes. The maximum velocity begins to decay beyond x/H=6, where the wake is no longer evident in the profiles. At x/H=10, the u profile is Gaussian. The axial rms velocity u' increase progressively with the downstream distance, and shows the highest values in the wake region (x/H<6) and outer edges of the jets due to strong mixing effects. However, the vertical rms velocity v' remains very small in the near field. Beyond x/H=4, turbulence is generated and the values of v' increase with the downstream distance. At x/H=10, both u' and v' are similar. Thus the turbulence can be considered as close to isotropic.

CONCLUSIONS

A wind tunnel with two separately heated air flows, separated by an insulating splitter plate, has been designed, constructed and tested. The exit velocity and turbulence profiles have been measured by LDV. Nearly uniform velocity profiles at the nozzle exits have been achieved. Heat transfer across the splitter plate results in thermal boundary layers inside the wind tunnel that distort the exit temperature profile. The measured turbulence structure, 127mm downstream of the nozzle exit, is close to isotropic.

ACKNOWLEDGMENT

REFERENCES

1. Koster, J.N. and Sani, R.L. Editors, "Low-Gravity Fluid Dynamics and Transport Phenomena", Progress in Astronautics and Aeronautics, AIAA, Washington, DC, Vol. 130, 1990.
2. Prakash, A., Peltier, J., Fujita, D., Koster, J., Biringen, S., "Convective Instabilities in a Two-Layer Fluid System", AIAA Paper 91-0313, 1991.
3. NASA's Micro Gravity Fluid Physics Workshop, NASA-Lewis, June 15, 1993.
4. Turner, J.S., "Buoyancy Effects in Fluids", Cambridge University Press, 1973.
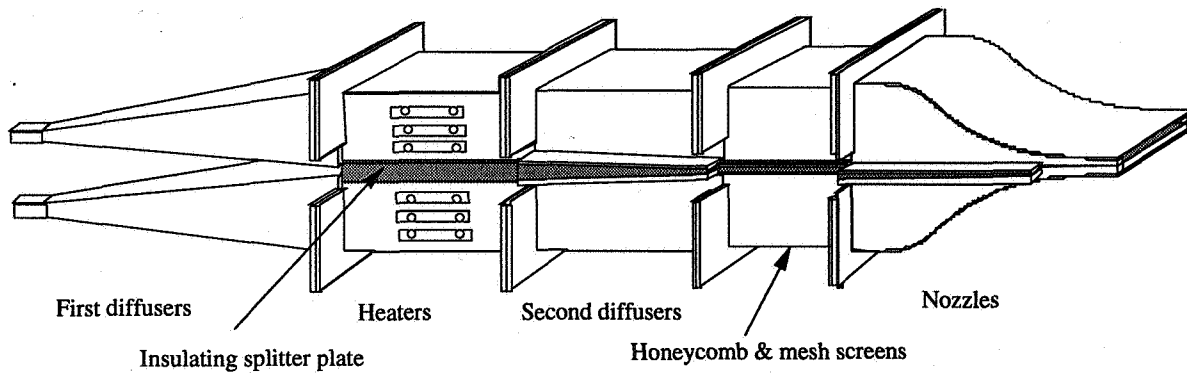
Figure 1   3-D view of the experimental apparatus.
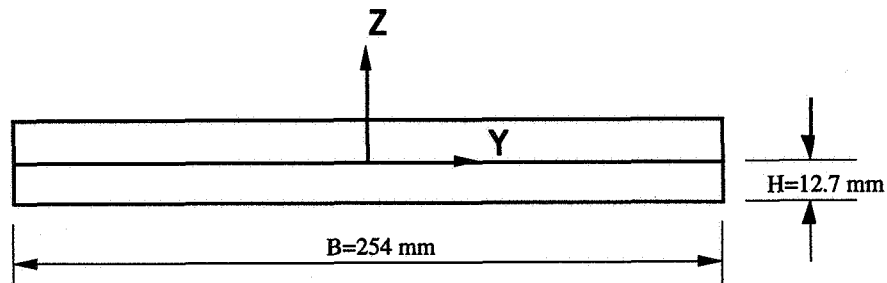
Figure 2   Nozzle exit cross section.
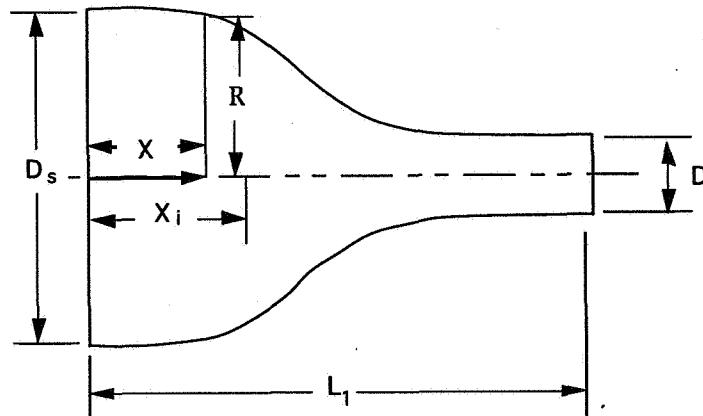
Figure 3   Convergent nozzle [eqs. (1),(2)].

276
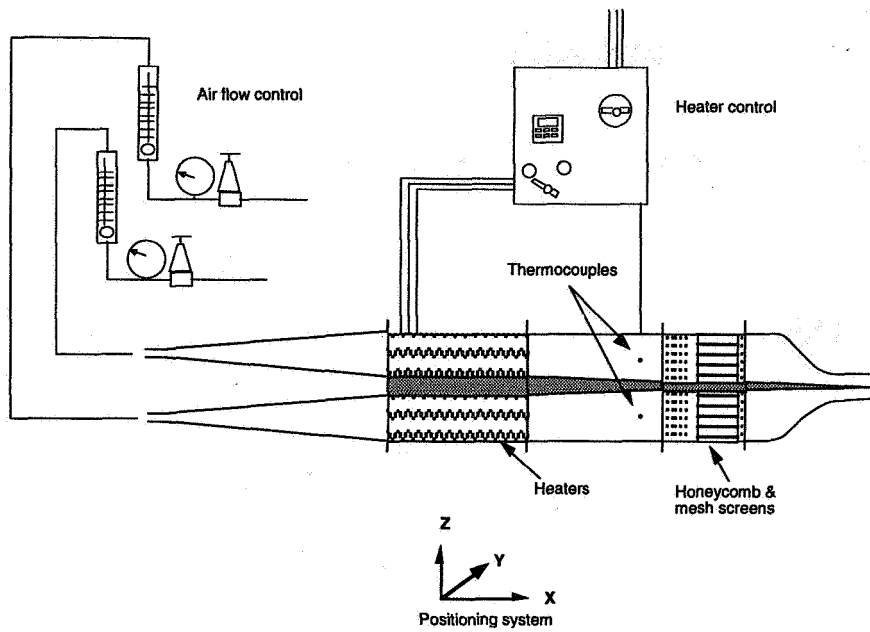
Figure 4   Apparatus and control systems.

Axial distance along the splitter plate   mm
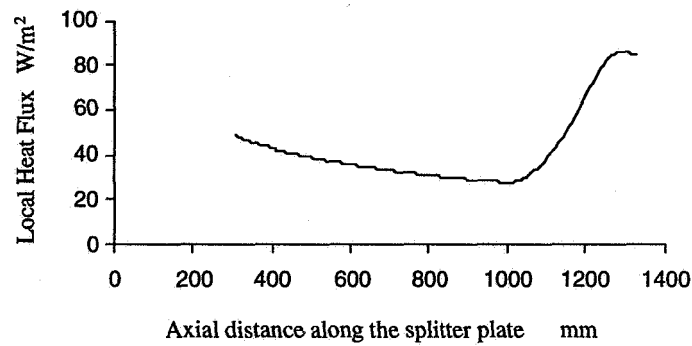
Figure 5   Predicted local heat flux between two flows through the splitter plate.
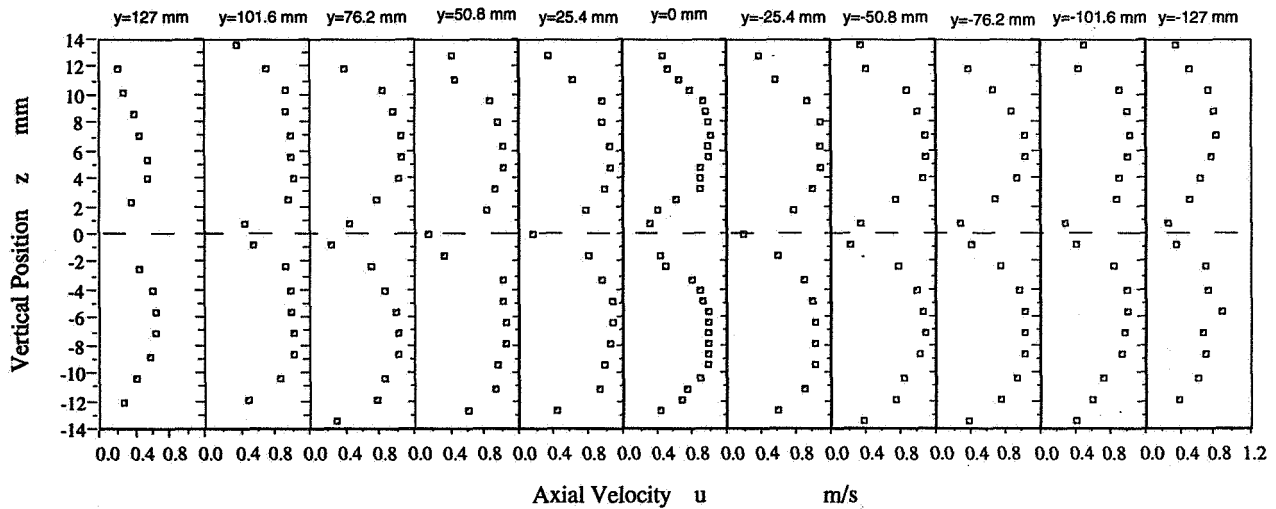
Axial Velocity   u   m/s

Figure 6   Axial mean velocity u profiles near the nozzle exit as a function of y and z (x=3.175 mm, u_m=1m/s).

277
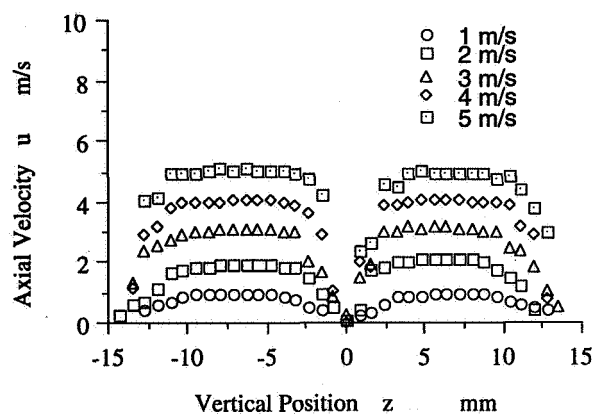
Figure 7 Axial mean velocity profiles at the center position of the 2-D nozzle (x=3.175mm, y=0) for various flow conditions.
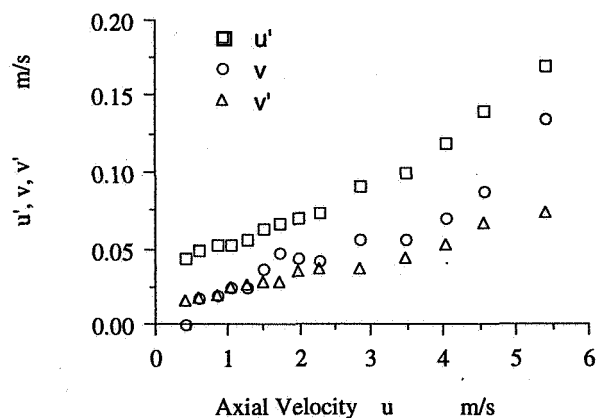
Figure 8 Vertical mean velocity and velocity fluctuations at the center of the flow (x=3.175mm, y=0, z=6.35mm) as a function of axial mean velocity.
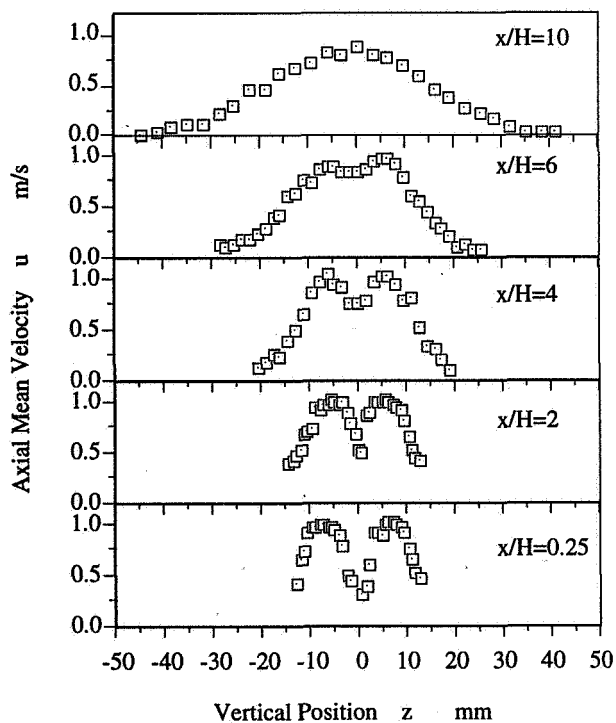
Figure 9 Axial mean velocity profiles as a function of downstream distance (u_m=1m/s).
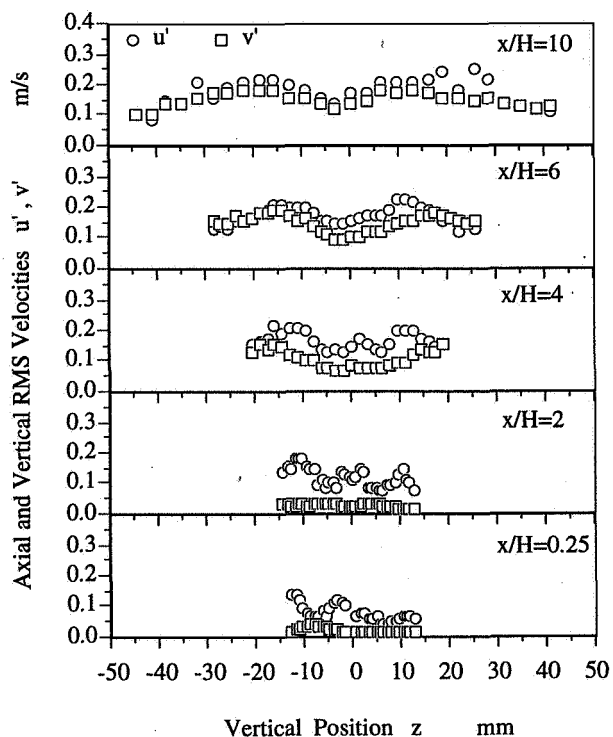
Figure 10 Axial and vertical velocity fluctuations as a function of downstream distance (u_m=1m/s).

PARTICLE EXPERIMENTS IN THERMAL AND VELOCITY GRADIENTS

Ivan O. Clark, NASA Langley Research Center, Hampton, Virginia, 23681
Edward J. Johnson, Lockheed Engineering & Sciences Co. Hampton, Virginia, 23666

ABSTRACT

The physical scales of velocity, length, time, thermal gradient magnitude and velocity gradient magnitude likely to be involved in gas-solid multiphase flight experiments are assessed for 1-100 μm particles.

INTRODUCTION

A complex interaction of forces normally governs the motion of solid particles which are conveyed pneumatically [1]. Forces due to viscous drag, gravity, inertia, velocity gradients, rotation, buoyancy, thermal gradients and several other causes may be present depending on the physical environment. The present research focuses on the effects of thermal and velocity gradients on the motion of solid particles in a laminar flow field. Thermal gradients induce an additional force on the particles, known as a thermophoretic force, which causes the particle trajectory to deviate from the fluid streamlines [2,3]. This force is dependent on the strength of the thermal gradient, the size of the particle and the thermophysical properties of both the particle and the fluid. Many numerical simulations rely on simple empirical expressions or an interpolation scheme based on Knudsen number developed by Talbot [2] to provide an expression for the thermophoretic force acting on a particle. Numerical investigations in laminar tube flows [4,5] and investigations of thermophoretic effects in stagnation point flows [6,7,8,9] show that additional terms must also be addressed in these non-isothermal systems to adequately characterize the motion of suspended particles. The adverse effects of thermophoresis on particle-based velocimetry instrumentation is also of concern [10].

Particles transiting a flow field containing a velocity gradient or shear will experience an additional force causing them to deflect from the surrounding fluid streamlines if they possess a non-zero velocity relative to the fluid. Saffman [12] demonstrated, for laminar flows, that the physical origins of this force lie in the variation of the pressure distribution acting on the surface of the particle. This force causes the particle to migrate to specific regions of shear. Segré and Silberberg [13] observed that small, neutrally buoyant spheres in Poiseuille flow migrate to a position 0.6 tube radii from the axis. This result has also been obtained analytically [12]. Experimental observations of liquid droplets in Poiseuille flow demonstrated that lift forces may direct the particles toward or away from the centerline depending on the particle and shear properties [15,16]. Lift forces acting on freely rotating particles in close proximity to walls have been investigated [17] and the effects of nonuniform particle concentrations in compressible shear flows and particle inertia on the accuracy of particle-based velocimetry instrumentation have also been studied [18].

EXPERIMENTAL CONSIDERATIONS

A goal of this research is to identify the science requirements and experimental parameters necessary to design future flight experiment packages which can provide improved data on the effects of thermal and velocity gradients. The intent is to exploit the suppression of gravitational forces and convection effects in a reduced gravity environment to examine effects on gas-solid flows normally masked by gravitationally induced effects and to study flow regimes unattainable in a ground-based laboratory.

A uniformly accepted mathematical treatment for the motion of a solid particle through a compressible gas containing both velocity and thermal gradients does not exist in a simple form. For purposes of discussion, one can assume that any experiment package suitable for flight or drop tower tests will require that the experiment be contained in an enclosure. That is, the experiment will take place in an enclosed space or in a tube or duct. If the experiment involves a flowing gas or liquid then some entry length and characteristic time is required for the system to reach hydrodynamic and thermal equilibrium. A discussion of the characteristic lengths and times associated with a large enclosure is quite complex and will not be addressed here. However, a simple laminar flow model in a tube will provide a great deal of insight into the length and time scales likely to be encountered in a wide class of experimental configurations. This is the classic Poiseuille flow for which hydrodynamic and thermal entry lengths are well established. The hydrodynamic and thermal entry length equations are derived from conservation of momentum and energy equations by Kays and Crawford [19] in the following forms, neglecting axial conduction:

| Hydrodynamic entry length, x | $x = \dfrac{Re\ D}{20}$ | Reynolds number | $Re = \dfrac{U\ D}{\nu}$ |

Thermal entry length, x $x = \dfrac{Re\ Pr\ D}{20}$

where x is the axial location of fully developed flow, U is the fluid velocity, D is the tube diameter, Re is the Reynolds number based on the tube diameter, ν is the kinematic viscosity of the fluid, and Pr is the Prandtl number. The Prandtl number is the ratio of the momentum diffusivity to the thermal diffusivity. In fluids with Pr > 1, the hydrodynamic profile develops faster than the thermal profile. The thermal entry length solution above applies to cases where Re Pr > 100.

By selecting Reynolds numbers and tube diameters, the equations above may be used to estimate the hydrodynamic and thermal entry lengths and the characteristic velocity of the system. A worst-case time scale can also be derived by dividing the maximum of the two length scales above by the characteristic velocity scale. Table 1 presents the results of such calculations for some common materials whose Prandtl numbers span four orders of magnitude at 300K. The Reynolds numbers are fixed at 1000 and 500 to maintain a laminar flow. For comparison, a Reynolds number of 2300 would normally indicate a turbulent flow in a tube. Tube diameters are selected to be 2.54 cm and 1.27 cm. Selection of Re and D fixes the hydrodynamic entry length scale independent of the fluid under consideration. As expected from the linear relations above, reducing the Reynolds number for a given diameter reduces the fluid entry length, thermal entry length and characteristic velocity but maintains the same time scale. Reducing the diameter at a given Reynolds number reduces the fluid entry length, thermal entry length and time scale but increases the velocity scale. For enclosed laminar experiments involving gases, it is desirable to reduce the Reynolds number and increase the tube diameter. Among the possible costs of this solution are that the desired fluid dynamic regime may not be attained and/or gravitational terms may become significant in the transport of solid particles relative to the reduced hydrodynamic drag.

It is possible to assess the response of a solid particle to an abrupt change in the fluid velocity, in a general way, by consideration of the so-called particle relaxation time. That is, the time required for a particle to adjust its velocity to match a change in the fluid velocity to within a very small percentage. Neglecting gravity, an expression for the particle relaxation time is derived by Hinds [20] in the following form for particle motion in the Stokes region and Re (based on the particle diameter) less than one:

Cunningham slip correction factor, C_c

Relaxation time, η $\eta = \dfrac{\rho_p\ d^2\ C_c}{18\ \mu}$ $C_c = 1 + \dfrac{\lambda}{d}\ [2.514 + 0.800\ \exp(-0.55\ \dfrac{d}{\lambda})]$

In these equations, d is the particle diameter, ρ_p the particle density, μ the fluid dynamic viscosity, C_c the Cunningham slip correction factor, and λ is the mean free path of a fluid molecule at the temperature and pressure under consideration. In all that follows, atmospheric pressure will be assumed and the focus will be on the gas-solid flow case. A nondimensional parameter known as the Knudsen number may be defined as Kn = $2\lambda/d$ which relates the mean free path to the particle radius. By selecting specific particle and gas parameters, the equations above and the Reynolds condition for Stokes flow provide a means to calculate a particle relaxation time and determine the maximum velocity for which Stokes hydrodynamic drag applies. The results of such calculations are presented in Table 2 for two types of particles in a size range from 1-100 μm in both hydrogen and air over a range of temperatures. The specific particles used in these calculations are alumina (Al_2O_3) with a density of 3970 kg/m^3 and polystyrene latex (PSL) with a density of 1050 kg/m^3. The diameters used are assumed to be equivalent spherical diameters and the intent is for the PSL particle to represent a low density particle and for the alumina to represent a medium density particle. Both materials are in common use as seed particles for particle-based velocimetry instruments. These simple calculations of the Knudsen number and the maximum velocity for which Stokes drag applies contain no particle properties other than the diameter. Hence, the results for alumina and PSL, or any other particle type, depends only on the thermodynamic properties of the fluid at the local temperature and pressure. The results indicate that maximum velocity for Stokes conditions on the particle is highly dependent on the local temperature and fluid properties. It may range from a few meters per second through supersonic velocities depending on the local conditions. These simple calculations also indicate that small particles may be expected to adapt to changes in the fluid velocity extremely rapidly. An incorrect conclusion may be drawn from such an analysis that the motion of sufficiently small

particles in laminar flow is governed solely by hydrodynamic drag for a given fluid and temperature. Indeed, hundreds of successful numerical models and particle-based experiments have been conducted based on this assumption. However, there are many forces besides drag which may be present in a given situation and which may impact the particle motion.

As described by Soo [21] and others, Tchen is generally credited with deriving the first widely accepted Lagrangian equation for the motion of a solid particle in an unsteady gas flow field. In what follows, the discussion of Tchen's equation provided by Nichols [22] will parallelled. The basic equation, using index notation, is written in the form:

$$m_p \frac{dv_i}{dt} = -3 \pi \mu d (v_i - u_i) + m_f \frac{Du_i}{Dt} - \frac{1}{2} m_f \frac{d}{dt} (v_i - u_i) - \frac{3 d^2}{2} \sqrt{\pi \rho_f \mu} \int_0^t \frac{\frac{d}{d\tau} (v_i - u_i)}{\sqrt{t - \tau}} d\tau - g_i (m_p - m_f)$$

with

$$\frac{Du_i}{Dt} = \frac{\partial u_i}{\partial t} + u_j \frac{\partial u_i}{\partial x_j} \qquad\qquad \frac{du_i}{dt} = \frac{\partial u_i}{\partial t} + v_j \frac{\partial u_i}{\partial x_j}$$

Here, $v_i = v_i(t)$, $u_i = u_i(t)$ and g_i are the component at time t in the x_i direction of the particle velocity, fluid velocity, and gravitational force, respectively. m_p is the mass of the particle, m_f is the mass of a volume of fluid equal to the particle volume, and ρ_f is the fluid density. The terms on the right of this expression represent forces acting on the particle associated with Stokes drag, the pressure distribution, the additional mass of fluid which must be accelerated along with the particle, a so-called Basset history integral over time τ (related to the acceleration history of the particle) and gravity. Tchen's equation is normally solved numerically due to the complexities introduced by the Basset history term. More recent equations of motion have been developed, for example the equation of Maxey and Riley [23], which correct some of the short comings of the Tchen expression. However, the present discussion focuses on the general relationship of forces which are likely to be present in common gas-solid flows and the simpler equation is quite adequate.

An idealized, quasi-one-dimensional problem provides a convenient way to assess the relative contributions of the various forces acting on a solid particle in a gas flow field. The case of the gas flow undergoing a step change in velocity is considered. For this case the Tchen equation is solved either numerically using a 4th order Runge-Kutta technique, if the Basset term is included, or analytically if the Basset term is dropped. The analytic solution for the relative velocity between the particle and the gas is in the form of a decaying exponential which provides a more exact determination of the particle relaxation time than the expression above. For this case, the force terms in the Tchen equation are supplemented with expressions for a shear-induced lift force and a thermophoretic force arising from thermal gradients in a laminar flow. As noted by Nichols [22], the shear-induced lift force or Saffman force has the form:

Shear-induced lift, $F_{L,i}$ $\qquad F_{L,i} = 1.6125 \, d^2 \sqrt{\rho_f \mu} \, |\frac{\partial u_i}{\partial x_j}|^{1/2} (v_i - u_i)$

while Talbot [2] provided an expression for the force due to a thermal gradient in the form:

Thermophoretic force, $F_{T,i}$ $\qquad F_{T,i} = \frac{\pi \mu v d}{2 |T|} \alpha(Kn) \frac{\partial T}{\partial x_i}$

with $\qquad\qquad\qquad \alpha(Kn) = 12 \, C_s \frac{k_f / k_p + C_t \, Kn}{(1 + 3 \, C_m \, Kn)(1 + 2 \, k_f / k_p + 2 \, C_t \, Kn)}$

representing a thermophoretic correction factor based on the Knudsen number. Thermal conductivities of the gas and particle are k_f and k_p, respectively, and $C_s = 1.147$, $C_t = 2.20$ and $C_m = 1.146$ are empirically derived constants.

The equations for shear-induced lift and thermophoretic force combined with a solution to Tchen's equation for the one-dimensional step change in gas velocity provide a means to quantify the relative contributions of the force terms. By selecting the gas, temperature, magnitude of the step change in velocity, particle size, and particle type, the magnitudes of the velocity and thermal gradients required to produce a lift or thermophoretic force equal to the drag, gravitational, or Basset force acting on the particle may be determined. Table 3 presents the results of such a calculation for a 1 μm particle experiencing a 1 mm/s relative velocity in both hydrogen and air over a range of temperatures. Table 4 presents similar calculations for the case in which the temperature is held fixed and the particle diameter is varied for the case of an alumina particle in hydrogen at 300K. Table 5 presents the case in which the gas, temperature, particle size and particle type are fixed and the relative velocity is varied from 1 mm/s to 10 m/s.

281

CONCLUSIONS

The following observations may be made from these calculations. First, the thermodynamic properties of the gas under consideration are extremely important in determining the contributions of the various force terms. Second, for small relative velocities, the magnitude of the velocity gradient required to produce a lift force equal to either the hydrodynamic drag or gravitational force are quite large. However, at higher relative velocities, it is possible for relatively modest velocity gradients to result in lift forces which exceed the gravitational forces acting on a particle. Third, thermal gradients are much more likely to produce a significant force acting on the particle relative to drag and gravity. This is especially true for small particles in high temperature flows. The exact conditions for maximum thermally-induced forces are not linear in temperature and depend on the gas under consideration. Resolution of the physics involved in gas-solid flows could be expected to improve significantly from experiments in microgravity where access to experimental conditions involving low speed flows with small velocity and/or thermal gradients and unrestricted particle size are not precluded by ground-based convection and sedimentation effects.

REFERENCES

[1] Barnett, D.O.: Seeding Requirements for Laser Velocimeter Utilization in Fluid Dynamics Facilities, Arnold Engineering Development Center, Arnold Air Force Station, TN, Final Report, Contract F40600-80-C-0002, Jan., 1981.

[2] Talbot, L., Chen, R.K., Schefer, R.W., and Willis, D.R.: "Thermophoresis of particles in a Heated Boundary Layer," J. Fluid Mechanics, Vol. 101, Part 4, 1980, pp. 737-758.

[3] Fotiadis, D.I., and Jensen, K.F.: "Thermophoresis of Solid Particles In Horizontal Chemical Vapor Deposition Reactors," J. Crystal Growth, Vol. 102, 1990, pp. 743-761.

[4] Stratmann, F., and Fissan, H.: "Convection, Diffusion and Thermophoresis in Cooled Laminar Tube Flow," J. Aerosol Sci., Vol. 19, No. 7, 1988, pp. 793-796.

[5] Pratsinis, S.E., and Kim K.: "Particle Coagulation, Diffusion and Thermophoresis in Laminar Tube Flows," J. Aerosol Sci., Vol. 20, No. 1, 1989, pp. 101-111.

[6] Ishii, R.: "Motion of Small Particles in a Gas Flow," Physics of Fluids, Vol. 1, January, 1984, pp. 33-41.

[7] Garg, V.K., and Jayaraj, S.: "Thermophoresis of Aerosol Particles in Laminar Flow Over Inclined Plates," Int. J. Heat Mass Trans., Vol. 31, No. 4, 1988, pp. 875-890.

[8] Turner, J.R., Fissan, H.J., and Liguras, D.K.: "Particle Deposition from Plane Stagnation Flow: Competition between Electrostatic and Thermophoretic Effects," J. Aerosol Sci., Vol. 19, No. 7, 1988, pp. 797-800.

[9] Garcia-Ybarra, P., and Rosner, D.E.: "Thermophoretic Properties of Nonspherical Particles and Large Molecules," AIChE Journal, Vol. 35, No. 1, January, 1989, pp. 139-147.

[10] Johnson, E.J., Hyer, P.V., Culotta, P.W. and Clark, I.O.: "Laser Velocimetry Measurements in Non-isothermal CVD Systems," Laser Anemometry: Advances and Applications, Vol. 2, 1991, eds., A. Dibbs and B. Ghorashi, ASME, pp. 483-489.

[11] Chang, J., Ishii, T., Matsumura, S., Ono, S., and Teii, S.: "Theory of Aerosol Particle Thermal Deposition on a Flat Body in a Variable Property Fluid," J. Aerosol Sci., Vol. 18, No. 6, 1987, pp. 619-621.

[12] Saffman, P.G.: "The Lift on a Small Sphere in a Slow Shear Flow," J. Fluid Mech, Vol. 22, part 2, 1965, pp. 385-400.

[13] Segré, G. and Silberberg, A.: "Behavior of Macroscopic Rigid Spheres in Poiseuille Flow: Part 2. Experimental Results and Interpretation," J. Fluid Mech., Vol. 14, No. 115, 1962, pp. 136-157.

[14] Ho, B.P. and Leal, L.G.: "Inertial migration of rigid spheres in two-dimensional unidirectional flows," J. Fluid Mech., Vol. 65, part 2, 1974, pp. 365-400.

[15] Puri, I.K. and Libby, P.A.: "On the Forces of Droplets in Poiseuille Flow," Phys. of Fluids A, Vol. 2, No. 7, July, 1990, pp. 1281-1284.

[16] McLaughlin, J.B.: "The lift on a small sphere in wall-bounded linear shear flows," J. Fluid Mech., Vol. 246, 1993, pp. 249-265.

[17] Cherukat, Pradeep, and McLaughlin, John B.: "The inertial lift on a rigid sphere in a linear shear flow field near a flat wall," J. Fluid Mech., Vol. 263, 1994, pp. 1-18.

[18] Samimy, M. and Lele, S.K.: "Motion of Particles in a Compressible Free Shear Layer," Phys. of Fluids A, Vol. 3, No. 8, 1991, pp. 1915-1923.

[19] Kays, William M., and Crawford, Michael E.: Convective Heat and Mass Transfer, McGraw-Hill, NY, 1980.

[20] Hinds, William C.: Aersosol Technology, John Wiley & Sons, NY, 1982.

[21] Soo, S.L.: Multiphase Fluid Dynamics, Gower Technical, 1990.

[22] Nichols, Robert H.: The Effect of Particle Dynamics on Turbulence Measurements with the Laser Doppler Velocimeter, Ph.D. Dissertation, University of Tennessee, Knoxville, June, 1986.

[23] Maxey, Martin R., and Riley, James J.: "Equation of motion for a small rigid sphere in a nonuniform flow," Phys. of Fluids A, Vol. 26, No. 4, 1983, pp. 883-889.

Table 1: Characteristic times, thermal entry lengths and velocities associated with combinations of Reynolds numbers and length scales for some common liquids and gases.

			Tube diameter 0.0254 m				Tube diameter 0.0127 m		
			Re 1000 Fluid scale 1.27 m		Re 500 Fluid scale 0.635 m			Re 1000 Fluid scale 0.635 m	
	Prandtl number 300K	Time scale	Thermal entry length	Velocity scale	Thermal entry length	Velocity scale	Time scale	Thermal entry length	Velocity scale
		(s)	(m)	(m/s)	(m)	(m/s)	(s)	(m)	(m/s)
Mercury	2.48E-02	2.87E+02	3.15E-02	4.40E-03	1.57E-02	2.21E-03	7.17E+01	1.57E-02	8.86E-03
Hydrogen	7.01E-01	2.91E-01	8.90E-01	4.37E+00	4.45E-01	2.19E+00	7.27E-02	4.45E-01	8.74E+00
Air	7.07E-01	2.03E+00	8.98E-01	6.23E-01	4.49E-01	3.13E-01	5.07E-01	4.49E-01	1.25E+00
Freon	3.50E+00	5.78E+02	4.44E+00	7.70E-03	2.22E+00	3.84E-03	1.45E+02	2.22E+00	1.54E-02
Water	5.83E+00	2.20E+02	7.40E+00	3.37E-02	3.70E+00	1.68E-02	5.50E+01	3.70E+00	6.73E-02
Ethylene Glycol	1.51E+02	3.45E+02	1.92E+02	5.55E-01	9.59E+01	2.78E-01	8.64E+01	9.59E+01	1.11E+00

Table 2: Relaxation times, maximum velocities which maintain Stokes conditions and Knudsen number for 1, 10 and 100 μm alumina and polystyrene latex particles.

| | HYDROGEN | | | | AIR | | | |
Temp.	Alumina Relax. time	PSL Relax. time	Stokes Maximum Velocity	Kn	Alumina Relax. time	PSL Relax. time	Stokes Maximum Velocity	Kn
			PARTICLE DIAMETER - 1 μm					
K	(s)	(s)	(m/s)		(s)	(s)	(m/s)	
100	5.84E-05	1.55E-05	1.76E+01	1.03E-01	3.18E-05	8.40E-06	2.32E+00	4.65E-02
300	3.65E-05	9.66E-06	1.10E+02	3.73E-01	1.51E-05	3.98E-06	1.53E+01	2.02E-01
500	3.35E-05	8.85E-06	2.59E+02	6.78E-01	1.22E-05	3.22E-06	3.70E+01	3.83E-01
1000	3.55E-05	9.38E-06	8.25E+02	1.53E+00	1.13E-05	2.98E-06	1.22E+02	8.56E-01
1500	3.96E-05	1.05E-05	1.62E+03	2.46E+00	1.18E-05	3.12E-06	2.45E+02	1.37E+00
2000	4.37E-05	1.16E-05	2.63E+03	3.44E+00	1.26E-05	3.32E-06	4.02E+02	1.97E+00
			PARTICLE DIAMETER - 10 μm					
K	(s)	(s)	(m/s)		(s)	(s)	(m/s)	
100	5.24E-03	1.39E-03	1.76E+00	1.03E-02	3.02E-03	7.99E-04	2.32E-01	4.65E-03
300	2.59E-03	6.85E-04	1.10E+01	3.73E-02	1.23E-03	3.26E-04	1.54E+00	2.02E-02
500	1.91E-03	5.04E-04	2.59E+01	6.78E-02	8.57E-04	2.27E-04	3.70E+00	3.84E-02
1000	1.31E-03	3.47E-04	8.25E+01	1.53E-01	5.75E-04	1.52E-04	1.22E+01	8.56E-02
1500	1.10E-03	2.91E-04	1.62E+02	2.46E-01	4.67E-04	1.23E-04	2.45E+01	1.37E-01
2000	9.95E-04	2.63E-04	2.63E+02	3.44E-01	3.99E-04	1.06E-04	4.02E+01	1.97E-01
			PARTICLE DIAMETER - 100 μm					
K	(s)	(s)	(m/s)		(s)	(s)	(m/s)	
100	5.18E-01	1.37E-01	1.76E-01	1.03E-03	3.00E-01	7.94E-02	2.32E-02	4.65E-04
300	2.49E-01	6.57E-02	1.10E+00	3.73E-03	1.20E-01	3.18E-02	1.54E-01	2.02E-03
500	1.77E-01	4.68E-02	2.59E+00	6.78E-03	8.22E-02	2.17E-02	3.70E-01	3.84E-03
1000	1.12E-01	2.97E-02	8.25E+00	1.53E-02	5.25E-02	1.39E-02	1.22E+00	8.56E-03
1500	8.65E-02	2.29E-02	1.62E+01	2.46E-02	4.05E-02	1.07E-02	2.45E+00	1.37E-02
2000	7.22E-02	1.91E-02	2.63E+01	3.44E-02	3.28E-02	8.67E-03	4.02E+00	1.97E-02

Table 3: Magnitude of velocity and thermal gradients required to produce a lift or thermophoretic force equal in magnitude to the drag or gravitational force acting on a 1 μm alumina particle experiencing a 1.0 mm/s relative velocity in hydrogen and air.

Temp.	HYDROGEN				AIR			
	Velocity gradient		Thermal gradient		Velocity gradient		Thermal gradient	
	Drag	Gravity	Drag	Gravity	Drag	Gravity	Drag	Gravity
K	(1/s)	(1/s)	(K/m)	(K/m)	(1/s)	(1/s)	(K/m)	(K/m)
100	6.02E+08	1.24E+04	2.15E+04	1.09E+04	7.91E+07	2.49E+03	2.57E+05	7.55E+04
300	3.77E+09	1.49E+04	8.68E+03	2.11E+03	5.25E+08	2.76E+03	6.13E+04	7.21E+03
500	8.86E+09	1.62E+04	7.47E+03	1.28E+03	1.26E+09	2.91E+03	4.35E+04	3.48E+03
1000	2.82E+10	1.81E+04	7.57E+03	8.18E+02	4.17E+09	3.28E+03	3.56E+04	1.81E+03
1500	5.55E+10	1.94E+04	8.29E+03	6.82E+02	8.38E+09	3.52E+03	3.54E+04	1.38E+03
2000	9.00E+10	2.03E+04	9.06E+03	6.14E+02	1.37E+10	3.65E+03	3.75E+04	1.18E+03

Table 4: Magnitude of velocity and thermal gradients required to produce a lift or thermophoretic force equal in magnitude to the drag or gravitational force acting on an alumina particle experiencing a 1.0 mm/s relative velocity in hydrogen at 300K.

HYDROGEN

| Particle diameter | Velocity gradient | | Thermal gradient | |
| | Drag | Gravity | Drag | Gravity |
(m)	(1/s)	(1/s)	(K/m)	(K/m)
5.0E-07	1.51E+10	7.44E+03	1.10E+04	6.67E+02
1.0E-06	3.77E+09	1.49E+04	8.68E+03	2.11E+03
1.0E-05	3.77E+07	1.49E+05	1.84E+04	4.45E+05
1.0E-04	3.77E+05	1.49E+06	1.09E+05	2.63E+08

Table 5: Magnitude of velocity and thermal gradients required to produce a lift or thermophoretic force equal in magnitude to the drag or gravitational force acting on a 1 μm alumina particle over a range of relative velocities in hydrogen at 300K.

HYDROGEN

| Relative velocity | Velocity gradient | | Thermal gradient | |
| | Drag | Gravity | Drag | Gravity |
(m/s)	(1/s)	(1/s)	(K/m)	(K/m)
1.0E-03	3.77E+09	1.49E+04	8.68E+03	2.11E+03
1.0E-02	3.77E+09	1.49E+03	8.68E+04	2.11E+03
1.0E-01	3.77E+09	1.49E+02	8.68E+05	2.11E+03
1.0E+00	3.77E+09	1.49E+01	8.68E+06	2.11E+03
1.0E+01	3.77E+09	1.49E+00	8.68E+07	2.11E+03

CROSS-EFFECTS IN MICROGRAVITY FLOWS

S. K. Loyalka
Particulate Systems Research Center
College of Engineering
University of Missouri-Columbia
Columbia, Missouri 65211

Abstract: In microgravity materials growth (i.e., crystal growth via vapor deposition) experiments, it is of interest to understand and control the flows that arise from the molecular rather than the mere continuum nature of the gases and the vapors. The project research is a theoretical and experimental investigation of the flow of gas/vapor mixtures in realistic geometries and environments, as well as the application of new fundamental understandings to simulating flows in the ampoules. Towards this goal, the research tasks are: to obtain a theoretical description of the flows by solving appropriate kinetics equations; to verify the results by acquiring experimental data in a diffusion cell; and to explore applications of the results above to simulations of flows in the ampoules. The paper provides a description of the cross-phenomena and the progress realized to-date by the project personnel.

I. **Background:** Film growth by chemical/physical vapor deposition is a process of considerable interest in microgravity experiments. The absence of natural convection should allow better control of the growth processes but, as Roesner has pointed out for the highly nonisothermal ampoules, thermal slip (creep) can become a matter of significant concern even for Knudsen numbers as small as 10^{-3}. Thus, it is important to understand and control the flows that arise from the molecular, rather than the mere continuum, nature of the gases and the vapors. Molecular flows have been extensively studied, both experimentally and theoretically. The theoretical investigations, except in rare circumstances, were confined to models of the Boltzmann equation which are not adequate to describe flows of gas mixtures. Also, the

experimental investigations did not address the non-continuum aspects of non-isothermal mixture flows. Thus, there exists a strong need for new theoretical investigations, their experimental confirmation, and the applications of the new findings.

To describe the molecular flows, we consider the diffusion of one or more species (molecular mass m_i, number density n_i) in an arbitrary gas mixture. Mathematically, for the distribution $f_i(\underline{r},\underline{c})$, the problem consists in solving the boundary value problem:

$$c_i \cdot \frac{\partial f_i}{\partial r} = \sum_{j=1}^{n} J(f_i f_j)$$

$$f_i^+(r, c_i) = A f_i^-(r, c_i), \qquad c_i \cdot n_r > 0, \quad r \in \partial S$$

$$(1)$$

where c_i is the molecular velocity (of species i), r is the position coordinate, and J is the nonlinear collision operator. n_r is a unit vector normal to the surface and directed into the gas-vapor mixture, f_i^- is the incident, and f_i^+ is the emergent distribution. A is a general vapor(gas)-surface scattering operator (including reaction, condensation, accommodation coefficients, etc.).

The driving terms in the problem are, respectively, the partial pressure gradients $\nabla P_{i,asy}(\underline{r})$ and the temperature gradient $\nabla T_{asy}(\underline{r})$ and hence the overall partial pressure and the temperature differences.

The quantities of major interest in this problem are the mass fluxes J_i and the total heat flux J_Q which are, respectively, expressed as:

$$J_i = \int m_i c_i f_i(r, c_i) dc_i$$

$$J_Q = \int \tfrac{1}{2} m_i c_i^2 c_i f_i(r, c_i) dc_i$$

$$(2)$$

It is useful, however, to consider the diffusive and the conductive components (both with respect to the mean mass velocity V) only, which are expressed respectively as:

$$J_{i,d} = \int m_i(c_i - V)f_i(r,c_i)dc_i = J_i - \rho_i V_i$$
$$J_h = \sum \int \tfrac{1}{2}m_i(c_i - V)^2(c_i - V)f_i(r,c_i)dc_i \qquad (3)$$

For the heat flux, it is somewhat easier to consider:

$$J_h = J_{h'} - \tfrac{5}{2}kT_0\sum n_i C_i$$
$$= J_{h'} - \tfrac{5}{2}kT_0(u - V_i) \qquad (4)$$

where u is the mean molecular velocity of the mixture. Thus J_h is measured with respect to the mean mass molecular velocity V, and J_h is measured with respect to the mean molecular velocity. For small gradients, one can write:

$$J_{i,d} = \sum L_{j,dd}X_j + L_{i,dh}X_h$$
$$J_h = \sum \tfrac{P_0}{\rho_i}L_{i,hd}X_i + L_{i,hh}X_h \qquad (5)$$

where

$$X_i = \nabla(P_{i,asy}(\underline{r}) - P_{i,0})/P_{asy}$$
$$X_h = \nabla(T_{i,asy}(\underline{r}) - T)/T_0 \qquad (6)$$

and $L_{i,dd}, L_{hh}$ are the phenomenological coefficients due to the direct effects, and $L_{i,dh}$, $L_{i,hd}$, are the coefficients related to the cross-effects. These

coefficients are known for the continuum conditions, but information is required for conditions under all range of Knudsen numbers.

The Project Research: The research being conducted is a theoretical and experimental investigation of the flow of gas/vapor mixtures in realistic geometries and environments. The main objective is to obtain a greater understanding of the mass and heat transfer for a vapor-gas mixture, and particularly the cross-effects with respect to their role in microgravity environments. Towards this goal, the research tasks are to :

1) Solve the Boltzmann and the Wang Chang Uhlenbeck equation to determine the flow (mass or heat) rates and the matrix of the phenomenological coefficients L, for arbitrary Knudsen number (ratio of mean free path to characteristic flow dimension), arbitrary gas (vapor) mixtures, realistic intermolecular and gas-surface interaction potentials, and for small (linear problems), as well as large, gradients (non-linear problems),

2) Verify the results by acquiring experimental data in a diffusion cell,

3) And, explore applications of the results above to simulations of flows in the ampoules.

Progress to-date: The project personnel (In addition to S, K, Loyalka, graduate student P.A. Tebbe and Drs. I. N. Ivchenko, R.V. Tompson, K.A. Hickey, S.A. Hamoodi, R.L. Buckley have contributed to theoretical investigations and graduate students C. Huang and D. Gabis and Drs. R. V. Tompson and T. K. Ghosh have contributed to the experimental tasks) have to-date solved numerically the Boltzmann Equation for a monatomic gas for rigid sphere molecules and cylindrical geometry, under non-condensing conditions. All phenomenological coefficients have been computed. Initial computations for

realistic potentials (monatomic gas), as well as the velocity and the creep slip, have been completed. The creep slip is found to be dependent on the type of gas, and results confirm the accuracy of recently reported variational results. The variational technique also has been extended, and it has been shown that the planar flows can be computed very efficiently, for all Knudsen numbers, by use of the Burnett solutions. The diffusion slip and the creep slip also have been computed for monatomic gas mixtures. A computer program to allow simulation of deposition in cross flows in idealized geometries (cylindrical tube) has been written and tested for some simple test problems.

The two bulb apparatus for isothermal experiments has been designed, built, and tested. Experimental data on two gas mixtures (Ar-He, N_2-He) at several pressures (1 torr to 200 torr total pressure) and mole ratios have been obtained, and are found in good agreement with the theoretical predictions (in the slip regime).

Ongoing and planned research includes calculations on mixtures for arbitrary pressures, measurements with non-condensing and condensing species (such as mercurous chloride) under temperature gradients, measurements of momentum accommodation coefficients (which affect the flows) for gas mixtures, generalization of the computer program on deposition in other geometries, and development of ideas for a micro-gravity experiment on cross-effects.

TWO-LAYER VISCOUS INSTABILITY IN A ROTATING COUETTE DEVICE

Christopher Gallagher,
Tom Kropnewicki,
David T. Leighton, and
Mark J. McCready

University of Notre Dame
Department of Chemical Engineering
Notre Dame, IN 46556

ABSTRACT

A novel experiment to study the interfacial shear instability between two liquids is described. Density-matched immiscible liquids are confined between concentric cylinders such that the interface is parallel to the cylinder walls. Interfacial waves that develop because of viscosity difference between the shearing fluids are studied as a function of rotation rate and depth ratio using optical techniques. Conditions of neutral stability and the most unstable wavenumber agree reasonably well with predictions from linear stability analysis of the Navier-Stokes equations. Illumination using laser sheets allows precise measurement of the interface shape. Future experiments will verify the correctness of weakly nonlinear theories that describe energy transfer and saturation of wave growth by nonlinear effects. Measurements of solitary wave shapes, that occur far above neutral stability, will be compared to similar measurements for systems that have gravity as an important force to determine how gravity effects large disturbances. These results will be used to interpret slug and annular flow data that have been obtained in other μg studies.

INTRODUCTION

Cocurrent flows of immiscible fluids are found in process flows, (e.g., condensers, oil-water separators, iron-slag separators), hydrocarbon production and transportation pipelines and there may be future opportunities to replace contacting devices that rely on emulsification (e.g., liquid extractors) with separate flowing phases that have high interphase transport coefficients. Critical information necessary for design and operation of these devices is whether the phases will remain separate (perhaps due to density differences) or if mixing will occur. While prediction of the phase configuration has been done using flow maps [1] of *dimensional* variables and stability analysis has been done with constitutive criteria [2,3,4,5], the validity of these procedures is generally confined to conditions close to the conditions of the experiments on which they were based. Further, the true predictive capabilities of these methods are lacking. If a base state with separate phases can be defined, a rigorous linear stability analysis that employs numerical solutions of the governing equations [6,7] can be done to determine if the base state is stable. While linear stability analysis can predict the conditions when waves will form and grow with distance, nonlinear theories are needed to determine if saturation of these waves will occur [8,9]. These rigorous nonlinear theories are valid only if the wave slope remains small; if the waves get too large, no predictions can be made. Consequently, experiments are needed to determine the long distance evolution of disturbances. Unfortunately, conduits available in laboratories are often too short and industrial pipelines too irregular to determine definitively what the long distance state of a linearly unstable flow is.

To solve this problem, we have devised a new experiment that uses a two-layer flow of density matched fluids confined between concentric cylinders. The interface is parallel to the cylinder walls and rotation of the outer cylinder, for fixed inner cylinder, induces shearing that can lead to instability. The waves that form are completely analogous to interface waves formed by a shear flow in a flat channel. For the rotating device these have crests that are parallel to the rotation axis and exhibit interface deformation in the radial direction (r) that is initially periodic in the direction of rotation (θ). This device can simulate extremely long distance evolution of disturbances by simply waiting a sufficiently long time. For example, experiments shown below indicate that waves with significant

amplitudes will form only after several minutes at rotation rates large enough to cause instability. This corresponds to over 100 meters of length -- a distance not usually available for a well-controlled experiment.

Interfacial wave growth curves for systems such as gravity driven films, pressure driven pipe or channel flow and two-layer Couette flows have two distinct shapes. Figure 1 shows temporal wave growth curves calculated numerically [10] using a two-layer Orr-Sommerfeld analysis and full linearized boundary conditions. In figure 1a the region of positive growth is bounded away from 0 wavenumber. Figure 1b shows the second shape where the growth rate has a maximum away from 0 but is positive all the way down to 0 once any wavenumber becomes unstable. The primary question suggested is: what generic differences are there in the very long time evolution of waves for the two different types of growth curves? Previous work [11] suggests that wave modes can be generated in linearly stable regions by nonlinear interactions, but it is not clear if they stay at small amplitudes or grow into the dominant waves. Gravity driven films, once unstable, always look like figure 1b, channel flows can exhibit either of the two behaviors.

The two-layer Couette geometry changes from 1a to 1b as h, the ratio of the inner (less viscous film) layer thickness/gap thickness, is altered. Thus it is possible to compare the behavior of both types of growth curves using well-controlled long time experiments. In this paper we describe the device, the experimental procedures and give some preliminary results on regions of instability and wavelengths of observed waves.

EXPERIMENTAL

Wave measurements have been made in a rotating concentric cylinder test cell. The diameter of the inner cylinder is 19.50 cm and the diameter of the outer cylinder is 21.50 cm resulting in a gap thickness of 1.00 cm. The gap width is 5 cm. The cylinders are loaded into a Weissenberg rheogoniometer such that the inner cylinder is fixed, the outer cylinder may be rotated, and the axis is aligned with gravity. The concentricity of the cylinders is aligned to a tolerance of about 75 μm while the tilt of the cylinders is aligned to a tolerance of about 25 μm.

To perform measurements in our system, the outer wall is transparent to permit direct imaging of the interface. We use several lighting techniques to probe the experiment -- white light, a vertical plane of laser light, and a horizontal laser sheet. The two laser methods provide useful quantitative data that direct visualization with white light does not allow. Figure 2a is a diagram of the vertical laser setup. It shows a plane of laser light projected on to the interface at a large incident angle. The laser light is visible at the outer surface of the outer wall and at the interface. The distance between the two laser images is proportional to the fluid depth ratio. Further, the image on the interface is a profile of the interface shape. Figure 2b is a diagram of the horizontal laser setup. The horizontal laser set up is designed to show a wave tracing at a constant vertical position.

The two fluids used for the experiments whose results are presented here are Dow 710, which is a phenylmethyl polysiloxane fluid and a mixture of ethylene glycol, water, and Pink Bismuth -- an Osco® brand upset stomach remedy. The Pink Bismuth is used as a source of refractive particles. The viscosity and density of Dow 710 are 0.555 Ns/m^2 and 1110 kg/m^3 respectively. The viscosity and density of the ethylene glycol solution are 0.0151 Ns/m^2 and 1108 kg/m^3 respectively. Dow 710 is loaded on the outer cylinder after the ethylene glycol mixture has been added to the channel.

To map the stability boundary of our system, the velocity of the outer plate was set to about 0.05m/s and periodically increased until waves formed. The exact value of the initial velocity is dependent upon the stability of the interface. If conditions change much from the conditions when the fluids were density matched, larger velocities are needed to maintain the interface.

RESULTS AND OBSERVATIONS

The growth curves in figure 1 predict that waves will form if the rotation velocity is sufficiently large and become detectable after a sufficiently long time. Figure 3 is a plot of Reynolds number versus dimensionless inner film thickness. The three curves correspond to dimensionless growth rates of 0.0, 0.001, 0.015. The circles show the experimentally - observed onset of waves. For a height of 0.7, waves were observed very close to the predicted onset conditions. A growth rate of 0.001 corresponds to a time constant of approximately 5 minutes and a flow distance of 100 m! For smaller heights, a larger growth rate was required to observe waves. This may have been because we did not wait long enough for waves to form, or it could be because nonlinear effects caused saturation at amplitudes too small to observe. Further experiments and nonlinear analysis are needed to resolve this issue.

Observed wavenumbers match well with the predicted fastest growing waves. Figures 4a-d are plots of the theoretical growth rate curves for the most unstable wave mode and experimental data. Wavenumbers for experimental data are depicted with a dashed line. Most of the stability points lie near the maximum growing wave number. The wavenumber for figure 4b lies closer to 1/2 the most unstable wavenumber. This could have been excited when the rotation rate was lower and thus the most unstable wave mode occurred at a lower wavenumber. This behavior has been seen in previous experiments with conditions such that the system was unstable for all Reynolds numbers. In those experiments, a small amplitude long wave was excited at a low plate velocity and grew in amplitude with increasing velocity. An alternative explanation is that there could have been nonlinear interactions that caused transfer of energy to lower wavenumber. Further experiments that carefully watch the time evolution of the wavenumber will be done to see which scenario is occurring.

CONCLUSIONS

Two-layer shear flow interfacial instability can be studied in the geometry of a rotating Couette flow that allows observation of wave evolution at times and (effectively) distances much longer with much better control than is possible in channel flows. Density matching of the fluids, necessary to create the vertical interface geometry, essentially removes gravity as an important force. By doing long time experiments, it is possible to examine the importance of modes near zero wavenumber that have much lower growth rates than shorter modes. These experiments will enable careful checks of nonlinear theories that predict energy transfer between modes and saturation of amplitudes at sufficiently long times. Direct white light imaging using a standard video camera allows measurement of the wavenumber and wave speed. The precise interfacial wave shapes, which are particularly important away from neutral stability where the shape is nonsinuous, can be accomplished using laser sheets to illuminate the flow cell. It is hoped that these measurements of nonsinuous waves will help to interpret annular and slug flow behavior that is observed in μg studies that have been done.

ACKNOWLEDGMENTS

REFERENCES

1. J. M. Mandhane, G. A. Gregory and K Aziz, Int. J. Mult. Flow, 1 (1974) 537-553.
2. Y. Taitel and A. E. Dukler, AIChE J., 22 (1976) 47-56.
3. D. Barnea, Chem. Eng. Sci., 46 (1991) 2123-2131.
4. D. Barnea, Int. J. Mult. Flow, 3 (1987) 1-12.
5. N. Brauner and D. M. Maron, Chem. Eng. Sci., 46 (1991) 1849-1859.
6. S. G. Yiantsios and B. G. Higgins, Phys. Fluids, 31 (1988) 3225-3238.
7. Y. Y. Su and B. Khomami, Journal of Computational Physics, 100 (1992) 297-305.
8. P. J. Blennerhassett, Proc. R. Soc. Lond. A, 298 (1980) 451-494.
9. M. Renardy and Y. Renardy, Phys. Fluids A, 5 (1993) 2738-2762.
10. W. C. Kuru, M. Sangalli and M. J. McCready, submitted to Int. J. Mult. Flow.
11. L. A. Jurman, S. E. Deutsch and M. J. McCready, J. Fluid Mech., 238 (1992) 187-219.

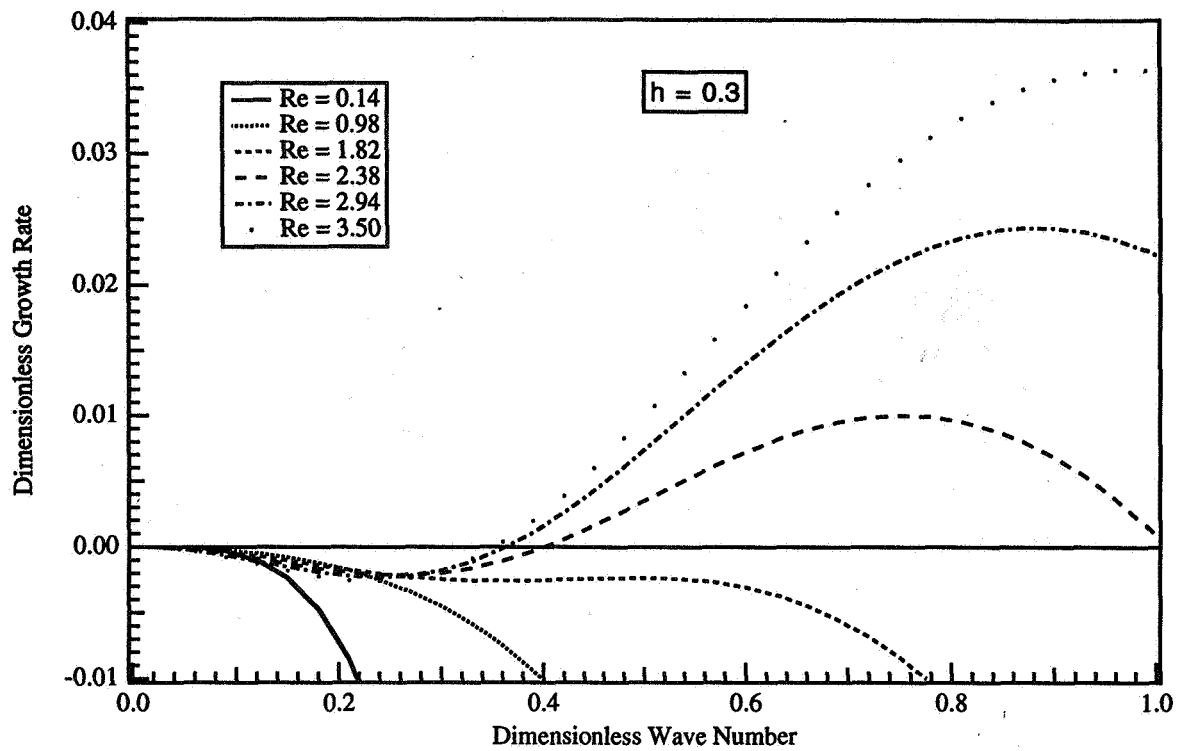Figure 1a: Plot of growth rate versus wave number for conditions
which can have positive growth bounded away from 0 wavenumber.

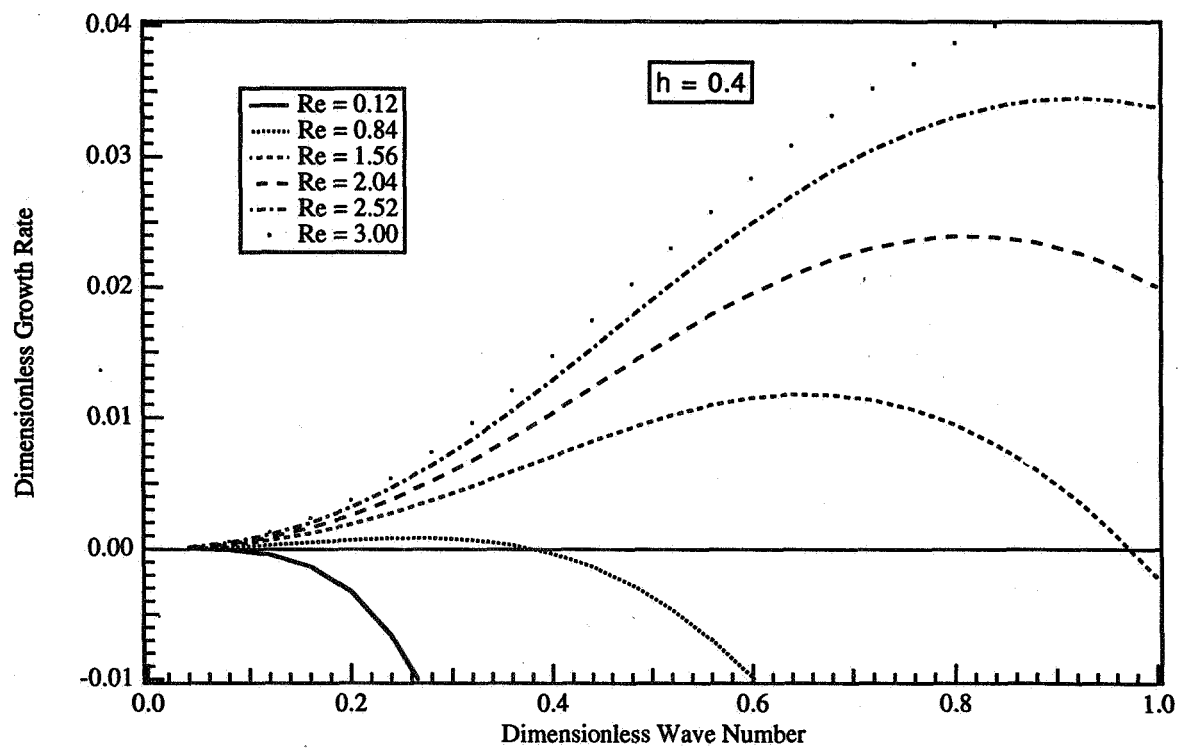Figure 1b: Plot of growth rate versus wave number for conditions
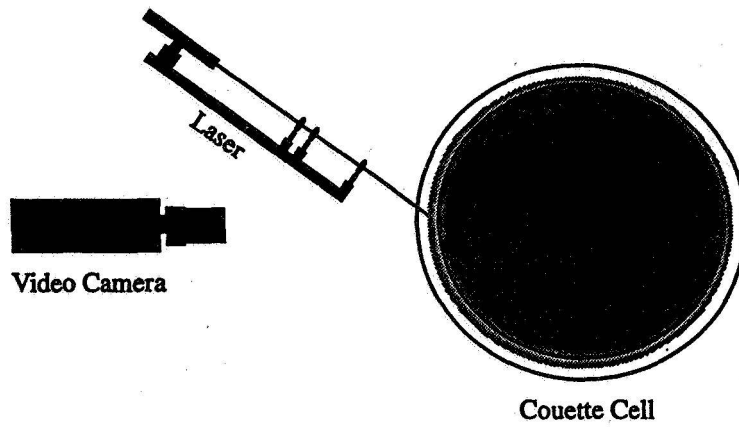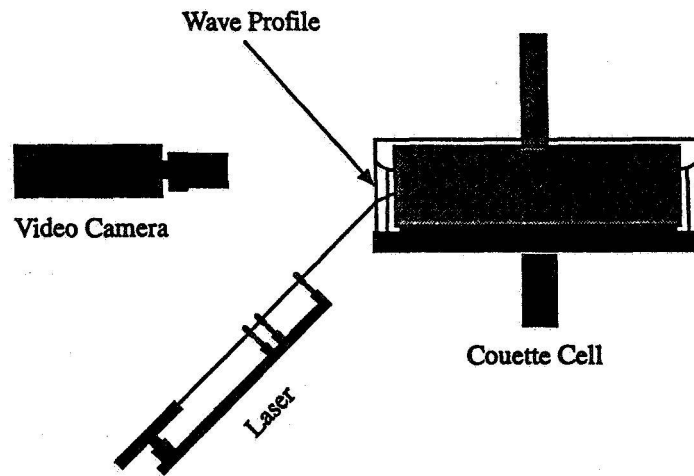where unstable waves extend all the way down to 0 wavenumber.

figure 2a: Vertical laser setup.

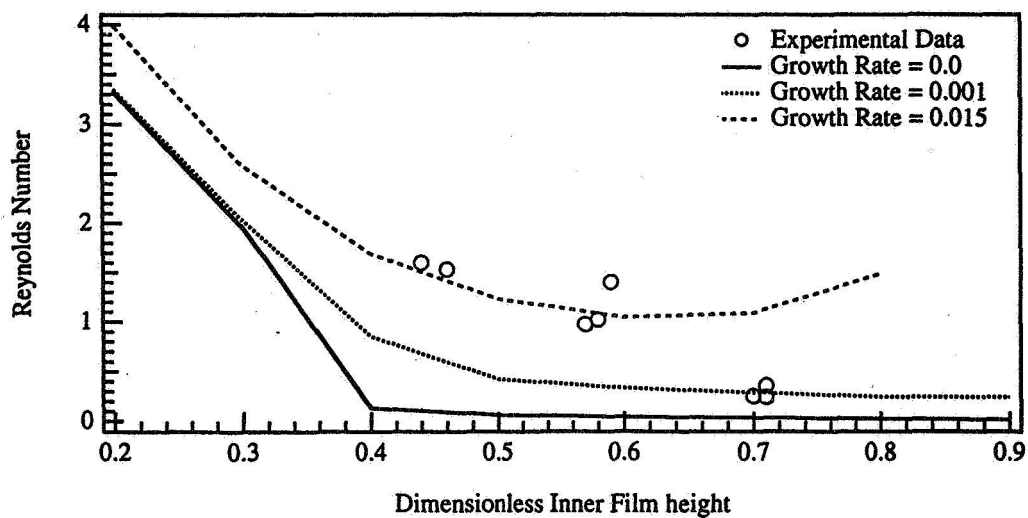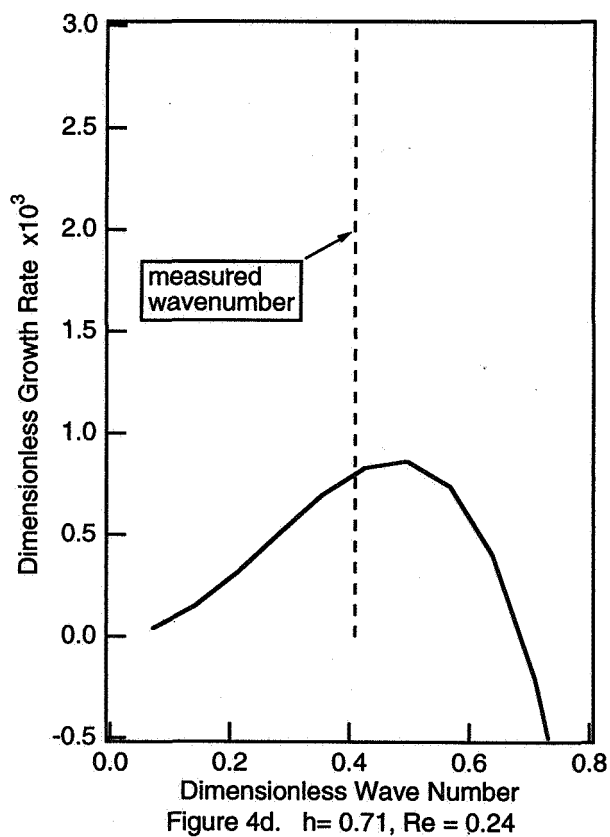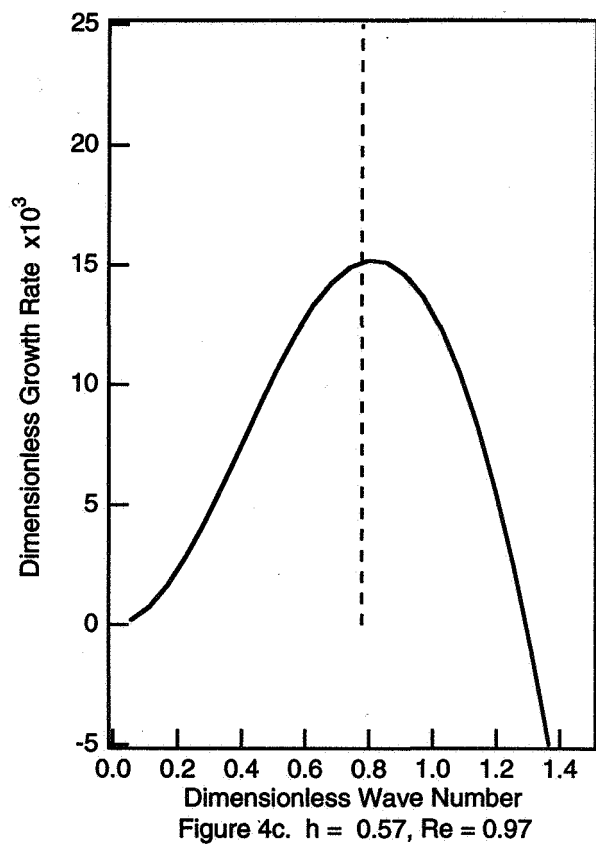figure 2b: Horizontal laser setup.

figure 3: Stability curves for three characteristic growth rates plotted with experimental data
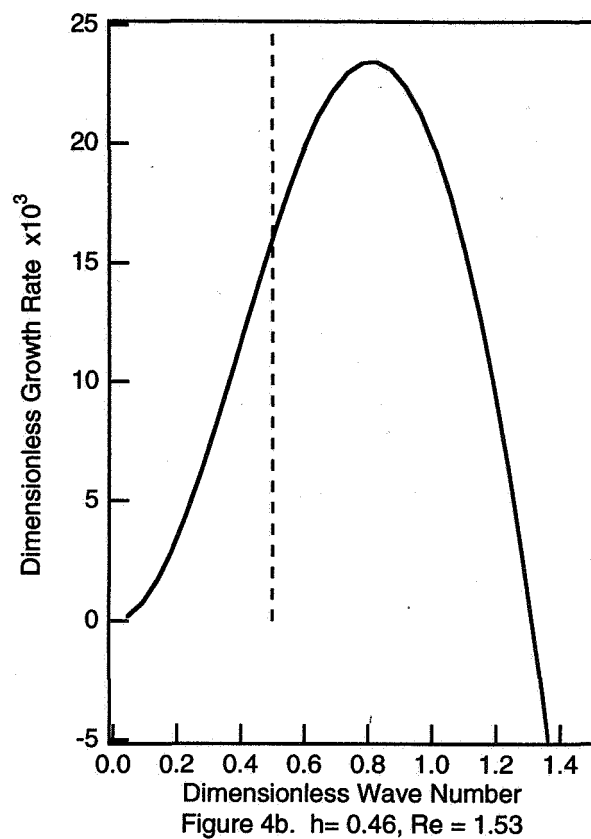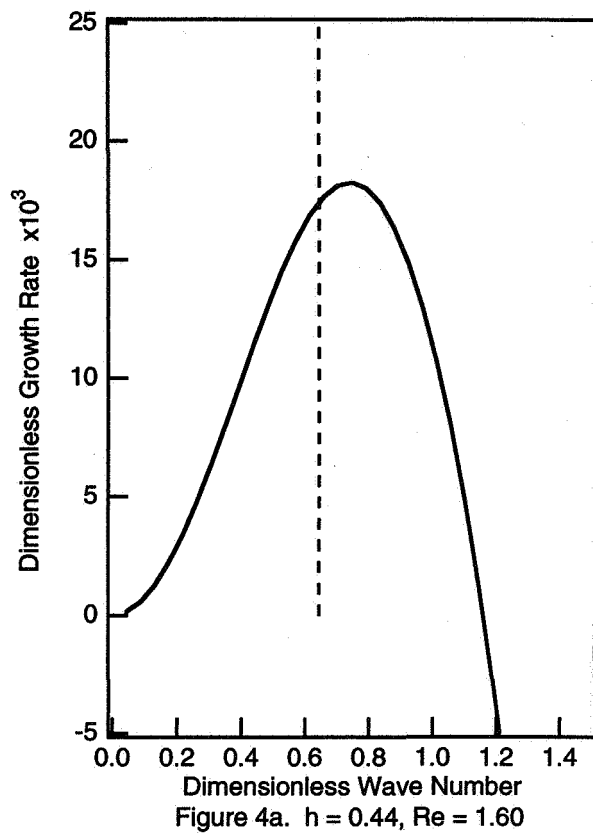
Figure 4a. h = 0.44, Re = 1.60

Figure 4b. h= 0.46, Re = 1.53

Figure 4c. h = 0.57, Re = 0.97

Figure 4d. h= 0.71, Re = 0.24

296

AN APPLICATION OF MINISCALE EXPERIMENTS ON EARTH TO REFINE MICROGRAVITY ANALYSIS OF ADIABATIC MULTIPHASE FLOW IN SPACE

Dr. Paul H. Rothe, P.I.
Ms. Christine Martin
Creare Inc., Hanover, NH 03755

Ms. Julie Downing
Dartmouth College
Hanover, NH 03755

ABSTRACT

Adiabatic two-phase flow is of interest to the design of multiphase fluid and thermal management systems for spacecraft. This paper presents original data and unifies existing data for capillary tubes as a step toward assessing existing multiphase flow analysis and engineering software. Comparisons of theory with these data once again confirm the broad accuracy of the theory. Due to the simplicity and low cost of the capillary tube experiments, which were performed on earth, we were able to closely examine for the first time a flow situation that had not previously been examined appreciably by aircraft tests. This is the situation of a slug flow at high quality, near transition to annular flow. Our comparison of software calculations with these data revealed overprediction of pipeline pressure drop by up to a factor of three. In turn, this finding motivated a reexamination of the existing theory, and then development of a new analytical model which is at once more plausible physically and is in far better agreement with the data. This sequence of discovery illustrates the role of inexpensive miniscale modeling on earth to anticipate microgravity behavior in space and to complement and help define needs for aircraft tests.

INTRODUCTION

Rothe (1988) stated the view that steady multiphase flow in microgravity is a well-developed engineering technology. Multiphase flow in space is in fact much simpler than that on earth, thanks to the absence of the gravity body force. The means of engineering analysis already existed in art prior to 1988. That is, engineers could already predict with confidence the two-phase flow regime, the pressure drop, and the inventory of liquid in pipelines and vessels. At this NASA review meeting several design engineers asserted that indeed the minor uncertainties associated with predicting these adiabatic multiphase design factors posed no practical difficulty in their system analysis, nor their specification of hardware, nor their confidence in ultimate system performance. Moreover, thermal components such as evaporators and condensers, and other hardware such as inertial separators could already be designed. This is not to say that it was useless to refine either science or engineering design technology. Rather, no Herculean effort to do so was warranted.

The problem of modeling multiphase flow in spacecraft is not its inherent physical complexity. The scientific community has already successfully addressed a more difficult problem here on earth, namely the omni-directional modeling of multiphase pipeline flows for oil/gas transportation and in process and power plants. Rather the difficulty perceived in 1988 was a dearth of data for spacecraft multiphase flow, particularly at low (e.g., lunar), minigravity (e.g., 0.01 g) and microgravity (e.g., 10^{-4} to 10^{-6} g).

Six years have passed and the literature on adiabatic multiphase flow has expanded markedly. Some fine scientific and engineering technology work has been performed at many organizations, among them the University of Houston, Texas A&M, and Creare, with NASA and Air Force collaboration and sponsorship. Dukler (1988) reports aircraft tests of multiphase flow in a pipeline, typical of many by the University of Houston and other organizations. Reinarts and Best (1993) also report aircraft tests of pipeline flow and present their data and others comparatively. Crowley et al (1992) offer a "design manual" organizing the then available theory, releasing associated engineering software, and assessing the theory by comparison with then available aircraft data. Crowley, Sam and Schuller (1991) report aircraft tests of a generic system including an evaporator, a condenser, a pipeline and a pump and use these data to challenge the main elements of their model. Nothing in any of this new information has produced a single surprise. The technology available before 1988 has transferred straightforwardly to the prediction of spacecraft flows.

Spacecraft tests of various multiphase flows have been proposed. Some such proposals have tended to be prohibitively expensive and broad rather than focused, amounting to general purpose facilities. We suggest that spacecraft tests are best performed for closely defined confirmatory purpose, as a result of comprehensive prior study using earth-based facilities. Aircraft (and drop towers) offer a practical research tool for minigravity tests, but with some limitations. Accelerations less than 0.01 g are difficult to maintain, g-jitter of comparable order is often experienced, test duration at minigravity is of the order of 10 seconds (and begins and ends with a jerk and an inventory transient), and costs are high by comparison with earth tests in a static facility. Moreover, for reasons of safety, only certain fluids can be used.

The idea in scale modeling is to vary governing forces widely while preserving key force ratios, thereby subjecting theory to severe challenges at modest experimental cost. The ratio of acceleration body force to surface force is the Bond number, expressed as

$Bo=aD^2\Delta\rho/\sigma$. This ratio suggests that rather than vary acceleration, there is merit in varying pipeline diameter, which appears to the second power in the Bond number. In particular if diameter is reduced by a factor of 10 then Bond number is reduced by a factor of 100, a change equivalent to reducing gravity by a factor of 100 as in an aircraft test. This suggests the use of tubes of the order of 2.5 mm on earth to model prototypical systems in the range 25 to 100 mm pipeline diameter in space. Such data on earth could be compared with similar data from aircraft tests. Moreover, the two modeling approaches are complementary. Small earthbound facilities can use a wide range of fluids safely and are subject to steady gravity force indefinitely. They are very inexpensive to build and test.

This paper illustrates the usefulness of miniscale tests on earth to anticipate minigravity aircraft tests and microgravity applications. The work is a collaborative effort of researchers at Creare, Dartmouth College and NASA.

Available Data

Table 2 of the report by Martin and Rothe (1994) presents a survey of available experimental data for adiabatic multiphase flow in aircraft pipelines and from capillary tubes on earth. The fluids include water/air, various freons, ammonia (the expected prototype fluid), and some hydrocarbons and pure gases. References are herein.

The data span the main flow regimes of applied interest and include visual data for regime determination, pressure drop measurement, and void fraction (also known as holdup or fluid inventory). The measurements of void fraction are so far very limited in aircraft, relying on the data of one investigator with one fluid and over only a limited range of test experience that did not extend to annular flow. With the exception of the early work by Suo and Griffith (1963) in capillary tubes of diameter 0.5 and 0.8 mm., all of these data, both aircraft and capillary tube, were obtained since 1988.

Crowley et al. (1992) and Reinarts (1993) unify these aircraft data by comparison with a single body of analytical methods, that established by Crowley et al. (1992). Embodied in that system of theoretical tools for the prediction of flow regime, pressure gradient and holdup is a self-consistent body of similitude principles. By this means, the high degree of unification of data achieved to date and the close agreement with theory together indicate effective scale modeling principles.

In this paper we examine this art by additional comparisons of the theory (design methods) with data for capillary tubes. This poses an entirely new challenge to the prior art because the capillary-tube data are quite different from the original data base, and because these data do not suffer from the problems of test duration, g-jitter, and the like experienced by aircraft. In this way we complement and increase confidence in the prior findings. We also extend them.

Comparisons of Theory with Data

Figures 1, 2 and 3 compare the flow regime predictions of Crowley et al. (1992) with the miniscale data of four investigators who coincidentally used capillary tubes of approximately 2.5 mm diameter. The maps illustrate the conditions tested; neither Ungar and Cornwell (1992) nor Duschatko et al. (1992) observed the flow regimes. Direct visual observations by Fukano and Kariyasaki (1993), Martin and Rothe (1994) and Downing (1994) agree consistently and comprehensively with these flow regime predictions, for example, see Figure 2. So these comparisons unify flow regime modeling among capillary tubes on earth, prototype-scale tubes in aircraft, and theory derived from first principles and incorporating fluid dynamic similitude. Once again there is no surprise whatsoever. That is, models available before 1988 continue to predict all available data without difficulty.

Figures 4 to 7 compare the pressure drop measurements of these same four investigators with calculations employing the software developed and described by Crowley et al. (1992). Once again, excellent agreement is achieved for the purpose of engineering design. And again these comparisons unify the available capillary tube data, complement and support the available aircraft data, and confirm the similitude theory inherent in the original theory as compiled and combined in the comprehensive methodology proposed by Crowley et al. (1992). However, this time there was one surprise.

Our initial comparisons with these pressure data were in part unsatisfactory. To achieve the agreement shown in Figures 4 through 7 required an original analytical model. This model was developed by Wallis and employed by Downing (1994). The model was reviewed by Crowley and is a feature of the current version of his software, MICROP (1994). This refinement appreciably affects only certain predictions, only those for slug flow and then only for those slug flows at very high quality, near the transition to annular flow. Nonetheless for those flows the Wallis-Downing (1994) model is superior by a factor of up to three, no small correction. Moreover, the model is more plausible physically and mitigates an unreasonable jump in the predictions between slug and annular flow.

This discrepancy in prior art, the only significant discrepancy found to date since all of the testing initiated in 1988, was not found by an aircraft test. It was found on earth using a small tube.

The Wallis-Downing (1994) Model of Slug Flow

The Wallis-Downing (1994) model considers three elements:

1. friction in a pipe,
2. acceleration in a pipe,
3. acceleration at inlet and outlet.

Of these, the first is the significant technology refinement. The second element is analyzed for completeness and found to be negligible, as was the finding of the original modeling by Crowley and others. The third element is necessary only to the reduction of data, as in the present instance, where the pressure drop is measured in two plena surrounding a pipe. This inlet/outlet acceleration term is found to be small compared with the measured pressure drop in the pipe, and any deviation between this element and the experimental reality represents an experimental uncertainty.

For comparison, the friction terms of the pressure drop model developed by (1) Crowley et al. (1992) used in MICROP (1992) and (2) Wallis-Downing (1994) are:

$$\left[\frac{\partial P}{\partial z}\right]_{frict} = -\frac{2C_f \rho_f j^2}{D}(1-\alpha) \qquad (1)$$

$$\left[\frac{\partial P}{\partial z}\right]_{frict} = \frac{2C_f \rho_f j \, j_f}{D} \qquad (2)$$

Due to space limitations the reader is referred to Downing (1994) for this derivation. Its effect is shown in Figure 8.

Figure 9 presents selected data of Downing (1994), those in the slug flow regime but at relatively high quality near the slug-annular transition. These data are compared in Figure 9 with the model of MICROP (1992), but with the annular regime selected. These data are not annular; they are in the slug regime yet close to annular. Not unexpectedly, the measurements show somewhat higher pressure drop than would be the case if the flow were truly annular. Figure 10 presents the same data in comparison with two slug-flow models, that of MICROP (1992) and the Wallis-Downing model (1994). Both models yield values higher than the measured data. The Wallis-Downing model is a substantial improvement; it is as much as a factor of three lower than the original MICROP (1992) model.

Figure 11 compares the data of Downing (1994) with each of the MICROP models, the original as described by Crowley and Izenson (1992) and the updated software MICROP (1994) incorporating the Wallis-Downing theory above. Plainly the Wallis-Downing model has the expected effect when compared with the Downing data for slug flow at high quality.

Of the four data sets for capillary tubes, only two have data for slug flow in the moderate to high quality range of interest. A similar plot for the data of Fukano and Kariyasaki (1993) confirms this finding. Because the slug flow tests performed by Fukano and Kariyasaki (1993) were generally at low flow rates (of both gas and liquid) well below the quality levels of Downing (1994), the impact of the model change is less severe.

We have examined the available aircraft data and do not present comparisons with them at this time.

Several investigators did not produce or report pressure drop data. Others discouraged the use of their data for this purpose, either because the flow conditions were not available in the range of present interest, or because the investigator questioned the accuracy of their data. Comparisons with the data of two investigators were performed and the initial results were equivocal. There is a need for additional aircraft data to examine this range of behavior. Such tests can now be performed with the benefit of prior calculations and in an effort to challenge a modeling hypothesis.

CONCLUSIONS

Original data have been developed for adiabatic two-phase flow in a capillary tube. Such "miniscale" testing complements aircraft tests at minigravity and is a step toward modeling microgravity effects on two-phase flow in spacecraft. These data extend the flow range of prior miniscale tests.

Available capillary tube data have been unified. These include data derived independently by four investigators at one size, approximately 2.5 mm or about one-tenth of prototype scale. The additional work described by Downing (1994) and Rothe and Martin (1994) further unify data at other sizes, diameters from 0.5 to 5.0 mm, which data however are less complete or less satisfactory in various ways.

The art predating 1988 was employed by Crowley et al. during the 1980s and thoroughly documented by Crowley et al. (1992) via their report and also their release of software called MICROP (1992). Their prior assessment of these analytical models and design tools unified and demonstrated agreement with all contemporary aircraft data, circa 1992. The present work extends this assessment to the available miniscale data from capillary tubes on earth. Once again the methodology of Crowley et al. (1992) has been qualified successfully against available data, save a minor refinement.

This qualification revealed a discrepancy limited to the slug flow regime, and further limited to high quality flows near the slug-annular regime transition. An improved model was written from first principles and assessed by Wallis-Downing (1994), improving the prior art both in terms of physical plausibility and in terms of agreement with the miniscale data. In selected cases the calculation of pressure drop has been improved by a factor of up to three.

The particular work reported here can be generalized to show the role of miniscale tests (and possible microscale tests) on earth to complement aircraft tests (and possible spacecraft tests) for the modeling of microgravity effects on two-phase adiabatic flows. The miniscale data provide an inexpensive way to rapidly explore parametric trends as a function of fluid properties, flow rates, physical size and the like. Together a body of data combining miniscale tests on

earth with aircraft tests model directly the effects of gravity and overcome concerns about sensitivity to g-jitter, jerk, and short duration of minigravity aircraft tests. The diversity of data derived thereby, encompassing a range of gravity and diameter, provides a strong challenge to analytical modeling.

ACKNOWLEDGEMENTS

REFERENCES

Barajas, A.M. and Panton, R.L.; *The Effects of Contact Angle on Two-Phase Flow in Capillary Tubes*; International Journal of Multiphase Flow, V19(2), 1993.

Chen, I.Y. et al.; *A Reduced Gravity Flight Experiment: Observed Flow Regimes and Pressure Drops of Vapor and Liquid Flow in Adiabatic Piping*; AIChE Symp. Series, V84(263), 1988, pp. 203-216.

Colin, C. et al.; *Gas-Liquid Flow at Microgravity Conditions -- I.: Dispersed Bubble and Slug Flow*; Int. J. Multiphase Flow, V17(4), 1991, pp. 533-544.

Crowley, C.J. et al.; *Design Manual for Two-Phase Components of Spacecraft Thermal Management Systems*; prepared for Phillips Laboratory, PL-TR-92-3002, Sept. 1992.

Crowley C.J., Sam, R.G., and Schuller, M.S.; *Microgravity Experiments with a Simple Two-Phase Thermal System*; Proc. of the Eighth Symposium on Space Nuclear Power Systems, Part Three, New York, NY: American Institute of Physics, 1991, p.1207.

Crowley, C.J.; *Scaling of Multiphase Flow at Large Pipe Size and High Gas Density*; 4th Int'l Conf. on Multi-Phase Flow, Nice, France, June 1989.

Damianides, C.A. and Westwater, J.W.; *Two-Phase Flow Patterns in a Compact Heat Exchanger and in Small Tubes*; 2nd UK Conf. on Heat Transfer, U. Strathclyde, Glasgow, Sept. 14-16, 1988.

Downing, J.P.; *Microscale Modeling of Microgravity Multiphase Flow*; a thesis submitted to Dartmouth College in partial fulfillment of the requirements for the degree of Master of Science, June 1994.

Dukler, A.E. et al.; *Gas-Liquid Flow at Microgravity Conditions: Flow Patterns and Their Transitions*; Int. J. Multiphase Flow, V14(4), 1988, pp. 389-400.

Duschatko, R.J. et al.; *Pressure Drop Experiments in Condensing Ammonia Flow in Small Diameter Tubes*; AIAA 27th Thermophysics Conf., Nashville, TN, AIAA-92-2908, July 1992.

Fukano, T. and Kariyasaki, A.; "Characteristics of Gas-Liquid Two-Phase Flow in a Capillary Tube"; Nuclear Engineering and Design, 1993, p. 144.

Govier, G.W. and Omer, M.M.; *The Horizontal Pipeline Flow of Air-Water Mixtures*; Canadian Journal of Chemical Engineering, V.40-41, June 1962, p. 101.

Hill, W.S. and Best, F.R.; *Definition of Two-Phase Flow Behaviors for Spacecraft Design*; Foster-Miller, Inc., Report No. AFK-0062-FM-8933-418, June 1991.

Martin, C.M. and Rothe, P.H.; *Microscale Modeling of Microgravity Fluid Flow: Analysis and Experiment*; prepared for NASA Lewis Research Center, Grant NAS3-26549, by Creare Inc. (TN-535), Hanover, NH, March 1994.

MICROP (1992, 1994); Engineering software released by Creare Inc. to the Air Force and its contractors, 1992, as described by Crowley at al. (1992) and updated as described by Downing (1994).

Reinarts, T.R. et al.; *Zero-G Two Phase Flow Regime Modeling in Adiabatic Flow*; 10th Symposium on Space Nuclear Power and Propulsion, Albuquerque, NM; eds. Ed-Genk, M.S. and Hoover, M.D.; 1993.

Suo, M. and Griffith, P.; *Two Phase Flow in Capillary Tubes*; Trans. ASME, Journal of Basic Engineering, Paper No. 63-WA-96, 1964, pp. 576-582.

Ungar, E.K. and Cornwell, J.D.; *Two-Phase Pressure Drop of Ammonia in Small Diameter Horizontal Tubes*; AIAA 92-3891; AIAA 17th Aerospace Ground Testing Conference, July 6-8, 1992.

Wallis, G.B.; One-Dimensional Two-Phase Flow; McGraw-Hill Book Company, New York, NY, 1969.

Wallis, G.B. and Downing, J.P.; a model written by Professor Wallis and incorporated in the Master's thesis of Ms. Downing, 1994.
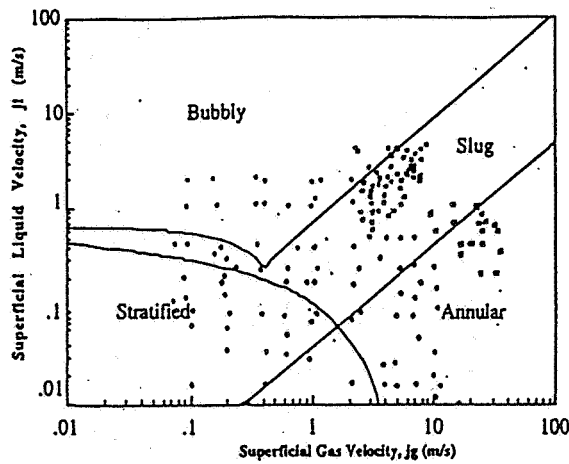
Figure 1. The data of Downing (1994) and Fukano and Kariyasaki (1993) each span the flow regimes and agree closely with the transitions identified by the methodology of Crowley et al (1992).
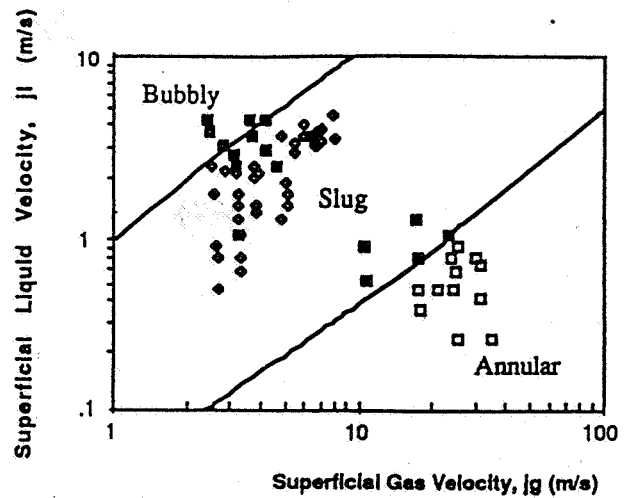
Figure 2. The data of Downing (1994) for a 2.4 mm diameter tube on earth are in close agreement with the flow regimes predicted by the methodology of Crowley et al (1992).
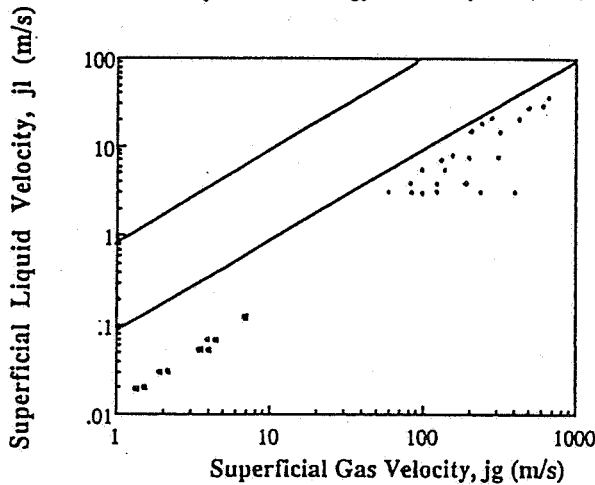
Figure 3. The data of Duschatko et al (1992) and Unger and Cornwell (1992) correspond with the annular flow regime according to the method of Crowley et al (1992). The data are for ammonia flowing in a 2.4 mm tube on earth.
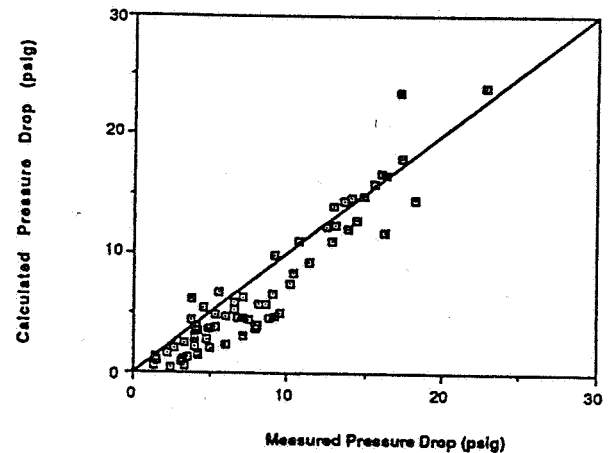
Figure 4. The data of Downing (1994) for bubbly, slug and annular flow regimes in a 2.4 mm diameter tube are in close agreement with the method of Crowley et al (1992), incorporating the Wallis-Downing (1994) model for slug flow.
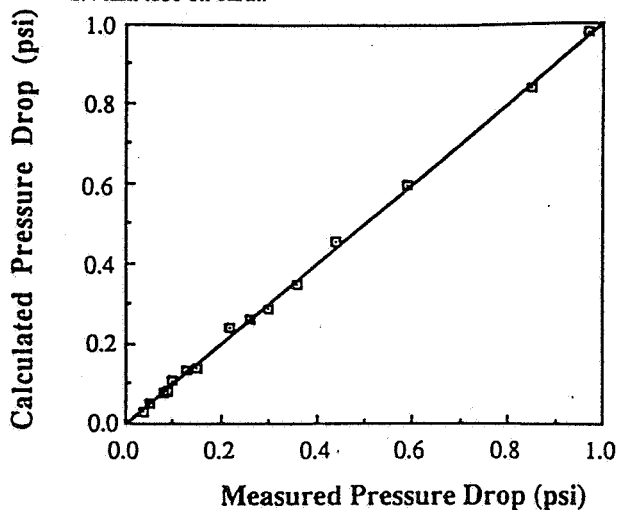
Figure 5. The method of Crowley et al (1992) shows close agreement with the ammonia data of Unger and Cornwell (1992) in the annular flow regime. Tube diameter is 2.6 mm on earth.
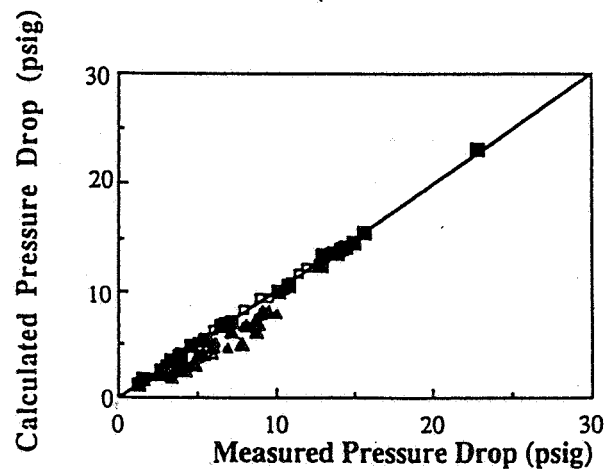
Figure 6. The method of Crowley et al (1992) shows close agreement with the data of Fukano and Kariyasaki (1993) in both the slug and annular regimes. These are Air Water Data for a tube of 2.4 mm diameter. The data of Downing (1994) are also shown.

301
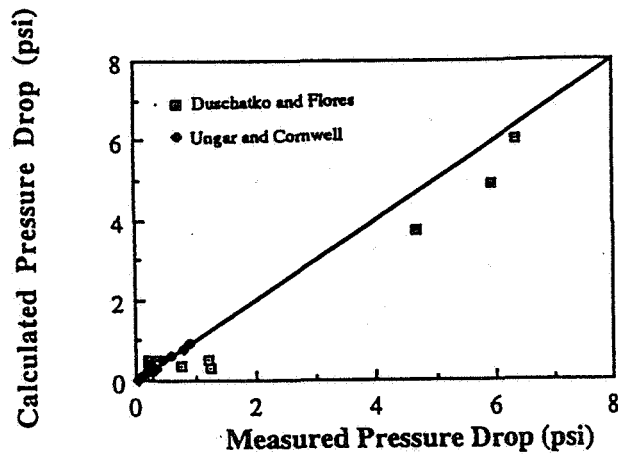
Figure 7. The data of Duschatko et al (1992) and Unger and Cornwell (1992) for ammonia flowing in a 2.4 mm tube on earth agree with the method of Crowley et al (1992). The data of these two investigators is limited to the annular flow regime.
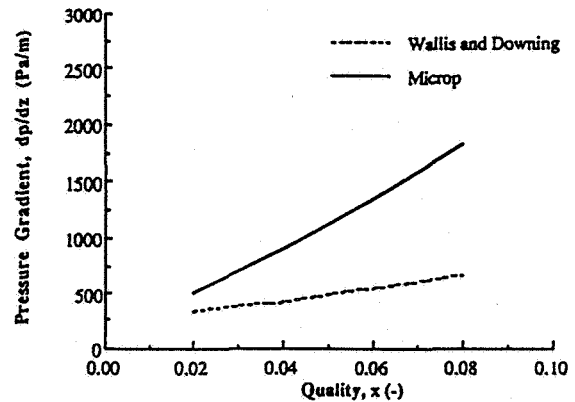
Figure 8. The Wallis-Downing model reduces pressure gradient in the slug flow regime, particularly at high quality near the slug-annular transition.
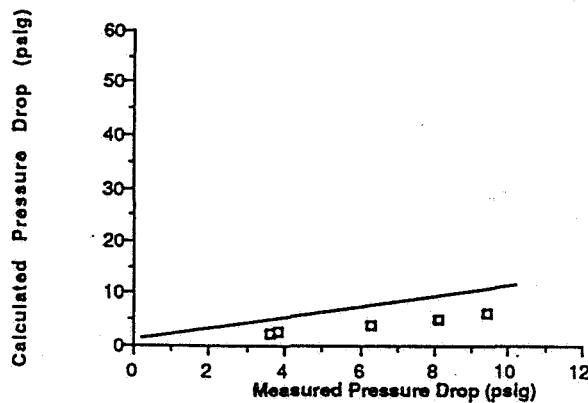
Figure 9. Measured pressure drop by Downing (1994) for slug flows at high quality exceed the annular flow calculation of MICROP (1992).
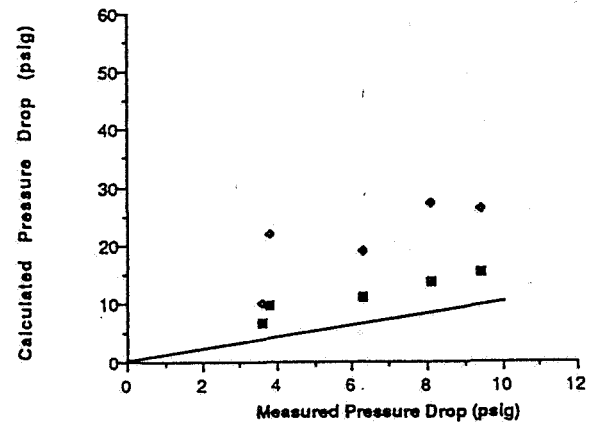
Figure 10. The model of Wallis-Downing (1994) gives much lower calculated pressure drop (for slug flow at high quality near the slug-annular transition) than does the slug flow of MICROP (1992). This is illustrated by comparison with selected data from Downing (1994) from a 2.4 mm tube on earth.
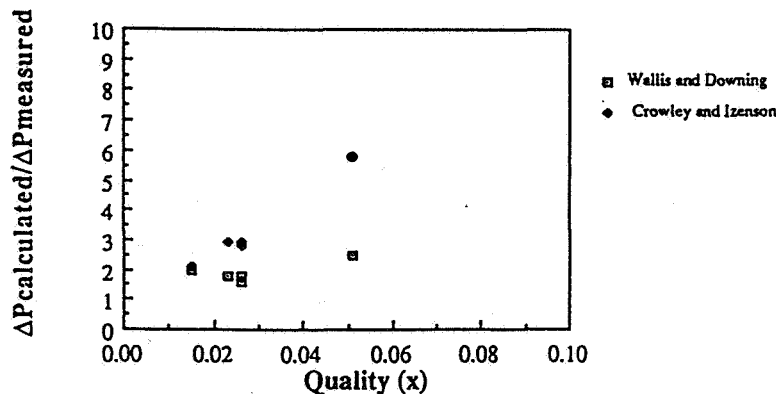
Figure 11. The ratio of calculated to measured pressure drop shows the expected deviation at high quality in the slug flow regime. The data are those of Downing (1994) with slug flow in a 2.4 mm tube on earth. The models are those of Crowley et al (1992) and Wallis-Downing (1994).

302

Complex Fluids

MICROGRAVITY FOAM STRUCTURE AND RHEOLOGY

Douglas J. Durian and Anthony D. Gopal
UCLA Department of Physics
405 Hilgard Avenue
Los Angeles, CA 90024-1547

ABSTRACT

Our long-range objective is to establish the fundamental interrelationships between the microscopic structure and dynamics of foams and their macroscopic stability and rheology. Foam structure and dynamics are to be measured directly and noninvasively through the use and development of novel multiple light scattering techniques such as diffusing-wave spectroscopy (DWS). Foam rheology is to be measured in a custom rheometer which allows simultaneous optical access for multiple light scattering. Microgravity conditions will ultimately be required to eliminate the increasingly rapid gravitational drainage of liquid from in between gas bubbles as the liquid:gas volume fraction is increased toward the rigidity-loss transition.

INTRODUCTION: FOAM STRUCTURE AND PROPERTIES

Foams are nonequilibrium dispersions of discrete gas bubbles in a smaller, continuous, volume of liquid which contains surface-active macromolecules [1-2]. They are familiar in everyday life from cleaning, food, and cosmetic products, and are important in a truly wide variety of industrial and research settings, whether fabricated for specific applications or inhibited and destroyed where undesirable. A hierarchy of structure and self-organization at progressively smaller length scales, as shown schematically in Figure 1, is ultimately responsible for the unique properties which make foams such fascinating and useful materials. The largest structural length scale, above which the foam appears homogeneous, is set by the average bubble size and can typically vary from 1 cm to 10 μm depending on method of preparation and foam age. At the very smallest structural length scale, surface-active molecules are preferentially adsorbed at the gas/liquid interfaces and give rise to several physical-chemical effects which deter the coalescence of neighboring bubbles and thereby lend stability to the foam. An important intermediate length scale is the thickness of the liquid film separating neighboring gas bubbles; its value depends on details of the interfacial forces, and hence on the molecular composition of the liquid, but is typically on the order of 100 nm as is familiar from the colorful interference patterns in isolated soap films.

In addition to this cascade of structural length scales, a key compositional parameter is the volume fraction occupied by the liquid phase. For relatively wet foams, such as depicted in Figure 1, the gas bubbles are very nearly spherical and the foam microstructure is most readily described as the random close packing of a polydisperse collection of spheres. For relatively dry foams, by contrast, the bubbles are very nearly polyhedral and the foam microstructure is more readily described as a continuous random network of thin liquid films. The influence of liquid volume fraction on bubble shape is depicted schematically in Figure 2. The amount of liquid which separates the "wet" and "dry" regimes depends not only on the bubble size distribution, but also on the competition between surface tension, which favors spherical bubbles, and repulsive interfacial forces, which favor polyhedral bubbles. The influence of this competition on bubble shape is also depicted schematically in Figure 2.

Stability

Aqueous foams are intrinsically nonequilibrium materials. With time, the liquid and gas portions separate by some combination of three basic mechanisms: gravitational drainage of liquid from in between gas bubbles, direct coalescence of neighboring bubbles via film rupture, and diffusion of gas from smaller to larger bubbles, which is known as coarsening. In practice, film rupture can be made negligible by suitable choice of liquid composition; however, it is not possible to eliminate the other two mechanisms. Coarsening always occurs because the bubble size distribution is naturally polydisperse. Gravitational drainage also cannot be prevented, on earth, because the mass densities of the liquid and gas portions are always significantly different and cannot be matched.

Rheology

Aqueous foams which are relatively stable can be considered as a form of matter which is unusual in sharing the hallmark features of both solids, liquids, and vapors [3]. Even though foams consist mainly of gas and a small amount of liquid, they can support shear elastically, like a solid, through the distortion of tightly packed bubbles away from area-minimizing shapes. If applied stresses are sufficiently great, the bubbles can hop around each other allowing the foam to flow and deform indefinitely like a liquid. And, in addition, foams are as readily compressible as gasses. The combination of elastic/solid-like and viscous/liquid-like behavior in foams is further surprising in that it is unlike the linear viscoelasticity exhibited by many complex fluids: Foam behavior is liquid-like at high shear strain rates and solid-like at low shear strain rates, while the rheology of polymers and colloids is the reverse.

SCIENCE OBJECTIVES

In spite of their commercial importance, and long-standing basic scientific interest, there is little fundamental understanding of the detailed interrelationships between foam microstructure and dynamics and the key features of their macroscopic stability and rheology [2-3]. Our long-range goal is to elucidate such interrelationships through critical use of new multiple light scattering techniques and microgravity conditions. Basic questions we intend to answer quantitatively include: How does liquid composition and content affect the rates of the three evolution mechanisms, and how does the foam microstructure then evolve with time? What are the dynamical time scales associated with the structural length scales, and how do they influence foam rheology? More specifically, what is the rate and duration of the so-called T1 neighbor-switching topology changes depicted in Figure 3? How does the striking shear elasticity of foams vanish with increasing liquid content? How, and to what extent, does foam stability and rheology scale with surface tension and average bubble size?

RELEVANCE TO APPLICATIONS

Applications involving foams fall into two categories: those where a foam is designed and produced to perform a particular task exploiting its unusual materials properties, and those where a foam is to be destroyed or the inadvertent foaming of a multi-component liquid is to be prevented. In addition to familiar cleaning, food, and cosmetic applications, important examples of the first type also include firefighting, physical and chemical separation processes, froth flotation, isolation and cleanup of toxic spills, application of dyes to textiles, and enhancing oil recovery. Examples of the undesirable generation of foams abound in the paper, paint, textile, leather, adhesive, and polymer industries as well as in waste water treatment and in polluted natural waters. In all cases, control of foam stability is crucial, but is only imperfectly achieved through trial and error; the fundamental understanding which we seek may lead to improved means of preserving, destroying, and inhibiting foams as needed. For applications involving special purpose foams, control of material properties is also currently achieved through trial and error; the fundamental understanding of foam rheology we seek may provide rational guidance for improved foam materials. In addition, the experimental techniques developed in our work should prove useful for monitoring foams and foam processing, and can be applied to a wide variety of other multiple light scattering materials such as colloids, emulsions, and biological tissues.

RESEARCH APPROACH

The lack of fundamental quantitative understanding of foam stability and rheology is due in part to the inherent complexity of the phenomena and is exacerbated by experimental difficulties which follow from the unavoidably large density and refractive index mismatches of the liquid and gas components of foam. The difficulty caused by the density mismatch is that the gravitational drainage of liquid from in between gas bubbles is rapid and cannot be prevented on earth. The difficulty caused by the refractive index mismatch is that incident light strongly scatters from the bubble interfaces; this unavoidably restricts optical imaging of foam structure to surface behavior, thereby making bulk properties inaccessible. As described below, we have formulated an experimental approach which can overcome both difficulties and should yield rapid progress in elucidating the origin of foam stability and rheology in terms of their underlying structure and dynamics.

306

Multiple Light Scattering

My experimental approach centers on the use and development of quantitative probes of structure and dynamics which actually take advantage of the generic multiple light scattering character of foams, namely static transmission (ST) and diffusing-wave spectroscopy (DWS) [4]. With ST, the fraction of incident light which is transmitted is measured and analyzed within a diffusion theory for the value of the transport mean free path of light. This general technique gives information about the density and spatial arrangement of scattering sites, which, for a foam, are the bubble interfaces. I have previously shown how such measurements give information on the average bubble size [5], but I also expect that information on the bubble shapes and average separation may also be extracted (such efforts are in progress, but will not be further discussed in this report). With DWS, intensity fluctuations in a speckle pattern are measured and analyzed within a diffusion theory for the average motion, or dynamics, of the scattering sites. I have previously shown how such measurements give information on the rate of T1 rearrangements, as shown in Fig. 3, in a coarsening foam [5].

An important feature of ST and DWS is that they are noninvasive measurements and can therefore be used to study stability issues directly in terms of the time evolution of structural parameters [6]. Furthermore, they can be performed simultaneously with stress-strain measurements in a custom-designed glass-walled rheometers; this will permit unprecedented and direct study of the interplay between structure, dynamics, and rheology.

The Need for Prolonged Microgravity Conditions

While ground-based multiple light scattering and rheology measurements can be performed, they are restricted to foams for which the rate of drainage, while never zero, is negligibly small; in practice this limits attention to relatively dry foams with small average bubble sizes. This is especially unfortunate because a key parameter affecting the behavior of foams is their liquid-to-gas volume fraction: for dry foams, the bubble shapes are nearly polyhedral and their tight packing gives rise to shear elasticity; for wetter foams, the bubbles become increasingly spherical and the shear rigidity ultimately vanishes when the bubbles are no longer closely packed. The rate of coarsening and gravitational drainage also depend on the liquid content: wetter foams coarsen more slowly and drain more rapidly. Near the rigidity loss transition, drainage becomes so rapid that the 'foam' is a seething froth of bubbles which quickly ceases to exist; this is unavoidable since liquid and gas cannot be density matched. On earth, it is not possible to experimentally study the dependence of foam structure, rheology, and stability on liquid content without interference from gravity. Microgravity conditions are critically needed in order to systematically measure a sequence of foams with increasing liquid content, especially for wet foams and near the rigidity loss transition.

RECENT SCIENCE RESULTS

In the current funding period we have made important progress both in terms of the development of multiple light scattering techniques and their application to a model foam system. As for the former, analysis of multiple light scattering data crucially assumes that photon propagation can be described by a diffusion approximation with source and boundary terms set by a phenomenological penetration depth and extrapolation length, respectively. While the accuracy of this approach can in principle be no greater than about 1%, far greater errors are introduced in practice due to inappropriate treatment of source and boundary terms. I have determined how to average over the penetration depth [7], and how to experimentally deduce the extrapolation length [8]. My objective, which is now nearly achieved, is to put ST and DWS theories on firmer theoretical ground and advance the reproducibility and accuracy of their application down from the 10% level to the 1% level. This is crucial if ST and DWS are to be truly quantitative probes of foam structure and dynamics. In addition, I have introduced a new optical configuration for DWS experiments which provides for significantly better photon-counting statistics and is less susceptible to systematic errors from imperfect laser beam conditioning.

To move towards our goal of simultaneous light scattering and rheology measurements, graduate student Anthony Gopal and I have recently completed a series of experiments on the response of foam dynamics to shear deformations in a sample cell consisting of two parallel glass plates, one of which can be translated at uniform velocity in order to shear the foam. The normalized electric field autocorrelation function is found to decay nearly exponentially with time. The value of the cumulant is set by the ratio of sample cell thickness to the transport mean free path of light and the rate τ_o^{-1} of rearrangement events: $\Gamma \cong (L/\ell^*)^2 \tau_o^{-1}$. Figure 4 shows how the rate

of rearrangement varies with the applied shear strain rate, $\dot{\gamma}$. If $\dot{\gamma}$ is small compared to the rate τ_{oo}^{-1} of rearrangements in the quiescent foam, then the measured rate is unchanged. If it is larger, however, the rearrangement event rate increases and appears to be equal to the shear strain rate. At still higher strain rates, the shape of the correlation function begins to change and it appears that the foam is beginning to melt; in this regime, the duration of rearrangement events may be the significant time scale [9].

Following the cessation of an imposed shear strain, we have also measured intensity fluctuations and find that the rate of rearrangements decreases if the total shear strain suffered is greater than about 5%, as shown in Figure 5. For strains greater than on the order of one, we find that the rate of rearrangement decreases by a factor of roughly two and remains depressed until the foam coarsens significantly. This implies that there are important correlations between neighboring bubbles which result from the coarsening process and that this self-organized structure is naturally marginally stable.

RESEARCH PLANS

In brief, our plans for ground-based research on the connection between foam dynamics and rheology are as follows. We first intend to construct an all-glass Couette cell in which a foam sample can be sheared at higher rates and for longer periods of time. We should then be able to reproduce and extend our recent work, and also begin to explore other foam systems. At the same time we would like to commence stress-strain measurements using a commercial rheometer in order to gain the necessary experience to convert our Couette cell into an instrument for simultaneous light scattering and rheology measurements. Such an instrument would allow us to explore both rheology and stability issues on the widest range of foams possible on earth, and would also serve as a prototype for the ultimate flight experiments in which the volume fraction of liquid is to be varied through the rigidity loss transition.

CONCLUSIONS

Foams are familiar and important materials which remain of basic scientific interest due to lack of microscopic understanding of their fascinating and unusual properties. We have formulated, and are now implementing, a comprehensive research program which will overcome traditional experimental difficulties and serve to elucidate the fundamental interrelationships between foam composition, structure, dynamics, stability, and rheology. Rapid progress is now being made in the ground-based component of our approach in which new multiple light scattering techniques are developed and used to noninvasively probe foam structure and dynamics. The second key component to our approach will be the use of microgravity conditions in order to examine sequences of foams with fixed composition and topology but increasing liquid content. The need for microgravity is clear and compelling: It is crucial to vary the liquid content towards the rigidity loss transition, however this cannot be done on earth due to the intrinsic density mismatch of the liquid and vapor portions of foam and the rapidly increasing rate of drainage on earth as the transition is approached.

REFERENCES

[1] A. J. Wilson, Ed., *Foams: Physics, Chemistry, and Structure* (Springer-Verlag, New York, 1989).
[2] D. J. Durian and D. A. Weitz, in *Kirk-Othmer Encyclopedia of Chemical Technology* J. I. Kroschwitz, Ed. (Wiley, New York, 1994).
[3] A. M. Kraynik, J. Fluid Mech. 20, 325 (1988).
[4] D. J. Pine, D. A. Weitz, J. X. Zhu and E. Herbolzheimer, J. Phys. (Paris) 51, 2101 (1990).
[5] D. J. Durian, D. A. Weitz and D. J. Pine, Science 252, 686 (1991).
[6] D. J. Durian, D. A. Weitz and D. J. Pine, Phys. Rev. A 44, R7902 (1991).
[7] D. J. Durian, "Penetration depth for diffusing-wave spectroscopy", preprint (1994).
[8] D. J. Durian, "Influence of boundary reflection and refraction on diffusive photon transport", to appear in Phys. Rev. E (August 1994).
[9] S.S. Park and D.J. Durian, Phys. Rev. Lett. 72, 3347 (1994).
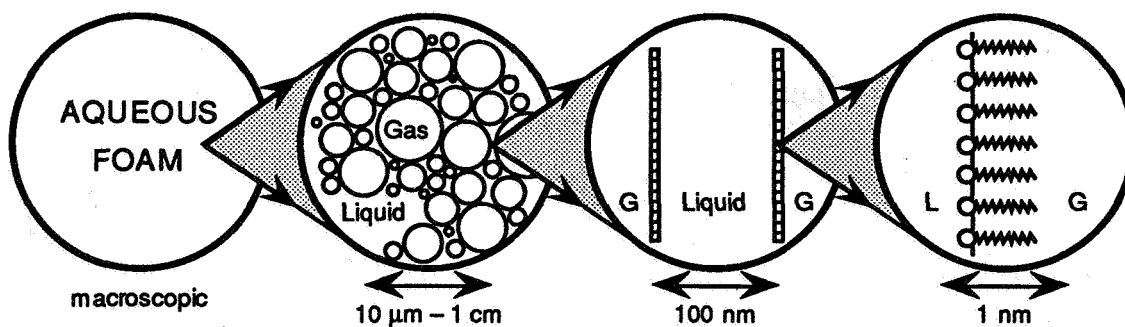
Fig. 1 – Hierarchy of structure and self-organization in an aqueous foam. Large gas bubbles are separated by thin liquid films which are stabilized against rupture by physical-chemical effects arising from the presence of adsorbed surfactants.
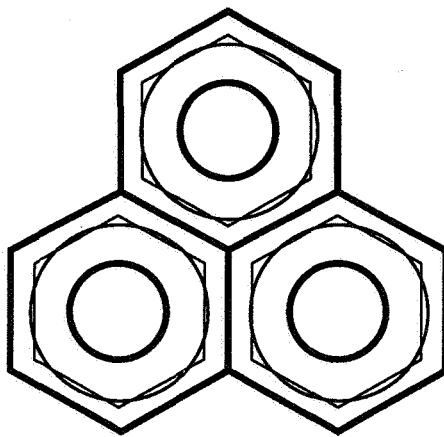
Fig. 2 – Influence of liquid content and physical-chemical effects on the shape of gas bubbles in a foam. In wet foams the bubbles are well-separated and nearly spherical, while in dry foams the bubbles are polyhedral; this is indicated by the heavy lines. For foams with fixed, nonzero, liquid content, however, the bubble shape can also vary in response to the competition between surface tension and repulsive interfacial forces; this is depicted by the light lines.
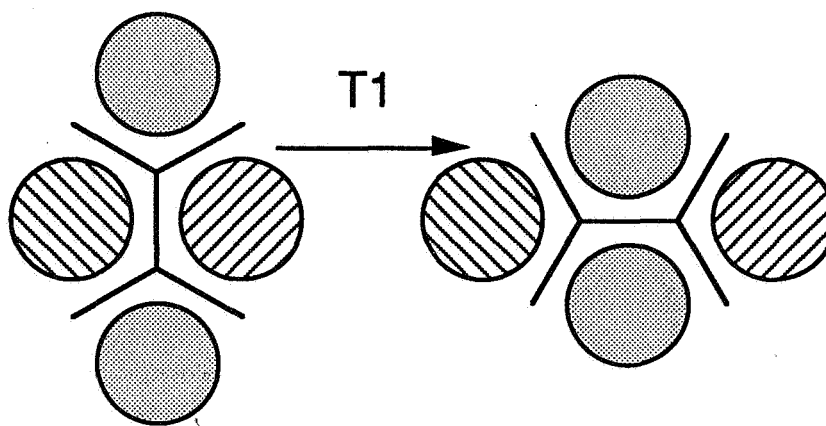
Fig. 3 – Schematic depiction of the T1 neighbor-swapping topology change; note that the number of bubbles and their relative sizes are unaffected by such rearrangements.
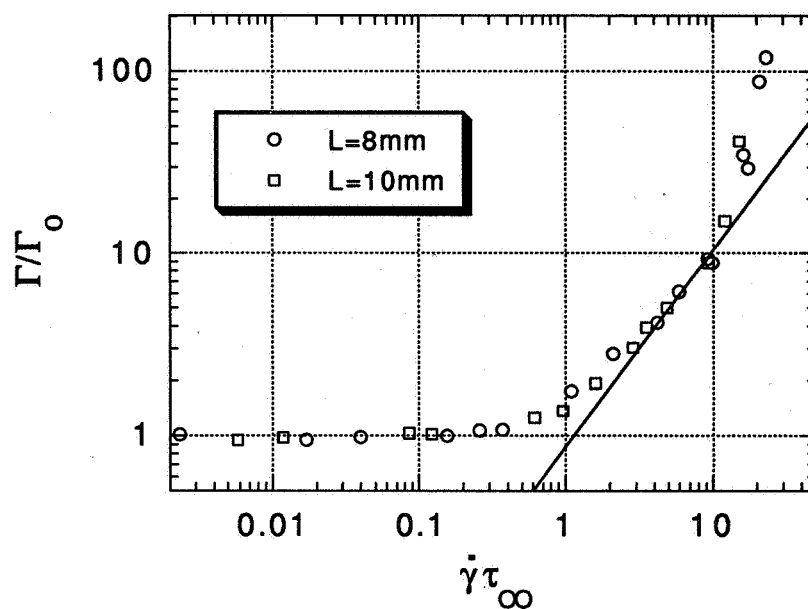
Fig. 4 – The rate of topological rearrangements vs the shear strain rate as measured by DWS.
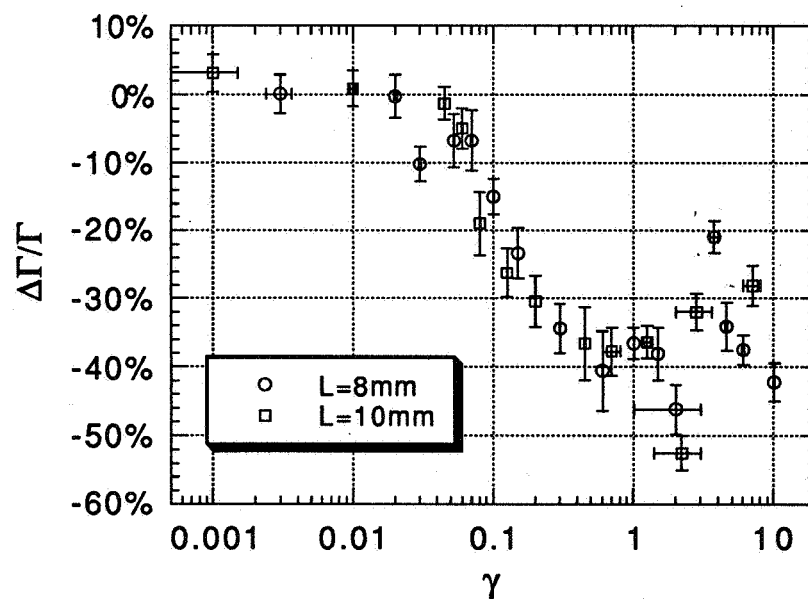
Fig. 5 – The change in rate of rearrangements following a step-strain as measured by DWS.

THE EXTENSIONAL RHEOLOGY OF NON-NEWTONIAN MATERIALS

Stephen H. Spiegelberg, Samuel Gaudet, and Gareth H. McKinley

Division of Applied Sciences
Harvard University
Cambridge, MA 02138

ABSTRACT

It has been proposed to measure the extensional viscosity function of a non-Newtonian polymer solution in a reduced gravity environment as part of the Advanced Fluid Module. In ground-based extensional measurements, the no-slip boundary condition at solid-fluid interfaces always results in appreciable shear gradients in the test fluid; however the removal of gravitational body forces permits controlled extensional deformation of containerless test samples and the first unambiguous measurements of this kind. Imperative to successful implementation of this experiment is the generation and subsequent deformation of a stable cylindrical column of test fluid. A study of the generation and deformation of liquid bridges demonstrates that Newtonian liquid bridges undergo capillary breakup as anticipated when stretched beyond a critical aspect ratio; non-Newtonian liquid bridges, however, are stabilized by the strain-hardening phenomenon exhibited by these materials. Numerical simulations of Newtonian breakup are compared with experimental results, and show that previous ground-based attempts at measuring the extensional viscosity of Newtonian fluids are of limited accuracy.

INTRODUCTION

The prevalence of extensional flows in common polymer-processing operations such as extrusion, blow-molding and fiber-spinning has motivated the investigation of the rheological properties of non-Newtonian fluids under idealized extensional flow conditions. Unlike Newtonian fluids, these materials cannot be characterized by a single material parameter such as the Newtonian viscosity μ, and the non-linear response must be characterized over a wide range of carefully-controlled deformations. A rigorous continuum mechanical consideration of the displacement gradients in a viscoelastic material shows that all possible deformations can be represented in terms of the invariants I_1 and I_2 of the finite finger strain tensor [1]. In this parameter space it is found that the strain invariants for homogeneous shear-free deformations do not intersect with those of simple-shear deformations for any non-zero deformation rates. The rheological functions that relate shear-free deformations to stresses in the fluid are therefore fundamental material properties of a non-Newtonian fluid and need to be measured independently from the viscometric shear-flow functions $\eta(\dot{\gamma})$, $\Psi_1(\dot{\gamma})$, and $\Psi_2(\dot{\gamma})$, which represent the shear viscosity, and the first and second normal stress components of the fluid.

The uniaxial extensional stress growth material function $\overline{\eta}^+$, or the *transient extensional viscosity*, is defined as

$$\tau_{zz}(t) - \tau_{rr}(t) = \overline{\eta}^+ (t, \dot{\varepsilon}_0)\dot{\varepsilon}_0 \tag{1}$$

where $\tau_{zz}(t) - \tau_{rr}(t)$ is the time-varying normal or tensile stress difference, and $\dot{\varepsilon}_0$ is the constant imposed extensional strain rate. In the limit $t \rightarrow \infty$, the transient extensional viscosity approaches the steady state value $\overline{\eta}(\dot{\varepsilon})$. To achieve a homogeneous shear-free flow, all off-axis velocity gradient must be zero and the fluid elements must be elongated along the z-axis such that the rate of strain is independent of position. The velocity field for such a deformation may be represented in a general form as [1];

$$v_r = -\tfrac{1}{2}\dot{\varepsilon}_0 r \qquad v_\theta = 0 \qquad v_z = \dot{\varepsilon}_0 z \tag{2}$$

and the Lagrangian separation $L(t)$ of two neighboring fluid points initially separated by a distance L_0 is given by

$$L(t) = L_0 e^{\dot{\varepsilon}_0 t} \tag{3}$$

Numerous experimental configurations have been devised to realize such kinematics and measure the resulting dynamic properties that characterize the extensional material functions of complex fluids (see Gupta and Sridhar [2]

and Meissner [3] for details). All the configurations considered to date have a fundamental physical constraint – the need for a solid container that holds the test fluid in a given position or geometric shape under the action of an external gravitational body force. The frictional boundary conditions that applies along all contact points of a liquid-solid interface results in large shearing forces that mask any extensional response of the fluid. This constraint will be almost entirely absent in a microgravity environment.

Removal of gravitational body forces will greatly simplify the measurement of the response of a complex fluid to a uniaxial extensional deformation. The experiment reduces to three fundamental steps: *(i)* generation of a column of test liquid; *(ii)* imposition of the deformation kinematics specified in equation (2); and *(iii)* measurement of the tensile stress difference in the elongating fluid column. The transient extensional viscosity may then be computed from equation (1).

In this paper we present results from the first phase of this project, namely the generation and controlled deformation of a fluid column in the absence of container boundaries. We present an experimental ground-based study of liquid bridge stability, and compare the results to numerical simulation. The results show that strain-hardening significantly stabilizes non-Newtonian liquid bridges against capillary breakup.

EXPERIMENTAL

Test fluid

Two viscous test fluids have been examined in this study. The first is a non-Newtonian test fluid composed of 0.31% polyisobutylene ($Mw \approx 1.7 \times 10^6$ g/mole, polydispersity index ≈ 1.9) dissolved in low molecular weight Newtonian solvent of hydrogenated polybutene. This semi-dilute polymer solution falls into a class of fluids termed *Boger fluids*, which exhibit a nearly constant shear viscosity over several decades of shear rate, yet are highly elastic [4]. The second fluid used in the study consists simply of the Newtonian solvent (polybutene) as a reference standard. The density of both fluids is $\rho = 0.894$ g/ml as determined *via* hydrometry. The zero shear viscometric data for the two fluids, as determined from cone & plate rheometry with a Rheometrics Mechanical Spectrometer RMS-800 are shown in Table 1 at a reference temperature of 25°C.

Apparatus

Figure 1 shows a schematic diagram of the device used to generate the liquid bridges. The test fluid is charged into the cavity (1) created when the acrylic sleeve is restored to the closed position (*i.e.* slid to the right in Figure 1). The liquid bridge is formed *via* positive displacement as the sleeve is slowly withdrawn to the left. In the current configuration, liquid bridges with a diameter of $D_0 = 2R_0 = 3.80$ cm may be generated. The moveable piston (2) allows the formation of bridges of varying length (corresponding to dimensionless aspect ratios from $L/D \equiv \Lambda = 0$ to 3.3), as well as the elongation of a previously-generated bridge. The piston drive shaft is connected to a DC servomotor driven by a computer controlled motion controller. Figures 2*a* and *b* show typical examples of a liquid bridge before and after an elongational deformation.

All of the ground-based experiments have been carried out in a *Plateau Tank* [5] consisting of a constant temperature bath filled with an immiscible fluid that is carefully density-matched to the test fluid, in effect creating a microgravity environment. For this experiment, the neutral density fluid (NDF) was composed of approximately 60% 1-propanol ($\rho = 0.806$ g/ml) and 40% water. The maximum Bond Number for this system, defined as the ratio of buoyancy forces to surface tension forces, was approximately $Bo = \Delta \rho g R_0^2 / \sigma \approx 0.1$.

In addition to the Bond number, the dynamic properties governing the extensional deformation of the liquid bridge may be characterized by several dimensionless groups, namely the *Capillary number* (ratio of viscous stresses/interfacial stresses), the *Reynolds Number* (ratio of inertial stresses/viscous stresses), and the *Deborah Number* (time scale of fluid/time scale of deformation). These terms are defined as:

$$Bo = \Delta \rho g R_0^2 / \sigma \qquad Re = \rho R_0 U_P / \eta_0$$
$$Ca = \eta_0 U_P / \sigma \qquad De = \lambda_1 \dot{\varepsilon}_0 \qquad (3)$$

where R_0 is the column radius, U_P is the characteristic velocity imposed by the piston; ρ, σ and η are the test fluid density, surface tension and viscosity respectively, λ_1 is a characteristic relaxation time of the non-Newtonian fluid, and the characteristic stretch rate experienced by the fluid is $\dot{\varepsilon}_0$.

To date, only a linear stretch history has been imposed in the experimental section of this work; *i.e.* the sample length $L(t)$ increases linearly with time; the characteristic stretch rate $\dot{\varepsilon}_0 \sim U_p/L(t)$ thus decreases during the deformation. In the numerical simulations, however, both a linear and an exponential stretch history have been examined. In the latter case, the piston velocity is ($U_p = \dot{\varepsilon}_0 Z_p$) and the length increases in time as $L = L_0 \exp(+\dot{\varepsilon}t)$ This deformation history produces a constant extension rate everywhere in the sample, if the sample remains cylindrical.

Calculations

In a previous paper we have described the implementation of the boundary integral method to investigate the dynamic evolution of deforming liquid filaments and the breakup of viscous (low Reynolds number) Newtonian fluid columns stretched beyond a critical aspect ratio [6]. The fluid motion is characterized by the capillary number, the initial and final aspect ratios (Λ_0, Λ_f) of the column, and the viscosity ratio of the fluid column (μ_2) compared to the outer fluid bath (μ_1).

RESULTS AND DISCUSSION

Newtonian and non-Newtonian liquid bridges have been subjected to identical deformation histories to assess the effects of extensional hardening on bridge stability. Liquid bridges with an initial aspect ratio of $\Lambda_0 = 0.87$ and a dimensionless volume $\mathcal{V} \equiv V_0/\pi R_0^2 L = 1$ were stretched to a final aspect ratio of 2.00 at a constant velocity of $U_p = 0.13$ mm/s corresponding to a capillary number of $Ca = 0.19$. Since the deformation rate varies throughout the test, the Deborah number decreases from 0.011- 0.006.

Figure 3 shows photographs of the evolution of the liquid bridge interfaces as of a function of time for the two test fluids. The photographs labeled as '0 minutes' correspond to the bridge immediately after cessation of the steady stretch; during the ensuing pictures, the bridges experiences no additional stretching but continue to evolve towards their final static equilibrium configuration. During the initial deformation, the fluid column adopts a concave cylindrical configuration, due to the fixed volume of fluid and the pinning condition experienced at the endplates. After 15 minutes, both bridges have relaxed to a surface energy–minimizing unduloid configuration. The non-Newtonian fluid retained this shape for the remainder of the experiment, up to times of 20 hours. Longer periods of μg are difficult to maintain due to evaporation and thermal gradients in the Plateau tank. The Newtonian fluid, however, experienced continual constriction in the center of the bridge; this constriction accelerates over the course of the experiment, and eventually results in bridge break-up after 173 minutes.

This hydrodynamic instability was first discussed for inviscid fluids by Lord Rayleigh [7], who predicted using surface energy arguments that cylindrical fluid filaments with $\Lambda > \pi$ were susceptible to random sinusoidal perturbations that acted to reduce the surface area of the cylinder; runaway capillary breakup ensued. Gillette and Dyson [8] extended this analysis to non-cylindrical bridges constrained between equal circular plates, and presented a stability envelope for constricted bridges, in terms of dimensionless sample volume $\mathcal{V}$ vs. aspect ratio Λ. The bridges shown in Figure 3 correspond to loci initially in the stable region of this stability diagram, which were subsequently stretched along a hyperbolic path $\mathcal{V}\Lambda = constant$ into the unstable region.

In the constricted region of the bridge, capillary pressure increases as the radius of curvature decreases. This increased pressure drives fluid out of the neck region into the lower pressure areas near the endplates, and therefore reduces the radius in the constricted region even more. The process accelerates as the radius of curvature decreases, eventually resulting in sample failure. It is clear that the stability of the non-Newtonian fluid bridge is not governed by identical arguments, since the bridge remained intact despite the fact that purely from energetic considerations of fluid statics it was also deformed beyond the Gillette & Dyson stability locus. The non-Newtonian strain hardening nature of the Boger fluid leads to this restabilization of the liquid bridge; the transfer of fluid from the constricted region of high pressure to lower pressure regions results in a uniaxial extensional flow. Under such conditions a Newtonian fluid has a steady extensional viscosity of $\bar{\eta} = 3\mu$ [9]; however, measurements for non-Newtonian fluids indicate that the viscosity will rise by 3 or more orders of magnitude [10]. This rise in viscosity effectively retards the flow of fluid, and thus stabilizes the liquid bridge from any further constriction.

Numerical calculations described elsewhere [6] were utilized to simulate the experimentally-observed breakup of the Newtonian liquid bridge following imposition of an identical deformation to that described above. The narrowest radius of the bridge in the middle of the constricted region (R_{mid}) is shown in Figure 4 as a function of dimensionless time. The initial rapid decrease in radius occurs during the imposed extensional deformation of the

313

bridge up to a dimensionless time given by $\sigma t/\mu R_0 \sim 1$. Capillary forces progressively reduce the radius in the remainder of the experiment. It can be seen that the results from the simulation correlate remarkably well with the experimental results; deviations are seen only at the end of the experiment when the length scale of the filament becomes small. Under such conditions, the experimental error increases and the numerical method also becomes increasingly inaccurate.

Having validated the accuracy of the boundary element method, additional numerical calculations have been performed to investigate the behavior of a Newtonian liquid bridge under an *exponential* imposed deformation. Such tests have been proposed as a method for measuring the extensional viscosity of viscous fluids [10, 11]. Measurement of the net traction force on the endplate (after a correction for the contribution of surface tension forces) yields an estimate of the extensional viscosity of the fluid. In Figure 5(a) we show the axial free-surface profile $R(z)$ and axisymmetric velocity field in an elongating liquid bridge with initial aspect ratio $\Lambda_0 = 0.6$ after a dimensionless strain of 2. It is clear from these calculations that the velocity field is not an homogeneous uniaxial elongation because of the three-phase contact line that pins the fluid interface to the edge of the piston. At large strains this deformation becomes increasingly important and in Fig. 5(b) we show an expanded view of the weak flow near the stationary left-hand piston indicating that a *flow reversal* can develop. This recirculation reverses the sign of the viscous contribution to the traction force exerted on the end plate, and results in substantial deviation of the calculated transient Trouton ratio $T_R = \bar{\eta}^+(\dot{\varepsilon}_0, t)/\mu$ from the predicted value of $T_R \equiv 3$ for a Newtonian fluid. Similar calculations for non-Newtonian liquid bridges are currently underway.

CONCLUSIONS

We have presented measurements and simulations of the stability of both Newtonian and non-Newtonian fluids in a reduced gravity environment. Newtonian bridges experience immediate breakup when stretched beyond a critical aspect ratio and undergo capillary breakup in good agreement with the predictions of classical energetic stability arguments and boundary element calculations. Non-Newtonian fluid bridges with similar shear viscosities exposed to identical stretching histories did not breakup, but rather were stabilized by the strain-hardening extensional viscosity exhibited by these materials. It is clear that selection of an initial aspect ratio will be critical when performing extensional flow measurements in the Newtonian case to ensure an initially stable column. This research represents a preliminary ground-based investigation forming part of the Science Requirement Document (SRD) submitted to NASA for a proposed microgravity flight experiment to measure the extensional viscosity of non-Newtonian polymer solutions.

ACKNOWLEDGEMENTS

REFERENCES

(1)   Petrie, C. J. S. *Elongational Flows: Aspects of the Behavior of Model Viscoelastic Fluids*; Pitman: London, 1979; Vol. 29.
(2)   Gupta, R. K.; Sridhar, T. In *Rheological Measurement*; ed.; A. A. Collyer and D. W. Clegg, Ed.; Elsevier Applied Science: London, 1988; pp 211-245.
(3)   Meissner, J. *Chem. Eng. Commun.*, 33, 159-180, (1985).
(4)   Boger, D. V. *J. Non-Newtonian Fluid Mech.*, 3, 87-91, (1977/78).
(5)   Plateau, J. A. F. In *Ann Rep. Smithsonian Institution*1863; pp 207-285.
(6)   Gaudet, S.; McKinley, G. H.; Stone, H. A. In *AIAA, 32nd Aerospace Sciences*; Reno, NV, 1994; p 1.
(7)   Rayleigh, L. *Proc. Lond. Math. Soc.*, 10, 4-13, (1879).
(8)   Gillette, R. D.; Dyson, D. C. *Chem. Eng. J.*, 2, 44-54, (1971).
(9)   Trouton, F. T. *Proc. Roy. Soc.*, A77, 426, (1906).
(10)   Tirtaatmadja, V.; Sridhar, T. *J. Rheol.*, 37, 1081, (1993).
(11)   Sridhar, T., Tirtaatmadja, V., Nguyen, D.A. and Gupta, R.K., *J. Non-Newtonian Fluid Mech.*, 40, (1991), 271-280.

Table 1:   Physical properties of 0.31 wt.% PIB/PB Boger fluid at $T_0 = 25°C$.

Viscometric Properties	η_0 [Pa.s]	47.2
	η_s [Pa.s]	43.2
	Ψ_{10} [Pa.s^2]	20.3
	Ψ_2 [Pa.s^2]	0
Bulk Properties	ρ [kg/m^3]	894
	σ [N/m]	3.0×10^{-3}
Oldroyd-B Model Parameters	λ_1 [s]	2.54
	β	0.92
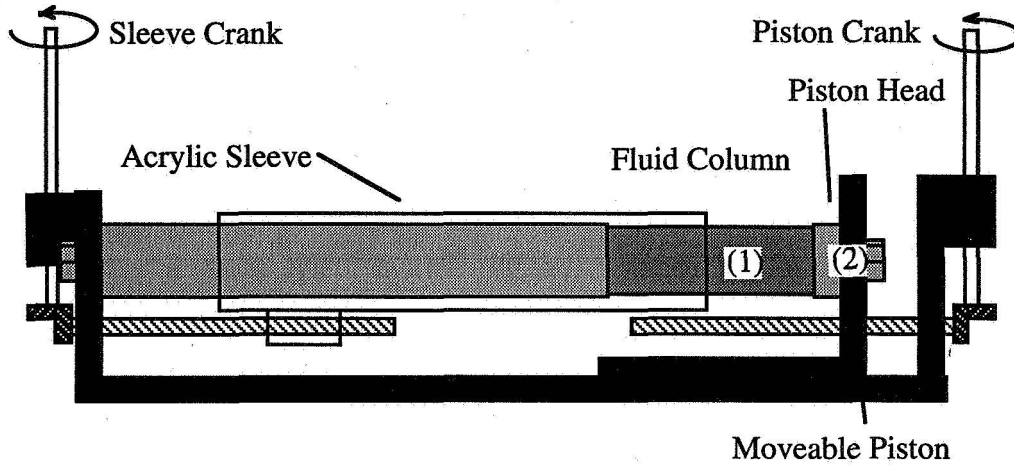
Figure 1:   Device for generation of liquid bridges. Fluid is charged into cavity created by acrylic sleeve, which is then withdrawn to expose sleeve to air or fluid interface. Bridge can be stretched with translating piston.
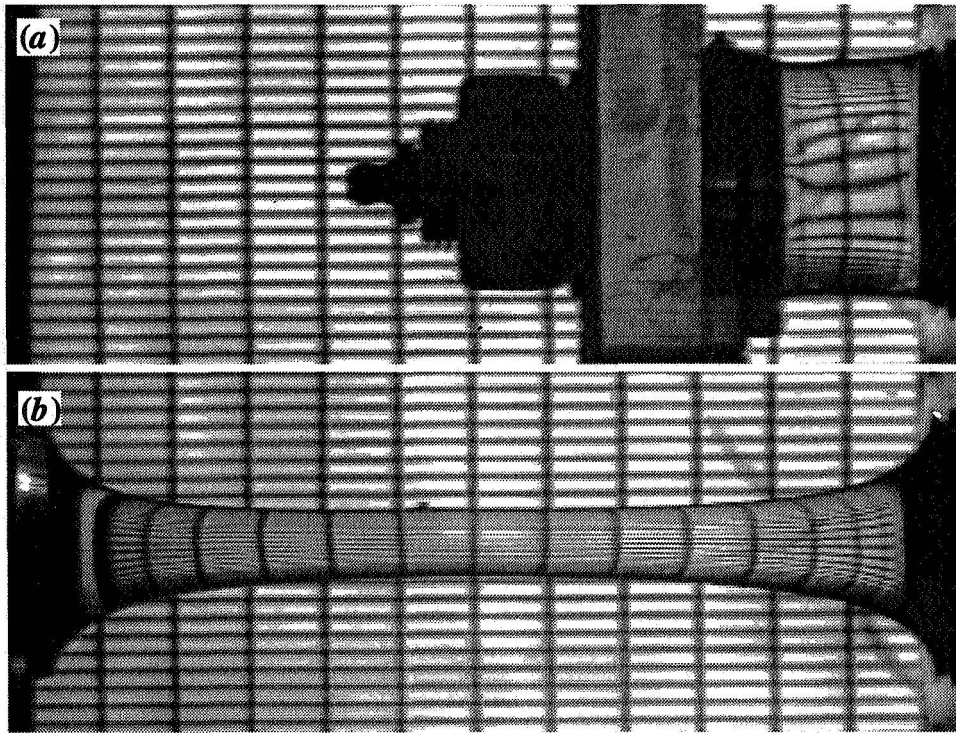
Figure 2:   Non-Newtonian liquid bridge from $\Lambda_0 = 0.46$ to $\Lambda_f = 3.10$ at a constant strain rate of 0.02 s^{-1} corresponding to a De = 0.05, Ca$_{max}$ = 2.9, and Bo = 0.1.

315

Newtonian Fluid

Non-Newtonian Fluid
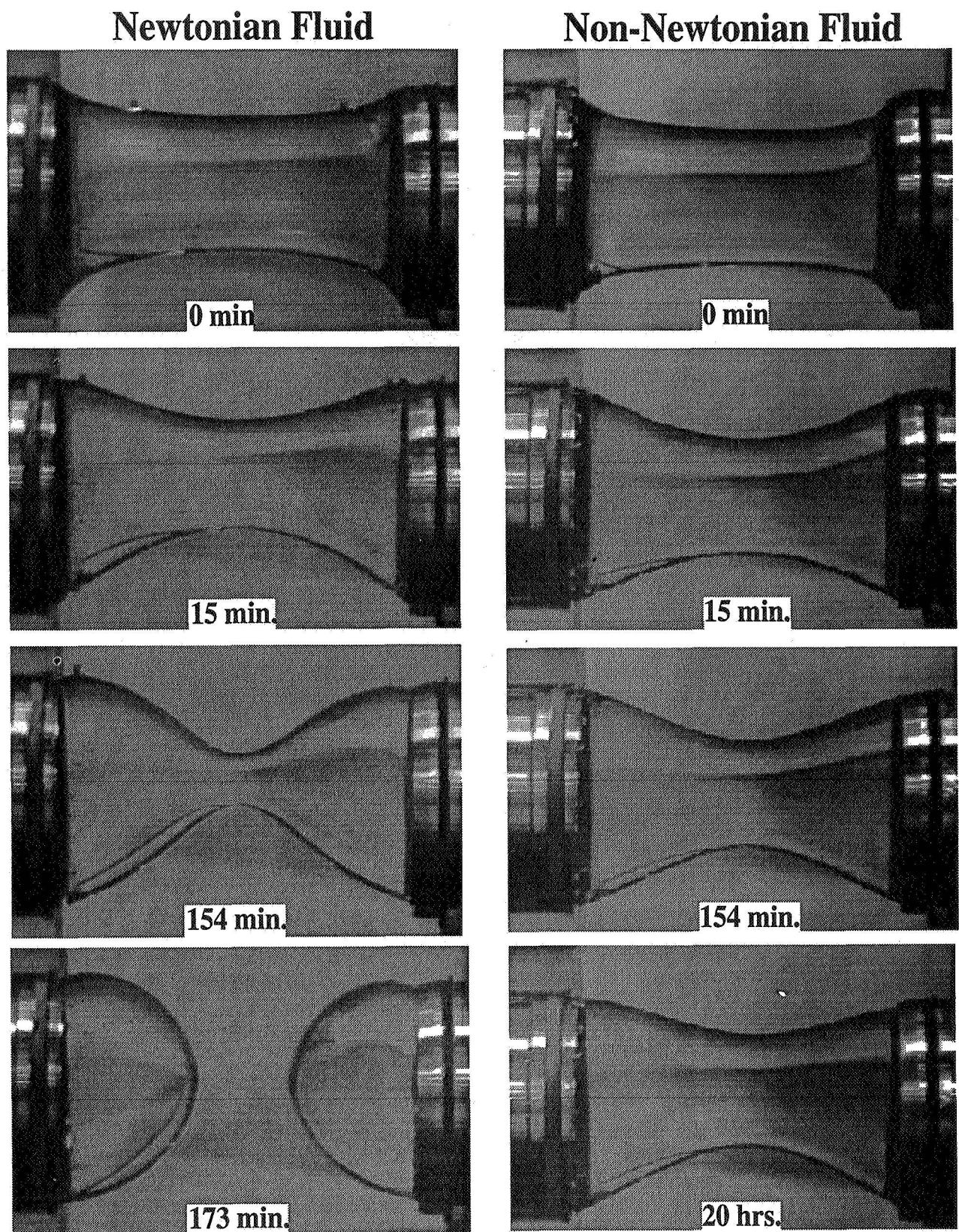
Figure 3:   Liquid bridge stability evolution for Newtonian and non-Newtonian fluids. $\Lambda_0 = 0.87$, $\Lambda_f = 2.00$, Bo = 0.1.

316
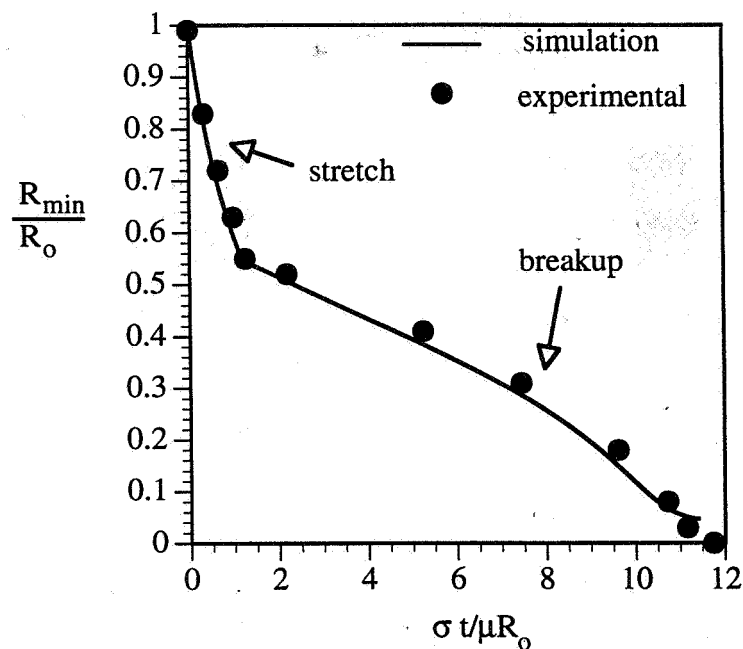
Figure 4: Neck radius of Newtonian liquid bridge as a function of dimensionless time. Radius decreases initially due to bridge stretch, then is further reduced by capillary forces. Bridge was stretched from an initial radius R_0 of 1.9 cm at a rate of 0.013 cm/s, corresponding to a Ca = 0.19. Bo = 0.1.
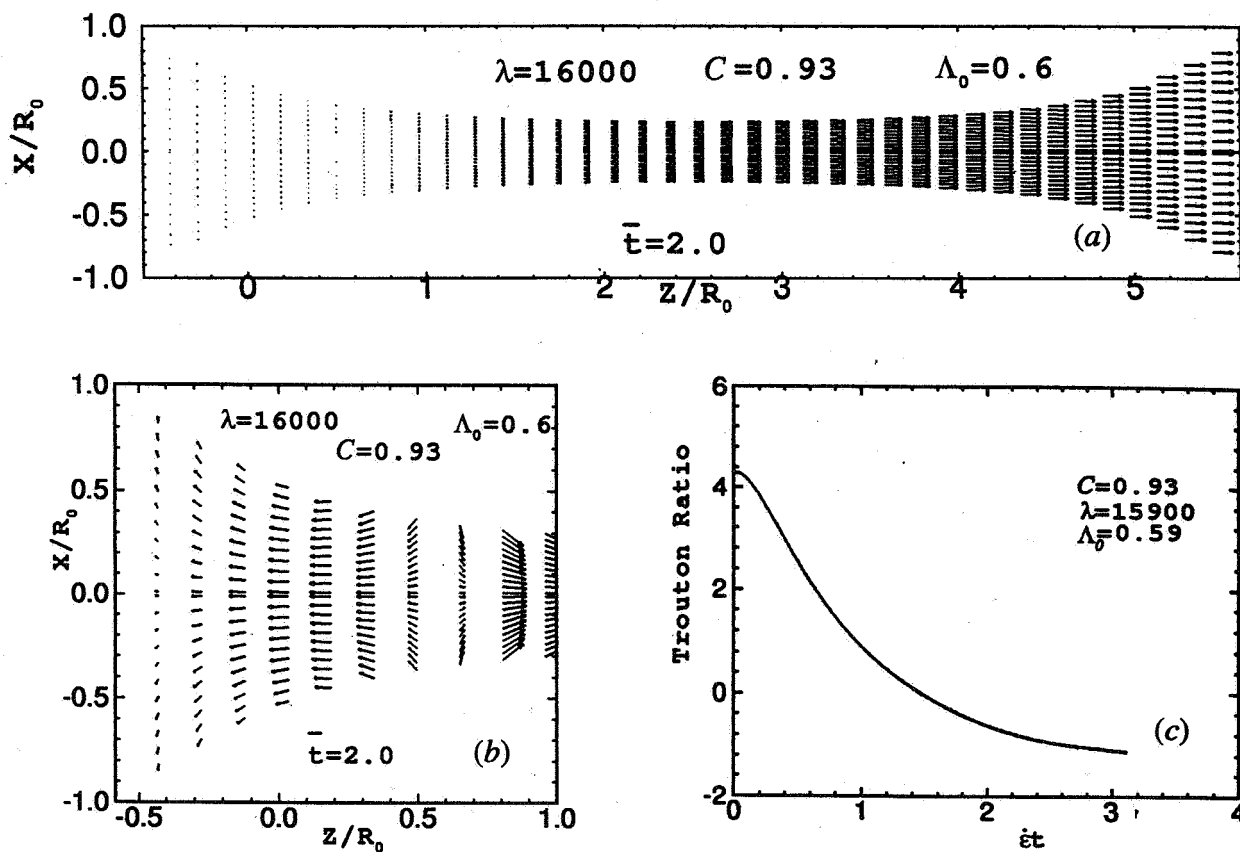
Figure 5: Extensional deformation of a Newtonian liquid bridge; (*a*) Final aspect ratio after a strain of $\dot{\varepsilon}_0 t = 2.0$; (*b*) magnification of flow reversal near stationary end plate ; (*c*) calculated Trouton ratio $\bar{\eta}(\dot{\varepsilon}_0, t)/\mu$.

NUCLEATION AND CHIRAL SYMMETRY BREAKING UNDER CONTROLLED HYDRODYNAMIC FLOWS

Xiao-lun Wu, Brian Martin and Arnold Tharrington
Department of Physics and Astronomy
University of Pittsburgh
Pittsburgh, PA 15260

ABSTRACT

The effects of hydrodynamic convection on nucleation and broken chiral symmetry have been investigated for a simple inorganic molecule, sodium chlorate ($NaClO_3$). Our experiment suggests that the symmetry breaking is a result of hydrodynamic amplification of rare nucleation events. The effect is more pronounced when the primary nucleation occurs on the solute-vapor interface, where mixing in the surface sublayer becomes important. The transition from the achiral to the chiral states appears to be smooth as the hydrodynamic parameters, such as flow rate, are varied.

INTRODUCTION

Mirror symmetry is often absent in nature; the universe is asymmetric at all levels, from the subatomic to the macroscopic. Famous examples include the handedness of nucleic acids, DNA and RNA, and the spontaneous broken rotational symmetry of nematic-isotropic phase transitions in liquid crystals. In this paper we present a classical nucleation experiment in which the chiral symmetry breaking is triggered by rarity surface nucleation and promoted by hydrodynamic convection.

It is known that the individual sodium chlorate ($NaClO_3$) molecule is symmetric (achiral), but its crystal form shows distinctive optical activity [1]. If a solution of $NaClO_3$ is left undisturbed, a small number of crystals slowly form as the solvent, water in this case, evaporates. If these crystals are examined under crossed polarizers, one finds that about half are left-handed and the other half are right-handed. Equal percentage of the two species indicates that the energy barrier for the nucleation is the same for the different species.

It was found by Kondepudi et al. [2] that under gentle stirring this is no longer true. The crystallization seems to proceed in one direction, favoring either all crystals being left-handed or right-handed for each individual experiment. The optical purity in each sample could be well over 99%. However, if an ensemble of experiments is carried out under identical conditions, one again finds an equal distribution of left-handed and right-handed crystals. This remarkable observation indicates that the system undergoes a transition from a totally symmetric (achiral) state to a totally asymmetric (chiral) state simply by introducing a hydrodynamic flow, without careful control of temperature and other conditions. Kondepudi's experiment touches upon several interesting issues ranging from nucleation, convective diffusion, and autocatalysis, a mechanism believed to be relevant for the symmetry breaking [1,3]. The experiment also raises a number of interesting questions, such as: (1) how do the two vastly different length scales, the size of a primary nucleus ($\sim 10 \overset{\circ}{A}$) and the hydrodynamic length (~ 1 cm), couple; (2) what is the mechanism by which the secondary nuclei proliferate; and (3) how does the sharpness of the transition change as the control parameters, such as the flow rate and the nucleation rate, are varied.

To answer some of these questions, systematic measurements were carried out using two different flow geometries, mechanical stirring and electroconvection. In the mechanical-stirring experiments each sample contains approximately one vortex and the flow is rather chaotic even at low stirring rates. The simple mechanical setup allows mass production of crystals under nearly identical conditions, and good counting-statistics can be achieved. On the other hand, in the electroconvection experiments, large numbers of vortices are generated and the flow characteristics can be tuned continuously. Our experiment suggests that primary nucleations occur predominantly on the solute-vapor interface, giving rise to high optical purity even with a moderate stirring rate. This effect has been overlooked in a previous experiment [2]. Our experiment also suggests that flows with random mixing characteristics, are far more effective in producing chiral symmetry breaking than a laminar shear flow with a comparable Reynolds number.

EXPERIMENTAL

The crystallization experiments were performed using a $NaClO_3$ solution with a weight fraction of 50% [4]. The $NaClO_3$ was first dissolved in distilled water and constantly stirred at room temperature for 8 hours to ensure complete desolution of the solute. The solutions were then filtered through a $0.2\mu m$ filter before usage. The crystal growth was initiated by slow evaporation. At the given concentration, the nucleation occurs approximately 4-6 hours after the samples were prepared, and this time interval appears to be independent of the flow rate. In the experiments the crystals were grown to an average size of ~ 1 mm; this takes approximately a couple of hours for quiescent samples and less than an hour for stirred samples, after the first nucleation event is identified.

Different handed crystals can be distinguished by their optical activity. A right-handed (dextro) crystal will rotate polarized light clockwise while a left-handed (levo) crystal will rotate light counterclockwise. A low-power (12×) microscope with a pair of polarizers allows us to determine the handedness of crystals even when they are as small as 100 μm. Under the transmission with a white light source, the two different crystal species appear blue and brown by slightly "uncrossing" the polarizers a few degrees. Since in some cases thousands of crystals are produced in a single sample, only a representative region of a few hundred crystals are analyzed.

Two different flow geometries were employed in the experiments. In the first experiment, $NaClO_3$ solution (7.5 cc) was placed in a cylindrical dish of 5 cm in diameter. A small Teflon coated magnetic stirring bar (1 cm long and 0.2 cm diameter) was placed in the center of the dish and was driven by a horse-shoe magnet. The stirring bar is light enough to float on the solute-vapor interface, providing effective mixing near the surface sublayer [5]. To improve the statistics, ten such samples were run simultaneously with the horse-shoe magnets connected in tandem, driven by a single DC motor. Flow visualization using a Kalliroscopic fluid indicates there is a great deal of mixing even at a very low stirring rate $\sim 1/30$ Hz.

In the second experiment, flow was produced by electroconvection. In this geometry all the mechanical moving parts are eliminated, allowing better control of the flow characteristics. The flow cell has a dimension of 12×20 cm^2 with a biased ac current flowing along the long dimension of the cell. The electrodes are made of platinum in order to reduce the contamination of the solution. Directly underneath the cell is an array of 400 cylindrical magnets each having a field ~ 0.4 T. The magnets are arranged in a square lattice with alternating poles pointing vertically. When a current passes through a thin layer of $NaClO_3$ solution an array of counter rotating vortices is formed. Depending on the strength of the current, both localized and delocalized vortices can be generated. Since the thickness of the fluid is much smaller, ~ 3 mm, compared with the width of the cell, the flow may be considered as two dimensional.

RESULTS

To ascertain that nucleation behaves normally with no bias, a set of quiescent measurements were carried out, and the results were similar to that found by Kipping and Pope [1], and Kondepudi [2]. In a total of 5395 crystals obtained from ~ 100 crystallizations, 2523 were right handed and 2872 were left handed. The bias towards right-handed crystals, though small ($\sim 6\%$), is statistically significant in that the standard deviation predicted from the bimodal distribution is $\sim 1\%$. We noted that similar bias was also observed in Kondepudi's experiment at the level of $\sim 10\%$. If an order parameter is defined as $O = (n_L - n_R)/(n_L + n_R)$, we can plot the distribution function $P(O)$ for the above hundred runs. Figure 1a shows $P(O)$ for the quiescent samples ($f = 0$ hz) together with a Gaussian distribution (solid line) for comparison. As can be seen, the experimental data are in general agreement with the Gaussian distribution except for large Os, where the difference is quite notable.

Constant Stirring of the solution has a dramatic effect on the overall chirality of the crystals. At stirring rates $f >> 1$ Hz each sample contains either almost all left or right-handed crystals, yielding high optical purity with a great certainty. It is amazing that the ordering process occurs spontaneously in individual cells without much human intervention. Figure 1c shows a typical run with 19 samples at $f = 1$ Hz. Among 19 samples, 7 are right-handed and 12 are left-handed with optical purity in each cells being greater than 95%. As the stirring rate decreases, we found that chiral symmetry is only partially broken in the sense that

a large fraction of samples show no symmetry breaking. Figure 1b shows the distribution for 19 samples at $f = 0.7$ Hz. Among the 19 samples, 2 are right-handed and 1 is left-handed with optical purity again greater than 95%. The other 16 samples show no (or weak) symmetry breaking, and their distribution is clustered near $O = 0$. The general trend seen in the experiment is that as the stirring rate increases from $f = 0$ Hz, the central peak in the distribution decreases in magnitude and its width increases. At the same time two chirally pure states with $O = \pm 1$ gains increasing more weight in the distribution function.

To characterize the order of an assemble of samples by considering $O = +1$ and $O = -1$ to be degenerate, we can define an ensemble averaged order parameter as $< |O| >= \sum_{i=1}^{N} |O_i| N_i / \sum_{i=1}^{N} N_i$, where $|O_i|$ and N_i are the absolute value of the order parameter and the total number of crystals in sample i, and N is the total number of samples. The average is weighted by the number of crystals in each samples, because samples with more crystals are statistically more significant than those with less crystals. In Fig. 2 we plot $< |O| >$ as function of stirring rate for 240 samples spanning f from 0 to 3 Hz. As can be seen, for $f > 2$ Hz the systems are almost completely ordered while for $f < 2$ Hz the systems are only partially ordered. The ordering process as a function of f appears to be smooth. The noise seen in the data is interesting by itself in that it reflects the fact that the distribution function has multiple peaks around $|O| = 0$ and $|O| = 1$ similar to that seen in Fig. 1b. The characteristic frequency $f_c \sim 2$ Hz, separating ordered from partially ordered states, may be interpret as a competition between the rate of nucleation and the rate of convection. In the high stirring rate (convection dominated regime), a single nucleation event apparently suppresses primary nucleation of opposite species and dominates the later evolution of the system. Our experiment may therefore provide an excellent way of measuring the primary nucleation rate.

It should be noted that in the experiments, both with and without stirring, the initial nucleation almost always occurs on the solute-vapor interface. As the crystals grow to a fraction of a millimeter, they fall to the bottom due to gravity. The surface nucleation by itself is not surprising since it is well known that surfaces (and other impuries) can lower the nucleation energy barrier substantially. However, the surface nucleation may explain the efficiency by which the chiral symmetry breaking occurs in the first place. This is because near the surface there is only relatively small volume which needs to be mixed in order to have the transition. This explanation is further enhanced by the observation that if a large crystal, say left handed, is placed in the bottom of the sample and it is not convected by the stirring, the chirality of the system at the later time is not always determined by the crystal we initially put in.

The chiral symmetry breaking experiment has also been carried out in electroconvection cell with different flow characteristics. Shown in Fig. 3 are two pictures that were taken at different driving currents. For low currents, the vortices are localized in space and form a fairly regular lattice. For a high current, however, the vortices become delocalized and the flow is almost turbulent. Our preliminary experiment shows that when the flow is localized (laminar regime), the chiral symmetry is not broken, whereas in the strong flow region the chiral symmetry can be broken with high optical purity. The observation points to the importance of hydrodynamic mixing, rather than local shear, for the broken chiral symmetry. It is apparent that with a comparable Reynolds number, similar to that used in the mechanical stirring experiments, a pure laminar shear flow is not sufficient for bringing about the transition. The nucleation experiment in electroconvection cells is still under way and the results will be reported elsewhere.

INTERPRETATION

To interpret our experimental results, the following mechanisms appear to be relevant: (1) Nucleation is a statistically rare event. Due to a high activation energy for nucleation, $\sim 100 k_B T$, a supersaturated solution can persist for hours before a nucleation event is triggered by thermal fluctuations. Because of such a slow nucleation rate, it is possible that only a single primary nucleation event occurs among $\sim 10^{23}$ molecules. This primary nucleus carries a definitive symmetry, or "genetic" code. (2) Secondary nuclei are generated from a primary nucleus due to hydrodynamic convection. For certain unknown reasons, the secondary nuclei have the same symmetry as the primary one and their number proliferates. (3) There is an interaction between distant parts of the fluid, allowing the "genetic" code to pass into other regions of the fluid. The passage of the information needs to be sufficiently fast covering a large fraction of the sample before another primary nucleation event takes place. It is obvious that hydrodynamic convection which cause mixing will allow for such a long-range interaction.

A possible mechanism by which flow can induce the symmetry breaking is the following: The primary and the secondary nuclei are convected by the flow, causing the depletion layers which surround the nuclei to spread out to the regions where the primary nucleations are *most* likely to take place. Because of supersensitivity of the rate of primary nucleation to the solute concentration, spreading of the depletion zone effectively reduces the chance of primary nucleation for the other species. On the other hand, by eliminating the depletion layer near the surface of a nucleus, the growth of such a crystal is further enhanced. Therefore the system has a built-in positive feedback mechanism which propels the nucleation towards one direction. In this sense the spontaneous chiral symmetry breaking is a result of rare statistical fluctuations and non-local hydrodynamic effects. In our experiment, the primary nucleation sites are predominantly on the free surface of the solution. The volume that needs to be mixed in order to produce chiral symmetry breaking, therefore, is rather small. This accounts for the fact that only moderate stirring is sufficient to bring about the symmetry-breaking transition.

What is not known in our experiment is why the secondary nucleation duplicates the symmetry of the primary nucleus. Important as it is, the secondary nucleation is only known empirically [6]. The effect has been phrased as a chirally autocatalytic process [2,3], in which the incipient nucleus undergoes a series of splittings and gives birth to the next generation of crystals. If the effect is hydrodynamic in nature it is not difficult to show that the incipient nucleus must be very weak with the critical shear stress several orders of magnitude smaller than that of a fully grown crystal. To see this we estimate the stress on a nucleus due to shear, $\sigma = \eta\gamma$, where $\eta(=0.1$ poise) is the shear viscosity of the solution and $\dot{\gamma}$ is the shear rate. In our experiment $\gamma \sim f \sim 1$ hz, we found $\sigma \sim 10^{-1}$ erg/cm^3. This is very small compared to the energy density ϵ of a fully grown crystal, $\epsilon = k_B T \rho \sim 10^{10}$ erg/cm^3 for $\rho \sim 10^{24}$ cm^{-3}. It is clear that an understanding of secondary nucleation requires the investigation of the formation of chiral crystals on microscopic scales, a domain which is beyond the scope of the current experiment.

CONCLUSIONS

Using different flow geometries, we have found that the chiral symmetry breaking correlates strongly with hydrodynamic convections. In particular, random mixing seems to be far more effective in bringing about the transition than a laminar shear flow. The high optical purity obtained with only a gentle stirring is likely to be a result of surface nucleation. Our experiment reveals for the first time the delicate balance between the rate of nucleation and the rate of convection. In the convection dominated regime, the systems self-organize into a chiral state with optical purity $> 95\%$, whereas in the nucleation dominated regime, the system is achiral. The processes studied in the experiment may provide insight into the possible origins of biomolecular chirality and may even lead to the production of chirally pure materials.

REFERENCES

1. F.S. Kipping and W.J. Pope, J. Chem. Soc. Trans. **73**, 606 (1898).

2. D. Kondepudi, R. Kaufman, and N. Singh, *Science* **250**, 975 (1990).

3. G. Metcalfe and J.M. Ottino, Phys. Rev. Lett. **72**, 2875 (1994)

4. The sodium chlorate, NaClO$_3$, was purchased from Fisher Scientific. The chemical is 99.9% pure and was used without further purification.

5. It was found that for a heavy magnetic bar which sinks to the bottom, the stirring can crush small crystals, causing chiral symmetry breaking. We learn this the hard way.

6. A. Randolph and M. Larson, *Theory of Particulate Process*, (Academic Press, San Diego, 1988).

Figure 2. The order parameter vs. stirring rate f. The order parameter increases with f and saturates at high frequencies. Near the transition zone, ~ 1 Hz, the measurements are noisy with anomalous fluctuations.
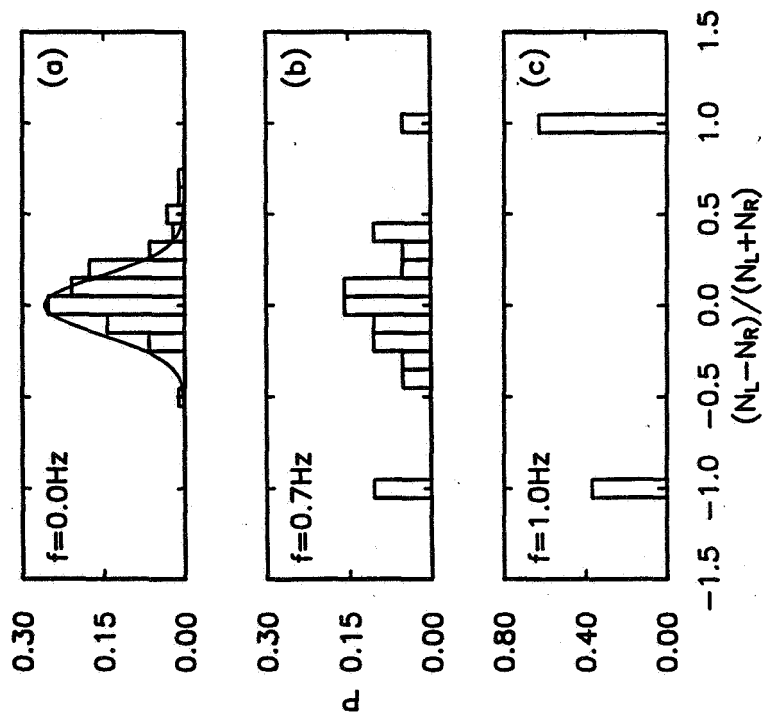

Figure 1. The order-parameter probability function $P(O)$. From top to bottom, the measurements were for samples with stirring rates $f =0$, 0.7 and 1 Hz, respectively.
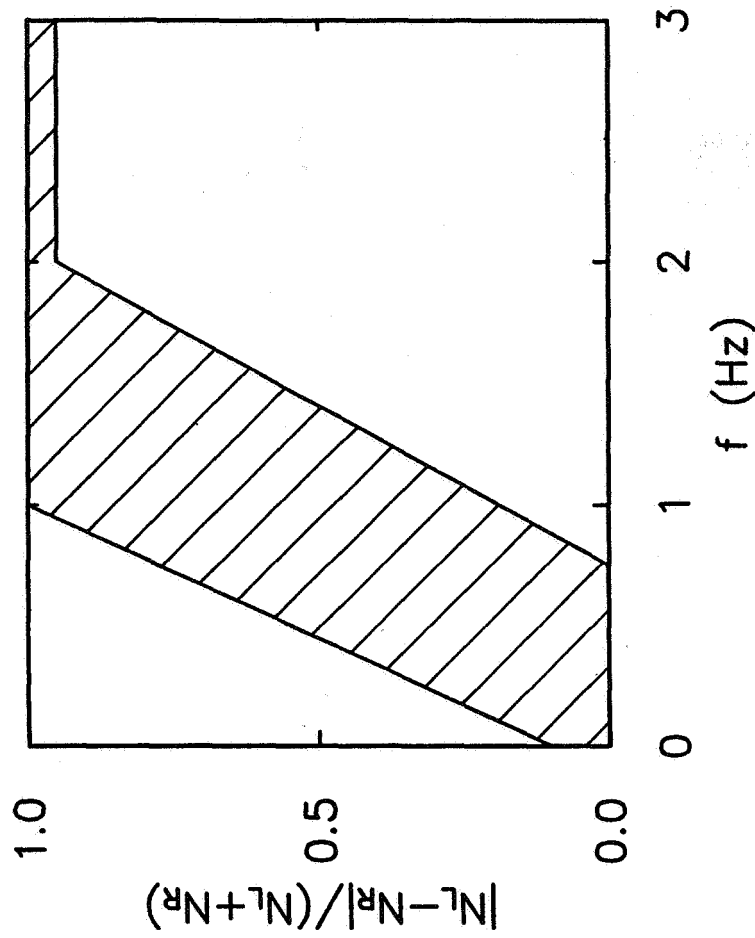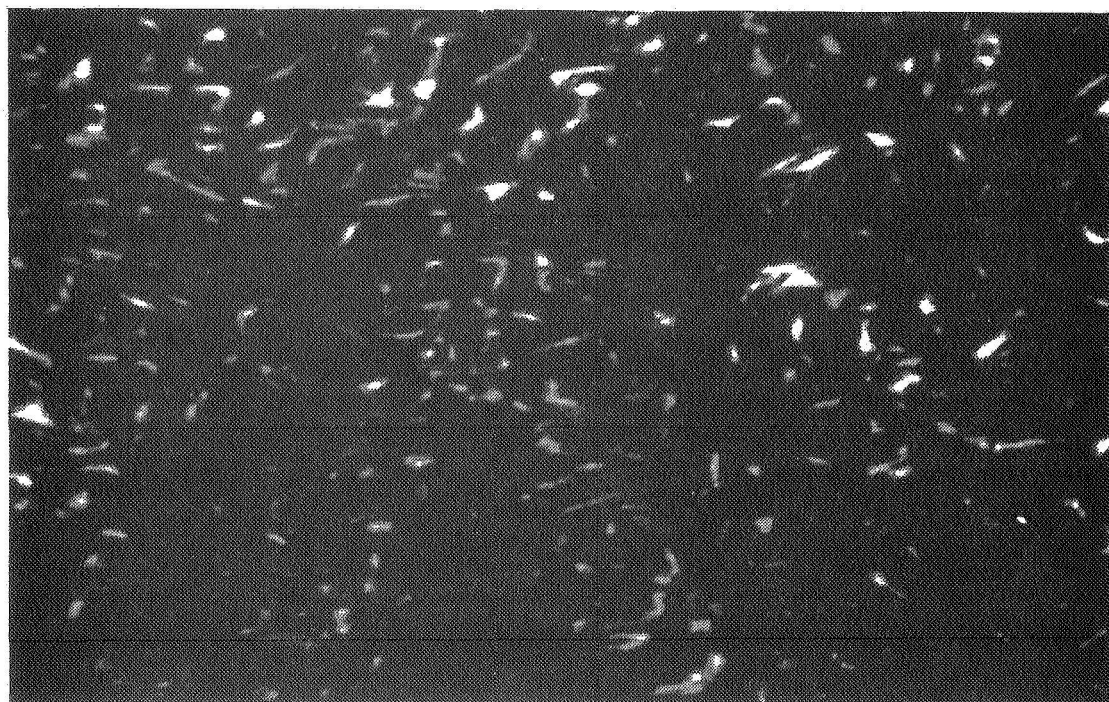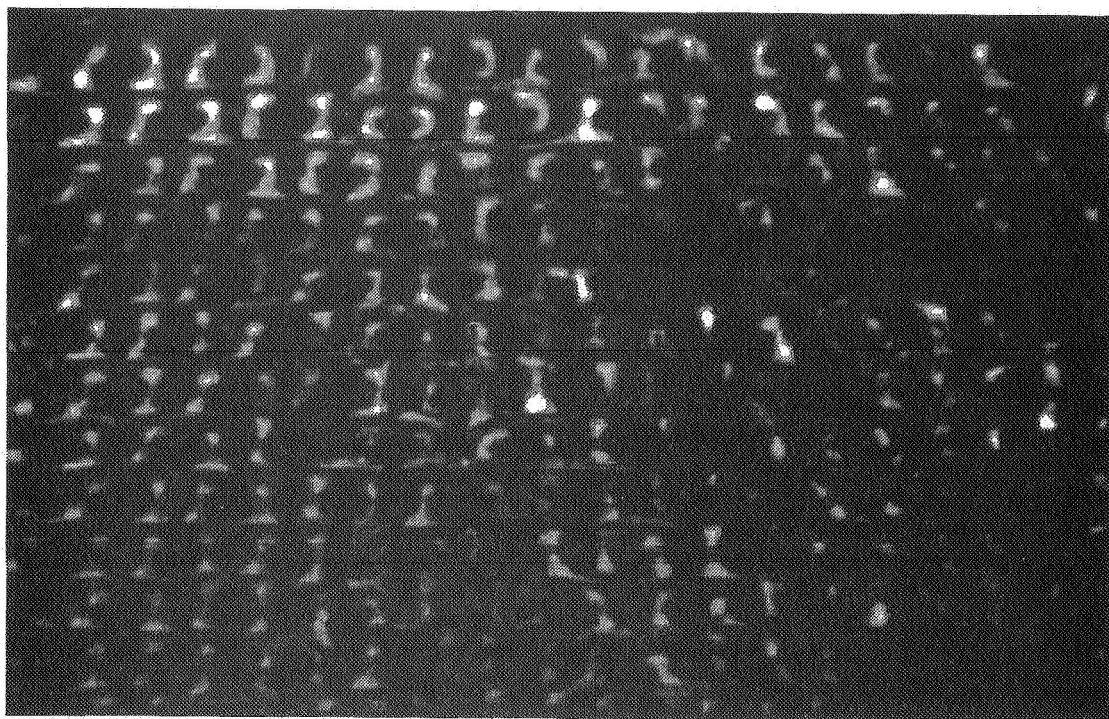
Figure 3. Flow patterns in electroconvection. The vorticies are regular and localized with a weak current (top) and become delocalized with a strong current (bottom).

PLASMA DUST CRYSTALLIZATION[1]

J. Goree[2]
University of Iowa
Iowa City, IA 52242

H. Thomas and G. Morfill
Max-Planck-Institut für extraterrestrische Physik
85740 Garching, Germany

ABSTRACT

In a ground-based definition study, a concept for a new type of microgravity experiment is developed. We formed a new state of matter: a crystalline lattice structure of charged micron-size spheres, suspended in a charge-neutral plasma. The plasma is formed by a low-pressure radio-frequency argon discharge. Solid micro-spheres are introduced, and they gain a negative electric charge. They are cooled by molecular drag on the ambient neutral gas. They are detected by laser light scattering and video photography. Laboratory experiments have demonstrated that a two-dimensional non-quantum lattice forms through the Coulomb interaction of these spheres. Microgravity is thought to be required to observe a three-dimensional structure.

INTRODUCTION

According to theory, plasmas can crystallize as they cool. What makes a crystal extraordinary is that virtually every known plasma, astronomical and man-made, is a gas-like fluid, not a solid.

Consider individual charged particles: those with identical charges repel one another and attempt to maintain a separation between themselves. But they cannot move infinitely far apart if they are electrically or magnetically confined in a volume. Nor can they move apart if there is a neutralizing background of the opposite polarity. This is called a one-component plasma (OCP). Such OCPs have been studied in other experiments, as we will review in Section III. We interest ourselves here in a kind of plasma that is closely related to the one-component plasma, but differs in the way that the neutralizing background behaves.

Usually in a plasma the thermal energy is high enough that the plasma behaves like a gas, with random particle velocities and trajectories with long mean-free-paths. This is called a "weakly-coupled plasma," and it is like a gas. By cooling the particles and lowering the thermal energy, according to theory, the charged particles in a plasma will adopt fixed positions with a uniform separation in order to minimize their potential energy. This is a crystal, and it is the extreme case of a "strongly-coupled plasma." It arises from the internal electrostatic interaction between particles and the containment of an external potential well.

The OCP can undergo phase transitions between gaseous, liquid and solid states. These states differ from ordinary states of matter in that the particles are much larger (micron size) than atoms, they are

---

spaced more widely (hundreds of microns) and their inter-particle interaction is strictly classical electrodynamics. The thermodynamics is quantified by the density of the grains and by their temperature, which are combined into the dimensionless parameters

$$\Gamma = Q_p{}^2 / (k_B \, T \, \Delta)$$
$$\kappa = \Delta / \lambda_D,$$

where Q_p is the charge on the particles, T is their temperature, Δ is the typical inter-particle spacing, and $\lambda_D \approx (\varepsilon_0 k T_i / n_i e^2)^{1/2}$ is the Debye shielding length. Physically, Γ is the ratio of the electrostatic potential energy to the thermal kinetic energy of a grain. By cooling the particles, one increases Γ. We cool the grains by drag on rarefied neutral gas in the plasma.

Monte Carlo simulations predict that, in the absence of additional disruptive forces, the OCP behaves as a:

gas   for $\Gamma < 2$
liquid   for $\Gamma > 2$
solid   for $\Gamma > 178$.

For high values of Γ, the OCP is a solid crystal, sometimes referred to as a "Wigner crystal," which is a non-quantum ordered structure in the cases we will consider.

A plasma containing micron-size grains has several advantages in forming a crystalline lattice: the charge Q_p is typically thousands of electron charges so it is easy to make Γ large, and the individual grains are big enough to be imaged photographically.

One can compute Q_p from plasma theories that were originally developed for charged bodies such as spacecraft and dust particles. [1-2] The sphere collects both electrons and ions, and so it gathers a net current until a steady state is reached where electron and ion currents exactly cancel. This steady state Q_p is negative, since electrons are faster than ions and must be repelled to reduce the electron current to equal the ion current. The negative charge is just like that of an object in a space plasma. Its value is given by $Q_p = C V_f$, where $C = 4\pi\varepsilon_0 r_p$ is the capacitance of a sphere of radius r_p, and V_f is its steady-state electric potential.

In our experiment the problem is complicated from that of the simple OCP model because the neutralizing background of electrons and ions is free to respond to the electric potential of the charged grains. As a result, Γ is not by itself a sufficient thermodynamic parameter to describe the phase transitions. Farouki and Hamaguchi [3] recognized this, and introduced κ as the other thermodynamic variable. Together, Γ and κ are a complete set of variables for the thermodynamic system, equivalent to using to the temperature and density as the variables. Farouki and Hamaguchi have also developed a Molecular-dynamics simulation of the phase transition from solid to crystalline dusty plasmas. [3,4] They have also introduced the idea that the negatively-charged grains are not purely repulsive, because they are surrounded by a net positively-charged cloud of ions in a Debye sheath, which also interact as the grains are brought within one Debye length of one another. [4]

Based on the OCP theory and the results of Farouki and Hamaguchi, it is expected that room temperature is cool enough for our spheres to crystallize, if they have charges of a thousand electron charges, or more.

We have carried out laboratory experiments that have demonstrated the formation of a 2-dimensional crystal, verifying in part the theories. These lab experiments are described below, and in a forthcoming paper. [5]

APPARATUS DESIGN

Our laboratory definition studies reveal that a design using an RF powered plasma is feasible because it levitates and confines dust particulates for hours. [5] In fact, we chose the RF design because it is known from its commercial use in plasma processing of materials that it easily levitates nad confines charged grains. [6] In the laboratory, gravity causes the particulates to be confined in a thin horizontal layer. In a microgravity environment we expect that they will disperse throughout the central region of the plasma. Drop-tower and parabolic flights may be used to test this assumption.

RF discharge operation is understood well. Electric sheaths form at the two electrodes, and their thicknesses oscillate with the applied rf voltage. The sheath edges collide with the electrons in the plasma and accelerate them stochastically to the energies required to sustain the plasma by electron-impact ionization of the neutral gas. RF power is applied continuously to sustain the discharge in a steady state. Ions and dust particles move too slowly to respond to the RF electric fields; instead they respond to a time-average DC electric field that forms naturally. This DC electric field points everywhere outward from the center of the plasma, providing stable confinement of the negatively-charged dust particulates. Dust is confined in the large central region of the plasma, where the field is less than 1 V/cm, small enough not to tear apart a lattice.

The RF design will allow an adjustable RF output power. This will allow a variable plasma density, which is useful for multiple experimental runs to test the density dependence in theories involving Γ and κ. A generator with a maximum output of 10 W should allow plasma densities of $\leq 10^{10}$ cm^{-3}.

There are two practical difficulties of using an RF discharge that we must evaluate during the laboratory definition study stage. These are thermal gradient forces and ion-drag forces. Either of them could disrupt crystal formation. Thermal gradients within the gas can disrupt the crystal formation due to the "thermophoresis force" [7] of the gas on the particles. During the laboratory experiments we will quantify this effect and arrive at engineering criteria for thermal design of the flight hardware. Ion-drag forces [8] arise from the ions that are streaming from the center of the plasma toward the negatively-biased electrodes. The ions are scattered by Coulomb collisions with the massively charged grains, and they impart some momentum to the grains. Expressions have been developed for ion drag for an isolated grain, [8] but it is unknown how substantial this force will be for ions passing through a cloud of grains, as in our experiment.

RESULTS OF LABORATORY DEFINITION EXPERIMENTS

A macroscopic Coulomb crystal of solid particles in a plasma has been observed in our laboratory definition experiments. Images of a cloud of 7-μm "dust" particles, which are charged and levitated in a weakly-ionized argon plasma, reveal a hexagonal crystal structure. The crystal is visible to the unaided eye. The particles are cooled by neutral gas to 310 K, and their charge is >9,000 e, corresponding to a Coulomb coupling parameter Γ >18,000. For such a large Γ value, strongly-coupled plasma theory predicts that the particles should organize in a Coulomb solid, in agreement with our observations.

A low-power argon discharge at 2.05 ± 0.05 mBar was formed by applying a 13.56-MHz signal to the lower electrode of a parallel-plate reactor. The lower electrode is a disk 8 cm in diameter, while the upper is a ring, with inner and outer diameters of 3 cm and 10 cm, respectively. The electrode separation is 2 cm. The dc self-bias of the lower electrode was -14.5 ± 0.5 V, measured at the electrical feed-through. The rf power was 0.4 ± 0.3 W.

A few milligrams of particles were placed in a sieve above the hole in the upper electrode. This is agitated to release particles into the plasma. The particles are 7.0 μm diameter melamine/formaldehyde spheres, with a size distribution of ± 0.2 μm.

The particles were seen as a thin disk-shaped cloud, levitated above the center of the lower electrode, near the sheath-plasma boundary. Particles were organized in approximately 18 planar layers ($\approx$ 6 layers of two-particle agglomerates and $\approx$ 12 layers of single particles), parallel to the electrode. The diameter of the cloud was approximately 3 cm. Observations were made using a sheet of HeNe laser light to illuminate a plane. The sheet has a thickness of 110 ± 23 μm and a breadth of 2 cm. It is adjustable to various heights above the lower electrode. Scattered light is viewed at 90° through a hole in the upper electrode. Individual particles were easily seen with the unaided eye and with a CCD video camera fitted with a macro lens. A 200-mm macro lens with extension tubes provided ×1 magnification for the data shown below, while a long-distance microscope lens with a ×13 magnification revealed that the particles in the plasma were either individual grains or agglomerates of two grains. The latter were found to populate the lower lattice planes of the cloud, presumably due to their greater mass to charge ratio.

An image of the particle cloud in a single plane reveals an organized structure with nearly uniform particle spacing. The image area is 7.7×7.7 mm^2 and contains 724 particles. Assuming equal particle spacing in all directions, this corresponds to $n_p = (4.3 \pm 0.2) \times 10^4$ cm^{-3}.

A numerical analysis of this image verifies it as a "plasma crystal." We identified the particle locations and to describe the Voronoi (Wigner-Seitz) cells). The cells are mainly six-sided, with nearly equal areas and uniform spacing. The mean separation Δ (lattice constant) between the particles is 250 μm. The measurements were compared with a synthetic random particle distribution using the same properties - number and density - as in the experiment, This simulates a dusty plasma in its "gas phase".

This result showing the structure is from a single video frame. The dynamics of this structure are revealed by the video, which showed the individual particles oscillating gently about fixed equilibrium centers in what appeared to be a Brownian motion. Occasionally a grain diffused through the structure, visibly perturbing the position of the nearest particle.

In order to estimate the coupling parameter, Γ, we need to know the particles' kinetic energy (or temperature) and charge. The particles are cooled by the neutral gas. Based on frame-by-frame measurements of the mean particle velocity, we estimate the particle kinetic temperature to $T_p = 310$ K, which is close to room temperature. Particles were also found to be at room temperature in the discharge of Boufendi et al. [9], who used laser-Doppler velocimetry to detect particles that were much smaller than ours, and reported a correspondingly smaller value of Γ.

We estimate the grain charge to lie between the extreme values $-9{,}000 \geq Q_p/e \geq -28{,}000$. The shielding length is estimated to lie in the range 60 μm $\leq \lambda \leq 400$ μm, resulting in $4 \geq \kappa \geq 0.6$. The

Coulomb coupling parameter Γ is then estimated to be >18000. Our observation of a crystalline structure is consistent with this large value of Γ.

NEED FOR MICROGRAVITY

Our experiment reveals that the dust cloud is crushed. It is much wider than it is high. This is thought to be due to a combination of gravity and the ion drag force. For spheres of the size we are using, it is inevitable that gravity will be a significant, and likely dominant, factor in this crushing.

To avoid the crushing, the *global electric force* that confines the grains in the plasma must be stronger than gravity. This is necessary so that particulates will be distributed uniformly throughout the vacuum vessel and don't pile up at the bottom due to gravity. Quantitatively, the potential energy difference across the vacuum vessel, Mg_0l, must be much smaller than the confining electric potential in the main field-free plasma region, $Q_p\phi$ which is $\approx Q_p k_B T_e / e$. Thus, the microgravity acceleration g_0 must satisfy

$$g_0 << Q_p k_B T_e / e M_p l$$

Now assuming a 20-μm radius plastic sphere, $T_e = 1$ eV, and a floating potential of -10 V, this reduces to $g_0 << 0.667$ cm s^{-2} = 7×10^{-3} g.

A second reason that gravity can disrupt crystal formation is that it competes with the *local electric field*. To achieve 3-D crystallization, the gravitational must be small compared to the local pressures on a grain. Electrostatic pressure is responsible for lattice formation, while gravitational pressure can inhibit it by crushing the lattice into a 2-D structure.

To summarize the anticipated microgravity requirements:

- The experiment requires $<< 7 \times 10^{-3}$ g of reduced gravity.
- Parabolic flights provide $\approx 10^{-2}$ g of microgravity, which will be inadequate to assure a uniform density of spheres in the plasma.
- Spaceflight will provide $< 10^{-4}$ g, which is adequate.

CONCLUSIONS

Ground-based definition studies now in progress are revealing the soundness and feasibility of microgravity experiments for forming 3-D crystalline structures of charged microspheres levitated in a charge-neutral plasma. These experiments are expected to offer new opportunities for basic physics (WIgner lattice studies) and engineering (dust contamination during microelectronics processing).

REFERENCES

1. E.C. Whipple, Potentials of surfaces in space, Rep. Prog. Phys., 44, 1197 (1981).
2. C.K. Goertz, Dusty plasmas in the solar system, Rev. of Geophys., 27, 271-292 (1989).
3. R.T. Farouki & S. Hamaguchi, "Phase transitions of dense systems of charged "dust" grains in plasmas," Appl. Phys. Lett., 61, 1764 (1992).
4. S. Hamaguchi and R.T. Farouki, "Self-consistent pair potential for charged particulates in plasmas," submitted to Phys. Rev. E (1993).
5. H. Thomas, G. Morfill, V. Demmell, J. Goree, et al., Physical Review Letters, submitted 1994.
6. G.S. Selwyn et al., J. Vacuum Sci. and Technol., A7, 2758 (1989) and Appl. Phys. Lett. 57, 1876 (1990)
7. L. Talbot, R.K. Cheng, R.W. Schefer, and D.R. Willis, "Thermophoresis of particles in a heated boundary layer," J. Fluid Mech. 101, 737 (1980)
8. M.D. Kilgore, J.E. Daugherty, and D.B. Graves, "Ion Drag on an isolated particulate in a low-pressure discharge," J. Appl. Phys., 73, 7195 (1993).
9. L. Boufendi et al., J. Appl. Phys. 73, 2160 (1993).

Containerless Capillary Wave Turbulence

Seth Putterman, UCLA

Paper not available

Flocculation and Aggregation in a Microgravity Environment (FAME)

Rafat R. Ansari
NASA Lewis Research Center/CWRU
Mail Stop 105-1, 21000 Brookpark Road
Cleveland, OH 44135, USA

Harbans S. Dhadwal and Kwang I. Suh
Department of Electrical Engineering
State University of New York at Stony Brook
Stony Brook, NY 11794, USA

Abstract

An experiment to study flocculation phenomena in the constrained microgravity environment of a space shuttle or space station is described. The small size and light weight experiment easily fits in a Spacelab Glovebox. Using an integrated fiber optic dynamic light scattering (DLS) system we obtain high precision particle size measurements from dispersions of colloidal particles within seconds, needs no onboard optical alignment, no index matching fluid, and offers sample mixing and shear melting capabilities to study aggregation (flocculation and coagulation) phenomena under both quiescent and controlled agitation conditions. The experimental system can easily be adapted for other microgravity experiments requiring the use of DLS. Preliminary results of ground-based study are reported.

Introduction

A functional engineering model of an integrated fiber optic system for conducting in-situ dynamic light scattering (DLS) measurements has been built for microgravity science & applications, in particular, to study flocculation and coagulation of spherical polystyrene particles in aqueous solutions in the presence of long chain polyacrylamide polymer (commonly known as flocculant). The development of the engineering model and its optical, mechanical, and electrical design have been recently presented by Ansari et al[1]. A Glovebox (GBX) experiment "Flocculation and Aggregation in a Microgravity Environment (FAME)" was selected by NASA for USML-2 (2nd United States Microgravity Laboratory) space shuttle flight mission scheduled to be flown in Fall 1995. However, due to the extraordinary demand on the GBX resources and a priority for mainstream experiments where GBX was required to support that activity, FAME was dropped out of USML-2 flight program. We plan to propose it for another flight at the next round of Fluids NRA. In addition to flocculation monitoring, we anticipate the use of FAME hardware, after some modification, for monitoring growth of porous materials in another future experiment by Dutta et al[2].

The Art of Polymer Induced Flocculation

Flocculation is widely used in the recovery of suspended material in coal and ore mining, pulp and paper making, enhanced oil recovery, pharmaceuticals, water and waste-water treatment, and pollution control of lakes and reservoirs. Flocculation is the polymer-induced aggregation of dispersed particles in a fluid based system. Details on this mechanism has been given by Attia[3], Finch[4], and Gregory[5,6]. Industrial polymeric flocculants are generally long chain polymers. Filtration, floatation, and sedimentation operations become very effective with an increase in the particle size. The particles which are to be flocculated may have a wide size range covering colloidal (nm) to microscopic (μm) to visible (mm) particles. Perikinetic flocculation process (due to Brownian diffusion) can be very slow for dilute colloidal dispersions. It may take several hours to grow large flocs under these conditions. Orthokinetic flocculation (due to some agitation) enhances collision efficiencies and thus promotes flocculation. However, all theoretical calculations for flocculation rate constants generally apply to spherical shapes assuming a laminar flow and hence strictly to the early stages of a flocculation process.

Colloid stability is very complex because several forces can be operational. Most frequently occuring forces are van der Waals forces, electrostatic forces, and forces due to adsorbed polymers. Dispersion stability can be described by DLVO[7,8] theory as a balance between electrostatic repulsion (ESR) and van der Waals attraction (VWA). In dilute electrolytic solutions ESR exceeds VWA. The ionic strength of the dispersion is modified to enhance particle-particle collision efficiency as high as possible for normal aggregation (coagulation) to occur. However, DLVO theory breaks down for polymer-induced flocculation because the mechanism of bridging or charge neutralization (patchwork model[9]) due to adsorbed polymer depends upon the long-chain nature of the polymer molecule. Furthermore, the polymer molecular weight should be very high ($\cong$1-20 $\times$ 10^6) to promote effective polymer-particle attachments. Only a small

---

polymer chain segment is required to be adsorbed on the particle surface, while a significant amount of chain segment is extended into the fluid phase to capture other particles of the dispersion. More adsorbed polymer on the particle surface may have adverse effect on the ability to flocculate by giving rise to steric repulsion.

Scientific Objectives

The scientific objectives of the FAME investigation is to obtain data sets for a proof-of-concept study on a model system which can be used to guide the development of quantitative models of the flocculation process. This study involves aggregation (both flocculation and coagulation) of primary particles from colloidal (nm) to large (1-100 μm) aqueous particulate dispersions, thus covering a wide range of size and interaction regimes.

Currently two competing models describe flocculation in terms of either a bridging mechanism and/or an interlocking polymeric network. In the bridging model a polymer chain is considered to be adsorbed simultaneously on two or more particles. In the network model, polymer chains form an entangled network which acts as a particle trap. Because of strong gravitational settling and a lack of non-invasive techniques these theories have not been tested thoroughly. Furthermore which theory plays a dominant role is not clearly understood. Laser light scattering (LLS) experiments in the absence of gravitational effects will be able to answer questions of fundamental importance to the flocculation phenomena and thus provide new quantitative insights into various interactions and microscopic structures present in pre-flocculation, during flocculation and after the flocculation stage. The microgravity environment on-board the space shuttle orbiter or space station will eliminate the problems of sedimentation and convective diffusion. The effects of agitation on the growth of large flocs under controlled shear conditions in the absence of sedimentation in a microgravity environment has been identified as an important area of research to the materials processing in space by Naumann and Herring[10]. It has been suggested by Sikora and Stratton[11] that the reversibility or otherwise of floc breakage under shear may be an indication of whether polymer bridging or charge neutralization is the predominant flocculation mechanism. Charge neutralization generally gives weaker flocs than bridging, but the flocs readily re-form. One important practical aspect of colloid interaction is its effect on the strength of aggregates. Unfortunately this is not well understood. Varooqui and Pefferkorn[12] describe the time evolution of the size distribution of flocculating particles at large time by scaling formulas. The objective of this investigation is to clearly delineate these predictions.

Our approach is to monitor, in real time, the growth of flocs due to polymer-induced aggregation and the growth of coagulase due to salt-induced aggregation. For primary colloids, we employ the technique of DLS and for large particles, we plan to use microscopy and videography to monitor the changing size and shape of the flocculating/coagulating particles. Strength of aggregates will be measured by applying controlled shear. Flocs are expected to be much stronger than coagulase. The diffusion data from DLS measurements from primary colloids will be compared with a quantitative model for flocculation developed earlier by Ansari and Hallett[13] to yield important information on the particle-particle, particle-polymer, and polymer-polymer interactions in a flocculating system.

In case of microscopic particles (>1 μm), Earth's gravity plays a dominant role in promoting differential settling and hence flocculation. The separation of liquid-solid components in a microgravity environment by destabilizing a suspension would offer great technical challenges because of the absence of differential settling. Particles of different size or density settle at different rates and the resulting relative motion can cause particle collisions and hence aggregation. A better understanding of the flocculation process in a microgravity environment will be useful in obtaining successful separation process technology for space-based processing operations.

FAME Hardware Development

The design criteria of FAME hardware is to acquire a miniaturized DLS system having both launch and collection optics in one entity (probe), modular (satisfy the requirements of several experiments), user friendly, rugged yet flexible, power efficient, eliminate the use of an index matching fluid for flare control, eliminate the need for on-orbit optical alignment, and offer in-situ sample mixing capabilities. In order to gain detailed knowledge in the theory and practice of DLS, the interested reader is referred to general reading in this area[14-16] and the references contained therein.

The experimental setup shown in Figure 1 comprises four major parts; the laser/detector module, a fiber optic backscatter probe, the flocculation module (sample chambers with mixing motor), and a correlator hardware/software. This experiment module with a dimension of 21.2 cm wide x 12.8 cm deep x 19.0 cm high can be easily seated on its
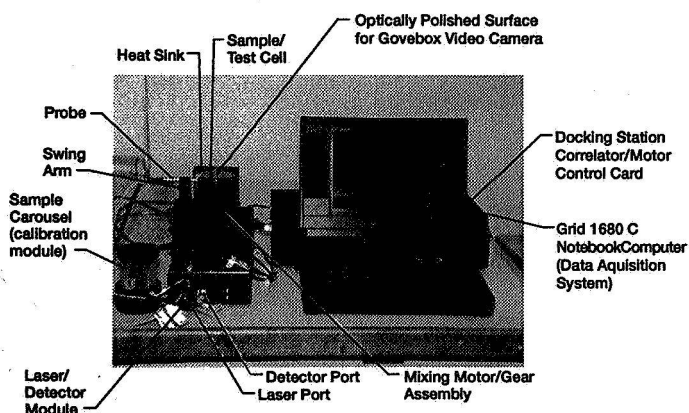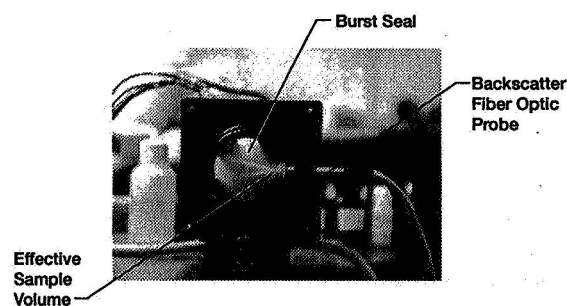
Figure 1. Experimental Setup.

Figure 2. Effective Scattering Volume as Shown by Two Intersecting Laser Beams in the Flocculation Cell.

magnetic legs inside the GBX. The GBX working area is 39.4 cm wide x 27.9 cm deep x 23.5 cm high with one main door opening of 21.4 cm x 18.9 cm and two side door openings 21.4 cm x 13.1 cm.

The laser light out of the laser/detector module is transmitted by a compact backscatter fiber optic probe to the flocculation module, where the flocculation process of a particulate dispersion is observed. A lens-less fiber optic probe comprising two optical fibers, as illustrated in Figure 2, provides a compact and remote means of studying the dynamical characteristics of colloidal/polymer systems, through the use of photon correlation spectroscopy or dynamic light scattering. Detailed descriptions of the backscatter fiber optic probe and its application to study concentrated particulate dispersions[17], microemulsion characterization[18], the early detection of cataracts in bovine and human eye lenses[19-21], and BSA and lysozyme protein solution characterization have been reported elsewhere[22].

Experimental

A simplified cross sectional view of the flocculation module is shown in Figure 3. The flocculation module consists of 3 major units; the base, the sample cell, and the swing arm. The sample cell is divided into 2 sections by a piston to contain the particle solution on the top section and the polymer solution on the bottom. The cell holds about 100 ml of sample volume. The sample cell has a thin sapphire window where the backscatter fiber optic probe is positioned so that the scattering volume is effectively located well inside the sample cell. The base module contains a stepper motor and its driver. The chopper driver's heat dissipation fins are connected to the base module which acts as a heat sink for the motor. The stepper motor is connected to the piston in the sample cell by a gear set. The piston has a hole that is covered by a thin aluminum bursting seal, and 3 stirring wings attached on top. The base of the piston divides the sample cell into two chambers. The upper and lower chambers are filled with the aqueous particle dispersion
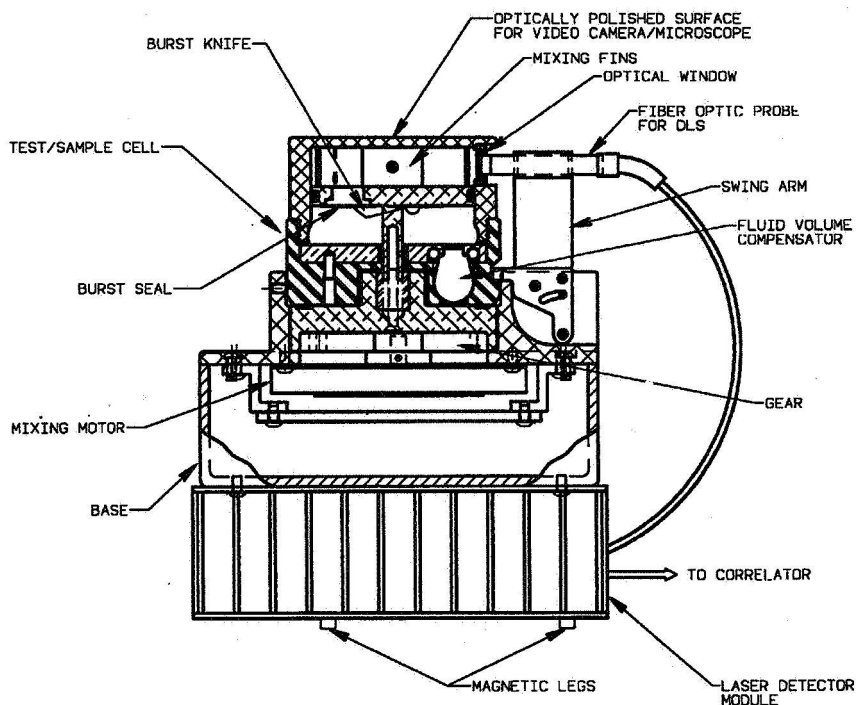

Figure 3. FAME Experiment Module.

and the long chain polymer solution respectively, through the fill holes located on the side of these chambers. The sample loading is done very carefully to ensure dust free and bubble free samples. During the experiment the piston retracts (pulls downward) in the sample cell by the stepper motor gear assembly. The bursting seal punctures upon contact with a knife edge mechanism and the polymer solution comes into contact with the particle solution. After the piston is completely pulled down and locked to the motor, it starts spinning, and the stirring action begins with three wing tips, each measuring 12 mm x 21 mm x 1 mm, on the top of the piston assembly. The spinning or mixing speeds can be varied from 5 rpm to 700 rpm. This spinning action is desired for two purposes. First it enables complete mixing of the two dispersions and secondly to study the effects of agitation and controlled shear on flocculation. The swing arm holds the fiber optic backscatter probe against the sapphire window of the sample cell. It can swing back and forth around a pivot point on the base module so that the sample modules can easily be exchanged without pulling out the probe every time a new measurement is performed. Another purpose of the swing arm is that when in position, the arm locks the sample cell with the base so that the sapphire window stays well aligned with the backscatter probe. This arrangement provides an easy access, safety, and flexibility to the crew member during experimental procedures. The test chambers are made of polycarbonate material with an optically polished flat surface on the top for studying in-situ the dynamics of the suspension (particles $\gg 30$ μm) under investigation using the GBX video camera or the microscope.

Figure 4. Particle Size Test Results.

Figure 5. Particle Size Distribution with and without Polymer Aided Flocculation.

Results

The FAME engineering model was tested on aqueous samples of polystyrene latex spherical colloidal particles ranging in size from 18 nm to 551 nm (Bangs Laboratory, Carmel, IN) at a concentration of 0.01%. The upper chamber of the test cell was filled with this dispersion and the lower chamber was filled with doubly distilled deionized water. The fiber optic probe provided measurements of particle size prior to mixing with water in the upper chamber and then after mixing with pure water in the lower chamber. These measurements are reported in Figure 4. The mean average diffusion coefficient, mean average size, and corresponding dimensionless polydispersity factor (PDF) computed from fifty autocorrelation functions for each particle dispersion are tabulated in Table 1. The average translational diffusion coefficient (D_T) and PDF are determined by analyzing the intensity-intensity autocorrelation data using the method of cumulants[23]. The D_T values are converted to average size (diameter) using the Stokes-Einstein equation[14-16]. PDF is a sensitive measure of the sample's polydispersity i.e. smaller the PDF, narrower the size distribution. Table 1 consistently shows very small values of PDF as expected from monodisperse samples. The fiber optic probe provides high precision particle size measurements within 5-15 seconds. 15, 60, and 300 seconds duration measurements give consistent values of particle sizes within 1-3%.
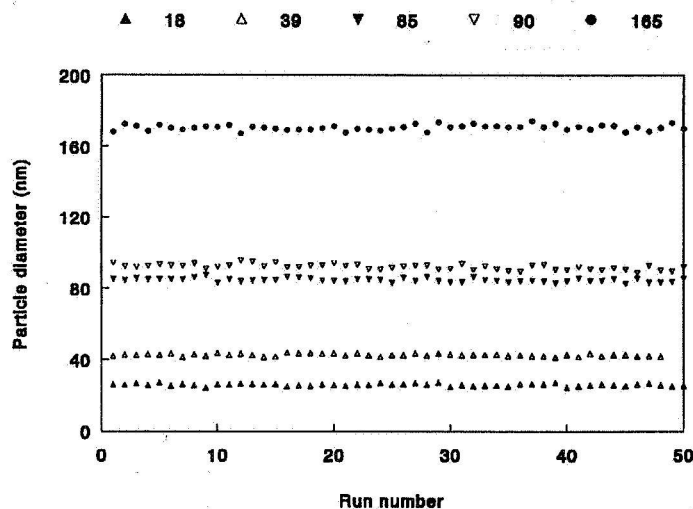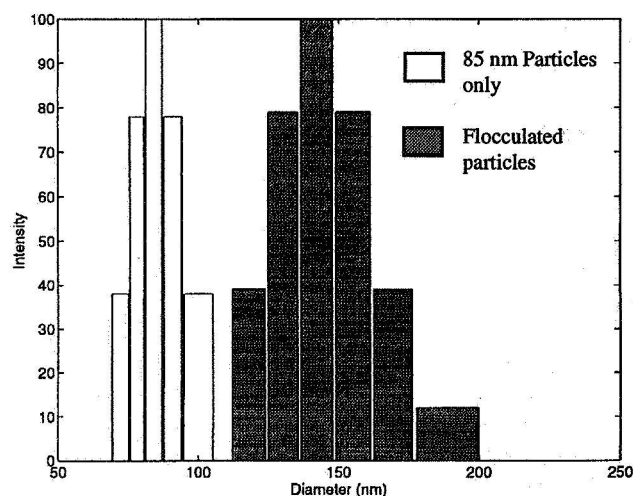
TABLE 1. FAME ENGINEERING MODEL PRELIMINARY TEST RESULTS

Sample, Aqueous Dispersions of Polystyrene Standards (nm)	Diffusion Coefficient. m^2sec^{-1} (10^{-13})	Mean Diameter nm	Polydispersity Factor PDF
18	169.12±4.21	25.36±0.64(5 sec. runs)	0.0016
39	104.36±1.73	42.55±0.70 (15 sec. runs)	0.0047
85±4	53.23±0.64	85.87±1.66 (15 sec. runs)	0.00026
85 nm particles mixed with polymer (Flocculated)	92.38±3.90	119.70±4.70 (15 sec. runs)	0.02180
90	47.72±0.78	92.15±1.69 (15 sec. runs)	0.00125
	47.68±1.63	92.33±2.80 (5 sec. runs)	0.00109
165±3	26.95±0.32	171.52±1.99 (5 sec. runs)	0.0005
551±10	9.24±0.39	517.96±21.34 (15 sec. runs)	0.00013

Preliminary flocculation tests were conducted using a long-chain, high molecular weight ($\approx$6 million daltons), polyacrylamide polymer and polystyrene spherical particles. The freely diffusing polymer chains in the polymer solution contributes only negligibly (<5%) to the total light scattering intensity at a concentration of about 50 ppm (parts per million). At this low polymer concentration the viscosity of the solution remains very closely to that of pure water. All measurements were conducted at room temperature. As an example, flocculation test results on 85 nm particles of polystyrene are reported here. In these experiments the two chambers were cleaned, and burst seals were replaced. The upper chamber was filled with the 85 nm particle dispersion while the lower chamber was filled with a polymer solution. DLS measurements were repeated. The size distribution of the polystyrene particles in the upper chamber is presented in a histogram (see Figure 5). The burst seals were broken to let particle and polymer molecules combine. After few minutes of mixing the particles grew in size and appeared to form flocs. NNLS[24] (non negative least squares) program from the commercially available software (Brookhaven Instrument Corporation, NY) is used to recover particle size distribution. Clearly the narrow size distribution of the 85 nm monodisperse particles is broadened (shaded area in Figure 5) due to polymer aided flocculation. This can also be seen from the changes in PDF values (see Table 1). This factor increases by two orders of magnitude. This indicates clustering of 85 nm monodisperse particles into bigger aggregates (flocs). More data is being gathered at this time using the FAME engineering model involving different particle sizes as a function of polymer molecular weight (chain size), the particle and polymer concentrations and the electric charge on their surfaces. This will be reported at a later date. The detailed studies of flocculation, however, will ultimately require µg conditions in which bigger floc behavior will be monitored without the detrimental effects of sedimentation and convection.

Figure 6 shows flocs or aggregates of 260 nm polystyrene spherical particles at a concentration of 1×10^{-5} gcm^{-3} using PAM solution of molecular weight 5×10^6 at a concentration of 100 ppm. These very dilute dispersions were mixed in a cuvette by hand shaking and electron micrographs were taken after few hours. Various shapes of aggregates are evident. The pioneering work by Weitz and Oliveria[25] on aggregates of colloidal gold and Auburt and Cannell[26] on colloidal silica has established that aggregates can be treated as fractal objects. We plan to extend the fractal analogy to long-chain polymer induced flocculation. For this purpose a simultaneous multiangle light scattering ap-
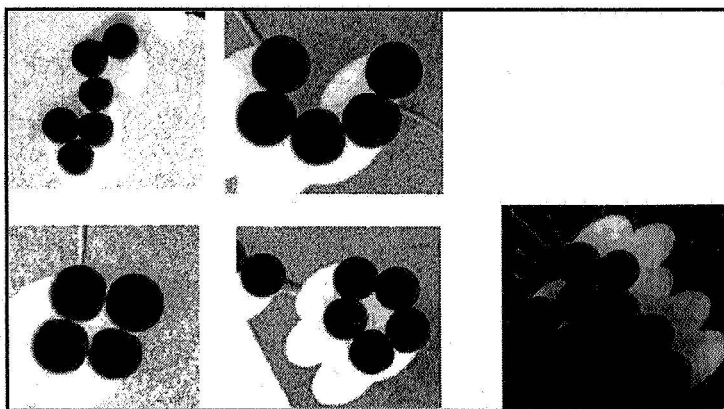

Figure 6. Floc Shapes.

paratus built by one of us (HSD) will soon be used to obtain dynamic and static light scattering data on a flocculating system. We hope to gain detailed information on the floc shape, its structure (open or compact), and the dynamics of floc formation. We are also looking into the polymeric networks, diffusion of particles through them at three regimes (C<C*, C=C*, and C>C*; C* is the critical concentration at which polymeric entangled networks become appreciable), and their effect on flocculation of these particles. The experiments reported here involve model polystyrene colloids. We plan to extend this work to clays, which are involved in majority of industrial flocculation operation in real world.

Conclusion

A compact functional engineering model built for a Glovebox experiment to study flocculation and aggregation phenomena in a microgravity environment, using the technique of dynamic light scattering, has been tested on the ground employing several colloidal dispersions of polystyrene latex particles ranging in size from 18 nm to 551 nm. One unique feature of the optical design is that both launch and collection optics are integrated into a miniaturized probe. With only 2.6 mW input laser power, this optical design matches or exceeds the efficiency of typical conventional DLS setups[20]. Conventional DLS systems use at least one to two orders of magnitude more power and physically occupy a large volume (1 m^3). The FAME system provides rapid measurements of diffusion coefficient and particle size in the backscatter regime (within 5-15 seconds), needs no optical alignment, and offers insitu sample mixing, controlled shear, and video monitoring capabilities (particles size >>30 microns). The preliminary data is very encouraging and has opened up new possibilities for gaining new insights into the process of flocculation. The system will be tested shortly on NASA's Lear Jet flights to check and simulate its functionality and ease of operation to actual flight conditions in a microgravity environment.

Acknowledgments

References

1. Ansari, R.R., Dhadwal, H.S., and Suh, K.I., "An Integrated Fiber Optic System for Dynamic Light-Scattering Measurements in Microgravity", Proceedings of The International Symposium on Space Optics 18–22 April 1994, Garmisch-Pantenkirchen, FRG, EOS/SPIE Paper #2210-22.
2. Dutta, P.K., Jakupca, M., Salvati, L., Reddy, K.S.N., and Ansari, R.R., "Synthesis of Microporous Materials in Reverse Micelles", 32nd Aerospace Sciences Meeting & Exhibit, AIAA 94-0569, January 10-13, 1994, Reno, Nevada.
3. Attia, Y.A.,(Editor), "Flocculation in Biotechnology and Separation Systems", Process Technology Proceedings, 4, Elsevier, 1987.
4. Finch, C. A., Editor, "Chemistry and Technology of Water Soluble Polymers," Plenum Press, New York 1983.
5. Gregory, J., "In the Scientific Basis of Flocculation", Ives, K. J., ed., NATO Adv. Study Inst. Series, Sijthoff and Noordhoff Alphen aan den Rijn, The Netherlands 1978.
6. Gregory, J., "Fundamentals of Flocculation", CRC Critical Reviews in Environmental Control, Vol. 19, Issue 3, pages 185-230 (1989).
7. Deryagin, B.V., and Landau, L.D.., "Theory of the Stability of strongly lyophobic sols and of adhesion of strongly charged particles in solutions of Electrolytes", Acta Physicochim, URSS, 14, 633, 1941.
8. Verwey, E.J.W., and Overbeek, J. Th. G., Theory of the Stability of Lyophobic Colloids, Elsevier, Amsterdam, 1948.
9. Gregory, J., "Rates of Flocculation of Latex Particles by Cationic Polymers", J. Colloid Interface Sci., 42, 448, 1973.
10. Naumann, R.J., and Herring. H.W., "Materials Processing in Space: Early Experiments", NASA SP-433, p.26, 1980.
11. Sikora, M.D., and Stratton, R.A., "The Shear Stability of Flocculated Colliods", Tappi, J. 64(1981) p. 97–101.

12. Varooqui, R., and Pefferkorn, E., "Experimental and Theoretical Aspects on Cluster Size Distribution of LatexParticles Flocculating in Presence of Electrolytes and Water Soluble Polymers", Prog. Colloid Plom. Sci., 79:194–201 (1989).

13. Ansari, R.R., and Hallett, F.R., "Quasi-Elastic Laser Light Scattering Study of Polymeric Flocculant Suspensions", in Particulate and Multiphase Processes, Vol. 3, Colloid and Interfacial Phenomena, T. Ariman and T.N. Veziroglu, Editors, Springer-Verlag, 1985.

14. Chu, B., "Laser Light Scattering: Basic Principles and Practice", Academic Press, New York, 1991.

15. Schmitz, K.S., "An Introduction to Dynamic Light Scattering by Macromolecules", Academic Press, 1990.

16. Pecora, R, Editor, "Dynamic Light Scattering: Applications of Photon Correlation Spectroscopy", Plenum Press, 1985.

17. Dhadwal, H.S., Ansari, R.R., Meyer, W.V., "A fiber Optic Probe for Particle Sizing in Concentrated Suspensions", Rev. Sci. Instrum. 62 (12), December 1991.

18. Ansari, R.R., Dhadwal, H.S., Cheung, H.M., and Meyer, W.V., "Microemulsion Characterization by the use of a Noninvasive Backscatter Fiber Optic Probe", J. App. Optics, Vol. 32, No. 21, July 1993.

19. Ansari, R.R., Dhadwal, H.S., Campbell, M.C.W., and DellaVecchia, M.A., "A Fiber Optic Sensor for Ophthalmic Refractive Diagnostics", Proc. of Fiber Optic Medical and Fluorescent Sensors and Applications, January 23-24, 1992, Los Angeles, CA., SPIE Vol. 1648.

20. Ansari, R.R., and Dhadwal, H.S., "A Fiber Optic Probe for the Detection of Cataracts", The third National Technology Transfer Conference & Exposition, December 1-3, 1992, Baltimore, MD., NASA conference Publication 3189, Vol. I.

21. Dhadwal, H.S., Ansari, R.R., DellaVecchia, M.A., "Coherent Fiber Optic Sensor for Early Detection of Cataractogenesis in a Human Eye Lens", J. Opt. Engineering, Vol. 32, No. 2, February 1993.

22. Dhadwal, H.S., Wilson, W.W., Ansari, R.R., and Meyer, W.V., "Dynamic Light Scattering Studies of BSA and Lysozyme Using a Backscatter Fiber Optic System", Proc. of Static and Dynamic Light Scattering in Medicine and Biology, 21-22 January, 1993, Los Angeles, CA, SPIE Vol. 1884.

23. Koppel, D.E., "Analysis of Macromolecular Dispersity in Intensity Correlation Spectroscopy: The Method of Cumulants", J. Chem. Phys., Vol. 57, 4814-4820, 1972.

24. Lawson, C.L., and Hanson, R.J., "Solving Least Squares Problems", Prentice Hall, 1974.

25. Weitz, D.A., and Olivera, M., "Fractal Structures Formed by Kinetic Aggregation of Aqueous Gold Colloids", Phys. Rev. Lett., 52, 1433, 1984.

26. Aubert, C. and Cannell, D.S., "Restructuring of Colloidal Silica Aggregates", Phys. Rev. Lett., 56, 738,1986.

DYNAMICS OF HARD SPHERE COLLOIDAL DISPERSIONS

J.X. Zhu and P.M. Chaikin
Department of Physics

S.-E. Phan and W.B. Russel
Department of Chemical Engineering
Princeton University
Princeton NJ 08544

INTRODUCTION

One of the most fundamental systems in nature is that of hard spheres, particles that do no interpenetrate but otherwise do not overlap. Hard spheres display many of the thermodynamic, hdyrodynamic, and transport properties of both molecular and colloidal systems, including transitions from disordered fluid to crystalline solid or disordered glasslike states and a host of nonideal static and dynamic phenomena. Physical realization of this most basic of interacting systems is possible with the inert gases only at extreme temperatures or pressures, but several well-studied colloidal particles provide very faithful approximations and are amenable to study at convenient length and time scales through dynamic and static light scattering. The synthesis of monodisperese spheres, stabilization by repulsions of range short relative to the radius, and index matching in organic solvents to minimize van der Waals attraction snd multiple scattering provides convincing hard sphere behavior over moderate time scales [1,2]. However, experiments with equilibration times of of days to weeks, such as crystallization, suffer from sedimentation due to the density difference between the solvent and particles [3].

The specific shortcomings of existing studies pertain primarily to the disorder-order transition, a subtle entropy driven process that leads to coexistence between a disordered phase with liquid-like order at a volume fraction $\phi=0.494$ and a face-centered-cubic solid at $\phi=0.545$. Experiments confirm fairly well the phase boundaries and suggest a glass transition at $\phi=0.56-58$, but detect a crystal structure more closely described by random stacking of hexagonally packed layers [4]. In addition, small angle light scattering studies of crystal growth do not yield the form factors expected for the linear growth of uncorrelated crystallites, but a considerably more complex form [5]. Either or both of these could arise from subtle effects of gravitational settling, which produces settling velocities comparable to diffusion velocities early in the process of nucleation and growth of crystallites. Furthermore, the equilibrium state under gravity consists of an almost closepacked, inhomogeneous crystal or glass, far from the homogeneous sample desired.

So our objective is to perform on homogeneous, fully equilibrated dispersions the full set of experiments characterizing the transition from fluid to solid and the properties of the crystalline and glassy solids. These include measurements quantifying the nucleation and growth of crystallites, the structure of the initial fluid and the fully crystalline solid, the Brownian motion of particles within the crystal, and the elasticity of the crystal and the glass. Experiments are being built and tested for the ideal microgravity environment. Here we describe the ground based effort, which exploits a fluidized bed to create a homogeneous, steady state dispersion for the studies. The difference between the microgravity environment and the fluidized bed is gauged by the Peclet number Pe, which measures the rate of convection/sedimentation relative to Brownian motion.

We have designed our experiment to accomplish three types of measurements on hard sphere suspensions in a fluidized bed: the static scattering intensity as a function of angle to determine the structure factor, the temporal autocorrelation function at all scattering angles to probe the dynamics, and the amplitude of the response to an oscillatory forcing to deduce the low frequency viscoelasticity. Thus the scattering instrument and the colloidal dispersion were chosen such that the important features of each physical property lie within the detectable range for each measurement.

COLLOIDAL DISPERSION

Our colloidal system consists of highly monodisperse poly(methyl methacrylate) (PMMA) particles with a layer of covalently bound poly(12 hydroxy stearic acid) (PHSA) chains. The branched PHSA chains provide a sufficiently thick layer (9-10 nm) to reduce the van der Waals attraction below the thermal energy, leaving as the dominant interaction a slightly soft, or nearly hard, repulsion when the polymer layers of different particles interact. PMMA/PHSA dispersions comprise a widely accepted and extensively documented model system for investigating hard sphere behavior [6,7,8].

341

The particles were synthesized in the laboratory of R.H. Ottewill by a one-shot (batch) dispersion polymerization [9]. This modified precipitation polymerization depends on the monomer (methyl methacrylate, MMA) being soluble in the dispersion medium while its polymer is not. The solvency of the dispersion medium controls the particle size, i.e. high monomer concentrations produce large particles. In this case, the medium consisted of hexane (aromatic free), dodecane, 40/60 petroleum ether, and a high boiling hydrocarbon. The comb stabilizer was prepared as a graft copolymer of PHSA with PMMA. Heating the monomer, stabilizer, and dispersion medium in an Ehrlenmeyer flask to 80°C initiated nucleation and growth of the particles. After completion of growth a further reaction covalently linked the backbone of the stabilizer to the particle. Excess stabilizer was removed by repeated centrifugation, removal of the supernatant, and redispersion in dodecane. Later we later replaced the dodecane with a more suitable solvent by a similar procedure.

Matching the refractive index of the PMMA (n=1.5240) with that of the solvent prevents multiple scattering and suppresses van der Waals forces. Combining a mixture of cis- and trans-1,2,3,4-decahydronapthalene (decalin with n=1.4750) with 1,2,3,4-tetrahydronapthalene (tetralin with n=1.5410) in the proper proportion accomplishes the match, as judged qualitatively by the clear appearance of the dispersion and quantitatively by a minimum in the intensity of scattered laser light. For the particles discussed here, with a nominal diameter of 1000 nm, the index matching solvent consists of 74.2% tetralin and 25.8% decalin with refractive index n=1.5240 for the sodium line at 25°C. For sedimentation of these particles in this solvent mixture at 25°C Pe=0.2. Whether this is sufficiently small not to affect the equilibrium remains to be seen.

FLUIDIZED BED AND SCATTERING INSTRUMENT

The fluidized bed consists of a uniform glass NMR tube with 13 mm ID and 1 mm wall thickness and a distributer consisting of a 0.2 μm membrane filter mounted at the bottom. Flow is controlled by a syringe pump (Harvard Apparatus Model 33). The membrane retains the PMMA spheres in the tube as the syringe pump drives fluid flow upwards to offset sedimentation due to the density mismatch between the particles (~1.1 g/cm^3) and the fluid (~0.95 g/cm^3). Therefore, in the laboratory reference frame, the dispersion is static at a volume fraction set by the fluid velocity and the volume fraction dependence of the settling velocity. At the superficial velocity of 63 μm/day set here the colloidal suspension is fully crystalline, i.e. at a volume fraction above 0.55.

The light scattering part of the apparatus is shown in Figure 1. An Argon ion laser operating at 488 nm wavelength is stabilized with a power controller that limits the peak-to-peak fluctuations to within 0.2% of the average intensity, allowing measurements of the intensity temporal autocorrelation function to below 10^{-4} of the baseline. The incident laser beam passes through the center of a cylindrical glass vat (32 cm diameter) filled with a hydrocarbon oil that approximately matches the index of the dispersion. The fluidized bed of PMMA particles is located at the center of the vat and aligned at the center of a goniometer. To ensemble average the intensities, as required for non-ergodic systems such as colloidal glasses or crystals [10], we translate the fluidized bed vertically and rotate independently about the axis, via stages driven by computerized DC servo motors.

The scattered light is detected at any desired angle by a photon multiplier tube (Hamamatsu H4730-01 PMT and Amplifier/Discriminator Assembly) through optics mounted on an arm that rotates with the goniometer. The detection optics consist of a lens that images the scattering volume to the photo cathode of the PMT and two apertures, the first (2 mm diameter) mounted immediately in front of the lens to limit the acceptance angle to 0.8° and the second (50 μm diameter) to define the scattering volume. The size of the latter compares with the speckle size of the scattered light. The signal is collected by a digital correlator [ALV 5000] which constructs the temporal autocorrelation function and computes the static intensity. To probe the structure factor at low angles, we use a CCD camera [GBC CCD-500E] to capture the intensity pattern of a screen glued to the outside of the vat.

The shear modulus and viscosity of the hard sphere dispersion are detected through so-called Bragg spectroscopy. A function generator produces a sinusoidal voltage to drive a speaker attached to the rotational stage holding the fluidized bed, thereby gently rotating it at a prescribed frequency and creating an oscillatory disturbance within the dispersion. When the amplitude of the oscillation is small relative to the inverse of the scattering wavevector, the scattered intensity fluctuates at the same frequency, and the ensemble averaged temporal autocorrelation function of the scattered intensity from the center of the bed indicates the amplitude of response. The rheological properties are then extracted by modelling the colloidal system as a linear viscoelastic solid.

RESULTS AND DISCUSSION

The scattering intensity pattern from the fluidized bed at low angles is shown in Figure 2 with the incident beam directed normal and into the photo but blocked by a vertical stop at the center. The Bragg scattering from the crystalline dispersion forms five symmetric rings on each side. We list the Bragg angles in Table 1 along with the

ratio of the scattering wavevector at the particular Bragg angles, q, to that of the first Bragg angle. For comparison columns 3 and 4 list the corresponding face-centered cubic (fcc) planes and the ratio of the reciprocal lattice vector G to that of the (1,1,1) plane, whereas column 5 lists the ratios for the randomly stacked hexagonal (rsh) planes.

Table 1: Comparison of Bragg angles with those expected for fcc and rsh crystals

Bragg angle [$^{\circ}$]	q/q_1	fcc planes	G/G_{111}(fcc)	G/G_{111}(rsh)
17.9	1	(1,1,1)	1	1
20.8	1.1604	(2,0,0)	1.154701	—
29.4	1.6311	(2,2,0)	1.632993	1.632993
34.6	1.9115	(3,1,1)	1.914854	1.914854
36.3	2.0023	(2,2,2)	2	2

The table indicates an fcc structure for the hard sphere crystal in the fluidized bed, since the ratios of the scattering wavevectors match all lines for the fcc crystal. However, the intensity of the second Bragg peak is much less than the first one, suggesting that some crystal grains may have rsh structures which contribute to the intensity of all but the second peak. Thus the structure observed may be a mixture of face-center-cubic and randomly stacked hexagonal crystallites. Assessing the relative amounts requires quantitative analysis of the intensities, which is now underway.

Proper interpretation of dynamic light scattering from colloidal crystals requires ensemble averaged temporal autocorrelation functions, since particles are localized in the vicinity of their lattice points. The scattered intensity has fixed and fluctuating components, so time averaging does not suffice. To solve this problem, we averaged autocorrelation functions measured at many different positions separated by 50 μm, the dimension of the scattering volume. Typical temporal autocorrelation functions averaged over 500 positions in Figure 3 exhibit the expected spread, e.g. about 4.2% at longer times as compared with $1/(500)^{1/2}=4.5\%$. Thus, in order to achieve accuracy better than 1%, we must measure autocorrelation function at 10,000 positions.

To relate these measurements to the dynamics of particles within the crystal, we adopt a simple model from solid state physics that considers only random motion about the lattice points with no correlation between different particles. This model leads to an autocorrelation function containing two terms. The first comprises the dynamic structure factor, reflecting the correlation of particle positions with the lattice site, and decays to zero at long times. The second is the self-dynamic structure factor, resulting from the polydispersity in the index of refraction of particles, and decaying to a finite value reflecting the limited volume available to each particle. Clearly the prediction conforms qualitatively to the observations. Quantitative fits of the functional form predicted to the observed autocorrelation functions should determine whether the model is sufficient and, if so, magnitudes of the short-time self diffusion coefficient and maximum mean square displacement for particles within the crystal. The former might then be compared with values for the metastable fluid phase at the same volume fraction and the latter with the maximum displacement expected for a crystal from the Lindemann criterion.

SUMMARY

In summary, we have assembled an instrument capable of measuring the structure, dynamics, and rheological properties of colloidal crystals in a homogeneous fluidized state. Preliminary experiments produced a hard sphere colloidal polycrystal with a mixture of face-centered cubic and random stacked hexagonal layer domains. Dynamic measurements confirm the need to ensemble average to obtain useful autocorrelation functions and suggest non-decaying fluctuations.

ACKNOWLEDGEMENTS

1. C.G. de Kruif, J.W. Jansen, and A. Vrij, *Physics of Complex and Supramolecular Fluids* (ed. S. Safran and N.A. Clark) Wiley, p. 315 (1986).

2. P.N. Pusey and W. van Megen, *Physics of Complex and Supramolecular Fluids* (ed. S. Safran and N.A. Clark) Wiley, p. 673 (1986); *Nature* **320** 340 (1986).

3. S.E. Paulin and B.J. Ackerson, *Phys. Rev. Lett.* **64** 2663 (1990).

4. P.N. Pusey, W. van Megen, P. Bartlett, B.J. Ackerson, J.G. Rarity, and S.M. Underwood, *Phys. Rev. Lett.* **63** 2753 (1989).

5. D.J.W. Aastuen, N.A. Clark, J.C. Swindal, and C.D. Muzney, *Phase Trans.* **21** 139 (1990); K. Schatzel and B.J. Ackerson, *Phys. Rev. Lett.* **68** 337 (1992).

6. P. Bartlett, R.H. Ottewill, and P.N. Pusey, *J. Chem. Phys.* **93** 1299 (1990).

7. W.B. Russel, D.A. Saville, and W.R. Schowalter, *Colloidal Dispersions* Cambridge, Chap 14 (1989).

8. J.W. Goodwin and R.H. Ottewill, J. *Chem. Soc. Far. Trans.* **87** 357 (1991).

9. L. Antl, J.W. Goodwin, R.D. Hill, R.H. Ottewill, S.M. Owens, and S. Papworth, *Colloids Surf.* **17** 67 (1986).

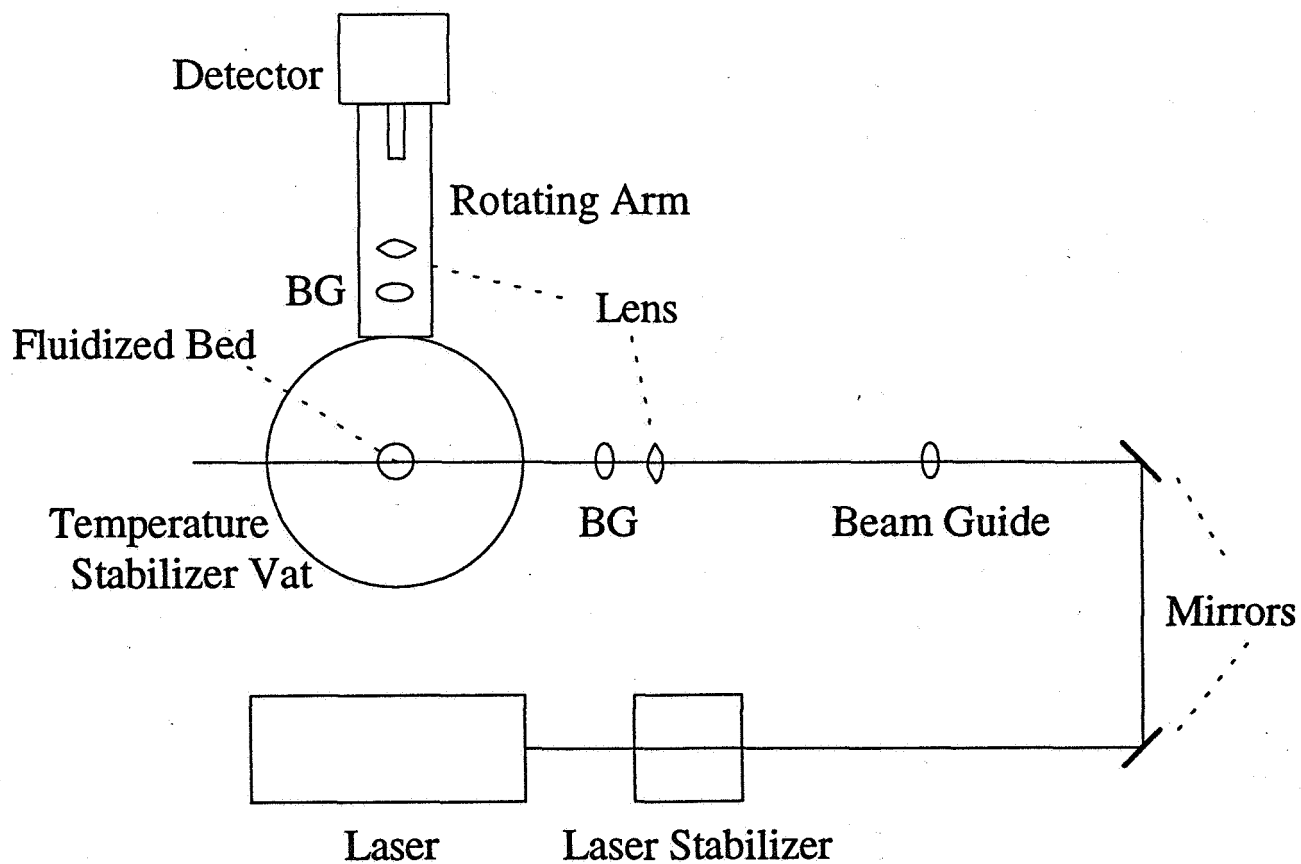10. P.N. Pusey and W. van Megen, *Physica A* **157** 705 (1989).

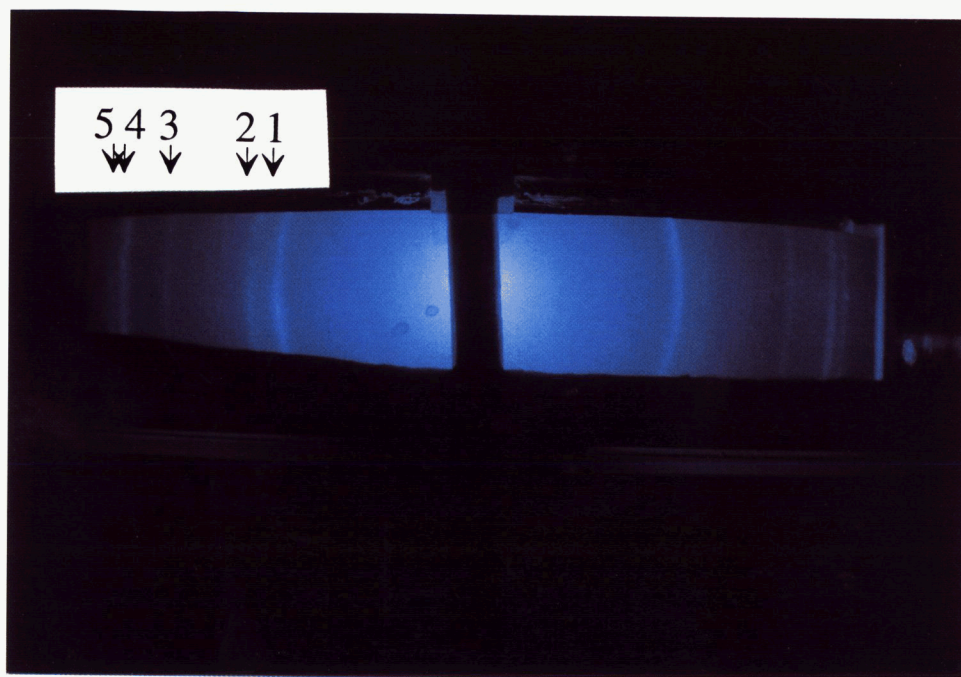Figure 1 - Light scattering apparatus

Figure 2 - Photograph of Bragg diffraction rings from dispersion of 1000 nm PMMA spheres in decalin/tetralin mixture projected onto screen attached to vat: 1 - 111, 2 - 200, 3 - 220, 4 - 311, 5 - 222.
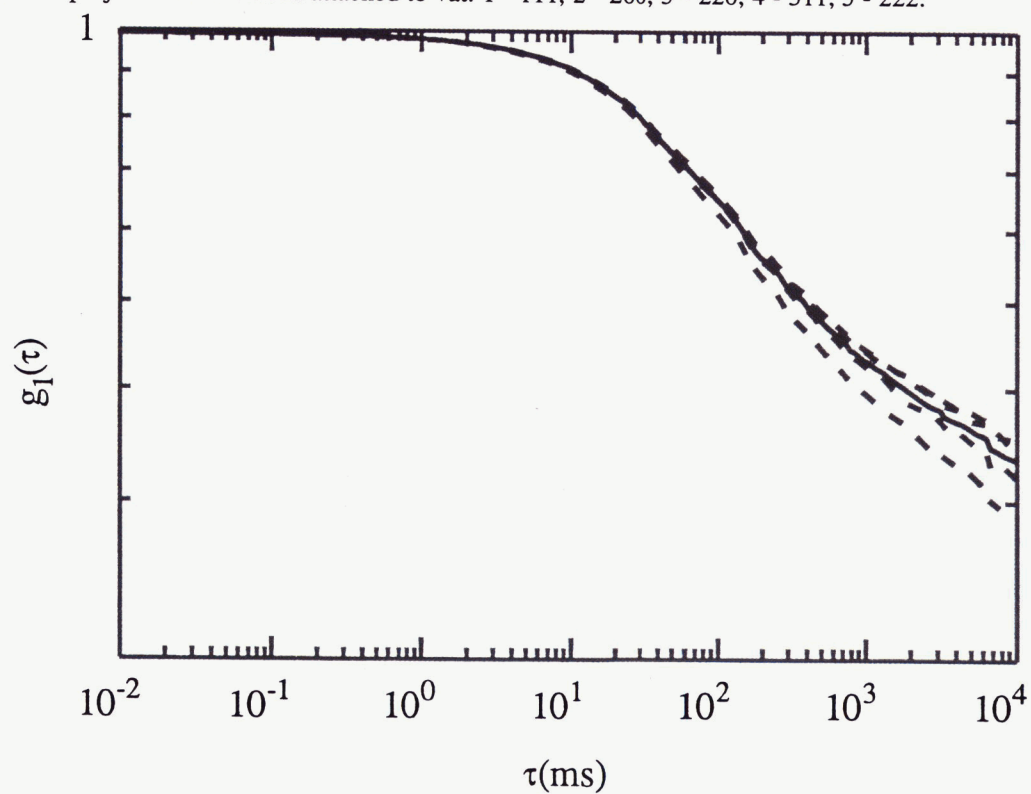

Figure 3 - Temporal autocorrelation function at 110° with 1000 nm PMMA spheres in decalin/tetralin mixture averaged over four different sets of 500 positions (- - -) and all 2000 positions (------).

MEASUREMENT OF RESISTANCE TO SOLUTE TRANSPORT ACROSS SURFACTANT-LADEN INTERFACES USING A FLUORESCENCE RECOVERY AFTER PHOTOBLEACHING (FRAP) TECHNIQUE

Edward P. Browne, Thierry Nivaggioli and T. Alan Hatton
Department of Chemical Engineering
Massachusetts Institute of Technology
Cambridge, MA 02139

ABSTRACT

A non-invasive Fluorescence Recovery After Photobleaching (FRAP) technique is under development to measure interfacial transport in two phase systems without disturbing the interface. The concentration profiles of a probe solute are measured in both phases as a function of time as the system recovers from a perturbation. The perturbation is caused by the irreversible bleaching of a predetermined region on both sides of the interface by an argon-ion laser, and the system relaxation is then monitored by a microscope-mounted CCD camera.

INTRODUCTION

Interfacial transport processes are important in areas as diverse as industrial and analytical separations, tertiary oil recovery, controlled and targeted release drug delivery, and cell membrane transport. However, the mechanism by which these processes takes place is still poorly understood. Solute transport across an interface is influenced by many forces, among them electrostatic, hydrophobic, fluid dynamic and steric interactions. To determine unambiguously the role played by each of these effects requires a reliable technique for the measurement of solute transport resistance under a variety of solution conditions. Unfortunately, to date, no method exists which is both reliable and unambiguous. Techniques which rely on fluid convection, such as the stirred cell [1-4] or the rotating diffusion cell [5], depend on detailed knowledge of the hydrodynamic conditions near the interface. However, such detailed knowledge is rarely available, particularly in surfactant-containing systems. Attempts have been made to eliminate this ambiguity through the use of purely diffusive systems [6, 7], in which transport resistance is measured by monitoring solute concentration profiles as they develop near an interface as a function of time. Most of these techniques suffer from the presence of a blind zone near the interface caused by the meniscus. This blind zone could not be reduced below 200 μm until the work of Aunins [8], in which a photolithography technique was used to produce a blind zone that was only 40 μm thick. An interferometric detection system was used to establish the concentration profiles. Unfortunately, this technique was not very robust, and its scope of applicability was somewhat limited owing to the high solute concentration required. The goal of the present work is to use the photolithography technique of Aunins in conjunction with a perturbation/detection system based on a Fluorescence Recovery After Photobleaching (FRAP) technique [9, 10] to measure resistances to solute interfacial transport unambiguously. FRAP exploits the loss of fluorescence exhibited by certain fluorophores when over-stimulated (photobleaching), so that a system, originally at equilibrium, can be perturbed by strong light and its recovery monitored as it relaxes to a new equilibrium, yielding information about the transport characteristics of the system.

EXPERIMENTAL

FRAP System

The Fluorescence Recovery After Photobleaching (FRAP) apparatus is shown in Figure 1. In a Video-FRAP experiment, an organic phase and a water phase are placed in a glasswalled cell (1). The system contains a fluorescent probe solute which partitions between the two phases. The cell is allowed to come to equilibrium. The cell is located at the object plane of an epi-illuminated microscope, and the dye molecules are excited by light at 488 nm from a 5W argon-ion laser. The beam splitter / attenuator (2) reduces the power of the laser beam by a factor of 10,000 through multiple partial reflections from four optical flats (3) when its internal shutter (4) is closed. A dichroic mirror (5) reflects the 488 nm-wavelength light onto the cell. The resulting fluorescence emission, being at a longer wavelength, passes through the dichroic mirror and is detected by a CCD camera (6) mounted on the microscope (7 and 8). The effectiveness of the dichroic mirror in differentiating between the excitation and emission wavelengths is enhanced by filters (9 and 10).

Before an experiment begins, the contents of the cell are at equilibrium. To start an experiment, the shutter (4) in the beamsplitter / attenuator opens for approximately 100 ms, exposing the contents of the cell to the laser beam at full power. This results in irreversible photobleaching of some of the fluorophore molecules i.e. the fluorophore no longer fluoresces. A mask (11) is used to define the region of the cell onto which the beam impinges. During photobleaching, the camera is protected by the microscope shutter (12). The recovery of fluorescence in the photobleached region is monitored as a function of time using a Data Translation Frame Grabber, revealing information about the mobility of the fluorescent molecules in each phase and, if the mask is designed to expose a much greater area of one phase than the other during photobleaching, the resistance to interphase transport. The operation of the Video-FRAP system is controlled through a National Instruments PC-based software package (Labview) and data acquisition board.

To obtain sensitive measurements of interfacial resistance, it is necessary to measure solute concentrations as close to the interface as possible. Because the cell walls are made of glass, which is hydrophilic, there would ordinarily be a meniscus between the aqueous and reversed micellar phases, which would distort the fluorescence emission image near the interface. To minimize the size of the meniscus, the surface of the glass cell wall is treated by a photolithography technique so that the lower part of the wall (corresponding to the water phase) is hydrophilic, and the upper part of the wall is hydrophobic. As a result, when the cell is filled appropriately, a 90° contact angle is obtained. Menisci as shallow as 25 μm have been obtained with this method.

DATA ANALYSIS

To obtain concentration profiles from the two-dimensional images of the fluorescence recovery that are stored in the frame grabber, the images are calibrated with an image taken before photobleaching, when all concentrations were known.

The two-dimensional unsteady state diffusion equation is solved using a Crank-Nicholson alternating-direction implicit finite difference scheme [11, 12], with the interfacial resistance, R, as a variable parameter which is introduced in the boundary conditions. The experimental interfacial resistance is obtained by finding the R value which results in the best fit of the diffusion equation to the experimental concentration profiles via a Newton-Raphson iteration scheme.

The diffusion coefficients of fluorophore in both the aqueous phase and the organic phase are measured directly in the diffusion cell.

PRELIMINARY RESULTS

Preliminary experiments were carried out with an aqueous phase consisting of 10 μM fluorescein (the probe solute) and 200 mM sodium chloride, and a reversed-micellar organic phase consisting of heptane with 200 mM AOT surfactant. The system was allowed to come to equilibrium, with the fluorescein distributing between the two phases. Photobleaching took place for 300 ms, and although the bleaching beam was somewhat ill-defined in these preliminary experiments, most of the photobleaching occurred in the aqueous phase.

Figure 2(a) shows the initial, post-bleach, two-dimensional concentration profile in false color. The concentrations have been normalized, so that a value of 1.0 (dark blue in figure 2(a)) represents no change in probe solute fluorescence between the pre-bleach image and the post-bleach image. The maximum photobleaching that occurred was 10%, represented by a normalized concentration of 0.9 (red in figure 2(a)).

The situation one minute after bleaching is shown in Figure 2(b). The system has started to relax from its immediate, post-bleach state, as seen by the false color image becoming less 'red'. At longer times, the image will eventually become blue, as the fluorescence intensity returns to its pre-bleach value.

Figure 3 shows the one-dimensional concentration profiles normal to the interface obtained by averaging the two-dimensional concentration fields. The data contain a large amount of noise, so it was not possible to obtain an interfacial resistance value for this preliminary experiment. However, the process of relaxation can clearly be seen in the aqueous phase, as the system returns to equilibrium.

FUTURE WORK

The system is currently being optimized to reduce noise in the fluorescence images. The first complete set of experiments will measure the rates of extraction and reextraction of fluorescein into and out of an AOT reversed-micellar phase in contact with an aqueous phase as a function of the aqueous ionic strength. This will illustrate the role charge interactions play in reversed micellar solubilization [2].

The sensitivity of the technique could be much improved by an increase in the amount of photobleaching. Unfortunately, buoyancy driven convection occurs at higher levels of photobleaching, which tends to mask the purely diffusive process. This restriction can, however, be removed by operating in a microgravity environment.

CONCLUSIONS

The apparatus is in the final stages of construction, and is currently being tested and its operational parameters optimized. Preliminary experiments indicate that this approach will provide a reliable technique for investigating solute transport in surfactant-containing systems free of the ambiguity that is inherent in convective systems, and that the performance of the system can be much enhanced by operation in a microgravity environment.

REFERENCES

1. Lewis, J.B., "The Mechanism of Solute Transport across Liquid-Liquid Interfaces . I. The Determination of Individual Mass Transfer Coefficients of Binary Systems." *Chemical Engineering Science,* **3** (1954), pp. 218-259.

2. Nitsch, W. and Plucinski, P., "Two-Phase Kinetics of Solubilization in Reversed Micelles" *Journal of Colloid and Interface Science,* **136** (1990), pp. 338-351.

3. Dungan, S.R., Bausch, T., Hatton, T.A., Plucinski, P., and Nitsch, W., "Interfacial Transport Processes in the Reversed Micellar Extraction of Proteins" *Journal of Colloid and Interface Science,* **145** (1991), pp. 33-49.

4. Plucinski, P. and Nitsch, W., "Mechanism of Mass Transfer between Aqueous Phase and Water-in-Oil Microemulsion" *Langmuir,* **10** (1994), pp. 371-376.

5. Albery, W.J., Choudhery, R.A., Atay, N.Z., and Robinson, B.H., "Rotating Diffusion Cell Studies of Microemulsion Kinetics" *Journal of the Chemical Society, Faraday Transactions I,* **83** (1987), pp. 2407-2419.

6. Ward, A.F.H. and Brooks, L.H., "Diffusion Across Interfaces" *Transactions of the Faraday Society,* **48** (1952), pp. 1124.

7. Chandrasekhar, S. and Hoelscher, H.E., "Mass Transfer Studies Across Liquid/Liquid Interfaces" *AIChE Journal,* **21** (1975), pp. 103.

8. Aunins, A.H., *Solute Transport Across Surfactant Laden Interfaces: Developement of a Novel Interferometric Technique for Measuring Interfacial Resistance*, Ph.D. Thesis, Massachusetts Institute of Technology, Cambridge MA, 1991.

9. Koppel, D.E., Axelrod, D., Schlessinger, J., Elson, E.L., and Webb, W.W., "Dynamics of Fluorescence Marker Concentration as a Probe of Mobility" *Biophysical Journal,* **16** (1976), pp. 1315-1329.

10. Wolf, D.E., *Designing, Building, and Using a Fluorescence Recovery after Photobleaching Instrument,* in *Methods in Cell Biology,* Academic Press: 1989, pp. 271-306.

11. Crank, J., *The Mathematics of Diffusion,* 2nd ed., London: Oxford University Press, 1975.

12. Gerald, C.F. and Wheatley, P.O., *Applied Numerical Analysis,* 3rd ed., Addison-Wesley, 1984.
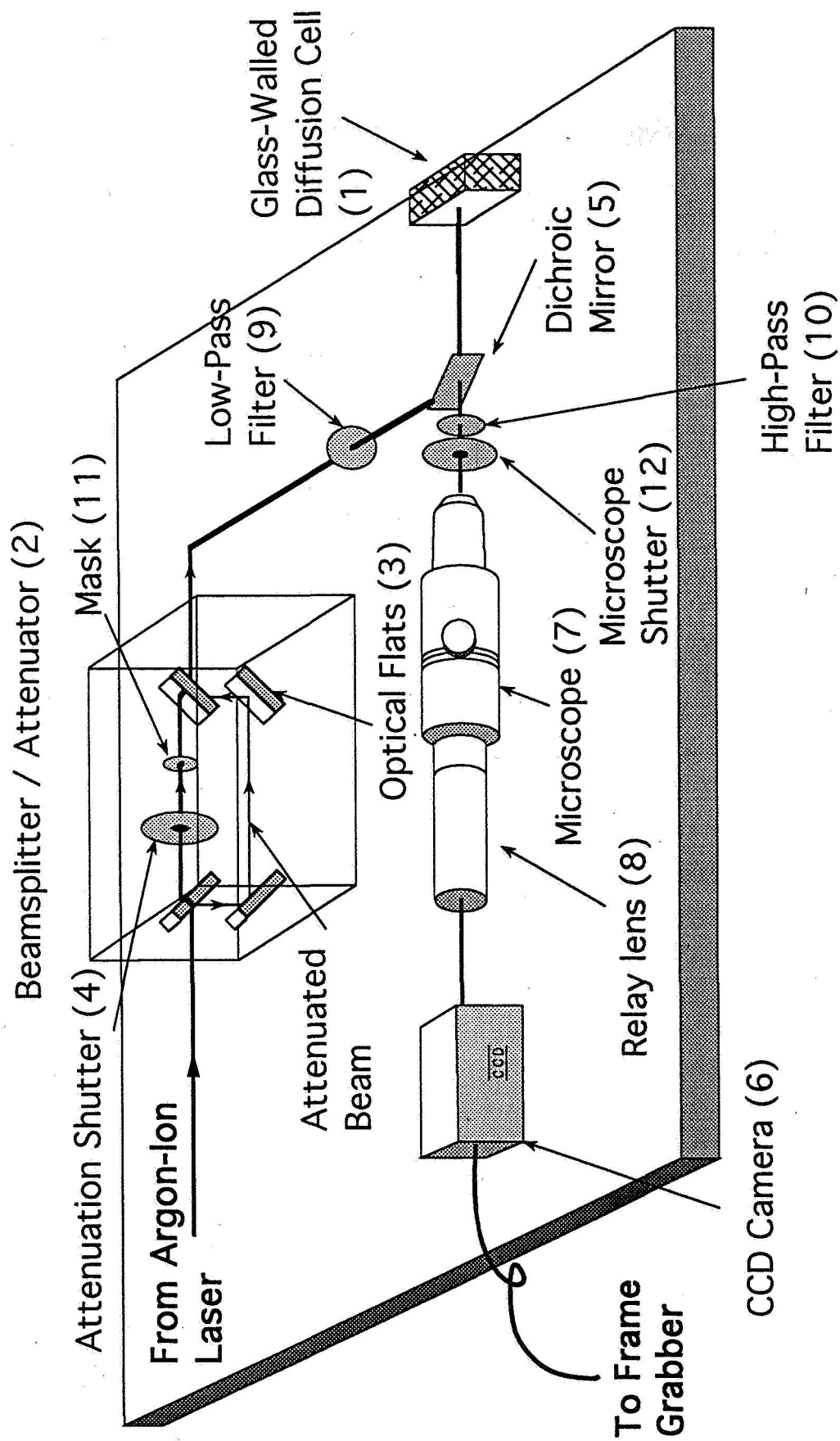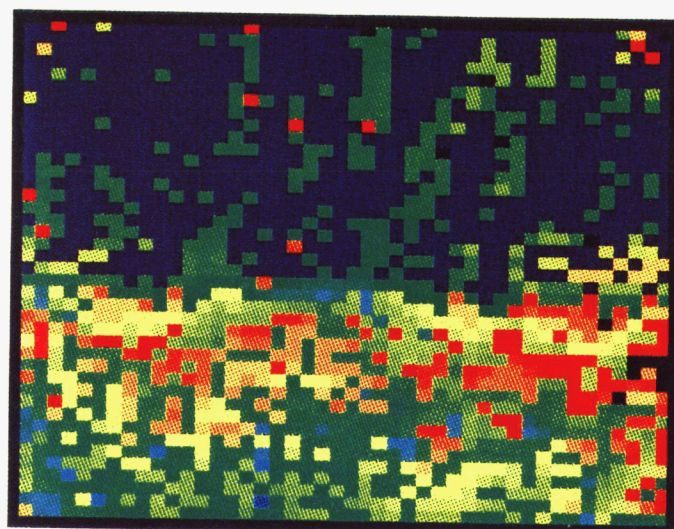
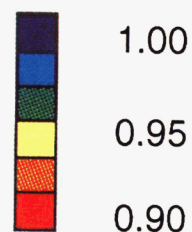Figure 1. Video-FRAP System

Figure 2(a)

t = 0 sec

Water Phase

Interface

Oil Phase

Figure 2(b)

t = 60 sec

Water Phase

Interface

Oil Phase

Normalised Concentration

1.00

0.95

0.90

Field of View: 1mm x 1mm

Figure 3

Normalised Concentration

1.05

1

0.95

0.9

0.85

Water Phase

Oil Phase

0 sec
20 sec
40 sec
60 sec

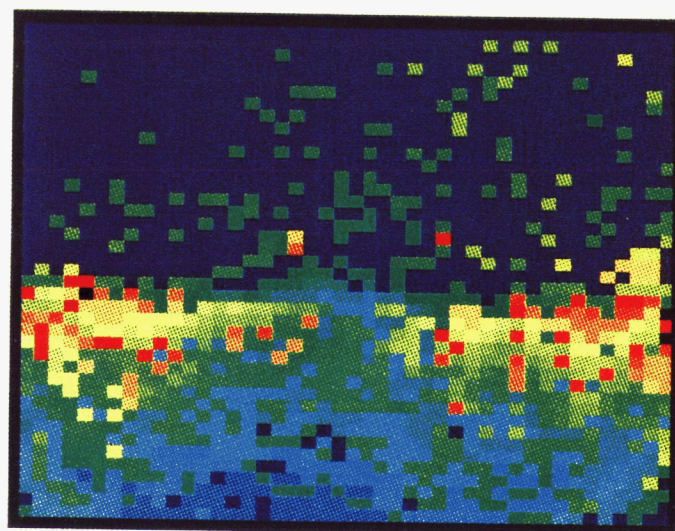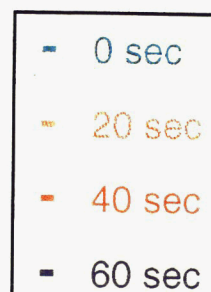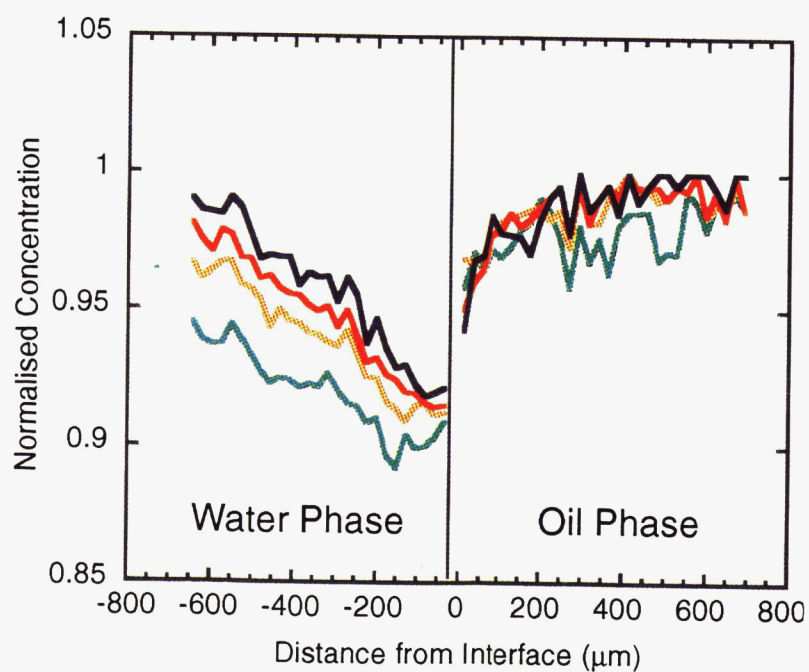-800 -600 -400 -200 0 200 400 600 800

Distance from Interface (μm)

352

NEW TECHNIQUES FOR DIFFUSING-WAVE SPECTROSCOPY

T.G. Mason[a,b] Hu Gang,[b] A.H. Krall[b] and D.A. Weitz[b]

a. Dept. of Physics, Princeton University, Princeton NJ 08544.
b. Exxon Research and Engineering Co., Rt. 22E Annandale, NJ 08801.

ABSTRACT

We present two new types of measurements that can be made with diffusing-wave spectroscopy, a form of dynamic light scattering that applies in the limit of strong multiple scattering. The first application is to measure the frequency-dependent linear viscoelastic moduli of complex fluids using light scattering. This is accomplished by measuring the mean square displacement of probe particles using DWS. Their response to thermal fluctuations is determined by the fluctuation-dissipation relation, and is controlled by the response of the surrounding complex fluid. This response can be described in terms of a memory function, which is directly related to the complex elastic modulus of the system. Thus by measuring the mean square displacement, we are able to determine the frequency dependent modulus. The second application is the measurement of shape fluctuations of scattering particles. This is achieved by generalizing the theory for DWS to incorporate the effects of amplitude fluctuations in the scattering intensity of the particles. We apply this new method to study the thermally induced fluctuations in the shape of spherical emulsion droplets whose geometry is controlled by surface tension.

A microgravity environment has significant potential benefits for a wide variety of scientific problems involving colloidal particles or other complex fluids, where sedimentation can play an important role. Several experiments are currently planned to exploit this environment. Laser light scattering is an important experimental technique for studying the physics of these complex fluids; as a result a laser light scattering apparatus is being constructed by NASA to allow measurements of different types to be made in space. This apparatus will allow the traditional light scattering techniques to be employed, including both static and dynamic light scattering. In addition, the apparatus will allow several ancillary measurements to be performed. Among the most important is the measurement of the rheological properties of the complex fluids being studied. Currently this measurements will be done by mechanically agitating the sample cell and measuring the response of the complex fluid. This will provide a measure of the complex, frequency-dependent linear viscoelastic modulus of the suspension, $G^*(\omega) = G'(\omega)+iG''(\omega)$. Here, the real part, $G'(\omega)$, reflects the energy storage or the elastic component of the modulus, while the imaginary part, $G''(\omega)$, reflects the viscous dissipation of the modulus. While these mechanical measurements of the modulus provide a direct measure of the viscoelastic response of the fluid, they are limited in the frequency range that is accessible. Moreover, since the primary function of the NASA apparatus is light scattering, a preferable method for measuring the visco-elastic response would be to use light scattering techniques.

In this paper, we discuss a new method for measuring the viscoelastic response of a complex fluid using solely light scattering methods. We discuss the use of diffusing-wave spectroscopy (DWS), which is form of dynamic light scattering applicable in the strongly multiple scattering limit[1,2]. Two new applications of DWS are presented. We first discuss the use of DWS, or more traditional dynamic light scattering techniques, to measure the frequency-dependent linear viscoelastic modulus of complex fluids. We also discuss the extension of DWS to include amplitude fluctuation due to the fluctuating shape of the scattering particles, and use this to measure the shape fluctuations of emulsion droplets, where surface tension controls the spherical shape of the particles.

We begin by presenting a novel method for measuring the linear viscoelastic properties of a complex fluid over an extended range of frequencies. We show that the response of the fluid to thermal fluctuations, as probed by the average motion of small particles dispersed within the fluid, provides a very close representation of the response of the bulk fluid to an imposed shear strain. The essential physics of this approach is that the bulk mechanical susceptibility of the fluid appropriately describes the microscopic viscoelastic forces acting on a small particle excited by the thermal stochastic forces which lead to Brownian motion. By describing the stochastic motion of the small probe particle with a Langevin equation generalized to include viscoelasticity and imposing energy equipartition using the fluctuation-dissipation theorem, the average particle motion, given by the mean square displacement, $\left\langle \Delta r^2(t) \right\rangle$, determines the time-dependent memory function, $\zeta(t)$, of both the surrounding and bulk complex fluid. This time-dependent memory function is proportional to the more commonly encountered stress relaxation modulus and contains the same information as $G^*(\omega)$. We use dynamic light scattering to measure $\left\langle \Delta r^2(t) \right\rangle$, and compare the $G^*(\omega)$ obtained with that measured directly by mechanical means using a rheometer.

We describe the motion of a small, neutrally buoyant particle dispersed in a complex fluid by means of a generalized Langevin equation,

$$m\dot{v}(t) = f_B(t) - \int_0^t \varsigma(t - \tau)v(\tau)d\tau \tag{1}$$

where m is the particle mass and $v(t)$ is the particle velocity. This equation expresses the balance of forces on the particle, relating the stochastic Brownian forces, $f_B(t)$, to the response of the surrounding fluid, which is described by a generalized time-dependent memory function, $\varsigma(t)$, and reflects the dependence of the properties of the material at time t on the behavior at previous times. A simplified form of this equation is commonly used to describe the motion of a particle in a purely dissipative viscous fluid; here we generalize it by using the memory function to describe the average, effective-medium response of a complex fluid that can also store energy. Allowing the medium to store energy profoundly changes the temporal correlation of stochastic forces acting on the particle at thermal equilibrium. Because energy from thermal fluctuations can be stored in the medium over time scales determined by the memory function, the dissipation required to maintain thermal equilibrium also occurs over these time scales. As a result, the stochastic forces acting on the particle are correlated over finite rather than infinitesimal time scales to prevent an unphysical energy buildup. Thus, the fluctuation-dissipation theorem differs from the commonly encountered delta-function correlation of a purely viscous fluid, and here takes the form[3]:

$$\langle f_B(0)f_B(t)\rangle = k_B T\varsigma(t) \tag{2}$$

where the coefficient ensures thermal equilibrium, with k_B Boltzmann's constant and T the temperature.

By taking the Laplace transform of Eq. (1), and using Eq. (2), the viscoelastic memory function can be related to the velocity autocorrelation function, and, hence, the mean square displacement of the particle. We assume that the Laplace transform of the microscopic memory function is proportional to the bulk frequency-dependent viscosity, $\tilde{\eta}(s) = \tilde{\varsigma}(s)/6\pi a$, where s represents the frequency in the Laplace domain. We choose the coefficient to ensure the correct Stokes drag on a particle of radius, a, in a purely viscous fluid, recognizing that this coefficient may differ somewhat in describing the behavior of a particle in a viscoelastic fluid. The frequency-dependent shear modulus is directly related to the viscosity by $\tilde{G}(s) = s\tilde{\eta}(s)$, and hence to the mean square displacement, $\langle\Delta\tilde{r}^2(s)\rangle$:

$$\tilde{G}(s) = \frac{s}{6\pi a}\left[\frac{6k_B T}{s^2\langle\Delta\tilde{r}^2(s)\rangle} - ms\right] \tag{3}$$

The terms within the brackets come from the solution of the Langevin equation for the memory function, $\tilde{\varsigma}(s)$; the first captures the thermal fluctuation-dissipation in the medium surrounding the particle, while the second is due to the particle's inertia. In most complex fluids, the inertial term is negligible compared to the fluctuation-dissipation term, except at very high frequencies. Fitting the optically measured $\tilde{G}(s)$ with an appropriate functional form, the complex, frequency-dependent shear modulus can be determined using analytic continuation by setting $s = i\omega$, and identifying $G'(\omega)$ and $G''(\omega)$ as the real and imaginary parts. Provided the functional form describes $\tilde{G}(s)$ over all measured frequencies, the Kramers-Kronig relationship will be satisfied over the measured range of frequencies. The complete procedure establishes a very general relationship between the mean square displacement of suspended particles and the bulk rheological properties of the complex fluid surrounding them.

To test the applicability of this scheme, we use diffusing-wave spectroscopy to determine the mean square displacement of the particles in a concentrated suspension of silica particles of relatively uniform radius, $a = 0.21$ μm, suspended in ethylene glycol. These particles behave essentially as hard spheres. Their volume fraction was increased by centrifugation to $\phi \approx 0.56$, quenching in disorder, to form an isotropic hard sphere glass. Diffusing-wave spectroscopy was used in the transmission geometry to measure the correlation function for a 4-mm thick sample, shown in Fig. 1; characteristic of a colloidal hard sphere glass, it exhibits an initial, rapid decay to a plateau value, followed by a final decay at longer times. The particles are relatively small, so that DWS is slightly sensitive to collective motion; nevertheless to a good approximation the correlation function can be inverted to obtain the mean square displacement of the particles. This requires knowledge of the transport mean free path of the light, l^*, which was obtained from static transmission measurements. The mean square displacement obtained from the correlation function is shown in Fig. 2. The linear increase at the shortest times reflects the initial diffusive motion of the particles; at longer times their motion is constrained by the local cage structure of the colloidal glass. The decay in the correlation function at the longest times can not be simply interpreted as a mean square displacement of individual particles setting the upper bound on the data accessible.

We numerically calculate the Laplace transform of the mean square displacement, and use Eq. (3) to determine $\tilde{G}(s)$, which is shown by the open points in Fig. 3. The accuracy of the Laplace transform is limited at the shortest and the longest time scales because of the limits of the available data. Nevertheless, the data exhibit

several very general features that characterize $\tilde{G}(s)$. The region having relatively low slope at lower frequencies indicates energy storage and hence a range where the real component of the complex modulus dominates. The region having nearly unity slope at higher frequencies indicates viscous dissipation, and hence a range where the imaginary component of the complex modulus dominates. This is very generally true of the data for $\tilde{G}(s)$; regions of small slope indicate that the elastic component of the modulus dominates, while regions of near-unity slope indicate that the viscous component dominates; the deviations from these slopes reflect contributions from both components.

To obtain the real and imaginary parts of the complex modulus, the frequency-dependent magnitude given by $\tilde{G}(i\omega)\tilde{G}(-i\omega) = \left|G^*(\omega)\right|^2$ can be fit using a superposition of complex moduli which satisfy the Kramers-Kronig relationship and have a single Maxwellian relaxation time. Rather than follow this more general procedure, we instead use our physical intuition about the behavior expected for a colloidal hard sphere glass to determine $\tilde{G}(s)$. We include a constant to account for the elasticity at low frequencies; a term proportional to $s^{0.3}$ to account for the behavior of the plateau, as predicted by mode coupling theories[4]; a term proportional to $s^{0.5}$ to account for the predicted asymptotic high frequency elastic modulus of hard spheres [5]; and a term proportional to s to account for the high frequency viscous component. A fit to a sum of these terms yields the solid line in Fig. 3. The real and imaginary components of $G^*(\omega)$ can then be calculated directly. Due to the form of $\tilde{G}(s)$, these do not satisfy Kramers-Kronig at low frequencies, but they do properly predict the moduli within the limits of the measured data.

To compare the elastic moduli calculated from the light scattering data with those determined directly by an oscillatory mechanical measurement, we use a controlled strain rheometer with a double-wall Couette sample cell geometry. A small, sinusoidal strain was applied and the in and out of phase components of the resultant stress were determined as the frequency was varied. The amplitude of the strain was maintained well below 1% to ensure that the data were obtained in the linear regime; this was verified by varying the strain amplitude. The upper frequency was limited by the motor's ability to produce a reliable sinusoidal strain, while the lower frequency was limited by the sensitivity of the torque transducer. The resultant real and imaginary components of the complex modulus are shown in Fig. 4. The dashed lines show the values of $G'(\omega)$ and $G''(\omega)$ obtained from the light scattering data. Remarkably good agreement is found, except for the loss modulus at the lowest frequencies. The light scattering data represent the overall trend of the rheological data quite well, particularly for the larger storage modulus.

These results clearly illustrate the possibility of using light scattering methods to determine the visco-elastic response of a suspension of hard spheres. We have also successfully tested the technique on very different forms of complex fluids, including polymer solutions and concentrated emulsions; in all cases tried the results are in good agreement with the mechanical measurements. The essential physics of this technique relies on the equivalence of the frequency-dependence of the microscopic memory function which describes the response of a probe particle in the complex fluid and the macroscopic complex viscoelasticity of the complex fluid. Provided particle inertia can be ignored and the viscoelastic coupling between neighboring particles varies as q^2, the complete equations of motion for a lattice of interacting particles can be reduced on average to a single particle equation of motion like the generalized Langevin equation having a memory function which describes the average bulk dynamics inherent in the microscopic coupling. This equivalence is perhaps somewhat surprising; the motion of a probe particle, as probed by light scattering normally reflects relatively large wavevector, q, behavior. Moreover, light scattering typically probes the longitudinal response of a system. By contrast, the elastic modulus of a material reflects the transverse response of the material in the limit of $q \rightarrow 0$. However, the mean square displacement does couple to shear modes; this is certainly true in the limit of a simple viscous fluid, where the shear viscosity determines the particle's motion. Thus, by analogy, we expect the shear elasticity of a complex fluid to determine the mean square displacement of a probe particle. However, the elasticity is typically measured by applying a uniform strain across the material; this is not the case for a small probe particle. As a result, the flow pattern of the viscoelastic fluid around the particle may differ significantly from the case of a simple viscous fluid; this will modify the coefficient relating the viscosity to the memory function, and may even make it frequency dependent. Thus, this method may not provide quantitatively exact measures of the elastic moduli; nevertheless, the overall trends are captured, and, as shown by our results, the agreement is surprisingly good.

Perhaps most importantly, this method provides a measure of the elastic moduli over a much broader range of frequencies than is obtained with mechanical measurements. Moreover, it provides a convenient method to relate the energy storage and loss due to strain to the microscopic mean square displacement of the particles in the suspension. These two advantages can provide considerable new insight into the underlying physics of the complex fluid. For example, for the hard sphere suspension, the plateau in $\left\langle \Delta r^2(t) \right\rangle$ is known to reflect the quenched disorder of a colloidal glass; the particle can diffuse freely at very short length scales until it reaches the cage formed by the

neighboring particles. Then the particle motion is restricted until the cage decays at much longer time scales. This behavior is accounted for theoretically by mode coupling theory (MCT) [4,6]. Our results indicate that the cage effects also play an important role in the rheological behavior of a hard sphere suspension; the existence of the cage leads to an additional mechanism for energy storage; presumably the strain distorts the shape of the cage, allowing energy to be stored, and causing the real part of the complex modulus to dominate. Mode coupling theory accounts for this behavior at high frequencies and predicts a β-relaxation contribution proportional to $s^{0.3}$ in addition to a constant nonergodicity parameter which characterizes the low frequency plateau elasticity. This $s^{0.3}$ component improves our fit to the transformed light scattering data, and directly contributes to the frequency dependence of the storage modulus. In fact, the predictions of MCT can be used to better describe the behavior of the loss modulus at lower frequencies. The rise in $G''(\omega)$ measured mechanically suggests an additional decay process at lower frequencies; MCT predicts that this α-relaxation process, or von Schweidler decay, results from the ultimate cage breakup at long times, and provides a functional form to describe it, suggesting an additional term proportional to $s^{-0.55}$ in $\tilde{G}(s)$. Subtracting this α-decay term leads to much better agreement at low frequencies between $G''(\omega)$ obtained from light scattering and that measured rheologically, as shown by the solid line in Fig. 4.

The second new application of DWS discussed here is the generalization of the theory for the technique to include amplitude fluctuations of the scattering particles. We use this scattering method to study the thermally driven shape fluctuations of monodisperse emulsion droplets, and to determine the effects of increasing volume fraction on the fluctuations. The thermally induced increase in the surface area of a fluid droplet is $\Delta R^2 \sim k_B T/\Gamma$, where Γ is the surface tension. For a typical surface tension of 10 dynes/cm, this corresponds to an increased area of only about 30 Å^2; for a 1 μm diameter droplet, this represents a change in the radius of less than 0.1%. The relaxation time, τ, of these fluctuation is also very rapid; it is determined by the viscosity of the two fluids. If the viscosity of the droplet is much greater than that of the continuous phase, the relaxation time is $\tau \sim R\eta/\Gamma$; for $\eta = 0.1$ P and $R \approx 1$ μm, $\tau \approx 10^{-6}$ sec. The combination of the very short time scale and the very small amplitude of the thermal fluctuations of emulsion droplets have, to date, precluded their observation.

Our samples are emulsions of silicone oil in water, stabilized with sodium dodecylsulphate, and purified using the technique of fractionated crystallization to yield highly monodisperse droplets with a radius of $R = 1.4$ μm[7]. The surface tension of the interfaces is measured to be 9.8 dynes/cm. We perform our DWS measurements in the transmission geometry using an expanded beam from an Ar$^+$ laser, which gives $k_0 = 16.3$ μm^{-1} for the incident wavevector in water. The detected light is collected from a point on the exit side of the 5-mm-thick sample cell. The transport mean free path, l^*, is determined independently by a static transmission measurement [2], allowing the correlation function to be inverted to determine the dynamics of the individual emulsion droplets [8].

We might expect the dynamics of emulsion droplets to be the same as those of hard spheres. This is indeed the case for an emulsion made of a high viscosity oil, $\eta = 1000$ cP. This is illustrated in Fig. 5, where the open circles represent $\left\langle \Delta r^2(t) \right\rangle$, the mean square displacement of an individual droplet. The data follow the shape predicted for hard spheres, shown by the solid line. By contrast, an emulsion made from a much lower viscosity oil, $\eta = 12$ cP, exhibits distinct additional dynamics, as shown for $\phi = 0.35$ by the solid circles in Fig. 5. At early times, the data are significantly higher than those expected for solid spheres; at later times the data merge. Similar behavior is observed for all ϕ. These additional dynamics result from the shape fluctuations; for the higher η, the relaxation time is so long that any shape fluctuations are masked by the large displacements that occur during τ.

To quantitatively describe these new dynamics, we must generalize the formalism for DWS to include fluctuations in the scattering *amplitude*, in addition to the phase fluctuations which result from translational motion. The analysis of the correlation function measured by DWS entails the calculation of the contribution of diffusive light paths comprised of a large number of scattering events; these are all represented by an angle-averaged scattering event [2]. Thus, to include the amplitude fluctuations, we write the correlation function for this q-averaged, scattering event as

$$ g_1(t) = \frac{\left\langle b^*(q,t)b(q,0) \right\rangle_q}{\left\langle b^*(q,0)b(q,0) \right\rangle_q} \left\langle \exp\{-i\bar{q}\cdot\Delta\bar{r}(t)\} \right\rangle_q . \tag{4} $$

Here, the time dependent scattering amplitude is $b(q,t)$, and the brackets with the subscript q denote an ensemble and q-average. We assume that the amplitude fluctuations are independent of the translational motion of the droplets, and we neglect the effects of correlations between the particles [9]. The amplitude fluctuations contribute an additional correlation function which is assumed to consist of a sum of a constant portion and a much smaller fluctuating portion. Performing the q-average,

356

$$g_1(t) = \left[\frac{\sigma_0 + \Delta\sigma(t)}{\sigma_0 + \Delta\sigma(0)}\right] \exp\left\{-\frac{k_0^2 l}{3l^*}\langle\Delta r^2(t)\rangle\right\}, \tag{5}$$

where σ_0 is the total cross section and $\Delta\sigma(t)$ is the correlation function of the fluctuating portion of $b(q,t)$, ensemble and q-averaged. We have also used the relationship, $\langle q^2\rangle_q = k_0^2 l/2l^*$, where l is the scattering mean free path [10].

To calculate the correlation function for a diffusive path of length s, consisting of $n = s/l$ scattering events, we take the product of Eq. (5) n times [2]. Since $\Delta\sigma(t)\ll\sigma_0$, the first term can be approximated as an exponential, $\exp\{(\Delta\sigma(t)-\Delta\sigma(0))/\sigma_0\}$; this ensures that the contribution of a single diffusive path is still linear in s, and allows the standard DWS analysis to be retained. Thus, the total DWS correlation function is a sum over the contributions of all paths, weighted by the probability that a photon follows the path, $P(s)$:

$$g_1(t) = \int P(s)\exp\left\{-\frac{sk_0^2}{3l^*}\left[\langle\Delta r^2(t)\rangle + \frac{3l^*}{lk_0^2}\frac{\Delta\sigma(0)-\Delta\sigma(t)}{\sigma_o}\right]\right\}ds. \tag{6}$$

Since $P(s)$ is known [2], this equation can be solved in exactly the same manner as done for DWS from solid particles. The effects of the amplitude fluctuations are contained in the second term in the square brackets. It is clear from Eq. (6) that DWS probes the relative fluctuations of the cross section; like $\langle\Delta r^2(t)\rangle$ their contribution increases from zero at $t=0$ but saturates at long times. It is also clear why very small fluctuations can be detected; the signal arises from the sum of n independent amplitude fluctuations. These minute fluctuations would not be detectable without the advantage of the multiple scattering.

We note that this derivation is independent of the nature of the amplitude fluctuations; not only shape fluctuations, but other phenomena, such as rotational motion of aspherical particles can also result in a similar contribution. Moreover, the DWS data can be inverted, and the translational and amplitude contributions can be separated. We do this here by subtracting the translational motion; the full effects of the hydrodynamic interactions are included by using the scaling form which describes the data for solid spheres [8]. We plot $R^2\Delta\sigma(t)/\sigma_0$ for $\phi = 0.35$ in Fig. 6; we multiply the normalized fluctuating cross section by R^2 to give the correlation function of the fluctuations of the droplet radius. We note that the data exhibit a distinctly non-exponential decay.

Similar behavior is found for all other droplet volume fractions. Surprisingly, the shape of the correlation function is independent of ϕ; all the data can be scaled onto a single master curve. This enables us to determine the ϕ-dependence of the shape fluctuations. We find that the characteristic frequency of the decay decreases approximately linearly with increasing volume fraction, as shown by the open triangles in Fig. 6. By contrast, we find that the amplitude of the shape fluctuations increase dramatically with ϕ; this is shown by the solid circles in Fig. 6.

To quantitatively describe the correlation function of the fluctuating shape, we expand the instantaneous radius of the drop in spherical harmonics [11]. Each independent deformation mode creates an excess area given by $k_BT/2\Gamma$. Together with the conservation of volume, this condition determines the amplitude of the expansion coefficients. Each mode relaxes independently with an exponential decay rate, ω_l, that must be calculated in the overdamped, or low Reynolds number, limit [12]. We obtain

$$\Delta\sigma(t) = \frac{k_BT}{4\pi\Gamma R^2}\sum_{l=2}\frac{2l+1}{l(l+1)-2}g_l\exp(-\omega_l t), \tag{7}$$

with

$$\omega_l = \frac{l(l+2)(2l+1)}{2(2l^2+4l+3)}\frac{\Gamma}{\eta R}. \tag{8}$$

In general, ω_l depends on the viscosities of both fluids [13]; here we have assumed that the viscosity of the oil is much greater than that of the water. Note that asymptotically $\omega_l\sim l$, reflecting the fact that the dynamics are driven by surface tension; by contrast, $\omega_l\sim l^3$ when the dynamics are driven by the interfacial rigidity [11]. The cross section for each mode is calculated within the Rayleigh-Gans (RG) approximation [14],

$$g_l = \pi\int_0^\pi\sin\theta(1+\cos^2\theta)[3j_l(x)]^2 d\theta, \tag{9}$$

where $x = 2k_0R\sin(\theta/2)$, and where we have omitted an optical constant which is canceled in the normalization by σ_0. The coefficients, g_l, depend only on k_0R, and become negligible when $l\gg k_0R$, since the length scale of the features described by such modes is much smaller than the wavelength of the radiation. This sets the upper bound to the expansion; we find that the series converges for $l\approx 20$. Because of their large mismatch in index of refraction, Mie theory, suitably generalized to treat non-spherical scatterers, should be used. However, the average cross section

calculated within the RG approximation differs by less than 0.5% from that calculated using Mie theory. Thus, we conclude that the RG approximation is sufficiently accurate.

These expressions apply only to an isolated droplet. However, since the functional form of our data is independent of ϕ, we can use them to describe all the data by allowing both the characteristic frequency and the amplitude to vary. The solid line through the data in Fig. 6 illustrates the fit for $\phi=0.35$. Excellent agreement is obtained. The non-exponential decay clearly reflects the contribution of the different modes. Quantitative agreement between the theory and the experiment should be obtained when the ϕ-dependent characteristic frequency, $\omega(\phi)$, and amplitude, $\Delta\sigma(\phi)$, are extrapolated to zero volume fraction. Our extrapolated value of $\omega(\phi)$ is identical to the predicted value of $\Gamma/\eta R = 1.2$ MHz. Similarly, the extrapolated value of the amplitude ratio $R^2\Delta\sigma(0)/\sigma_0$ is 65 Å^2, in good agreement with the predicted value of $(k_BT/4\pi\Gamma\sigma_0)\Sigma(2l+1)g_l/(l(l+1)-2) = 52$ Å^2. The remaining discrepancy may reflect the error introduced by the RG approximation.

The ϕ-dependence of both the frequency and the amplitude must reflect the consequences of the interactions between the droplets, and these are not, as yet, well understood theoretically. The normalized characteristic frequency is well represented by a linear behavior, $\omega(\phi)/\omega(0)=1-0.78\phi$. The frequency depends only on the surface tension, R, and the viscosities of the two liquids; it is unlikely that Γ changes with ϕ, so that the most likely origin of this behavior is the ϕ-dependence of the effective viscosity of the emulsion. A similar linear form was recently predicted for the $l=2$ modes, but the predicted coefficient is 1.4 [15]. However, this theory was restricted to the case of equal viscosities of the oil and water, which may account for the discrepancy.

The pronounced ϕ-dependence of the amplitude of the shape fluctuations is more surprising. This may reflect the effects of collisions between the droplets, which become increasingly likely as ϕ increases; because the droplets are flexible, these collisions may result in additional deformations. We model the effects of collisions by introducing a contribution to the amplitude proportional to the fraction of the droplets that, at any instant, are colliding with a neighbor. This fraction we estimate as $\phi g(2,\phi)$, where $g(2,\phi)$ is the pair correlation function at contact. The dashed line through the data in Fig. 6 is a fit of $\Delta\sigma(\phi)/\Delta\sigma(0)$ to the functional form $1+C\phi g(2,\phi)$ with $g(2,\phi)=(1-\phi/2)/(1-\phi)^3$ as holds for hard spheres [16]. Good agreement is found with $C=1.7$, suggesting that colliding droplets deform an extra amount that is about 1.7 times the deformation exhibited by an isolated droplet. More generally, it should be possible to regard these increased shape fluctuations as the consequence of the osmotic pressure of flexible spheres. The expression $1+C\phi g(2,\phi)$, with $C=4$ and $g(2,\phi)$ as given above, is in fact the ratio of the full osmotic pressure of a hard-sphere suspension to the kinetic part nk_BT, where n is the number density [16]. This observation suggests that $\Delta\sigma(\phi)/\Delta\sigma(0)$ may be related to the reduced osmotic pressure of the flexible droplets.

The results presented here are two extensions of DWS. Amplitude fluctuations can arise from many phenomena in addition to the shape fluctuations presented here; for example, rotational diffusion of aspherical particles will also lead to similar effects, and the theory presented here should be applicable. The ability to measure the linear viscoelastic modulus optically enables its determination over a much broader frequency range, without mechanical motion. This could be particularly beneficial for experiments studying complex fluids in microgravity.

We gratefully acknowledge very useful discussions with T. Lubensky, R. Klein, W. Russel, W. Graessley, J. Bibette, S. Milner and W. Cai.

REFERENCES:
1. Maret, G. and Wolf, P., Z. Phys. B65, 409 (1987).
2. Pine, D.J., Weitz, D.A., Chaikin, P.M. and Herbolzheimer, E., Phys. Rev. Lett. 60, 1134 (1988).
3. Chaikin, P.M. and Lubensky, T., Principles of Condensed Matter Physics, (Cambridge University, Cambridge, 1994).
4. Gotz, W. and Sjogren, L., Phys. Rev. A43, 5442 (1991).
5. van der Werff, J., de Kruif, C., Blom, C. and Mellma, J., Phys. Rev. A39, 795 (1989).
6. van Megen, W. and Pusey, P.N., Phys. Rev. A43, 5429 (1991).
7. Bibette, J., J. Coll. Interface Sci. 147, 474 (1991).
8. Zhu, J.X., Durian, D.J., Muller, J., Weitz, D.A. and Pine, D.J., Phys. Rev. Lett. 68, 2559 (1992).
9. Weitz, D.A., Zhu, J.X., Durian, D.J., Gang, H. and Pine, D.J., Physica Scripta T49, 610 (1993).
10. Wolf, P.E., Maret, G., Akkermans, E. and Maynard, R., J. Phys. (Paris) 49, 63 (1988).
11. Milner, S.T. and Safran, S.A., Phys. Rev. A36, 4371 (1987).
12. Cox, R.G., J. Fluid Mech. 37, 601 (1969).
13. Choi, S.J. and Schowalter, W.R., Physics of Fluids 18, 420 (1974).
14. Huang, J.S., Milner, S.T., Farago, B. and Richter, D., Phys. Rev. Lett. 59, 2600 (1987).
15. Schwartz, M. and Edwards, S.F., Physica A 167, 589 (1990).
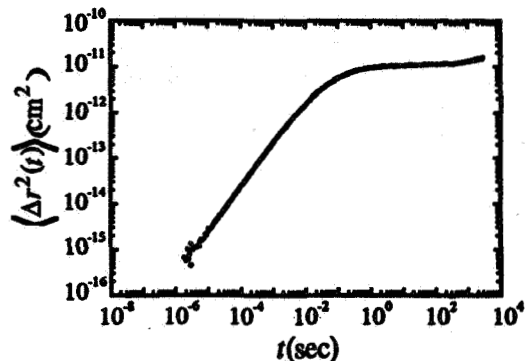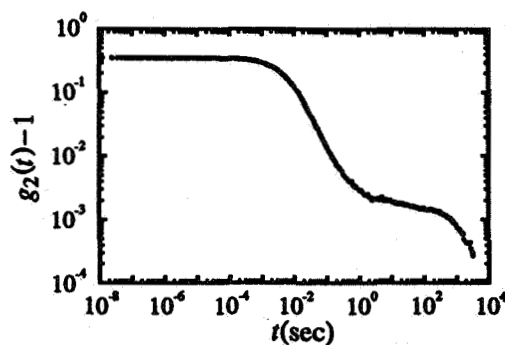16. Brady, J.F., J. Phys. Chem. 99, 567 (1993).

Fig. 1   (LEFT) DWS autocorrelation function for a suspension of hard sphere colloids at $\phi \approx 0.56$.
Fig. 2   (RIGHT) Mean square displacement of hard spheres determined from the data in Fig. 1. At early times the particles diffuse; at later times the particles are trapped in cages formed by the neighboring particles.
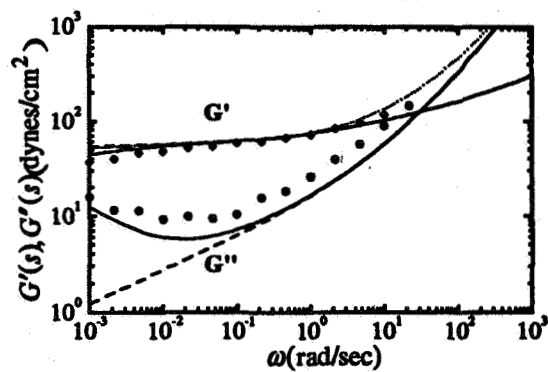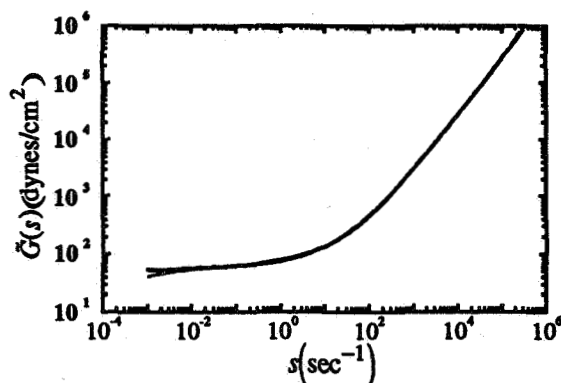

Fig. 3   (LEFT) Laplace transform of the complex modulus, $\tilde{G}(s)$, determined from the mean square displacement, shown in Fig. 2, for hard sphere colloids.
Fig. 4   (RIGHT) Comparison of the complex moduli for hard sphere colloids determined with light scattering (solid lines) and with a rheometer (points). The dashed line does not include a decay at longer time; the solid line does. The light scattering data are determined from the $\tilde{G}(s)$ shown in Fig. 3.
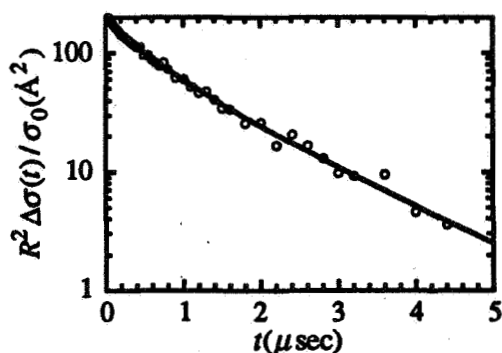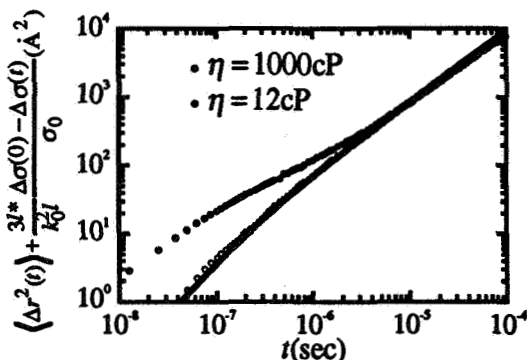
Fig. 6.   (LEFT) Inverted correlation functions of monodisperse emulsions. The data are the sum of the mean square displacement and a term related to the correlation function of the fluctuating scattering amplitude. The solid points are for an emulsion with an oil viscosity of 12 cP, while the open points are for an emulsion with an oil viscosity of 1000 cP. The solid line is the theoretical prediction for rigid spheres.
Fig. 6.   Correlation function of the radius fluctuations of an emulsion with $\phi = 0.35$, compared with theory.
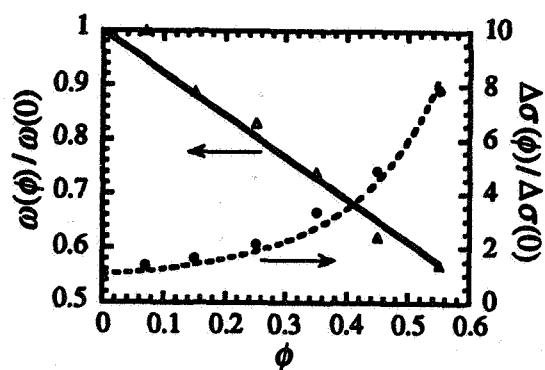
Fig. 7. The ϕ-dependence of the characteristic frequency (open triangles) and the fluctuating amplitude (solid circles). Both quantities have been reduced by their extrapolations to zero volume fraction. The solid line is a fit to a linear decay, with a coefficient of 0.78; the dashed line is a fit to a simple model which attempts to include the effects of interactions between the droplets.

Biological Colloids
&
Elctrohydrodynamics

ELECTROHYDRODYNAMIC DEFORMATION AND INTERACTION
OF A PAIR OF EMULSION DROPS

J. C. Baygents
Department of Chemical Engineering
The University of Arizona
Tucson, AZ 85721

ABSTRACT

The response of a pair of emulsion drops to the imposition of a uniform electric field is examined. The case studied is that of equal-sized drops whose line of centers is parallel to the axis of the applied field. A new boundary integral solution to the governing equations of the leaky dielectric model is developed; the formulation accounts for the electrostatic and hydrodynamic interactions between the drops, as well as their deformations. Numerical calculations show that, after an initial transient during which the drops primarily deform, the pair drift slowly together due to their electrostatic interactions.

INTRODUCTION

Externally-applied electric fields provide a well-known means for maniupulating suspenions of drops and bubbles. Common applications span a variety of multiphase flows, including enhanced coalescence, emulsion breaking and demixing operations for dispersions [1], electrophoretic migration of charged drops [2], enhanced heat and mass transfer owing to electroconvection [3], and aqueous two-phase partitioning [4]. Additional impetus for understanding the behavior of drops and bubbles in externally-applied electric fields arises from spaced-based materials processing, where nonuniform fields may be used to position fluid globules [5].

Previous research on the deformation of emulsion drops by electric fields has focused primarily on the behavior of isolated drops in uniform applied fields. In this context, the seminal contribution was made by Taylor [6], who demonstrated that conductive processes play a substantive role in determining how a drop, dispersed in another liquid, deformed in response to the imposed field. Taylor's analysis was pedicated on a model which has since come to be known as *the leaky dielectric*. Subsequent investigations have confirmed the essential premise of Taylor's analysis, i.e. that conduction processes cannot be altogether ignored, and have shown the leaky dielectric to be a useful quantitative model [7,8].

Several investigators have focused on the effect of a uniform electric field on two neighboring drops [9-12], motivated by the observation that the drop pair tends to coalesce due to the imposition of the field. As is the case for an isolated drop, the drops deform as the applied field strength increases, though now there are electrostatic and hydrodynamic interactions between the drops. Sozou [10] employed the leaky dielectric model to study the two drop problem in the limit that drop deformation was negligible, while others [11,12] have considered finite drop deformation but have neglected viscous effects. Taken together, these studies omit two important features of the problem for emulsion drops: first, dielectrophoretic forces, which bring the drops together, depend on charge conduction *and* drop shape; and second, resistance to the relative motion between the drops is dominated by viscous effects.

Here we apply the leaky dieletric model to investigate axisymmetric electrohydrodyanmic interactions between two emulsion drops of equal size. Boundary integral methods are used to obtain a numerical solution that accounts for the aforementioned problem features,viz., electrical conduction, drop deformation, and viscous-dominated hydrodynamic interations.

363

GOVERNING EQUATIONS

Balance Laws and Boundary Conditions

The balance laws of the leaky dielectric are well-known [13]. The velocity is governed by the Stokes equations, viz.

$$0 = -\nabla p + \mu \nabla^2 \mathbf{u} \qquad \nabla \cdot \mathbf{u} = 0, \tag{1}$$

and the electric field is solenoidal and irrotational, i.e.

$$\nabla \cdot \mathbf{E} = 0 \qquad \nabla \times \mathbf{E} = 0. \tag{2}$$

As a consequence of Eqn. (2), the electric field can be written as the gradient of a harmonic function, i.e.

$$\mathbf{E} = -\nabla \phi \qquad \nabla^2 \phi = 0, \tag{3}$$

where ϕ is the electric potential.

The electromechanical boundary conditions that apply at the drop surface couple the electrostatic field to the velocity. Classical electrostatics gives that

$$-\epsilon \nabla \phi \cdot \mathbf{n} + \bar{\epsilon} \nabla \bar{\phi} \cdot \mathbf{n} = \frac{q}{\epsilon_0}, \tag{4}$$

and

$$[\nabla \phi - \nabla \bar{\phi}] \times \mathbf{n} = 0, \tag{5}$$

where ϵ is the dielectric constant, ϵ_0 is the permittivity of free space, $\mathbf{n}$ is the unit normal pointing outward from the drop, and q is the local free surface charge density. Here overbars are used to indicate that a particular quantity refers to the drop interior.

The charge density q is not known independently of ϕ. Thus, while the electric potential must still satisfy Eqns. (4) and (5), the description of the electrostatic conditions at the interface must be augmented to unambiguously determine the electric field. If lateral transport of charge within the interface is neglected, conservation of charge requires that

$$\sigma \nabla \phi \cdot \mathbf{n} = \bar{\sigma} \nabla \bar{\phi} \cdot \mathbf{n}. \tag{6}$$

The velocity is continuous and the stresses balance at the interface, so

$$\mathbf{u} = \bar{\mathbf{u}} \tag{7}$$

and

$$\mathbf{n} \cdot (\mathbf{T}^N + \mathbf{T}^M) - \mathbf{n} \cdot (\bar{\mathbf{T}}^N + \bar{\mathbf{T}}^M) = \gamma (\nabla_s \cdot \mathbf{n}) \mathbf{n}. \tag{8}$$

In Eqn. (8), γ is the interfacial tension, $\mathbf{T}^N$ and $\bar{\mathbf{T}}^N$ are Newtonian stress tensors, i.e.

$$\mathbf{T}^N = -p\mathbf{I} + \mu(\nabla \mathbf{u} + \nabla \mathbf{u}^T) \qquad \bar{\mathbf{T}}^N = -\bar{p}\mathbf{I} + \bar{\mu}(\nabla \bar{\mathbf{u}} + \nabla \bar{\mathbf{u}}^T), \tag{9}$$

and $\mathbf{T}^M$ and $\bar{\mathbf{T}}^M$ are Maxwell stress tensors, i.e.

$$\mathbf{T}^M = \epsilon \epsilon_0 [\mathbf{E}\mathbf{E} - \frac{1}{2}(\mathbf{E} \cdot \mathbf{E})\mathbf{I}] \qquad \bar{\mathbf{T}}^M = \bar{\epsilon} \epsilon_0 [\bar{\mathbf{E}}\bar{\mathbf{E}} - \frac{1}{2}(\bar{\mathbf{E}} \cdot \bar{\mathbf{E}})\mathbf{I}]. \tag{10}$$

The remaining boundary conditions are: that the dependent variables remain bounded within the drops; and that, in the distance, the velocity vanish and $-\nabla \phi$ go over to $\mathbf{E}^\infty$, the externally-applied electric field.

Boundary Integral Formulation

A definition sketch for the problem to be solved is given in Fig. 1, and, as noted, the drops deform under the action of the imposed field. Because the drop shapes are not known *a priori*, analytic solutions to the governing equations are impracticable. The problem does, however, lend itself to boundary integral methods since the Green's functions for the balance laws are known.

The boundary integral representation for $E_n(\mathbf{x}_s)$, the normal component of the electric field at some position $\mathbf{x}_s$ on a drop surface, is

$$E_n(\mathbf{x}_s) = \frac{2}{1 + \bar{\sigma}/\sigma} \mathbf{n} \cdot \left[\mathbf{E}^\infty(\mathbf{x}_s) + \frac{1}{4\pi}(\bar{\sigma}/\sigma - 1) \int_S |\mathbf{x}_s - \mathbf{y}|^{-3}(\mathbf{x}_s - \mathbf{y})E_n(\mathbf{y})dS_y \right]. \tag{11}$$

The component of the electric field tangent to the surface, i.e. $E_t \equiv \mathbf{t} \cdot \mathbf{E}(\mathbf{x}_s)$, follows directly from the integration of an expression involving E_n, viz.

$$E_t(\mathbf{x}_s) = \mathbf{t} \cdot \left[\mathbf{E}^\infty(\mathbf{x}_s) + \frac{1}{4\pi}(1 - \bar{\sigma}/\sigma) \int_S |\mathbf{x}_s - \mathbf{y}|^{-3}(\mathbf{x}_s - \mathbf{y})E_n(\mathbf{y})dS_y \right]. \tag{12}$$

For the velocity, the boundary integral equation reads

$$\frac{1}{2}(1 + \frac{\bar{\mu}}{\mu})\mathbf{u}(\mathbf{x}_s) = \int_S \left[\mathcal{C}_{el}^{-1}\mathbf{n}(\nabla_s \cdot \mathbf{n}) - [\![\mathbf{n} \cdot \mathbf{T}^M]\!] \right] \cdot \mathbf{J}(\mathbf{x}_s|\mathbf{y})dS_y - (1 - \frac{\bar{\mu}}{\mu}) \int_S \mathbf{n} \cdot \mathbf{K}(\mathbf{x}_s|\mathbf{y}) \cdot \mathbf{u}(\mathbf{x}_s)dS_y, \tag{13}$$

where

$$\mathbf{J}(\mathbf{x}_s|\mathbf{y}) = \frac{1}{8\pi} \left[\frac{\mathbf{I}}{|\mathbf{x}_s - \mathbf{y}|} + \frac{(\mathbf{x}_s - \mathbf{y})(\mathbf{x}_s - \mathbf{y})}{|\mathbf{x}_s - \mathbf{y}|^3} \right] \quad \mathbf{K}(\mathbf{x}_s|\mathbf{y}) = -\frac{3}{4\pi}\frac{(\mathbf{x}_s - \mathbf{y})(\mathbf{x}_s - \mathbf{y})(\mathbf{x}_s - \mathbf{y})}{|\mathbf{x}_s - \mathbf{y}|^5}. \tag{14}$$

Note that Eqns. (11)-(14), which are constructed from the Green's functions for $\mathbf{u}$ and ϕ so as to satisfy Eqns. (4)-(8), are given in dimensionless form. The reference scales for the problem are: stress, $\epsilon\epsilon_0(E^\infty)^2$; velocity, $a\epsilon\epsilon_0(E^\infty)^2/\mu$; potential, aE^∞; and length, a. Accordingly, $\mathcal{C}_{el} \equiv a\epsilon\epsilon_0(E^\infty)^2/\gamma$ is an electric capillary number that characterizes the ratio of normal stresses due to electric and capillary forces; when $\mathcal{C}_{el}$ is small compared to unity, the imposed field causes little deformation of the emulsion drops.

RESULTS

Equations (11)-(13) were integrated numerically to obtain solutions for the electric and velocity fields. One of the virtues of the formulation summarized above is that, for a given drop shape, one can solve for the electric field without making reference to the velocity. Moreover, the components of the electric field can be obtained sequentially. Equation (11) is solved first for E_n, then E_t follows from Eqn. (12). Once the electric field is determined, the jump in the Maxwell stress is computed and substituted into the first integral on the RHS of Eqn. (13), along with the capillary stresses associated with the given drop shape. Owing to the need for the hydrodynamic stresses to balance these Maxwell and capillary stresses, the surface velocity field evinces a non-trivial normal component. Inasmuch as

$$\frac{d\mathbf{x}_s}{dt} = (\mathbf{n} \cdot \mathbf{u})\mathbf{n} = (\mathbf{n} \cdot \bar{\mathbf{u}})\mathbf{n}, \tag{15}$$

the drop shape is updated by moving the points $\mathbf{x}_s$, which are located on the interface, a distance $\delta\mathbf{x}_s = (\mathbf{n} \cdot \mathbf{u})\mathbf{n}\delta t$, where δt denotes the time step for the calculation. After updating the interface position, the calculation for the electric field is repeated, and so on, ...

Figures 2-4 show the results of such a calculation. In Fig. 2, the drop shapes and positions are shown as functions of time, which is scaled on $a\mu/\gamma$. The drops are assumed to be spherical and situated at $z_0 = 3.25$ when the field is imposed ($t = 0$). The behavior exhibited by the drop pair shown is characteristic of the results obtained in the study. The drops deform more rapidly than they translate. So long as the drops are not positioned such that their initial deformations bring their surfaces into virtual contact, translation is the rate limiting process by which the drops come together. (The phrases *virtual contact* and *come together* do not necessarily imply coalescence, since factors such as DLVO interactions have not been considered in the

365

calculations). The drops translate slowly toward one another because the electrical forces that drive them together are dielectrophoretic and, thus, die off roughly as one over the drop separation raised to the fourth power.

In Fig. 3, the velocity of the front and back edges of the right-hand drop are plotted against time; the front edge is that point closest to the origin (cf. Fig. 1). After the inital transient due to deformation, the front and back of the drop move with essentially the same velocity as the drop pair slowly drifts together. At approx. $t = 35$, the front edge of the drop accelerates as it comes under the increasingly stronger influence of the neighboring drop. Judging from Fig. 4, it would appear that this occurs when the dimensionless separation is about unity. Just before $t = 44$, when the numerical scheme says the drops touch, the front edge of the drop slows appreciably as the thin film between the pair drains, giving rise to lubrication forces.

CONCLUSIONS

A new boundary integral formulation for the electrohydrodynamic interaction between pairs of emulsion drops has been developed. The method accounts for the effects of conduction processes, viscous stresses and drop deformation on the interactions. Numerical results show that after an initial transient due to deformation, the drops converge comparatively slowly owing to the weakness of the electrostatic (dielectrophoretic) interactions. Since dielectrophoretic translation rates are shape dependent, the results imply that meaningful descriptions of emulsion behavior in electric fields ought to account for drop deformation induced by the imposed field.

ACKNOWLEDGEMENTS

REFERENCES

1. T. C. Scott, *Sep. & Purif. Meth.*, **18** (1989) 65-109.
2. J. C. Baygents and D. A. Saville, *J. Chem. Soc. Faraday Trans.*, **87** (1991) 1883-1898.
3. L. S. Chang and J. C. Berg, *AIChE J.*, **31** (1985) 551-557.
4. D. E. Brooks, K. A. Sharp, S. Bamberger, C. H. Tamblyn, G. V. F. Seaman and H. Walter, *J. Colloid Interface Sci.*, **102** (1984) 1-13.
5. T. B. Jones and G. W. Bliss, *J. Appl. Phys.*, **48** (1977) 1412-1417.
6. G. I. Taylor, *Proc. Roy. Soc. London.*, **A291** (1966) 159-166.
7. S. Torza, R. G. Cox and S. G. Mason, *Phil. Trans. Roy. Soc. London*, **A269** (1971) 295-319.
8. O. Vizika and D. A. Saville, *J. Fluid Mech.*, **239** (1992) 1-21.
9. G. I. Taylor, *Proc. Roy. Soc. London.*, **A306** (1968) 423-434.
10. C. Sozou, *J. Fluid Mech.*, **67** (1975) 339-348.
11. P. R. Brazier-Smith, *Phys. Fluids*, **14** (1971) 1-6.
12. P. R. Brazier-Smith, S. G. Jennings and J. Latham, *Proc. Roy. Soc. London.*, **A325** (1971) 363-376.
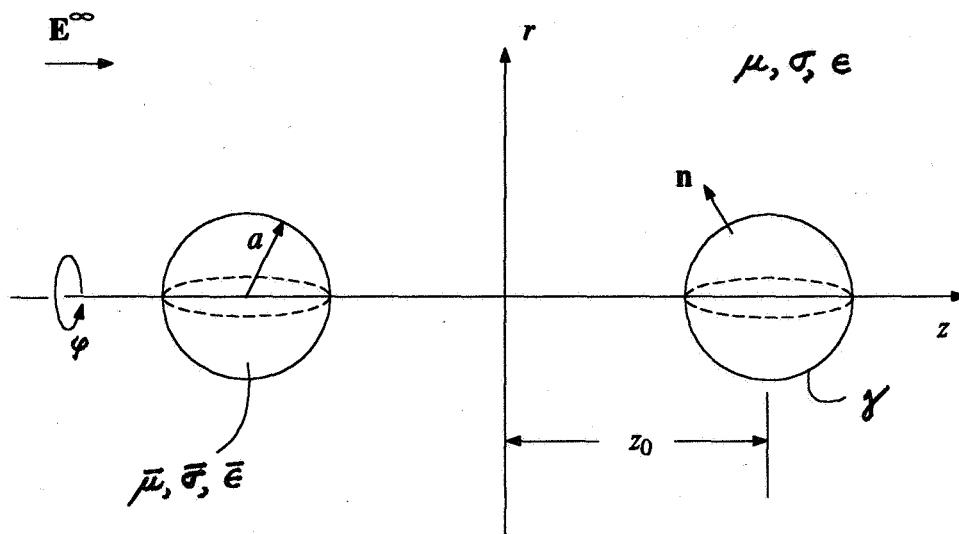13. J. R. Melcher and G. I. Taylor, *Ann. Rev. Fluid Mech.*, **1** (1969) 111-146.
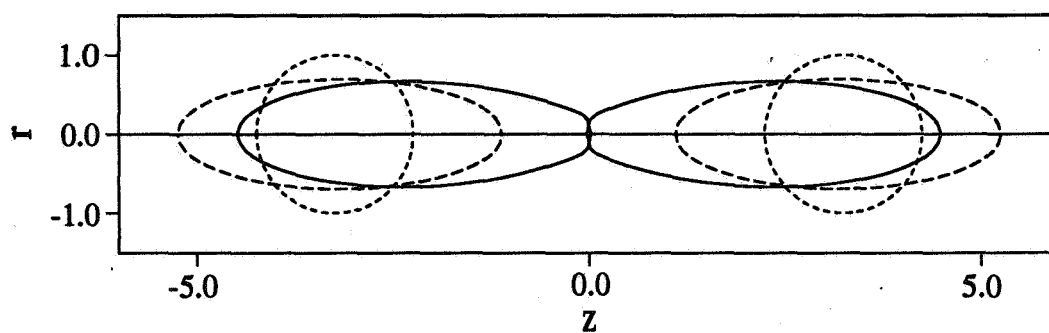
Figure 1: Definition sketch.

Figure 2: Drop shape and position as a function of time. $\mathcal{C}_{el} = 5; \bar{\mu}/\mu = 1; \bar{\epsilon}/\epsilon = 3; \bar{\sigma}/\sigma = 3; z_0 = 3.25$.
Legend: $--------$, $t = 0$; $---------$, $t = 10.4$; $——————$, $t = 44.0$.
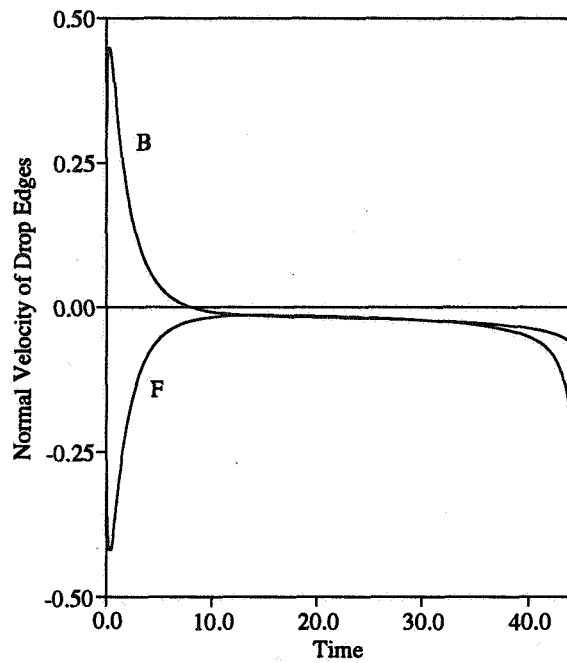
Figure 3: Velocity of front (F) and back (B) edges of drop as a function of time. Parameter specifications are as for Figure 2.
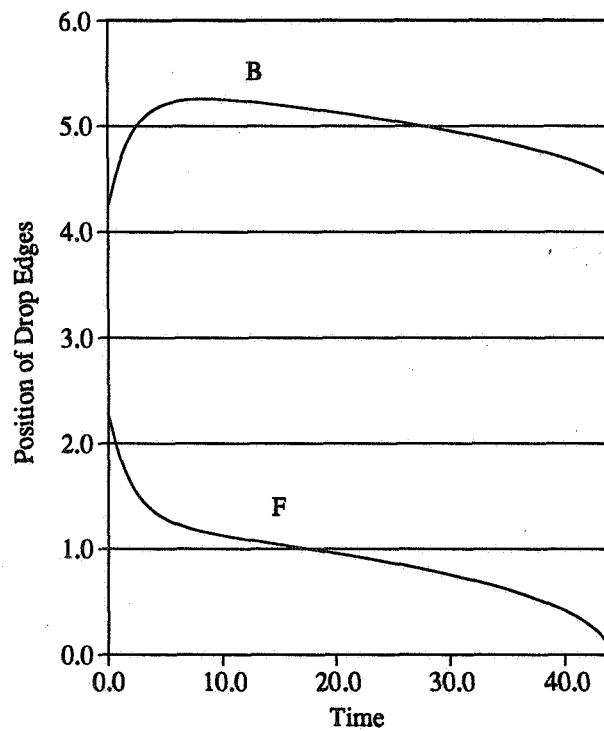

Figure 4: Position of front (F) and back (B) edges of drop as a function of time. Parameter specifications are as for Figure 2.

ROLE OF DIELECTRIC CONSTANT IN ELECTROHYDRODYNAMICS OF CONDUCTING FLUIDS

Percy H. Rhodes and Robert S. Snyder
National Aeronautics and Space Administration
George C. Marshall Space Flight Center
Huntsville, Alabama 35812

Glyn O. Roberts
Roberts Associates, Inc.
11794 Great Owl Circle
Reston, Virginia 22094

ABSTRACT

Electrohydrodynamic sample distortion during continuous flow electrophoresis is an experiment to be conducted during the second International Microgravity Laboratory (IML-2) in July 1994. The specific objective of this experiment is the distortion caused by the difference in dielectric constant between the sample and surrounding buffer. Although the role of sample conductivity in electrohydrodynamic has been the subject of both flight and ground experiments, the separate role of dielectric constant, independent of sample conductivity, has not been measured. This paper describes some of the laboratory research and model development that will supprt the flight experiment on IML-2.

INTRODUCTION

The role of electric conductivity tends to overshadow the effect of dielectric constant in many electrohydrodynamic (EHD) experiments. Melcher and Taylor [7] make the following observations. "Electrostatic effects in fluids are known for their vagaries; often they are so extremely dependent on electrical conduction that investigators are discouraged from carefully analytical models and simple experiments." Our early experiments [5] studying the EHD deformations of cylindrical streams readily showed the conductivity effect but the dielectric constant effect was not discernible. We have modified our flow chamber and enhanced our method of observation and can now see an unequivocal dielectric constant effect which is in agreement with the theory given in [5].

In this paper we first give a brief description of the physics of charge buildup at the interface of an immersed spherical drop or flowing cylindrical sample stream and then show how these charge distributions lead to interface distortions and accompanying viscous flows which constitute EHD. We next review theory and experiment describing the deformation of spherical drops of one fluid in another and show that there is no significant dielectric constant effect on the mode of deformation. We review our work [5] describing the deformation of a cylindrical stream of one fluid flowing in a carrier buffer and compare the deformation equations to those of the spherical drops. Finally, we show a definite dielectric constant effect in our case for a cylindrical sample stream of polystyrene latex as a function of the frequency of the excitation field.

INDUCED CHARGE FOR A DROP OR CYLINDER

In this study we consider the EHD flows associated with spherical drops or circular cylinders of an inside fluid in a surrounding outside fluid. We review theoretical and experimental work done by others and ourselves, and attempt to explain their structure and sign physically. Figure 1 shows the spherical or cylindrical geometry, and adds electrodes to indicate an imposed field direction from left to right.

It can be shown that there is no induced charge in the homogeneous regions. Charge is induced only at the interface.

From charge continuity, Ohm's law, and Maxwell's equations, the surface charge is

$$4\pi q_s = j_n (K_o / \sigma_o - K_i / \sigma_i), \tag{1}$$

where K and σ are the dielectric constant and electric conductivity, respectively. The current density normal to the interface is j_n. The subscript i denotes the region inside the drop or stream while o denotes the surrounding region (outside). Defining the conductivity and dielectric constant ratios as

$$R = \sigma_i / \sigma_o, \tag{2}$$

$$S = K_i / K_o, \tag{3}$$

Equation (1) can be rewritten as

$$4\pi q_s = (R - S) j_n K_o / \sigma_i. \tag{4}$$

The current in Fig. 1 is from left to right. So on the right half of the interface the outward normal current j_n is positive, and the interface charge density q_s has the same sign as $(R-S)$. Thus q_s is negative on the right in Fig. 1a, where

$$R < 1 < S,$$

and positive on the right in Fig. 1b, where

$$R > 1 > S.$$

On the left half of the interfaces in Fig. 1, the outward normal current j_n is negative, and the induced charge in Fig. 1a and 1b has the opposite sign, as shown.

FLOW CALCULATION

Once the electric field solution and the associated induced charge density have been found, the corresponding flow is determined by solving the Navier-Stokes equations, with the electric forces included. The electric forces can be equivalently expressed either in terms of the Maxwell stress tensor (convenient for interface boundary conditions) or as the sum of the electric forces on the charge density and on the dipole distribution associated with the dielectric constant.

On the scales of interest, fluid momentum can normally be neglected. The flow is therefore a balance between the electric forces, viscosity, and pressure gradients, with the incompressibility condition. Interface surface tension must be included in determining the change of shape of drops.

We have chosen not to give details in this review. But inspection of Fig. 1a suggests that with the electric field from left to right, the electric forces pull the positive and negative charges towards each other, flattening the circle normal to the electric field. And in Fig. 1b, the electric forces on the positive and negative surface charge distributions pull them apart, tending to elongate the circle toward the electrodes. This is confirmed by the detailed computations for the drop and cylindrical geometries. For the two special cases shown in Fig. 1a and 1b, the inclusion of the dipole electric forces does not change the solution qualitatively.

On the other hand, when R and S are either both greater than unity or both less than unity, dielectric forces can change the qualitative picture. In particular, Equation (4) shows that for $R = S$ there is no induced charge on the surface. But the detailed calculations show non zero EHD flow in this case, except in the trivial case $R = S = 1$.

THEORY OF DROP DEFORMATION

This early work on EHD flows was concerned with drop deformation, and used immiscible fluids. A neutrally buoyant spherical drop of one fluid in the other was distorted against surface tension by the application of a uniform AC field, and the shape distortion was measured and compared with theory.

The theory for conducting fluids was given by Taylor [1], and is known as Taylor's "leaky dielectric" model. Taylor obtains the drop deformation (defined as the difference of the drop axis lengths (diameters) divided by their sum, and positive for a prolate spheroid) in the form

$$\Omega = (9/64\pi)(K_o a E^2/\gamma)\Phi/(2+R)^2. \tag{5}$$

In this equation, γ is the surface tension, a the drop radius, E the imposed root mean square electric field, and the dimensionless discriminating function is

$$\Phi = 1 + R^2 - 2S + N(R - S). \tag{6}$$

Here

$$N = (6M + 9)/(5M + 5), \tag{7}$$

$$M = \mu_i/\mu_o, \tag{8}$$

and μ_i and μ_o are the inner and outer viscosities. Thus N decreases from 1.8 to 1.2 as the viscosity ratio M increases from zero to infinity, and is 1.5 when M is 1. Using these values for N, Equation (6) becomes

for $M = 0$, $$\Phi = R^2 + 1.8R + 1 - 3.8S, \tag{9}$$

and for $M \to \infty$, $$\Phi = R^2 + 1.2R + 1 - 3.2S. \tag{10}$$

Note that Taylor used the reciprocal S definition to our Equation (3), we have therefore changed his results appropriately to obtain our Equations (5) and (6). If Φ is positive, the spherical drop is elongated in the electric field direction, into a prolate spheroid. If Φ is negative, the drop is flattened normal to the electric field direction, into an oblate spheroid.

370

DROP DEFORMATION EXPERIMENTS

Many reported EHD studies have measured the electrical deformation of spherical drops, using various combinations of immiscible fluids. In this review, we emphasize the significance of dielectric constant effects. In our view, none of these reported results unequivocally demonstrated such effects, since in all cases the sign of the discriminating function (6) was the same as if the dielectric constant ratio had been 1. Note that from Equation (6) the critical value of the dielectric constant ratio S is

$$(1+ NR + R^2)/(2+N).$$

Figure 3 shows the critical S value as a function of R over the range of M. For smaller S values, the drop becomes prolate, elongated in the field direction. For larger S values it becomes oblate, flattened normal to the field. An unequivocal demonstration of a dielectric constant effect in EHD requires a sign change in the drop distortion. For $R < 1$ this requires that S is less than the critical value, while for $R > 1$ it requires that S is greater than the critical value. Otherwise we can say that the sign of the discriminating function is "controlled" by R.

In these admittedly difficult experiments, measuring and controlling the conductivities and controlling the interface surface tension are often the hardest problems. In Equation (5), $\Phi/(2+R)^2$ simplifies to 1 for large conductivity ratio R and to $(1-2S-NS)/4$ for small R. Intermediate R values have been avoided in the reported results, apparently due to the conductivity difficulties. For large R, the critical S value is very large, while for R close to zero, it is just $1/(2+N)$, or about 0.3, as Fig. 3 shows.

Allan and Mason [2] reported drop deformation experiments with 13 different combinations of fluids. In all cases the observed deformation correlated with Φ, and was also that expected for the measured conductivity ratio R. The experimental R values ranged up from 15, or down from 1/15. In terms of Equations (5) and (6), these experiments did not demonstrate a dielectric effect; the results were qualitatively the same as if S had been unity.

Torza, Cox, and Mason [3] reported 22 fluid combinations, which were all controlled by the conductivity ratio R. Similarly, Vizika and Saville [4] reported 11 fluid combinations; also controlled by R. In the small R cases in [2] through [4], the smallest S value was 0.44, or substantially above the critical value of $1/(2+N)$. A smaller value would have provided an unequivocal demonstration of dielectric constant effects in EHD.

DIELECTRIC CONSTANT OF AQUEOUS SUSPENSIONS

Clays and aqueous suspensions can be polarized, and act as homogeneous fluids with very high dielectric constants. This phenomenon is associated with the electrochemical charge double layer on each particle. As the particle and its surrounding charge cloud respond to the external field, and undergo electroosmosis, they also become a dipole. The higher the frequency for AC, the less time there is for the charge to move. Thus K decreases with increasing frequency, as shown in Fig. 2.

The dielectric constant of a suspension is measured experimentally by using an accurate bridge technique to determine the complex resistance of an electrolytic cell, as a function of frequency. This is not easy, and comparisons with theory have been mixed.

Over the last several years we have studied the deformation of cylindrical sample streams consisting of dispersions of polystyrene latex (PSL) microspheres [5,6]. The sample is drawn into a fine filament as it is injected into a flowing carrier buffer. The major difference between our system and the immiscible drop system discussed previously is the absence of surface tension in our case. The application of a uniform electric field to the cylindrical sample filament will distort the sample stream into a ribbon. The orientation of the ribbon depends on the ratios of dielectric constant and electrical conductivity between the buffer and sample. These distortions are the result of EHD flows in both the sample and buffer. The leaky dielectric model of Taylor is again used to determine the degree and orientation of the sample stream distortion. For a circular sample stream of properties shown in Fig. 1, we showed [5] that the radial EHD velocity u at the interface is given by

$$u = FD \cos 2\theta, \tag{11}$$

where the amplitude function is

$$F = \frac{aE^2 K_0}{12\pi(\mu_i + \mu_0)(R+1)^2} \tag{12}$$

and the discriminating function is

$$D = R^2 + R + 1 - 3S. \tag{13}$$

Here θ is the polar coordinate angle measured from the electric field direction. Note that the angular dependence $\cos 2\theta$ implies distortion of the circular sample section to an ellipse. From qualitative theoretical study [5] and from all our observations, this distortion continues until the sample becomes a flattened ribbon, either aligned with the field or perpendicular to it. Note the

similarity between this discrimination function D given by Equation (13), and the earlier function Φ for drop deformation, given by Equation (6). Both are different from the approximate discriminating function (R-S) suggested by Equation (4) and by the qualitative approximation of considering only the forces on free charges in computing the flow. To directly compare the discriminating function for liquid drops Φ to the discriminating function D for liquid streams, note the similarities between Equations (9), (10), and (13).

PSL SAMPLE STREAM DISTORTION EXPERIMENTS

In our experiments with sample stream distortion, we could vary the conductivity of both fluids. But we could not at first find a dielectric constant effect. Part of the problem was the low sensitivity of our early system, which was an electrophoresis type chamber limited to 30 V/cm. In addition, we were expecting K values from 200 to 1000 and higher, based on published literature for PSL suspensions. In fact, it appears that our samples were much closer to the water and buffer K value of 80. We improved the sensitivity of our method by using a small square chamber, allowing fields up to 300 V/cm, and by observing the distorted stream using a microscope system with a CCD camera and video monitor, at 62.5 magnification. Physically, the sample stream distortion was increased by a factor of 100, because of the E^2 dependence shown in Equation (12). Thus, our sensitivity improved by a factor of 6,250. With this system we have been able to demonstrate the EHD effects of the variations of dielectric constant with frequency, as shown in Fig. 2. These demonstrations are now repeatable.

Figure 4 shows eight views of steady EHD flows in our apparatus. The eight percent sample is injected through the circular nozzle just visible on the right. The transparent buffer, with matched conductivity, also enters the chamber from the right. In Fig. 4a there is no applied field, and the PSL passes along the chamber as a circular cylinder of constant diameter. The changes in cylinder diameter near the nozzle are associated with the nozzle drag on the buffer and PSL flow and with the viscous adjustment to a more uniform downstream flow profile. In the rest of Fig. 4 there is a fixed external AC electric field in the viewing direction; only the frequency is varied. The internal dimension for the square chamber is .5 cm, which gives a voltage gradient of 200 volts/cm throughout the run. No changes are made in the buffer or sample fluids or flow rates. In Fig. 4b, at 100,000 Hz, R and S are 1, and there is no EHD flow. At lower frequencies S increases, according to Fig. 2 and Equation (3). This makes the discriminant (13) increasingly negative, so that the circular sample stream is progressively flattened into a ribbon normal to the field, as it passes downstream to the left. For the lowest frequency of 28 Hz, this flattening is very rapid.

This series of photographs vividly shows the dielectric constant effect on EHD, and its variation with frequency, for a PSL sample filament. It also suggests a method for the measurement of dielectric constant. The stream at each frequency can be brought to zero deformation by adjustment of the conductivity ratio R. This value of R can then be used in Equation (13) (with $D = 0$) to calculate S and, hence, K_i. The PSL particles were made using a recipe without emulsifier, and each polymer (styrene) chain is terminated with a sulfate and end group at each end. The sample was sonicated and centrifuged, and then placed in R-1 (phosphate) buffer to form the sample stock. The final conductivity was adjusted using distilled water. The R-1 buffer used had a pH of 7.08.

CONCLUSIONS

We believe that the sample stream distortions which are shown in Fig. 4 are the first experimental evidence of the dielectric constant effect in conducting fluids to appear in the literature. We are continuing work on our miniature flow chamber to improve the uniformity of the electric field while still maintaining clear observation of the sample stream when viewed parallel to the field. We will now quantify a selection of PSL with respect to debye length (κ^{-1}), zeta potential ζ, and particle radius a. The dielectric constant of this selection can then be determined as a function of frequency ν by the method previously described. This data will then be described by a Cole-Cole relaxation frequency distribution which can be compared to the standard model of Delacy and White [8] and to dielectric spectroscopy measurements of Myers and Saville [9].

REFERENCES

1. Taylor, G.I. 1966 Studies in electrohydrodynamics. I. The circulation produced in drop by an electric field. Proc. R. Soc. London 291, 159-166.
2. Allan, R.S., & Mason, S.G. 1962 Particle behaviour in shear and electric fields. I. Deformation and burst of fluid drops. Proc. R. Soc. London A 267, 45-61.
3. Torza, S., Cox, R.G. & Mason, S.G. 1971 Electrohydrodynamic deformation and burst of liquid drops. Phil. Trans. R. Soc. London 269, 259-319.
4. Vizika, O. & Saville, D.A. 1992 The electrohydrodynamic deformation of drops suspended in liquids in steady and oscillatory electric fields. J. Fluid Mech. 239, 1-21.
5. Rhodes, P.H., Snyder, R.S., & Roberts, G.O. 1989 Electrohydrodynamic distortion of sample streams in continuous flow electrophoresis. J. Colloid Interface Sci. 129, 78-90.
6. Rhodes, P.H., Snyder, R.S., Roberts, G.O. & Baygents, J.C. 1991 Electrohydrodynamic effects in continuous flow electrophoresis. Applied and Theoretical Electrophoresis 2/3, 87-91.
7. Melcher, J.R. & Taylor, G.I. 1969 Electrodynamics: a review of the role of interfacial shear stresses. Ann. Rev. Fluid Mech. 1, 111-146.

8. Delacey, E.B. & White L.R. 1981 *Dielectric response and conductivity of dilute suspensions of colloidal particles.* J. Chem. Soc. Faraday Trans. 2, 77, 2007-2039.

9. Myers, D.F. & Saville, D.A. 1989 Dielectric Spectroscopy of Colloidal Suspensions: II. Comparisons Between Experiment and Theory. J. Colloid Interface Sci. 131, 461-470.
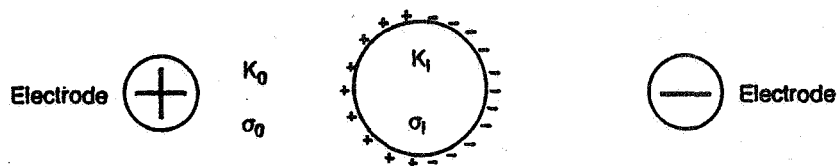
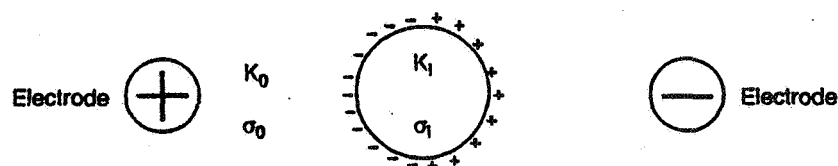**Fig. 1a.** Charge distribution for $K_I > K_0$ and $\sigma_I < \sigma_0$ producing distortion normal to the field (oblate)

Fig. 1b. Charge distribution for $K_I < K_0$ and $\sigma_I > \sigma_0$ producing distortion parallel to the field (prolate)

Figure 1. Charge Distribution at the Interface and Resulting EHD Flows
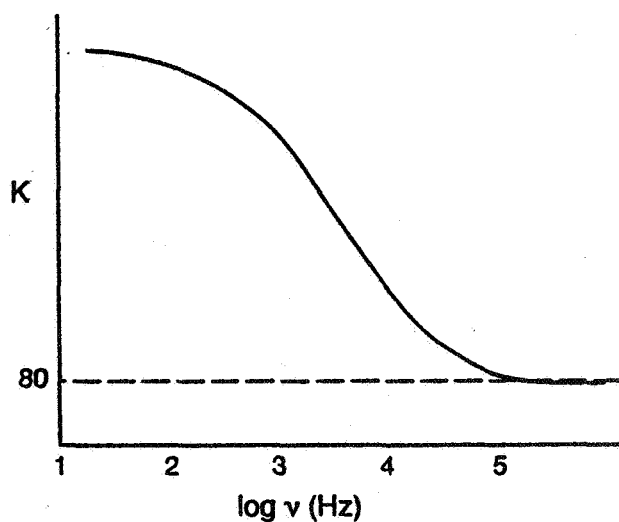
Figure 2. Variation of Dielectric Constant with Frequency ν for PSL Suspensions
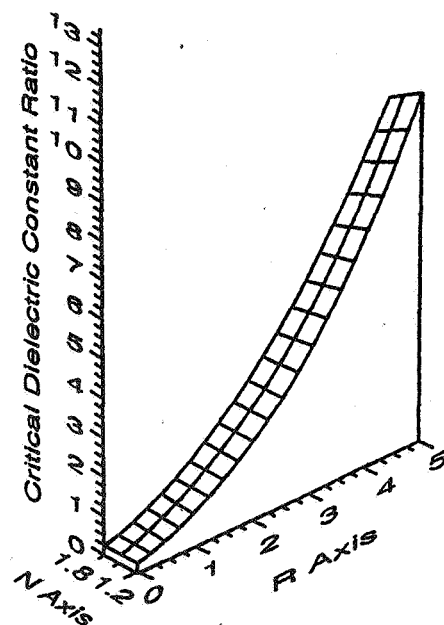
Figure 3. Relationship of Critical S to R

373
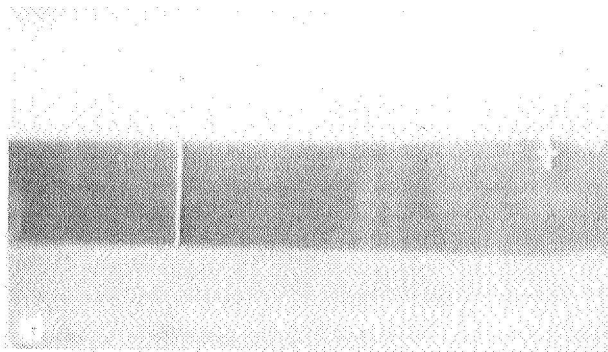
4a Zero Electric Field

4b. 100 Volts RMS. 100,000 Hz Frequency

4c. 100 Volts RMS. 50,000 Hz Frequency
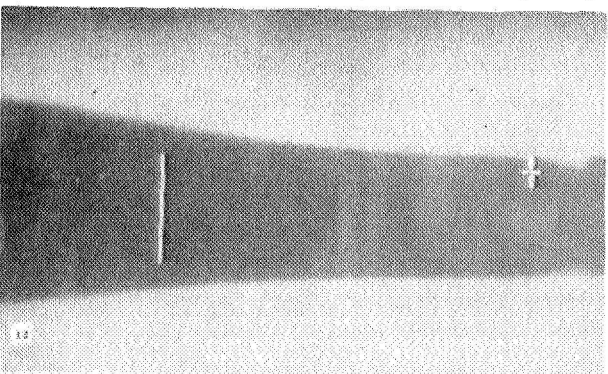

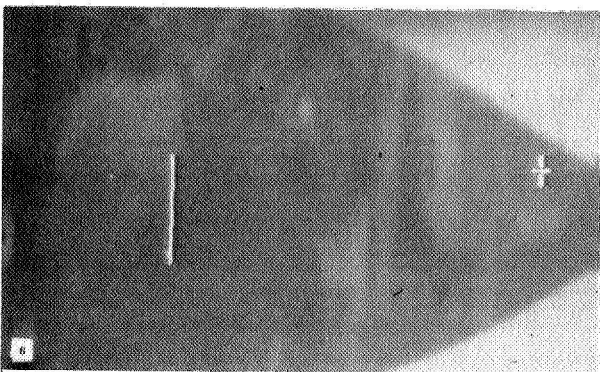**4d. 100 Volts RMS. 10,000 Hz Frequency**

4e. 100 Volts RMS. 5,000 Hz Frequency

4f. 100 Volts RMS. 1,000 Hz Frequency

4g. 100 Volts RMS. 100 Hz Frequency

4h. 100 Volts RMS. 28 Hz Frequency

Fig 4 Sample stream distortions viewed parallel to the AC electric fields at varying frequency, using an 8% PSL sample.

Studies in Electrohydrodynamics

Dudley Saville, Princeton University

Paper not available

Dielectric and Electrohydrodynamic Properties

Dudley Saville, Princeton University

Paper not available

ELECTROPHORETIC INTERACTIONS AND AGGREGATION OF
COLLOIDAL BIOLOGICAL PARTICLES

Robert H. Davis, Scott C. Nichols, Michael Loewenberg, and Paul Todd
Department of Chemical Engineering
University of Colorado
Boulder, Colorado 80309-0424

ABSTRACT

The separation of cells or particles from solution has traditionally been accomplished with centrifuges or by sedimentation; however, many particles have specific densities close to unity, making buoyancy-driven motion slow or negligible, but most cells and particles carry surface charges, making them ideal for electrophoretic separation. Both buoyancy-driven and electrophoretic separation may be influenced by hydrodynamic interactions and aggregation of neighboring particles. Aggregation by electrophoresis was analyzed for two non-Brownian particles with different zeta potentials and thin double layers migrating through a viscous fluid. The results indicate that the initial rate of electrophoretically-driven aggregation may exceed that of buoyancy-driven aggregation, even under conditions in which buoyancy-driven relative motion of noninteracting particles is dominant.

INTRODUCTION

Electrophoresis is a common analytical technique for separating charged biological particles and macromolecules. In an electric field, suspended particles will migrate at a velocity proportional to their surface charge and the applied field strength. Smoluchowski [1] showed that, for thin double layers, the electrophoretic velocity of an isolated particle is:

$$\mathbf{V}^{E,o} = \left(\frac{\epsilon\zeta}{\mu}\right)\mathbf{E}_\infty \quad , \tag{1}$$

where ϵ is the dielectric constant, ζ is the zeta potential of the charged particle surface, $\mathbf{E}_\infty$ is the applied electric field, μ is the viscosity of the fluid, and the group in parenthesis is the electrophoretic mobility, μ_e, a physical constant of a given particle. Morrison [2] later showed that the electrophoretic mobility was independent of the size and shape of the particle.

In a heterogeneous suspension, particles with different surface charges will have different electrophoretic velocities, leading to the possibility that they will collide and aggregate [3]. Such aggregation inhibits the ability for different subpopulations of cells or other biological particles to be separated and is the subject of this article. Particle aggregation has been investigated theoretically for buoyancy-driven motion by Davis [4] and Melik and Fogler [5] who used a trajectory analysis to determine the aggregation rates. A similar analysis for electrophoretic particle aggregation is performed in this work and compared with the results for gravity-induced aggregation.

THEORETICAL DEVELOPMENT

We restrict our attention to suspensions which are dilute, so that only two particles interact at one time. The particles are assumed to have negligible Brownian motion and the surrounding fluid is assumed to have negligible inertia. The zeta potentials are of moderate strength or less, and the electrical double layers are thin ($\kappa a \gg 1$). These conditions are typically met for biological cells and other charged particles of 1-50 μm radius.

To study coagulation and stability of dilute suspensions of spherical particles, a quantitative description of the relative motion between two spheres is needed. When the particles are far apart, this relative motion

is simply the difference between the separate velocities, given by: $\mathbf{V}_{12}^o = \mathbf{V}_1^o - \mathbf{V}_2^o$. For electrophoresis, $\mathbf{V}_{12}^o = (1 - \beta) \mathbf{V}_1^{E,o}$, where $\mathbf{V}^{E,o}$ is defined by eq. (1), β is the ratio of zeta potentials, ζ_2/ζ_1. For gravity sedimentation, $\mathbf{V}_{12}^o = (1 - \lambda^2 \gamma) \mathbf{V}_1^{G,o}$, where $\mathbf{V}^{G,o}$ is the Stokes sedimentation velocity [4]:

$$\mathbf{V}^{G,o} = \frac{2\Delta\rho a^2 \mathbf{g}}{9\mu} \quad , \tag{2}$$

$\Delta\rho$ is the density difference between the particle and the fluid, a is the particle radius, $\mathbf{g}$ is the gravitational acceleration, λ is the particle size ratio, a_2/a_1, and γ is the reduced density ratio, $\Delta\rho_2/\Delta\rho_1$.

As two particles approach each other, hydrodynamic interactions significantly affect the relative velocity, and this can be expressed through the use of mobility functions. Using the coordinate system shown in Fig. 1, we write [6]:

$$U_{12,r} = -L(r)\cos\theta - \frac{G(r)}{N_A}(f_A - N_R f_R) \quad , \tag{3}$$

$$U_{12,\theta} = M(r)\sin\theta \quad , \tag{4}$$

where $U_{12,r}$ and $U_{12,\theta}$ are the components of the relative velocity directed parallel and perpendicular to the line of centers, respectively; the velocities are made dimensionless by V_{12}^o, and r is the distance between the centers of the two particles made dimensionless by the average particle radius. The mobility functions $L(r)$ and $M(r)$ describe relative motion due to the driving force. The mobility function $G(r)$ describes relative motion due to interparticle forces, which are summarized later in this section. When the dimensionless interparticle separation distance, $\delta = r - 2$, is large compared to unity, $L(r)$, $M(r)$, and $G(r)$, approach unity, but, at near contact, $L(r)$ and $G(r)$ approach zero, and $M(r)$ tends to a finite limit.

Figure 2 shows $L(r)$ for electrophoretic and buoyancy motion. For electrophoresis, $L(r)$ was obtained from the method of reflections [7] at large separations, a boundary collocation solution [8] at moderate separations, and a lubrication solution [9] at small separations. For buoyancy, $L(r)$ is taken from the solutions summarized by Jeffery and Onishi [10]. The mobility functions for electrophoresis approach unity much more rapidly (with a leading-order correction proportional to $1/r^3$) than do those for buoyancy (which have a leading-order correction proportional to $1/r$) as the interparticle separation is increased; this is because electrophoresis is a force-free motion.

When the interparticle separation distance is small, short-range interparticle forces will affect the relative particle motion. Electrostatic repulsion due to overlapping double layers can keep particles from aggregating, if strong enough. However, in most cases, van der Waals attractive forces will cause aggregation to occur. It will be assumed that these colloidal forces act only along the line of centers. The driving force for aggregation made dimensionless by the van der Waals force is described by the dimensionless parameter

$$N_A = \frac{6\pi\mu V_{12}^o a^2}{A} \quad , \tag{5}$$

where A is the Hamaker constant and a is the average particle radius. A dimensionless function describing the attractive van der Waals forces, taken from Gregory [11], is

$$f_A = \left(\frac{1}{6\delta^2}\right)\left(\frac{\nu}{5.32\delta + \nu}\right) \quad , \tag{6}$$

where $\delta = h/a$ is the dimensionless particle separation distance, and $\nu = \lambda_L/a$ is the dimensionless retardation parameter, with $\lambda_L \approx 0.1$ μm being the London retardation wavelength. This expression is valid for $\delta \ll 1$, and, since van der Waals attractions are negligible at larger separations, eq. (6) will be used throughout. The dimensionless parameter describing the strength of the electrostatic repulsion relative to the van der Waals attraction is

$$N_R = \frac{\epsilon \zeta_1^2 a}{A} \quad . \tag{7}$$

The dimensionless function describing the electrostatic repulsion force due to overlapping double layers, taken from Hogg et al. [12], is

$$f_R = \kappa a \left(\frac{\beta e^{-\kappa a \delta} - \left(\frac{1+\beta^2}{2}\right) e^{-2\kappa a \delta}}{1 - e^{-2\kappa a \delta}} \right) \tag{8}$$

This expression for the double layer repulsion is valid for $\kappa a > 10$, $\zeta_1 < 60$ mV, and constant surface potential.

RESULTS

Colloidal suspensions tend to form aggregates of particles due to van der Waals attraction, but electrostatic repulsion between two particles can lead to a stable suspension. To characterize the stability of the suspension, we examine the relative motion along the line of centers using eq. (3). A stable suspension is one in which the relative velocity along the line of centers, $U_{12,r}$, becomes zero at finite separations for all values of $-1 \leq \cos \theta \leq 1$. Moreover, the location at which $U_{12,r} = 0$ is stable only if $dU_{12,r}/dr < 0$, indicating that a pair of particles will move apart if they become slightly closer than the stable separation distance.

Melik and Fogler [5] have previously studied the stability of particles undergoing gravity sedimentation. We show here how their results can be extended to electrophoretic motion. In particular, if eq. (3) is written for gravity motion and electrophoretic motion, and set to zero relative velocity for each case, we have

$$N_A^E = \frac{L^G}{L^E} N_A^G \tag{9}$$

along the neutral stability curves. Since $L^G/L^E \ll 1$ at small separations (see Fig. 2), this implies that electrophoretic motion becomes unstable at larger dimensionless driving forces than does buoyancy motion (Fig. 3). Moreover, since interparticle forces act at distances where near-contact hydrodynamics apply, L^E/L^G is independent of the small separation distance because $L(r)$ is proportional to the gap between the particles for both types of motion [9].

Loewenberg and Davis [9] have analyzed electrophoretic near contact motion and compared the results with buoyancy-driven near-contact motion. They find for small size ratios, $\lambda < 0.2$, L^E/L^G can be approximated by

$$\frac{L^E}{L^G} = \frac{1.89}{\lambda (1 - 0.206\gamma)} \tag{10}$$

Then at small size ratios, L^E/L^G is proportional to λ^{-1}, which implies that electrophoresis is able to force particles together much easier than gravity is able to. In fact, $L^E/L^G > 8$ for all size ratios at $\gamma = 1$; thus, electrophoresis is much less stable than buoyancy. Loewenberg and Davis [9] have postulated that the greater tendency for particles to aggregate when undergoing electrophoresis is due to electroosmotic convection which draws fluid out of the gap between two approaching particles. In contrast, the fluid must be squeezed out of the gap between two approaching particles in buoyancy-driven motion, which causes greater resistance to close approach.

AGGREGATION RATE RESULTS

Trajectory Analysis

The pairwise aggregation rate is equal to the flux of particle pairs through an upstream collision cross-section [4]:

$$J_{12} = n_1 n_2 V_{12}^o \pi \sigma_c^2 \quad , \tag{11}$$

where n_i is the number density of particles of type i and σ_c is the critical impact parameter at upstream infinity defined in Fig. 4 such that particle capture occurs only for $\sigma \leq \sigma_c$. The collision efficiency is defined

as the actual collision rate given by eq. (11) divided by that in the absence of particle-particle interactions ($\sigma_c = a_1 + a_2$):

$$E_{12} \equiv \left(\frac{\sigma_c}{a_2 + a_1}\right)^2 \qquad (12)$$

The critical impact parameter and the collision efficiency were determined from a trajectory analysis [4,5]. Dividing eq. (3) by eq. (4) yields

$$\frac{dr}{d\theta} = -r\frac{\left(L(r)\cos\theta + \frac{G(r)}{N_A}(f_A - N_R f_R)\right)}{M(r)\sin\theta} \quad , \qquad (13)$$

which was integrated backwards from a critical point at $\theta = \pi$ and the separation for which the driving force pulling the two particles apart is balanced by the interparticle colloidal forces pulling them together [4].

Figures 5 and 6 show the collision efficiency as a function of the dimensionless driving force, N_A, at different double-layer thicknesses and strengths of the electrostatic repulsion. Apparently, electrophoretic aggregation is approximately an order of magnitude more efficient than buoyancy-driven aggregation. The stability region ($E_{12} = 0$) for electrophoretic aggregation is shifted according to eq. (9), which is another manifestation that a given colloidal suspension is less stable to an applied electric field than to a gravitational driving force. As the driving force parameter increases, the collision efficiency at first increases as the electrophoretic or gravitational mechanisms pushing the particles together overcome the repulsive forces which hold them apart; a maximum is then reached, and further increases of the parameter N_A lead to a decrease in E_{12} because the attractive van der Waals forces required for aggregation become relatively weak. By comparing Figs. 5 and 6, it is seen that adding electrolyte to decrease the double-layer thickness (increase κa) enhances the collision rate. This is because attractive van der Waals forces become stronger relative to repulsive electrostatic forces as the double-layer becomes thinner and shields the repulsive surface charge.

CONCLUSIONS

A suspension undergoing electrophoresis is less stable to aggregation than a comparable suspension undergoing gravity sedimentation. In addition, the collision efficiencies are much higher for electrophoretic aggregation than for gravity-induced aggregation. These results stem from the fact that electrophoretic motion is force-free and hydrodynamic interactions have a smaller effect on the relative motion than for gravity motion.

ACKNOWLEDGMENTS

REFERENCES

1. Smoluchowski, M. von. Vesuch einer mathematischen theorie der koagulationskinetik killoider Lösungen. *Z. Phys. Chem.* **92** (1903) 129.

2. Morrison, Jr., F.A. Electrophoresis of a particle of arbitrary shape. *J. Colloid Interface Sci.* **34** (1970) 210-214.

3. Todd, P & Hjertén, S. Free zone electrophoresis of animal cells I: Experiments on cell-cell interactions. in *Cell Electrophoresis*, ed. W. Schütt & H. Klinkman, Walter deGruyter & Co., Berlin (1985) pp. 23-31.

4. Davis, R.H. The rate of coagulation of a dilute polydisperse system of sedimenting spheres. *J. Fluid Mech.* **145** (1984) 179-199.

5. Melik, D.H. & Fogler, H.S. Gravity-induced flocculation. *J. Colloid Interface Sci.* **101** (1984) 72-83.

6. Batchelor, G.K. Sedimentation in a dilute polydisperse system of interacting spheres. Part 1. General theory. *J. Fluid Mech.* **119** (1982) 379-408.

7. Chen, S.B., & Keh, H.J. Electrophoresis in a dilute dispersion of colloidal spheres. *AICHE Journal* **34** (1988) 1075-1085.

8. Keh, H.J. & Yang, F.R. Particle Interactions in electrophoresis III: Axisymmetric motion of multiple spheres. *J. Colloid Interface Sci.* **139** (1990) 105-116.

9. Loewenberg, M. & Davis, R.H. Near-contact, electrophoretic particle motion. *J. Fluid Mech.* (1994, in press).

10. Jeffery, D.J., & Onishi, Y. Calculation of the resistance and mobility functions for two unequal rigid spheres in low-Reynolds-number flow. *J. Fluid Mech.* **139** (1984) 261-290.

11. Gregory, J. Approximate expressions for retarded van-der Waals interaction. *J. Colloid Interface Sci.* **83** (1981) 138-145.

12. Hogg, R., Healy, T.W., & Fuerstenau, D.W. Mutual coagulation interaction. *J. Colloid Interface Sci.* **83** (1981) 138-145.
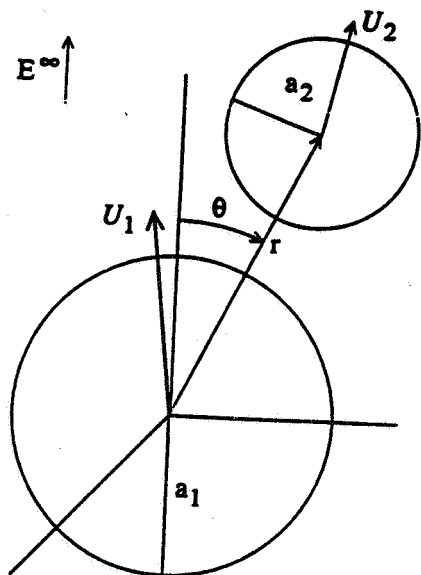
Fig. 1–Schematic of the relative motion of two charged spheres in an electric field.
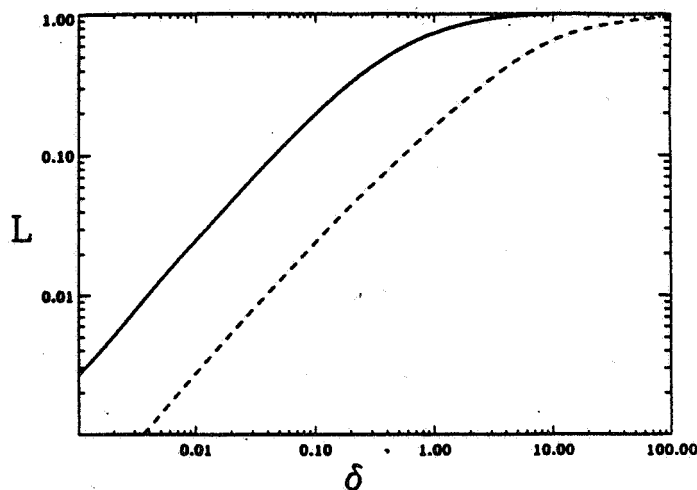
Fig. 2–Relative mobility function along the line of centers for gravity motion (dashed line) and electrophoretic motion (solid line) with $\lambda = 2$, $\gamma = 1$, and $\beta = 0.5$.
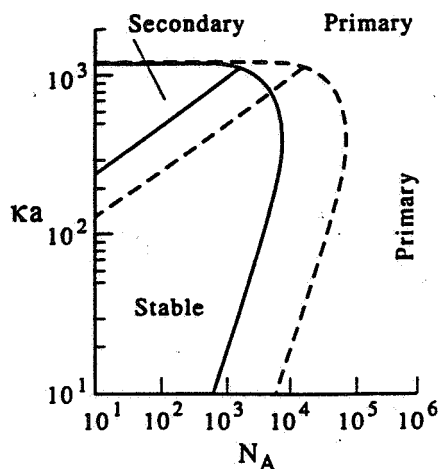
Fig. 3–Stability plot showing stable region, primary capture, and secondary capture for gravity-induced aggregation (dashed lines) and electrophoretic aggregation (solid lines) with $\lambda = 0.5$, $\gamma = 1$, $\beta \to 1$, $\nu = 0.1$, and $N_R = 400$.

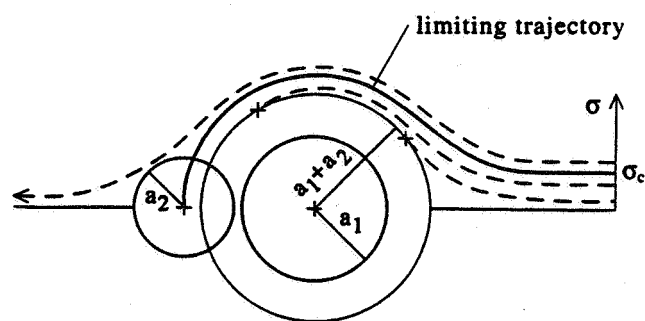Fig. 4–Schematic of the relative trajectories of two spheres for different impact parameters; σ_c is the critical impact parameter defined such that aggregation occurs for $\sigma < \sigma_c$ and not otherwise.
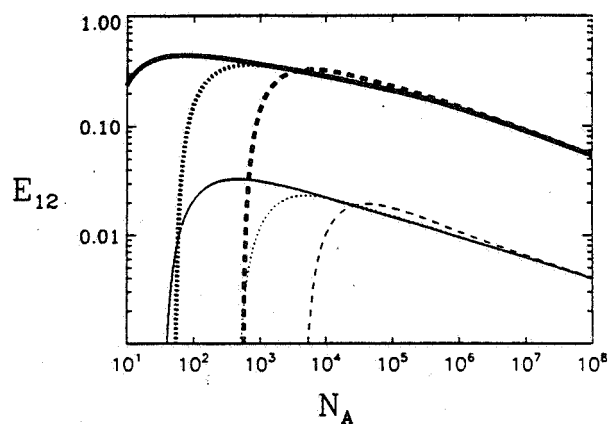

Fig. 5–The collision efficiency versus the ratio of driving force to attractive force for electrophoresis (thick lines) and gravity sedimentation (thin lines) for $\lambda = 2$, $\gamma = 1$, $\beta = 0.5$, $\nu = 0.044$, $\kappa a = 10$, and $N_R = 10$ (solid lines), 100 (dotted lines), and 1000 (dashed lines).
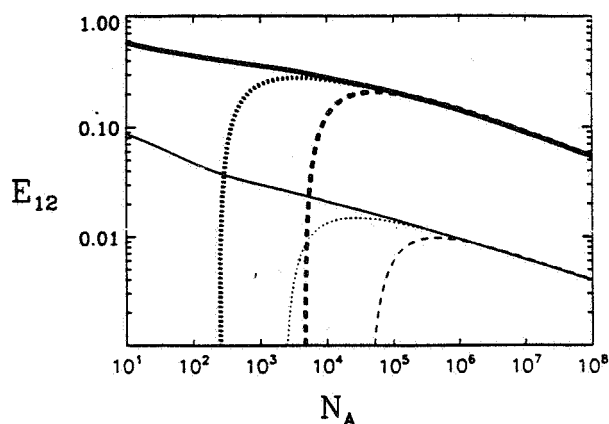
Fig. 6–The collision efficiency versus the ratio of driving force to attractive force for electrophoresis (thick lines) and gravity sedimentation (thin lines) for $\lambda = 2$, $\gamma = 1$, $\beta = 0.5$, $\nu = 0.044$, $\kappa a = 100$, and $N_R = 10$ (solid lines), 100 (dotted lines), and 1000 (dashed lines).

Physicochemical Systems

SURFACTANT-BASED CRITICAL PHENOMENA IN MICROGRAVITY

Eric W. Kaler and Michael E. Paulaitis

Center for Molecular and Engineering Thermodynamics
Department. of Chemical Engineering
University of Delaware
Newark, Delaware 19711

ABSTRACT

The objective of this research project is to characterize by experiment and theoretically both the kinetics of phase separation and the metastable structures produced during phase separation in a microgravity environment. The particular systems we are currently studying are mixtures of water, nonionic surfactants, and compressible supercritical fluids at temperatures and pressures where the coexisting liquid phases have equal densities (isopycnic phases). In this report, we describe experiments to locate equilibrium isopycnic phases and to determine the "local" phase behavior and critical phenomena at nearby conditions of temperature, pressure, and composition. In addition, we report the results of preliminary small angle neutron scattering (SANS) experiments to characterize microstructures that exist in these mixtures at different fluid densities.

INTRODUCTION

Ground-based measurements of surfactant solutions undergoing phase separation where density differences between the coexisting phases are minimized provide an excellent guide for defining key measurements and systems for study in shuttle experiments where density differences are irrelevant. Our approach has been to employ compressible supercritical fluids and use pressure as a field variable to match phase densities, and to use surfactants to slow the rate of phase separation to allow easy observations. Moreover, because two equilibrium phases containing different surfactants can have markedly different viscosities, these mixtures will make possible examination of the role of rheology in setting metastable structures during phase separation. A practical motivation for matching densities with a supercritical fluid at elevated pressures, rather than a liquid solvent, is to examine a variety of polymerization processes in microemulsion and micellar phases where the supercritical fluid can be polymerized; butadiene, for example, would be a potential supercritical fluid for such polymerizations.

In the following, we present current results of calculations to predict state points corresponding to isopycnic phases and experiments to locate them for the three-

component mixture: water, carbon dioxide, and the ethoxylated alcohol surfactant, C_8E_5. Small-angle neutron scattering (SANS) measurements were also made on mixtures of the surfactant $C_{12}E_6$, CO_2, and D_2O to probe for the presence of aggregates in these solutions. These experimental results are also reported.

EXPERIMENTAL WORK AND CONCLUSIONS

Phase Behavior and the Search for Isopycnic Phases

Ternary mixtures of a nonionic C_iE_j surfactant, CO_2, and H_2O will form three coexisting equilibrium phases at elevated pressures and ambient or slightly higher temperatures [1]. The three phases are: (1) a H_2O-rich liquid phase, (2) a CO_2-rich gas phase, and (3) a fluid phase with properties that can be varied between those of the other two phases depending on the pressure. In previous experimental work on the phase diagram for mixtures of C_8E_3, CO_2, and H_2O [1], we determined that the densities of the H_2O-rich liquid phase and the third fluid phase would approach one another with increasing pressure. We have extended those observations in the present work to predict the temperature and pressure at which isopycnic phases will form using a modified Peng-Robinson equation of state [2]. Equation-of-state parameters were regressed from data available in the literature and from our measurements of vapor-liquid equilibrium for binary mixtures of C_8E_3 and H_2O at elevated pressures and temperatures of 40 and 50°C. The calculated results are shown in Figure 1 as a plot of phase densities for the water-rich liquid phase (L1 in this figure) and the surfactant-rich, third fluid phase (L2 in this figure) as a function of pressure at 40°C. As expected, the density of the L1 phase is much less sensitive to pressure than the L2 phase, and the density of the L2 phase increases with pressure as this phase becomes more "liquid-like" at higher pressures and therefore can dissolve larger amounts of water and surfactant. These phase densities converge at an isopycnic point at a pressure of approximately 400 bar. As a result of these calculations, we conducted experiments to search for isopycnic phases for mixtures of C_8E_3 and C_8E_5 with CO_2 and H_2O at temperatures near 40°C and pressures up to 400 bar.

A high-pressure sapphire view cell (Insaco Inc.) was constructed based on an earlier design [1]. The cell is thermostated to ± .001 °C in a Hart Scientific high precision bath, and the temperature inside the cell was monitored with a platinum resistance thermometer (Newport Electronics). Pressure was measured with a precision Heise gauge. Slow demixing rates and wetting phenomena provide qualitative indications of near-isopycnic phase separation. However, a quantitative determination of isopycnic phases can be made from the observation of a phase inversion in which the high density, water-rich phase at the bottom of the cell inverts with the middle liquid phase. Isopycnic phase compositions can be measured with reasonable accuracy using a stoichiometric technique which does not require sampling of the phases [3]. Accurate quantitative measurements of isopycnic phase densities are made using an Anton-Paar densimeter.

A phase inversion was observed for mixtures of C_8E_5, CO_2, and H_2O at a temperature of $31.89 \pm .01°C$ and a pressure of 396 ± 10 bar. Wetting phenomena observed for other isopycnic systems -- such as the formation of large spherical droplets and a faint, wavy meniscus separating the two isopycnic phases [4] -- were also observed in the vicinity of the phase inversion for this mixture. A more accurate determination of the pressure and measurements of isopycnic phase densities using the Anton-Paar densimeter are now in progress. The formation of isopycnic phases for this mixture at reasonably moderate pressures is a result of two conditions: (1) the density of the pure surfactant is sufficiently high (.985 g/cc at 20°C) that the third fluid phase, which is surfactant-rich, has a density close to that of the water-rich liquid phase at ambient pressures; (2) the H_2O/C_8E_5 mixture critical temperature (61°C [5]) is high enough compared to the temperature of interest that the surfactant-rich fluid phase has a large water content. These conditions are expected to hold for other C_iE_j surfactants when $i > 8$ and $j > 5$, and we have begun to search for the isopycnic state points of these amphiphiles in mixtures with H_2O and CO_2.

Neutron Scattering

A sapphire neutron scattering cell (Insaco Inc.) was constructed to enable scattering experiments to be done at pressures up to 550 bar and at scattering angles of 30°. The temperature inside the cell was monitored with a platinum resistance thermometer (Newport Electronics) and maintained with an aluminum water jacket to ± 0.1 °C. Samples for neutron scattering were equilibrated in the sapphire view cell [1] before they were transferred to the scattering cell.

SANS measurements were made on mixtures of $C_{12}E_6$, CO_2, and D_2O in the water-rich one phase region (7.5 wt % surfactant on a CO_2 free basis) in solutions of varying CO_2 content of up to 4 wt %.. Representative data are shown in Figures 2 and 3 as plots of the neutron scattered intensity (on an absolute scale) as a function of q. The striking feature of the scattering curves is their upturn with decreasing q. This feature is usually attributed either to the presence of attractive interactions between colloidal-scale objects, the $C_{12}E_6$ micelles in this case, or to critical scattering. In either case, the rate of increase of the spectra measured at constant pressure (Figure 3) increases with increasing temperature rather steadily on approach to the critical temperature of CO_2 (31°C). On the other hand, at a constant temperature of 31°C, the spectra change substantially from 62 to 76 bar (the critical pressure of CO_2 is 74 bar), but do not vary significantly with a further increase in pressure to 90 bar (Figure 2). The role of attractive interactions can be more fully investigated using established methods that relate inter-aggregate interaction potentials to the scattering spectra [6].

The presence of aggregates in the solution is supported by the shape of the scattering curves measured at larger values of q (not shown). These data suggest that $C_{12}E_6$ micelles roughly 30 Å in size exist even in the presence of 4 wt % CO_2.

ACKNOWLEDGEMENTS

REFERENCES

1. Ritter, J. M. and Paulaitis, M. E. "Multiphase Behavior in Ternary Mixtures of CO2, H2), and Nonionic Amphiphiles at Elevated Pressures," *Langmuir* 6 (1990) p. 934 - 941.

2. Kao, C.-P., Pozo, M. E. and Paulaitis, M. E. "Equation-of-State Analysis of Phase Behavior for Water-Surfactant-Supercritical Fluid Mixtures," *ACS Symp. Ser.* 514 (1993) p. 74 - 91.

3. DiAndreth, J. R., Ritter, J. M. and Paulaitis, M.E. "Experimental Technique for Determining Mixture Compositions and Molar Volumes of Three or More Equilibrium Phases at Elevated Pressures," *IEC Res.* 26 (1987) p. 337 - 343.

4. Beysens, D. "Stability of Critical Fluid Mixtures: Experimental Simulation of Microgravity Conditions," *Acta Astronautica,* 12 (1985) p. 525 - 530.

5. Schubert, K.V., Strey, R. and Kahlweit, M. "A New Purification Technique for Alkyl Polyglycol Ethers and Miscibility Gaps for Water-C_iE_j," *J. Col. Int. Sci,* 141 (1991) p. 21 - 29.

6. Kaler, E. W. "Small-Angle Scattering from Complex Fluids," in "Modern Aspects of Small-Angle Scattering," (H. Brumberger, ed.), Kluwer Academic Publishers, Dordrecht, The Netherlands (1994).
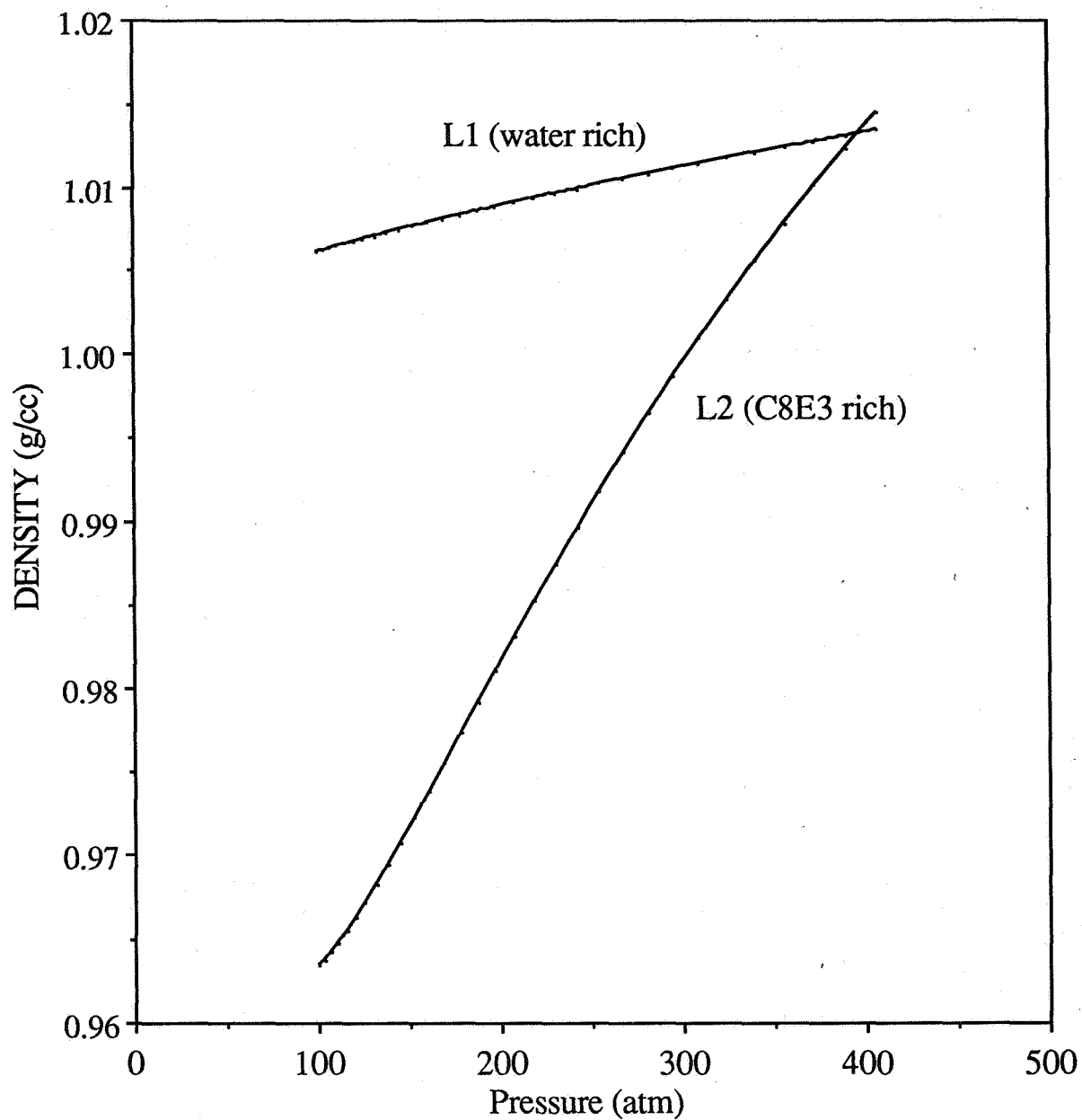
Figure 1. Calculated Phase densities as a function of pressure for the water-rich L1 liquid phase and the surfactant-rich L2 liquid phase in the presence of a CO_2-rich gas phase at 40°C for the C_8E_3/H_2O/CO_2 system.
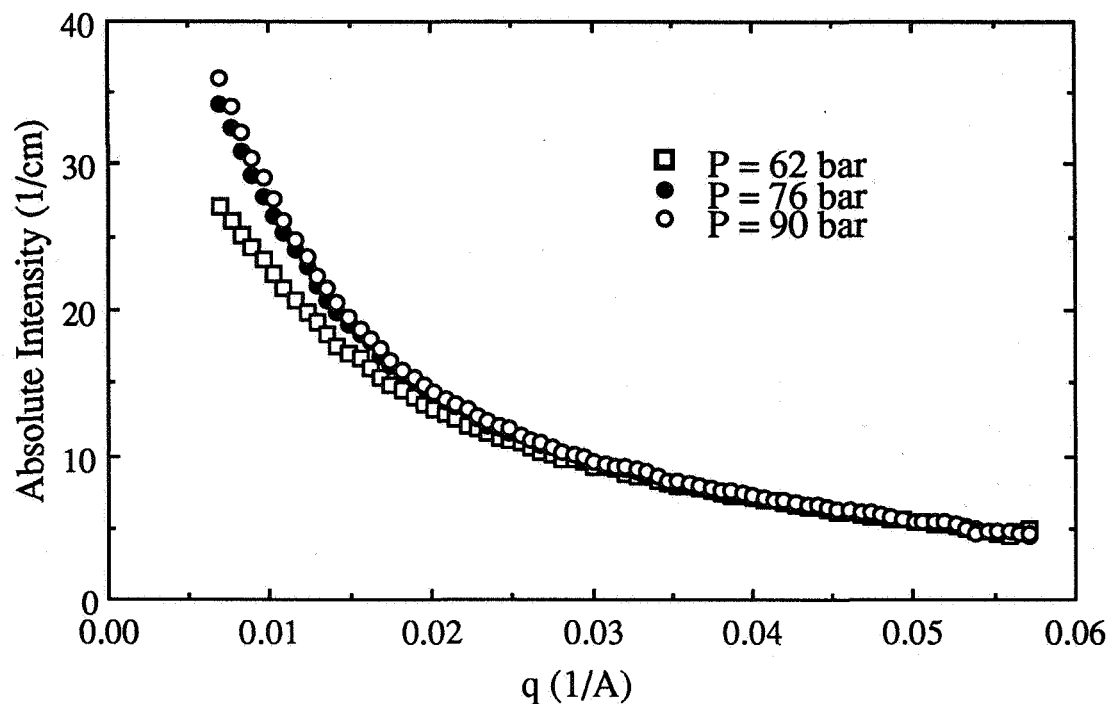
Figure 2. SANS spectra on absolute scale for a sample of 8 wt% $C_{12}E_6$, 4 wt% CO_2, and D_2O at 31°C as a function of the scattering vector q and pressure.
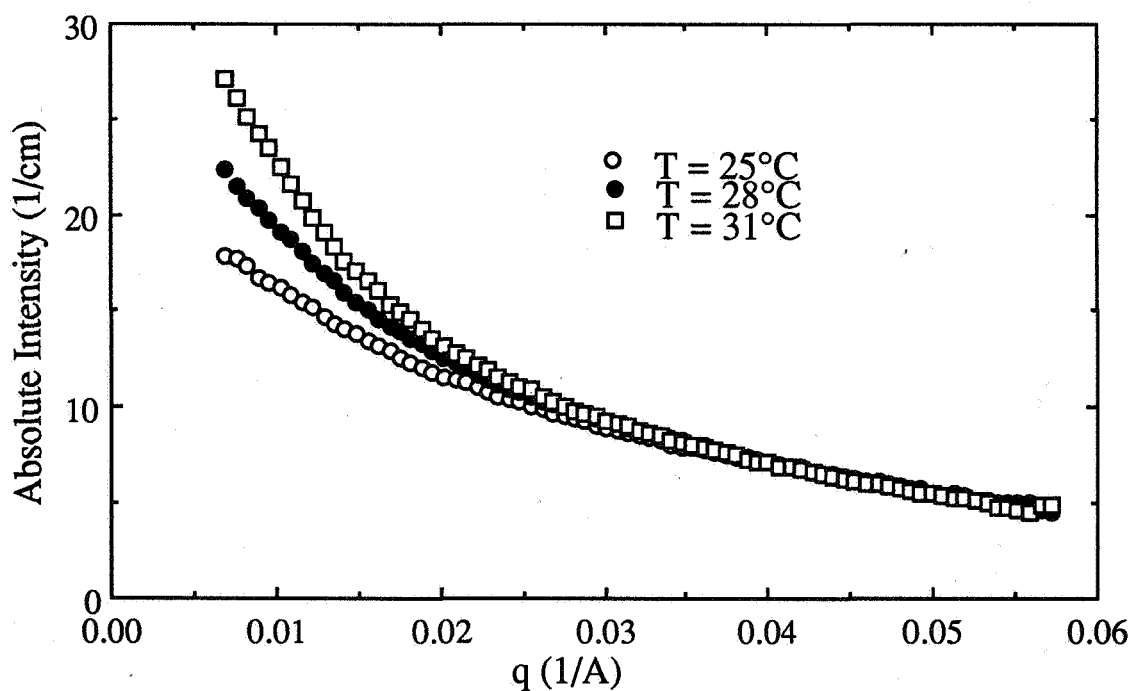

Figure 3. SANS spectra on absolute scale for a sample of 8 wt% $C_{12}E_6$, 4 wt% CO_2, and D_2O at a pressure of 62 bar as a function of the scattering vector q and temperature.

GRAVITY-DEPENDENT TRANSPORT IN INDUSTRIAL PROCESSES

Simon Ostrach and Yasuhiro Kamotani
Department of Mechanical and Aerospace Engineering
Case Western Reserve University
Cleveland, Ohio 44106

ABSTRACT

Gravity-dependent transport phenomena in various industrial processes is investigated in order to address a broader range of microgravity phenomena and to develop new applications of microgravity. A number of important topics are identified and analyzed in detail. The present article describes the results of some of topics which are: coating flow, zeolite growth and rotating electrochemical system.

INTRODUCTION

New directions for microgravity research that will also enhance commercial successes for the space program were indicated by Ostrach (1987). In particular, it was noted that microgravity research is dispersed over a number of disciplines but the underlying and unifying basis for new and unusual aspects in microgravity is gravitationally modified biophysicochemical transport phenomena. This means that the effects of fluid flow and heat and mass transfer on physical transport and biological and chemical reactions and, inversely, the transport associated with such processes will be different in a low-gravity environment. When it is realized that such phenomena are vital elements in the chemical, pharmaceutical, food-processing, and biotech industries as well as in material processing it is evident that commercialization possibilities will be increased by consideration of such topics and the scope of the microgravity research program will be broadened if it is directed to understand such phenomena in order to develop a knowledge base for the applications.

On this basis, grants jointly supported by NASA Code SN and C were granted, and as a result of the research efforts, a number of topics were identified that were important and which were of particular interest to us. These are: coating flows, rotating electrochemical systems, transport phenomena in zeolite growth, two-phase flows (bubble generation in liquid flow), and effect of g-jitter on liquid-gas interface. All of the topics, in the first phase of the research, were carefully reviewed and, thereafter, were thoroughly investigated in the second phase. Both scaling and numerical analysis of coating flows was performed by Kizito et al. (1991) for the applications both on earth and in space. In addition, experiments were carried out to verify some of their results (Ostrach et al., 1994; Kamotani et al., 1994). Kim (1992) completed a theoretical analysis of bubble formation in flowing continuous liquid phases under both terrestrial and microgravity environments. Lateral g-jitter (both regular and random modes) effects with and without thermocapillary convection on liquid motion in an open container under weightless conditions were studied numerically and analytically (Chao et al., 1991; Kamotani et al., 1994). Gulic et al. (1991) performed both scaling and experimental studied on natural convection in fluids contained in a flat, shallow, rapidly rotating annulus exposed to an axial stable temperature gradient. A detailed scaling analysis of natural convection in dilute electrochemical systems with multiple species was completed by Jiang et al. (1992, 1994) in which temperature gradients exist. An experimental study of transport phenomena in zeolite growth has been recently finished by Zhang et al. (1992, 1993, and 1994).

Based on these works, additional ground-based research and definitive low-gravity experiments have been identified. Due to the limited space, the information on three topics, coating flow, zeolite growth, and rotating electrochemical system, will be described individually in the following sections.

COATING FLOW

In industrial coating processes, surfaces are covered with one or more uniform liquid layers that are, subsequently cured or dried. Recently, new advanced technologies have emerged that use coating operation such as in the manufacture of semiconductor components, magnetic information storage systems and photoresist microelectronics. In these processes, the final film thickness can be very thin and must be highly accurate. The liquid layer may not be smooth and, in which case, waves or ribs or streaks may occur. In most coating configurations, the gravitational force acts parallel to the flow thereby creating shear stresses in the film making it more prone to shear instability. The instabilities tend to be three dimensional, making numerical simulation difficult and inaccurate thus requiring a careful experimental study. The present experiment investigates in details the nature and conditions under which an interfacial film instability occurs in coating flow.

Since the primary objective of the experiment is to determine the conditions under which the interfacial instability occurs for a coating film, the experimental apparatus was designed to minimize vibrations from the motor, building and other undesired movements of the coating belt and pulley. The major components of the experiment are sub-divided as follows; coating applicator, the working fluid and flow visualization; recording and analysis equipment. Fig. 1 shows the schematic experimental setup. The dip coating applicator was a rectangular open container constructed from clear scratch-proof LEXAN. Silicone oil (polydimethylsiloxane polymer) was the primary test fluid.

Coating flows have very small characteristic dimensions with a free surface. To enhance the image of the meniscus profile, a method called laser induced fluorescence was used. The two-dimensional flow field was viewed and recorded by a CCD camera placed perpendicular to the laser sheet. The camera was found to be very suitable because it was able to penetrate into the flow field past any edge effects at the same time giving good resolution. Finally, the position and shape of the free surfaces were accurately measured by pixel analysis of digitized images.

When the belt is steadily withdrawn from the applicator, a thin liquid film adheres to it because of the no slip condition at the belt wall and fluid viscosity. The free interface deforms at the meniscus creating capillary pressure because of its curvature. Also, the downstream film size and its stability depend on the withdrawal rate, physico-chemical properties of the fluid and the balance of viscous and body forces.

The inverse Stokes number St^{-1} can be defined as a ratio of gravitational force to viscous force, in which $St^{-1} = \rho g h_o^2/\mu U_o$, h_o and U_o represent the characteristic film thickness and the velocity of the belt, respectively. The experimental data of the final film thickness is plotted in Fig. 2 together with the theoretical results (Levich, 1962; Kizito et al., 1991) showing $St^{-1/2} = 0.93\ Ca^{1/6}$ when Ca number is small (where $Ca=\mu U/\sigma$). From this figure, for all the fluids tested, the non-dimensional final thickness ($St^{-1/2}$) was no longer a function of Ca number beyond a certain Ca number. In the cases of this study, $St^{-1/2}$ was about 0.65 for high capillary number flow whereas for high Reynolds number flow $St^{-1/2}$ was about 0.69. However, we have not included values of $St^{-1/2}$ greater than 0.69 because the film interface had already become wavy. The existence of a maximum $St^{-1/2}$ has also been shown theoretically by Kamotani et al. (1994) for low Re number flow (where Re is Reynolds number = $h_o \rho U_o/\mu$). When the non-dimensional final thickness exceeded a certain critical value, the film interface became wavy. That St^{-1} number attains a maximum is a necessary condition for the wave motion to exist at the interface of the coating film. This condition implies that the appearance of waves is somehow related to the diminishing importance of surface tension forces relative to gravity and viscous forces in the meniscus region. The waves on the interface are constantly maintained by gravity. (Ostrach et al., 1994; Levich, 1962).

The techniques described above were suitable for the first phase of the coating instability study. Capillary forces are the restoring force which causes the damping of the waviness of the interface. That, the effect of surface tension is relatively small when Ca number is large and when the film becomes wavy seems to suggest the following. Any small disturbances generated in the meniscus region are no longer damped and thus propagated downstream to trigger the wavy motion there. The conclusion from this experiment that gravity significantly

influences the stability of the coating film is important in the design and implementation of industrial coating processes.
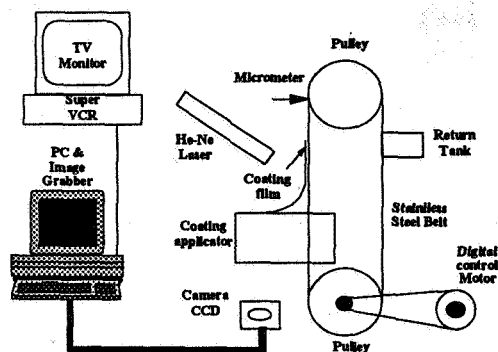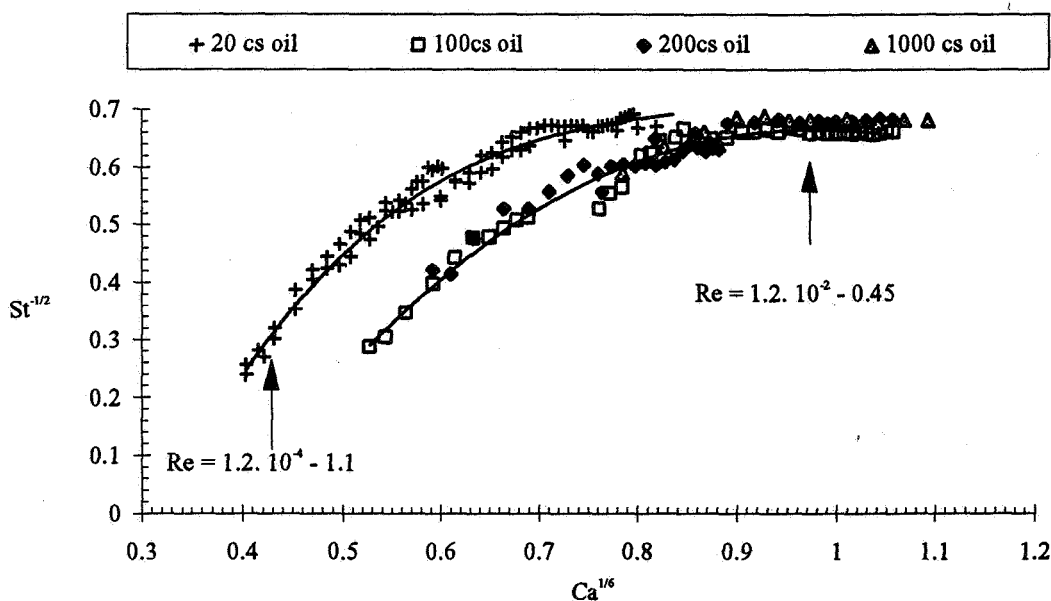

Figure 1. Schematic experimental setup.

Figure 2. Non-dimensional final thickness ($St^{-1/2}$) vs. non-dimensional velocity ($Ca^{1/6}$) at low and high Reynolds number.

ZEOLITE GROWTH

Aluminosilicate crystals, commonly referred to as zeolites, have been extensively used in the petroleum, chemical and environmental industries because of their unique microporous structures. Considerable research efforts have been devoted to the field of zeolite synthesis, aimed mainly at creating new structures and, thus, finding new commercial applications. In recent years potential applications of zeolites in chemical sensor

technology, electronics and optics are being examined. Therefore, zeolite crystals of considerably large size are expected in order to have characterization studies that would help open up their uses in such novel technologies.

However, under terrestrial conditions, there is no available technology to grow large zeolite crystals, which was believed to be the consequence of crystal particles sedimentation through their mother liquid where they nucleate and crystallize (Sand et al., 1987). Orbiting spacecraft seems to offer an attractive environment to researchers for seeking a new approach to accomplish the task since the sedimentation is significantly reduced under microgravity conditions. There have been a number of attempts to grow zeolites in space, but with no quantitative study whatsoever regarding the gravity-dependent transport phenomena in zeolite growth. Zhang *et al.* (1992) investigated gravitational effects on zeolite growth, first considered by Sand et al. (1987), and found that gravity-induced secondary nucleation (GSN) is the only possible detrimental effect. GSN means as follows: after an induction period some primary nuclei are formed within the reaction mixture. These nuclei shortly become crystals of certain sizes and then, due to gravity, settle down to the bottom of the reactor to form a close-packed layer where growth terminates. After that, some nuclei are formed again (i.e. secondary nucleation) at the top part of the reaction mixture, and they would follow the same course as their predecessors. This process continues until the concentration of nutrients in this part goes below a threshold value. In this manner, the total number of crystals increases for a fixed amount of nutrients, therefore, the average crystal size decreases. In reality, the phenomenon of GSN is more complicated than that described as above. Usually, zeolites grow within cavities of the porous gel network formed by gel particles of the colloidal size due to London-van der Waals forces. The gel particles serve as a source for nutrients, dissolving and then transferring to growing crystal surfaces through the solution. Under normal gravity, a discrete boundary is seen separating the clear solution at the top from the opaque white column called the gel portion. As the growth process proceeds, this boundary moves downward. Figure 1 shows this phenomenon, which is called the gel shrinkage, giving a microscopic view of the opaque white gel portion. We modeled the growth-in-gel crystallization and found that the gel shrinkage, a gravity-dependent phenomenon, can be used as a parameter to identify different stages of a growth process, nucleation and crystallization (Zhang et al., 1993). A method of increasing the crystal size by adding nutrients after the onset of crystallization was subsequently developed.

Additionally, a non-dimensional parameter was derived as a criterion for the occurrence of GSN, based on the modeling of growth-in-gel crystallization. Thereby, the benefit of microgravity concerning the increment of the crystal size is discussed in terms of whether or not GSN (detrimental) will occur on earth. Our theory was found to be consistent with the results of STS-40 (SLS-1 mission) and STS-50 (USML-1 mission) experiments (Zhang et al., 1994), systematic space experimental studies performed by Sacco et al. (1993).

As mentioned above, adding nutrients at some moment after the onset of crystallization can increase the crystal size. However, for a system designed to grow large crystals (e.g. 30 mm), this method did not work because gravity caused large crystals to settle out the added nutrients. Consequently, microgravity seems to provide an ideal environment to grow much larger zeolite crystals. However, there will be no discrete boundary seen at μ-g. In order to define an appropriate parameter for space growth, corresponding to the gel shrinkage for 1-g growth, to determine the moment of adding nutrients (after the onset of crystallization), zeolite crystallization at μ-g was modeled (Zhang et al., 1994). Unlike the growth process at 1-g, the porosity of the gel portion will increase under microgravity, because cavities of the porous gel network, within which crystals grow, will enlarge due to continuous dissolution of gel particles and to the lack of a packing effect resulting from gravity (Fig. 3 a). Hence, the overall porosity change was defined as the parameter to determine the moment of adding nutrients for μ-g growth. It was found that this parameter is proportional to the mass transfer rate at crystal growing surfaces, which will eventually approach zero. Hence, this moment can be easily identified and therefore is proposed to be the moment at which to add nutrients at μ-g. Nevertheless, how to measure the overall porosity change needs to be investigated, so that the method of nutrient addition can be applied to the growth process in space (which is aimed at growing large crystals), thus further increasing the crystal size.
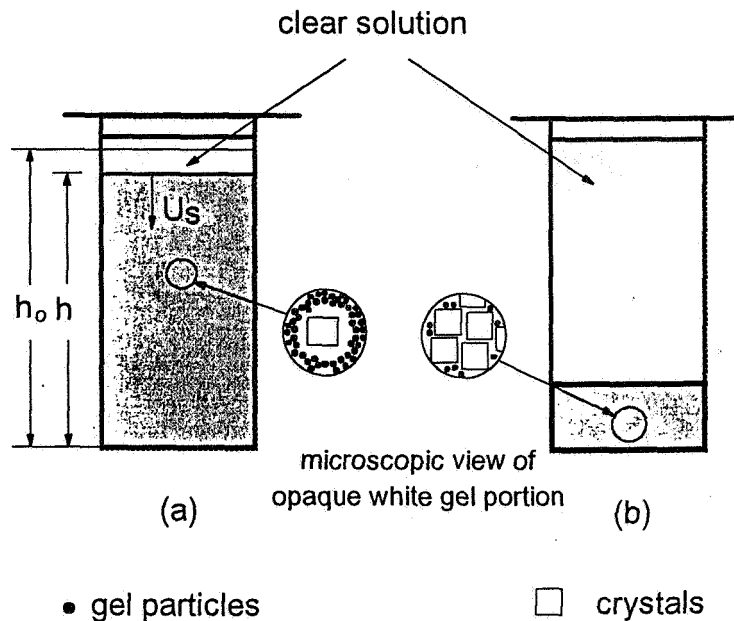
clear solution

microscopic view of
opaque white gel portion

(a)

(b)

• gel particles

☐ crystals

Figure 3. The observation of growth-in-gel zeolite crystallization.

ROTATING ELECTROCHEMICAL SYSTEM

The present research was motivated by a recent discovery of a rotating nickel-zinc battery system that has considerable advantages over conventional ones. A nickel-zinc battery provides very high energy density and power density, and low toxicity at a comparatively low cost. Therefore, the advanced rechargeable Ni-Zn battery is one of leading candidates for large-scale energy storage technologies, such as, electric vehicles and electric utility load leveling. The battery system can also find its space applications in life support systems and in energy storage and power generation. The major problem for the stationary Ni-Zn batteries is the limited cycle life of the Zn electrode during multiple recharge cycles, which has been traced to: first, formation and propagation of Zn dentrites that leads to cell shorting, and second, Zn electrode instability that causes gradual capacity loss (Mclarnon and Cairns, 1991). By rotating battery, the following effects were noticed: (i) at the rotation corresponding to 50 g (earth's gravitation) the dentrite growth was nearly eliminated, (ii) the discharge current density was increased by a factor of five over non-rotating battery performance, and (iii) the electrochemical by-products were continuously removed due to a strong centrifugal force.

The rotating Ni-Zn battery system can be considered as a rotating electrolyte inside shallow cylinders subjected to axial concentration and temperature gradients. The lack of knowledge of transport phenomena in such configurations not only hinders the commercialization of Ni-Zn battery, but could also lead to erroneous conclusion with regard to the practicability of the battery. To understand the transport processes in the system, Gulic et al. (1991) and Ostrach et al. (1992) performed both scaling analysis and experiments on heat transfer in a rotating cylinder heated from above for the cases with large Prandtl number and small Ekman number. In the experiment a photochromic technique was used to visualize the flow field. When $(Pr \beta_T \Delta T)^{1/4} > 1$, the flow field is dominated by thermal buoyancy force in the radial direction and Nusselt number, Nu, is characterized by the one-fourth power of $Pr \beta_T \Delta T E^{-2}$, while for $Pr \beta_T \Delta T < 1$, the vertical Ekman suction dominates the heat transfer process and Nu is proportional to $Pr \beta_T \Delta T E^{-1/2}$. Good agreement between the scaling results and the experimental data have been demonstrated. It is believed that successful control of dentrite growth at the higher rotation rates in the rotating battery can be attributed to well-behaved solutal convection. The conclusions drawn from the experiment appeared to support this argument.

In general, transport phenomena in an electrochemical system is different from that in a nonelectrolytic system. It is known that under the limiting current condition mass transfer process in the electrochemical system is controlled by solutal diffusion and convection, which by no means indicates that the transport phenomena in the system become the same as that in the nonelectrolytic system. First, the electrochemical system must satisfy the electroneutrality condition in the bulk solution except in the so-called double layer. Secondly, the migration contribution to mass transfer does not occur for the nonelectrolytic system. Most of the theoretical work on transport phenomena in electrochemical systems is highly idealized and inadequate for practical applications. In order to obtain meaningful models a detailed scaling analysis was performed by Jiang et al. (1992, 1994) for multiple-component electrochemical systems. Both binary and well-supported ternary systems were considered in which convection along a vertical flat plate is generated by both horizontal temperature and concentration gradients. For the ternary system, such as cupric-sulphate-acid solution, the hydrogen and sulphate ions must share a common solutal boundary layer to satisfy electroneutrality. Therefore only two solutal layers, the inner and outer layers can be defined. Concentration profiles of the sulphate, hydrogen, and cupric ions were estimated in both layers respectively. In the inner layer, the bulk concentration of both sulphate and hydrogen ions increase toward the values at the interface between the inner and outer layers, while that of cupric ion remains constant. The concentration of the sulphate ions reaches a maximum at the interface as shown in Fig. 4. As a result, near the cathode surface the solutal buoyancy force is upward in the inner portion of the entire solutal layer, and downward in the rest of the layer. A new approach which considers the effects of heat and mass transfer simultaneously with the momentum transport is developed to study transport correlation for the thermosolutal convection. It is found that the ratio of thermal to solutal boundary layers as well as the ratio of the dimensionless mass transfer number, Sherwood number, to Nusselt number, are proportional to the two-fifth power of Lewis Number. The Scaling results were compared with both analytical and experimental data, and satisfactory agreement was demonstrated (Fig. 5).

S   electrode surface,   B   bulk solution
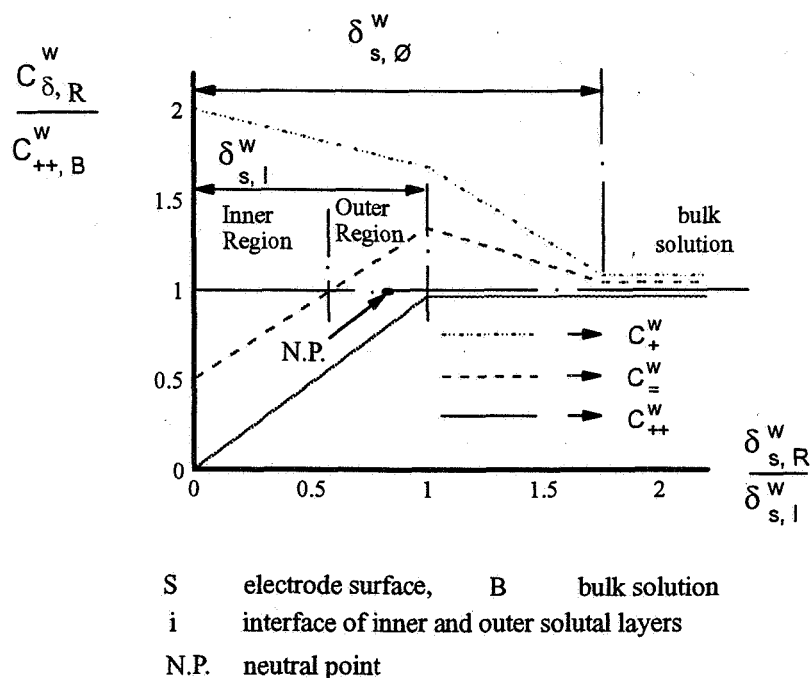i   interface of inner and outer solutal layers
N.P.   neutral point

Figure 4. Estimated concentration profiles of all ions in a
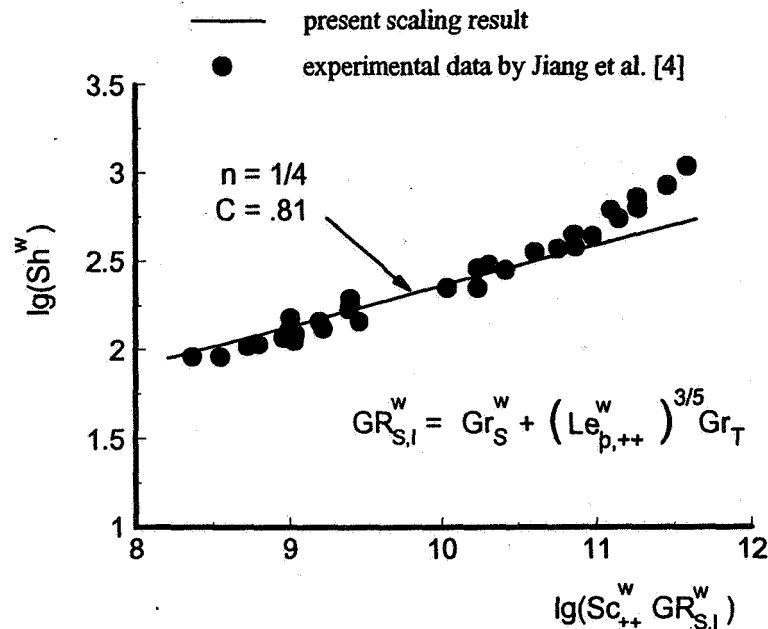cupric-sulphate-acid electrolyte

Figure 5. Comparison between the experimental

data and the present scaling result

REFERENCES

Chao, L. Y., Ostrach, S., and Kamotani, Y., 1991, Lateral G-Jitter Effects on Liquid Motion and Thermocapillary Convection in an Open Square Container under Weightless Condition, Ph.D. Thesis, Case Western Reserve s, Cleveland, Ohio, EMAE/TR-91-201.

Gulic, I., Ostrach, S., and Kamotani, Y., 1991, Thermal Convection in A Rotating Annulus, M.S. Thesis, Case Western Reserve University, Cleveland, Ohio, EMAE/TR-91-204.

Jiang, H. D., Ostrach, S., and Kamotani, Y., 1992, Scaling Analysis of Thermosolutally-Driven Natural Convection in Electrochemical Systems, *Transport Phenomena Science and Technology*, Ed. by B. X. Wang, pp. 164-169.

Jiang, H. D., Ostrach, S., and Kamotani, Y., 1994, Thermosolutal Transport Phenomena in Large Lewis Number Electrochemical Systems, *Int. J. Heat and Mass Transfer* (submitted).

Kamotani, Y., Chao, L. Y., and Ostrach, S., 1994, G-Jitter Effects on Free Surface Motion in A Cavity, *J. Spacecraft and Rockets* (accepted).

Kamotani, Y., Kizito, J. P., and Ostrach ,S., 1994, Prediction of Meniscus Shapes in Dip Coating at Low to High Capillary Numbers, *AIChE*, (submitted).

Kim, I., Ostrach, S., and Kamotani, Y., 1992, Modeling of Bubble and Drop Formation in Flowing Liquids in Terrestrial and Microgravity Environments, Ph.D. Thesis, Case Western Reserve University, Cleveland, Ohio, EMAE/TR-92-207.

Kizito, J. P., Ostrach, S. and Kamotani, Y., 1991, Coating flow in Microgravity, M.S. Thesis, Case Western Reserve University, Cleveland, Ohio, EMAE/TR-91-202.

Levich, V. G., 1962, *Physicochemical Hydrodynamics*, Prentice-Hall, Englewood Cliffs, NJ.

Mclarnon, F. R. and Cairns, E. J., 1991, The Secondary Alkaline Zinc Electrode, *J. Electrochem. Soc.*, **138**, pp. 645-664.

Ostrach, S. and Kamotani, Y., 1987, Gravity-Dependent Transport in Industrial Processes, A Proposal to NASA, Cleveland, Ohio.

Ostrach, S., Gulic, I., Kamotani, Y., and Jiang, H. D., 1992, Thermal Convection in A Shallow Rotating Annulus, 18th International Congress of Theoretical and Applied Mechanics, Haifa, Israel, August.

Ostrach, S., Kizito, J. P. and Kamotani, Y., 1994, Free Coating flow at high Capillary and Reynolds numbers, *ASME* (submitted).

Sacco, A., Thompson, R. W., and. Dixon, A. G, 1993, Zeolite crystal growth in space - what has been learned AIAA 93-0473, 31st Aerospace Sciences Meeting & Exhibit, Jan. 11-14, Reno, NV.

Sand, L. B., Sacco, A., Thompson, R. W., and Dixon, A. G., 1987, *Zeolites*, 7, p.387.

Zhang, H., Kamotani, Y. and Ostrach, S., 1992, Transport Phenomena in Materials Processing and Manufacturing, *ASME*, HTD-Vol. 196, p.83.

Zhang, H., Kamotani, Y. and Ostrach, S., 1993, Growth-in-gel zeolite crystallization and transport phenomena, *Journal of Crystal Growth*, **128**, pp. 1288-1292.

Zhang, H., 1994, Modeling of the zeolite crystal growth process in microgravity and comparison with space flight results, *Journal of Spacecraft and Rockets* (accepted).

ELECTROKINETIC TRANSPORT OF HETEROGENEOUS PARTICLES IN SUSPENSION

D. Velegol, S. Garoff, J.L. Anderson
Department of Chemical Engineering
Carnegie Mellon University
Pittsburgh, PA 15213

ABSTRACT

The Smoluchowski equation for electrophoresis predicts that the electrophoretic velocity of a particle is proportional to its zeta potential but not its size, shape, or orientation. Furthermore, the equation predicts that the rotation rate is identically zero. The Smoluchowski equation fails for *heterogeneous particles* (i.e., those with non-uniform zeta potentials). Recent theories and experiments show that particles with a dipole moment of zeta potential rotate into alignment with an externally applied electric field. For doublets (particles composed of two spheres) the rotation rate depends on 1) whether the spheres are rigidly locked or freely rotating, and 2) the gap distance between the spheres. The relative configuration of two coagulated spheres is determined by the colloidal forces of the system. The goal of our research is to use measurements of electrophoretic rotation to determine the gap between two spheres of a colloidal doublet and also to determine whether or not the doublet is rigid.

INTRODUCTION

Almost all colloidal particles immersed in aqueous solution are electrically charged. The electrostatic potential at a particle's surface is called the zeta potential. To maintain electroneutrality oppositely-charged ions (counter-ions) from the solution form a thin layer near the surface. Together the charged solid surface of the particle and the surrounding layer of oppositely-charged fluid compose the electrical *double layer*.

When an electric field is applied to a suspension of colloidal particles, the field interacts with the electrical double layer, and the resulting forces move the particle. This movement is called *electrophoresis*, one of several *phoretic* processes [1]. The Smoluchowski equation predicts

$$U=\frac{\varepsilon\zeta}{\eta}E^{\infty} \tag{1a}$$
$$\Omega=0 \tag{1b}$$

where U is the translational velocity of the particle, Ω is its rotation rate, ε is the permittivity of the bulk fluid, η is the viscosity, and E^{∞} is the applied electric field. The Smoluchowski equation requires three main conditions:

1. The particle must be rigid and non-conducting.
2. The double layer thickness (of order κ^{-1}, the Debye screening length) must be much smaller than the size of the particle (i.e., the radius for a spherical particle).
3. The zeta potential must be uniform over the surface.

Equation (1) applies to any particle that satisfies these conditions, independent of its size or shape. Typically, ζ is of order $kT/e = 25.7$ mV at 25 °C, and in water the electrophoretic mobility (U/E^{∞}) for this zeta potential is 2.0 μm s^{-1}/V cm^{-1}.

HETEROGENEOUS PARTICLES

Many particles have non-uniform zeta potentials over their surfaces—they are heterogeneous. Kaolinite clay particles, which have the shape of a disk, may have different zeta potentials on each face and yet a third zeta potential on the edge. Aggregates are nonuniform when the original subunits have different zeta potentials. *Heterogeneous particles (those with a non-uniform zeta potential over their surface) do not obey the Smoluchowski equation.*

Figure 1 shows examples of heterogeneous particles and references to theories describing their electrophoretic motion. Here we summarize the theory for doublets [2]:

$$U_p = \frac{\varepsilon}{\eta}\left[\zeta_1\left(1-K^p\right)+\zeta_2 K^p\right]E^\infty \tag{2a}$$

$$U_n = \frac{\varepsilon}{\eta}\left[\zeta_1\left(1-K^n\right)+\zeta_2 K^n\right]E^\infty \tag{2b}$$

$$\Omega = -\frac{d\theta}{dt} = \frac{\varepsilon}{\eta}\left(\frac{\zeta_2-\zeta_1}{a_2+a_1}\right)N E^\infty \sin(\theta) \tag{2c}$$

Equation (2a) describes the translation of a colloidal doublet when its axis is parallel to the electric field, and (2b) describes the translation when the axis is normal to the electric field. Equation (2c) gives the angular velocity of the doublet as a unit. The values of K^p, K^n, and N—three geometric parameters—depend on the ratio of the sphere radii (a_2/a_1) and the dimensionless gap ($\lambda=\delta/(a_1+a_2)$, where δ is the separation between the surfaces of the spheres). In addition these geometric parameters depend on whether the spheres composing the doublet are rigidly locked or freely rotating. Figure 2 shows how the value of N (the rotation rate parameter) depends on λ. Not only is N sensitive to the gap, but $N>1$ for *freely rotating spheres* and $N<1$ for *rigid doublets*. The values of N are calculated from the results of Keh and Yang [3].

COLLOIDAL DOUBLETS AND THE GAP BETWEEN TWO COAGULATED SPHERES

The DLVO theory of coagulation predicts two potential energy minima for the two spheres of a doublet [4]. Figure 3 shows the how the potential energy varies with gap distance for two spheres with the same zeta potential. When the spheres touch (i.e., $\lambda=0$), the particles lie in a deep *primary* energy minimum; in this case, the doublet is expected to be rigid.

When the spheres have the same charge, they can also be stable in a *secondary* energy minumum. The secondary minumum lies at distances comparable to the Debye screening length κ^{-1}, and it is not as deep as the primary minumum. The gap is finite ($\lambda>0$) for spheres in a secondary minumum, so not only can the doublet rotate as a unit but each sphere can also rotate independently.

Van de Ven and Mason [5] used shear flows to determine whether colloidal doublets were rigidly locked or freely rotating. They measured the period of rotation (T) of the Jeffrey orbitals of symmetric doublets ($a_2/a_1=1$). Because T is a function of λ, the gap distance could, in principle, be determined from these measurements. Van de Ven and Mason found that a significant number of doublets had $\lambda>0$; that is, the two spheres of a doublet appeared to be freely rotating according to the measured value of T. Unfortunately, the difference between T for a doublet of freely rotating spheres compared to rigidly locked spheres is not as large as one would like in order to make definitive conclusions about the relative configuration of the spheres.

Electrophoretic rotation, on the other hand, appears to be a sensitive probe of the rigidity of doublets—if $N>1$ then the spheres of the doublet are freely rotating; otherwise the doublet is rigid. In addition, the value of N can provide an estimate for the gap distance.

EXPERIMENTS AND PRELIMINARY DATA

We form aggregates by mixing two dilute suspensions of different polystyrene spheres [6]. The two spheres can have zeta potentials of the same sign but different magnitudes, or zeta potentials of opposite sign. The important distinction between these two cases is that in the former, DLVO theory predicts the existence of a secondary potential minumum which should allow free rotation of the spheres, whereas in the latter case no secondary minumum is predicted. The particle diameters for our experiments are in the range of 1 to 5 μm. Using a VCR and simple imaging analysis, we determine the orientation angle $\theta(t)$ (Figure 4). These data are fit to the integrated form of equation (2c). Figure 5 shows data from one experiment ($a_2/a_1 \approx 1.5$). The best fit between the data and (2c) is N = 1.68 $\pm$ 0.20 (95% confidence interval).

Because N>1 in these experiments, we conclude that the two spheres in the doublet were *freely rotating*. The curve in Figure 2 (this curve is for equal-sized spheres, but for other size ratios the curve changes little) shows that N = 1.7 corresponds to λ=0.001, or roughly δ=2 nm. For this experiment we measured only $\zeta_2 - \zeta_1$ (i.e., not each zeta potential separately), so we cannot compare the value of δ to the predictions of existing theories of doublet configuration based on colloidal forces.

Future experiments are aimed at measuring N as a function of electrolyte concentration (i.e., Debye screening length). The zeta potentials of the single spheres (i.e., ζ_1 and ζ_2) will be determined *in situ*. Latexes with ζ_1 and ζ_2 of opposite sign and the same sign will be studied. The goal is to probe the configuration of doublets—specifically the gap distance and whether they are rigid or not—and to compare the results with theories for the colloidal forces between the particles.

ACKNOWLEDGEMENT

REFERENCES

1. Anderson, J.L., Colloid Transport by Interfacial Forces, *Annual Review of Fluid Mechanics*, 21, 61 (1989).
2. Fair, M.C. and Anderson, J.L. *International Journal of Multiphase Flow*, 16, 663, 1131 (1990).
3. Keh, H.J. and Yang, F.R. Particle Interactions in Electrophoresis IV. Motion of Arbitrary Three-Dimensional Clusters of Spheres, *Journal of Colloid and Interface Science*, 145, 362 (1991).
4. Russel, W.B., Saville, D.A., and Schowalter, W.R. *Colloidal Dispersions*. Cambridge University Press (1989), 262-263.
5. Van de ven, T.G.M and Mason S.G. The Microrheology of Colloidal Dispersions V. Primary and Secondary Doublets of Spheres in Shear Flow, *Journal of Colloid and Interface Science*, 57, 517 (1976).
6. Fair, M.C. and Anderson, J.L. Electrophoresis of Heterogeneous Colloids: Doublets of Dissimilar Particles, *Langmuir*, 8, 2850 (1992).
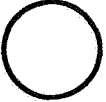
Spheres		Anderson *et al.* *JCIS* **105**, 45 (1985) *JCIS* **158**, 1 (1993)
Ellipsoids		Fair and Anderson *JCIS* **127**, 388 (1989)
Doublet		Fair and Anderson *Int. J. Multiphase Flow*, **16**, 663, 1131 (1990) *Langmuir*, **8**, 2850 (1992)
Triplet		Keh and Yang *JCIS* **145**, 362 (1991)
Spherical Macromolecule		B. Yoon *JCIS* **142**, 575 (1991)
Clay disk		Anderson and Fair Proceedings 1991 Coating Conference, TAPPI, Atlanta

Figure 1: Theory for non-uniformly charged particles
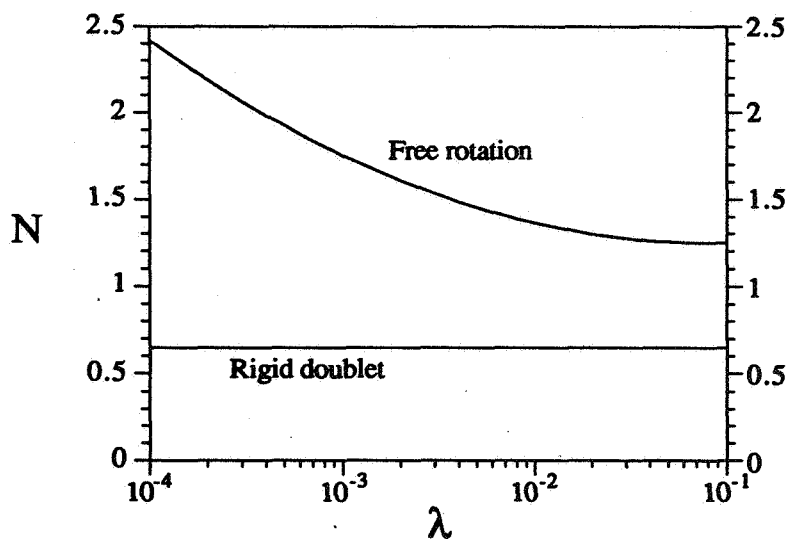
Figure 2: Rotation rate parameter N versus gap for a doublet of two equal size spheres.

404
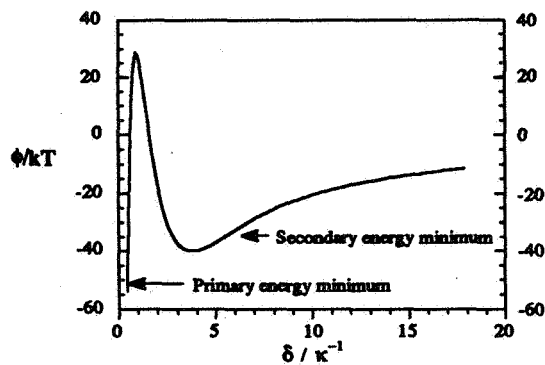
Figure 3: Potential energy vs. gap distance for two identically charged colloidal particles.
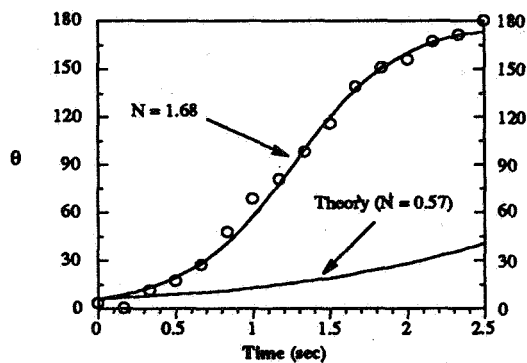
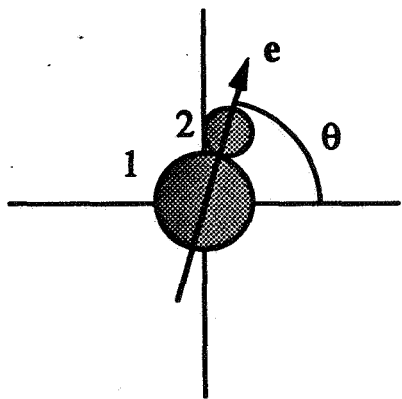Figure 4: Sample data fitted to integrated form of equation (2c).

Figure 5: Orientation of the doublet. Theta is the solid angle between the direction of the applied field and the axis of the doublet.
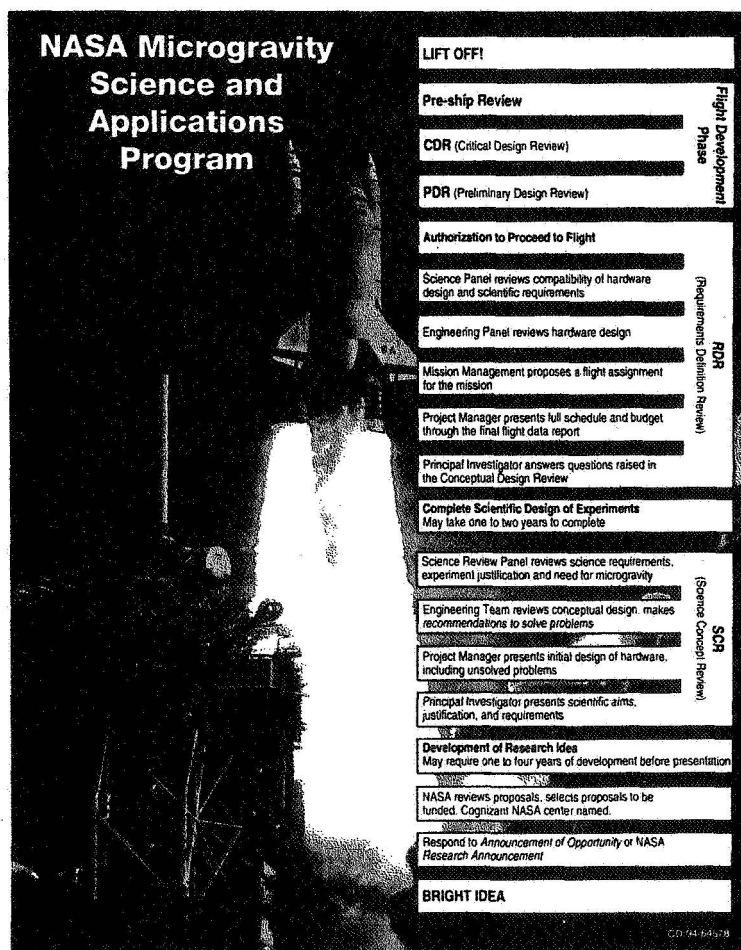
Microgravity Fluids Program Information

7.

THE PATH TO AN EXPERIMENT IN SPACE
(From Concept to Flight)

Jack A. Salzman
Space Experiments Division
Lewis Research Center
Cleveland, Ohio 44135

TIME FROM FLIGHT PI SELECTION TO LAUNCH

NEW HARDWARE

- GLOVEBOX - 3 YEARS OR LESS
- SOUNDING ROCKETS - 3 TO 4 YEARS
- GET-AWAY SPECIAL - 3 TO 4 YEARS
- MIDDECKS - 5 TO 6 YEARS
- USMP - 6 TO 8 YEARS
- USML - 6 TO 8 YEARS

REFLIGHTS (MINOR OR NO MODS)

- SOUNDING ROCKETS - 6 MONTHS
- GET-AWAY SPECIAL - < 1 YEAR
- MIDDECKS - 1 YEAR
- USMP - 2 YEARS
- USML - 2 YEARS

Key Flight Experiment Phases and Schedule Drivers

Experiment Definition (PI & PS)

- Focus science objectives into experiment concept
- Conduct ground-based program (analysis, 1-g and μ-g tests)
- Determine flight experiment science requirements
- Demonstrate basic experiment feasibility

Flight Experiment Concept Definition (PI, PS, and PM)

- Define engineering requirements and hardware concepts, (size, weight, power, etc.)
- Determine appropriate carrier choice(s)
- Demonstrate technology readiness
- Prepare project plan (schedule, cost, etc.)

Flight Experiment Development (PI, PS & PM)

- Generate final hardware design
- Complete hardware development, assembly, test (performance and qualification)
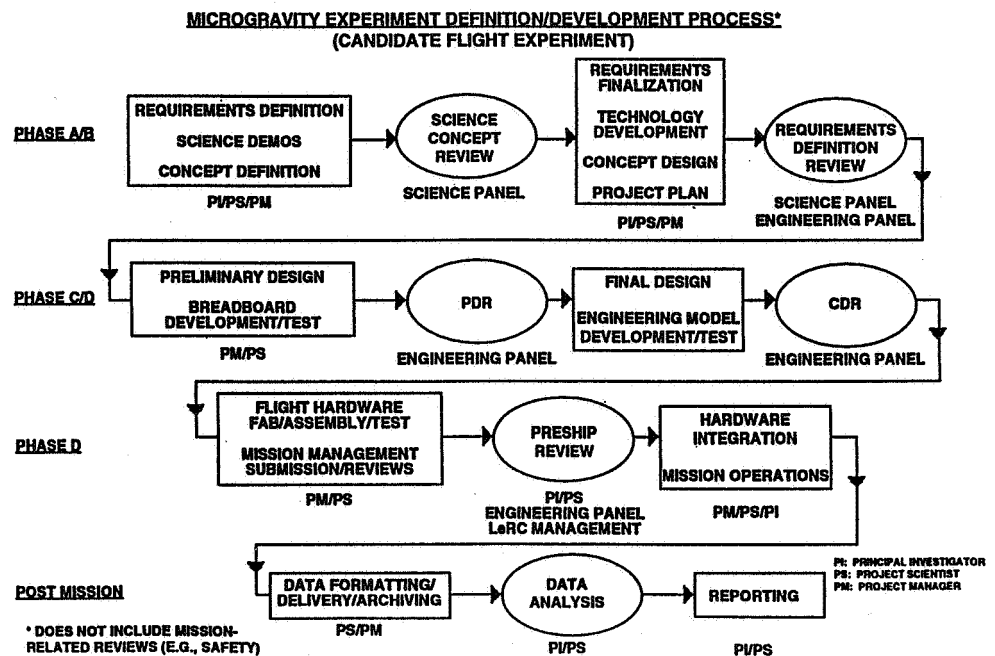- Prepare documentation

410

Key Flight Experiment Phases and Schedule Drivers

Mission Integration and Operations (PI, PS, PM, & MM)

- Conduct mission planning
- Complete mission, integration and safety reviews
- Complete physical integration
- Complete documentation
- Conduct mission operations

> Review, Review, Review, •••••••••••••••••••••••••••••••••••••
> Document, Document, Document ••••••••••••••••••••••••••

PI (Principal Investigator), PS (Project Scientist), PM (Project Manager), MM (Mission Manager)

MICROGRAVITY EXPERIMENT DEFINITION/DEVELOPMENT PROCESS*
(CANDIDATE FLIGHT EXPERIMENT)

PHASE A/B

REQUIREMENTS DEFINITION	SCIENCE CONCEPT REVIEW	REQUIREMENTS FINALIZATION
SCIENCE DEMOS		TECHNOLOGY DEVELOPMENT
CONCEPT DEFINITION		CONCEPT DESIGN
PI/PS/PM	SCIENCE PANEL	PROJECT PLAN

REQUIREMENTS DEFINITION REVIEW

PI/PS/PM — SCIENCE PANEL / ENGINEERING PANEL

PHASE C/D

PRELIMINARY DESIGN / BREADBOARD DEVELOPMENT/TEST — PM/PS

PDR — ENGINEERING PANEL

FINAL DESIGN / ENGINEERING MODEL DEVELOPMENT/TEST

CDR — ENGINEERING PANEL

PHASE D

FLIGHT HARDWARE FAB/ASSEMBLY/TEST / MISSION MANAGEMENT SUBMISSION/REVIEWS — PM/PS

PRESHIP REVIEW — PI/PS ENGINEERING PANEL LeRC MANAGEMENT

HARDWARE INTEGRATION / MISSION OPERATIONS — PM/PS/PI

POST MISSION

* DOES NOT INCLUDE MISSION-RELATED REVIEWS (E.G., SAFETY)

DATA FORMATTING/ DELIVERY/ARCHIVING — PS/PM

DATA ANALYSIS — PI/PS

REPORTING — PI/PS

PI: PRINCIPAL INVESTIGATOR
PS: PROJECT SCIENTIST
PM: PROJECT MANAGER

411

DEFINITION AND ENGINEERING DEVELOPMENT PHASE

SCIENCE CONCEPT REVIEW
SCR
▽

REEQUIREMENT
DEFINITION REVIEW
RDR
▽

SCIENCE DEFINITION

- DEVELOP SCIENCE REQUIREMENTS
- PROVIDE JUSTIFICATION FOR FLIGHT
- DEMONSTRATE SCIENTIFIC FEASIBILITY
- IDENTIFY ENGINEERING CONCEPTS
- IDENTIFY HIGH RISK DEVELOPMENT ITEMS
- DEFINE THE PLAN TO RDR
- IDENTIFY HAZARDS

ENGINEERING DEVELOPMENT

- UPDATE SCIENCE REQUIREMENTS
- DEFINE FUNCTIONAL REQUIREMENTS
  AND CONCEPTUAL DESIGN
- CONFIRM THE FEASIBILITY OF HIGH RISK
  ELEMENTS
- DEFINE THE BUDGET (INCLUDING
  CONTINGENCY) AND SCHEDULE
- PREPARE PHASE O SAFETY PACKAGE

▽ HQ CONTROLLED; REQUIRES APPROVAL BEFORE PROCEEDING

GROUND-BASED REDUCED GRAVITY RESEARCH FACILITIES

ZERO GRAVITY
RESEARCH FACILITY
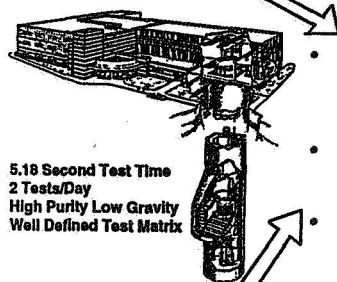
5.18 Second Test Time
2 Tests/Day
High Purity Low Gravity
Well Defined Test Matrix

DROP TOWER
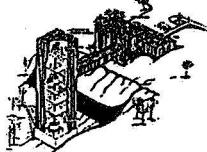
2.18 Second Test Time
12 Tests/Day
Exploratory Tests
Large Test Matrixes

DC-9, KC-135,
LEARJET AIRCRAFT

18-22 Second Test Time
Large Experiments
Operator Interaction
Large Test Matrix

- UNIQUE LABORATORIES FOR THE DEVELOPMENT
  AND SUPPORT OF RESEARCH AND TECHNOLOGY
  VALIDATION ACTIVITIES

- VALUABLE SOURCE OF DATA IN THE PI FLIGHT
  EXPERIMENT DEFINITION PROCESS

- IMPORTANT TEST FACILITIES IN THE FLIGHT
  HARDWARE DESIGN, DEVELOPMENT AND TEST
  PROCESS

Optimize Designs
Define Measurement Requirements
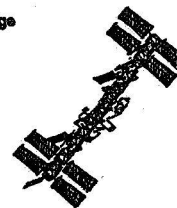Refine Experiment Timelines,
Procedures

Develop Low-G Specific Technologies/
Techniques
Confirm Benefits of Flight
Acquire Fundamental Knowledge

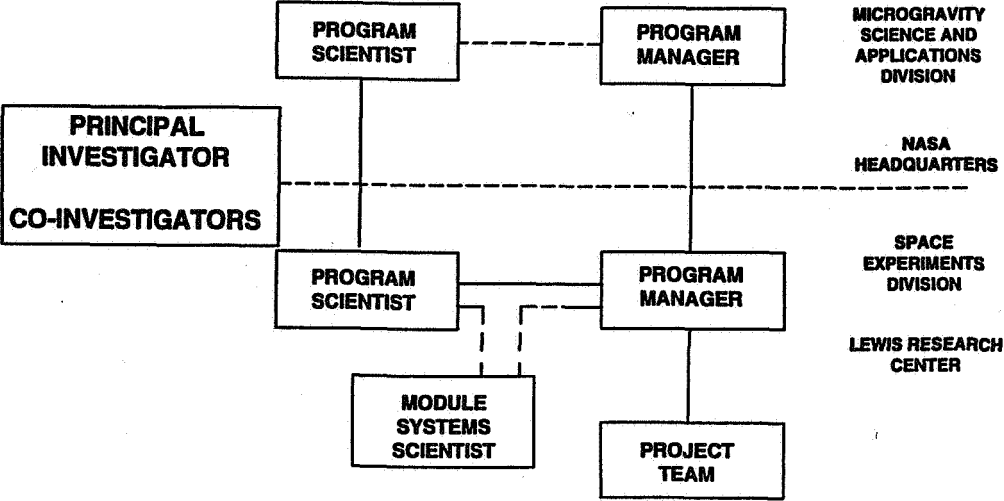STS, ELV EXPERIMENTS
SPACE STATION PRECURSOR EXPERIMENTS

1994   2000

412

PROJECT ORGANIZATION

```
┌─────────────┐                    ┌─────────────┐          MICROGRAVITY
│   PROGRAM   │- - - - - - - - - - │   PROGRAM   │          SCIENCE AND
│  SCIENTIST  │                    │   MANAGER   │          APPLICATIONS
└─────────────┘                    └─────────────┘          DIVISION

┌──────────────────┐
│   PRINCIPAL      │                                         NASA
│  INVESTIGATOR    │- - - - - - - - - - - - - - - - - - - -  HEADQUARTERS
│                  │
│ CO-INVESTIGATORS │
└──────────────────┘
                    ┌─────────────┐    ┌─────────────┐       SPACE
                    │   PROGRAM   │    │   PROGRAM   │       EXPERIMENTS
                    │  SCIENTIST  │────│   MANAGER   │       DIVISION
                    └─────────────┘    └─────────────┘
                                                             LEWIS RESEARCH
                    ┌─────────────┐                          CENTER
                    │   MODULE    │
                    │   SYSTEMS   │    ┌─────────────┐
                    │  SCIENTIST  │    │   PROJECT   │
                    └─────────────┘    │    TEAM     │
                                       └─────────────┘
```

PRINICIPAL INVESTIGATOR / CO-INVESTIGATORS

RESPONSIBILITIES

- ENSURE A HIGH SCIENTIFIC RETURN FROM THE FLIGHT PROJECT
- PROVIDE ANALYSIS AND REPORTING OF THE FLIGHT EXPERIMENT RESULTS IN A TIMELY MANNER

SOME SPECIFIC DUTIES

- PREPARE AND MAINTAIN THE SCIENCE REQUIREMENTS DOCUMENT
- RECOMMEND AND PROVIDE EXPERIMENT HARDWARE AND TECHNOLOGIES WHEN APPROPRIATE
- CONDUCT ANALYSES AND GROUND-BASED EXPERIMENTS TO REFINE EXPERIMENT TEST
  PARAMETERS, DATA REQUIREMENS, AND OPERATING PROCEDURES
- CONDUCT ANALYSES TO SUPPORT EXPERIMENT DESIGN
- REVIEW AND APPROVE EXPERIMENT DESIGNS AND TECHNOLOGIES
- REVIEW AND APPROVE HARDWARE PERFORMANCE TESTS
- SUPPORT CREW AND GROUND OPERATIONS TRAINING
- PARTICIPATE IN EXPERIMENT OPERATIONS
- PARTICIPATE IN FORMAL EXPERIMENT REVIEWS
- ANALYZE THE FLIGHT DATA AND REPORT THE RESULTS IN THE SCIENTIFIC LITERATURE

413

PROJECT SCIENTIST

RESPONSIBILITIES

- ENSURE THE SCIENTIFIC INTEGRITY OF THE EXPERIMENT
- REPRESENT THE PI IN HIS INTERACTIONS WITH THE PM AND OTHER NASA PERSONNEL
- FACILITATE THE TIMELY ANALYSIS AND DISSEMINATION OF SCIENTIFIC RESULTS

SOME SPECIFIC DUTIES

- ASSIST THE PI IN PREPARING AND MAINTAINING A SCIENCE REQUIREMENTS DOCUMENT
- COLLABORATE WITH THE PM IN GENERATING FUNCTIONAL/SYSTEM/TECHNOLOGY REQUIREMENTS FROM SCIENCE REQUIREMENTS
- ASSIST THE PM IN DEFINING AND SELECTING CONCEPTS AND LEVELS OF TECHNOLOGY
- SUPPORT THE PI IN EVALUATING CONCETPS, DESIGNS, AND OPERATING PROCEDURES
- PARTICIPATE IN ALL PROJECT REVIEWS AND ASSIST THE PI AT ALL FORMAL REVIEWS
- MONITOR AND ASSIST IN ASSESSMENT OF ALL HARDWARE PERFORMANCE TESTS
- MONITOR PI ACTIVITY TO ENSURE FULFILLMENT OF REPORTING REQUIREMENTS
- ASSIST THE PI IN RESEARCH TESTS CONDUCTED IN NASA FACILITIES
- RESOLVE DISPUTES BETWEEN PI AND PM OR REFER DISPUTES TO PROGRAM SCIENTIST

PROJECT MANAGER

RESPONSIBILITIES

- ADMINISTER ALL PROJECT MANAGEMENT FUNCTIONS NECESARY FOR THE SUCCESSFUL PERFORMANCE OF THE EXPERIMENT
- ENSURE THE DELIVERY OF HARDWARE CAPABILITIES AND OPERATIONS TO SATISFY THE EXPERIMENT SCIENCE REQUIREMENTS

SOME SPECIFIC DUTIES

- PREPARE AND MAINTAIN THE PROJECT PLAN
- MONITOR AND REPORT PROJECT COST AND SCHEDULE STATUS
- DIRECT THE DEVELOPMENT OF EXPERIMENT FUNCTIONAL REQUIREMENTS AND CONCEPTS
- MANAGE THE DESIGN, DEVELOPMENT, PRODUCTION, AND TESTING OF THE EXPERIMENT HARDWARE (ALL PHASES)
- PREPARE ALL NECESSARY DOCUMENTATION REGARDING SAFETY, INTEGRATION, AND OPERATIONS
- PROVIDE CREW AND GROUND OPERATIONS TRAINING
- SUPPORT THE PI DURING EXPERIMENT OPERATIONS
- PARTICIPATE IN ALL PROJECT REVIEWS

414

SCIENCE REQUIREMENTS DOCUMENT

I. INTRODUCTION: SUMMARY DESCRIPTION OF EXPERIMENT; THE KNOWLEDGE SOUGHT AND ITS VALUE; AND THE JUSTIFICATION OF THE NEED FOR THE SPACE EXPERIMENT

II. BACKGROUND: SUMMARY OF RELATED RESEARCH, PAST AND CURRENT; RELATIONSHIP OF PROPOSED EXPERIMENT TO THE SCIENTIFIC FIELD, APPLICATIONS OF RESEARCH RESULTS

III. JUSTIFICATION FOR CONDUCTION THE EXPERIMENT IN SPACE: LIMITATIONS OF GROUND-BASED TESTING (NORMAL GRAVITY, DROP TOWERS, AIRCRAFT); LIMITATIONS OF MODELING; SUMMARY OF SPACE-BASED EXPERIMENTS

IV. EXPERIMENT DETAILS: EXPERIMENT PROCEDURES; REQUIRED MEASUREMENTS; GROUND-BASED TEST PLAN, INCLUDING FUNCTIONAL TESTING OF FLIGHT APPARATUS; POST-FLIGHT DATA HANDLING AND ANALYSIS

V. EXPERIMENT REQUIREMENTS: EXPERIMENT SAMPLE (FUEL, MATERIAL, FLUID); ATMOSPHERE; TEMPERATURE CONTROL; ACCELERATION LEVEL CONTROLS; TEST MATRIX; IMAGING; MEASUREMENTS; ASTRONAUT INVOLVEMENT; DATA

THROUGHOUT III, IV, AND V EACH REQUIREMENT SHOULD BE JUSTIFIED OR SUBSTANTIATED WITH RESPECT TO THE EXPERIMENT OBJECTIVES.

A TABULAR SUMMARY OF QUANTITATIVE REQUIREMENTS IS A USEFUL FEATURE OF THE SRD.

THE FINAL SCIENCE REQUIREMENTS DOCUMENT

- NASA COMMITS RESOURCES TO FULLY SATISFY REQUIREMENTS (IRONCLAD CONTRACT)

- PI FREEZES SCIENCE UNTIL LAUNCH (3 TO 6 YEARS)

A DOUBLE-EDGED SWORD

THE IDEAL SCR

- **WELL DEFINED AND DEFENDABLE SET OF SCIENCE REQUIREMENTS**
  - DEFINITIVE TEST MATRIX AMENDABLE TO FLIGHT CONSTRAINTS
  - DEFINITIVE LIST OF EXPERIMENT CONTROL PARAMETERS
  - DEFINITIVE LIST OF MEASUREMENT REQUIREMENTS (TYPES, ACCURACY, RESOLUTION)

- **IDENTIFIED TECHNIQUES AND TECHNOLOGIES TO SATISFY REQUIREMENT**
  - DEMONSTRATED CAPABILITY (ACCURACY, RESOLUTION)
  - HARDWARE ACCEPTABLE TO FLIGHT CONSTRAINTS

- **WELL DESIGNED FLIGHT EXPERIMENT CONCEPT**
  - PREDICTED PERFORMANCE WHICH MEETS REQUIREMENTS
  - MANIFEST OPTION WITH REASONABLE RESOURCE MARGINS

- **SOUND PROJECT PLAN**
  - CLEAR ORGANIZATION RESPONSIBILITIES
  - DETAILED AND REALISTIC PLAN TO RDR

COMMUNICATIONS (PI <--> PS <--> PM)
GROUND-BASED TESTS

FLIGHT DEVELOPMENT PHASE

PRELIMINARY DESIGN REVIEW	CRITICAL DESIGN REVIEW	PRE-SHIP REVIEW
PDR ▽	CDR ▽	PSR ▽

PRELIMINARY DESIGN

- COMPLIANCE WITH SCIENCE & DESIGN REQUIREMENTS
- FUNCTIONAL & INTERFACE REQUIREMENTS
- BREADBOARD TESTING
- ENGINEERING MODEL DRAWINGS

→

ENGINEEING MODEL

- ENGINEERING MODEL FABRICATION, INTEGRATION AND TEST
- FLIGHT DESIGN
- FLIGHT DRAWINGS (90%)
- INTEGRATION AND TEST PLANNING

→

FLIGHT FABRICATION, INTEGRATION AND TEST

- FLIGHT FABRICATION, INTEGRATION AND TEST
- EXPERIMENT SIMULATIONS

416

The Spacelab Mission Integration and Operations Schedule Template

Mission Integration Process

Manifest Decision: Authority to Proceed	L-48
Requirements Review	L-36
Phase 0 Safety Review	
Preliminary Design Review	L-24
Phase I Safety Review	
Critical Design Review	L-18
Phase II Safety Review	
Ground Operations Review	L-15
Flight Operations Review	L-14
Integration Readiness Review	L-8
Phase III Safety Review	
Flight Readiness Review	L-0.5
Launch	

Mission Planning and Operations Process

Investigators Working Group Meetings (Several in Process)	L-30+
Crew Training (Several in Process)	L-18
Mission Simulations (Several in Process)	L-6
Launch	

MSAD Experiment Definition and Development Process

NRA Award for Ground-Based Study	L-110
NRA Award for Flight	L-74
Preliminary SRD	
Conceptual Design Review	L-66
Final SRD / Breadboards	
Requirements Definition Review	L-64
Data Package	
Brassboards	
Preliminary Design Review	L-42
Data Package	
Functional Objectives	
Engineering Model	
Critical Design Review	L-30
Data Package	
Data Package	
Prototype Hardware	
Preship Review	
Ship Flight Hardware to KSC	L-12

Mission Integration Process

Manifest Decision: Authority to Proceed	L-48
Data Package	
Requirements Review	L-36
Phase 0 Safety Review	
Data Package	
Preliminary Design Review	L-24
Phase I Safety Review	
Data Package	
Critical Design Review	L-18
Phase II Safety Review	
Ground Operations Review	L-15
Flight Operations Review	L-14
Data Package	
Integration Readiness Review	L-8
Phase III Safety Review	
Flight Readiness Review	L-0.5
Launch	

Integrated Spacelab Experiment Process

Mission Planning and Operations Process

Investigators Working Group Meetings (Several in Process)	L-30+
Functional Objectives	
Crew Training (Several in Process)	L-18
Mission Simulations (Several in Process)	L-6
Launch	

417

EXPERIMENT COST AND SCHEDULE

- COST AND SCHEDULE ARE HEAVILY DRIVEN BY MANPOWER REQUIREMENTS FOR
  - DOCUMENTATION
  - DESIGN AND DRAWINGS
  - ANALYSIS
  - REVIEWS

- CHANGING REQUIREMENTS ARE A PM's NIGHTMARE

- COST AND SCHEDULE ESTIMATES ONLY BECOME REALISTIC AFTER RDR

- CARRIER CHOICE HAS LARGE IMPACT ON COST AND SCHEDULE
  - DIFFERENT GAS CAN, MIDDECK, USML, USMP REQUIREMENTS
  - DIFFERENT REFLIGHT OPPORTUNITIES
  - UNCLEAR MANIFEST OPPORTUNITIES EARLY IN PROCESS

- COST AND SCHEDULE CAN BE TRIMMED BY DEVELOPING HARDWARE BEFORE PI's ARE AVAILABLE
  - CHOOSE PI's (I.E., SCIENCE) TO MATCH HARDWARE CAPABILITIES
  - UNPROVEN APPROACH (POTENTIAL PROBLEMS WITH PROGRAM GOALS)

- PROCESS FOR SPACE STATION FREEDOM EXPERIMENTS IS STILL EVOLVING (CAN IT BE SIMPLER OR FASTER?)

KEYS TO EXPERIMENT SUCCESS

- EFFECTIVE BALANCE BETWEEN EXPERIMENT COMPLEXITY AND MATURITY OF THE SCIENCE
  - EVOLUTIONARY APPROACH TO RESEARCH
  - WELL POSED HYPOTHESIS
  - REQUIREMENTS CLEARLY NEED DRIVEN

- EXTENSIVE PI INVOLVEMENT
  - CLEAR REQUIREMENTS AND DIRECTION EARLY IN PROCESS
  - REGULAR INTERACTIONS WITH PS AND PROJECT TEAM
  - PARTICIPATION IN MISSION PLANNING AND TRAINING

- EFFECTIVE PROJECT TEAM
  - SOLID PI-PS RELATIONSHIP
  - SKILLED PM
  - DEDICATED, CAPABLE PROJECT MEMBERS

- ADEQUATE PRE-PROJECT EFFORTS
  - GROUND-BASED TESTING
  - EXPERIMENT DEFINITION

- EARLY IDENTIFICATION AND RESOLUTION OF TECHNOLOGY TALL POLES

- EARLY ATTENTION TO MISSION PLANNING

```
COMMUNICATIONS
PI <--> PS <--> PM <--> MISSION
```

FLUIDS FLIGHT HARDWARE

DR. NANCY SHAW
CHIEF, FLUIDS EXPERIMENT DEFINITION BRANCH
(216) 433-3285

THE ORBITER

AFT FLIGHT DECK

GET AWAY SPECIAL PAYLOADS

MIDDECK

SPACELAB

PALLETS

AIRLOCK
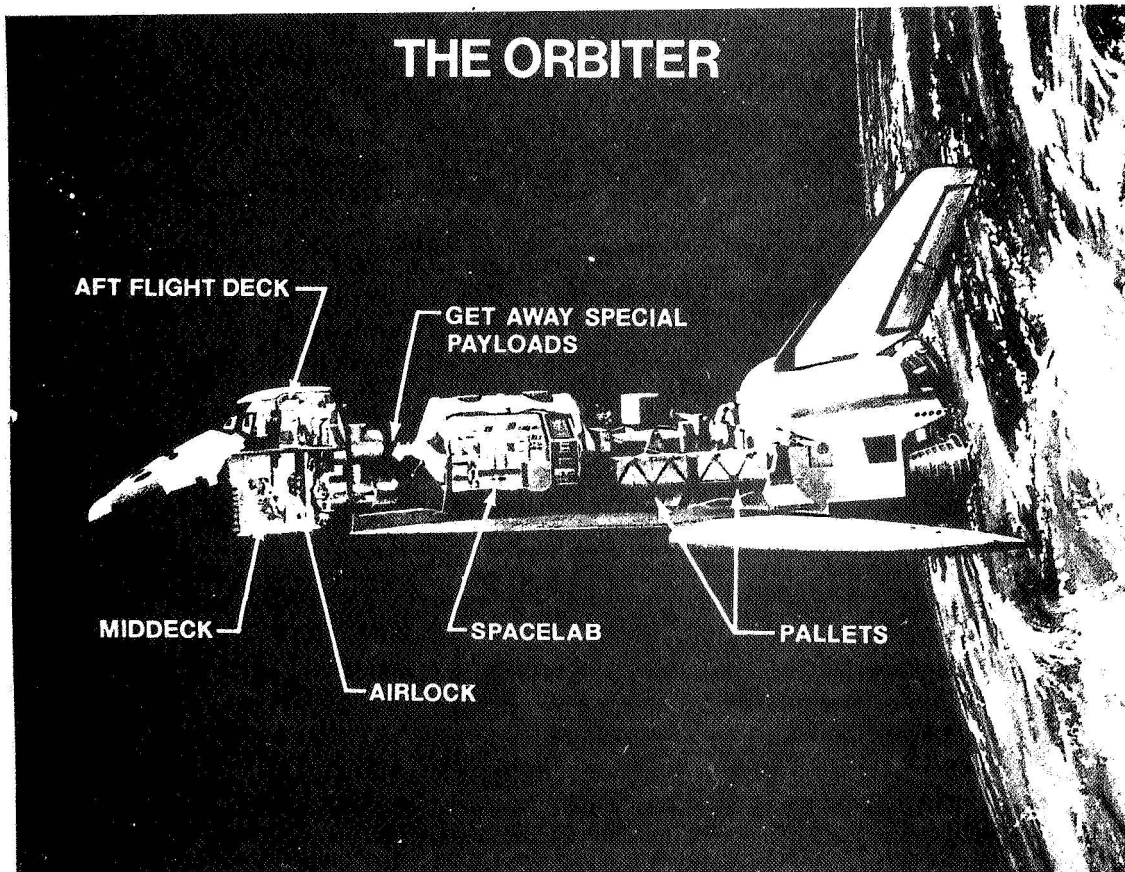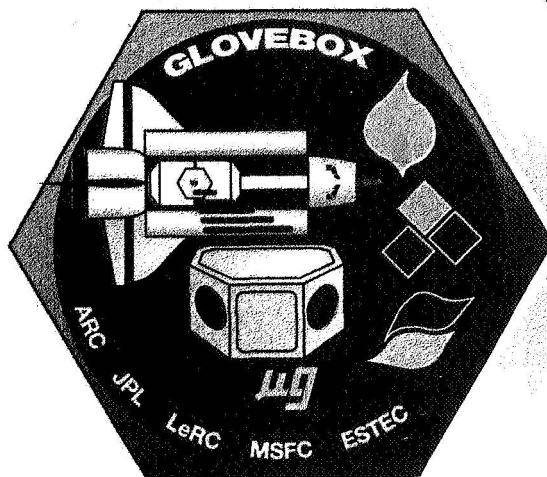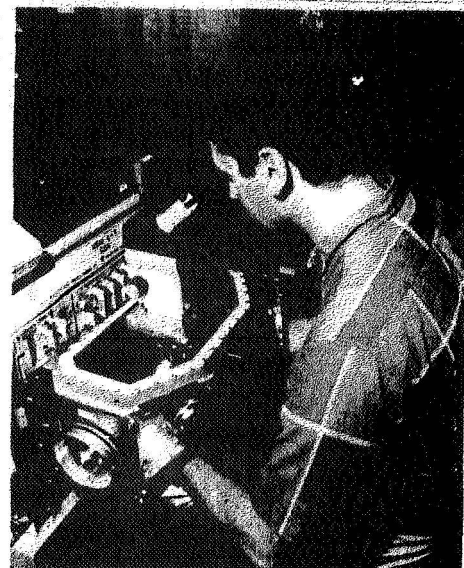
GLOVEBOX

Glovebox-2 Investigations

35-mm Camera   Video Monitor   Microscope

CCD Cameras   CCD Cameras

Gloves   CCD Cameras (Video Cameras)   Gloves
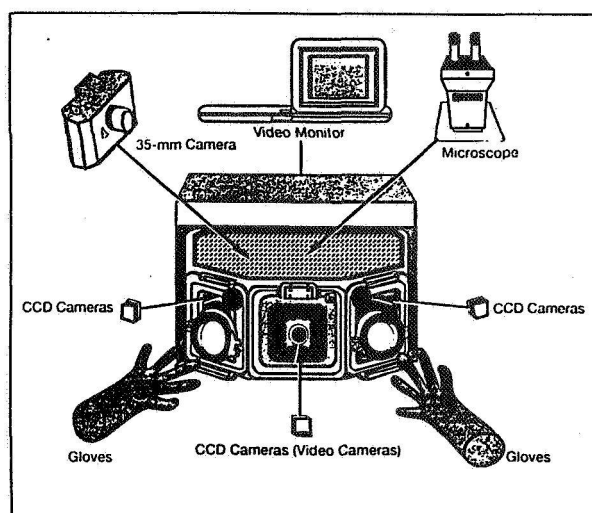
Fluids
- Colloidal Disorder-Order Transitions
- Interface Configuration Experiment
- Oscillatory Thermocapillary Flow

Combustion
- Comparative Soot Diagnostics
- Fiber Supported Droplet Combustion
- Forced Flow Flamespreading Test
- Radiative Ignition and Transition to
  Spread Investigation

LeRC Contacts:
  PS: Howard D. Ross
  PM: Brian F. Quigley

420

CF = Constant Flux

(Laser heating)

L Oil flow
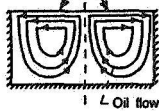
CT = Constant Temperature

(Cartridge heating)

T_C T_H

L Oil flow

Test chambers

Turning mirrors

CO_2 Laser

Variable Focus

Flow Visualization 3 Camera/Lens Assemblies

Free Surface Deformation Measurement System

Gratings

Variable Locations

6 Interchangeable Test Chamber Modules (1.2, 2.0, or 3.0 cm Diameter)

Submerged Heater

IR Imager with 3 Position Zoom Telescope

Beam Combiner (Zinc Selenide Window)
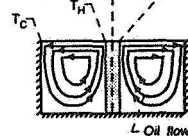
Thermistors
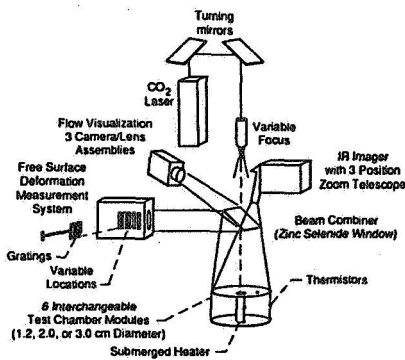
Optical Systems for STDCE-2

TV monitor

Data memory cartridge

LCD display

STDCE-2 AVIONICS PACKAGE

VCR installed on-orbit

Experiment access door and interlock

STDCE-2 EXPERIMENT PACKAGE

Grating access door
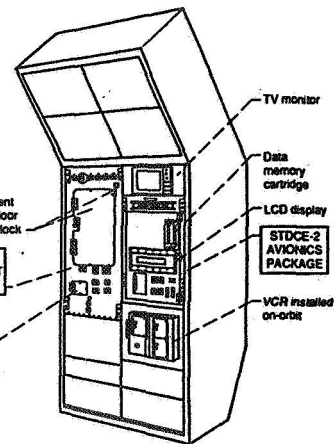
STDCE-2 in Spacelab Rack

Study Oscillatory Thermocapillary Flows and Validate Physical Models on the Second U.S. Microgravity Laboratory Mission (USML-2)

PI: Prof. Simon Ostrach
    Prof. Yasuhiro Kamotani
    Case Western Reserve University

LeRC Contacts:
    PS: Alexander D. Pline
    PM: Thomas F. Jacobson
    DPM: Robert L. Zurawski

CD-93-63753

STS-62

OAST-2

DEE

LDCE-C

LDCE-B

ITEPC

USMP OARE EDO

SSBUV/A
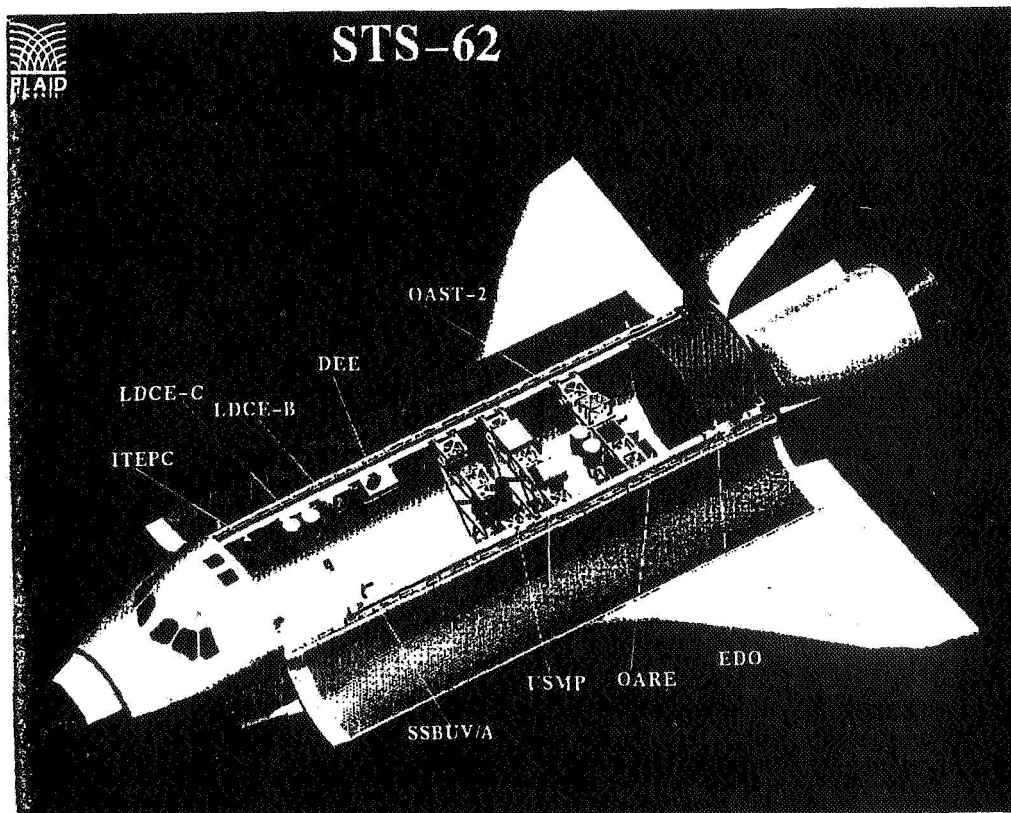
Pool Boiling Experiment
Get Away Special Payload   STS-47, STS-57, and STS-60
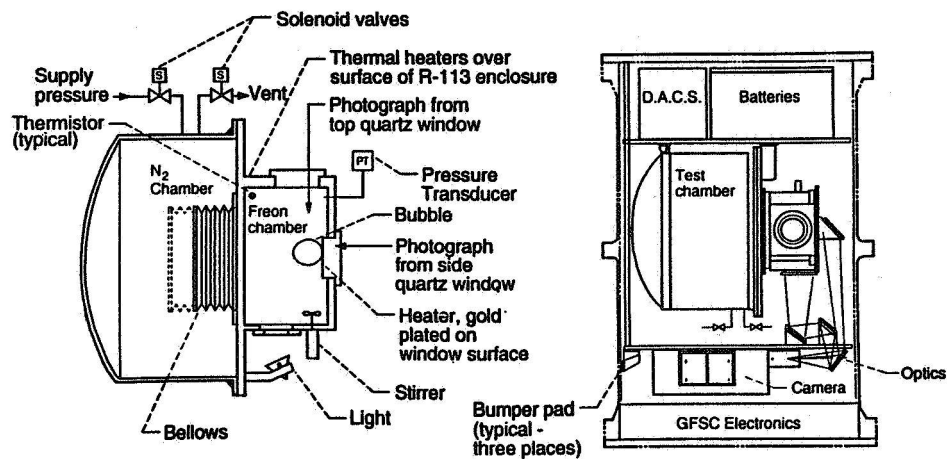
Test chamber schematic

Set-up of experiment in container

**Study of heat flux and liquid subcooling effects on the onset
of nucleate pool boiling in reduced gravity.**

PI.: Prof. Herman Merte, Jr.
University of Michigan

CD-93-64459

LeRC Contacts:
PS: Francis P. Chiaramonte
PM: Angel M. Otero

422
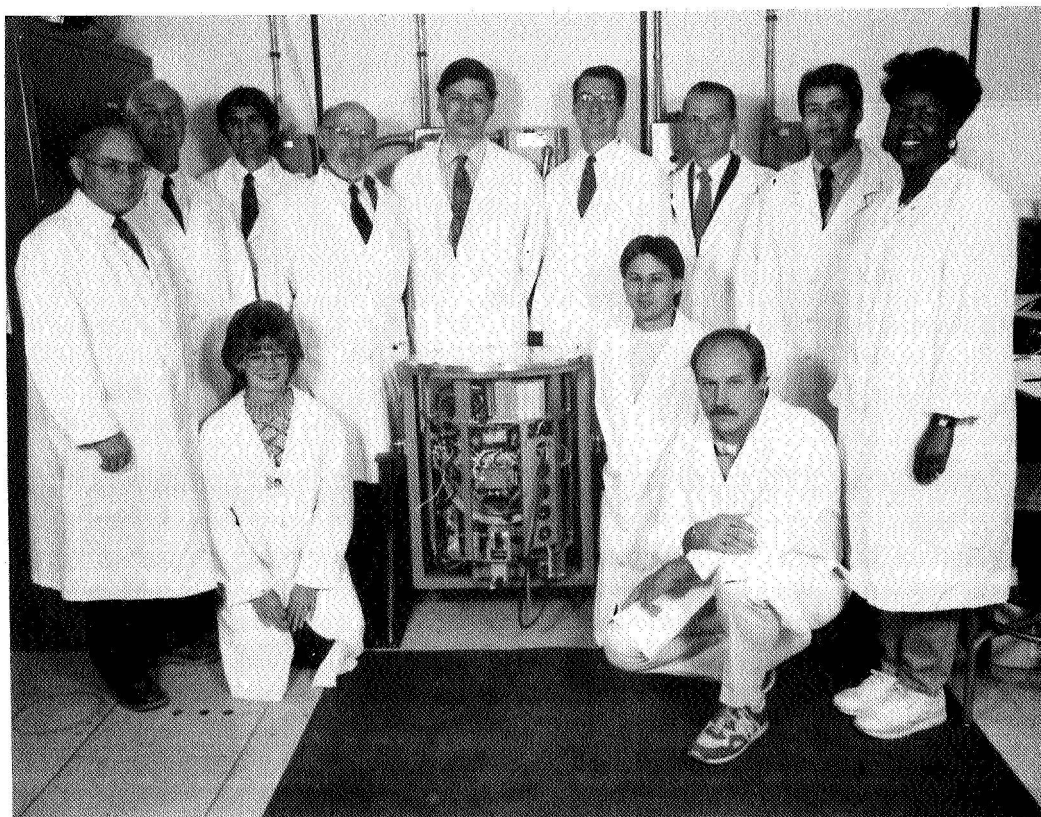
Critical Fluid Viscosity Measurement Experiment

Protoflight CFVME Viscometer

Discipline: Fundamental Science
Phase: Definition
Principal Investigator: Dr. M. Moldover/NIST
Co-Investigator: Dr. R. Berg/NIST
LeRC Project Manager: Dr. R. Lauver
LeRC Project Scientist: Dr. A. Wilkinson
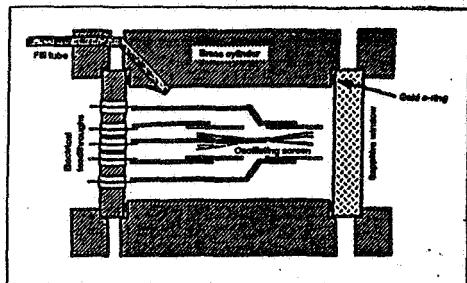
Objectives & Description:

The purpose of the experiment is to produce data on xenon closer to its liquid-vapor critical point than is possible in 1-g due to the singular compressibility of the fluid near the critical point. The data will provide complementary results with Critical Fluid Scattering Experiment to test the mode-coupling theory of critical phenomena and will provide guidance to re-normalization group theory development on dynamic critical fluid behavior.

The task requires the use of a low-frequency, low shear rate viscometer and a thermostat with approximately 30µK temperature control precision near room temperature. Viscosity measurements with an accuracy of 0.2% will be taken between 60 mK and 800 µK of Tc. Sample loading to within 0.3% of critical density and temperature gradients of less than 0.22 µK/cm are also required to take full advantage of the low-g environment.

Hitchhiker-G Typical Structural Configuration

PLATE MOUNTED EXPERIMENT

EXPERIMENT MOUNTING PLATE

STANDARD 5 CU. FT. CANISTER EXPERIMENT

STANDARD 5 CU. FT. CANISTER EXPERIMENT WITH MOTORIZED DOOR

CARRIER AVIONICS

Figure 2.4

423
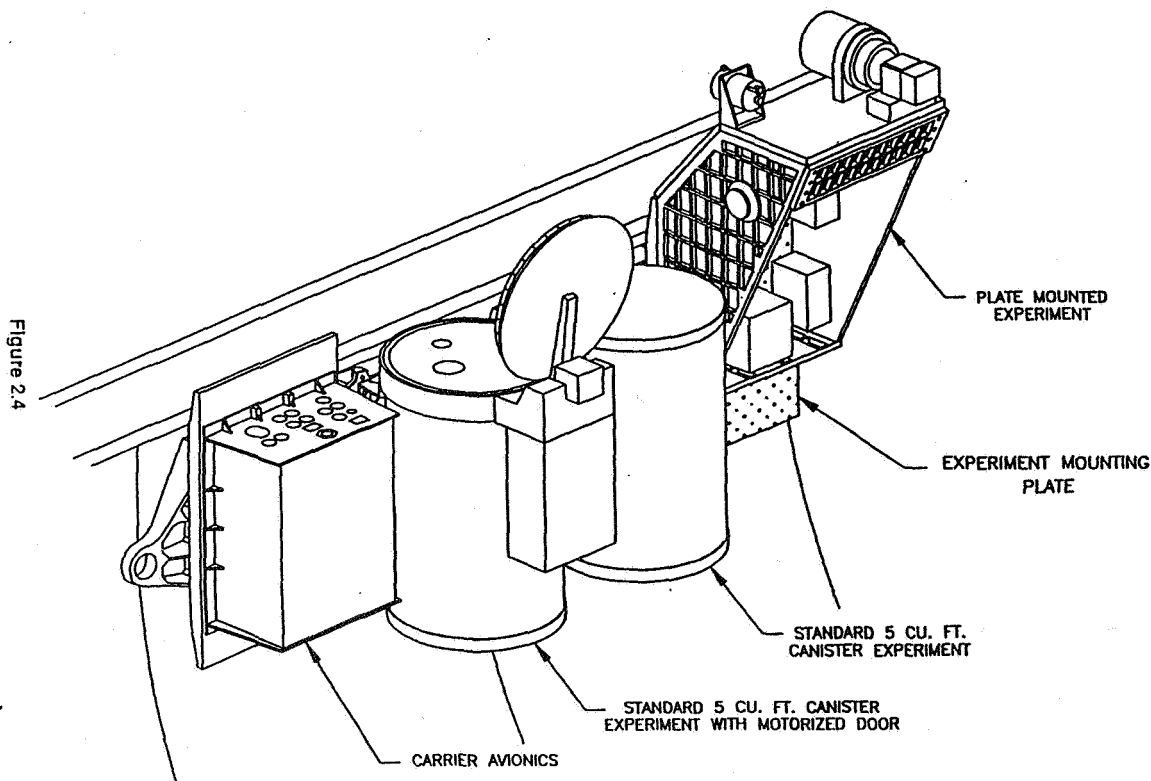
Zeno-Critical Fluid Light Scattering Experiment
Shuttle-USMP

ZENO thermostat

Flight configuration

A	Aperture
B	Beam Splitter
L	Lens
M	Mirror
S	Shutter
PD	Photodiode
PMT	Photomultiplier
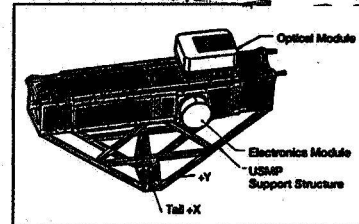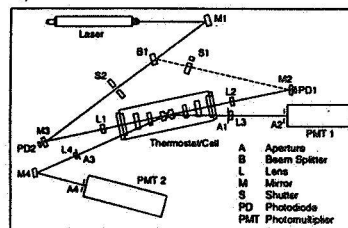
Optical layout
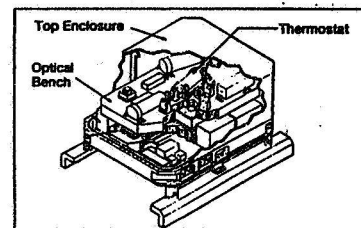
Optical module

Extend light scattering measurements of xenon to temperatures closer
to the critical point by reducing density stratification in the sample

PI: Prof. Robert W. Gammon
University of Maryland

LeRC Contacts: PM: Richard W. Lauver
PS: R. Allen Wilkinson

CD-93-64129

Isothermal Dendritic Growth Experiment
Space Shuttle-USMP
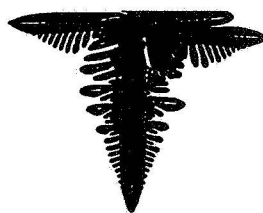
Dendrite
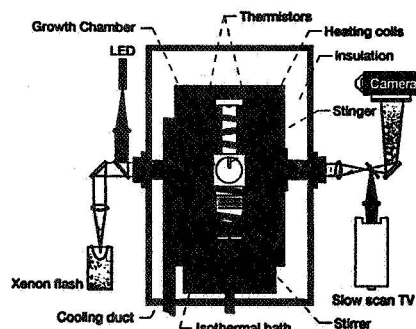
Thermostat
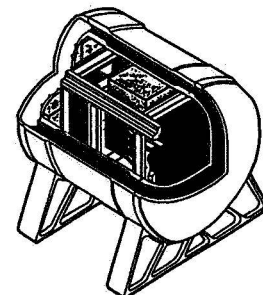
Flight Apparatus

Development and verification of a mathematical model relating
dendrite growth rates and tip radii to tip undercooling

PI: Prof. Martin E. Glicksman
Rensselaer Polytechnic Institute

LeRC Contacts: PM: Edward A. Winsa
PS: Diane C. Malarik

CD-93-64460

Flight Apparatus Both Autonomous and Teleoperable

Containment Vessel
Primary Vessel
Rack
Computers (5)
Thermostat
Slow Scan Television (2)
35mm Cameras (2)
SAMS
Saddle

Length ~ 1m
Weight ~ 325kg

NASA
C-93-01594
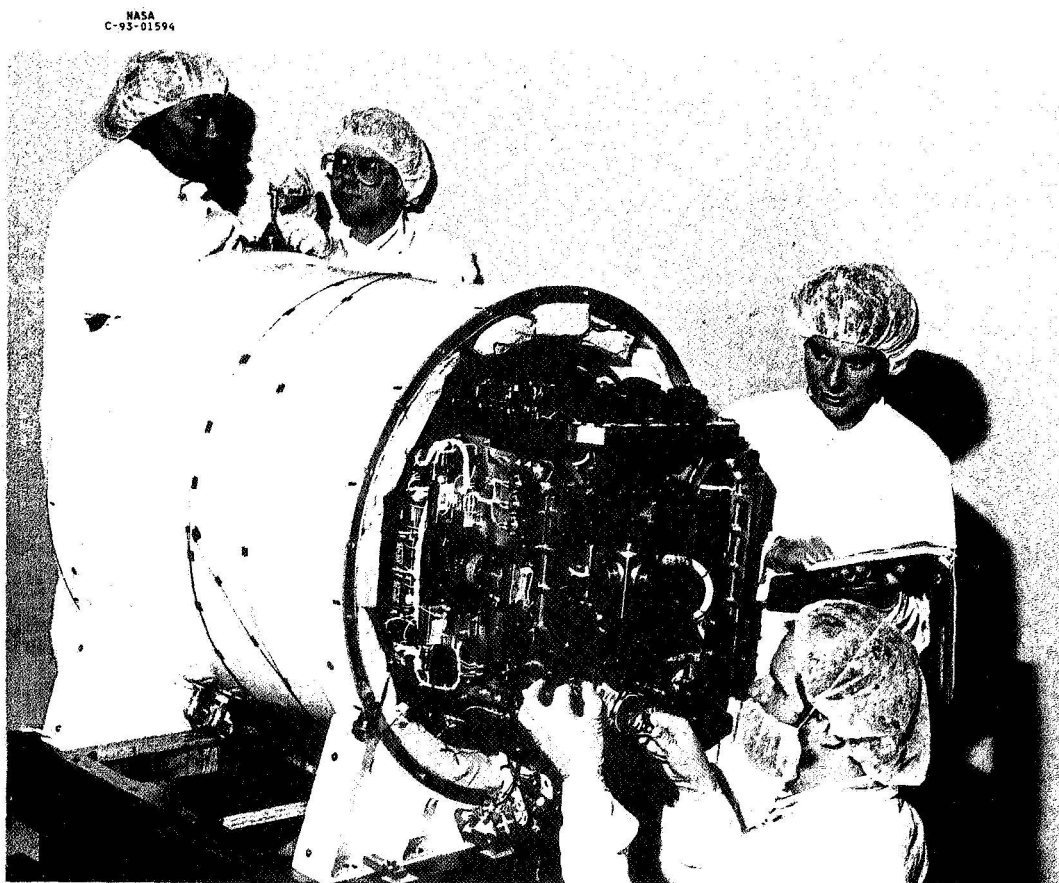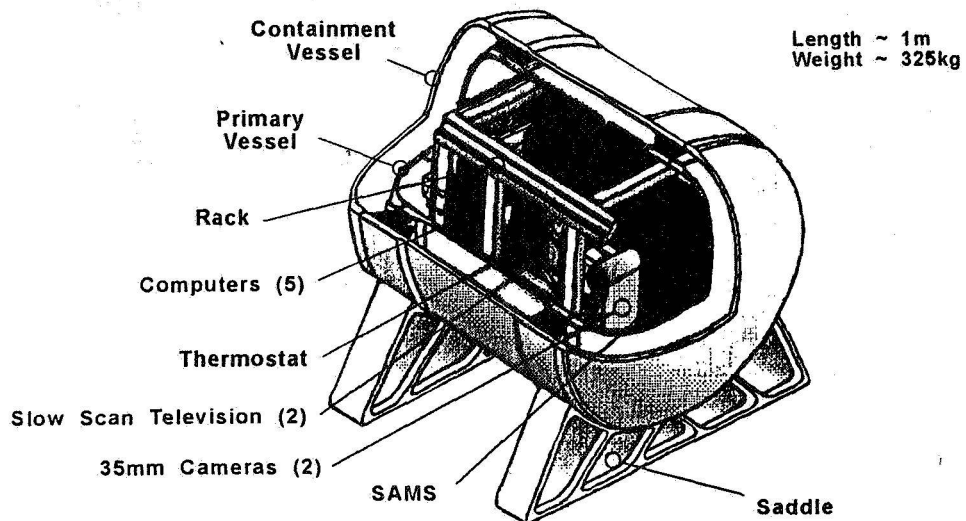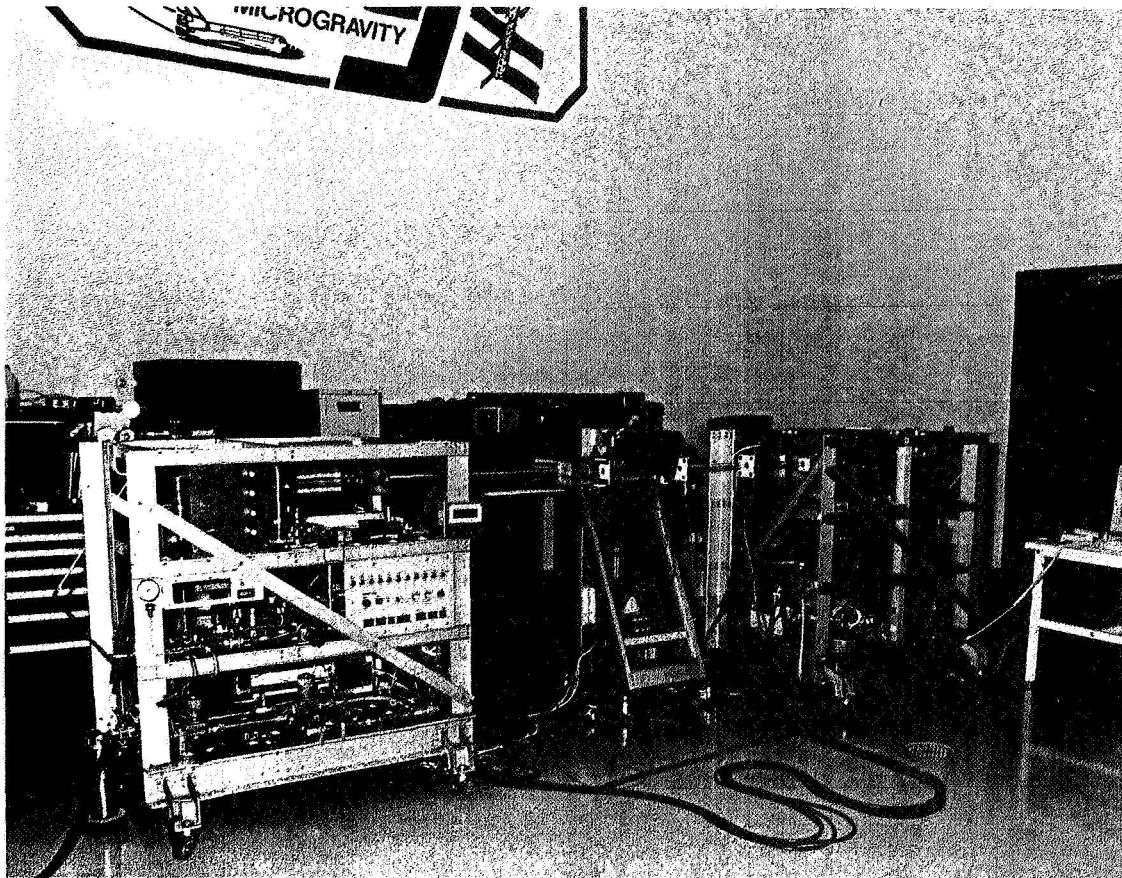
MICROGRAVITY ACCELERATION ENVIRONMENT SUPPORT

- **SCIENCE REQUIREMENTS DEFINITION ASSISTANCE**

- **MICROGRAVITY ENVIRONMENT ADVICE**

  - **EFFECT OF LOCATION, ORIENTATION, EXCITATION**

- **MISSION OPERATION SUPPORT**

- **POST-MISSION PI SUPPORT**

  - **PROCESSED ACCELERATION DATA**

  - **SUMMARY ANALYSIS OF ENVIRONMENT**

LeRC CONTACT:
RICHARD DeLOMBARD
(216) 433-5285

426

Space Acceleration Measurement System (SAMS)

Applications of the SAMS

- Measurement of low-g accelerations
- Monitoring of low-g environment
- Monitoring of experiment-induced vibrations
- Validation of vibration isolation techniques

Electronics box
(with enclosure)

Control panel

Optical disk drives
(4 maximum)

Cable
(6 m maximum)

Triaxial sensor head
(3 maximum)

Space hardened configuration

Cargo Bay

Spacelab Module

Middeck locker area
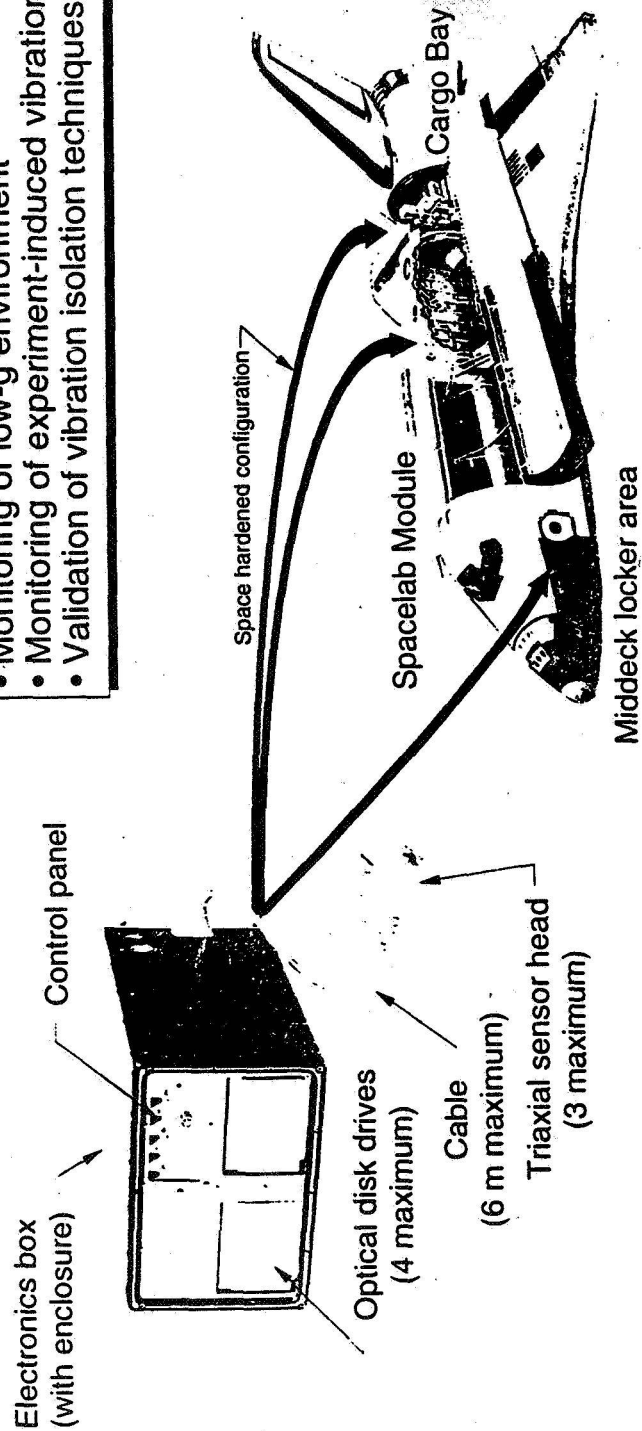
Typical locations for the SAMS

LeRC Contact:
PM: Ronald Sicker

CD-94-64569

427

CONCEPTUAL DESIGN OF THE SPACE STATION FLUIDS MODULE

Dennis W. Rohn
NASA Lewis Research Center
Cleveland, OH

Daniel P. Morilak
NASA Lewis Research Center
Cleveland, OH

Jennifer L. Rhatigan
NASA Lewis Research Center
Cleveland, OH

Todd T. Peterson
NASA Lewis Research Center
Cleveland, OH

June 1994

1. Introduction

The purpose of this paper is to describe the conceptual design of the Fluids Module for the International Space Station Alpha (ISSA). This module is part of the Space Station Fluids/Combustion Facility (SS FCF) under development at the NASA Lewis Research Center. The Fluids/Combustion Facility is one of several science facilities which are being developed to support micro-gravity science investigations in the US Laboratory Module of the ISSA. The SS FCF will support a multitude of fluids and combustion science investigations over the lifetime of the ISSA and return state-of-the-art science data in a timely and efficient manner to the scientific communities. This will be accomplished through modularization of hardware, with planned, periodic upgrades; modularization of like scientific investigations that make use of common facility functions; and through the use of orbital replacement units (ORUs) for incorporation of new technology and new functionality.

Portions of the SS FCF are scheduled to become operational on-orbit in 1999. The Fluids Module is presently scheduled for launch to orbit and integration with the Fluids/Combustion Facility in 2001.

The objectives of this paper are to describe the history of the Fluids Module concept, the types of fluids science investigations which will be accomodated by the module, the hardware design heritage, the hardware concept, and the hardware breadboarding efforts currently underway.

2. Background

NASA Lewis Research Center (LeRC) received approval from NASA Headquarters to begin a definition study and conceptual design effort for a Fluid Physics/Dynamics Facility in June of 1987. The objective of this study was to assess the feasibility, effectiveness, and benefits to potential users of a modular, multi-user facility for performing fluid physics science and applications experiments aboard the Space Station Freedom [1]. Facility class hardware has been considered as an alternative to experiment specific hardware for several reasons; 1) modular, multi-user facilities can provide resources or services to users which are non-standard to space station, 2) the modular approach allows for growth in capabilities over time, 3) common subsystems developed across facilities can improve maintainability and minimize logistics requirements, 4) minimizing the individual investigators experiment hardware can reduce the individual experiment development time, and 5) the facility approach can minimize cost to the overall science discipline program while maintaining operational flexibility.

A study team worked with a facility project scientist from The LeRC Space Experiments Division (SED) fluids science group to define science requirements for formulation of a concept. The process used to define the requirements started with the Fluids Discipline Working Group (DWG), which defined fundamental areas of micro-gravity fluid physics and fluid dynamics research. A reference set of fluids experiments was developed from this definition of research areas. Some of these reference experiments were determined to be more appropriate in other facilities which were also being conceptualized for operation on the space station, such as a containerless processing facility, a fundamental science facility, a biotechnology facility, and a furnace facility. Thus the reference experiments allocated to be performed in the Fluid Physics/Dynamics Facility were deemed to have appropriate commonality and scientific significance to require a unique facility dedicated to fluids physics investigations. This initial reference experiment list contained the following experiment types [2]:

1. Surface Tension Induced Instabilities and Flows
2. Free-Surface Phenomena
3. Immersed Bubble/Droplet Dynamics and Interactions
4. Multi-component/Coupled Flow (Moderate temperatures and pressures)
5. Multi-phase Flow
6. First-Order Phase Transitions (Moderate temperatures and pressures; no externally induced flow)

These were then appropriately combined into what was considered the reference categories of micro-gravity fluids science:

I.   Iso-thermal/Iso-solutal Capillary Phenomena
II.   Capillary Phenomena with Thermal/Solutal Gradients
III.   Thermal/Solutal Convection and Diffusive Flows
IV.   First Order Phase Transitions in a Static Fluid
V.   Multi-phase Flow

The study team held interviews with NASA funded fluids Principle Investigators (PI's) and project scientists to develop the specific experimental requirements for each of the above listed categories. These experiment specific requirements were then used as the basis for this team to develop a conceptual design of a Space Station Freedom based Fluids Physics/Dynamics Facility.

It was at this point in the effort, in 1990, that a Space Station Freedom Fluid Physics/Dynamics Facility Assessment Workshop was held at the Lewis Research Center. The purpose of the workshop was to obtain science and engineering assessments of the Fluid Physics/Dynamics Facility design and operational concepts as well as the selected micro-gravity fluids science requirements used to develop those concepts.

As a result of this workshop, the study team further developed the experiment specific requirements with example science requirements documents for the following experiments [3]:

1. Free Surface Phenomena
2. Bubble/Droplet Migration
3. Surface Tension Driven Convection
4. Surface Tension Induced Instabilities
5. Adiabatic Multi-phase Flow
6. Pool Boiling
7. Non-Adiabatic Multi-phase Flow
8. Thermal/Solutal Convection

The conceptual design effort continued by focusing on accommodating these eight experiments in the Fluid Physics/Dynamics Facility until the release of the 1992 NASA Research Announcement (NRA). This NRA resulted in the selection of six potential PI's for the Fluid Physics/Dynamics Facility. During this time the Space Station Freedom Program was evolving to become what is currently known as the International Space Station Alpha (ISSA). Changes also occurred in the organization of the Fluid Physics/Dynamics Facility in that it was now envisioned as a combined facility with the Modular Combustion Facility, sharing common functions, such as data handling, communications, and carrier interfaces. These combined facilities are now called the Space Station Fluids/Combustion Facility (SS FCF) which houses a Fluids Module for performing micro-gravity fluids science, and a Combustion Module for performing micro-gravity combustion science, with shared resources for both.

3. Fluids Science Accommodations

In order to design the SS FCF Fluids Module such that a broad range of fluid physics research areas are accommodated, a fluids science requirements "envelope" was established. This fluids science envelope currently consists of six flight definition experiments and five potential flight experiments from the 1992 NRA. These five potential flight experiments are currently in the ground-based fluids experiment program at NASA in the science areas emphasized by the Fluids DWG and the workshop described above, and are expected to be representative of future flight experiments. Five of the six flight definition experiments were selected from the 1992 Fluids NRA process. The sixth flight definition experiment is from the 1991 Materials NRA process. This materials investigation is believed to have enough commonality with the fluids investigations in the science envelope to be considered for manifesting on the Fluid Module. These eleven science experiment areas have been summarized and forwarded through NASA Headquarters to the Fluids DWG for formal approval as the Fluids Module science requirements envelope. This science envelope consists of the following investigations:

Flight Definition Experiments:

1. Evaporation from a Meniscus within a Capillary Tube in Micro-gravity
2. Microscale Hydrodynamics Near Moving Contact Lines
3. The Extensional Rheology of Non-Newtonian Materials
4. Dynamics of Hard Sphere Colloidal Dispersions
5. Colloidal Physics in Micro-gravity
6. Reverse Micelle Based Synthesis of Microporous Materials in Micro-gravity

Envelope Experiments:

1. Interaction of Bubbles and Drops in a Temperature Gradient
2. Phase Segregation Due to Simultaneous Migration and Coalescence
3. Interfacial Transport and Micellar Solubilization Processes
4. Studies in Electrohydrodynamics
5. Thermocapillary and Double-Diffusive Phenomena

The bulk of the eleven investigations listed above can be traced back to the five reference categories of micro-gravity fluids science mentioned in section 2. In addition, several investigative research areas have either been added to the SS FCF fluid science envelope or have been shifted to other carriers. For example, electrohydrodynamics has been added, while multi-phase flow has been shifted to larger carriers (ex. Shuttle cargo bay pallets) due to size and scaling factors required for this research area.

The SS FCF Fluids Science Requirements Envelope Document (SRED) has been drafted based on individual experiment Science Requirement Documents (SRDs), NRA proposals, and requirements gathered from current ground-based research projects. The primary purpose of the SS FCF fluids SRED is to document the envelope of science requirements from which the SS FCF Fluids Module is designed. The fluids SRED will be used in the engineering specification development process, along with combustion science and Space Station carrier and safety requirements. As specific investigations are assigned to the Fluids Module, investigation-specific requirements will be accomodated in the system specification and the hardware design.

4. Hardware Heritage

The design of the SS FCF will draw upon the design of as many previous space experiments as possible. Since the science requirements envelope includes many investigations that have previously been performed on orbit or are being developed, it only makes sense to utilize the previous development efforts to minimize cost and design effort. The hardware heritage for the Fluids Module of the SS FCF can be broken into two areas, that of diagnostics and that of test apparatus.

A. Diagnostic Heritage: There is one experiment that is currently in development which the SS FCF design team plans to utilize as a basis for a facility diagnostic system. The Physics of Hard Spheres Experiment (PHaSE) project at LeRC, is currently developing a laser light scattering instrument (LLSI) that will be used in an experiment to fly aboard the Shuttle. The PHaSE LLSI, shown in figure 4.A-1 is designed to provide some early science data, but due to schedule constraints, cannot accomplish all of the science that the SS FCF LLSI will be required to accomplish. The SS FCF will use the PHaSE design as the basis for a LLSI that will meet all of the diagnostic requirements for such an instrument in a facility. Further information on the SS FCF LLSI is provided in section 5.B.

There are a number of other flight and ground experiments that have flown or are being developed for flight that may serve as a basis for design of facility diagnostic systems. Other than the LLSI instrument discussed above, the rest of the diagnostics have been evaluated only at the conceptual level. As these facility diagnostic concepts develop into detailed designs, the design from these other experiments will be evaluated to see if they meet the facility requirements. Some of these other experiments are the Surface Tension Driven Convection Experiment (STDCE) I & II, the Bubble Droplet Particle Unit (BDPU), Microscale Hydrodynamics Near Moving Contact Lines, The Extensional Rheology of Non-Newtonian Materials, Evaporation from a Meniscus within a Capillary Tube in Micro-gravity, and the Drop Physics Module (DPM).

B. Test Apparatus Heritage: Design of the test apparatus will be very specific to the science investigation that will be performed. As these specific investigations become manifested in the facility, the design of the apparatus will certainly draw on that of previous experiments, including those identified above.

5. Hardware Description

The concept for the SS FCF has been developed based on the envelope of science requirements discussed in section 3 and those for the Combustion Module portion of the project. The concept is a three rack facility as shown in figure 5-1. The left hand rack contains the hardware required to support combustion experiments. The right hand rack contains the hardware required to support fluid physics and dynamics experiments and the central rack provides core functions and control to the other two racks. A Hardware Capabilities Document (HCD) is being drafted that will provide details on capabilities of the SS FCF. The HCD will be kept current so it can be used as a source of information for potential users. The discussion that follows will address only the central, or core rack and the fluids rack. The hardware in the racks can be grouped into three categories: level 1, 2 and 3.

Level 1 hardware is that hardware which, although designed for change out for maintenance or upgrade, is planned to be a permanent feature of the facility. The rack structure of the fluids rack, a number of packages in the lower portion of the fluids rack and the entire core rack are included in this category.

Level 2 hardware is that hardware which supports a large number of the flight and envelope experiment and/or promotes future use of the facility. For the SS FCF Fluids Module, this hardware is comprised of experiment modules (EMs) which can be inserted into and removed from the rack and are supported by the level 1 hardware. Currently three EMs have been concepted. One, called a LLSI EM, supports a group of experiments which have small test volumes and require a LLSI. A second one, called a Thermo-capillary/Thermo-solutal (TCTS) EM, supports a group of experiments that require moderate test volumes with orthogonal imaging. The third EM supports a group of experiments that require large test volumes and have little common hardware.

Level 3 hardware is that which is experiment specific. The majority of this hardware consists of test cells and unique diagnostics or test set-up and is supported within the EM that is accommodating the investigation. This hardware is generally provided by the project team responsible for the specific science and not by the SS FCF project. This hardware could become part of a level 2 EM if a future need for the same hardware develops.

A. Level 1 Capabilities/Description: The level 1 hardware concept and interfaces are shown in block diagram form in figure 5.A-1. Level 1 hardware provides the primary interface to space

station systems and the crew. The level 1 hardware also provides space for, interfaces to, and control of the level 2 hardware. Following is a description of the various functions performed by the level 1 hardware.

Structural Support: The Level 1 hardware provides structural support for all of the level 1 packages and the level 2 EMs. This support is accomplished through the use of two International Standard Payload Racks (ISPRs) which directly mount into the space station U.S. Laboratory Module.

Facility Control and Data Acquisition: Facility control and data acquisition will be accomplished by implementing a distributed control, Versa Module Europe (VME) bus system architecture. One VME bus system will be located in the core rack to provide facility level control and one will be located in the fluids rack to provide control to the level 1, 2 and 3 hardware located in that rack. A Fiber Distributed Data Interface (FDDI) system has been chosen for inter-rack communications due to the high data rates that will be required. The control and data interface with space station will be via a Mil-1553 B interface system. Data storage will be stored on 120 mega-byte, replaceable media units.

Crew Interface: The crew interface will provide a system for the crew to view digital and video data and control the facility. This system will include a video monitor and a laptop computer.

Video Image Control, Processing and Storage: Level 1 will provide for routing, processing and storage of video images generated by the facility. Another VME bus system will be used to provide this control, digitization and compression of images so that the images can then be stored. Digitization and compression of images is required so the data can be stored on a reasonable size drive and sent to the ground within a reasonable time frame.

Electrical Power: Level 1 hardware will provide for conditioning, conversion and distribution of 120 VDC power provided by space station. The core rack will provide for 28 VDC and 120 VDC to the fluids rack and the fluids rack will additionally provide 5 VDC and 12 VDC.

Thermal Control: Level 1 hardware will interface with the space station low and moderate temperature water systems to reject excess heat. Both the core and fluids rack will have an avionics air system tied into the water systems to provide forced air convection cooling. In addition, the core rack will contain heat exchanger/pump assemblies to route cooled water to specific hardware in levels 1, 2 and 3 that require large amounts of cooling.

Vibration Data Processing: A Space Acceleration Measurement System II (SAMS II) Remote Triaxial Sensor Electronics Enclosure (RTS-EE) will be located in the core rack to provide data processing and measurement support for sensor heads that will be located in level 2 hardware.

B. Level 2 Capabilities/Description: Each EM is designed to

435

interface in the same manner with level 1 hardware. The structural interface consists of slide rails that allow the EMs to be installed easily and fasteners to fix the EMs to the ISPR corner posts. All fluid and electrical interfaces are then made though a common interface panel. This configuration is shown in figure 5.B-1 for the LLSI and TCTS EMs. The EM itself provides one level of containment for any hazardous materials located within it.

LLSI EM: The LLSI EM is designed to perform full angle static and dynamic laser light scattering. As discussed previously the instrument to do these measurements is based on the design for the PHaSE instrument. The instrument is shown configured in the EM in figure 5.B.1-1. The laser source, detectors and other hardware that make the measurements are mounted in a fixed location and a carousel allows eight tests cells to be moved into position for data collection. These test cells are the level 3 hardware that would be provided by the specific science investigation team. Rheology and variable volume fraction could be accommodated in these test cells. Details of a generic test cell and the measurement system are shown in figure 5.B.1-2. The LLSI is located in the central portion of the EM which will be thermally controlled to maintain a desired temperature. Electronics and other heat sources will be located behind a thermal barrier to ease thermal control of the test cells. Space is also provided to store additional carousels and test cells. The usable internal volume of the EM is approximately 450 mm. high x 900 mm. wide x 600 mm. deep. Each carousel, including test cells, is estimated to have a mass of 7 kg. The level 3 test cells are approximately 70 mm. diameter by 100 mm. tall.

TCTS EM: The TCTS is designed to perform microscopic and macroscopic orthogonal imaging and laser interferometry of a test cell or multiple test cells. These options are shown in figures 5.B.2-1, -2 and -3. The level 2 hardware provided within the EM consists of two video cameras mounted on 3-axis translation stages for test cell imaging and tracking of bubble, drops, or fluid interfaces that are of interest; two sets of microscopic and macroscopic lenses for the cameras; appropriate lighting for the camera images; an interferometry system; six dispenser mechanisms to provide a supply source for bubbles and drops; two deployment mechanisms to deploy the bubbles and drops; a translation stage to provide any required test cell motion, including aspect ratio changes; and thermal control hardware to reject heat and support test cell thermal boundary condition maintenance. The usable internal volume of the EM is approximately 550 mm. high x 900 mm. wide x 850 mm. deep. Space allotted for the test cells, which are level 3 hardware, is approximately 125 mm. square by 300 mm. tall, with a mass of less than 16 kg.

Large EM: The large EM is configured to support a variety of experiments which require larger test volumes and have less

diagnostics commonality. At this time, the only hardware envisioned to be provided within this EM by level 2 is general thermal control. The rest of the volume would be allocated to level 3 hardware. Level 2 hardware developed for other EMs may be used in this EM if it meets the needs of the specific science investigation being performed. The usable internal volume of the EM is approximately 1000 mm. high x 900 mm. wide x 600 mm. deep.

Future EMs: The three EMs described above have been configured for the classes of experiments that are currently in the SRED. As specific science investigations are identified that will operate in the facility, these may require modification. At that time additional EMs will be designed to meet the needs of the science. These EMs will utilize as much of the design of the other EMs as possible and could range in size up to the large EM size.

C. Software: The SS FCF project will provide the majority of the software required to perform the science investigations. This software will reside on the VME bus systems that are part of the level 1 hardware. There are two cases where this is not true: 1) if there are specific control algorithms/software required that have been developed by a specific science investigation team and which can be integrated with the facility software, and can be loaded into the VME bus system in the fluids rack, and 2) if a controller is included in the level 3 hardware, then the specific science investigation team could write software that would reside on the controller and interface with the facility.

D. Logistics Scenario: A logistics scenario is the concept for getting experiments to the space station, operating them in the SS FCF, and bringing them back to the ground. The current concept for getting experiments to the space station is launch as cargo aboard a space vehicle. Once on-orbit, an EM would be installed into the Fluids Module by an astronaut. Installation of the EM would include making all hardware connections with the FCF (e.g. power, data, vacuum/vent, nitrogen), verifying these connections, and performing functional check-out of the EM, including hardware and software. The astronaut would then install the experiment specific hardware into the EM, by making all hardware connections between the experiment specific hardware and the EM, verifying these connections, and performing functional check-out of the experiment specific hardware.

The operations of the experiments are very dependent on the experiment being performed and the EM into which it is installed. The concept for operations is to maximize the effectiveness of the crew time by automating experiment functions when it is experimentally and technologically practical as well as cost efficient.

Resources which need replenishment will be planned for and the resupply of these will be negotiated with the ISSA and the resupply vehicle programs.

Experiments which are completed will be removed by an astronaut and packed for return to Earth in the appropriate carrier. However, the EMs may remain installed in the FCF and another PI's experiment installed for operation in the EM. This could continue as long as there are experiments planned for operations in that EM. These experiments could all be on-orbit at the same time or could be taken up on consecutive flights.

When all planned operations for an EM are complete it will be de-integrated from the FCF and packed for shipping back to Earth. Another EM will be installed into the FCF in its place, or possibly, if a large EM is removed, two EMs may be installed in it's place. This concept of continual resupply of experiments and EMs for the FCF will ensure that the NASA micro-gravity fluids science program has a consistent and constant platform for performing micro-gravity fluid physics research.

6. Breadboard Plans/Accomplishments

The SS FCF Project is currently in the process of capturing all of the requirements that it will have to meet to perform the science described in the SRED. A necessary part of this conceptual phase of the project is to demonstrate that systems can be designed to meet key performance parameters. This may include development of new technologies to meet these needs. Most often, this is addressed by breadboard testing of systems that potentially will be used in the final design. Three breadboards are currently in work and another is being planned to support the SS FCF project. In addition, other projects are currently performing breadboards which are associated with the specific type of investigation they are considering for flight in the SS FCF. These breadboards are described below.

A. Automated Positioning and Tracking (APT): The envelope of science requirements includes a number of investigations where high resolution images of small features (on the order of 0.01 mm.) in the test cell are required. A high resolution camera with a microscopic lens is required to adequately image these features. As part of the science investigation, these features will be in motion. The simplest approach to image this would be to have a fixed camera with a large field of view, however the resolution could not be obtained within the volume constraint of the facility. The current imaging concept to accomplish has the cameras mounted on translation stages. The cameras translate to keep the desired feature in the field of view. An option to this has been proposed where the camera is fixed and a scanning mirror is adjusted to keep the feature in the field of view.

Although these both appear to be feasible, there are many challenges which have to be met. It was therefore decided that this system would require a breadboard to demonstrate that it could meet the science requirements. Some of the functions that the breadboard must prove the feasibility of are: 1) recognize

the feature that is desired, 2) determine the camera/mirror motion required to keep it within the field of view, 3) translate the cameras/mirrors while keeping the image in focus and retaining image resolution, and 4) maintain knowledge of the camera image relative to a fixed point of reference.

The current effort on the breadboard is to test the baseline concept of translating camera and is shown schematically in figure 6.A-1. The scanning mirror concept will be added in the near future. The breadboard consists of two cameras mounted on 3 axis translation stages, a 486 PC, an image processing workstation, video monitors and video recorders. The effort will focus initially on control of a single camera in two axis. Once this is demonstrated, a second camera will be added for tracking in three dimensions.

Once the camera acquires an image, it is then sent to a monitor for real time visual indication of tracking, to a video recorder for post test analysis to determine success, and to the image processing workstation. The workstation must process the image to recognize the desired feature and then send the location of the feature to the 486 PC. The PC then determines the required relative motion of the camera and commands the motion.

Hardware is currently being delivered and configured for this breadboard. The algorithms needed to recognize and track the desired feature are currently being developed. The current schedule has the initial software developed by the end of July 1994, testing with a single camera complete by the end of September 1994, and testing with two cameras complete by the end of October 1994.

B. Data Compression and Image Processing (DC/IP): Most experiments in the SS FCF science envelope rely heavily on video images for quantitative science data. Storing and transmitting all of these images to the ground is a major challenge. Current Spacelab and shuttle experiments rely primarily on video tapes to store the data. This is a feasible approach because the shuttle returns to the ground within a relatively short period of time. For experiments on Space Station however, the opportunity to return tapes to the ground in a short time will be severely limited. Alternatives to this are being developed. Digitizing of the images is the approach being taken. These images are also required to be compressed to avoid having excessively large files created, transmitted and stored. Once on the ground the images then need to be processed to return them to usable form, without losing the video data of interest.

Many methods have been developed in the recent past for image compression. The challenge is to select a method that will allow the video image information to be of sufficient quality to extract the required science data on the ground. Within the SS FCF science envelope, there are needs for several different types of video images to allow different data to be extracted. These types of data vary from microscopic to macroscopic views which

require illumination configurations that include incident, backlit, and scattered lighting with both lasers and white light sources. The SS FCF will need to have a number of compression methods available so that the best method can be selected for each type of science data required.

The breadboard is shown schematically in figure 6.B-1. It consists of a video source, a 486 PC, digital storage, and a video output recording system. The video source provides video images to the 486 PC which digitizes, compresses, and stores the images on the digital storage device. The digital data is then sent back to the 486 PC which de-compresses it, regenerates the video image, and sends it to the output system. These images, in contrast to the input image, will be used to determine if the data in the input image was maintained adequately.

The majority of the hardware and commercial software needed for this breadboard has arrived and has been assembled. Testing of compression algorithms is expected to continue into July 1994. The image processing portion is expected to be complete by the end of August 1994.

C. Data Management: The concept of the SS FCF as presented has data processing and storage functions along with central control functions located within the core rack on a VME bus system. In addition, this system is the interface to the Space Station control and data systems. There is also a VME bus system located in the fluids rack that passes data to the core VME bus system and controls the lower level functions. With the quantity of data and control that is required to pass between the various systems it was determined that a breadboard was needed to make sure that the hardware can be integrated and to benchmark the system performance. This breadboard will demonstrate the implementation of Mil-1553 B interface hardware operations and protocol for use as a data and control bus, and the FDDI system operation and protocol for use as a high speed data bus for rack to rack communications.

The breadboard system is shown schematically in figure 6.C-1. It consists of two VME bus systems connected by fiber optics and one of the VME bus systems connected to a 486 PC via a Mil-1553 B interface. Initial testing will consist of sending simple commands and data across the systems. Once this is working and understood, the communications will be made to be more and more complex, to the point where a large amount of traffic including the data and commands being transferred in the APT and DC/IP breadboards can be accomodated. Initial testing is expected to be complete by the end of July 1994.

D. Fluid Handling: The method to handle the various fluids to configure a test cell for testing and to allow it to be used for more than one test point is a key development issue. These methods will be common to a number of experiment types. This breadboard is in the initial stages. It will initially focus on

C1-6

the generation of a drop(s) or bubble(s) in a test cell completely filled with a liquid and the removal of the same drop(s) or bubble(s). Most of the experiments that fall in the class that utilize this require that a linear thermal gradient be established in the test cell before deployment. This requires that the bubble/drop deployment does not disturb the liquid, destroying the thermal gradient. Results from this breadboard are expected by the end of 1994. Once methods are developed, they will be evaluated to see which functions will become part of the facility design.

E. Vector Alignment: A number of experiments in the science envelope are affected by even the low levels of micro-gravity that will exist on Space Station. By aligning the experiment with the gravity gradient, the effects can be minimized. Active control/alignment systems may be required, depending on the criticality to the science objectives. The SS FCF project is currently evaluating the criticality of this capability to the experiment apparatus. If it is decided to provide such a system, a breadboard is planned to support the concept development.

F. SS FCF Breadboard Integration: As SS FCF breadboards meet their individual objectives, many will be combined to test a larger system. This is currently planned for the APT, DC/IP, Data Management and Fluid Handling breadboards. The Fluid Handling breadboard will provide a feature for the APT system to track and send an image to the DC/IP system, all under the control of the Data Management system. This complete system should be up and running by the end of 1994.

G. Vibration Isolation: The SS FCF project is currently gathering vibration environment requirements from the envelope science requirements and comparing them to expected environments. If the predicted environment does not meet the requirements, vibration isolation, either active or passive, will be required. Currently the ISSA program is evaluating vibration isolation at the rack level, which includes the SS FCF. A great deal of breadboard work on vibration isolation has been performed at LeRC by Grodsinsky [4].

H. External Breadboards: There are currently a number of projects which fall into the SS FCF science envelope that are testing independent breadboards. Although the exact science may not be performed in the SS FCF, many of the techniques developed in the breadboards may be applicable.

Extensional Rheology: One of these projects is looking at the extensional rheology of fluids. This project has three major areas that are being breadboarded. The deployment of a column of both high and moderate viscosity liquid, the stretching of this column at constant strain rates and the measurement of the force required to do so.

<u>3-Dimensional Particle Image Velocimetry (3-D PIV)</u>: Another project plans to evaluate three dimensional flows by tracking particles in a fluid. A technique to do this is currently under development in a breadboard. Lighting of the test cell and processing of the video image are the areas of focus.

7. Summary

A conceptual design of a Fluids Module, which is part of the Space Station Fluids/Combustion Facility, has been presented. The concept was developed to maximize use of common hardware and software in order to minimize development time and effort for a large number of fluids science investigations, and to provide maximum scientific return.

These objectives are met through provision of standard experiment modules (EMs) which support like experimental investigations. The EMs provide a maximum of common hardware and software with clearly defined interfaces and standard data acquisition and control capabilities.

The Fluids Module concept supports all of the classes of fluid physics and dynamics scientific investigations currently envisioned by the NASA Fluids Discipline Working Group to be performed aboard the International Space Station Alpha.

REFERENCES

[1] Thompson, R. L., et al, "Conceptual Design for the Space Station Freedom Fluid Physics/Dynamics Facility", NASA TM 103663, April 1993.

[2] NASA, "Space Station Freedom Fluid Physics/Dynamics Facility Assessment Workshop Proceedings", January 24-25, 1990.

[3] Hill, M. E. and Tschen, P. S., "A Review of Design Concepts for the Advanced Fluids Module (AFM) Project", 31st Aerospace Sciences Meeting & Exhibit January 11-14, 1993, Reno, NV; AIAA 93-0258.

[4] Grodsinsky, C., "Microgravity Vibration Isolation Technology: Development to Demonstration", NASA TM 106320, September 1993.
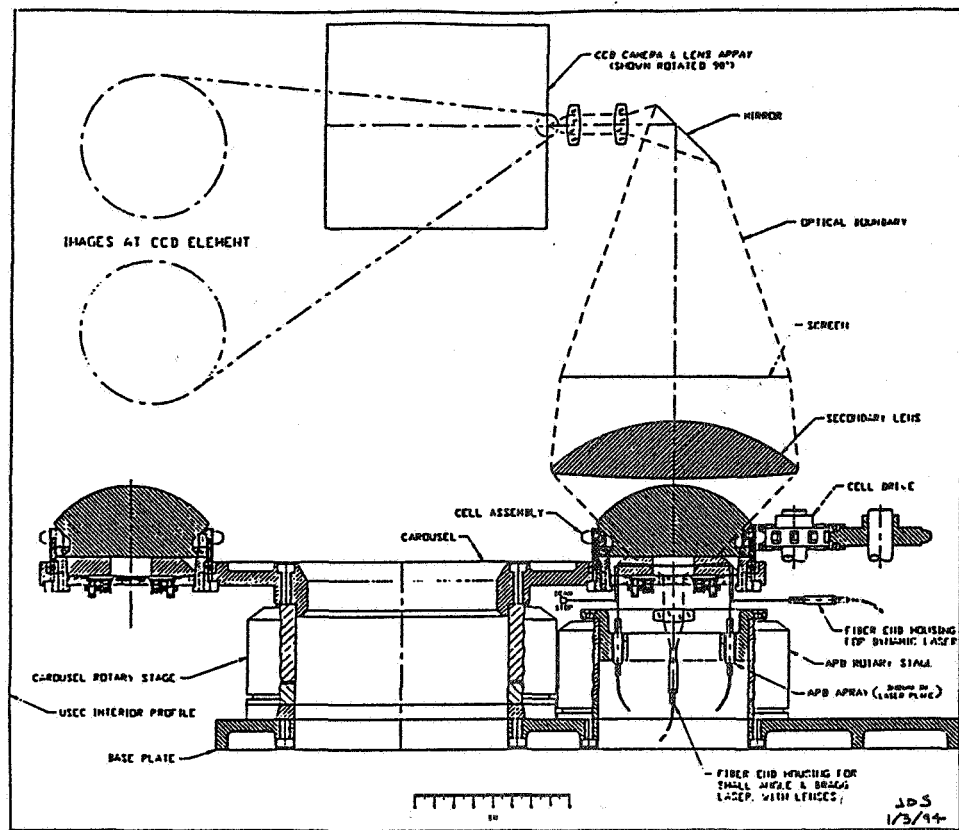
Figure 4.A-1   Diagram of PHaSE Laser Light Scattering Instrument
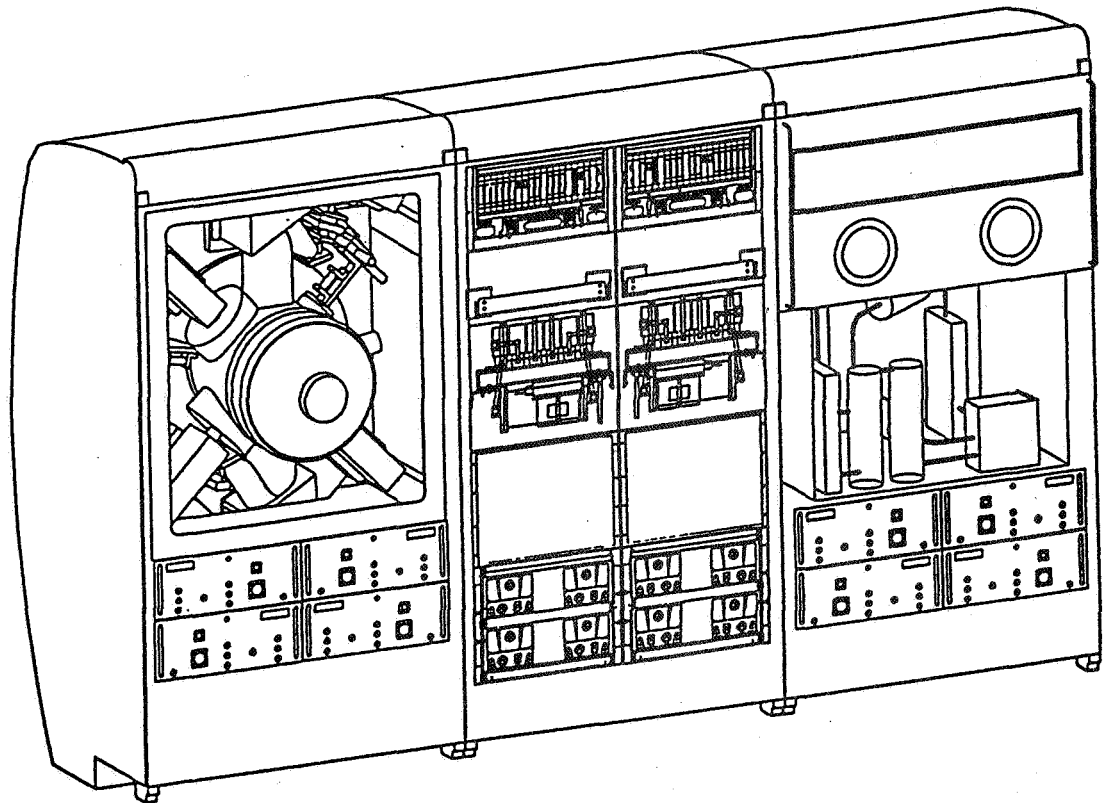
Figure 5-1   Space Station Fluids and Combustion Facility
                 Concept

443
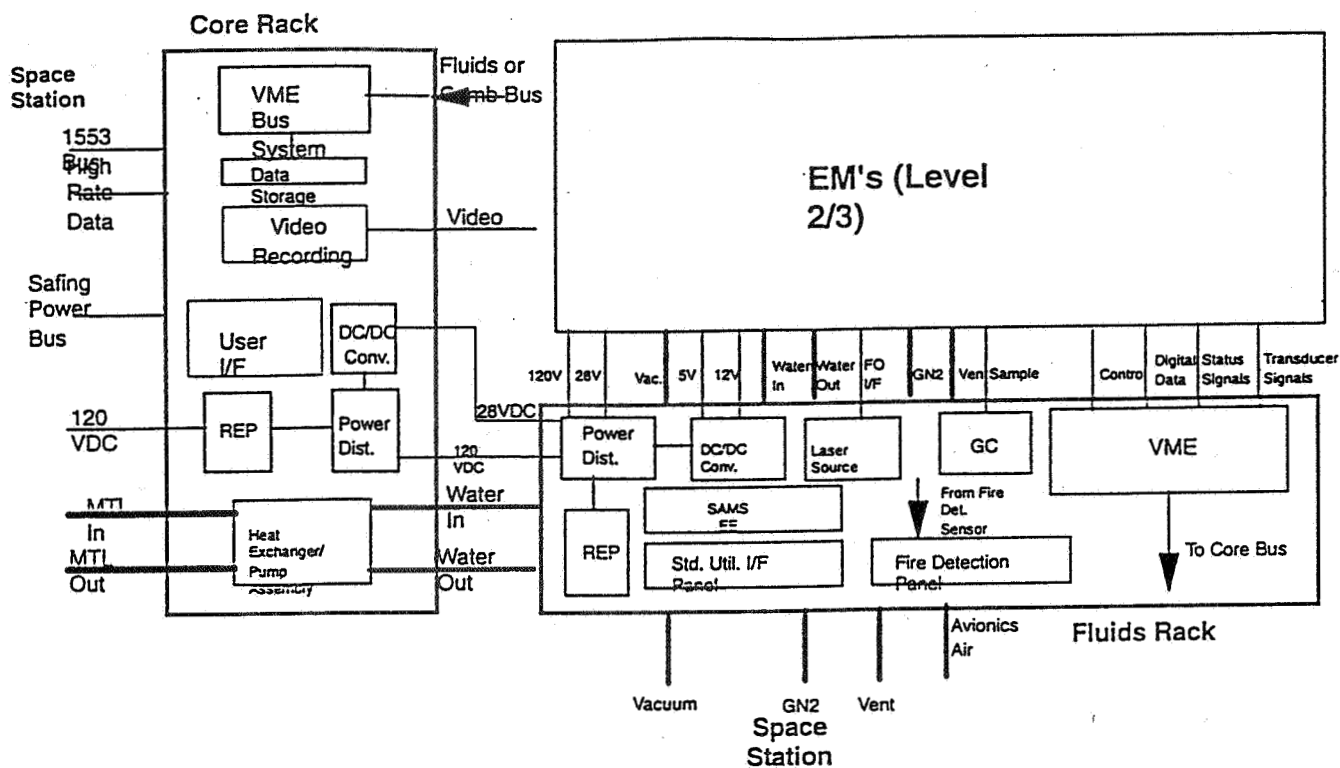
Figure 5.A-1   Level 1 Block Diagram
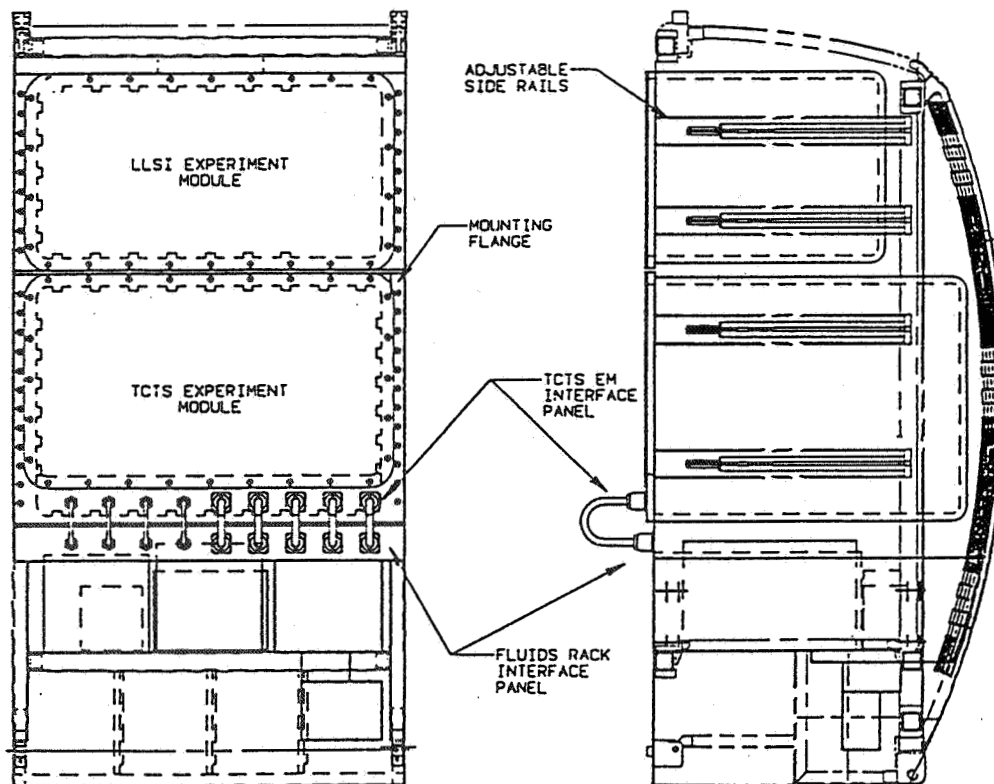
Figure 5.B-1   Fluids Rack Layout with LLSI and TCTS Experiment Modules

444
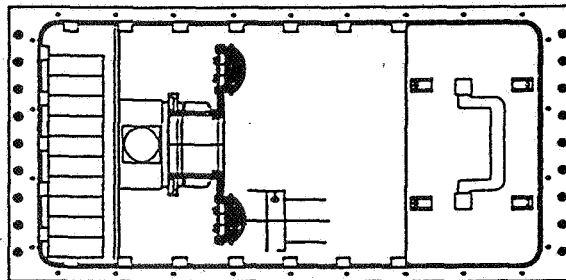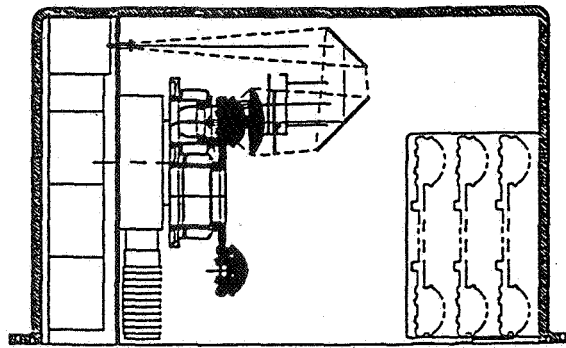
Figure 5.B.1-1   Diagram of LLSI Experiment Module
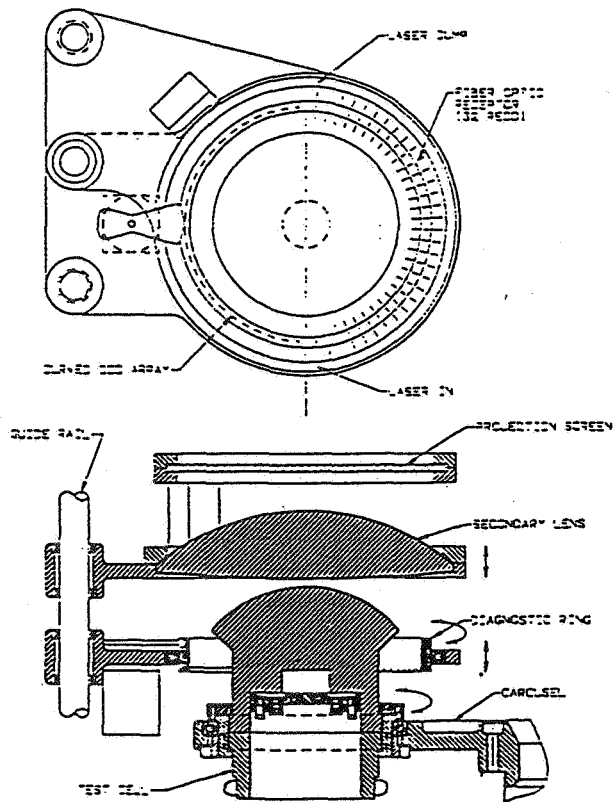
Figure 5.B.1-2   Diagram of LLSI Test Cell and Diagnostics
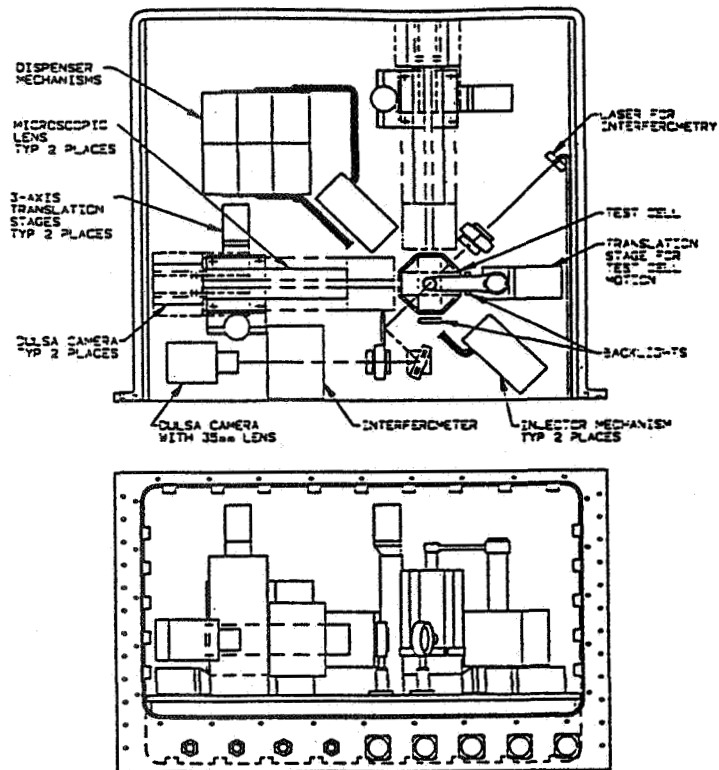
Figure 5.B.2-1 TCTS Experiment Module Layout for Microscopic Viewing
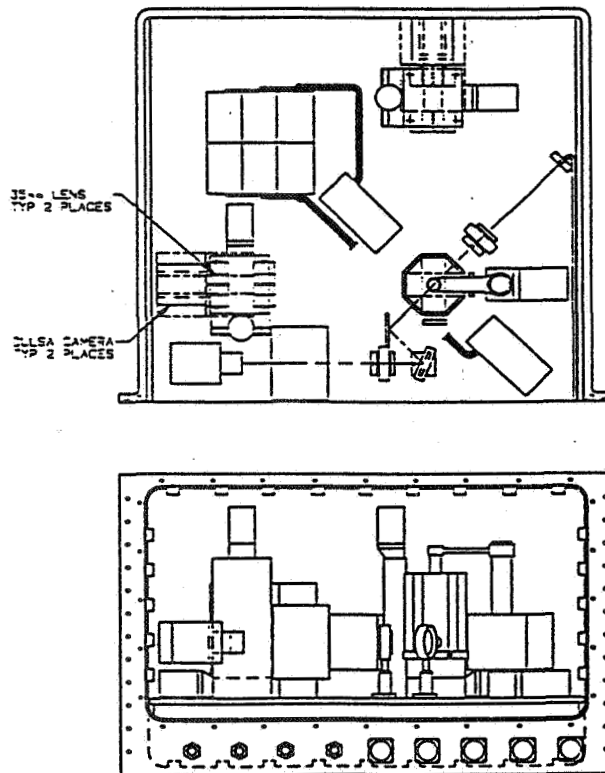
Figure 5.B.2-2   TCTS Experiment Module Layout for Macroscopic Viewing
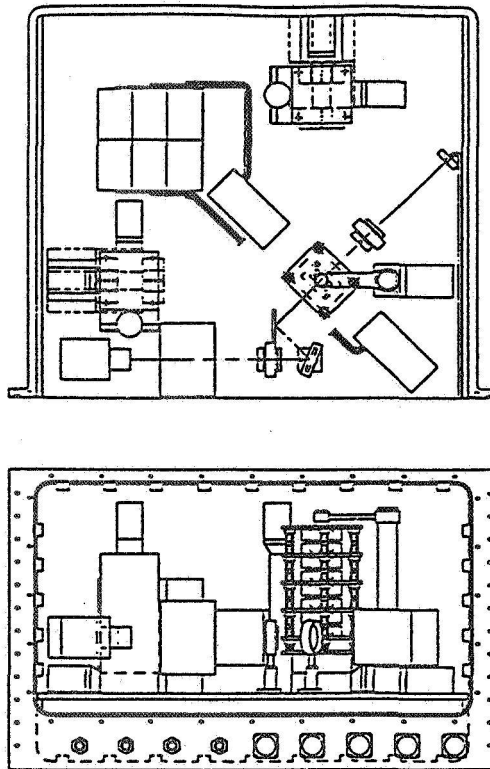
Figure 5.B.2-3 TCTS Experiment Module Layout for Multiple Test
            Cells
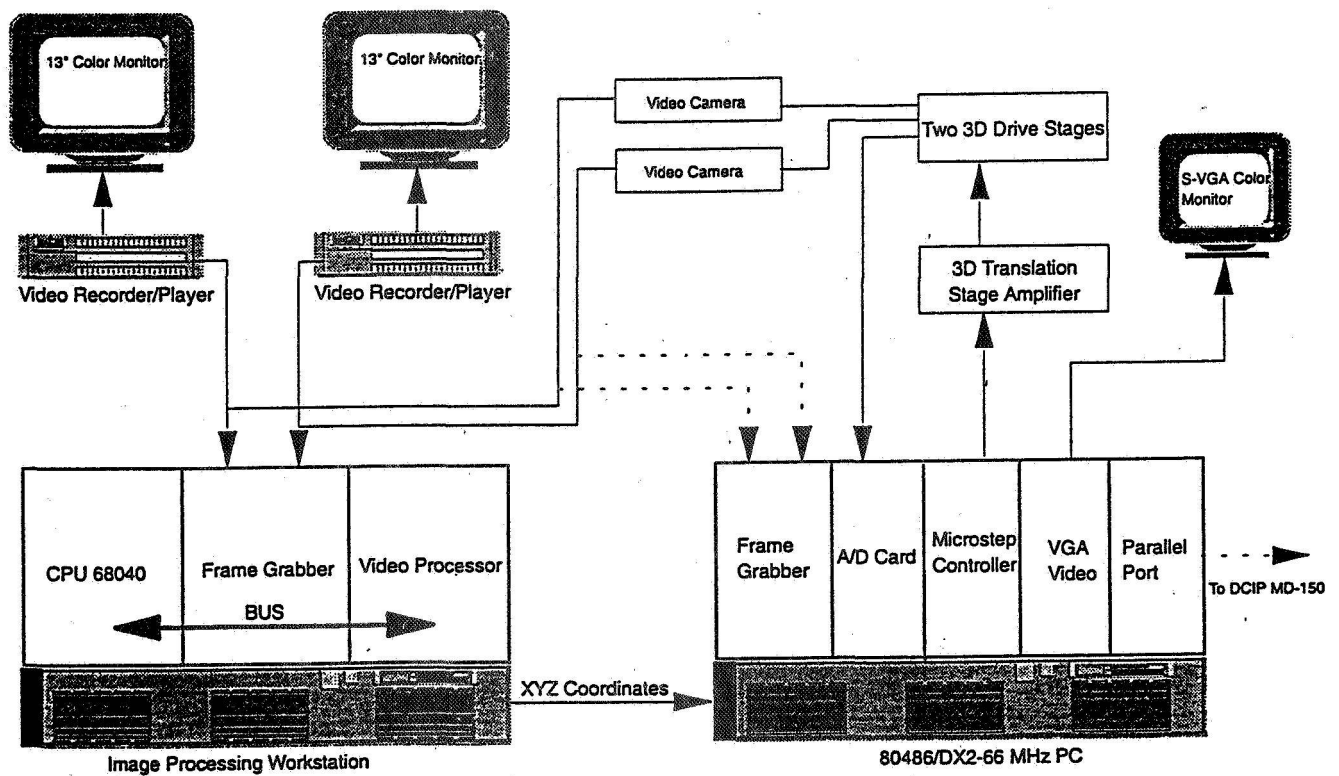
Figure 6.A-1 Automated Positioning and Tracking Breadboard

447

Figure 6.B-1 Data Compression and Image Processing Breadboard

Figure 6.C-1 Data Management Breadboards

Schedule Overview

8:00 a.m.   Registration

Opening Plenary Session
(Orleans Ballroom)
8:00 a.m. - 1:30 p.m.

9:00 a.m.	Opening Session Welcome	Chair: Jack Salzman, NASA-Lewis Donald Campbell, Center Director, NASA-Lewis
9:15 a.m.	Conference Objectives & Overview	Bradley Carpenter, NASA Headquarters
9:35 a.m.	Conference Organization	Bhim Singh, NASA-Lewis
9:45 a.m.	**Keynote**: Science Policy Environment— NASA & μg Research	Simon Ostrach, Case Western Reserve
10:30 a.m.	Break	
11:00 a.m.	Opportunities in Microgravity Fluid Physics	Stephen Davis, Northwestern University
11:20 a.m.	**Keynote**: Interdisciplinary Opportunities for Fluid Physics in Life Sciences	Harry Holloway, Associate Administrator, NASA Headquarters
12:00 noon	Lunch break—open	
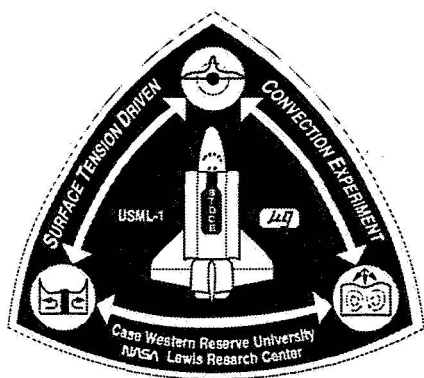
Parallel Session I
1:30 - 3:00 p.m.

Drops and Bubbles I
Chair, Marc Smith
(Royal Street)

Eugene Trinh
Nonlinear Dynamics of Drops and
Bubbles and Chaotic Phenomena

Gretar Tryggvason
Computations of Drop
Collision and Coalescence

An-Ti Chai
Marangoni Instability Induced
Convection in Evaporating Liquid
Droplets

3:00 p.m.   Break

Thermocapillary Flows I
Chair, Shankar Subramanian
(Royal Street)

Robert Kelly
Stabilization of Thermocapillary
Convection by Means of Nonplanar
Flow Oscillations

Paul Neitzel
Control of Oscillatory
Thermocapillary Convection in
Microgravity

Abdelfattah Zebib
Oscillatory Thermocapillary
Convection

Michael Schatz
Onset of Hexagons in Surface-Tension-
Driven Benard Convection

6:30 p.m.   Reception (Mark Twain Ballroom)
7:30 p.m.   Dinner (Orleans Ballroom)
              After-Dinner Speaker

Multiphase Flow/Heat Transfer I
Chair, George Bankoff
(Bourbon Street)

Davood Abdollahian
Study of Two-Phase Flow and Heat
Transfer in Reduced Gravities

Scott Bousman
Characterization of Annular Two-Phase
Gas-Liquid Flows in Microgravity

Richard Lahey
Analysis of Phase Distribution Phe-
nomena in Microgravity Environments

Parallel Session II
3:30 - 5:30 p.m.

Solidification
Chair, Norman Chigier
(Bourbon Street)

Sam Coriell
Convection and Morphological
Stability during Directional Solidifica-
tion

Stephen Davis
Theory of Solidification

Saleh Tanveer
Crystal Growth and Fluid Mechanics
Problems in Directional Solidification

M. Grae Worster
Interactions Between Solidification
and Compositional Convection in
Mushy Alloys

Evening

Complex Fluids I
Chair, David Weitz
(Foster Street)

Douglas Durian
Microgravity Foam Structure and
Rheology

Gareth McKinley
The Extensional Rheology of Non-
Newtonian Materials

Xial-lun Wu
Nucleation and Chiral Symmetry
Breaking Under Controlled Hydro-
dynamic Flows

Complex Fluids II
Chair, Doug Durian
(Foster Street)

John Goree
Plasma Dust Crystallization

Seth Putterman
Containerless Capillary Wave
Turbulence

Rafat Ansari
Flocculation and Aggregation in a
Microgravity Environment

Donald Koch
Effects of Gravity and
Shear on Multiphase Flow

Chair: Jack Salzman, NASA Lewis

Robert Rhome, NASA Headquarters

Keynote Address
(Orleans Ballroom)
8:00 - 8:40 a.m.

8:00 a.m.	Keynote Address **Keynote:** Future Directions for Multiphase Flow and Heat Transfer in Microgravity	Chair: Stephen Davis, Northwestern University George Bankoff, Northwestern University

Plenary Session
8:40 a.m. - 12:00 noon

8:40 a.m.	Microgravity Research Programs, Plans, & Status: Presentations by International Space Organizations	Chair: Bradley Carpenter, NASA Headquarters
10:10 a.m.	Break	
10:30 a.m.	Plenary Session	Chair: Robert Snyder, NASA-MSFC
10:30 a.m.	Path to Flight Experiment	Jack Salzman, NASA-Lewis
11:00 a.m.	Flight Hardware	Nancy Shaw, NASA-Lewis
11:30 a.m.	Space Station Fluids Facility	Jennifer Rhatigan, NASA-Lewis
12:00 noon	Lunch break—open	

Afternoon

Parallel Session III
1:00 - 2:30 p.m.

Thermocapillary Flows II **Chair, Abdelfattah Zebib** **(Royal Street)**	**Multiphase Flow/Heat Transfer II** **Chair, Mark McCready** **(Bourbon Street)**	**Physicochemical Systems I** **Chair, Gareth McKinley** **(Foster Street)**
Chuan Chen Experimental Investigation of the Marangoni Effect on the Stability of a Double-Diffusive Layer	S. Chan Experimental and Theoretical Studies of Rewetting of Unheated Grooved Plates	Eric Kaler Surfactant-Based Critical Phenomena in Microgravity
Sindo Kou Thermocapillary Convection in Floating Zones under Simulated Reduced-Gravity Conditions	Kevin Hallinan Effects of Thermocapillarity on an Evaporating Meniscus in Microgravity	Simon Ostrach Gravity-Dependent Transport in Industrial Processes
Marc Smith The Behavior of Unsteady Thermocapillary Flows	Peter Wayner Interfacial Force Field Characteriza- tion of a Constrained Vapor Bubble Thermosyphon Using IAI	Jorge Vinals Stochastic Model of the Residual Acceleration Environment in Microgravity

2:30 p.m.	Break

Wednesday, June 22, 1994
Afternoon

Parallel Session IV
3:00 - 4:00 p.m.

Thermocapillary Flows III
Chair, Choua Chen
(Royal Street)

K.C. Hsieh
Oscillatory/Chaotic Thermocapillary
Flow Induced by Radiant Heating

Jean Koster
Multilayer Fluid Dynamics and
Solidification of Metallic Melts

Multiphase Flow/Heat Transfer III
Chair, Peter Wayner
(Bourbon Street)

Jacob Chung
Bubble Dynamics, Two-Phase Flow,
and Boiling Heat Transfer in a
Microgravity Environment

Herman Merte
Pool and Flow Boiling in Variable and
Microgravity

Physicochemical Systems II
Chair, Robert Snyder
(Foster Street)

John Anderson
Electrokinetic Transport of Heteroge-
neous Particles in Suspension

4:00 p.m.   Break

Parallel Session V
4:30 - 6:00 p.m.

Drops and Bubbles II
Chair, Gary Leal
(Royal Street)

Hossein Haj-Hariri
Thermocapillary Motion of
Deformable Drops

Satwindar Sadhal
Ground Based Studies of
Thermocapillary Flows in
Levitated Drops

Shankar Subramanian
Thermocapillary Migration and
Interactions of Bubbles and Drops

Multiphase Flow/Heat Transfer IV
Chair, Herman Merte
(Bourbon Street)

Norman Chigier
Transport Phenomena in Stratified
Multi-Fluid Flow in the Presence and
Absence of Gravity

Ivan Clark
Particle Experiments in Thermal and
Velocity Gradients

Sudarshan Loyalka
Cross Effects in Microgravity Flows

Biological Colloids &
Electrohydrodynamics I
Chair, Thomas Glasgow
(Foster Street)

James Baygents
Studies on the Response of Emulsions
to Externally-Imposed Electric and
Velocity Fields

Robert Snyder
Electrohydrodynamics Observed
during Electrophoresis
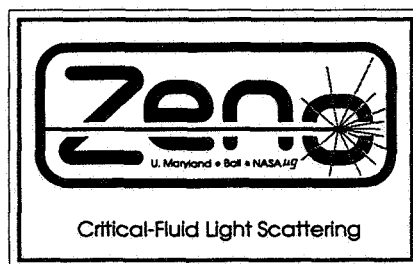
Critical-Fluid Light Scattering

Keynote Address
(Orleans Ballroom)
8:00 - 8:40 a.m.

8:00 a.m.   Keynote Address   Chair: Paul Neitzel, Georgia Institute of Tech.
              Keynote: Rheological Instabilities and   Joe Goddard, University of California
              Patterned States in Complex Fluids

8:40 a.m.   Break

Parallel Session VI
9:00 - 10:30 a.m.

Interfacial Phenomena I
Chair, Satwindar Sadhal
(Royal Street)

Iwan Alexander
Dynamics and Statics of
Nonaxisymmetric Liquid Bridges

Paul Concus
Equilibrium Fluid Interface Behavior
under Low-and Zero-Gravity
Conditions

Sung Lin
The Breakup of a Liquid Jet at
Microgravity

10:30 a.m.   Break

Multiphase Flow/Heat Transfer IV
Chair, Kevin Hallinan
(Bourbon Street)

Mark McCready
Two-Layer Viscous Instability in a
Rotating Couette Device

Paul Rothe
An Application of Miniscale Experi-
ments on Earth to Refine Microgravity
Analysis of Adiabatic Multiphase Flow
in Space

Joel Koplik
Wetting and Spreading at the
Molecular Scale

Biological Colloids &
Electrohydrodynamics II
Chair, James Baygent
(Foster Street)

Dudley Saville
Studies in Electrodynamics

Dudley Saville
Dielectric/Electrohydrodynamic
Properties

Robert Davis
Electrophoretic Interaction and
Aggregation of Colloidal Biological
Particles

Parallel Session VII
11:00 a.m. - 12:30 p.m.

Interfacial Phenomena II
Chair, Sung Lin
(Royal Street)

Stephen Garoff
Microscale Hydrodynamics Near
Moving Contact Lines

Robert Davis
Phase Separation Due to Simulta-
neous Migration and Coalescence

Paul Steen
Influenced of Flow on Interface Shape
Stability in Low Gravity

Phase Transitions
Chair, M. Grae Worster
(Bourbon Street)

Donald Jacobs
Turbidity of a Binary Fluid Mixture:
Determining η

David Jasnow
A Coarse Grained Approach to
Thermocapillarity Effects in Binary
Systems

Graham Ross
Helium II Slosh in Low Gravity

Complex Fluids III
Chair, Douglas Durian
(Foster Street)

Paul Chaikin
Dynamics of Hard Sphere Colloidal
Dispersions

Alan Hatton
Measurement of Resistance to Solute
Transport Across a Water-in-Oil
Microemulsion/Aqueous Phase
Interface Using a Fluorescence
Recovery After Photobleaching
(FRAP) Technique

David Weitz
Colloid Physics in Microgravity

12:30 p.m.   Hotel Lunch—Airport Marriott (Mark Twain Ballroom)

|		
1:30-3:30 p.m.	Closing Plenary (Orleans Ballroom)	
1:30 p.m.	Responding to NRA	Bradley Carpenter, NASA Headquarters
2:00-3:30 p.m.	Panel/Audience Exchange	Chair: Bradley Carpenter NASA Headquarters

Topics:

- Microgravity Program Budget and Future Plans
- Present and Future Theme Areas
- NRA Questions and Suggestions
- Flight/Ground Test Hardware Availability
- Questions & Answers

Panel Members:

- Professor Stephen Davis, Northwestern University
- Professor S. George Bankoff, Northwestern University
- Professor Joe Goddard, University of California—San Diego
- Professor Richard Lahey, Rensselaer Polytechnic Institute
- Professor Paul Neitzel, Georgia Institute of Technology
- Dr. Robert Snyder, NASA-MSFC
- Mr. John Watkins, Jet Propulsion Laboratory

3:30-5:00 p.m.	Optional LeRC Tour
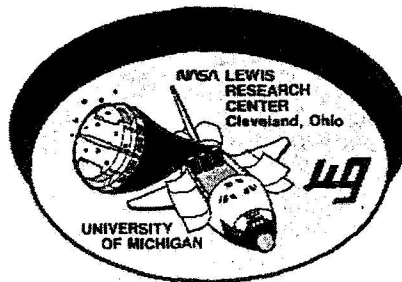
B-0716-6
Jun 94

Second Microgravity Fluid Physics Conference
Attendance List
June 21-23, 1994
Cleveland, Ohio

KATHLEEN ABBEY
CARYTECH, INC.
P.O. BOX 5527
CARY, NC 27512

DAVOOD ABDOLLAHIAN
S. LEVY, INC.
3425 S. BASCOM AVE.
CAMPBELL, CA 95008

THOMAS H. ACQUAVIVA
MS 500-222
NASA-LEWIS
21000 BROOKPARK RD.
CLEVELAND, OH 44135

M. KHAIRUL ALAM
OHIO UNIV.
255 STOCKER CENTER
ATHENS, OH 45701

IWAN ALEXANDER
M-65 R.I. BUILDING UAH
UNIV. OF ALABAMA, HUNTSVILLE
HUNTSVILLE, AL 35803

JEFF ALLEN
MS 500-102
NASA-LEWIS
21000 BROOKPARK RD.
CLEVELAND, OH 44135

M. CENGIZ ALTAN
SCHOOL OF AEROSPACE & MECHANICAL
ENGINEERING
UNIV. OF OKLAHOMA
NORMAN, OK 73019

C. DAVID ANDERECK
DEPT. OF PHYSICS
OHIO STATE UNIV.
174 W. 18TH AVE.
COLUMBUS, OH 43210

JOHN ANDERSON
DEPT. OF CHEMICAL ENGINEERING
CARNEGIE MELLON UNIV.
PITTSBURGH, PA 15213

RAFAT ANSARI
MS 105-1
NASA-LEWIS
21000 BROOKPARK RD.
CLEVELAND, OH 44135

TOM AVEDISIAN
DEPT. OF MECHANICAL ENGINEERING
CORNELL UNIV.
ITHACA, NY 14853

GREGORY BAKER
DEPT. OF MATHEMATICS
OHIO STATE UNIV.
231 W. 18TH AVE.
COLUMBUS, OH 43210

R. BALASUBRAMANIAM
MS 500-102
NASA-LEWIS
21000 BROOKPARK RD.
CLEVELAND, OH 44135

S. GEORGE BANKOFF
CHEMICAL ENGINEERING DEPT.
NORTHWESTERN UNIV.
EVANSTON, IL 60208

MARTIN BARMATZ
MS 183-401
JET PROPULSION LABORATORY
4800 OAK GROVE DRIVE
PASADENA, CA 91109

OSMAN A. BASARAN
4501, MS-6224
OAK RIDGE NATIONAL LABORATORY
P.O. BOX 2008
OAK RIDGE, TN 37831-6224

JAMES C. BAYGENTS
DEPT. OF CHEMICAL ENGINEERING
UNIV. OF ARIZONA
TUSCON, AZ 85721

PIERRE BENARD
UNIVERSITE DU QUEBEC A TROIS RIVIERES
3351, BOUL. DES FORGES
TROIS-RIVIERES, PQ G9A 5H7 CANADA

457

LUIS P. BERNAL
AEROSPACE ENGINEERING
UNIV. OF MICHIGAN
ANN ARBOR, MI 48109-2118

RAVI S. BHAGAVATULA
OHIO STATE UNIV.
174 W. 18TH AVE.
COLUMBUS, OH 43210

FABIAN BONETTO
CENTER FOR MULTIPHASE RESEARCH
RENSSELAER POLYTECHNIC INSTITUTE
NUCLEAR ENG. AND ENG. PHYSICS
TROY, NY 12180-3590

JOHN BORDEN
IPST BLDG. 085 RM 1102
UNIV. OF MARYLAND
COLLEGE PARK, MD 20742

SCOTT BOUSMAN
DEPT. OF CHEMICAL ENGINEERING
UNIV. OF HOUSTON
14526 OAK CHASE DR.
HOUSTON, TX 77062

KIRK BRATTKUS
SOUTHERN METHODIST UNIV.
3200 DYER
DALLAS, TX 75275

RICHARD BRAUN
MS 101-A238
NATIONAL INST. OF STANDARDS & TECH
GAITHERSBURG, MD 20899

STEVEN BROAD
OHIO AEROSPACE INSTITUTE
21000 BROOKPARK RD.
CLEVELAND, OH 44135

TIMOTHY BROWER
COLORADO STATE UNIV./CEISS
FORT COLLINS, CO 80523

EDWARD P. BROWNE
DEPT. OF CHEMICAL ENGINEERING
MASSACHUSETTS INSTITUTE OF TECH.
CAMBRIDGE, MA 02139

RAFFI BUDAK
DEPT. OF PHYSICS
UNIV. OF CALIFORNIA
LOS ANGELES, CA 90024-1547

WESLEY BURGHARDT
DEPT. OF CHEMICAL ENGINEERING
NORTHWESTERN UNIV.
EVANSTON, IL 60208

DAVID CANNELL
DEPT. OF PHYSICS
UNIV. OF CALIFORNIA/SANTA BARBARA
SANTA BARBARA, CA 93106

VAN P. CAREY
MECHANICAL ENGINEERING DEPT.
UNIV. OF CALIFORNIA AT
BERKELEY, CA 94720

BRAD CARPENTER
CODE UGS
NASA HEADQUARTERS
WASHINGTON, DC 20546-0001

IGOR CARRON
DEPT. OF NUCLEAR ENGINEERING
TEXAS A&M UNIV.
TAM U
COLLEGE STATION, TX 77843-3133

AN-TI CHAI
MS 500-327
NASA-LEWIS
21000 BROOKPARK RD.
CLEVELAND, OH 44135

PAUL CHAIKIN
DEPT. OF PHYSICS
PRINCETON UNIV.
PRINCETON, NJ 08544

ARNON CHAIT
MS 105-1
NASA-LEWIS
21000 BROOKPARK RD
CLEVELAND, OH 44135

RICK CHAN
MS 106-1
NASA-LEWIS
21000 BROOKPARK RD.
CLEVELAND, OH 44135

SHIH H. CHAN
UNIV. OF WISCONSIN
P.O. BOX 784
MILWAUKEE, WI 53201

B.J. CHANG
LIFE SYSTEMS, INC.
24755 HIGHLAND RD.
CLEVELAND, OH 44122

DAVID CHAO
MS 500-102
NASA-LEWIS
21000 BROOKPARK RD.
CLEVELAND, OH 44135

DAVID J. CHATO
SPTD-6
NASA-LEWIS
21000 BROOKPARK RD.
CLEVELAND, OH 44135

CHUAN CHEN
DEPT. OF AEROSPACE & MECHANICAL
UNIV. OF ARIZONA
TUSCON, AZ 85721

MING-TANG CHEN
DEPT. OF PHYSICS
CASE WESTERN RESERVE UNIV.
10900 EUCLID AVE.
CLEVELAND, OH 44106

TUNG-LUNG CHEN
18645 DETROIT AVE. APT. #316
LAKEWOOD, OH 44107

G.G. CHERNYI
RUSSIAN ACADEMY OF SCIENCES
LENINSKI PROSPECT 14
117901 MOSCOW V71, RUSSIA

MIKE CHEUNG
CHEMICAL ENGINEERING DEPT.
UNIV. OF AKRON
AKRON, OH 44325-3906

FRANCIS CHIARAMONTE
MS 500-327
NASA-LEWIS
21000 BROOKPARK RD.
CLEVELAND, OH 44135

NORMAN CHIGIER
MECHANICAL ENGINEERING DEPT.
CARNEGIE MELLON UNIV.
SCHENLEY PARK
PITTSBURGH, PA 15213-3890

SRINIVAS CHIPPADA
DEPT. OF MECH. ENG. & MATL. SCI.
RICE UNIV.
P.O. BOX 1892
HOUSTON, TX 77251-1892

THOMAS CHOU
PHYSICS DEPT.
HARVARD UNIV.
CAMBRIDGE, MA 02138

J.N. CHUNG
DEPT. OF MECH. & MATL. ENG.
WASHINGTON STATE UNIV.
PULLMAN, WA 99164-2920

MAREK CIEPLAK
PHYSICS DEPT.
RUTGERS UNIV.
PISCATAWAY, NJ 08854

IVAN CLARK
MS 473
NASA LANGLEY RESEARCH CENTER
HAMPTON, VA 23681-0001

MICHAEL CLIFTON
BIOPHYSICS ES76
MARSHALL SPACE FLIGHT CENTER
HUNTSVILLE, AL 35812

RITA L. COGNION
ADF, INC.
3001 AEROSPACE PKWY.
BROOK PARK, OH 44142

ANNE COLE
ORBITAL SCIENCES CORP.
2771 NORTH GAREY AVENUE
POMONA, CA 91767

PIERRE COLINET
UNIV. OF BRUSSELS
50 AV. F.D. ROOSEVELT
BRUXELLES, BELGIUM

PETER W. COLOVAS
OHIO STATE UNIV.
179 W. 18TH AVE.
COLUMBUS, OH 43210

PAUL CONCUS
LBL, 50A-2129
UNIV. OF CALIFORNIA
BERKELEY, CA 94720

SAM CORIELL
NAT. INST. OF STANDS. & TECH.
GAITHERSBURG, MD 20899

ROGER CROUCH
CODE UGS
NASA HEADQUARTERS
WASHINGTON, DC 20546

CHRISTOPHER CROWLEY
CREARE, INC.
P.O. BOX 71
HANOVER, NH 03755

A.J. DAHM
DEPT. OF PHYSICS
CASE WESTERN RESERVE UNIV.
10900 EUCLID AVENUE
CLEVELAND, OH 44106-7079

R. CLARK DARTY
BLDG. 4203, MS FA25
NASA MARSHALL SPACE FLIGHT CTR.
HUNTSVILLE, AL 35812

RONALD DAVENPORT
LIFE SYSTEMS, INC.
24755 HIGHPOINT RD.
CLEVELAND, OH 44122

ROBERT DAVIS
DEPT. OF CHEMICAL ENGINEERING
UNIV. OF COLORADO
BOULDER, CO 80309-0424

STEPHEN DAVIS
DEPT. ES/AM, MCCORMICK SCHOOL
NORTHWESTERN UNIV.
EVANSTON, IL 60208

MICHAEL DEGEN
SMITH 3025
OHIO STATE UNIV.
174 W. 18TH AVE.
COLUMBUS, OH 43210

KENNETH J. DEWITT
DEPT. OF CHEMICAL ENGINEERING
UNIV. OF TOLEDO
TOLEDO, OH 43606

VIJAY K. DHIR
46-147 ENGR. IV
UNIV. OF CALIFORNIA/LOS
LOS ANGELES, CA 90024

JEFFREY R. DIDION
CODE 724.2
NASA GODDARD SPACE FLIGHT CTR.
GREENBELT, MD 20771

LOREN DILL
CLEVELAND TELECOMMUNICATIONS CORP.
5351 NAIMAN PARKWAY
SOLON, OH 44139

FRANKLIN DODGE
SOUTHWEST RESEARCH INSTITUTE
6200 CULEBRA RD.
SAN ANTONIO, TX 78238

MICHAEL P. DOHERTY
MS 500-102
NASA-LEWIS
21000 BROOKPARK RD.
CLEVELAND, OH 44135

JAMES P. DOWNEY
ES-75
NASA MARSHALL SPACE FLIGHT CENTER
HUNTSVILLE, AL 35812

KEITH DOWNING
OHIO AEROSPACE INSTITUTE
21000 BROOKPARK RD.
CLEVELAND, OH 44135

MICHAEL DREYER
CENTER OF APPLIED SPACE TECH.
ZARM UNIV. OF BREMEN
AM FALLTURM
BREMEN, D-28359 GERMANY

J.C. DUH
MS 500-102
NASA-LEWIS
21000 BROOKPARK RD.
CLEVELAND, OH 44135

PATRICK W. DUNN
MS 86-14
NASA-LEWIS
21000 BROOKPARK RD.
CLEVELAND, OH 44135

WILLIAM W. DURGIN
WORCESTER POLYTECHNIC INST.
100 INSTITUTE ROAD
WORCESTER, MA 01609

DOUGLAS DURIAN
DEPT. OF PHYSICS
UNIV. OF CALIFORNIA
405 HILGARD AVE.
LOS ANGELES, CA 90024-1547

WALTER DUVAL
MS 105-1
NASA-LEWIS
21000 BROOKPARK RD.
CLEVELAND, OH 44135

ASUQUO EBIANA
MC219D
CLEVELAND STATE UNIV.
EUCLID AVE. AT EAST 24 ST.
CLEVELAND, OH 44115

ELIZABETH ERVIN
1036 HIGHVIEW DRIVE
BEAVERCREEK, OH 44534

JEAN FABRE
INSTITUT DE MECANIQUE DES FLUIDES
ALLEES C. SOULA
TOULOUSE, 31400 FRANCE

BARBARA R. FACEMIRE
ES-76
NASA MARSHALL SPACE FLIGHT CTR.
HUNTSVILLE, AL 35812

ROBERT L. FAGALY
GENERAL ATOMICS
P.O. BOX 85608
SAN DIEGO, CA 92186

ALEXANDER FEDOSEYEV
CENTER FOR MICROGRAVITY & MATLS.
UNIV. OF ALABAMA IN HUNTSVILLE
CMMR, RI M-65
HUNTSVILLE, AL 35899

FRANK FENG
DEPT. OF MECHANICAL ENG. MIT 3-360
MASSACHUSETTS INSTITUTE OF TECHNOLOGY
CAMBRIDGE, MA 02139

GEORGE H. FICHTL
FA21
NASA MARSHALL SPACE FLIGHT CENTER
HUNTSVILLE, AL 35812

PATRICK FINNEGAN
ANALEX CORPORATION
3001 AEROSPACE PKWY.
BROOK PARK, OH 44142

COLLEEN FITZPATRICK
RICE SYSTEMS
18198 AZTEC CT.
FOUNTAIN VALLEY, CA 92708

MIKE FLEMING
LORAL VOUGHT SYSTEMS CORP.
P.O. BOX 650003
DALLAS, TX 75265-0003

J.M. FLORYAN
DEPT. OF MECHANICAL ENGINEERING
UNIV. OF WESTERN ONTARIO
LONDON, ON N6A 5B9 CANADA

LARRY B. FORE
DEPT. OF CHEMICAL ENGINEERING
UNIV. OF HOUSTON
4800 CALHOUN
HOUSTON, TX 77204

RAINER FORKE
GERMAN SPACE AGENCY
KOENIGSWINTERER STR. 522-524
BONN, 53227 GERMANY

JUSTIN FORTMEYER
USC
1724 MERIDIAN APT. H
SOUTH PASADENA, CA 91030

MICHAEL R. FOSTER
AERO. ENG.
OHIO STATE UNIV.
2036 NEIL MALL
COLUMBUS, OH 43210-1276

CARL FRANCK
PHYSICS DEPT.
CORNELL UNIV.
CLARK HALL
ITHACA, NY 14853

DONALD O. FRAZIER
NASA MARSHALL SPACE FLIGHT CTR.
HUNTSVILLE, AL 35803

TRAUGOTT FREDERKING
UCLA
LOS ANGELES, CA 90024

ROBERT FRIEDMAN
MS 500-217
NASA-LEWIS
21000 BROOKPARK RD.
CLEVELAND, OH 44135

ROBERT J. FRYE
MS 500-102
NASA-LEWIS
21000 BROOKPARK RD.
CLEVELAND, OH 44135

TOM GALOMBOS
ANALEX CORPORATION
3001 AEROSPACE PARKWAY
BROOK PARK, OH 44142

STEPHEN GAROFF
CARNEGIE MELLON UNIV.
PITTSBURGH, PA 15213

461

LUIS A. GAST
DEPT. OF MECHANICAL ENGINEERING
UNIV. OF PUERTO RICO, MAYAGUEZ
P.O. BOX 5000
MAYAGUEZ, PR 00681-5000

MORRIS M. GIRGIS
CENTRAL STATE UNIV.
1400 BRUSH ROW ROAD
WILBERFORCE, OH 45384

RONALD GIUNTINI
SPACE ENGINEERING P.O. BOX 077777
WYLE LABORATORIES
7800 GOVERNORS DRIVE W.
HUNTSVILLE, AL 35807-7777

THOMAS GLASGOW
MS 105-1
NASA-LEWIS
21000 BROOKPARK RD.
CLEVELAND, OH 44135

JOE D. GODDARD
DEPT. OF AMES 0411
UNIV. OF CALIFORNIA/SAN DIEGO
LA JOLLA, CA 92093-0411

SULEYMAN GOKOGLU
NASA-LEWIS
21000 BROOKPARK RD.
CLEVELAND, OH 44135

JOHN GOREE
DEPT. OF PHYSICS & ASTRONOMY
UNIV. OF IOWA
IOWA CITY, IA 52242-1479

MEREDITH GRAHAM
MS 105-1
NASA-LEWIS
21000 BROOKPARK RD.
CLEVELAND, OH 44135

MIKE GRAHAM
DEPT. OF CHEM. ENG.
UNIV. OF WISCONSIN
1415 JOHNSON DR.
MADISON, WI 53706-1691

STANLEY A. GREENBERG
AEROJET
P.O. BOX 296 1100 W. HOLLYVALE ST.
AZUSA, CA 91702

VLADIMIR GRIAZNOV
UNIV. OF MICHIGAN-DEARBORN
4901 EVERGREEN RD.
DEARBORN, MI 48128

JOHN B. GRUTZNER
DEPTARTMENT OF CHEMISTRY
PURDUE UNIV.
BROWN BUILDING
WEST LAFAYETTE, IN 47907

MARK HABERBUSCH
MS SPTD-6
OHIO AEROSPACE INSTITUTE
21000 BROOKPARK RD.
CLEVELAND, OH 44135

HOSSEIN HAJ-HARIRI
THORNTON HALL
UNIV. OF VIRGINIA
CHARLOTTSVILLE, VA 22903

ROSHANAK HAKIMZADEH
MS 500-216
TAL-CUT CO.
21000 BROOKPARK RD.
CLEVELAND, OH 44135

NANCY R. HALL
MS 500-102
NASA-LEWIS
21000 BROOKPARK RD.
CLEVELAND, OH 44135

KEVIN HALLINAN
MECH. & AEROSPACE ENG. DEPT.
UNIV. OF DAYTON
300 COLLEGE PARK
DAYTON, OH 45469-0210

MICHAEL T. HARRIS
4501, MS 6224
OAK RIDGE NATIONAL LABORATORY
P.O. BOX 2008
OAK RIDGE, TN 37831-4829

MOHAMMAD HASAN
SPTD-6
NASA-LEWIS
21000 BROOKPARK RD.
CLEVELAND, OH 44135

UDAY HEGDE
NYMA, INC.
2001 AEROSPACE PKWY.
BROOK PARK, OH 44142

JOHN HEGSETH
DEPT. OF PHYSICS
UNIV. OF NEW ORLEANS
NEW ORLEANS, LA 70148

ROGER HELMICK
ANALEX CORPORATION
3001 AEROSPACE PKWY.
BROOK PARK, OH 44142

R.C. HENDRICKS
SPTD-3
NASA-LEWIS
21000 BROOKPARK RD.
CLEVELAND, OH 44135

CILA HERMAN
DEPT. OF MECHANICAL ENG.
JOHNS HOPKINS UNIV.
3400 NORTH CHARLES STREET
BALTIMORE, MD 21218

ROBERT H. HERTEL
ORBITAL SCIENCES CORP.
2771 NORTH GAREY AVENUE
POMONA, CA 91767

MYRON HILL
MS 500-327
NASA-LEWIS
21000 BROOKPARK RD.
CLEVELAND, OH 44135

WAYNE S. HILL
FOSTER-MILLER INC.
350 SECOND AVE.
WALTHAM, MA 02154

ANANDA HIMANSU
CLEVELAND TELECOMMUNICATIONS CORP.
5351 NAIMAN PARKWAY SUITES E AND F
SOLON, OH 44139

ED HODGSON
HAMILTON STD. DIV. OF UNITED TECH.
1 HAMILTON RD.
WINDSOR LOCKS, CT 06096

TOMOHIRO HONDA
DEPT. OF MECH. & AEROSPACE ENG.
CASE WESTERN RESERVE UNIV.
10900 EUCLID AVE.
CLEVELAND, OH 44106-7222

ANDREW M. HONOHAN
CLARKSON UNIV.
BOX 5725
POTSDAM, NY 13699

JOHN A. HOPKINS
CENTER FOR LASER APPLICATIONS
UNIV. OF TENNESSEE SPACE INST.
B.H. GOETHERT PARKWAY
TULLAHOMA, TN 37388-8897

K.C. HSIEH
MS 500-102
NASA-LEWIS
21000 BROOKPARK RD.
CLEVELAND, OH 44135

HOWARD HU
297 TOWNE BUILDING
UNIV. OF PENNSYLVANIA
220 S. 33RD ST.
PHILADELPHIA, PA 19104-6315

ULF E. ISRAELSSON
MS 125-112
JET PROPULSION LABORATORY
4800 OAK GROVE DRIVE
PASADENA, CA 91109-8099

DONALD JACOBS
THE COLLEGE OF WOOSTER
WOOSTER, OH 44691

DAVID JASNOW
DEPT. OF PHYSICS AND ASTRONOMY
UNIV. OF PITTSBURGH
PITTSBURGH, PA 15260

SUBASH JAYAWARDENA
M.S. 500-102
NASA-LEWIS
21000 BROOKPARK RD.
CLEVELAND, OH 44135

DAVID JEFFREY
UNIV. OF WESTERN ONTARIO
LONDON, ON N6A 5B7 CANADA

LINDA B. JETER
FA-24
NASA MARSHALL SPACE FLIGHT CENTER
HUNTSVILLE, AL 35812-

MILIND A. JOG
DEPT. OF MECH. ENGINEERING (ML 072)
UNIV. OF CINCINNATI
CINCINNATI, OH 45221-0072

W.L. JOHNSON
DEPT. OF PHYSICS
WESTMINSTER COLLEGE
NEW WILMINGTON, PA 16172

SANG W. JOO
DEPT. OF MECHANICAL ENGINEERING
WAYNE STATE UNIV.
DETROIT, MI 48202

463

PRAKASH B. JOSHI
PHYSICAL SCIENCES, INC.
20 NEW ENGLAND BUSINESS CTR.
ANDOVER, MA 01810-1077

DAMIR JURIC
UNIV. OF MICHIGAN
304 AUTOLAB
ANN ARBOR, MI 48109

YASUHIRO KAMOTANI
CASE WESTERN RESERVE UNIV.
CLEVELAND, OH 44106

RUDOLF KELLER
EMEC CONSULTANTS
4221 ROUNDTOP ROAD
EXPORT, PA 15632

ROBERT KELLY
SCHOOL OF ENGINEERING
UNIV. OF CALIFORNIA
MANE DEPT.
LOS ANGELES, CA 90024-1597

EDWARD G. KESHOCK
CLEVELAND STATE UNIV.
E. 24TH AND EUCLID
CLEVELAND, OH 44147

BAMIN KHOMAMI
DEPT. OF CHEMICAL ENGINEERING
WASHINGTON UNIV.
ST. LOUIS, MO 63130

JOEL KNAPP
ANALEX CORPORATION
3001 AEROSPACE PKWY.
BROOK PARK, OH 44142

RICHARD H. KNOLL
MS 500-322
NASA-LEWIS
21000 BROOKPARK RD.
CLEVELAND, OH 44135

DONALD KOCH
OLIN HALL
CORNELL U. SCHOOL OF CHEM. ENG.
ITHACA, NY 14853

CARRIE KOECHEL
ANALEX CORPORATION
3001 AEROSPACE PKWY.
BROOK PARK, OH 44142

FRED J. KOHL
500-327
NASA-LEWIS
21000 BROOKPARK RD.
CLEVELAND, OH 44135]

JEAN N. KOSTER
DEPT. OF AEROSPACE ENG. SCI.
UNIV. OF COLORADO
BOULDER, CO 80309

SINDO KOU
DEPT. OF MATERIALS SCIENCE & ENG.
UNIV. OF WISCONSIN
1509 UNIV. AVE.
MADISON, WI 53706

KAZUHIKO KUDO
DEPT. OF MECH. ENG.
HOKKAIDO UNIV.
KITA-13, NISHI-8, KITA-KU
SAPPORO, 060 JAPAN

MARK D. KUNKA
AERO ENG.
OHIO STATE UNIV.
2036 NEIL MALL
COLUMBUS, OH 43210-1276

ROBERT KUSNER
MS 500-102
NASA-LEWIS
21000 BROOKPARK RD.
CLEVELAND, OH 44135

M. GENE LEE
LIFE SYSTEMS, INC.
24755 HIGHLAND RD.
CLEVELAND, OH 44122

ANTHOHY LIAKOPOULOS
DEPT. OF MECHANICAL ENG.
LEHIGH UNIV.
PACKARD LAB
BETHLEHEM, PA 18015-3085

SETH LICHTER
MECHANICAL ENGINEERING
NORTHWESTERN UNIV.
2145 SHERIDAN ROAD
EVANSTON, IL 60208-3111

DAVID LIEBAL
MS 86-5
NASA-LEWIS
21000 BROOKPARK RD.
CLEVELAND, OH 44135

SUNG LIN
DEPT. OF MECH. & AERONAUT. ENG.
CLARKSON UNIV.
POTSDAM, NY 13699

JERRI S. LING
MS 500-102
NASA-LEWIS
21000 BROOKPARK RD.
CLEVELAND, OH 44135

PAT LONEY
NYMA, INC.
2001 AEROSPACE PKWY.
BROOK PARK, OH 44142

JOHN M. LOPEZ
DEPT. OF MATHEMATICS
PENN STATE UNIV.
218 MCALLISTER BLDG., PSU
UNIV. PARK, PA 16802

SAMUEL LOWRY
CFD RESEARCH CORP.
3325 TRIANA BLVD.
HUNTSVILLE, AL 35801

SUDARSHAN LOYALKA
PARTICULATE SYS. RESEARCH CTR.
UNIV. OF MISSOURI/COLUMBIA
0039 ENGINEERING COMPLEX
COLUMBIA, MO 65211

JAMES MAGUIRE
AET, LTD.
155-B NEW BOSTON ST.
WOBURN, MA 01801

JAMES MAHER
DEPT. OF PHYSICS AND ASTRONOMY
UNIV. OF PITTSBURGH
PITTSBURGH, PA 15260

BRIAN MARTIN
DEPT. OF PHYSICS
UNIV. OF PITTSBURGH
PITTSBURGH, PA 15260

MOSHE MATALON
NORTHWESTERN UNIV.
2145 SHERIDAN RD.
EVANSTON, IL 60208-3125

ED MATHIOTT
ANALEX CORPORATION
3001 AEROSPACE PKWY.
BROOK PARK, OH 44142

FRANCES MCCAUGHAN
CASE WESTERN RESERVE UNIV.
CLEVELAND, OH 44106

WILLIAM D. MCCORMICK
CENTER FOR NONLINEAR DYNAMICS
UNIV. OF TEXAS AT AUSTIN
AUSTIN, TX 78712

MARK MCCREADY
DEPT. OF CHEMICAL ENGINEERING
UNIV. OF NOTRE DAME
182 FITZPATRICK HALL
NOTRE DAME, IL 46556

JEFF MCFADDEN
A238 BUILDING 101
NATIONAL INST. OF STAND. & TECH.
GAITHERSBURG, MD 20899

GARETH MCKINLEY
DIVISION OF APPLIED SCIENCES
HARVARD UNIV.
PIERCE HALL 316
CAMBRIDGE, MA 02138

JOHN B. MCLAUGHLIN
CHEMICAL ENGINEERING DEPT.
CLARKSON UNIV.
POTSDAM, NY 13699-5705

JOHN MCQUILLEN
MS 500-327
NASA-LEWIS
21000 BROOKPARK RD.
CLEVELAND, OH 44135

C. MEGARIDIS
DEPT. OF MECH. ENG. (M/C 251)
UNIV. OF ILLINOIS AT CHICAGO
842 W. TAYLOR ST.
CHICAGO, IL 60607-7022

HERMAN MERTE, JR.
UNIV. OF MICHIGAN
2148 G.G. BROWN
ANN ARBOR, MI 48109

WILLIAM MEYER
MS 105-1
OHIO AEROSPACE INSTITUTE
21000 BROOKPARK RD.
CLEVELAND, OH 44135

JALICS MIKLOS
OHIO STATE UNIV.
100 W. 18TH AVE.
COLUMBUS, OH 43210

MICHAEL MIKSIS
ESAM
NORTHWESTERN UNIV.
2145 SHERIDAN RD.
EVANSTON, IL 60208

KYUNG-YANG MIN
MS 110-2
NASA-LEWIS
21000 BROOKPARK RD.
CLEVELAND, OH 44135

HANS D. MITTELMAN
ARIZONA STATE UNIV.
P.O. BOX 871804
TEMPE, AZ 85287-1804

BRUCE MURRAY
ADMIN A238
NIST
GAITHERSBURG, MD 20899

HENRY K. NAHRA
MS 77-5
NASA-LEWIS
21000 BROOKPARK RD.
CLEVELAND, OH 44135

R. NARAYANAN
DEPT. OF CHEMICAL ENGINEERING
UNIV. OF FLORIDA
GAINESVILLE, FL 32611

JON R. NASH
DEPT. OF MECHANICAL ENGINEERING
UNIV. OF TOLEDO
TOLEDO, OH 43606

LUIS NAVARRO
OHIO AEROSPACE INSTITUTE
21000 BROOKPARK RD.
CLEVELAND, OH 44135

JOHN NAVICKAS
MCDONNELL DOUGLAS AEROSPACE
5301 BOLSA AVE.
HUNTINGTON BEACH, CA 92647

PAUL NEITZEL
GEORGE W. WOODRUFF SCHOOL
GEORGIA INSTITUTE OF TECHNOLOGY
ATLANTA, GA 30332-0405

EMILY NELSON
MS 105-1
NASA-LEWIS
21000 BROOKPARK RD.
CLEVELAND, OH 44135

WILLIAM NIU
ORBITAL SCIENCES CORP.
2771 NORTH GAREY AVENUE
POMONA, CA 91767

HASAN OGUZ
JOHNS HOPKINS UNIV.
122 LATROBE HALL
BALTIMORE, MD 21218

SIMON OSTRACH
DEPT. OF MECH. & AEROSPACE ENG.
CASE WESTERN RESERVE UNIV.
418 GLENNAN BLDG.
CLEVELAND, OH 44106

BEN OVRYN
MS 110-3
NYMA, INC.
21000 BROOKPARK RD.
CLEVELAND, OH 44135

A.A. OYEDIRAN
AYT CORP.
23718 CEDAR RD.
CLEVELAND, OH 44122

D.T. PAPAGEORGIOU
DEPT. OF MATHEMATICS
NEW JERSEY INST. OF TECHNOLOGY
NEWARK, NJ 07102

CHANG-WON PARK
DEPT. OF CHEMICAL ENGINEERING
UNIV. OF FLORIDA
GAINESVILLE, FL 32611

ALEXANDER PATASHINSKY
DEPT. OF PHYSICS AND ASTRONOMY
NORTHWESTERN UNIV.
2145 SHERIDAN ROAD
EVANSTON, IL 60208-3112

MICHAEL E. PAULAITIS
DEPT. OF CHEMICAL ENGINEERING
UNIV. OF DELAWARE
NEWARK, DE 19716

ARNE J. PEARLSTEIN
UNIV. OF ILLINOIS
1206 W. GREEN ST.
URBANA, IL 61801

CATHERINE PEDDIE
MS 500-222
NASA-LEWIS
21000 BROOKPARK RD.
CLEVELAND, OH 44135

PRIYANTHA PERERA
DEPT. OF MATHEMATICS
CARNEGIE MELLON UNIV.
PITTSBURGH, PA 15213

ROBERT PETERSEN
JET PROPULSION LABORATORY
4800 OAK GROVE DRIVE
PASADENA, CA 91109

TODD PETERSON
MS 500-102
NASA-LEWIS
21000 BROOKPARK RD.
CLEVELAND, OH 44135

DUSAN PETRAC
JET PROPULSION LABORATORY
4800 OAK GROVE DR.
PASADENA, CA 91109-8099

VLADIMIR PINES
MS 105-1
NASA-LEWIS
21000 BROOKPARK RD.
CLEVELAND, OH 44135

JONATHAN PLATT
MS 500-327
NASA-LEWIS
21000 BROOKPARK RD.
CLEVELAND, OH 44135

ALEX PLINE
MS 86-5
NASA-LEWIS
21000 BROOKPARK RD.
CLEVELAND, OH 44135

JOHN A. POJMAN
DEPT. OF CHEMISTRY
UNIV. OF SOUTHERN MISSISSIPPI
BOX 5043
HATTIESBURG, MS 39406

VADIM POLEZHAEV
INSTITUTE FOR PROBLEMS IN
MECHANICS/RUSSIAN ACADEMY
117526 RUSSIA MOSCOW
PROSPEKT VERNADSKOGO 101

JOHN F. PRINCE
NYMA, INC.
2001 AEROSPACE PKWY.
BROOK PARK, OH 44142

RAJ RAJAGOPALAN
DEPT. OF CHEMICAL ENGINEERING
UNIV. OF HOUSTON
HOUSTON, TX 77204-4792

BALA RAMASWAMY
DEPT. OF MECHANICAL ENG.
RICE UNIV.
P.O. BOX 1892
HOUSTON, TX 77251-1892

ENRIQUE RAME
DEPT. OF PHYSICS
CARNEGIE MELLON UNIV.
PITTSBURGH, PA 15213

GARY RANKIN
M/C EC2
NASA JOHNSON SPACE CENTER
2101 NASA ROAD 1
HOUSTON, TX 77058

NASSER RASHIDNIA
MS 500-102
NYMA, INC.
21000 BROOKPARK RD.
CLEVELAND, OH 44135

LONNIE REID
NYMA, INC.
2001 AEROSPACE PKWY.
BROOK PARK, OH 44142

THOMAS REINARTS
MAINSTREAM ENGINEERING CORP.
200 YELLOW PLACE
ROCKLEDGE, FL 32955

RICH REINKER
BALL AEROSPACE
10 LONGS PEAK DRIVE
BROOMFIELD, CO 80021

KAMIEL REZKALLAH
MECHANICAL ENGINEERING DEPT.
UNIV. OF SASKATCHEWAN
SASKATOON, SK S7N 0W0

JENNIFER RHATIGAN
MS 500-216
NASA-LEWIS
21000 BROOKPARK RD.
CLEVELAND, OH 44135

PERCY H. RHODES
BLDG. 4481; MS ES76
NASA MARSHALL SPACE FLIGHT CTR.
HUNTSVILLE, AL 35812

BOB RHOME
CODE UG
NASA HEADQUARTERS
WASHINGTON, DC 20546-0001

JUDITH ROBEY
CODE UGT
NASA HEADQUARTERS
WASHINGTON, DC 20546-0001

TERRI D. RODGERS
MS 500-102
NASA-LEWIS
21000 BROOKPARK RD.
CLEVELAND, OH 44135

MELISSA ROGERS
MS 500-216
TAL-CUT CO.
21000 BROOKPARK RD.
CLEVELAND, OH 44135

RICK ROGERS
MS 105-1
NASA-LEWIS
21000 BROOKPARK RD.
CLEVELAND, OH 44135

DENNIS W. ROHN
MS 110-3
NASA-LEWIS
21000 BROOKPARK RD.
CLEVELAND, OH 44135

PAUL RONNEY
DEPT. OF MECH.ENGINEERING OHE 430M
UNIV. OF SOUTHERN CALIFORNIA
LOS ANGELES, CA 90089-1453

GRAHAM ROSS
O/92-05, B/260
LOCKHEED MISSILES & SPACE CO.
3251 HANOVER ST.
PALO ALTO, CA 94304-1187

PAUL ROTHE
CREARE, INC.
P.O. BOX 71
HANOVER, NH 03755

SATWINDAR SADHAL
MECHANICAL ENG. DEPT (OHE 430)
UNIV. OF SOUTHERN CALIFORNIA
LOS ANGELES, CA 90089-1453

JACK SALZMAN
MS 500-205
NASA-LEWIS
21000 BROOKPARK RD.
CLEVELAND, OH 44135

DUDLEY SAVILLE
DEPT. OF CHEMICAL ENGINEERING
PRINCETON UNIV.
PRINCETON, NJ 08544

MICHAEL SCHATZ
DEPT. OF PHYSICS
UNIV. OF TEXAS
AUSTIN, TX 78712

DEAN S. SCHRAGE
ADF, INC.
2001 AEROSPACE PKWY.
BROOK PARK, OH 44142

DONALD SCHULTZ
MS 500-203
NASA-LEWIS
21000 BROOKPARK RD.
CLEVELAND, OH 44135

LOU SEILER
HARRIS AEROSPACE SYSTEMS DIVISION
P.O. BOX 94000
MELBOURNE, FL 32902

ROBERT SEKERKA
DEPT. OF PHYSICS
CARNEGIE MELLON UNIV.
6319 WEH
PITTSBURG, PA 15213

GREGORY W. SELLMEYER
ANALEX CORPORATION
3001 AEROSPACE PKWY.
BROOK PARK, OH 44142

NANCY SHAW
MS 500-102
NASA-LEWIS
21000 BROOKPARK RD.
CLEVELAND, OH 44135

PETER SHIRRON
NASA GODDARD SPACE FLIGHT CENTER
GREENBELT, MD 20771

JOHN SIAMIDIS
ANALEX CORP.
3001 AEROSPACE PKWY.
BROOK PARK, OH 44142

KARL SILL
FLUID PHYSICS
DORNIER GMBH
FRIEDRICHSHAFEN, D
88039 GERMANY

BHIM S. SINGH
MS 500-102
NASA-LEWIS
21000 BROOKPARK RD.
CLEVELAND, OH 44135

SUMON K. SINHA
MECHANICAL ENGINEERING DEPT.
UNIV. OF MISSISSIPPI
201-C CARRIER HALL
UNIV., MS 32677

RAY SKARDA
MS 500-102
NASA-LEWIS
21000 BROOKPARK RD.
CLEVELAND, OH 44135

ANTHONY SMART
1582 PARKWAY LOOP, SUITE B
TUSTIN, CA 92680-6505

MARC SMITH
SCHOOL OF MECH. ENG.
GEORGIA INSTITUTE OF TECHNOLOGY
ATLANTA, GA 30332-0405

ROBERT SNYDER
MAIL CODE ES71
NASA MARSHALL SPACE FLIGHT CTR.
HUNTSVILLE, AL 35812

STEPHEN SPIEGELBERG
HARVARD UNIV.
29 OXFORD ST.
CAMBRIDGE, MA 02138

DAVID SQUARER
1193 BEECHWOOD BLVD.
PITTSBURGH, PA 15206

TOM ST. ONGE
MS 500-205
NASA-LEWIS
21000 BROOKPARK RD.
CLEVELAND, OH 44135

PAUL STEEN
CHEMICAL ENGINEERING
CORNELL UNIV.
OLIN HALL
ITHACA, NY 14853

R. SHANKAR SUBRAMANIAN
DEPT. OF CHEMICAL ENGINEEERING
CLARKSON UNIV.
BOX 5705
POTSDAM, NY 13699-5705

KWANG I. SUH
DEPT. OF ELECTRICAL ENGINEERING
SUNY-STONY BROOK
STONY BROOK, NY 11794

THOMAS J. SUTLIFF
MS 500-216
NASA-LEWIS
21000 BROOKPARK RD.
CLEVELAND, OH 44135

SUZANNE SWICKARD
MS 500-102
NASA-LEWIS
21000 BROOKPARK RD.
CLEVELAND, OH 44135

JOHN B. SWIFT
CENTER FOR NONLINEAR DYNAMICS
UNIV. OF TEXAS AT AUSTIN
AUSTIN, TX 78712

ANDREW J. SZANISZLO
MS 500-202
NASA-LEWIS
21000 BROOKPARK RD.
CLEVELAND, OH 44135

RANDALL TAGG
PHYSICS DEPT.
UNIV. OF COLORADO AT DENVER
P.O. BOX 173364
DENVER, CO 80217-3364

SALEH TANVEER
DEPT. OF MATHEMATICS
OHIO STATE UNIV.
231 WEST 18TH AVE.
COLUMBUS, OH 43210-1174

SARATH TENNAKOON
PHYSICS DEPT.
OHIO STATE UNIV.
174 WEST 18TH AVE.
COLUMBUS, OH 43210

ARNOLD THARRINGTON
UNIV. OF PITTSBURGH
100 ALLEN HILL
PITTSBURGH, PA 15260

JOHN THOMAS
MS 500-322
NASA-LEWIS
21000 BROOKPARK RD.
CLEVELAND, OH 44135

ROBERT V. THOMPSON, JR.
E1425C ENGINEERING
UNIV. OF MISSOURI/COLUMBIA
COLUMBIA, MO 65211

PADETHA TIN
MS 105-1
NASA-LEWIS
21000 BROOKPARK RD.
CLEVELAND, OH 44135

AUGUST TISCHER
DEPT. OF CHEMICAL ENGINEERING
UNIV. OF TOLEDO
TOLEDO, OH 43606

LE TRAN
NYMA, INC.
2001 AEROSPACE PKWY.
BROOK PARK, OH 44142

EUGENE H. TRINH
MS 183-401
JPL/CALTECH
4800 OAK GROVE DRIVE
PASADENA, CA 91109

JAMES D. TROLINGER
METROLASER
18006 SKYPARK CIRCLE #108
TRUINE, CA 92714

PETER TSCHEN
NYMA, INC.
2001 AEROSPACE PKWY.
BROOK PARK, OH 44142

SANDRA VALENTI
MS 501-4
NASA-LEWIS
21000 BROOKPARK RD.
CLEVELAND, OH 44135

M. VEDHA-NAYAGAM
ANALEX CORPORATION
3001 AEROSPACE PKWY.
BROOK PARK, OH 44142

JORGE VINALS
SCRI
FLORIDA STATE UNIV.
TALLAHASSEE, FL 32306-4052

DEEPAK VOHRA
DEPT. OF MECHANICAL
SOUTHERN ILLINOIS
CARBONDALE, IL 62901

DMITRY VOMPE
OHIO STATE UNIV.
111 W. HUDSON ST. #1E
COLUMBUS, OH 43202

MICHAEL WALLER
CLEVELAND TELECOMMUNICATIONS CORP.
5351 NAIMAN PARKWAY
SOLON, OH 44139

H.U. WALTER
ESA
8-10 RUE MARIO NIKIS
PARIS, 75015 FRANCE

C.H. WANG
UNIV. OF NEBRASKA-LINCOLN
632 HAMILTON HALL
LINCOLN, NE 68588

PETER WAYNER, JR.
DEPT. OF CHEMICAL ENGINEERING
RENSSELAER POLYTECHNIC INSTITUTE
TROY, NY 12180-3590

KAREN J. WEILAND
MS 110-3
NASA-LEWIS
21000 BROOKPARK RD.
CLEVELAND, OH 44135

MARK WEISLOGEL
MS 500-102
NASA-LEWIS
21000 BROOKPARK RD.
CLEVELAND, OH 44135

DAVID WEITZ
EXXON RESEARCH AND ENGINEERING CO.
ROUTE 22 EAST, CLINTON TOWNSHIP
ANNANDALE, NJ 08801

HARVEY J. WILLENBERG
M.S. JW-21
BOEING DEFENSE AND SPACE GROUP
P.O. BOX 240002
HUNTSVILLE, AL 35824-6402

WILLIAM K. WITHEROW
ES76 SSL BUILDING 4481
NASA MARSHALL SPACE FLIGHT CTR.
HUNTSVILLE, AL 35812

ROBERT WITT
147 ERB
UNIV. OF WISCONSIN-MADISON
1500 JOHNSON DRIVE
MADISON, WI 53706

MICHA WOLFSHTEIN
AEROSPACE ENG.
TECHNION
TECHNION CITY
HAIFA, 32000 ISRAEL

GARY WORKMAN
RI A-6
UNIV. OF ALABAMA/HUNTSVILLE
HUNTSVILLE, AL 35899

M. GRAE WORSTER
DEPT. OF APPLIED MATH.
CAMBRIDGE UNIV.
SILVER STREET
CAMBRIDGE, CB3 9EW ENGLAND

XIAO-LUN WU
DEPT. OF PHYSICS AND ASTRONOMY
UNIV. OF PITTSBURGH
PITTSBURGH, PA 15260

GERALD YOUNG
DEPT. OF MATHEMATICAL SCIENCES
UNIV. OF AKRON
AKRON, OH 44325-4002

BERNARD ZAPPOLI
CNES/DP/SC
18 AVENUE EDOUARD BELIN
TOULOUSE, 31055 FRANCE

ABDEL ZEBIB
MECHANICAL AND AEROSPACE
RUTGERS UNIV.
PISCATAWAY, NJ 08855-0909

HAO ZHANG
CASE WESTERN RESERVE UNIV.
10900 EUCLID AVENUE
CLEVELAND, OH 44106

GREG ZIMMERLI
NYMA, INC.
2001 AEROSPACE PKWY.
BROOK PARK, OH 44142

ROBERT L. ZURAWSKI
MS 86-15
NASA-LEWIS
21000 BROOKPARK RD.
CLEVELAND, OH 44135

AUTHOR INDEX

473

REPORT DOCUMENTATION PAGE

1. AGENCY USE ONLY (Leave blank)	2. REPORT DATE	3. REPORT TYPE AND DATES COVERED
	August 1994	Conference Publication

4. TITLE AND SUBTITLE

Second Microgravity Fluid Physics Conference

6. AUTHOR(S)

5. FUNDING NUMBERS

WU–962–24–00

7. PERFORMING ORGANIZATION NAME(S) AND ADDRESS(ES)

National Aeronautics and Space Administration
Lewis Research Center
Cleveland, Ohio 44135–3191

8. PERFORMING ORGANIZATION REPORT NUMBER

E–9046

9. SPONSORING/MONITORING AGENCY NAME(S) AND ADDRESS(ES)

National Aeronautics and Space Administration
Washington, D.C. 20546–0001

10. SPONSORING/MONITORING AGENCY REPORT NUMBER

NASA CP–3276

11. SUPPLEMENTARY NOTES

Responsible person, Bhim S. Singh, organization code 6712, Lewis Research Center, (216) 433–5396.

12a. DISTRIBUTION/AVAILABILITY STATEMENT

Unclassified - Unlimited
Subject Category 34

12b. DISTRIBUTION CODE

13. ABSTRACT (Maximum 200 words)

The conference's purpose was to inform the fluid physics community of research opportunities in reduced-gravity fluid physics, present the status of the existing and planned reduced gravity fluid physics research programs, and inform participants of the upcoming NASA Research Announcement in this area. The plenary sessions provided an overview of the Microgravity Fluid Physics Program, present and future areas of emphasis, information on NASA's ground-based and space-based flight research facilities, and the process by which future investigators enter the program. An international forum offered participants an opportunity to hear from French, German, and Russian speakers about the microgravity research programs in their respective countries. Two keynote speakers provided broad technical overviews on multiphase flow and complex fluids research. An interactive discussion session, with the Fluid Dynamics Discipline Working Group serving as the panel, answered questions from the audience. One keynote paper and selected plenary presentations of general interest are included in the proceedings. Sixty-two technical papers were presented in 21 sessions. Presenters briefed their peers on the scientific results of their ground-based and flight research. Fifty-eight of the papers are included here.

14. SUBJECT TERMS

Fluid dynamics; Fluid mechanics; Microgravity; Reduced gravity; Heat transfer; Multiphase flow; Complex fluids

15. NUMBER OF PAGES

488

16. PRICE CODE

A21

17. SECURITY CLASSIFICATION OF REPORT	18. SECURITY CLASSIFICATION OF THIS PAGE	19. SECURITY CLASSIFICATION OF ABSTRACT	20. LIMITATION OF ABSTRACT
Unclassified	Unclassified	Unclassified	